University of Nottingham
UK | CHINA | MALAYSIA

Investigating the role of eIF4A2 in the spatial regulation of metabolic adaptation to hypoxia in colorectal cancer

Submitted by:

Luke Thornton, MSci (Hons)

School of Medicine

Translational Medical Sciences

Thesis submitted to The University of Nottingham for the degree of Doctor of Philosophy

Abstract

Colorectal cancer is the third most common cancer worldwide and ranks second for cancer-related mortality. Hypoxia (< 1% pO_2) is found in up to 50% of colorectal tumours and is associated with poor patient prognosis, increased metastatic potential and resistance to therapy. Hypoxia stabilises the hypoxia-inducible factors, HIF-1α and HIF-2α, to alter the transcriptome to drive molecular adaptation to hypoxic stress. Hypoxia also leads to changes in the translation machinery to alter protein synthesis. The changes introduced by these mechanisms contribute to the major hallmarks of cancer including metabolic reprogramming. However, how the oxygen gradient in tumours contributes to spatially defined metabolic adaptations and how this leads to therapeutic failure is unknown. Preliminary data hypothesised that the translation initiation factor eIF4A2 is a modulator of hypoxic adaptation and regulates colorectal cancer cell survival through the regulation of metabolic mRNA translation. Here, the eIF4A2 interaction landscape was investigated and revealed hypoxic interactions with other regulators of mRNA translation including eIF4G3, eIF4E1 and CNOT7. eIF4A2 knockout was shown to reduce spheroid growth and led to an increase in HIF-2α expression. Furthermore, the expression of several predicted eIF4A2 target genes involved in amino acid biosynthesis and endocytosis were investigated. eIF4A2 knockout led to a reduction in the expression of the endocytosis regulator EHD1 and EHD1 knockdown reduced cancer cell survival. This work suggests eIF4A2 regulates the hypoxic translation of specific mRNAs, such as EHD1, through altered protein:protein interactions to regulate colorectal cancer cell survival. Moreover, a novel secondary ion mass spectrometry imaging technique for spatially resolving metabolite changes across the oxygen gradient within 3-D spheroid models and colorectal cancer xenografts is revealed. We pioneer high-pressure frozen orbiSIMS to simultaneously measure metabolites *in situ* across differentially oxygenated regions of tumours and colorectal cancer spheroid models. Correlation with RNA-sequencing helps predict the transcriptional changes behind this spatial metabolic adaptation and could be used to identify novel therapeutic targets important for tackling therapeutic resistance driven by hypoxia-induced metabolic reprogramming.

Acknowledgements

Firstly, I would like to thank my two supervisors Dr Kenton Arkill and Dr Alan Mcintyre for their support and mentorship and for challenging me to become a better scientist every day.

Secondly, I would like to thank the Biotechnology and Biological Sciences Research Council for funding my project over the last four years and the Nottingham BBSRC DTP team for their support and guidance.

I would also like to thank Julie Watts for sharing her expertise and advice when helping with my orbiSIMS work as well as Prof Anna Grabowska and Catherine Probert in the EVPC group for their help and support with the *in vivo* and IHC work.

I would like to give a special mention to both Pam Collier and Vicky Norris for going above and beyond in their support, both of me and my work.

I would also like to thank all the current and former lab members who have provided endless hours of friendship, support, tears and laughter over the last four years. Especially, Eric Vancauwenberghe, I could not have done this without you as well as Tammy, Charlie, Ashia, Amna, Rinad, Shaikha, Zubair, Claire, Lorna, Hannah, Leo and many more (you know who you are).

A special thank you also to my mum and dad, your unwavering love and support have made me into the person I am today. To my sister, whom I am so proud of for everything you have achieved, thank you for always being there for me.

Finally, a very special mention to my incredible wife Kayleigh, I could not have done any of this without you being there every single day. For all the late night and weekend working, counselling and always being there to pick me up when I'm down. I am forever grateful.

COVID impact statement

The work submitted in this thesis has been significantly impacted by the COVID-19 pandemic. The PhD project began in April 2019, however, in March 2020 the research laboratories were closed for 5 months until August 2020 during the national lockdown. Unfortunately, upon being allowed to return to work, I took ill on two separate occasions, severely impacting my ability to work for another 2 months. In addition, a significant amount of research time was lost due to the variety of logistical issues that arose from the pandemic, including laboratory capacity restrictions, restricted working areas to maintain social distancing and continued reagent supply problems. While all efforts were made to mitigate the lost research time, this was not always possible due to the practical nature of the research. This work has been completed with an additional two-month extension to try and overcome some of the above-mentioned problems. However, this thesis represents work completed with a loss of approximately 7 months.

Table of contents

List of abbreviations

Abbreviation	Definition
ABC	ATP-binding cassette
ACSS2	Acetyl-CoA synthetase
ACYL	ATP citrate lyase
ALDH18A1	Aldehyde dehydrogenase 18 family member A1
ALDOA/C	Aldolase A/C
ALT	Alternative lengthening of telomeres
AMPK	AMP-activated protein kinase
ARNT	Aryl hydrocarbon receptor nuclear translocator
ASS1	Arginosuccinate synthetase 1
ATC	Adoptive T-cell
ATM	Ataxia telangiectasia mutated
ATR	Ataxia telangiectasia and Rad3-related
A3SS	Alternative 3' splice site
A5SS	Alternative 5' splice site
BCAA	Branched-chain amino acids
BCAT1/2	Branched-chain aminotransferase 1/2
bHLH	basic helix-loop-helix domain
CA9	Carbonic anhydrase 9
CAR	Chimeric antigen receptor
CBS	Cystathionine-b-synthase
CCL2	Chemokine (C-C motif) ligand 2
CDK	Cyclin-dependent kinase
CIMP	CpG island methylator phenotype
CIMP+	CIMP-positive
CIN	Chromosomal instability
CML	Chronic myeloid leukemia
CpG	Cytosine-guanine dinucleotide
CPT1A	Carnitine palmitoyltransferase 1
CRC	Colorectal cancer
CSF1	Colony stimulating factor-1
C-TAD	C-terminal transactivation domain
CTH	Cystathionine-ɣ-lyase
CTLs	Cytotoxic T lymphocytes
CTLA4	Cytotoxic T lymphocyte antigen 4
Cul2	Cullin-2
CYP2D6	Cytochrome P450 family 2 subfamily D polypeptide 6
DAG	Diacylglycerol
DESI	Desorption electrospray ionisation

DHAP	Dihydroxyacetone phosphate
DMAPP	Dimethylallyl pyrophosphate
ECM	Extracellular matrix
eEF	Eukaryotic translation elongation factor
EGF	Epidermal growth factor
EGFR	Epidermal growth factor receptor
EGTA	Ethylene glycol tetraacetic acid
eIF	Eukaryotic translation initiation factor
4E-BP	eIF4E binding protein
EMT	Epithelial-mesenchymal transition
ENO1/2	Enolase 1/2
eRF	Eukaryotic translation release factor
ESI	Electrospray ionisation
FABP	Fatty acid binding protein
FAP	Familial adenomatous polyposis
FASN	Fatty acid synthase
FGF1/2	Fibroblast growth factor 1/2
FIH-1	Factor inhibiting HIF-1
F-2,6-BP	Fructose-2,6-bisphosphate
F-6-P	Fructose-6-phosphate
GAPDH	Glyceraldehyde-3-phosphate dehydrogenase
GCIB	Gas cluster ion beam
GC-MS	Gas chromatography mass spectrometry
GCN2	General control non-depressible 2
GDH	Glutamate dehydrogenase
GEF	Guanine nucleotide exchange factor
GF	Growth factor
GLS1	Glutaminase
GPT2	Glutamate pyruvate transaminase 2
GSH	Glutathione
G-3-P	Glycerol-3-phosphate
G-6-P	Glucose-6-phosphate
G6PD	Glucose-6-phosphate dehydrogenase
HAF	Hypoxia-associated factor
HDAC	Histone deacetylase
HER2	Human epidermal growth factor receptor 2
HIF	Hypoxia-inducible factor
HK	Hexokinase
HMG-CoA	3-hydroxy-3-methylglutaryl-CoA
HNPCC	Hereditary non-polyposis colon cancer
HRE	Hypoxia-response element
HRI	Heme-regulated eIF2α kinase

IAP-2	Inhibitor of apoptosis protein 2
IDH1	Isocitrate dehydrogenase 1
IL-10	Interleukin-10
IPP	Isopentenyl pyrophosphate
α-KG	α-ketoglutarate
LAT	L-type amino acid transporters
LC-MS	Liquid chromatography mass spectrometry
LDH-A	Lactate dehydrogenase
LMIG	Liquid metal ion gun
LOH	Loss of heterozygosity
LRP1	LDLR-related protein 1
MAB	Monoclonal antibody
MALDI	Matrix-assisted laser desorption ionisation
MAP	MYH-associated polyposis
MAPK	Mitogen-activated protein kinase
M/LCAD	Medium/long chain acyl-CoA dehydrogenase
mCRC	Metastatic colorectal cancer
MDM2	Mouse double minute 2 homolog
MDR-1	Multi-drug resistance 1
MDSCs	Myeloid-derived suppressor cells
MHC-1	Major histocompatibility complex 1
MLH1	MutL homolog 1
MMR	Mismatch repair
MSI	Microsatellite instability
MSI-H	MSI-high
MSI-L	MSI-low
MSH2	MutS homolog 2
MSH6	MutS homolog 6
MSS	Microsatellite stable
MTHFD2/1L	Methylene THF dehydrogenase 2/1-like
mTOR	Mammalian target of rapamycin
mTORC1	mTOR complex 1
mTORC2	mTOR complex 2
MXE	Mutually exclusive exon
m7G	7-methylguanosine
NADH	Nicotinamide adenine dinucleotide
NADPH	Nicotinamide adenine dinucleotide phosphate
N-TAD	N-terminal transactivation domain
ODDD	Oxygen-dependent degradation domain
OER	Oxygen enhancement ratio
OXPHOS	Oxidative phosphorylation
PABP	Poly-A binding protein

PAS	Per-ARNT-Sim domain
PDGF	Platelet-derived growth factor
PDH	Pyruvate dehydrogenase
PDK1	Pyruvate dehydrogenase kinase 1
PD1	Programmed cell death 1
PDX	Patient-derived xenograft
PERK	PKR-like ER kinase
PFK	Phosphofructokinase
PFKFB	6-phosphofructo-2-kinase/fructose-2,6-bisphosphatase
PGC-1α	Proliferator-activated receptor γ coactivator-1α
PGD	6-phosphogluconate dehydrogenase
PGK1	Phosphoglycerate kinase 1
P-gp	P-glycoprotein
PHGDH	Phosphoglycerate dehydrogenase
PIC	Pre-initiation complex
PI3K	Phosphoinositide-3-kinase
PKM2	Pyruvate kinase 2
PKR	Double-stranded RNA-dependent protein kinase
PMS2	Post-meiotic segregation increased 2
PPARγ	Peroxisome proliferator-activated receptor γ
PPP	Pentose phosphate pathway
PRODH2	Proline dehydrogenase 2
PSAT1	Phosphoserine transaminase 1
PSPH	Phosphoserine phosphatase
PYCR1	Pyrroline-5-carboxylate reductase 1
RB	Retinoblastoma
RBM4	RNA binding motif protein 4
RBP	RNA-binding protein
REDD1	Regulated in development and DNA damage 1
rHRE	RNA hypoxia response element
RI	Retained intron
RIP-Seq	RNA immunoprecipitation sequencing
ROS	Reactive oxygen species
RSV	Rous sarcoma virus
RTK	Receptor tyrosine kinase
SE	Skipped exon
SHMT2	Serine hydroxymethyl transferase 2
SIMS	Secondary ion mass spectrometry
SSP	Serine synthesis pathway
S6K	Ribosomal S6 kinase
TAG	Triacylglycerol
TAM	Tumour-associated macrophages

TC	Ternary complex
TGFα	Transforming growth factor α
TGFβ	Transforming growth factor β
THF	Tetrahydrofolate
TIC	Total ion count
TILs	Tumour-infiltrating lymphocytes
TNFα	Tumour necrosis factor α
ToF	Time-of-flight
Tregs	Regulatory T cells
TSC2	Tuberous sclerosis complex 2
TSG	Tumour suppressor gene
UPS	Ubiquitin-proteasome system
VEGF	Vascular endothelial growth factor
VEGFR	Vascular endothelial growth factor receptor
VHL	von Hippel-Lindau protein
VLDLR	Very low density lipoprotein receptor
3-MST	3-mercaptopyruvate sulfurtransferase
3-PG	3-phosphoglycerate
5-FU	5-fluorouracil
5,10-MTHF	5,10-methylene tetrahydrofolate
6-MP	6-mercaptopurine

List of figures and tables

1. Introduction

1.1 Cancer

1.1.1 What is cancer?

Cancer is a term used to describe a large family of diseases characterised by the uncontrolled growth and proliferation of cells and metastatic spread to distant tissues. It is the leading cause of death worldwide[1]. The ability of cells to divide uncontrollably is due to failures in the mechanisms that normally regulate cell proliferation and growth. The malfunctioning of these homeostatic mechanisms leads to dysregulated cell division and tumour formation[2]. However, for a tumour to develop into malignant cancer it must also acquire the ability to invade surrounding tissues and migrate or metastasise, throughout the body. Metastasis is estimated to be responsible for 90% of all cancer deaths due to tissue damage at the sites of secondary tumour formation alongside a current lack of understanding regarding the treatment of metastatic cancer[3].

1.1.2 Cancer statistics

In 2018, there were an estimated 18.1 million new cancer diagnoses and approximately 9.6 million cancer-associated deaths worldwide, making cancer the most significant disease impacting human life around the world[1]. Cancer incidence rates, described as the average risk of developing cancer, as well as mortality rates are increasing on a global scale due to a complex network of risk factors including a growing yet ageing population alongside rapid developments in socioeconomic status[1,4].

As of 2018, lung cancer remains both the most commonly diagnosed (11.6% of all cases) and leading cause of death (18.4%) worldwide in both males and females. Female breast cancer (11.6%), prostate cancer (7.1%) and colorectal cancer (6.1%) have the next highest incidence rates globally whereas colorectal cancer (9.2%), stomach cancer (8.2%) and liver cancer (8.2%) have the next highest rates of mortality. In the UK, there are over 360,000 new cases of cancer each year with the most commonly diagnosed cancers being breast, prostate, bowel and lung cancer (Cancer Research UK, 2018). However, several other cancer types including liver, thyroid, stomach and kidney are showing rapid increases in incidence. Mortality trends are similar to the global statistics with lung accounting for the majority of cancer-associated deaths followed by bowel, breast and

prostate cancers. The trends in incidence and mortality rates throughout the UK are associated with similar risk factors used to determine global statistical trends such as age, gender, ethnicity and economic background (Cancer Research UK, 2018).

1.1.3 Multistep tumourigenesis

Evidence suggests that cancer development and progression is a highly complex, multi-step process involving the acquisition of numerous genetic and epigenetic alterations. This includes genetic mutations, amplifications, chromosomal rearrangements, aneuploidy, and epigenetic modifications, which drive the progressive transformation of normal cells into malignant cells[5]. Malignancy is therefore acquired gradually through combinations of these mutations affecting two main types of genes: proto-oncogenes and tumour suppressor genes (TSGs)[6–8].

Proto-oncogenes

Oncogenes were first discovered during experiments with the type-C retrovirus Rous sarcoma virus (RSV) because of its ability to transform infected cells and induce cancer[9]. The term proto-oncogene is therefore used to describe normal cellular genes that, when activated to oncogenes, have the ability to cause cancer[10]. Many proto-oncogenes have now been identified that encode proteins which are responsible for regulating cell division, growth and apoptosis under normal conditions but when mutated, can contribute to tumour growth through the dysregulation of cell proliferation and division[11]. It is also known that oncogenes act in a dominant manner such that a mutation in one allele of the proto-oncogene is sufficient for oncogenic activation[12].

Point mutations involving the substitution, insertion or deletion of a single nucleotide are common genetic alterations leading to oncogene activation[13]. The most well-documented point mutations occur in the *RAS* and *BRAF* proto-oncogenes. The Ras family of small GTPase proteins, including H-ras, K-ras and N-ras, represent the upstream components of the RAS/RAF/MAPK signalling cascade and point mutations in the *RAS* gene are one of the most common triggers in a large number of cancers[14]. Mutated *RAS* genes encode constitutively active oncoproteins that can transduce signals for uncontrolled cell proliferation through a variety of interconnected signal transduction pathways[15]. *KRAS* mutations are commonly seen in cancers of the pancreas, lung and colon whereas *HRAS* mutations are most frequent in head and neck and dermatological cancers and *NRAS* is

associated with haematological malignancies[16]. In particular, *KRAS* mutations are found in 90% of all pancreatic adenocarcinomas and around 40% of all colorectal cancer cases[15].

As well as point mutations, proto-oncogenes can be activated by larger chromosomal alterations such as gene amplifications and chromosomal translocations. Increased copy number, or amplification, of a specific chromosomal region containing a proto-oncogene leads to overexpression of the amplified gene and cellular transformation[17]. DNA double-strand breaks are believed to be responsible for initiating the amplification process which most likely occurs due to defects in DNA replication or telomere dysfunction[18,19]. One of the most well-studied amplifications is that of the *MYC* oncogene which is amplified in many types of cancer. The *MYC* family of genes (*MYCC, MYCL* and *MYCN)* code for transcription factors important in the activation of many pro-proliferative genes and are involved in DNA replication[20]. Amplification of *MYCN* is reported to occur in approximately 20% of all neuroblastoma cases along with other neuronal tumours and is associated with a poor patient prognosis and advanced tumour stage[21].

Tumour-suppressor genes

The activation of proto-oncogenes alone is rarely enough to trigger the transformation of cells[22]. In contrast to oncogenic activation, the loss of certain genes, TSGs, can also contribute to neoplastic transformation. TSGs often carry out physiological roles designed to prevent tumour formation such as DNA repair, inhibition of cell division and the induction of apoptosis[23]. The first TSG was identified during studies on retinoblastoma (RB) which indicated that the inheritance of a single copy of the mutated *RB* gene alone was insufficient to transform retinal cells into tumour cells[22]. This led to the development of Knudson's two-hit hypothesis, suggesting that retinoblastoma was caused by two mutations, one of which is inherited through the germ line. Heterozygous individuals carrying the *RB* mutation do not develop tumours until a second, somatic mutation occurs leading to loss of heterozygosity (LOH) through alteration of both functional copies of the TSG *RB* present on homologous chromosomes[22]. It is now well established that all TSGs function in a recessive manner and require the inactivation of both alleles in order to become tumourigenic[22,24].

The RB protein, pRb plays a key role in the regulation of the G1-S phase checkpoint of the cell cycle through interactions with the E2F family of transcription factors preventing their activation of pro-proliferative genes[25]. Phosphorylation of pRb by cell cycle regulators such as cyclin-dependent kinases (CDKs) in response to growth signals releases E2F and triggers cell cycle progression[26]. Therefore, loss of functional pRb leads to unregulated cell cycle control and explains its function as a canonical TSG.

Loss of the TSG *TP53* encoding the p53 protein is estimated to play a role in around 50% of all human cancers and is the most frequently mutated gene in human malignancies[27]. Wild-type p53 is a key regulator of cell cycle progression and apoptosis. In response to DNA damage or cellular stress, p53 is post-translationally modified by numerous kinases involved in sensing DNA damage such as ataxia telangiectasia mutated (ATM) and ataxia telangiectasia and Rad3-related (ATR)[28]. These modifications prevent p53 binding to its negative regulator MDM2 which normally targets p53 for proteasomal degradation[29]. Stabilised p53 is then able to activate the expression of a large number of target genes involved in the inhibition of cell cycle progression at G1, allowing the DNA repair machinery to repair DNA damage prior to progressing through the cell cycle or, if unsuccessful, triggers cell death[29].

1.1.4 Hallmarks of cancer

The accumulation of advantageous genetic changes provides cells with distinct biological capabilities allowing them to overcome the physiological barriers to tumour formation and these abilities have been coined with the term the "Hallmarks of Cancer" (figure 1.1)[2].

Originally, six hallmarks were identified: sustained proliferative signalling, evasion of anti-growth signals, resistance to apoptosis, maintained angiogenesis, replicative immortality and the ability to invade and metastasise[2]. More recently, additional hallmarks such as evasion of the immune response and reprogramming metabolism and cellular bioenergetics have also been included[30]. Underpinning the hallmarks are the principles of genetic instability and inflammation as well as the influence of tumour-associated cells within the tumour microenvironment[31,32].

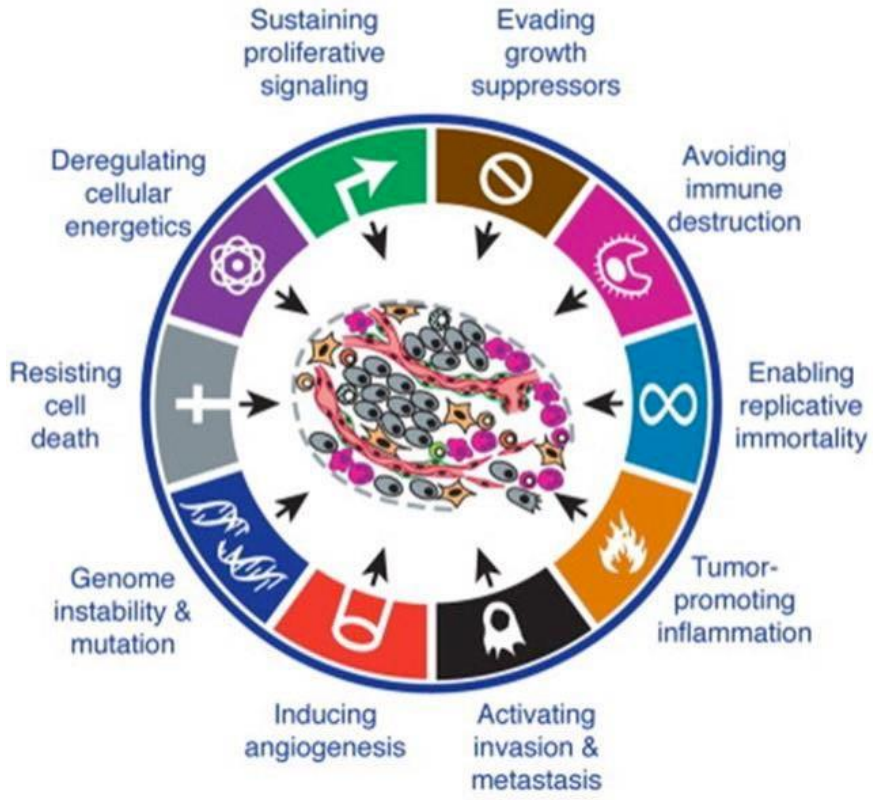

Figure 1.1 The hallmarks of cancer. Adapted by permission from Elsevier, Cell, 'Hallmarks of Cancer: The Next Generation', Hanahan & Weinberg, 2011.

Sustained proliferative signalling

The most fundamental trait of cancer cells is their ability to sustain cellular proliferation. Normal cells have strict mechanisms in place to regulate the production of growth signals and control entry and progression through the cell cycle. The ability of cancer cells to dysregulate these homeostatic mechanisms allows them to proliferate and expand uncontrollably[2]. Growth-promoting signals are usually relayed to cells through growth factor (GF) binding to cell surface receptor tyrosine kinases (RTKs) and activation of downstream signalling cascades[33]. Cancer cells can promote autocrine signalling loops by synthesising GFs themselves and expressing the appropriate receptor[34]. Glioblastomas and breast cancers are able to synthesise platelet-derived growth factor (PDGF) and transforming growth factor-α (TGFα) respectively[35,36].

GF receptors are also commonly overexpressed or mutated in many cancers, allowing cancer cells to become hyperresponsive to normal levels of GF or produce a mutant ligand-independent receptor capable of constitutive activation. For example, human epidermal growth factor receptor 2 (HER2) and epidermal growth factor receptor (EGFR) are commonly overexpressed in breast and head and neck cancers respectively[37].

Similarly, a mutant form of the EGFR is produced in human brain tumours lacking the extracellular ligand binding domain and is autophosphorylated leading to constant activation[38]. Mutations affecting downstream signalling components can bypass the need for GF stimulation altogether. For example, 40% of all melanoma cases are known to contain activating mutations in the B-Raf protein resulting in constitutive activation of the MAPK signalling pathway[39]. The disruption of negative feedback mechanisms normally in place to prevent excessive growth signalling can also lead to increased cellular proliferation. Mutations in Ras proteins are seen in around 25% of all tumours and leads to activation of pro-proliferative signalling through inhibition of the intrinsic GTPase activity of Ras which normally functions as an inhibitor of downstream signalling[40].

Evasion of growth suppressors

Cancer cells must simultaneously adapt to overcoming the anti-growth signals that exist to prevent excess cell growth and division. Many of these anti-growth pathways are orchestrated by a network of TSGs that must be inactivated in order for cancer cells to escape their anti-proliferative signals[2]. Similar to pro-growth signals, anti-growth signals also function through cell surface receptors or receptors embedded in the extracellular matrix (ECM)[2].

Tumour cells can evade these anti-growth signals due to both genetic and epigenetic silencing of TSG functions. Most anti-growth signals converge on two key regulatory proteins, pRb and p53 that act as guardians of cell cycle progression and DNA damage. Therefore disruption of the components of these two pathways is common in a large variety of cancers[41]. For example, in many cancer types, downregulation or expression of inactive, mutated isoforms of the transforming growth factor β (TGF-β) receptors (e.g. TGFBR1 and TGFBR2) lead to loss of response to TGF-β signalling and subsequently pRb inactivation[42]. Likewise, components of the p53 pathway are also inactivated in cancers. For example, loss of the *p14*^{ARF} gene results in unrestricted mouse double minute 2 homolog (MDM2)-mediated ubiquitination and degradation of p53[43]. Loss of the *TP53* gene is the most common mutation seen in the vast majority of cancers and leads to drastic loss of cell cycle regulation[27].

Resistance to apoptosis

Apoptosis is a crucial mechanism responsible for orchestrating cell death in response to irreparable DNA damage or cellular stress which is often encountered by tumour cells due to the high levels of genetic instability, oncogenic stress and hypoxia[44]. Therefore, cancer cells must acquire the ability to avoid this cellular response by inhibiting the apoptotic pathways.

Cancer cells have evolved a variety of strategies for overcoming the activation of apoptosis in response to cellular stress. The most common mechanism is through loss of p53 function which normally responds to cellular stress by upregulating a number of pro-apoptotic genes including *BAX, PUMA, NOXA* and *APAF-1*[45–47]. However, cancer cells also commonly overexpress anti-apoptotic members of the Bcl-2 family. For example, translocation of the *BCL-2* gene leads to constitutive expression in B-cell lymphomas, whereas amplification of the *BCL-XL* and *MCL-1* genes have been identified in several cancers[48–50].

Replicative immortality

One major barrier to tumour growth is the limited number of replicative cycles that normal cells can undertake before entering a terminally differentiated, nonproliferative state called senescence[30]. This process can be driven by the natural shortening of chromosomes or by oncogenic stress and DNA damage[51]. Telomeres protect the ends of chromosomes from fusion or recognition as sites of DNA damage. During each replicative cycle approximately 50-100 bp of telomeric DNA are lost from the chromosomes due to the inability of DNA polymerase to fully replicate the 3' ends of chromosomal DNA[2]. Eventually, the shortened telomeres are no longer able to protect the chromosome ends and cells enter replicative senescence[52]. It is the acquired maintenance of these shortened telomeres that allow cancer cells to replicate indefinitely[53]. Telomerase is a ribonucleoprotein complex capable of synthesising new telomeric DNA repeats to reverse the loss of DNA from the 3' ends of chromosomes[54]. Telomerase activity is silent in normal cells but is upregulated in 80-90% of all cancers[55]. In addition a telomerase-independent mechanism of telomere maintenance, the alternative lengthening of telomeres (ALT), is activated in 10-15% of all tumours and represent a different mechanism to bypassing senescence[56].

Inducing angiogenesis

Growing tumours require a constant supply of oxygen and nutrients delivered by the surrounding vasculature to survive. However, as the tumour grows to a larger size the natural blood supply is insufficient to supply the cancer cells with enough oxygen and nutrients to continue expanding[2]. The sprouting of new blood vessels from existing vessels, or angiogenesis, can be transiently activated in certain physiological processes such as wound healing whereas it is almost always activated in growing tumour cells[57].

Angiogenesis is controlled by a strict balance between pro- and anti-angiogenic signalling factors. Tumour cells alter this balance to promote angiogenesis in a variety of ways including the production of pro-angiogenic factors, the recruitment of angiogenic factors present in the ECM and the hijacking of nearby host cells such as macrophages[58]. One major form of signalling involves soluble factors such as vascular endothelial growth factor (VEGF) and fibroblast growth factors (FGF1/2) binding to receptors on the surface of endothelial cells in existing blood vessels to trigger cell proliferation[59]. In the vast majority of cancers, *VEGF* expression is upregulated in response to elevated growth factor signalling or hypoxia through hypoxia-inducible factor (HIF) activation[60]. As well as inducing endothelial cell proliferation VEGF also induces remodelling of the ECM through the activation of proteases to improve the permeability of the ECM to cell migration[61]. Similarly, FGF is also overexpressed in many cancers and promotes ECM remodelling cell proliferation and migration[62].

Invasion and metastasis

Metastasis is a complex process involving a sequential series of events, resulting in the formation of distant secondary tumours, defined as the invasion-metastasis cascade (figure 1.2)[63]. Dysregulation of a multitude of signalling pathways is required to enable each stage of the cascade and modify the local tumour microenvironment to promote invasion and migration[64]. One key mechanism by which carcinoma cells achieve this is by hijacking a normal biological programme called the epithelial-mesenchymal transition (EMT) involved in embryonic morphogenesis and wound healing[65].

The EMT pathway leads to loss of cell-cell junctions and loss of cell polarity, allowing cells within epithelial layers to dissociate into individual cells with mesenchymal characteristics including enhanced invasiveness[65]. E-cadherin is the most abundant

adhesion protein and its expression is downregulated in the vast majority of epithelial cancers[66]. Loss of E-cadherin is now considered a major hallmark of invasion and metastasis.

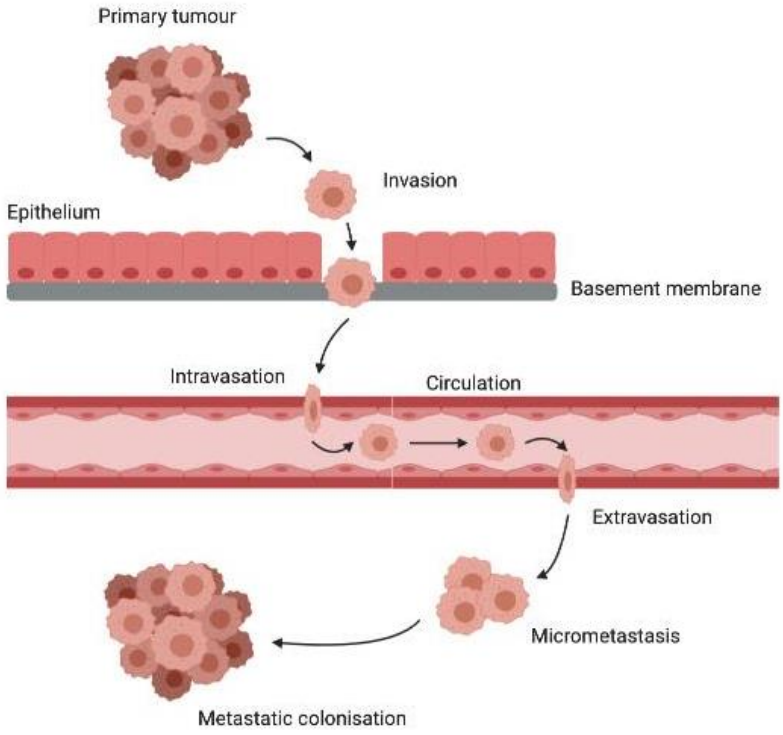

Figure 1.2 The invasion-metastasis cascade. Cancer cells acquire the ability to 1) invade into the extracellular matrix, 2) intravasate into nearby blood vessels, 3) survive in the circulation, 4) extravasate into distant tissue, 5) survive the foreign microenvironment to form a micrometastasis and 6) re-initiate their proliferative cycle to generate a macroscopic secondary tumour.

Immune evasion

Due to cross-talk between tumour cells and immune cells the ability of cancer cells to avoid destruction by the host immune response is now recognised as another hallmark of cancer[30]. The importance of immune evasion is evidenced by the elevated frequency of cancers seen in immunocompromised individuals[67]. One mechanism of immune suppression employed by cancer cells involves hijacking normal immune suppressive cells such as regulatory T cells (Tregs) and myeloid-derived suppressor cells (MDSCs) which are recruited to the tumour microenvironment via tumour-derived chemokines[68,69]. Additionally, tumour-derived TGF-β has been shown to stimulate the conversion of CD4+ T cells into Tregs *in situ*[70]. Many tumour cells also display defective antigen processing machinery affecting the function of the major histocompatibility complex 1 (MHC-1) pathway, leading to loss of tumour antigen recognition by cytotoxic T lymphocytes (CTLs)[71]. The production of immunosuppressive cytokines such as

interleukin-10 (IL-10), colony-stimulating factor 1 (CSF-1) and tumour necrosis factor α (TNFα) by both tumour cells and tumour-associated cells can also lead to inhibition of CTLs[72,73].

Reprogramming cellular metabolism

Rapidly proliferating cancer cells must adopt a metabolic program that fulfils the increased energy demand, biosynthetic requirements and redox balance needed to sustain cell growth[74]. Thus, the ability of cancer cells to alter the normal cellular metabolic machinery to enable growth in conditions such as hypoxia and acidosis is now also recognised as a key hallmark of cancer[30]. In aerobic conditions, normal cells generate energy via oxidative phosphorylation coupled with ATP synthesis in the mitochondria. Yet, even under aerobic conditions cancer cells display a preference for glycolytic energy production; a phenomenon known as the Warburg effect[75,76]. However, cancer cells must employ additional mechanisms to compensate for the 18-fold reduction in ATP production by glycolysis compared with mitochondrial respiration, predominantly through the upregulation of many genes involved in the glycolytic process (see section 1.5 for details)[77]. An additional advantage of the Warburg effect and elevated glycolysis is the production of intermediates for several biosynthetic pathways. For example, glucose-6-phosphate (G6P) can be diverted to the pentose phosphate pathway (PPP) and used to synthesise nucleotides and nicotinamide adenine dinucleotide phosphate (NADPH)[78,79]. Similarly, dihydroxyacetone phosphate (DHAP) can be used in lipid biosynthesis and organelle biogenesis essential for maintaining tumour growth and division[78,79]. In addition to glycolysis, cancer cells also utilise various other metabolic pathways including glutaminolysis, lipid metabolism and amino acid metabolism to regulate energy production (see section 1.5 for details).

Genomic instability and mutation

The progressive acquisition of the hallmarks of cancer depends on the accumulation of genomic instability and subsequent genetic damage over time[30]. Advantageous mutations allow subpopulations of cancer cells within a tumour to expand and outgrow other subpopulations. Therefore, multistep tumourigenesis can be defined as a series of clonal expansions where each cell division is triggered by genetic diversification and clonal selection of an advantageous genotype[80]. The major source of genomic instability in human cancers is chromosomal instability (CIN) however, there are numerous other

forms including microsatellite instability (MSI) and instability associated with an increased frequency of point mutations[81,82].

In most hereditary cancers genomic instability, primarily CIN and MSI, is directly linked to mutations in DNA repair genes. For example, germline mutations in the DNA base excision repair gene *MYH* are linked with *MYH*-associated polyposis and predispose individuals to colorectal cancer[83]. The "mutator hypothesis" states that genomic instability is present in precancerous lesions and that cancers develop by increasing the rate of spontaneous mutations[84]. However, genomic instability in sporadic cancers arises due to oncogene-induced DNA replication failure and subsequent DNA damage[85]. DNA double-strand breaks lead to activation of the DNA damage checkpoint machinery, such as p53[86]. Eventually, tumour suppressor gene loci will be targeted by this pathway to release cancer cells from the tumour-suppressive effects of the DNA damage repair pathways[86]. This model has been proposed to explain the frequent loss of common TSGs such as p53 and ATM seen within the vast majority of cancers and how this then contributes to genomic instability[87].

Inflammation

Tumours are commonly infiltrated by vast numbers of cells from the immune system and so inflammation, and the inflammatory response are now recognised as a tumour-promoting characteristic[88,89]. An inflammatory microenvironment is an essential component of all tumours and it is estimated that 15-20% of all cancer-related deaths are caused by underlying infection and chronic inflammation[88,90]. Inflammation can initiate tumour formation by inducing DNA damage and CIN, promote tumour development by increasing proliferation and resistance to apoptosis and increase invasive and metastatic potential by inducing angiogenesis and ECM remodelling[91].

During chronic inflammation, numerous intracellular signalling pathways are activated including the PI3K/Akt and MAPK pathways[92,93]. This stimulates the production of pro-inflammatory cytokines and chemokines and attracts immune cells to the tumour microenvironment[93]. Tumour-associated macrophages (TAMs) are one of the most abundant immune cells recruited to the tumour microenvironment by chemokines such as chemokine (C-C motif) ligand 2 (CCL2) and CSF-1[94,95]. TAMs promote tumourigenesis in a variety of ways by inducing angiogenesis and remodelling the

ECM[96,97]. TAMs also directly promote cell proliferation and migration through the secretion of GFs such as epidermal growth factor (EGF) and VEGF[98,99]. An inflammatory microenvironment can also cause an increase in the rate of mutations and genomic instability through the production of reactive oxygen species (ROS) and subsequent increase in DNA damage[100].

1.1.7 Cancer treatment strategies

Many different treatments are available depending on the type of cancer, tumour location and stage of clinical progression. Conventionally, surgery alone or in combination with either radiotherapy or chemotherapy is used to treat a large number of cancers. However, recent advances have led to the development of more specialised therapeutics including hormone therapy, immunotherapy, targeted therapy and precision medicine (Cancer Research UK, 2018).

Surgery

Surgery, or resection, is one of the mainstay treatments used to treat a large number of cancers as it reduces the amount of surrounding tissue damage when compared with radiotherapy or chemotherapy[101]. Surgery is a localised treatment used to treat many solid tumours that are contained within a single region of the body and is therefore not used to treat certain cancer types such as leukaemias and some lymphomas as well as advanced metastatic cancers where there is an increased likelihood of cancer cells spreading throughout the body (Cancer Research UK, 2018).

Radiotherapy

Radiotherapy is a treatment which uses high-energy ionising radiation, usually in the form of x-rays, to shrink and destroy cancer cells. At high doses, ionising radiation can kill cancer cells by damaging DNA, inducing cell cycle arrest and triggering apoptosis either directly or indirectly through the production of free radicals[101]. However, radiotherapy also leads to damage of nearby normal tissue and can cause unwanted side effects such as tiredness and soreness which usually disappear within a few weeks (Cancer Research UK, 2018). Therefore, radiation doses are usually divided into smaller doses called fractions administered over several weeks to allow healthy cells to recover in between (Cancer Research UK, 2018). Nearly 50% of all cancer patients will receive some form of radiotherapy during their course of treatment (Cancer Research UK,

2018). However, this is most often in combination with other therapies such as surgery or chemotherapy.

Chemotherapy

Chemotherapy is a form of anti-cancer drug treatment designed to either stop cancer cells from growing with the use of cytostatic drugs or to kill cancer cells with cytotoxic drugs[102]. Treatment may involve the use of a single chemotherapeutic agent or a combination of drugs often alongside other treatments including surgery and radiotherapy (Cancer Research UK, 2018). However, as chemotherapeutic drugs target dividing cells, some normal cells are also damaged during treatment leading to unwanted side effects such as hair loss, nausea and tiredness. During more intense courses of treatment, patients may also become immunocompromised as a result[101].

There are many different types of chemotherapy drugs that are categorised based on their mode of action and chemical structure which can be used in combination therapies to maximise the therapeutic response. Alkylating agents such as nitrogen mustards (e.g. Cytoxan®) and nitrosoureas (e.g. streptozocin) directly damage DNA by alkylating guanine bases causing DNA strand breaks and ultimately, cell death[103]. Alkylating agents are used to treat a number of cancers including lymphoma and leukaemia[103]. Antimetabolites are chemical compounds that mimic the normal function of purine or pyrimidine bases of DNA and RNA and block cell cycle progression by misincorporation during S phase[104]. Common antimetabolites used to treat cancers such as ovary, breast and colon include 5-fluorouracil (5-FU) and 6-mercaptopurine (6-MP)[104]. Anti-tumour antibiotics are drugs derived from natural products and include the family of anthracyclines (e.g. Doxorubicin) which function by disrupting the activity of DNA replication enzymes[101]. Topoisomerase inhibitors prevent the unwinding of DNA and thus block DNA replication. They are used to treat a many cancer types including ovarian, gastrointestinal and lung cancers[105]. Examples include the topoisomerase 1 inhibitors topotecan and irinotecan and topoisomerase II inhibitors etoposide and teniposide[105]. Plant alkaloids including vinca alkaloids (e.g. vincristine) and taxanes (e.g. paclitaxel) are agents derived from certain types of plants. They prevent cell division by disrupting mitosis often by acting as anti-microtubule-forming agents[106].

Molecular targeted therapy

With more recent advances in the understanding of the genetic basis of cancer and the role of the tumour microenvironment in cancer growth and development new therapeutics have been developed to target specific genes or proteins involved in tumourigenesis[107]. This has enabled the concept of tailoring treatment to individual patients with specific molecular targets. By targeting specific proteins or genes that are overexpressed or mutated in cancer cells the risk of harmful side effects to non-cancerous cells is greatly reduced[108]. The two main forms of targeted therapy are monoclonal antibodies (MABs) and small molecule inhibitors. Most of these therapeutic agents target several growth factor signalling pathways such as the EGFR, VEGF receptor (VEGFR) and HER2/neu pathways[108].

MABs typically target extracellular components of these pathways such as the ligands and the ligand-binding domains of the receptors. For example, trastuzumab (Herceptin) is a MAB targetting HER2/neu which is overexpressed in around 25% of all breast cancers[109]. Similarly, the anti-EGFR MAB cetuximab (Erbitux) is used to treat colorectal and head and neck cancers[108]. Some MABs also function to alter the tumour microenvironment. Targetting VEGF signalling inhibits cancer growth and development by blocking angiogenesis[110]. The use of the anti-VEGF MAB bevacizumab (Avastin) is approved for the treatment of non-small cell lung cancer and colorectal cancers[111,112].

On the other hand, small molecule inhibitors capable of entering cells often disrupt intracellular signalling molecules and RTK activity that affects cancer cell proliferation, migration and angiogenesis[107]. For example, the successful treatment of chronic myeloid leukaemia (CML) patients where malignancy is driven by the BCR-ABL translocation with the anti-ABL inhibitor imatinib indicates the potential benefits of small molecule targeted therapy[113]. Similarly, the anti-EGFR inhibitors erlotinib and gefitinib have been used in the treatment of non-small cell lung cancer as well as the anti-HER2/neu inhibitor lapatinib in breast cancer patients with HER2 overexpression[107].

Immunotherapy

The discovery of tumour-specific immune responses has also led to the development of immunotherapeutics that aid the host immune system in recognising and attacking cancer cells[114]. Two main types of immunotherapy currently exist: immune checkpoint

inhibitors and T-cell therapy[115]. Immune checkpoint proteins act as negative regulators of T-cell activation to modulate and fine-tune the immune response to exert specific biological effects[116]. Two of the most commonly-targeted checkpoint proteins are cytotoxic T-lymphocyte antigen 4 (CTLA4) and programmed cell death 1 (PD1)[116]. CTLA4 functions as a negative regulator of T-cell activation by disrupting the co-stimulatory effects of the cell surface receptor CD28[117]. mAbs targetting CTLA4, such as ipilimumab, have now been approved for the treatment of late-stage melanoma[118]. Similar to CTLA4, PD1, a transmembrane glycoprotein, also functions as a negative regulator of T-cell activation but through the inhibition of intracellular signalling pathways such as PI3K-AKT pathway[119]. The anti-PD1 mAbs nivolumab and pembrolizumab were the first approved PD1-targeted therapies for melanoma patients[120]. The use of pembrolizumab has since been extended to a range of other cancers including non-small-cell lung carcinoma that show high expression of the PD1 ligand PDL1[121].

Adoptive T-cell (ATC) therapy involves the extraction, culturing and reinfusion of a patient's own immune cells that can be engineered to recognise and destroy cancer cells[122]. The two main forms of ATC involve tumour-infiltrating lymphocytes (TILs) and chimeric antigen receptors (CAR). TILs were originally used in the treatment of melanoma patients where lymphocyte expansion was achieved using interleukin-2[123]. However, one limitation of this therapy is the need for anti-tumourigenic T-cells to be present within the tumour[122]. Due to the challenges associated with expanding T-cells *in vitro*, synthetic CARs have been developed that can direct cytotoxicity to specific molecules on the surface of cancer cells through genetic modification of isolated patient-derived T-cells[122]. For example, the first CAR-T therapies aimed at targetting CD19-expressing B-cells for the treatment of B-cell cancers such as lymphocytic leukaemia[124]. One major challenge with CAR-T therapy is the need for a tumour-specific target antigen to be present on the cell surface as loss of these antigens, such as CD19, are a common cause of treatment failure[125].

Precision medicine

One of the major challenges associated with cancer therapeutics is that every tumour has a different mutational landscape such that every tumour is genetically unique. Traditionally, appropriate treatments for different cancer types have been guided by large sample-based epidemiological studies which does not take into account the genetic

variability that exists between individual patients[126]. The aim of modern personalised medicine is to utilise current genomic, proteomic and metabolomic profiling techniques to fully understand each individual tumour to determine who will respond to a particular therapy[127]. Along with information about a patient's family history, personal factors (e.g. age, sex, race) and overall health, a complete genetic picture of the cancer can be compiled and used to prescribe the best course of therapeutics.

For example, tamoxifen is a standard hormone therapy prescribed to steroid receptor-positive breast cancer patients. A member of the cytochrome P450 family of enzymes, cytochrome P450, family 2, subfamily D, polypeptide 6 (CYP2D6), is responsible for metabolising tamoxifen into the active metabolites 4-hydroxytamoxifen and endoxifen[128]. However, it is now known that multiple allelic variants of CYP2D6 exist that differ in their ability to metabolise tamoxifen with both non-functional and severely impaired variants associated with higher recurrence of breast cancer[129]. Therefore, genotyping of CYP2D6 prior to treatment can be used to predict the outcome to therapy and guide clinical decisions regarding adjuvant endocrine treatments[127].

1.2 Colorectal cancer

1.2.1 Colorectal cancer incidence and survival rates

With over 1.8 million new cases of colorectal cancer diagnosed in 2018 and over 860,000 deaths worldwide, colorectal cancer is the third most commonly diagnosed cancer accounting for around 11% of all cases[1]. It is also the second most common cause of cancer-related mortality worldwide accounting for 9.2% of all cancer-associated deaths[1]. In the UK, colorectal cancer is the fourth most diagnosed cancer and the second most common cause of cancer-related death (Cancer Research UK, 2018). The risk of developing colorectal cancer varies significantly between regions and appears to be most prevalent in developed countries and correlates with an increasing human development index[1]. The rising incidence in many countries is associated with several risk factors including eating processed meat, alcohol, smoking, lack of exercise and obesity; many of which reflect the development of a more Western lifestyle in transitioning countries (Cancer Research UK, 2018). One major risk factor associated with colorectal cancer incidence, and particularly mortality, is age. In the UK, both incidence and mortality rates

rise significantly above the age of 54 with almost 50% of cases appearing in people aged 75 and over (Cancer Research UK, 2018).

However, approximately 58% of patients diagnosed with colorectal cancer in the UK are expected to survive for five years or more, dropping to 52% and 54% ten-year survival in males and females respectively (Cancer Research UK, 2018). As expected, survival rates decrease with increasing age as well as the stage of the disease at diagnosis, with those diagnosed with stage 4 colorectal cancer having a 10% five-year survival rate (Cancer Research UK, 2018).

1.2.2 Colorectal cancer development

Colorectal cancer (CRC) describes malignancies that originate in any region of the colon or rectum. Most CRCs begin as a benign, pre-cancerous growth called an adenomatous polyp within the intestinal mucosa[130]. These polyps consist of localised aggregations of epithelial cells that obtrude into the lumen[130]. As these cells divide, they acquire sufficient genetic and epigenetic changes that promote excessive proliferation and provide a selective survival advantage, ultimately giving rise to a malignant carcinoma[131,132]. This sequential series of events has been termed the adenoma-carcinoma sequence and can be characterised stagewise by a combination of histological, morphological and genetic traits[130,131,133].

Three major types of CRC have been described. Approximately 75% of CRCs are sporadic and occur in people with no familial history or genetic predisposition[134]. Another 20-30% of CRCs are found in patients with a family history of the disease[135]. 5-10% of all CRC cases are due to rare hereditary predispositions including hereditary non-polyposis colon cancer (HNPCC), Lynch syndrome which accounts for 3-4% of cases and familial adenomatous polyposis (FAP) accounting for 1% of CRCs[136]. Other rare hereditary conditions such as *MYH*-associated polyposis (MAP), hyperplastic polyposis and hamartomatous polyposis syndromes make up less than 1% of all cases[136].

The Fearon and Vogelstein model was developed describing a genetic model for colorectal tumourigenesis[137]. This model proposes that the accumulation of a specific series of mutations and epigenetic changes leading to the activation of oncogenes and inactivation of TSGs triggers the development of CRC[137]. Although these mutational

events often occur in a defined sequence, it is the overall combination of the changes that are important for tumour development[137]. Critical to this model is the underlying genomic instability seen within the vast majority of CRCs[138]. Three major pathways contributing to the genomic instability of CRCs are the chromosomal instability (CIN), microsatellite instability (MSI) and CpG island methylator phenotype (CIMP) pathways[139].

Chromosomal instability pathway

Approximately 70% of sporadic CRCs develop through the CIN pathway and are characterised by structural and numerical (aneuploidy) chromosomal abnormalities, chromosomal rearrangements and LOH at key TSG loci[82]. In addition, these tumours show an accumulation of mutations in specific oncogenes such as *KRAS* and *BRAF* and TSGs such as *APC, TP53* and *SMAD4*[140]. According to the Fearon-Vogelstein model, inactivation of *APC* is the initiating event, followed by oncogenic *KRAS* mutations during the adenomatous stage and eventually inactivation of *TP53* and deletion of chromosome 18q during the transition to malignancy[137].

Activation of the Wnt signalling pathway via mutations in the *APC* gene is critical to the onset of tumourigenesis[141]. *APC* mutations are found in 80-90% of CRC patients whilst gene silencing through promoter hypermethylation is seen in 18% of CRC cases[142,143]. Germline mutations in the *APC* gene are responsible for hereditary FAP with identical somatic mutations present in approximately 60% of sporadic CRCs[144]. Additionally, independent mutations of β-catenin are seen in around 50% of CRCs[145]. Disruption of the Wnt signalling pathway leading to the accumulation of nuclear β-catenin and transcriptional activation induces the proliferation, migration and invasion of CRC cells[146].

Activation of the proto-oncogene *KRAS* during the adenomatous stage is seen in around 40% of all CRC cases[147]. Activating mutations in codons 12 and 13 predominantly involving the substitution of glycine for aspartate are responsible for 90% of activating *KRAS* mutations in developing colorectal tumours[148]. Interestingly, in patients with wild-type *KRAS*, the lack of response to targeted EGFR therapy is reportedly due to *BRAF* mutations conferring resistance to treatment[149].

Inactivating *TP53* mutations are strongly associated with the progression of CRC from adenoma to carcinoma and loss of p53 function is seen in 50-75% of CRC cases[150,151]. The most common *TP53* mutations are missense mutations within the DNA binding domain and it has been reported that mutant p53 may inhibit remaining wild-type p53 through a dominant-negative mechanism[152]. Similarly, the loss of chromosome 18q21 is commonly associated with the adenoma-to-carcinoma transition and is detected in around 70% of CRC cases[153]. Several potential TSGs involved in CRC progression are found on chromosome 18q including *SMAD2* and *SMAD4*[154]. *SMAD4* has been shown to be inactivated in advanced-stage CRC and may contribute to tumour development by conferring resistance to the anti-growth TGF-β signalling pathway[155,156].

Microsatellite instability pathway

The MSI pathway is characterised by defects in the DNA mismatch repair (MMR) machinery and is found in 15-20% of sporadic CRC cases and is responsible for >95% of HNPCC cases[157]. DNA replication errors commonly occur in repetitive sequence elements called microsatellites[158]. Defective DNA repair due to mutant MMR genes leads to an accumulation of genetic alterations and a hypermutator phenotype[158]. HNPCC is caused by germline mutations in several MMR genes including MutL homolog 1 (*MLH1)*, MutS homolog 2 (*MSH2)*, postmeiotic segregation increased 2 (*PMS2)* and MutS homolog 6 (*MSH6)* and predisposes individuals to developing CRC[136].

However, MMR deficiency in sporadic CRCs is caused predominantly by epigenetic silencing of MMR genes, particularly *MLH1*, by promoter hypermethylation[159]. The MSI status of colorectal tumours can be identified using a standard panel of five microsatellite markers[160]. Tumours are then classified according to the number of altered microsatellites present. MSI-high (MSI-H) tumours have at least two altered microsatellites, MSI-low (MSI-L) tumours have a single altered microsatellite whilst those with no alterations are microsatellite stable (MSS)[160]. *TGFBR2* is the most affected gene in the MSI-H pathway, harbouring a poly-adenine tract that is susceptible to mutation when the MMR machinery is defective and is mutated in 85% of MSI-H CRC cases[161]. This generates a truncated, inactive form of the receptor that renders CRC cells resistant to the anti-growth signals of TGFβ[162].

CpG island methylator phenotype pathway

Transcriptional silencing of genes by DNA hypermethylation within CpG islands of gene promoters is now widely recognised as the third major pathway of TSG inactivation and cancer development[163]. Aberrant DNA methylation is seen in 30-40% of sporadic colorectal carcinomas, designated as CIMP-positive (CIMP+) tumours[164]. The CIMP status of CRCs is defined according to the methylation status of a panel of CpG target sites within selected genes, however, the genes making up this panel are widely debated[165,166].

At least three molecularly distinct subclasses of CRCs based on genetic and epigenetic changes have been defined based on this analysis[167]. CIMP+ tumours can be divided into two types. 80% of CIMP-high tumours display an MSI-H phenotype due to hypermethylation of *MLH1* and are commonly associated with *BRAF* mutations (53%) whereas CIMP-low tumours with wild-type *BRAF* are characterised by mutant *KRAS* (92%) and are usually MSS or MSI-L[167]. On the other hand, CIMP-negative tumours are predominantly MSS with wild-type *BRAF* and *KRAS* but have a high rate of *TP53* mutations (72%)[167]. In addition, chromosome 18q LOH correlates with CIMP-negative CRCs but is inversely related to both CIMP-high and CIMP-low tumours[168].

1.2.3 Consensus molecular subtyping of colorectal cancer

Due to the highly heterogeneous nature of CRC and the variety of pathways that lead to its development, many attempts have been made to classify CRCs into distinct categories based on combinations of genetic alterations, immunological traits and microenvironmental characteristics to better our understanding of the disease and to guide the development of more effective precision medicine[169]. However, in order to remove inconsistencies and discrepancies between different subtyping systems, a comprehensive cross-system analysis comparing six independently developed CRC subtyping algorithms enabled the classification of CRCs into four consensus molecular subtypes (CMS) (figure 1.3)[170].

The different CMS groups 1-4 can be defined based on combinations of their chromosomal instability status, genetic mutations, immune markers and clinical prognosis[170]. Importantly, CRC cell lines commonly used *in vitro* to study CRC have also been classified into CMS subtypes and have been shown to recapitulate the

characteristics and behaviour of primary CRC tumours allowing for more accurate and translational basic research[171]. Furthermore, few biomarkers currently exist that are utilised to assess CRC patients in the clinic. Although, the CMS categories display enrichment for some genetic markers it is the combination of CMS subtype analysis with next-generation omics data that provides potential therapeutic guidance[172]. For example, transcriptomic and proteomic analysis of the metabolic adaptation seen in CMS3 tumours could identify novel targeted therapy options.

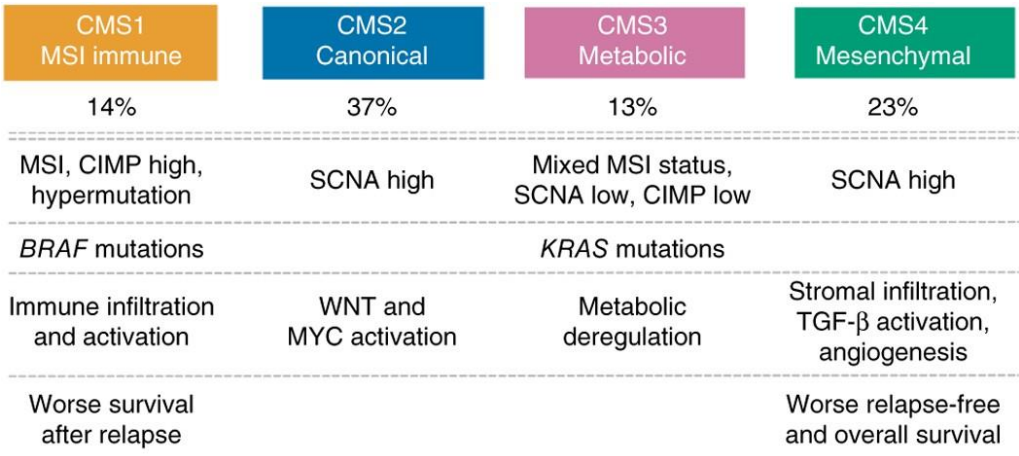

Figure 1.3 Consensus molecular subtype categorization of CRCs. Adapted by permission from Springer Nature, Nature Medicine, 'The consensus molecular subtypes of colorectal cancer', Guinney *et al*, 2015.

1.2.4 Current therapeutic strategies

Clinically, CRC can be categorised into five main stages: Stage 0, 1, II, III and IV with further division into substages based on a universal scoring system (Table 1.1) designed by the American Joint Committee on Cancer (AJCC). Treatment for stage 0 CRC is surgery, either a polypectomy or colonoscopic excision, to remove the adenomatous polyp from the mucosal layer[173].

Surgery to remove the tumour and possibly nearby lymph nodes is also often the only necessary treatment required for stage I CRCs. The type of surgery required depends on both the size and location of the tumour[173]. The initial treatment for stage II-III CRCs is surgical resection of the tumour and surrounding lymph nodes however, if the cancer is classified as high-risk then adjuvant chemotherapy may be recommended. The presence of MSI is a good prognostic marker and is often used to determine stage II patients with a low risk of recurrence with no benefit to administering chemotherapy[174]. On the other

hand, LOH at chromosome 18q is considered a poor prognostic factor in stage II CRCs and indicates those patients may benefit from adjuvant chemotherapy[175]. For stage II CRCs requiring chemotherapy and most stage III CRCs the recommended chemotherapeutic agent is 5-FU or capecitabine, an oral form of 5-FU, given as a monotherapy. In more advanced/high-risk stage II/III cancers 5-FU can be given in combination with oxaliplatin and/or leucovorin (FOLFOX regime) or capecitabine plus oxaliplatin (CapeOx regime)[176].

Stage	Description	Five-year survival (%)
0	Tumour confined to mucosa; cancer *in situ*	-
I	Tumour invades into submucosa	93.2
IIA	Tumour reaches outer layer of colon; no spread to nearby tissue/lymph nodes	84.7
IIB	Tumour grows through wall of colon to the peritoneum; no spread to nearby lymph nodes	72.2
IIC	See IIB; tumour grows into nearby organs or structures such as the stomach	-
IIIA	Tumour reaches outer layer of colon; found in nearby lymph nodes	83.4
IIIB	Tumour grows through peritoneum and/or nearby organs; found in 1-3 nearby lymph nodes	64.1
IIIC	See stage IIIB; cancer cells found in 4 or more nearby lymph nodes	44.3
IVA	Cancer has metastasised to one distant site	8.1
IVB	Cancer has metastasised to 2 or more distant sites	-

Table 1.1. Clinical stages of colorectal cancer. The clinical stages of colorectal cancer as defined by the American Joint Committee on Cancer (AJCC) based on the TNM scoring system comprised of T: growth and size of the tumour, N: spread to nearby lymph nodes and M: Metastasis to distant sites. Statistics taken from the AJCC Cancer Staging manual.

Approximately 20-30% of CRC patients present with metastases at the time of diagnosis and 50% of early-stage CRC patients will relapse with metastatic disease[177]. Metastases occur primarily to the liver (50% of cases) and the lung (10-15% of cases) but also to the bone and, less commonly, the brain[178]. Metastatic CRC (mCRC) has a dismal prognosis with a 5-year survival rate of <10%[179]. For stage IV patients with resectable metastases, surgical resection remains the first line of treatment coupled with a preoperative

FOLFOX regime and adjuvant 5-FU based chemotherapy[180,181]. For non-resectable stage IV tumours the standard of care is either a FOLFOX or 5-FU combined with irinotecan (FOLFIRI) regime in combination with a targeted MAB therapeutic against either VEGF or EGFR such as bevacizumab or cetuximab respectively[182].

More recently, advanced targeted therapeutics have been developed to help treat individual patients with advanced colorectal cancer (stave IV) based on the genotype of the tumour. For example, a phase III clinical trial of a multi-kinase inhibitor regorafenib capable of targeting VEGFR, fibroblast growth factor receptors (FGFRs) and PDGFRs provides significant survival benefit to patients with highly advanced metastatic colorectal cancer who have been unresponsive to first-line treatments[183].

1.3 Tumour hypoxia and the hypoxic response

1.3.1 Physiological oxygen levels

Maintenance of cellular oxygen (O_2) levels is critical to preserving tissue homeostasis in multicellular eukaryotes, as insufficient or excess O_2 can have profound effects on aerobic metabolism and cellular bioenergetics. In addition, the formation of harmful ROS can have damaging consequences for cells and tissues. Thus, several defensive and regulatory mechanisms have evolved to protect cells from fluctuations in O_2 tension.

Normoxia is used to describe 'normal' atmospheric O_2 levels; equivalent to 159.6 mmHg (21% O_2), however, this is not an accurate measurement for tissue oxygenation as cells and organs are exposed to a wide range of physiological oxygen tensions[184]. Tissue normoxia or 'physoxia' is therefore used to describe more accurately the physiological O_2 tension found in peripheral tissues. For example, the oxygen tension in arterial blood is approximately 70 mmHg (9.5% O_2) whereas oxygen levels in peripheral tissues can range between 3-10% O_2[184,185]. Below the lower limit of physoxia (~ 3% O_2), the term physiological hypoxia is used to describe the oxygen tension at which cells respond to restore their normal O_2 levels and is assumed to be in the range of 2-6% O_2 depending on the tissue type[184]. More importantly, pathological hypoxia is seen in acute and chronic pulmonary disease, cardiovascular disease and cancer, and is associated with loss of the homeostatic mechanisms in place to restore O_2 levels. It is defined approximately as <

7.6 mmHg (< 1% O_2) but can range between 0.3-4% O_2 with 0% O_2 defined as anoxia[184,186].

1.3.2 Development of tumour hypoxia

Due to the rapid proliferation and growth of cancer cells limiting the availability of oxygen, hypoxia (< 7.6 mmHg O_2) is a common microenvironmental feature of nearly all solid tumours; the most common form of cancer[186,187]. Physiological O_2 levels in the colon epithelium, for example, are maintained around 50 mmHg O_2 (6%) whereas colorectal tumour oxygen tension is measured at < 1.3% O_2 and is often found surrounding a central necrotic core[184,188]. Hypoxic regions are identified in approximately 45% of colorectal tumours and contribute to their metastatic potential whilst conferring resistance to chemotherapeutic and radiotherapeutic treatments.[189–191]. Hypoxia is also associated with worse patient prognosis[190,192].

The rapid, uncontrolled growth and metabolic demand of tumours quickly outweigh the oxygen available to proliferating cells due to insufficient blood supply. Therefore, tumours must stimulate the formation of their own vasculature in order to grow beyond 1mm in diameter[193,194]. However, the newly formed vascular architecture is chaotic and leaky, and displays many functional aberrations, thereby reducing blood flow and oxygen delivery to cells. This leads to the development of chronically hypoxic regions within tumours[193,195]. In addition, the increased distance between capillaries rapidly exceeds the limit of oxygen diffusion (~ 180 μm) and not only worsens the resulting hypoxia but contributes to the necrosis of cells surpassing this distance within the tumour core as depicted in figure 1.4[196]. However, tumours often experience transient fluctuations in oxygen tension due to the nature of the poorly developed vasculature. Acute or perfusion-limited hypoxia can occur temporarily when the immature, hyperpermeable vasculature surrounding tumours is reversibly closed or occluded causing fluctuations in oxygen delivery and dynamic hypoxia-reoxygenation cycles[189,197]. The coexistence of both chronic and acutely hypoxic regions within tumours generates large gradients of O_2 consumption and leads to a heterogeneous mixture of cell populations with different oxygenation status within tumours[198].

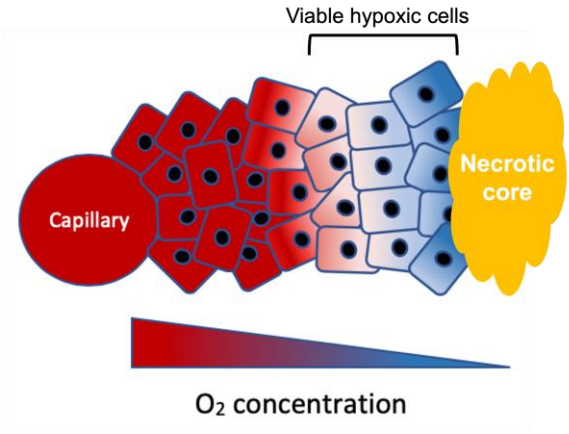

Figure 1.4 Development of hypoxia and necrosis within solid tumours. Cells close to the vasculature receive an adequate supply of oxygen and remain normoxic. As cells rapidly proliferate their distance from the blood vessel increases and the oxygen availability decreases leading to hypoxia. Above the diffusion limit of ~180 μm cells become anoxic, leading to the development of a central necrotic core. Figure created using BioRender.

1.3.3 Hypoxia-inducible factors

The primary cellular response to hypoxia involves large-scale transcriptomic changes orchestrated by the hypoxia-inducible factor (HIF) family of transcription factors that regulate the expression of >100 target genes which contribute to all of the major hallmarks of cancer and drive a more aggressive phenotype whilst promoting therapeutic resistance[199,200].

HIFs function as heterodimers consisting of two basic helix-loop-helix (bHLH) proteins of the Per-ARNT-Sim (PAS) domain-containing superfamily of transcription factors: an oxygen-sensitive α-subunit and a constitutively expressed β-subunit[201,202]. There are three isoforms of HIF-α: HIF-1α, HIF-2α (also known as EPAS-1) and HIF-3α which dimerise with the HIF-1β subunit (also known as the aryl hydrocarbon receptor nuclear translocator [ARNT])[203,204]. The HIF-α subunits share highly homologous domain organisation and are characterised by the presence of an N-terminal DNA-binding bHLH domain, two PAS domains for DNA-binding and heterodimerization, and an oxygen-dependent degradation domain (ODDD) that regulates protein stability (figure 1.5)[205,206].

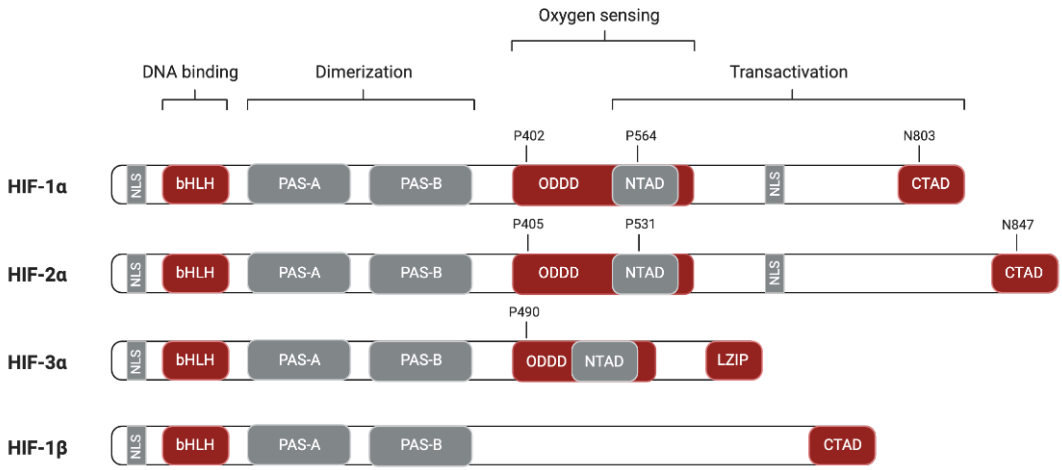

Figure 1.5 Domain architecture of the HIF isoforms. All isoforms possess a DNA-binding bHLH domain, a PAS domain for heterodimerization and an ODDD which overlaps with the NTAD domain and confers the oxygen dependence of HIFα subunit stability. The N-TAD and C-TAD domains are also responsible for the transactivation of the HIFα subunits. The C-TAD of HIF-3α is replaced with an LZIP domain that regulates protein-protein interactions. Figure created using BioRender.

The N- and C-terminal transactivation domains (N/C-TAD) of HIF-1α and HIF-2α are involved in the regulation of transcriptional activity. For example, the C-terminal transactivation domain (C-TAD) of HIF-1α is responsible for interacting with the transcriptional coactivator CREB binding protein (CBP/p300) to modulate the expression of HIF target genes[207]. HIF-1α is the most ubiquitously expressed HIF-α isoform in human tissues and is often described as the master regulator of the hypoxic response[208]. HIF-1α shares 48% amino acid sequence homology with HIF-2α and both have been shown to have various overlapping functions in the activation of hypoxia-dependent gene expression[203,209,210]. However, HIF-1α and HIF-2α have also been shown to play distinct roles in the response to hypoxia. This may be due to differential patterns of tissue-specific and temporal expression between the isoforms. HIF-1α appears to be expressed across most tissue types whereas HIF-2α expression was thought to be restricted to endothelial cells[203]. More recently, HIF-2α has been identified in a wider range of cell types including, renal, hepatic, intestinal and lung cells suggesting some overlap in the expression of HIF-1α and HIF-2α[211]. Both HIF-1α and HIF-2α are overexpressed in a large number of cancers and are often associated with poor patient prognosis and tumour aggressiveness[212]. In colorectal cancer, research suggests that HIF-1α and HIF-2α have different functional roles in tumour progression. Xenograft studies

indicated that HIF-1α was able to promote the proliferation and migration of colon cancer cells whereas HIF-2α restricted growth and loss of HIF-2α correlates with an advanced tumour stage[213]. Other studies suggest that the differential activity of the HIF-α isoforms are due to having distinct transcriptional target genes. For example, HIF-1α target genes include carbonic anhydrase IX (CA9) and a large number of metabolic genes including glycolytic enzymes such as lactate dehydrogenase (LDHA) whereas HIF-2α seems to be important in the expression of angiogenesis-inducing genes such as vascular endothelial growth factor (VEGF) and its receptor fms-like tyrosine kinase-1 (Flt1/VEGFR1) as well as peroxisome proliferator-activated receptor γ (PPARγ)[214–216].

1.3.4 Regulation of hypoxia-inducible factors

Under normoxic conditions, HIF-α proteins have a very short half-life and are rapidly turned over by the ubiquitin-proteasome system (UPS) (figure 1.6). This turnover is mediated by the oxygen-dependent hydroxylation of two proline residues, P402 and P564, within the ODDD by a family of prolyl hydroxylase enzymes comprising PHD1, 2 and 3[217,218]. The PHDs belong to the dioxygenase family of enzymes that require oxygen and 2-oxoglutarate as co-substrates along with an iron co-factor[219]. O_2-dependent prolyl hydroxylation mediates binding of the von Hippel-Lindau (pVHL) protein, which acts as the substrate recognition component of a Cullin RING E3 ubiquitin ligase complex comprising Cullin-2 (Cul2), Elongins B and C and the RING finger subunit Rbx1[220,221]. The binding of hydroxylated HIF-α to the β-domain of pVHL facilitates HIF-α polyubiquitination and degradation by the 26S proteasome[222,223].

In addition to protein stability, the transcription activating potential of HIF-1α is regulated by O_2-dependent hydroxylation of asparagine 803 (N803) in the C-TAD by an asparaginyl hydroxylase: factor inhibiting HIF (FIH-1)[224,225]. C-TAD hydroxylation prevents the recruitment of the transcriptional coactivator p300/CBP by blocking interactions with its CH1 domain and represses hypoxic gene expression in normoxia[226]. FIH-1 can also interact with pVHL to enhance the degradation of HIF-1α and may also aid in the recruitment of histone deacetylases (HDACs) to silence gene expression[224]. This represents one of several key regulatory differences between HIF-1α HIF-2α. Similarly, the E3 ubiquitin ligase hypoxia-associated factor (HAF) can interact with HIF-

1α and promote its proteasomal degradation whereas HAF binding to HIF-2α promotes transactivation and a switch from HIF-1α to HIF-2α-dependent signalling[227].

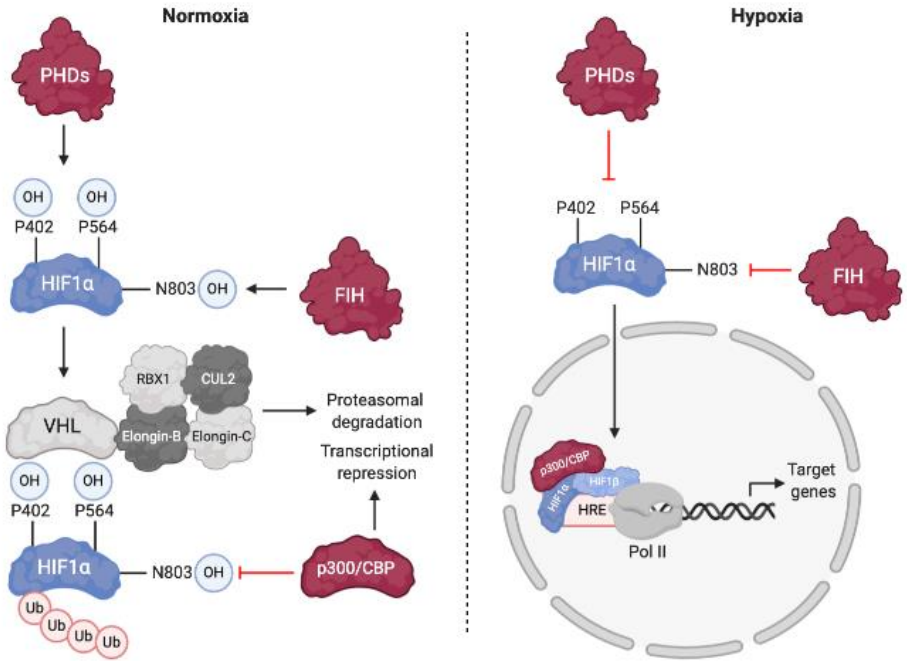

Figure 1.6 Oxygen-dependent regulation of HIF-1α protein stability and target gene expression. Under normoxic conditions, HIF-1α is hydroxylated by O_2-dependent PHD and FIH-1 enzymatic activity leading to proteasomal degradation and transcriptional repression. In hypoxia, the enzymatic activities of PHDs and FIH-1 are inhibited leading to HIF-1α stabilisation. HIF-1α translocates to the nucleus where it dimerises with HIF-1β and recruits coactivators such as p300/CBP to activate gene expression from HRE sequences in target gene promoters. Figure created using BioRender.

In hypoxic conditions, the enzymatic activities of the PHDs and FIH-1 are inhibited due to the absence of the oxygen cofactor. Therefore, the ODDD and C-TAD of HIF-1α remain unhydroxylated and HIF-α is stabilised. HIF-α can then translocate into the nucleus where it dimerises with HIF-1β and recruits co-factors such as p300/CBP at consensus 5'-G/ACGTG-3' hypoxia-response elements (HRE) in target gene promoters to activate gene expression (figure 1.6)[228].

1.3.5 Hypoxia and therapeutic resistance

Clinically, the most important feature of hypoxia is its ability to confer resistance to radiotherapy, chemotherapy and targeted therapies[229]. Hypoxia is therefore associated with poor prognosis in almost every clinical setting independent of cancer grade[229,230]. Many of the anti-therapeutic effects of hypoxia can be attributed to the effects of HIF-

1α in the regulation of cell cycle progression, apoptosis, autophagy, metabolic reprogramming and mitochondrial activity[217]. However, due to the requirement for oxygen in the production of radiation-induced ROS, HIF-independent mechanisms of resistance are also implicated as are hypoxia-associated changes in the tumour microenvironment[232].

Radioresistance

Oxygenated cancer cells display a 3-fold increase in responsiveness to radiotherapy compared to hypoxic regions[233]. This "oxygen effect", first hypothesised in 1953 by Gray and colleagues, is quantified by the oxygen enhancement ratio (OER); defined as the ratio of doses required to achieve the same biological effect in hypoxic and oxygenated cells[220,221]. Ionising radiation functions by inducing DNA double-strand breaks which, if unrepaired, triggers apoptosis and cell death[236]. DNA damage can occur either directly due to the ionisation of DNA or indirectly through the actions of free radicals or ROS generated from the ionisation of water molecules[236].

In normoxic cells, oxygen fixation occurs as oxygen has a high affinity for the free radicals generated during radiotherapy, binding covalently to the radicals and causing irreversible DNA damage[237]. As hypoxic cancer cells lack sufficient oxygen, the formation of ROS and production of DNA damage are significantly reduced[237]. As up to 60% of DNA damage may be caused through the indirect effects of radiation, the lack of oxygen explains the resistance of hypoxic cells to radiotherapy[238].

Chemotherapeutic resistance

Resistance to chemotherapeutic agents is complex and highly diverse and is caused by a variety of mechanisms including the pharmacokinetic properties of the drug such as absorption and metabolism, intrinsic factors such as cancer cell expression of drug efflux pumps and extrinsic factors within the tumour microenvironment such as acidosis, interstitial fluid pressure, vascular structure and hypoxia[239]. As hypoxic cells are found within the tumour core furthest away from the surrounding vasculature there is limited drug delivery to hypoxic cells[240]. Drug extravasation and tumour penetration also both rely heavily on convection or diffusion gradients[240]. However, the interstitial fluid pressure of many tumours is elevated due to the lack of functional lymph vessels and is similar to the pressure within the tumour vasculature leading to reduced extravasation of

drugs[241]. Furthermore, hypoxia is often associated with increased acidosis and promotes an acidic tumour microenvironment conducive to multi-drug resistance[242].

Many chemotherapeutic agents are directly dependent on cellular oxygenation for maximum efficiency, such as alkylating agents which transfer alkyl groups to DNA during cell division[243,244]. Many alkylating agents have reduced efficacy under hypoxic conditions due to competition with increased levels of nucleophiles such as glutathione which compete for DNA alkylation sites[245].

Both hypoxia and nutrient deprivation within tumours can cause a reduction in cell proliferation and therefore increased resistance to chemotherapeutic agents which function during a specific phase of the cell cycle[246]. A large number of alkylating agents and antimetabolites exert their cytotoxic effects by damaging DNA during S phase and triggering apoptosis[245]. Hypoxia-induced p27 expression can lead to inhibition of the G1/S phase transition and cell-cycle arrest therefore reducing the efficacy of many S-phase dependent drugs[247]. Importantly, hypoxia also selects for TP53 mutant cells that have a reduced apoptotic potential and therefore increased resistance to chemotherapy-induced DNA damage[248]. Furthermore, in response to DNA damage, hypoxia can inhibit the expression of pro-apoptotic proteins such as Bax and Bid and activate anti-apoptotic proteins such as survivin and inhibitor of apoptosis protein-2 (IAP-2) through both HIF-dependent and independent mechanisms to prevent apoptosis[249–251].

Hypoxia can also lead to the overexpression of drug efflux proteins belonging to the ATP binding cassette (ABC) family of transporters which has a significant impact on the therapeutic response[252]. The multi-drug resistance 1 (*MDR1*) gene encodes a membrane-bound P-glycoprotein (P-gp) that functions as a drug efflux pump to reduce the intracellular concentrations of foreign agents including drugs to sub-lethal levels[253]. Expression of *MDR1* positively correlates with hypoxia in a large number of cancer types including colon cancer[254,255]. Inhibition of HIF-1α has been shown to reverse multi-drug resistance in CRC by downregulating *MDR1* expression.

Resistance to molecular-targeted therapy and immunotherapy

Despite the recent, rapid advances in molecular-targeted therapeutics and immunotherapies, hypoxia still poses a significant problem to many of the targeted

treatments commonly used in the clinic. For example, HIF-1α inhibits estrogen receptor α (ERα) expression which correlates with poor prognosis and tamoxifen resistance in breast cancer[256]. Furthermore, the elevated lactate levels generated by hypoxia-induced aerobic glycolysis further contribute to tamoxifen resistance[257]. Trastuzumab is one of the most used therapies for HER2+ breast cancers and has more recently been approved for the treatment of HER2-amplified mCRC[258]. However, HIF-1α has been shown to induce resistance to trastuzumab through upregulating the expression of the PTEN negative regulator HES-1, leading to constitutive STAT3 activation that drives resistance[259].

Hypoxia also promotes immunosuppression and resistance to checkpoint inhibitors by promoting the expression and reprogramming of immunosuppressive immune cells including M2 macrophages, MDSCs and Tregs[260]. For example, HIF-1α and hypoxia-induced lactate production promote the polarization of TAMs from an M1 to an immunosuppressive M2 phenotype[261]. Furthermore, hypoxia promotes the secretion of tumour-derived cytokines such as CCL5, CCL28 and CXCL12 that stimulate the recruitment of Tregs and MDSCs[262]. In turn, Tregs and MDSCs secrete immunosuppressive cytokines such as TGF-β, IL-6 and IL-10 to inhibit CD8+ T-cell cytotoxic activity[263]. The suppression of T-cell activity in hypoxia is enhanced further by the HIF-1α-mediated upregulation of immune checkpoint proteins including PD-1 and CTLA4 as well as promoting the expression of PD-L1 on stromal cells and MDSCs[264,265]. This simultaneously confers resistance to immune checkpoint therapy. As most hypoxia-induced immunosuppressive effects are metabolism-driven, this provides a rationale for identifying novel ways of targetting metabolism in hypoxic tumours to overcome therapeutic resistance[260].

1.4 Cap-dependent protein translation and hypoxia

1.4.1 Overview of cap-dependent protein synthesis

Protein synthesis, or translation, is the most energy-consuming process in the cell and utilises enormous amounts of ATP generated through oxygen-dependent cellular metabolism[266]. Low oxygen conditions reduce the global rate of protein synthesis due to diminished ATP availability, necessitating the need for alternative hypoxia-regulated translation pathways[267]. The majority of eukaryotic capped mRNAs are translated via the

canonical cap-dependent translation pathway consisting of three stages: initiation controlled by initiation factors (eIFs), elongation by elongation factors (eEFs) and termination by release factors (eRFs) with the regulation of this process occurring predominantly at the rate-limiting stage of initiation[268].

Translation initiation

Translation initiation begins with the formation of a ternary complex (TC) consisting of the GTP-bound initiation factor eIF2 and the initiator methionine tRNA (met-tRNA$_i$) that recognises the AUG start codon (figure 1.7)[269]. eIF2 is a heterotrimeric complex of eIF2α, eIF2β and eIF2γ subunits and is a major control point for translation initiation[270]. eIF2β acts as a guanine nucleotide exchange factor (GEF) that recycles eIF2-GDP to eIF2-GTP to promote met-tRNA$_i$ binding[271]. The TC is then recruited to the 40S small ribosomal subunit with the aid of several initiation factors including eIF1, eIF1A, eIF3 and eIF5 to form a 43S pre-initiation complex (PIC) (figure 1.7). eIF3 is responsible for recruiting the TC, facilitates eIF1 and eIF5 binding and prevents premature association with the 60S large ribosomal subunit[272,273].

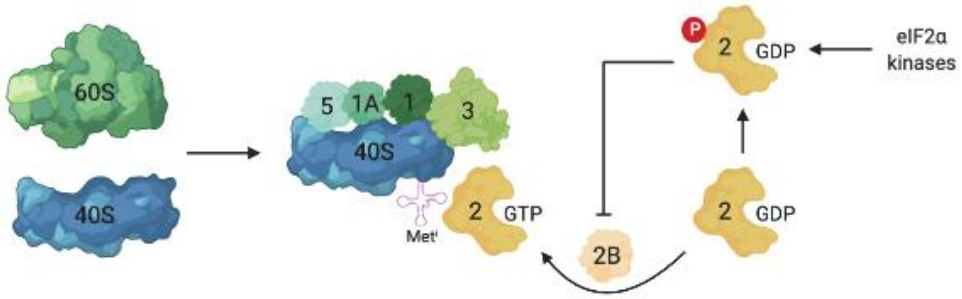

Figure 1.7 Formation of the 43S pre-initiation complex. Translation initiation begins with the formation of an eIF2-GTP-Met-tRNA$_i$ ternary complex that is recruited to the 43S small ribosomal subunit with the help of the initiation factors eIF1, eIF1A, eIF3 and eIF5. Figure created using BioRender.

Simultaneously to PIC formation, activation of the mRNA occurs through recognition of the 5'-7-methylguanosine (m^{7}G) cap, present on all eukaryotic capped mRNAs as an evolutionarily conserved modification, by the cap-binding protein eIF4E[274]. eIF4E functions as part of the eIF4F cap-binding complex that also consists of the scaffold protein eIF4G and the DEAD-box RNA helicase eIF4A. eIF4G provides binding sites for eIF4E and eIF4A and an RNA-binding motif that helps anchor eIF4A on the 5'UTR of mRNAs[275,276]. eIF4G also interacts with poly-(A) binding protein (PABP) which

associates with the 3'-polyadenylated mRNA tail and is able to form a closed loop structure bringing the 5' and 3' ends of the mRNA together (figure 1.8)[277,278]. This 'closed-loop' structure was initially thought to promote PIC recruitment as well as allow for multiple termination and recycling events without the need for reinitiation on the same mRNA[279]. However, there is much conflicting evidence regarding the interactions between PABP and eIF4G and the formation and role of looped mRNA structures[277,280,281].

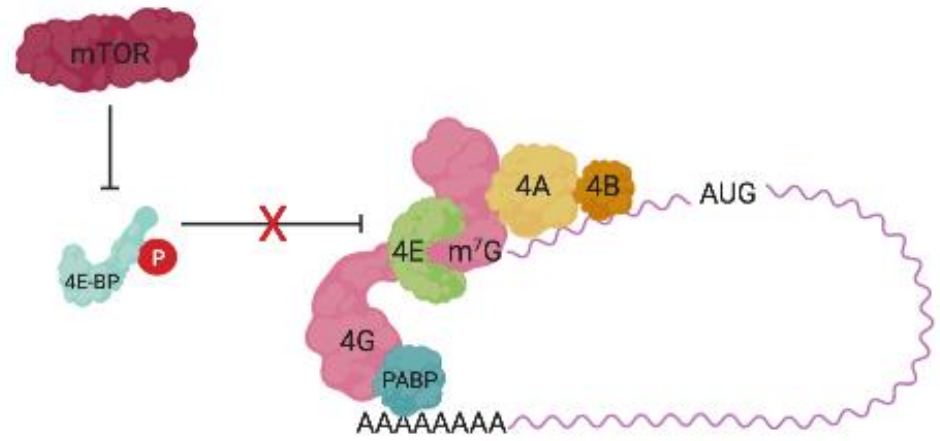

Figure 1.8 mRNA activation via eIF4F cap-binding complex assembly. mRNAs are activated by the recruitment of the eIF4E cap-binding protein and subsequent assembly of the eIF4F complex consisting of eIF4G and eIF4A at the 5' cap. eIF4G also interacts with PABP to form closed-loop structures. Figure created using BioRender.

Once bound, the 48S complex scans the mRNA in a 5' to 3' direction along the unwound 5'UTR until the met-tRNA$_i$ recognises the AUG start codon[282]. Upon start codon recognition, eIF1 is released and the GTPase activity of eIF2 is stimulated by eIF5 triggering release of inorganic phosphate, followed by the dissociation of eIF2-GDP as well as eIF5[283,284]. Recruitment of eIF5B-GTP through interactions with eIF1A promotes 60S large ribosomal subunit binding and formation of the 80S initiation complex (figure 1.9) [285]. Binding of the 60S subunit promotes GTP hydrolysis and release of eIF5B-GDP followed finally by release of eIF1A[286,287]. The 80S complex is then able to initiate the elongation phase of translation.

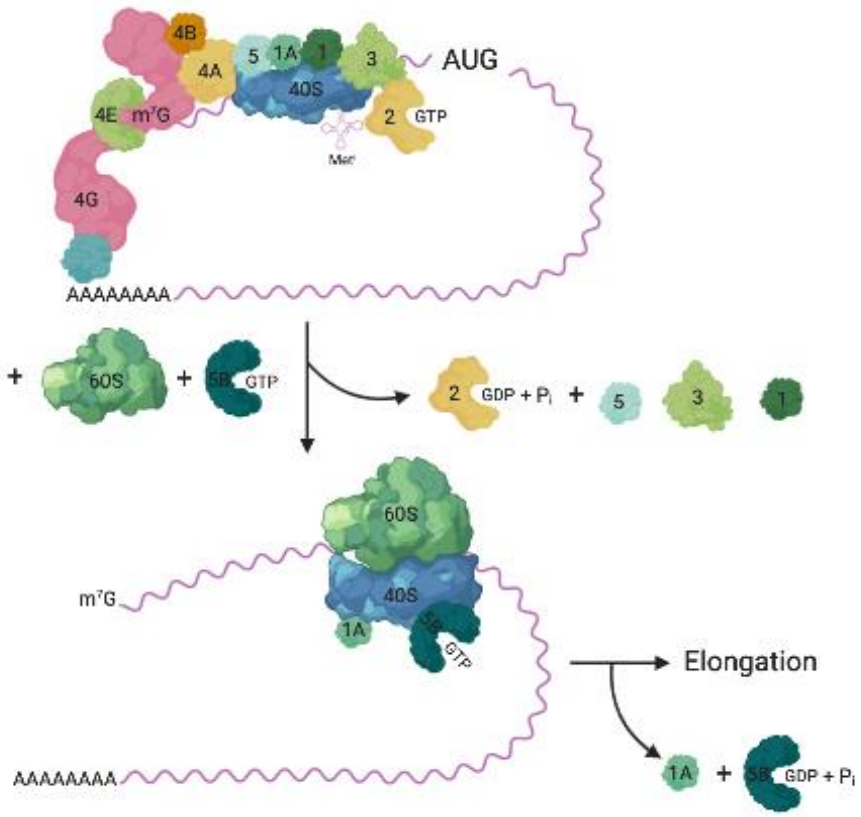

Figure 1.9 PIC recruitment and ribosome scanning. PIC recruitment is facilitated by several interactions between eIF4G, eIF4B and eIF3 as well as eIF1/1A activity. The 48S complex scans the 5'UTR until the AUG start codon is recognised. GTP hydrolysis and release of eIF1, eIF2-GDP and eIF5 followed by eIF5B-GTP binding promotes 60S ribosomal subunit joining. GTP hydrolysis promotes the release of eIF5B-GDP and eIF1A, leaving the elongation-competent 80S complex. Figure created using BioRender.

1.4.2 Regulation of protein synthesis in response to stress

Cancer cells adapt to survive in the presence of a variety of environmental stresses including oxidative stress, mechanical stress, nutrient deprivation and hypoxia which often reduce global cap-dependent protein translation rates[288]. Endoplasmic reticulum (ER) stress leads to activation of the unfolded protein response (UPR) which inhibits global cap-dependent protein translation to reduce the accumulation of unfolded proteins in the ER[289]. Similarly, in response to nutrient deprivation or hypoxia, cap-dependent protein translation is inhibited in order to conserve energy[290]. The regulation of cap-dependent protein translation occurs predominantly at the initiation stage through two mechanisms: eIF2α phosphorylation and mTOR/eIF4F signalling[290]. However, cancer cells are more metabolically active and often require increased rates of protein synthesis, particularly of proteins involved in regulating many of the hallmarks of cancer such as proliferation, metabolic reprogramming and angiogenesis[291]. Therefore, cancer

cells must utilise alternative modes of protein translation under stress conditions in order to synthesise specific subsets of pro-tumourigenic mRNAs essential for survival[290].

eIF2α phosphorylation

Regulation of eIF2α subunit phosphorylation is one major mechanism of translation regulation. A family of four kinases recognise various stresses to coordinate the integrated stress response: amino acid depletion monitored by general control non-depressible 2 (GCN2); heme deprivation monitored by heme-regulated eIF2α kinase (HRI); viral infection monitored by double-stranded RNA-dependent protein kinase (PKR) and ER stress monitored by PKR-like ER kinase (PERK)[289]. Activation of these kinases leads to phosphorylation of serine-51 on the eIF2α subunit, preventing GDP-GTP exchange by blocking eIF2β activity critical for ternary complex formation with the initiator met-tRNA$_i$ and therefore reducing translation initiation (see figure 1.9)[292]. However, dephosphorylation and restoration of eIF2 activity usually occur within 4-8 hours following stress and so regulation of the chronic stress response occurs through the mTOR signalling pathway[293].

mTOR/eIF4F signalling

Translation initiation is the rate-limiting step of protein synthesis and is highly dependent on the activity of the cap-binding eIF4E protein which is therefore under strict regulation, particularly in response to stress[294]. mTOR is a Ser/Thr kinase activated in response to stimuli such as oxygen and nutrient availability via the PI3K/Akt signalling pathway to phosphorylate target proteins involved in cell proliferation, growth and survival[295]. mTOR exists in two protein complexes mTOR complex 1 (mTORC1) and mTOR complex 2 (mTORC2)[296].

Under normal conditions, mTORC1 is regulated by the PI3K/Akt pathway to promote protein synthesis. Growth factor stimulation of the PI3K/Akt pathway leads to Akt activation[297]. This enables Akt to activate mTORC1 by phosphorylating and inactivating the PRAS40 inhibitory subunit of mTORC1 as well as the tuberous sclerosis complex 2 (TSC2) component of the TSC1/2 complex[298,299]. TSC1/2 acts as a GTPase-activating protein that stimulates the conversion of Rheb-GTP to Rheb-GDP [300]. Inactivation of the TSC1/2 complex by Akt phosphorylation keeps Rheb in the GTP-bound state which can activate mTORC1[300].

Active mTORC1 phosphorylates the eIF4E binding protein (4E-BP) which prevents it from binding and sequestering eIF4E, thus allowing cap-binding and translation initiation to proceed[301]. However, in response to stress, mTORC1 activity is reduced, allowing unphosphorylated 4E-BP to sequester eIF4E and prevent eIF4F complex formation[301]. mTORC1 also phosphorylates ribosomal protein S6 kinase (S6K) which promotes translation through increased S6 ribosomal protein, eIF4B and eEF2 activity[302]. Again, under stress conditions, the reduction in mTORC1 activity leads to reduced S6K phosphorylation and reduced translation rates[303].

1.4.3 Regulation of protein synthesis in hypoxia

Canonical cap-dependent protein synthesis requires large amounts of ATP generated in an oxygen-dependent manner, therefore to promote protein synthesis and cell survival in low oxygen conditions cancer cells adapt to hypoxia-induced changes by activating alternative translation pathways that mediate the selective recruitment of mRNAs for translation initiation[304]. The regulation of mRNA translation in hypoxic conditions occurs mainly at the stage of initiation and exhibits a biphasic response characterised by two independent pathways: eIF2α phosphorylation and eIF4F complex formation (see figure 1.10)[293].

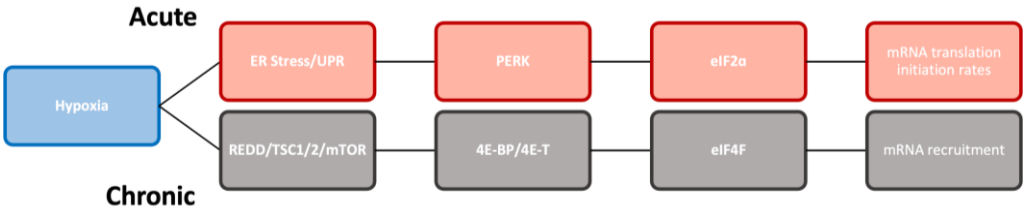

Figure 1.10 Effects of hypoxia on mRNA translation occurs via two distinct pathways. Acute hypoxia (1-2 hours) involves the PERK-mediated phosphorylation of eIF2α and regulation of translation initiation rates. Chronic hypoxia involves mTOR signalling and the regulation of eIF4E activity and mRNA recruitment. Figure adapted from Koritzinsky et al., 2006.

Within 1-2 hours of hypoxic exposure, there is a global decrease in protein translation mediated by activation of the UPR due to increased ER stress[293]. This acute response to hypoxia leads to hyperphosphorylation of PERK and subsequent phosphorylation and inhibition of eIF2α thereby reducing global protein synthesis[305]. This initial reduction in translation is followed by a partial recovery period where translation rates increase slightly and cap-dependent translation is responsible for approximately 90% of hypoxic protein translation[293,306] This recovery is crucial for allowing the PERK-mediated

selective translation of stress response genes such as ATF4 which upregulates the expression of key genes responsible for restoring cellular homeostasis[307].

Chronic exposure to hypoxia leads to the activation of an alternative signalling pathway that regulates hypoxic protein translation through the disruption of the eIF4F complex[308]. Prolonged hypoxia leads to a reduction in ATP availability and energy depletion resulting in the activation of AMP-activated protein kinase (AMPK)[309]. AMPK phosphorylates and activates the TSC1/2 complex leading to GTP hydrolysis and a reduction in Rheb-GTP levels[310]. This leads to inhibition of mTORC1 activity and reduced 4E-BP phosphorylation allowing 4E-BP to bind and sequester eIF4E thereby preventing eIF4F complex assembly[308]. Furthermore, hypoxia leads to increased expression of the HIF-1α target regulated in development and DNA damage 1 (REDD1) gene[309]. REDD1 promotes the dissociation of TSC2 from its inhibitory 14-3-3 protein and therefore prevents mTORC1 activation and promotes eIF4E inhibition by 4E-BP[311,312]. Additional eIF4E inhibition in response to hypoxia also occurs due to the translocation of eIF4E into the nucleus or into the cytoplasmic compartment of mRNA processing bodies (P-bodies)[313]. The eIF4E transporter 4E-T is capable of localising eIF4E to the nucleus or P-bodies and hypoxia causes an increase in the nuclear co-localisation of eIF4E and 4E-T, thus preventing it from participating in translation[314,315].

1.4.4 Alternative mechanisms of translation in hypoxia

Under hypoxic stress, cancer cells must continue to synthesise proteins that maintain cell survival and promote adaptation to hypoxia through the selective translation of key hypoxia-responsive mRNAs[290]. Due to the mTORC1-mediated inhibition of canonical cap-dependent translation, cancer cells activate alternative translation pathways including switches in the eIF4F translation machinery and complex formation[290].

Hypoxia-specific cap-binding complex formation

Investigations into the alternative cap-dependent translation of the *EGFR* mRNA during hypoxia and eIF4E inactivation led to the discovery of a novel role of HIF-2α as a cap-dependent translation initiation factor in hypoxic conditions[316]. HIF-2α was shown to interact directly with the 3'UTR of the *EGFR* mRNA and increase its translation, and siRNA knockdown of HIF-2α, but not HIF-1α, led to a reduction in global translation rates indicating a specific role for HIF-2α in hypoxic protein synthesis[316]. HIF-2α was

also shown to interact with the RNA binding motif protein 4 (RBM4) via a canonical CGG trinucleotide motif[316]. RBM4 is also capable of interacting with the 3'UTR of the *EGFR* mRNA and is essential for HIF-2α binding suggesting a mechanism whereby RBM4 interacts with specific sequences within the 3'UTR of hypoxia-responsive mRNAs, termed RNA hypoxia-response elements (rHREs), and recruits HIF-2α[316]. The HIF-2α-RBM4 complex is then able to recruit the cap-binding protein eIF4E2, a paralog of the normoxic eIF4E protein to form a HIF-2α-RBM4-eIF4E2 complex on the 3'UTR of target mRNAs (figure 1.11)[316]. Knockdown of eIF4E2 prevented the translation of target transcripts including *EGFR* whereas eIF4E knockdown had no effect, suggesting a hypoxia-specific switch in the cap-binding component of the eIF4F complex[316].

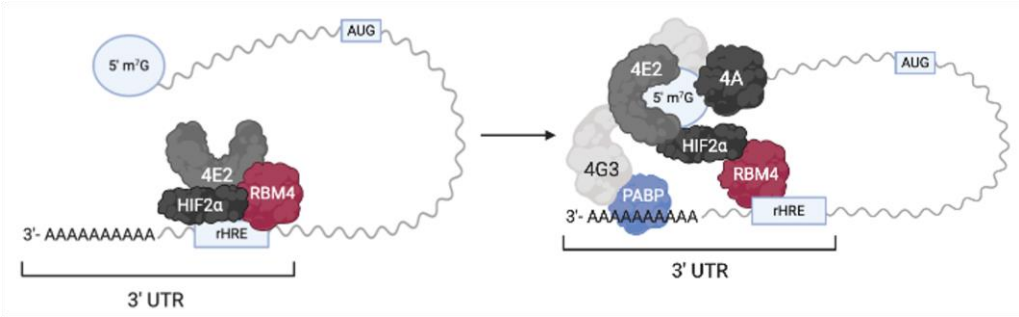

Figure 1.11 Formation of an alternative hypoxia-specific eIF4F cap-binding complex. A hypoxia-specific HIF-2α-RBM4-eIF4E2 complex forms at rHREs within the 3'UTR of target mRNAs. eIF4E2 then interacts with the 5' cap and forms a hypoxia-specific eIF4F^{H} complex with eIF4G3 and eIF4A.

The HIF-2α-RBM4-eIF4E2 complex can then interact with the 5' cap of the mRNA where it forms a hypoxia-specific eIF4F complex termed eIF4F^{H} consisting of eIF4A and a hypoxia-specific paralogue of eIF4G1, eIF4G3 (figure 1.11)[317]. Similar studies to those used to identify the role of eIF4E2, showed that eIF4G3 silencing, but not eIF4G1, resulted in decreased global translation rates in hypoxia[317]. Taken together these studies propose the existence of two distinct eIF4F cap-binding complexes: the normoxic eIF4F consisting of eIF4A, eIF4E and eIF4G1; and the hypoxic eIF4F^{H} complex consisting of eIF4A, eIF4E2 and eIF4G3[316,317].

1.4.5 RNA helicases in translation

Importantly, no studies have investigated or confirmed which paralogue of the eIF4A RNA helicase protein is present in the normoxic eIF4F and hypoxic eIF4F^{H} complexes nor have they determined the selectivity of different eIF4A paralogues for target mRNAs

in hypoxic conditions. It is possible that there is a hypoxia-induced switching in eIF4A paralogues similar to that seen with the eIF4E and eIF4G proteins.

DEAD-box RNA helicases

RNA helicases play central roles in the regulation of all aspects of RNA metabolism, splicing, transport and degradation as well as regulating RNA-protein interactions and ribosome biogenesis through the ATP-dependent unwinding of RNA duplexes[318]. The DEAD-box RNA helicases, which include eIF4A1 and eIF4A2, belong to the superfamily 2 (SF2) and are classified based on conserved sequence motifs[319]. The DEAD-box family is characterised by nine conserved sequence motifs: Q motif, motif I, motif Ia, motif Ib, motif II, motif III, motif IV, motif V and motif VI arranged within a helicase core comprised of two RecA-like domains that contribute to ATPase and helicase activity as well as regulatory functions[320]. Motif II, also known as the Walker B motif, contains the Asp-Glu-Ala-Asp (DEAD) sequence responsible for the family's name[321].

eIF4A RNA helicases and translation initiation

The RNA helicase eIF4A belongs to the DEAD-box family of helicases and is required for the unwinding of secondary structures in the 5'UTR of the mRNA to facilitate 43S PIC recruitment[322]. There are two mammalian isoforms of eIF4A that can be incorporated into the eIF4F complex and participate in translation initiation: eIF4A1 and eIF4A2, which display 91% amino acid homology[323,324]. A third functionally distinct isoform, eIF4A3, only shares ~60% homology with eIF4A1/2 and is involved in regulating nonsense-mediated decay as part of the exon-junction complex[325].

The intrinsic helicase activity of eIF4A1 is very low despite approximately 90% of eIF4A1 existing as free, isolated eIF4A protein within mammalian cells[326]. The other 10% of eIF4A1 functions as part of the eIF4F cap-binding complex where its helicase activity is stimulated through interactions with other translation initiation factors[327]. Both eIF4B and eIF4H can interact exclusively with eIF4A1 to stimulate helicase activity however, the exact molecular mechanism behind this activation remains unclear[328]. Furthermore, the formation of a stable eIF4A1-eIF4B complex also requires the presence of eIF4G, which acts synergistically with eIF4B or eIF4H to enhance eIF4A1 ATPase activity and RNA unwinding[329].

eIF4A1 and eIF4A2 expression and functions

The expression of eIF4A1 and eIF4A2 varies depending on the tissue type; eIF4A1 is generally more highly expressed than eIF4A2 and is expressed in actively dividing cells whereas eIF4A2 is more highly expressed in quiescent, non-proliferative cells[330,331]. Both eIF4A1 and eIF4A2 have long been proposed to be functionally interchangeable and play overlapping roles in translation initiation yet, eIF4A1 has been shown to be essential for translation whereas eIF4A2 is not[332]. Similarly, mutant eIF4A1 but not mutant eIF4A2 leads to a global reduction in protein synthesis[333]. Furthermore, eIF4A1 inhibition leads to an increase in *eIF4A2* gene expression but eIF4A2 is unable to rescue the inhibitory effect of eIF4A1 suppression on translation and cell proliferation[334]. Despite these suggestions that eIF4A1 and eIF4A2 may have individual and distinct roles in regulating protein translation almost all of the existing biochemical and structural studies investigating the eIF4A protein have focused solely on eIF4A1 with eIF4A2 being largely neglected[335].

More recently, eIF4A2 has been identified as the only component of the eIF4F complex required for the miRNA-mediated regulation of gene expression[336]. eIF4A2 has been shown to interact with the CCR4-NOT complex, one of the major deadenylase complexes regulating miRNA-mediated repression of translation and mRNA degradation[337]. Recruitment of eIF4A2 has been proposed to occur through interaction with the MIF4G domain, similar to the eIF4A binding site on eIF4G, of the CCR4-NOT complex component CNOT1 which is capable of forming an RNA-independent complex with eIF4A2[338,339]. Additional studies have since revealed another specific interaction between eIF4A2 and the deadenylase component CNOT7[336,340]. The recruitment of eIF4A2 into the CCR4-NOT complex inhibits the deadenylation activity of CNOT7 and bound mRNAs are maintained in a stable, polyadenylated state[341]. On the other hand, the recruitment of an alternative RNA helicase, DDX6, stimulates CNOT7 deadenylation activity and leads to mRNA deadenylation and degradation[341]. This suggests that the fate of mRNAs is determined by the recruitment of either eIF4A2 or DDX6 into the CCR4-NOT complex which promotes different pathways of translation repression and mRNA deadenylation[341]. Interestingly, only mRNAs bound by eIF4A2 are enriched for miRNA recruitment and are translationally activated in response to CCR4-NOT complex inhibition, whereas DDX6-bound mRNAs are not translationally repressed[339]. This provides the possibility that eIF4A2 could be playing a

dual role in the regulation of protein synthesis both as an activator of initiation and also as a member of the translation repression machinery depending on the cellular context distinct from the role of eIF4A1.

To further understand the potentially distinct roles of eIF4A1 and eIF4A2, native RNA immunoprecipitation sequencing (RIP-Seq) has been used to investigate the differences in target mRNA binding by the two eIF4A isoforms. Whilst the majority of mRNAs display overlap between eIF4A1 and eIF4A2 (3967 genes) there are also specific mRNA populations of 832 genes and 628 genes that are only bound by eIF4A1 or eIF4A2 respectively[339]. Importantly, eIF4A1-bound mRNAs display a polysomal distribution in accordance with its role in promoting translation initiation whereas eIF4A2-bound mRNAs display a subpolysomal distribution associated with translation repression[339]. Enrichment analysis shows that mRNAs bound by eIF4A2 encode for predominantly nuclear proteins involved in the negative regulation of transcription, neural tube development and miRNA biogenesis whereas eIF4A1-bound mRNAs display no enrichment for particular mRNAs suggesting eIF4A1 does not selectively target specific subsets of mRNAs[339]. Importantly, the role of eIF4A1 and eIF4A2-specific translation was not investigated in the context of cancer or under hypoxic conditions.

eIF4A1 and eIF4A2 in cancer

The expression of both eIF4A1 and eIF4A2 has been investigated in a large number of tumour types and has provided more insight into the potentially divergent roles of the two proteins[335]. eIF4A1 overexpression has been observed in several cancer types including gastric cancer, cervical cancer and breast cancer and is associated with tumour stage and poor patient prognosis[342–344]. Furthermore, *eIF4A1*, as well as *eIF4E* and *eIF4G1* gene expression, but not *eIF4A2*, is regulated by the oncogene c-myc which is often overexpressed in many tumours[345]. Importantly, previous studies using HCT116 colorectal cancer cells have shown that eIF4A1 expression is unaltered in response to hypoxia[346]. Additionally, under hypoxic conditions, eIF4A1 does not associate with the hypoxic polysome fraction in HEK293 cells[347].

In contrast to eIF4A1 expression, high eIF4A2 expression observed in NSCLC and breast cancer is associated with better patient outcome and overall survival[348,349]. More recently, further studies into the role of eIF4A2 in cancer progression have revealed that

high eIF4A2 expression is associated with worse prognosis and is an independent prognostic factor in patients with oesophageal squamous cell carcinoma[350]. Inhibition of eIF4A2 expression by miRNA-mediated repression has also been shown to inhibit cell proliferation in triple-negative breast cancer[351]. Recently, the clinical significance of eIF4A2 in colorectal cancer has been investigated and shows that eIF4A2 mRNA expression is higher in colorectal cancer tissue compared to non-cancerous tissue; is a prognostic factor for reduced overall survival and disease-free survival, and correlates with tumour stage[352]. Furthermore, knockdown of eIF4A2 in colorectal cancer cell lines reduced cell proliferation, colony formation and migration *in vitro*[352]. A second study has since confirmed these findings, showing that knockdown or chemical inhibition of eIF4A2 inhibits CRC cell migration and spheroid formation *in vitro* as well as inhibiting lung metastasis *in vivo*[353]. Importantly, the role of eIF4A2 in a hypoxia-specific context in CRC was not investigated.

Role of eIF4A2 in hypoxia

One study using squamous cell carcinoma cell lines demonstrated that eIF4A2 mRNA was upregulated under both hypoxic and acidic conditions as well as concurrent hypoxia-acidosis; a common feature of most solid tumours[354]. However, no further investigation into the role of eIF4A2 in hypoxia was carried out. Previous work carried out by the Mcintyre lab identified eIF4A2 as a key regulator of hypoxic CRC cell viability using an shRNA lentiviral screen (unpublished data). The lab has since investigated the role of eIF4A2 in hypoxia in CRC[355]. This work shows that eIF4A2 mRNA, but not eIF4A2 protein levels, are upregulated in response to hypoxia in CRC cell lines *in vitro* and this is HIF-2α-dependent in the LS174T cell line. The regulation of eIF4A2 by HIF-2α may be explained by the presence of RBM4 CGG binding motifs in the 3' UTR of eIF4A2 and other studies identified that eIF4A2 interacts with the hypoxia-specific HIF-2α-RBM4-eIF4E complex vie this rHRE sequence which may promote preferential translation in hypoxia[316]. The Mcintyre lab has also demonstrated that knockdown of eIF4A2 *in vitro* leads to a reduction in CRC cell growth and colony formation in both normoxia and hypoxia[355]. Furthermore, eIF4A2 knockdown led to a reduction in 3-dimensional spheroid growth and increased the amount of necrosis present within the hypoxic core of the spheroids[355]. Importantly, these studies utilised an inducible eIF4A2 knockdown system where only partial loss of eIF4A2 is observed. Due to the generally lower expression levels of eIF4A2 compared to eIF4A1, it may be that a more stringent

knockout system using CRISPR-Cas9 gene editing is required to fully examine the functional impact of eIF4A2 on CRC cell survival[331].

In order to elucidate the role of eIF4A2 in regulating protein synthesis in hypoxia, the Mcintyre Lab also demonstrated that eIF4A2 interacts with the CNOT7 component of the CCR4-NOT complex under normoxic conditions and that this interaction is reduced under hypoxic conditions[355]. Furthermore, RIP-Seq was employed to identify eIF4A2-bound mRNAs in hypoxic conditions and pathway analysis identified that hypoxic eIF4A2-bound mRNAs mostly encoded metabolic proteins, particularly those involved in amino acid biosynthetic pathways. This suggests that eIF4A2 may be regulating CRC cell adaptation to hypoxia by modulating the translation of proteins involved in cellular metabolism.

1.5 Metabolic adaptation to hypoxia

The rapid growth and proliferative rates of cancer cells coupled with a hypoxic microenvironment trigger large-scale remodelling of cellular metabolism in order to maintain ATP production and the biosynthetic requirements of rapidly growing tumours[30]. In normal cells, a constant supply of oxygen is required to sustain oxidative phosphorylation (OXPHOS) and ATP synthesis[356]. The high metabolic demand of cancer cells coupled with the lack of oxygen availability leads to metabolic reprogramming, coordinated predominantly by the HIF transcription factors[356].

1.5.1 Hypoxic regulation of glucose metabolism

The most well-documented metabolic adaptation seen in cancer cells is the phenomenon known as aerobic glycolysis or the Warburg effect[75]. Cancer cells switch from using OXPHOS to glycolysis as the main source of ATP synthesis, even under aerobic conditions, and pyruvate is preferentially converted to lactate instead of entering the TCA cycle[75]. The utilisation of glycolysis to generate ATP becomes even more important under hypoxic conditions when OXPHOS is inhibited. HIF-1α increases glucose flux into cancer cells by regulating the transcription of the *SLC2A1* and *SLC2A3* genes encoding the GLUT1 and GLUT3 glucose transporters[357,358]. Intracellular glucose is rapidly phosphorylated to glucose-6-phosphate (G6P) by hexokinase 1 and 2 (HK1/HK2) which are both upregulated by HIF-1α however, HK2 has been shown to

play the dominant role in G6P production in hypoxia[359]. G6P is an important metabolic intermediate that can be diverted towards several biosynthetic pathways, including the pentose phosphate pathway (PPP), glycogen synthesis and glycoprotein synthesis, and glycolysis[360]. However, in several cancer types, hypoxia has been shown to reduce the expression of PPP enzymes such as glucose-6-phosphate dehydrogenase (G6PD) and 6-phosphogluconate dehydrogenase (PGD) in favour of promoting glycolysis in response to hypoxic stress[361].

HIF-1α promotes glucose flux through the glycolytic pathway by upregulating all of the enzymes involved such as phosphofructokinases (PFK-1 and PFK-2), aldolases (ALDOA and ALDOC), phosphoglycerate kinase 1 (PGK1), enolases (ENO1 and ENO2) and pyruvate kinase 2 (PKM2) by binding to HREs in the promoter regions of these genes[362]. PFK-1 represents a key rate-limiting step of glycolysis regulating the irreversible conversion of fructose-6-phosphate to fructose-1,6-bisphosphate and is allosterically regulated by fructose-2,6-bisphosphate (F-2,6-BP)[363]. F-2,6-BP synthesis is regulated by the enzyme 6-phosphofructo-2-kinase/fructose-2,6-bisphosphatase (PFKFB)[364]. The isozyme PFKFB3 is stimulated by HIF-1α in hypoxia to promote F-2,6-BP synthesis, activate PFK-1 and increase glycolytic flux and is commonly overexpressed in a wide variety of cancers[365,366].

Due to the increased rate of glycolysis, hypoxic cancer cells must also activate several mechanisms to remove excess pyruvate whilst preventing pyruvate entry into the TCA cycle in order to reduce OXPHOS. HIF-1α increases the expression of lactate dehydrogenase (LDHA) which converts pyruvate and nicotinamide adenine dinucleotide (NADH) into lactate, the end product of aerobic glycolysis, and NAD^+[367]. Excess lactate is then exported from hypoxic cancer cells due to the HIF-1α-mediated upregulation of the monocarboxylate transporter 4 (MCT4) whilst NAD^+ is recycled by glyceraldehyde-3-phosphate dehydrogenase (GAPDH) to trigger additional cycles of glycolysis[368]. Furthermore, pyruvate entry into the TCA cycle is inhibited by the upregulation of pyruvate dehydrogenase kinase (PDK1) by HIF-1α which phosphorylates and inactivates pyruvate dehydrogenase (PDH) and prevents the conversion of pyruvate into acetyl-CoA in the mitochondria[369,370].

Interestingly, in HIF-1α-deficient CRC cell lines, glucose uptake is maintained through the HIF-2α-mediated upregulation of an alternative glucose transporter GLUT14[371]. Furthermore, HIF-1α deletion leads to an accumulation of glycolytic intermediates with reduced glycolytic enzyme expression and glycolytic flux[371]. Interestingly, the key step blocking glycolytic flux in HIF-1α deficient cells is regulated by ALDOA, and not PFK-1 as described earlier, and ALDOA expression has been shown to be increased in hypoxia in CRC and is associated with worse patient prognosis[371,372].

1.5.2 Hypoxic regulation of lipid metabolism

Cancer cells utilise fatty acids, either imported through exogenous uptake or synthesised *de novo*, in a large range of biological processes including oxidation for energy production, energy storage in the form of triacylglycerols (TAGs) and the synthesis of important signalling molecules and plasma membrane components[373]. As fatty acid oxidation takes place in the mitochondria in an oxygen-dependent manner, lipid accumulation and storage in response to hypoxia is seen in a large number of cancers and is under complex regulation by both HIF-1α and HIF-2α[374].

The uptake of extracellular fatty acids is increased in hypoxia through the HIF-1α-mediated activation of the transcription factor peroxisome proliferator-activated receptor γ (PPARγ) which upregulates the expression of the fatty acid binding proteins 3, 4 and 7 (FABP3/4/7)[375,376]. Additionally, HIF-1α increases lipoprotein endocytosis by upregulating the expression of the VLDL receptor (VLDLR) and LDLR-related protein (LRP1)[377,378].

Similarly, increased *de novo* fatty acid synthesis from the precursor acetyl-CoA also contributes to the lipid accumulation seen in hypoxia however, the normal conversion of pyruvate into acetyl-CoA is inhibited by the hypoxia-induced expression of PDK1[370]. Therefore, cancer cells employ an alternative pathway for synthesising acetyl-CoA to sustain fatty acid production through the reductive carboxylation of glutamine via glutaminolysis (see 1.5.3)[379]. The end product of glutaminolysis, citrate, plays a critically important role in cancer cells by acting as a substrate for acetyl-CoA production by the enzyme ATP citrate lyase (ACYL) which is upregulated in hypoxia[380,381]. Alternatively, acetyl-CoA can be generated by the conversion of acetate into acetyl-CoA by the enzyme

acetyl-CoA synthetase (ACSS2) which is also upregulated in hypoxic cancer cells and, in turn, promotes the acetylation and activation of HIF-2α[382]. Finally, the rate-limiting enzyme complex of fatty acid synthesis, fatty acid synthase (FASN), is also upregulated in hypoxia in a variety of cancers[383].

Conversely, lipid accumulation in hypoxia is further enhanced by the HIF-mediated inhibition of fatty acid β-oxidation[384]. Hypoxia leads to a reduction in the transcriptional coactivator proliferator-activated receptor-ɣ coactivator-1α (PGC-1α) in a HIF-1α and HIF-2α-dependent manner which in turn reduces the expression of the medium and long-chain acyl-CoA dehydrogenase enzymes (MCAD and LCAD) which catalyse the first step in fatty acid oxidation[384,385]. Furthermore, HIF-1α reduces the expression of carnitine palmitoyltransferase 1 (CPT1A) which is essential for the transport of fatty acids into the mitochondria for oxidation[386].

1.5.3 Hypoxic regulation of amino acid metabolism

Aside from the vital importance of central carbon metabolism to energy production and cancer cell survival, additional non-carbon sources of energy and biosynthetic intermediates must exist to sustain the increased energy demand and high proliferative rates of rapidly growing tumour cells[387]. Amino acids are now recognised as an important source of energy for cancer cells as well as providing a range of intermediates required for the biosynthesis of nucleotides, proteins and fatty acids[388].

Glutamine

Glutamine, the most abundant amino acid in blood plasma, is vital for the synthesis of TCA cycle intermediates, nucleotides, fatty acids, amino acids and ATP production[389]. Rapidly proliferating cells, including cancer cells, become highly dependent on glutamine which is converted to glutamate by the mitochondrial glutaminase (GLS1) enzyme[390]. Glutamate is then deaminated to α-ketoglutarate (α-KG) by glutamate dehydrogenase (GDH)[391]. When TCA cycle flux is reduced in conditions such as hypoxia, α-KG can be exported to the cytoplasm and converted to citrate by isocitrate dehydrogenase (IDH1) and then into acetyl-CoA for fatty acid synthesis[379].

Glutamine is imported into cancer cells via multiple transporters including the *SLC1A5* transporter which is highly expressed in a large number of cancers and is upregulated in

hypoxia[392]. Furthermore, glutamine import into the mitochondria, a required step in glutaminolysis, is regulated by a SLC1A5 variant that is upregulated in hypoxia in a HIF-2α-dependent manner[393]. In hypoxia, glutamine becomes the major source of citrate[394]. HIF-mediated inhibition of PDK1 contributes indirectly to increased citrate levels however, hypoxia also promotes glutaminolysis by upregulating glutaminase 1 (GLS1) in a HIF-2α and c-myc-dependent manner[395,396]. In addition, HIF-1α induces GDH and IDH1/2 expression[379,397]. A feedback mechanism also exists whereby several intermediates within the glutaminolysis pathway including 2-hydroxyglutarate (generated by mutant IDH1/2), and succinate function to stabilise HIF-1α through inhibition of the PHD and FIH enzymes[398].

Glutamate is also an essential precursor to glutathione (GSH) which is utilised by peroxidase enzymes in the maintenance of ROS homeostasis[399]. Approximately 50% of non-essential amino acid biosynthesis is also derived from glutamine metabolism in cancer cells due to its ability to function as a nitrogen donor in transamination reactions for the production of alanine, aspartate and serine[400]. Glutamate pyruvate transaminase 2 (GPT2) has recently been shown to promote tumourigenesis in glioblastoma in a HIF-2α -dependent manner[401]. Similarly, phosphoserine transaminase 1 (PSAT1) is overexpressed in a large number of cancers including breast and colon cancer and is commonly upregulated in hypoxia in an ATF4-dependent manner[402,403].

Branched-chain amino acids

The branched-chain amino acids (BCAAs) - leucine, isoleucine and valine – are obtained in the diet and are critical for maintaining the high proliferative rates of cancer cells by providing the building blocks for nucleotides, proteins and lipids[404]. BCAAs are transported into cells via a family of L-type amino acid transporters (LAT1-4) and broken down into α-ketoacids by the cytosolic and mitochondrial enzymes branched-chain aminotransferase 1 and 2 (BCAT1/BCAT2)[405]. The main transporter, LAT1 (*SLC7A5)*, is upregulated in many cancers and is activated in hypoxia in a c-myc and HIF-2α-dependent manner to increase BCAA import and mTORC1 signalling[406,407]. Similarly, BCAT1 is upregulated in hypoxia in a HIF-1α-dependent manner to remodel BCAA metabolism in cancer cells and help maintain the intracellular pool of α-KG for glutamate and acetyl-CoA production[408].

Serine and glycine

Serine and glycine are both crucial for cancer cell proliferation as sources of one-carbon donation for the synthesis of nucleotides and DNA methylation as well as for maintaining redox homeostasis[409]. Serine can be imported into cells via transporters such as ASCT1 and SNAT1/2 which are both upregulated in hypoxic conditions[410,411]. Cancer cells can also synthesise serine from glucose via the intracellular serine synthesis pathway (SSP) which is essential for tumour progression[412]. The glycolytic intermediate 3-phosphoglycerate (3-PG) is converted to serine in a series of three reactions catalysed by phosphoglycerate dehydrogenase (PHGDH), PSAT1 and phosphoserine phosphatase (PSPH)[413]. The expression of all three SSP enzymes is increased in a large number of cancers including CRC and breast cancer[414,415]. Furthermore, hypoxia leads to increased expression of all three SSP enzymes in a HIF-1α-dependent manner but also in response to hypoxia-induced stress response pathways and ATF4 activation[403,416].

Serine is critical to the synthesis of the one-carbon unit 5,10-methylene tetrahydrofolate (5,10-MTHF), essential for nucleotide biosynthesis, through the donation of its β-carbon to tetrahydrofolate (THF) to form glycine and 5,10-MTHF in a reaction catalysed by serine hydroxymethyltransferase 2 (SHMT2) in the mitochondria[417]. A series of one-carbon transfers then occur in the mitochondria catalysed by two related enzymes: methylene THF dehydrogenase 2 (MTHFD2) and methylene THF dehydrogenase 1-like (MTHFD1L) generating the key biosynthetic intermediate formate, as well as NADPH, which can be shuttled to the cytoplasm or nucleus for use in the synthesis of purines and thymidylate respectively[417]. Interestingly, all of the mitochondrial folate cycle enzymes, but not their cytosolic equivalents, are overexpressed in many cancer types and are upregulated in hypoxia in a HIF-1α-dependent manner to sustain nucleotide biosynthesis[403,418]. Furthermore, this hypoxic adaptation aims to maintain redox balance by generating excess glycine which can then be utilised, in combination with cysteine and folate cycle-generated NADPH, in the production of GSH[419].

Other amino acids

Arginine is another amino acid critical for cancer cell survival as it is a precursor to a range of important metabolites and molecules including polyamines, creatine, nitric oxide and other amino acids[420]. *De novo* arginine synthesis is carried out through the urea cycle. Interestingly, the rate-limiting enzyme in arginine synthesis, arginosuccinate synthetase 1

(ASS1) has been shown to be downregulated in hypoxia in several cancer types via HIF-1α-mediated miRNA repression to increase the aspartate pool for nucleotide biosynthesis as well as maintain intracellular pH[421].

Several enzymes involved in the key stages of proline biosynthesis are also upregulated under hypoxic conditions including aldehyde dehydrogenase 18 family member A1 (ALDH18A1), which is under HIF-1α regulation and leads to an accumulation of hydroxyproline due to inactivation of proline dehydrogenase 2 (PRODH2)[422]. Mitochondrial pyrroline-5-carboxylate reductase 1 (PYCR1) is also upregulated in hypoxia leading to increased proline synthesis and NADH oxidation for refuelling glycolysis[423].

1.5.6 Role of eIF4A2 in metabolic adaptation to hypoxia

As discussed in section 1.4.5, previous work carried out by the Mcinytre lab identified that a large number of mRNAs encoding metabolic genes are bound by eIF4A2 under hypoxic conditions in colorectal cancer cells. Many hypoxia-induced glycolytic enzymes were enriched for eIF4A2-binding in hypoxia suggesting that the increased hypoxic translation of these proteins may be playing a role in their upregulation[355]. Interestingly, the two most significantly enriched KEGG pathways for eIF4A2-binding in hypoxia were amino acid biosynthesis and endocytosis.

Several well-known hypoxia-associated enzymes involved in amino acid metabolism were identified including PHGDH, GPT2, ALDH18A1, BCAT1 and ASS1. However, the most enriched gene for eIF4A2 binding in hypoxia encoded the enzyme cystathionine-γ-lyase (CTH) and siRNA knockdown of eIF4A2 led to a reduction in CTH protein expression confirming the translational regulation of CTH in both normoxia and hypoxia[355].

CTH is a pyridoxal-5'-phosphate-dependent enzyme which functions as part of the transsulfuration pathway that synthesises cysteine from methionine and plays a central role in sulfur metabolism within cells (figure 1.12). It also plays a role in the production of the gaseous signalling molecule hydrogen sulfide, H_2S. CTH overexpression as well as increased cysteine and H_2S production have been implicated in tumour progression in a growing number of cancers[424].

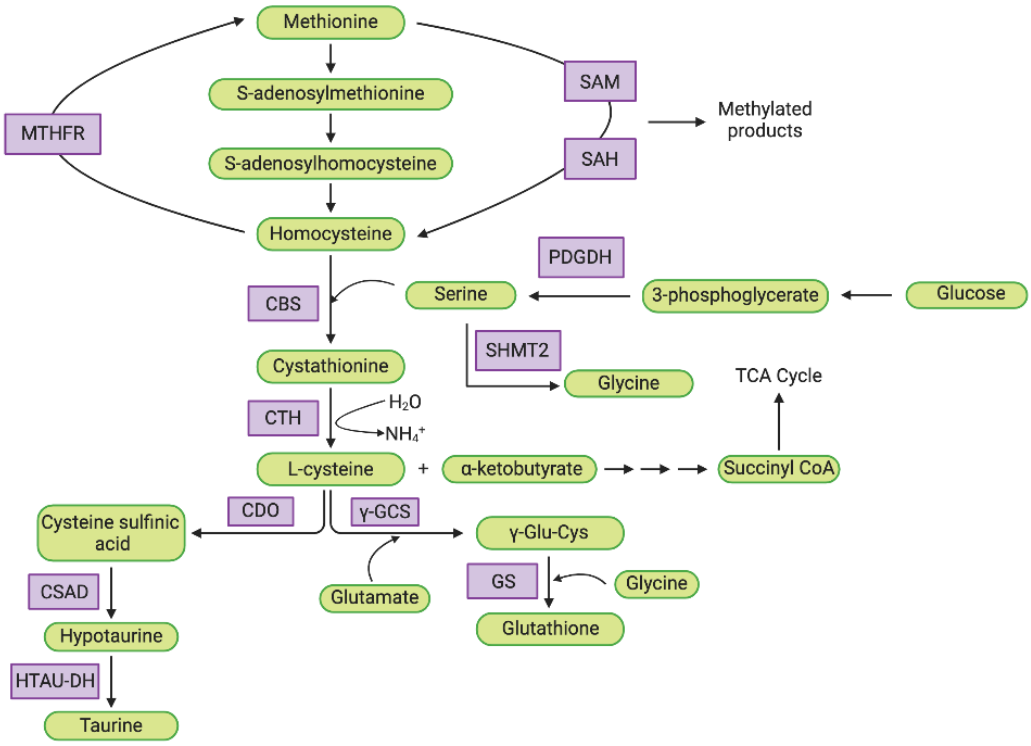

Figure 1.12 The transsulfuration pathway. Dietary methionine is converted into homocysteine through the sequential actions of S-adenosylmethionine (SAM) and S-adenosylhomocysteine (SAH). Homocysteine is condensed with serine in a reaction catalysed by cystathionine-β-synthase (CBS) to generate cystathionine. Cystathionine is metabolised to L-cysteine by CTH, producing ammonia and α-ketobutyrate as by-products. L-cysteine is utilised in protein translation but can also be metabolised into glutathione through the actions of γ-glutamyl cysteine synthetase (γ-GCS) and glutathione synthetase (GS) which catalyse the addition of glutamate and glycine to L-cysteine respectively.

CTH has been shown to be upregulated in hypoxic hepatoma cells and contribute to hypoxia-induced radioresistance through increased H_2S production[425]. CTH overexpression in CRC has been shown to be regulated by increased PI3K/Akt signalling[426]. Furthermore, elevated Wnt signalling has been shown to induce the expression of CTH in colorectal cancer leading to increased cell proliferation, migration and tumour xenograft growth *in vivo*[427]. Interestingly, induction of the UPR in response to ER stress leads to the eIF2α-mediated activation of ATF4 which regulates the expression of CTH and therefore promotes cysteine and GSH synthesis to maintain cellular homeostasis[428]. However, the role of CTH in regulating cancer cell growth and survival in response to hypoxia, specifically in CRC, has not been investigated.

1.6 Analysing spatial metabolic heterogeneity

Hypoxia-associated metabolic adaptations have important consequences for cancer progression and therapeutic intervention[429]. Recently, the ability to characterise tumours from 33 different cancer types based on the expression patterns of metabolic signatures was demonstrated and correlated with clinical outcome[430]. Furthermore, single-cell transcriptome profiling of TAMs showed that they exhibit markedly heterogeneous metabolic responses which correlate with function[431]. TAMs with elevated purine metabolism display a pro-tumourigenic phenotype which leads to reduced therapeutic efficacy[431]. Therefore, the ability to detect, measure and analyse metabolites with subcellular spatial resolution is becoming increasingly important for understanding metabolic heterogeneity at the single-cell level[432]. This is particularly important for cancer therapy as most tumours consist of a highly heterogeneous mix of cell populations with distinct metabolic and phenotypic characteristics[431,432]. Furthermore, oxygen concentration-dependent metabolic changes compound this heterogeneity as different tumour cell populations are exposed to a range of oxygen concentrations. Therefore, to measure and analyse the metabolic adaptation to hypoxia in tumours most accurately and representatively, spatial metabolomics techniques with subcellular resolution are required[433]. Additionally, the use of *in vitro* 3-dimensional cell culture models to study cancer metabolism has become increasingly important due to their ability to better represent the *in vivo* tumour microenvironment and the complex networks of cell interactions and nutrient gradients seen within poorly vascularised tumours, critical for studying metabolic heterogeneity[434].

1.6.1 Mass spectrometry-based metabolomics

Mass spectrometry (MS) techniques have played an important role in the bulk detection and quantification of metabolites extracted from homogenised tissue or cell lysates and have contributed to the understanding of cancer progression and the development of improved cancer therapeutics[435]. Traditional MS-based bulk metabolomics approaches for use in cancer studies consist of either gas chromatography MS (GC-MS) or, more commonly, liquid chromatography MS (LC-MS) methods[436,437]. However, one major problem with both GC-MS and LC-MS methods is that the sample preparation involves the extraction and quenching of intracellular metabolites as well as the homogenisation of tissue or cell samples[438]. Therefore, these techniques cannot provide any information

on the spatial distribution or localisation of metabolites within samples[439]. The development of imaging MS (MSI) techniques combines the high sensitivity of MS-based detection methods with spatial resolution to analyse metabolites at the single-cell level[440].

1.6.2 Imaging mass spectrometry-based metabolomics

Single-cell MSI is a powerful technique for analysing the distribution of metabolites with subcellular resolution[441]. However, moving from bulk metabolomics to the single-cell level provides several challenges[442]. For example, the highly dynamic nature of the metabolome in response to the local environment, such as the hypoxic microenvironment in tumours, requires accurate quenching of cellular metabolism in the required physiological state prior to measuring[443]. Furthermore, the human metabolome is estimated to consist of >200,000 molecules and this large chemical diversity makes the accurate detection of individual metabolites challenging[442,444]. The inability to amplify or tag metabolites compounds this problem, particularly for low-abundance metabolites[442]. Therefore, single-cell MSI metabolomics requires the use of label-free methods with enhanced chemical specificity and range of detection.

MSI techniques are characterised based on the ionisation source used to ablate molecules from the sample surface and the mass analyser used to detect and analyse the desorbed molecules[445]. The most commonly used MSI techniques include desorption electrospray ionisation (DESI), matrix-assisted laser desorption ionisation (MALDI) and secondary ion mass spectrometry (SIMS)[446]. Despite being the most commonly used MSI method for studying metabolomics, MALDI-MS has a limited spatial resolution of 5-200 μm compared to the sub-micron (50-100 nm) resolution of SIMS[447,448]. Furthermore, MSI techniques that utilise artificial matrices for sample capture, including MALDI, can cause unwanted 'matrix effects' which can lead to changes in ionisation of small molecules and disruption of their spatial distribution[449]. Therefore, in the case of spatial metabolomics, SIMS is the preferred technique for carrying out single-cell MSI[441].

SIMS is a label-free, matrix-free technique that utilises a primary ion beam to desorb molecules from the sample surface[450]. Desorbed molecules are ionised, generating secondary ions that can be detected by a mass analyser[451]. The superior spatial resolution and surface sensitivity make SIMS the optimal choice for single-cell metabolomics imaging[452]. However, there are several physical and biological limitations associated with

SIMS MSI that pose significant challenges for accurately detecting and characterising metabolites at single-cell resolution. Sample preparation has a significant impact on imaging quality as fluctuations in sample temperature can lead to molecule migration and reduced ionisation efficiency during analysis, resulting in loss of spatial information[453]. Preparing and maintaining samples under cryogenic conditions therefore greatly improve the spatial imaging capabilities of SIMS and keep samples in their intact, physiological state[453].

The composition of the primary ion beam can also impact the resolving power and imaging capabilities of the instrument[448]. Monoatomic ion beams, most commonly in the form of liquid metal ion guns (LMIG), can be focused to < 50 nm and so provide subcellular resolution for imaging however, they cause increased fragmentation of desorbed molecules, making accurate molecule characterisation more challenging[448,454]. Alternatively, gas cluster ion beams (GCIB), which can be focused to < 3 μm cause less fragmentation and improved ionisation efficiency compared with LMIG sources and GCIB-SIMS has been shown to improve the ability to detect metabolites such as increased *de novo* purine biosynthesis in purine-depleted cells[455,456].

Due to the molecular fragmentation caused by the ion beams during desorption, advances in SIMS technology have focused on the incorporation of tandem MS (MS/MS) capabilities for the accurate identification of biomolecules from fragmented ions as well as improving the spatial and mass resolving power of SIMS instruments[457]. Time-of-flight (ToF) SIMS with MS/MS imaging capability has become a powerful technique for small molecule analysis as it combines the high spatial resolution of ToF-SIMS with the ability to detect and interpret molecular fragments[458]. However, despite the rapid imaging rate of ToF analysers, they lack the mass resolving power needed to accurately identify biomolecules[459]. The development of high-resolution tandem mass analysers, such as the Orbitrap mass analyser, with a mass resolving power or 10^5-10^6 (accurate to <1 ppm), has enabled the detection and identification of biomolecules including metabolites[460]. These technologies have led to the development of hybrid SIMS instruments that combine the spatial resolving power of ToF-SIMS with increased mass resolving power for spatial metabolomics analysis.

1.6.3 3-dimensional OrbiSIMS

The 3-D OrbiSIMS is a hybrid mass analyser combining the high spatial resolving power of a ToF-SIMS analyser (TOF.SIMS 5, ION-TOF) with the high mass resolving power and mass accuracy of an orbitrap mass analyser (Q Exactive HF, Thermo Fisher Scientific) (figure 1.13)[459,461]. The dual beam setup, consisting of a 30 keV Bi LMIG and a 5-20 keV Ar GCIB, combined with the dual analyser configuration enables 10 different operational modes for carrying out a range of analyses and 2-D or 3-D imaging (table 1.2)[459]. This hybrid approach allows individual high spatial resolution 2-D images to be taken at different depths using the Bi LMIG with the ToF analyser which rapidly sputters away material from the sample surface. The depth between images is then precisely controlled by the gentle sputtering using the Ar GCIB and desorbed ions are analysed by the orbitrap to generate high-resolution mass spectra in-between LMIG image acquisitions[459]. This approach was used to map the distribution of drugs within single cells and reconstruct a 3-D image from the individual 2-D ToF images[459]. Furthermore, the metabolic profiles of single macrophage cells in response to different drug concentrations were analysed and specific metabolic responses were correlated with drug dosage[459]. More recently, the 3-D OrbiSIMS was used to assess the metabolome of differentiated macrophage cells *in situ* and was able to characterise the M1 and M2 phenotypes of mature macrophages based on their individual metabolic profiles[462].

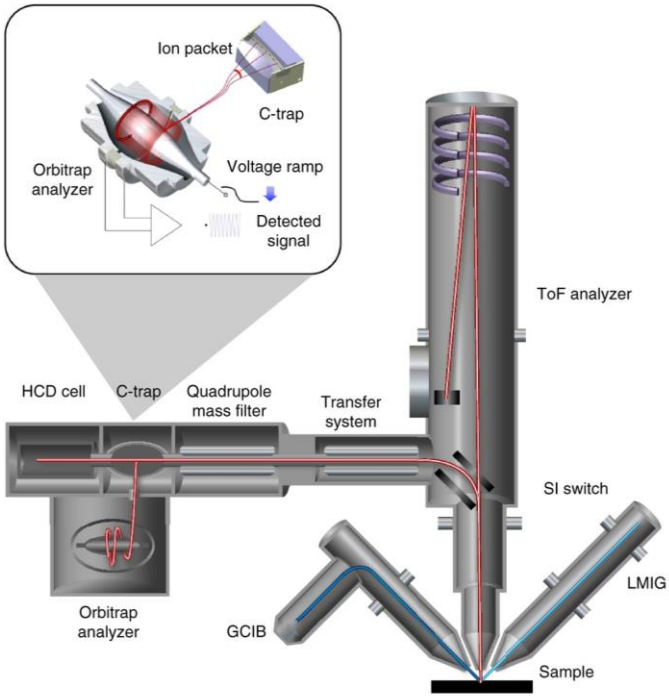

Figure 1.13 3-dimensional OrbiSIMS schematic. Adapted by permission from Springer Nature: Springer, Nature Methods, 'The 3D OrbiSIMS—label-free metabolic imaging with subcellular lateral resolution and high mass-resolving power', Passarelli *et al*, 2017.

However, one complication is that the high vacuum conditions required for OrbiSIMS analysis require specific sample preparation techniques; most commonly involving chemical fixation or plunge freezing followed by drying[463]. These methods can cause unwanted molecule migration and morphological alterations that disrupt the native spatial distribution of small molecules such as metabolites[464]. Analysing biological samples under cryogenic conditions in a native frozen-hydrated state can prevent this redistribution and generate more accurate mass spectra[465]. Avoiding water crystal formation during cryogenic sample preparation is also critical for the prevention of molecule migration and rupturing of cell membranes[466]. Plunge freezing is the most common cryogenic sample preparation technique for SIMS[466]. However, this technique is only fast enough to form non-crystalline, or vitreous, ice in thin samples < 20 μm and is not suitable for thicker samples such as tissue or multicellular 3-D models due to the formation of crystalline ice[467].

Mode	Primary ion	Mass analyser	Application
1	Bi or Ar (single beam)	ToF	Surface spectra
2		Orbitrap	
3	Bi or Ar (single beam)	ToF	Depth profiling
4	Bi and Ar (dual beam)	Orbitrap	
5		ToF + orbitrap	
6	Bi or Ar (single beam)	ToF	2-D imaging
7		Orbitrap	
8	Bi or Ar (single beam)	Orbitrap	3-D imaging
9	Bi and Ar (dual beam)	ToF	
10		ToF + orbitrap	

Table 1.2 Summary of the operational modes available with the 3-D OrbiSIMS. The 3-D OrbiSIMS has 10 different operational modes for different applications based on combinations of primary ion beam source and mass analyser used.

So far, little research assessing the applicability of the 3-D OrbiSIMS technique for the metabolic profiling and characterisation of tumour samples has been carried out. One study has recently utilised a tandem OrbiSIMS-liquid extraction surface analysis MS/MS (LESA-MS/MS) workflow to carry out metabolic profiling of paediatric brain tumour

samples[468]. This work demonstrated the ability of SIMS to predict tumour relapse based on the levels of key metabolites identified within the tumour samples[468]. Interestingly, this work was only carried out using chemically fixed tissue at room temperature. There is currently no research investigating the use of OrbiSIMS for analysing the spatial regulation of metabolic adaptation to hypoxia in cancer cells and tumour tissue and whether this could be used to direct personalised therapeutic intervention at the individual patient level.

1.6.4 3-dimensional models for studying cancer metabolism

Traditionally, 2-dimensional *in vitro* cell cultures have been the dominant pre-clinical methodology for probing cancer cell behaviour and understanding cellular mechanisms due to their ease of handling, reproducibility and cost-effectiveness[434]. However, when considering the complexity of the tumour microenvironment, limitations to using 2-D models become highly evident. The lack of cell-cell interactions and cell-ECM contacts in 2-D models that are found within the *in vivo* microenvironment leads to significant changes in the signalling pathways controlling key cellular programmes including gene expression, proliferation and metabolism[469,470]. Furthermore, changes in cell morphology, receptor expression, oncogene expression and cell polarity noticed in 2-D cell culture have led to questioning the applicability of 2-D cell culture for replicating cancer behaviour *in vivo*[434]. This has led to the rapid development of 3-dimensional cell culture models, including 3D spheroids, in attempts to better model the tumour microenvironment of various cancer types such as CRC[471].

Several characteristics of 3D spheroids are crucial for their ability to represent solid tumours *in vitro* (figure 1.14). Spheroids can be cultured exclusively as cancer cells or co-cultured with other cell types including stromal cells and immune cells[472,473]. The introduction of multiple cell types better mimics the cellular heterogeneity seen within solid tumours and promotes cell-cell communication and activation of intercellular signalling pathways within the microenvironment[473,474]. Similarly, cells within 3D spheroids have been shown to deposit ECM components including laminin and proteoglycans to form a tumour-like extracellular matrix which increases cell density and interstitial fluid more closely matching that seen in solid tumours as well as activating ECM-regulated signalling pathways[475,476].

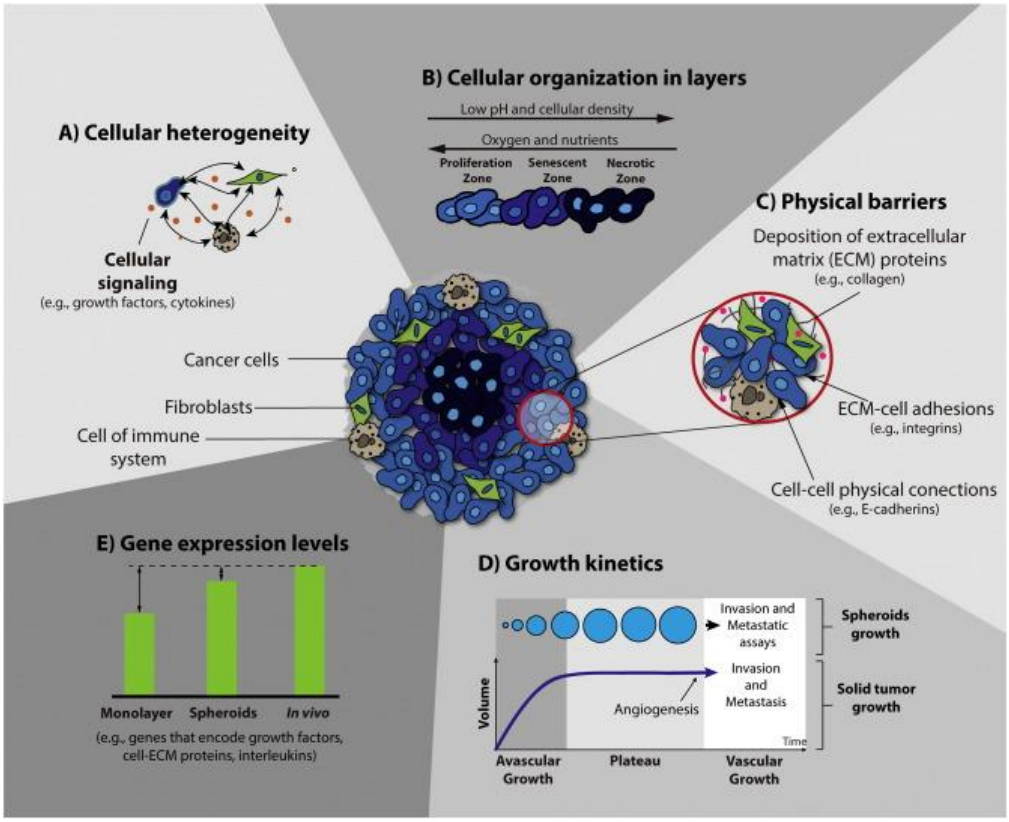

Figure 1.14 Schematic representation of 3D spheroid characteristics for more accurate modelling of the solid tumour microenvironment. Adapted by permission from Elsevier, Biotechnology Advances, '3D tumour spheroids: an overview on the tools and techniques used for their analysis', Costa *et al*, 2016.

In addition, the 3-dimensional structure of spheroids also parallels the internal structure seen in solid tumours consisting of an outer proliferative layer of cells, a senescent middle layer and a necrotic core, generated by the oxygen and nutrient gradients which form as the spheroids grow[477]. Importantly, the oxygen gradient generates a hypoxic microenvironment near the spheroid core which activates the hypoxic response and the metabolic switch to anaerobic glycolysis resulting in metabolic reprogramming and acidification, both of which are common features of solid tumours[478]. The layered structure of 3D spheroids makes them an ideal model for studying cancer pathways with spatial resolution, particularly in relation to hypoxia and the oxygen-dependent metabolic response.

Importantly, the gene expression profiles of 3D spheroids more closely match those observed in solid tumours compared with 2D cell culture as has been demonstrated for a variety of cancers including liver and CRC[479,480]. Furthermore, cancer cell metabolism changes rapidly in response to nutrient availability, oxygen concentration and

microenvironment interactions. Recent studies have shown that the metabolic fingerprints of *in vitro* 3D spheroids are highly comparable to tumour tissue as opposed to conventional 2D cell culture. For example, CRC cell lines cultured in 2D and 3D spheroids showed drastic differences in glucose metabolism[481]. In particular, anaerobic ATP production was increased in 3D spheroids coupled with elevated MCT transporter expression, indicative of the Warburg effect, a feature not observed in 2D culture[481]. Similarly, renal cell lines grown in 2D and 3D spheroid cultures displayed markedly different metabolic patterns[482]. Whilst 2D cells displayed elevated levels of glycolytic intermediates, lipids and amino acids, these metabolites were significantly reduced in spheroids and this was more representative of the metabolic fingerprint of isolated kidney tissue[482]. These studies highlight the importance of developing 3D culture models for probing the metabolic reprogramming seen within solid tumours and for the development of metabolism-targeted therapeutics.

1.7 Project aims

This study aims to investigate the role of eIF4A2 in the regulation of hypoxic protein translation in colorectal cancer cells and the regulation of amino acid biosynthesis protein translation, such as CTH. This study also aims to assess the functional role of eIF4A2 and target genes, such as CTH, in regulating cancer cell growth and survival *in vitro* with the development of CRISPR-Cas9 gene editing methods. Further to this, the spatial regulation of metabolic adaptation to hypoxia in colorectal cancer will be investigated by 3-D OrbiSIMS using *in vitro* 3-D models and *in vivo* samples and correlated with RNA sequencing data. Specifically, this work will focus on the following aims:

Chapter 3:

1. Identify the role of eIF4A2 and its binding partners in hypoxic cap-dependent protein translation

2. Determine the functional role of eIF4A2 in the regulation of CRC cell growth and survival *in vitro*

3. Determine the functional role of eIF4A2 target genes, such as CTH, in the regulation of CRC cell growth and survival *in vitro*

Following the results obtained in Chapter 3 it was decided to focus the orbiSIMS analysis on HIF-1α and HIF-2α as well-established regulators of metabolism in hypoxia in order to aid the development of a novel and complex mass spectrometry imaging technique. This allowed for analysis of HIF-dependent metabolic regulation across the oxygen gradient which has never been investigated previously.

Chapter 4:

4. Develop a 3-D OrbiSIMS workflow for the analysis of the spatial regulation of metabolic adaptation in hypoxic CRC

5. Determine the roles of HIF-1α and HIF-2α in the spatial regulation of metabolic adaptation to hypoxia in CRC using 3-D OrbiSIMS and RNA-sequencing

Chapter 5:

6. Utilise the workflow to investigate and spatially resolve metabolic profiles of more complex in vivo xenograft/PDX samples

2. Materials and Methods

2.1 Cell culture and reagents

2.1.1 Culture of adherent cells

All cell culture was performed in a Class II microbiological safety cabinet (BioMAT2, Contained Air Solutions, UK). Colorectal cancer cell lines LS174T (CL-188™), HCT116 (CCL-247™), HT-29 (HTB-38™), DLD-1 (CCL-221™) and HCT-15 (CCL-225™) and SW-620 (CCL-227™) were obtained from the American Type Culture Collection and cultured in complete medium consisting of Dulbecco's modified Eagle's medium (DMEM- high glucose, Sigma Aldrich, MO, USA) supplemented with 10% [v/v] foetal bovine serum (FBS, Sigma Aldrich, MO, USA) unless stated otherwise. Cells were maintained at 37°C in a humidified incubator at 5% CO_2.

Cell lines were subcultured routinely when they reached 70% confluency in T75cm^2 flasks (Corning®, Thermo Fisher Scientific, MA, USA). Culture media was aspirated, and cells were washed once with sterile phosphate-buffered saline (PBS, Sigma Aldrich, MO, USA). Cells were detached from the base of the culture flask and each other using 1x Trypsin-Ethylenediaminetetraacetic acid (EDTA) solution (Sigma Aldrich, MO, USA) for 3-5 min at 37°C in a 5% CO_2 humidified incubator. Dissociation of cells from the base of the flask was determined by microscopy. An appropriate volume (2x volume of trypsin) of fresh complete medium was used to neutralise trypsin activity. Cells were then passaged at an appropriate ratio (typically 1:10-1:15) into clean T75cm^2 flasks containing 15 mL of complete medium and maintained at 37°C.

All cell lines were routinely tested for mycoplasma using the PlasmoTest™ mycoplasma detection kit (InvivoGen, CA, USA). Briefly, 500 µL of cell culture medium was heated to 100°C for 15 min and 50 µL was then added to a well of a 96-well plate. 200 µL of HEK-blue™-2 cell suspension prepared in HEK-blue™ detection medium was added to each well of the 96-well plate. The plate was incubated overnight at 37°C in a 5% CO_2 incubator. The presence of mycoplasma was confirmed by a colour change from pink to purple/blue measured by a spectrophotometer at 620-655 nm.

2.1.2 Hypoxic cell culture

Hypoxia was induced by incubating cells at 37°C under hypoxic conditions (1% pO_2 [<7.6 mmHg]) in a 5% CO_2, nitrogen-balanced Hypoxia Workstation InvivO2 400/500 (Baker Ruskinn, UK).

Physoxia was induced by incubating cells at 37°C under physoxic conditions (8.5% pO_2 [64.6 mmHg]) in a 5% CO_2, nitrogen-balanced Hypoxia Workstation Inviv0_2 400 (Baker Ruskinn, UK)[184].

2.1.3 Cell counting

Cell lines were detached from the flasks and pelleted by centrifugation at 200 x *g* for 5 min in 15 mL falcon tubes. Cells were resuspended in complete medium and counted using a TC10™ automated cell counter (Bio-Rad, CA, USA) using dual-chamber TC10™/TC20™ cell counting slides (Bio-Rad, CA, USA) according to manufacturer's instructions. Briefly, 10 µL of cell suspension was transferred to a counting chamber and inserted into the machine. After counting, the cell suspension was diluted to the required concentration for further experiments.

2.1.4 Cryopreservation of cell lines

Cell lines were cultured to 70% confluency in T75cm^2 flasks then detached from the bottom of the flask (see 2.1.1) and pelleted by centrifugation at 200 x *g* for 5 min in 15 mL falcon tubes (Cellstar®, Greiner Bio-one, Austria). Cells were counted as described in 2.1.3 and resuspended at a concentration of 1x10^6 cells per mL in freezing media (90% [v/v] FBS, 10% [v/v] dimethyl sulfoxide [DMSO](Sigma Aldrich, MO, USA)) and 0.5 mL of the cell suspension was transferred into individual cryovials (Azenta Life Sciences, MA, USA). Cryovials were placed into a freezing container (Mr Frosty™; Thermo Fisher Scientific, MA, USA) containing the recommended level of 100% isopropanol (Sigma Aldrich, MO, USA) and frozen overnight at -80°C. Frozen cryovials were then transferred into a cryogenic storage system (Brooks Biostore™ III Cryo; Azenta Life Sciences, MA, USA) for long-term storage. Cell thawing was achieved by incubating cryovials in a 37°C water bath for 30 s. Cell suspensions were then transferred immediately into a T25cm^2 containing 5 mL pre-warmed complete medium and maintained at 37°C in a 5% CO_2 humidified incubator.

2.1.5 Inducible shRNA eIF4A2 knockdown

Pre-existing IPTG-inducible lentiviral shRNA particles generated using Sigma MISSION® custom lentiviral shRNA services were used previously to generate IPTG-inducible lentiviral shRNA particles (credit: Hannah Bolland). Two separate shRNA sequences, termed sh69 and sh84, were used to generate IPTG-inducible eIF4A2 knockdown cell lines (table 2.1). A control knockdown cell line, termed shCTL, was also generated by transduction with 3x LacO-inducible non-targeting shRNA control transduction particles (credit: Hannah Bolland, Sigma Aldrich, MO, USA). shRNA-mediated knockdown of eIF4A2 was induced with sterile dioxane-free IPTG (Formedium™, UK) made up to a working solution of 0.1 M in ultrapure H_2O. For eIF4A2 knockdown, cells were incubated with cell culture media containing 1 mM IPTG for 96 hours. Fresh IPTG-containing media was replaced daily.

Clone ID	Sequence (5'-3')
TRCN0000051869 (**sh69**)	CCGGCCGGGAGAGTGTTTGATATGTTCTCGAGAACATATCCAAACACTCTCCCGTTTTG
TRCN0000369484 (**sh84**)	CCGGAGTCGTGTTCTGATCACTACTCTCTCGAGAGTAGTGATCAGAACACGACTTTTTTG

Table 2.1 eIF4A2 shRNA sequences used to generate eIF4A2 knockdown cell lines.

2.1.6 Generation of siRNA knockdown cell lines

Dharmacon™ siGENOME SMARTpool siRNA (Horizon Discovery, UK) was introduced into cell lines using lipofection and a reverse transfection method (table 2.2). siRNAs were reconstituted at 20 µM in RNase-free water inside a class II MSC after centrifugation for 10 s at 16,000 x *g*. siRNAs were vortexed for 10 s and incubated on ice for 20 min before storing at -80°C. An AllStars negative control siRNA (100 µM stock, Qiagen, Germany) condition was included as a control. Transfection reagents were prepared in two sterile 1.5 mL Eppendorf tubes per siRNA per 10cm^2 cell culture dish (Corning®, Thermo Fisher Scientific, MA, USA). Tube A consisted of 8.75 µL siRNA diluted in 991.25 µL Opti-MEM™ reduced serum media (Thermo Fisher Scientific, MA, USA) and tube B consisted of 37.5 µL lipofectamine™ RNAiMAX reagent (Thermo Fisher Scientific, MA, USA) diluted in 962.5 µL Opti-MEM™. Oligonucleotide and lipofectamine™ solutions were mixed and incubated at room temperature. The

transfection mix was then added to the corresponding 10cm^2 dish by dotting the solution around the plate. Cell suspensions were then pipetted directly on top of the solution (reverse transfection).

Gene target	Catalogue number
EHD1	M-019022-02-0010
KIF5B	M-008867-00-0010
PLD2	M-005064-01-0010

Table 2.2 Catalogue ordering information for siRNA sequences used in this study.

Cells were harvested and counted as described in 2.1.3. After centrifugation, cell pellets were resuspended in Opti-MEM™. A 5 mL suspension containing 2.0x10^6 cells was added to each plate and mixed gently, giving a final siRNA concentration of 25 nM. 6 hours post-transfection the Opti-MEM™ and gRNA:lipofectamine™-containing media was aspirated from the cells and replaced with 10 mL fresh complete medium containing 10% FBS. Transfected cells were incubated at 37°C in a 5% CO_2 humidified incubator for 24 hours before harvesting for protein extraction.

2.2 3-Dimensional cell culture

2.2.1 *In vitro* spheroid formation

Cells were harvested and counted as described in 2.1. A fresh cell suspension was prepared containing enough cells to seed each inner well of an ultra-low attachment 96-well plate (Corning® Costar®, Thermo Fisher Scientific, MA, USA) with an appropriate number of cells as determined experimentally, typically 2000 cells/well, in a final volume of 100 µL complete medium. 200µL sterile PBS was added to the outer wells to prevent edge effects. LS174T cell line required the addition of Cultrex® basement membrane extract (BME, R&D Systems, MN, USA) at the optimised concentration of 200µg/mL to the cell suspension. Both the BME and cell suspensions containing BME® were always kept on ice and were added to 96-well plates kept on ice. Plates were centrifuged for 10 min at 2000 rpm to promote spheroid formation. The following day, denoted Day 1, an additional 100 µL of complete medium was added to each well. Spheroids were cultured for 10 days with 100 µL media changes taking place every other day (Days 3, 5, 7 and 9).

Spheroids were imaged on Days 3, 5, 7 and 10 on a widefield microscope (Nikon Eclipse Ti) at 4x magnification using NIS-elements imaging software (Nikon, NY, USA).

2.2.2 *In vitro* spheroid growth analysis

Spheroids were prepared and cultured as described in 2.2.1. Spheroids were imaged on Days 3, 5, 7 and 10 on a widefield microscope (Nikon Eclipse Ti) at 4x magnification using NIS-elements imaging software (Nikon, NY, USA). Images were exported to Fiji image processing software for further analysis (figure 2.1)[483].

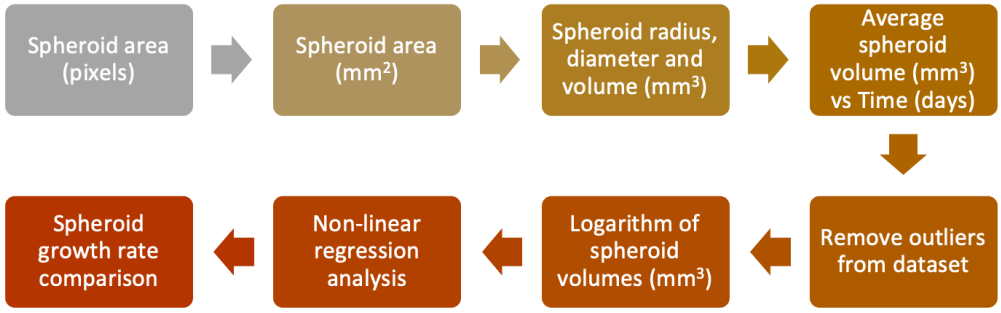

Figure 2.1 Spheroid growth analysis workflow. The area of each spheroid was measured in pixels and converted into mm^2 by using the number of pixels equating to $1mm^2$ of a haemocytometer. Spheroid area was used to calculate radius, diameter and volume. Spheroid volumes were used to calculate average spheroid volume (mm^2) which was plotted against time (days) using GraphPad Prism. Outliers in the data set were identified and removed using the ROUT method (Q = 1%) based on the false discovery rate (FDR) where Q is the maximum FDR i.e. if Q = 1% then 1% of the identified outliers will be false whereas the other 99% will be true outliers. This method allows for the possibility of identifying more than one outlier from a dataset. Spheroid growth rates were analysed by taking the logarithm of the spheroid volumes and plotting them against time (days). A non-linear regression analysis was then performed to fit a straight line through the data. The gradients of the straight lines were taken as the logarithmic values of spheroid growth rates and plotted as mean +/- standard deviation (SD).

2.2.3 Fixing and embedding spheroids for immunohistochemistry

After 10 days spheroids were aspirated from the 96-well plate using cut pipette tips and transferred to a 15 mL falcon tube. Excess media was removed, and spheroids were fixed in 5 mL 10% neutral-buffered formalin (Sigma Aldrich, MO, USA) overnight. For long-term storage spheroids were kept in 70% ethanol at 4°C. Fixed spheroids were embedded in 2% [w/v] agarose gel (6 spheroids per mould, Sigma Aldrich, MO, USA). Spheroids were aspirated from the falcon tube and placed in 0.2 mL PCR tubes (Starlab, Germany). Excess solvent was aspirated and replaced with ~200µL of 2% [w/v] agarose then allowed to set for 5 min. Agarose moulds containing spheroids were transferred

into labelled tissue cassettes. Samples were submerged in 50% [v/v] methanol (Sigma Aldrich, MO, USA) to prevent spheroids from drying out.

2.2.4 Tissue processing

Spheroids underwent a 13-hour tissue processing programme using a TP1020 semi-enclosed Benchtop Tissue Processor (Leica Biosystems, Germany). See table 2.3 for programme details. The spheroid samples were then embedded in paraffin wax and chilled using an EG1160 tissue embedding station (Leica Biosystems, Germany). Once cooled and the wax solidified, the excess wax was removed using a Paratrimmer™ (Thermo Fisher Scientific, MA, USA) and the blocks were stored at 4˚C until required for sectioning.

Solution	Duration (h)	No. of washes
50% methanol	1	1
70% methanol	1	1
90% methanol	1	1
100% methanol	1	4
100% xylene	1	2
Wax	2	2

Table 2.3 Tissue processor programme cycle details for spheroid and tissue embedding.

For sectioning, the paraffin blocks were mounted onto a manual rotary microtome (RM2135, Leica Biosystems, Germany) and cut into 4µm thick sections. The sections were flattened by floating into a water bath heated to 45˚C and then collected onto either SuperFrost™ or polysine microscopy slides depending on the downstream application (Thermo Fisher Scientific, MA, USA). Slides were left to air dry overnight at room temperature before storing at 4˚C.

2.3 Immunohistochemistry

2.3.1 H&E staining

Slides were first deparaffinized in a series of three xylene baths (5 min each) followed by rehydration in two methanol baths (1 min each). Slides were then transferred to a

staining stray submerged in a bath of distilled H_2O. The excess H_2O was removed and then haematoxylin (H) staining was performed with Mayer's Haemalum (Sigma Aldrich, MO, USA) by covering the slides in filtered staining solution and incubating them for 3 min. Excess haematoxylin was drained off the slides and then the slides were washed in a bath of running water for 1 min. Eosin staining was then performed by covering the slides with filtered eosin solution (acidified with 2 µL/mL glacial acetic acid; Sigma Aldrich, MO, USA) and incubating them for 3 min. Excess eosin was drained off the slides and then the slides were washed in a bath of running water for 1 min. Slides were then dehydrated in three methanol baths (1 min each) and then cleared in two xylene baths (3 min each) before cover-slipping with dibutyl phthalate in xylene (DPX; Sigma Aldrich, MO, USA). Cover-slipped slides were left to dry overnight at room temperature before storing at 4˚C.

2.3.2 Pimonidazole staining

Slides were first deparaffinized in a series of three xylene baths (5 min each) followed by rehydration in two methanol baths (1 min each). Slides were then rinsed under a running tap of distilled H_2O for 1 min followed by two PBS washes (2 min each). Antigen retrieval was performed by heating the slides in a microwave for 20 min submerged in 10 mM citrate buffer, pH 6 (Sigma Aldrich, MO, USA). Slides were then rinsed under running H_2O for 1 min followed by two PBS washes (2 min each). Slides were then blocked in a 3% hydrogen peroxide in PBS solution (Sigma Aldrich, MO, USA) for 10 min followed by two PBS washes (2 min each). Slides were then blocked in a 20% rabbit serum in PBS solution (Sigma Aldrich, MO, USA) for 30 min followed by incubation with an anti-pimonidazole FITC-conjugated mouse monoclonal primary antibody (1:50 in PBS; hypoxyprobe, MA, USA) for 60 min. Slides were washed twice with PBS (2 min each) followed by incubation with an HRP-conjugated rabbit anti-FITC secondary antibody (1:50 in PBS; Hypoxyprobe, MA, USA) for 60 min. Slides were washed twice with PBS (2 min each) followed by incubation with DAB reagent (Sigma Aldrich, MO, USA) for 10 min. Slides were rinsed under running H_2O for 1 min and then counterstained with haematoxylin solution (Sigma Aldrich, MO, USA) for 3 min. Slides were rinsed under running H_2O for 1 min and then dehydrated in three methanol baths (1 min each) followed by two xylene baths (3 min each) before cover-slipping with dibutyl phthalate in xylene (DPX; Sigma Aldrich, MO, USA). Cover-slipped slides were left to dry overnight at room temperature before storing at 4˚C.

2.3.3 Imaging and scoring

H&E-stained spheroid sections and pimonidazole stained spheroid sections were imaged on a Hamamatsu NanoZoomer-SQ Digital Slide Scanner (Hamamatsu, Japan) using a 40x objective. Individual slide images were exported from scans as compressed JPEGs from the NanoZoomer digital pathology image (.ndpi) file. Images were analysed using NDP.view 2 software. For H&E staining, training was provided by an independent histopathologist for the identification of necrosis within samples. Quantification of necrosis levels was calculated by visual scoring. The criteria used to determine necrosis included histomorphological appearance such as nuclear shape and staining. Independent validation of the results was carried out by a histopathologist following scoring.

For pimonidazole stained spheroid sections, images were subsequently analysed in ImageJ to quantify the staining. The total area of the spheroid sections were determined and used to calculate the percentage hypoxic region based on the area of positive pimonidazole staining as a fraction of total area. Independent validation of the results was subsequently carried out.

2.4 Clonogenics assay

2.4.1 Cell preparation

Clonogenics assays were performed in either T25cm^2 or T75cm^2 cell culture flasks (Corning®, Thermo Fisher Scientific, MA, USA). Cells were harvested and counted as described in 2.1 except cell suspensions were pelleted by centrifugation for 10 min at 200 x *g*. Typically, cells were seeded at a concentration of 500 cells/T25cm^2 in 7.5 mL complete medium or 2000 cells/T75cm^2 in 15 mL complete medium. Two flasks were seeded per experimental condition to obtain average colony counts. Cells were incubated overnight at 37°C in a 5% CO_2 humidified incubator. Hypoxic samples were incubated in hypoxic conditions as described in 2.1.2 for 72 hours before returning to the incubator alongside normoxic samples. Colonies were left to form for 14 days with minimal disturbance. Extra flasks were seeded to assess cell growth during this period.

2.4.2 Colony staining

Flasks were removed from the incubator after 14 days and the media aspirated from the cells. Colonies were then fixed and stained with 1% methylene blue (3 mL/T25cm^2 or 10

mL/T75cm^2, Sigma Aldrich, MO, USA) for 60 min at room temperature. 1% methylene blue solution was prepared by dissolving 1g of methylene blue powder in 100 mL 70% ethanol diluted in PBS. Methylene blue was aspirated from the flasks, which were then rinsed once with tap water and then another two times by fully submerging the flasks in tap water. Flasks were allowed to dry overnight at room temperature. Colonies were counted using an eCount colony counter (Heathrow Scientific, IL, USA).

2.5 Immunoblotting

2.5.1 Protein extraction

Cells were cultured to 70% confluency in 10 cm Petri dishes (Corning®, Thermo Fisher Scientific, MA, USA) under appropriate conditions. Dishes were placed on ice and cell culture media was aspirated. Cells were washed once with 5 mL ice-cold PBS and then lysed in 100 µL radioimmunoprecipitation assay (RIPA) buffer (Cell Signalling Technology, MA, USA) containing 1x protease inhibitor cocktail ([10 µL/mL], Sigma Aldrich, MO, USA). Cells were scraped from the dish using a cell scraper (Corning®, Thermo Fisher Scientific, MA, USA) and collected into a fresh 1.5 mL Eppendorf tube (Starlab, Germany). Cell lysates were homogenised by sonication for 5x 30 s cycles using a Bioruptor® Pico sonication device (Diagenode, Belgium). Cell lysates were cleared by centrifugation at 16,000 x *g* for 10 min at 4°C and then stored at -80°C.

For HIF protein immunoblotting, cells were lysed in urea buffer (see appendix A) containing SDS, DTT and 1x protease inhibitor cocktail. Cells were collected as described above and homogenised by sonication for 10x 30-second cycles. Cell lysates were cleared by centrifugation at 16,000 x *g* for 10 min at 4°C and then stored at -80°C.

2.5.2 Protein quantification – Bradford Assay

Protein extracts were quantified using a Bradford assay. Briefly, a stock solution of bovine serum albumin 50 mg/mL (BSA (Lee BioSolutions, MO, USA) was produced by dissolving 0.5g BSA powder in 10 mL distilled H_2O. 80 µL of BSA stock solution was dissolved in 920 µL PBS to produce a top working concentration of 4000 µg/mL. Serial dilutions were then performed using the working BSA solution to generate a series of standard concentrations: 2000 µg/mL, 1000 µg/mL, 500 µg/mL, 250 µg/mL, 125

μg/mL, 62.5 μg/mL, 31.25 μg/mL, 15.625 μg/mL. PBS was used as a negative control. Experimental samples were diluted 1:10 in PBS. The Bradford assay dye reagent concentrate (Bio-Rad, CA, USA) was prepared by diluting 1:5 in distilled H_2O. 10 μL of standard concentrations and experimental samples were plated in triplicate in a 96-well plate (Falcon®, Corning®, Thermo Fisher Scientific, MA, USA) and 200 μL of the assay dye was added to each well. The plate was read using an Infinite® F50 absorbance microplate reader (Tecan, Switzerland) at 620 nm and data was collected using Magellan™ data analysis software. Raw data was exported to Microsoft Excel for additional analysis.

2.5.3 Sample preparation

Typically, 40 μg of protein sample was prepared for western blotting as calculated by the Bradford assay (see 2.5.2). The calculated volume of cell lysate was mixed with a working solution of 4x Laemmli sample buffer (Bio-Rad, CA, USA) containing 900 μl 4x Laemmli plus 100 μl β-mercaptoethanol (Sigma Aldrich, MO, USA). The final volume was produced by adding distilled H_2O to give a final concentration of 1x Laemmli. Samples were boiled at 95°C for 5 min and then centrifuged briefly to collect excess from the lid of tubes.

2.5.4 Gel electrophoresis

Prepared samples were separated using sodium dodecyl sulfate-polyacrylamide gel electrophoresis (SDS-PAGE) based on their size using an appropriate percentage of polyacrylamide gel (see table 2.4). 1.0 mm polyacrylamide gels were prepared using the Mini-PROTEAN Tetra Handcast system (see appendix B) (Bio-Rad, CA, USA). Typically, a 4% stacking gel was used. 3 μL of Precision Plus Protein™ Dual colour standards (Bio-Rad, CA, USA) was used to allow the identification of protein molecular weights. Gels were run initially at 80 volts until the ladder began to separate, after which, the voltage was increased to 120 volts until the dye front ran out of the gel (approx. 120 min).

Protein Size	Gel Acrylamide Percentage
4-40 kDa	20%
12-45 kDa	15%
10-70 kDa	12%
15-100 kDa	10%
5-200 kDa	8%
> 200 kDa	6%

Table 2.4 Percentage of acrylamide required to produce different percentage resolving gels for the separation of different-sized proteins.

2.5.5 Gel transfer

Separated proteins were transferred onto a nitrocellulose membrane (0.45 μm pore size, Bio-Rad, CA, USA) using the Trans-Blot® Turbo™ Transfer machine (Bio-Rad, CA, USA). Transfer conditions were selected based on the molecular weight of the target protein (table 2.5). Proteins were transferred using either 1) mixed molecular weight programme, 1.3 amps, 25 volts, 7 min or 2) high molecular weight programme, 1.3 amps, 25 volts, 12 min. Turbo Transfer Buffer (Bio-Rad, CA, USA) was used to facilitate effective transfer from the gel to the membrane (see appendix A).

Protein	Molecular weight (kDa)	Protein	Molecular weight (kDa)
eIF4A2	45	HIF2α	110
eIF4A1	45	ASS1	47
eIF4E1	28	GPT1	48
eIF4E2	29	GPT2	47
eIF4G3	250	PHGDH	57
CNOT7	29	Cas9	160
CTH	44	EHD1	60
ALDH18A1	87	KIF5B	110
BCAT1	43	PLD2	95
IRP1	98	ASNS	64
SHMT2	55	ALDOC	40
CA9	55	ADSS1	48
HIF1α	120	β-actin	45

Table 2.5 Molecular weights in kilodaltons (kDa) of proteins investigated in this study.

2.5.6 Immunoblotting

After transfer, membranes were blocked in 5% milk or 5% BSA [w/v] (according to antibody recommendations, see table 2.6) in 1x Tris-buffered saline (TBS) buffer (see appendix A) containing 0.1% Tween20 (TBS-T, Sigma Aldrich, MO, USA) unless stated otherwise. The membranes were incubated with the appropriate primary antibody diluted as described in table 2.6 at 4°C overnight with gentle rocking.

Protein	Company	Catalogue #	Diluent	Dilution
eIF4A2	AbCam	ab31218	5% BSA	1:1000
eIF4A1	GeneTex	GTX107319	5% BSA	1:500
eIF4E1	Santa Cruz Biotechnology	sc-9976	5% BSA	1:500
eIF4E2	Santa Cruz Biotechnology	sc-100731	3% milk	1:500
eIF4G3	GeneTex	GTX1181109	5% BSA	1:1000
CNOT7	Cell Signalling Technology	86665S	3% milk	1:1000
CTH	Cell Signalling Technology	30068S	5% BSA	1:1000
ALDH18A1	Santa Cruz Biotechnology	sc-100498	3% milk	1:1000
BCAT1	Cell Signalling Technology	88785S	5% BSA	1:1000
IRP1	Cell Signalling Technology	20272S	5% BSA	1:1000
SHMT2	Atlas Antibodies	HPA020549	3% milk	1:2000
CA9	Absolute Antibodies	Ab00414-1.4	3% milk	1:500
HIF1α	BD Biosciences	610959	3% milk	1:500
HIF2α	Cell Signalling Technology	7096S	5% BSA	1:500
ASS1	Cell Signalling Technology	70720S	5% BSA	1:1000
GPT1	Santa Cruz Biotechnology	sc-374501	3% milk	1:500
GPT2	Santa Cruz Biotechnology	sc-398383	3% milk	1:500
PHGDH	Cell Signalling Technology	66350S	3% milk	1:1000
Cas9	Cell Signalling Technology	14697S	3% milk	1:500
EHD1	Abcam	ab109311	3% milk	1:1000
KIF5B	Abcam	ab5629	3% milk	1:2000
PLD2	Cell Signalling Technology	13904S	3% milk	1:1000
ASNS	Cell Signalling Technology	92479S	3% milk	1:1000
ALDOC	Invitrogen	PA5-27659	5% BSA	1:1000
ADSS1	Santa Cruz Biotechnology	sc-166470	5% BSA	1:200
β-actin	Santa Cruz Biotechnology	sc-47778	5% BSA	1:1000

Table 2.6 Summary of the primary antibodies used in this study along with dilution factor and diluent used.

The membranes were then washed three times in TBS-T (0.1% [v/v]) for 5 min each and then incubated with the appropriate secondary antibody (see below) for 1 hour at room temperature protected from light with gentle rocking. The membranes were washed three times for 5 min each and stored in 1xTBS before imaging using the Odyssey Fc imaging system (LI-COR Biosciences, NE, USA). β-actin was probed for as a loading control. Band densitometry analysis was performed using the ImageStudio Lite software (LI-COR Biosciences, NE, USA) and data was exported to Microsoft Excel for further analysis.

Secondary Antibodies

IRDye® 680RD and 800CW anti-rabbit, anti-mouse and anti-goat IgG (1:10000 in 5% BSA-TBST) were purchased from LI-COR Biosciences, NE, USA. Anti-rabbit IgG, HRP-linked and anti-mouse IgG, HRP-linked (1:2000) were purchased from Cell Signalling Technology, MA, USA. Chemiluminescent detection was carried out using SuperSignal™ West Pico PLUS Chemiluminescent substrate (Thermo Fisher Scientific, MA, USA).

2.6 Co-immunoprecipitation of endogenous proteins

Co-immunoprecipitation of endogenous proteins was carried out using a newly designed method. Experimental dishes were placed on ice and the culture media was aspirated. Cells were washed once in ice-cold PBS and lysed with modified RIPA buffer as described in 2.5.1. Details of Co-IP lysis buffer, wash buffer and neutralisation buffer can be found in Appendix A. Samples were quantified as described in 2.5.2. Whole cell lysate (20 µg) from cells cultured in normoxic and hypoxic conditions was used as an input control (not immunoprecipitated).

1.0 mg of cell lysate was incubated with the recommended dilution of either eIF4A2 (4 µg, rabbit polyclonal, Abcam, UK) or IgG control (5 µg, Sigma Aldrich, MO, USA) antibody in 200 µL of Co-IP lysis buffer for 2 hours at 4°C on a rotator disk (VWR™, UK). SureBeads™ Protein A or G (depending on IP antibody) magnetic beads (100 µl/sample, Bio-Rad, CA, USA) were incubated in 0.1% BSA-PBS for 1 hour at 4°C then washed three times with Co-IP wash buffer (PBS + 0.1% Tween20 [PBS-T]). Beads were engaged on a magnetic rack (Bio-Rad, CA, USA) and co-IP wash buffer was removed.

Immunocomplexes were then incubated with pre-cleaned beads for 2 hours at 4°C on a rotator disk (VWR™, UK). Immunoprecipitates on beads were washed four times in wash buffer before samples were resuspended in 100 µL wash buffer and transferred into fresh 1.5 mL Eppendorfs (Starlab, Germany). Samples were engaged on the magnetic rack and the wash buffer was removed. Protein samples were eluted in 25 µL elution buffer (0.2 M glycine, pH 2.5) at 56°C for 15 min. Supernatants were collected and immediately neutralised with 2 µL neutralisation buffer (1 M Tris, pH 8) and then stored at -80°C.

Samples were dissolved in 4x Laemmli sample buffer (Bio-Rad, CA, USA) + 10% β-mercaptoethanol (Sigma Aldrich, MO, USA) and boiled at 95°C for 5 min. Samples were separated by SDS-PAGE as described in 2.3. After primary antibody incubation membranes were washed three times for 15 min in TBS-T. Polyclonal antibodies were used to detect eIF4A2 and eIF4G3 whilst a monoclonal antibody was used to detect eIF4E2 (see Table 2.2). IgG fraction monoclonal mouse anti-rabbit IgG, light-chain specific antibody (Jackson ImmunoResearch, PA, USA. 1:50000), AffiniPure Fab Fragment Goat Anti-Mouse IgG1, Fcγ fragment specific Alexa Fluor® 680 (Jackson ImmunoResearch, PA, USA, 1:25000) and IRDye® 800CW donkey anti-rabbit IgG (LI-COR Biosciences, NE, USA, 1:10000) diluted in 5% BSA-TBST were used to detect eIF4A2, eIF4E2 and eIF4G3 primary antibodies respectively. After secondary antibody incubation membranes were washed three times for 10 min in TBS-T and then imaged using an Odyssey Fc imaging system (LI-COR Biosciences, NE, USA). For chemiluminescence, the HRP detection solution was prepared as described by the manufacturer (Super Signal™ West Dura Extended Duration Substrate, Thermo Fisher Scientific, MA, USA).

2.7 Generation of CTH and eIF4A2 knockout cell lines

2.7.1 Cell line preparation – Lentiviral transduction

The amount of lentivirus required was calculated based on the recommended multiplicity of infection (MOI) using the following equation:

$$Volume\ of\ virus\ required\ (mL) = \frac{MOI\ x\ number\ of\ cells\ per\ well}{viral\ particles\ per\ mL}$$

The required amount of lentivirus was added as a droplet in the centre of each well of a 48-well plate. Cells were then harvested and counted as described in section 2.1. A cell suspension containing 20,000 cells/200 µL DMEM was prepared multiplied by the number of wells required. Polybrene (Sigma Aldrich, MO, USA) was added to the cell suspension at a final concentration of 8 µg/mL (1:100 dilution from 800 µg/mL stock). 200 µL of cell suspension was added to each well of the 48-well plate (reverse transduction) and PBS was added to empty wells. Additional wells containing wild-type cells ± puromycin (Thermo Fisher Scientific, MA, USA) were included as a control for antibiotic selection. Cells were also transduced with a non-targeting lentivirus as a negative control (Sigma Aldrich, MO, USA). The plate was incubated overnight at 37°C in a 5% CO_2 humidified incubator. The following day, the cells were washed twice with PBS and then replaced with fresh DMEM containing 10% FBS. 48 hours post-transduction, the cells were treated with puromycin at a final concentration of 2 µg/mL. Fresh DMEM containing 2 µg/mL puromycin was added every 2-3 days for 10 days until the negative control cells and wild-type cells without antibiotic resistance had died. Transduced cells were then passaged and amplified for cryopreservation and seeding for protein extraction to validate knockout efficiency.

2.7.2 Transfection

CRISPR guide RNA (gRNA, Sigma Aldrich, MO, USA) was introduced into cell lines using lipofection and a reverse transfection method. See table 2.7 for gRNA sequence details. Cells were treated with doxycycline (1:1000 in fresh cell culture media, Sigma Aldrich, MO, USA) 48 hours prior to transfection to induce Cas9 expression. gRNAs were reconstituted at 100 µM in 30 µL RNase-free water inside a class II MSC after centrifugation for 10 s at 16,000 x *g*. gRNAs were vortexed for 10 s and incubated on ice for 20 min before storing at -80°C. For transfection, gRNAs were diluted to 10 µM (1 µL gRNA + 9 µL sterile RNase-free water) and kept on ice. A negative control gRNA was prepared at 100 nM (from 20 µM stock). Transfection reagents were prepared in two sterile 1.5 mL Eppendorf tubes per gRNA per well of a 24-well cellBIND® plate (Corning®, Thermo Fisher Scientific, MA, USA). Tube A consisted of 2.5 µL gRNA diluted in 22.5 µL Opti-MEM™ reduced serum media (Thermo Fisher Scientific, MA, USA) and tube B consisted of 1.5 µL lipofectamine™ RNAiMAX reagent (Thermo Fisher Scientific, MA, USA) diluted in 23.5 µL Opti-MEM™. Oligonucleotide and

lipofectamine™ solutions were mixed and incubated at room temperature. The transfection mix was added to the corresponding well of the 24-well plate by dotting it in the centre of the well. Cell suspensions were then pipetted directly on top of the solution (reverse transfection).

Gene target	gRNA name	Abbreviation	gRNA sequence (5'-3')
CTH	HSPD0000009440	g40	AAGACTCTACATGTCCGAA
CTH	HS0000181204	g204	TTCCAACATTTCGCCACGC
CTH	HS0000181208	g208	GCCCCTTGCTTGAACGTGG
eIF4A2	HSPD0000012261	g61	GTAAGCATAGATGCCACGA
eIF4A2	HSPD0000012260	g60	GGGGGCCAATACTAGTGCT
eIF4A2	HSPD0000012262	g62	TATTGTTGTTGGTACACCC

Table 2.7 Oligonucleotide gRNA sequences used to generate CRISPR knockout cell lines.

Cells were harvested and counted as described in 2.1. After centrifugation, cell pellets were resuspended in Opti-MEM™. A 200 µL suspension containing $8.5x10^4$ cells was added to each well and mixed gently. 6 hours post-transfection the Opti-MEM and gRNA:lipofectamine™-containing media was aspirated from the cells and replaced with 500 µL fresh complete medium containing doxycycline (1:1000, 500 µg/mL). Transfected cells were incubated at 37°C in a 5% CO_2 humidified incubator for 24 hours.

2.7.3 Single-cell sorting and expansion

Single-cell clonal selection was carried out to identify clones harbouring the greatest percentage knockout of target genes. Cells were harvested and counted as previously described and then serially diluted until a final concentration of 1 cell per 200 µl was achieved. The cell suspension was plated out into a 96-well plate. A pool of the original transfected cells was also kept in culture. After 7 days, wells were checked for the presence of a single colony. Any wells containing more than one colony were discarded. Single colonies were then expanded into increasingly larger flasks until viable for cryopreservation and protein extraction.

2.7.4 Validation and sequencing

Cells were harvested and cryovials were prepared as described in 2.1. 10 cm dishes (Corning®, Thermo Fisher Scientific, MA, USA) were prepared containing $2x10^6$ cells in 10 mL complete medium and incubated at 37°C for 24 hours. Protein expression was

analysed by immunoblotting as described in 2.5. A polyclonal antibody was used to detect eIF4A2 and a monoclonal antibody was used to detect CTH (see table 2.6). After blotting, membranes were re-probed with an actin antibody as a loading control.

For DNA sequencing, samples were extracted and prepared as described in 2.8. Primers were designed and DNA sequencing was analysed using SnapGene (GSL Biotech LLC, CA, USA, see table 2.10).

2.7.5 Pooling method

Cells were transfected with CRISPR gRNA as described above in section 2.7.1. 6 hours post-transfection the Opti-MEM and gRNA:lipofectamine™-containing media was aspirated from the cells and replaced with 500 µL fresh complete medium. Two days post-transfection, the cells were trypsinised and resuspended in 10 mL fresh DMEM and then divided into two T-25 flasks. One T-25 flask was used to expand the cells for cryopreservation post-first-transfection, labelled T1. To the other T-25 flask, 2 µg/mL doxycycline was added for 48 hours before repeating the transfection procedure with the same gRNA for a second time. This protocol was repeated three times in total to obtain T1 (post-first transfection), T2 (post-second transfection) and T3 (post-third transfection) cell lines. After each round of transfection, cells were seeded for protein extraction to assess knockout efficiency.

2.7.6 Lentiviral gRNA knockout cell line generation

Stable gRNA-expressing cell lines were generated by transducing lentiviral inducible-Cas9 transduced cells, as described in 2.7.1, with a lentiviral vector containing the required targeting gRNA sequence as well as an antibiotic puromycin selection marker and blue fluorescent protein (figure 2.2, Sigma Aldrich, MO, USA). See table 2.8 for gRNA sequence details and abbreviated names.

Gene target	gRNA name	Abbreviation	gRNA sequence (5'-3')
eIF4A2	HS5000017578	g78	GATTTGATCCTTAAAACCACGG
eIF4A2	HS5000017577	g77	CAGATGAAATGTTGAGCCGTGG

Table 2.8 Lentiviral gRNA sequences used to generate CRISPR knockout cell lines.

To induce target protein cutting, cells were cultured under selection with 4 μg/mL puromycin and simultaneously treated with 2 μg/mL doxycycline to induce Cas9 expression for 48 hours. After 48 hours, the media was replaced with fresh DMEM containing 2 μg/mL doxycycline for an additional 48 hours. After 96 hours of doxycycline treatment cells were harvested as described in section 2.1 and seeded for cryopreservation and protein extraction to assess knockout efficiency.

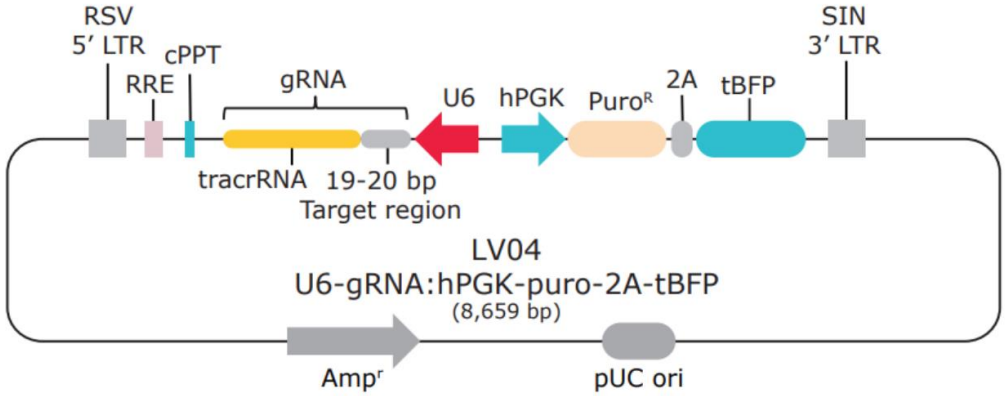

Figure 2.2. Structure of the LV04 lentiviral gRNA vector from Sigma. The vector contains a puromycin antibiotic selection marker (puro^R) as well as a blue fluorescent protein marker (tBFP).

2.8 Nucleic acid extraction and processing

2.8.1 DNA extraction

Cells were passaged and pelleted as described in 2.1.3. Cell culture media was removed, and pellets were frozen at -80°C. Cell pellets were thawed on ice and DNA extraction was performed using DNAzol reagent (Sigma Aldrich, MO, USA) and ethanol/sodium hydroxide (NaOH) extraction. Cell pellets were washed once in ice-cold PBS and centrifuged for 5 min at 16,363 x *g*. PBS was removed and 500 μL DNAzol reagent was added to resuspend each pellet. Cells were incubated with DNAzol for 3 min at room temperature and then transferred to clean 1.5 mL Eppendorf tubes (Starlab, Germany). DNA was precipitated from cells with the addition of 250 μL 100% ethanol and mixed by inverting the tubes several times. DNA precipitates were removed by spooling with a pipette tip and attached to the tube wall. The supernatant was removed, and the DNA precipitate was washed two times with 800 μL 75% ethanol. Excess ethanol was removed, and precipitates were left to air dry briefly (5-15 s). DNA was solubilised with the addition of 50-200 μL fresh 8 mM NaOH depending on the size of the cell pellet. 8

mM NaOH was prepared by adding 40 µL of 1 M NaOH stock (0.4 g NaOH in 10 mL distilled H_2O) to 5 mL distilled H_2O. The DNA solution was stored at -20ºC.

2.8.2 DNA quantification

DNA quantification was performed using the Nanodrop 2000 spectrophotometer (Thermo Fisher Scientific, MA, USA) by measuring absorbance at 260 nm. The ratio of absorbance at 260 nm and 280 nm was used to assess the purity of the DNA with a ratio of >1.8 being classified as pure.

2.8.3 Polymerase chain reaction

DNA samples were diluted to 100 ng/µL in 8 mM NaOH and quantified as described in 2.6.2. Polymerase chain reactions (PCR) were set up as described in table 2.9. Primers were purchased from Sigma Aldrich, MO, USA (table 2.10). Primers were reconstituted at 100 µM in 30 µL RNase-free water after centrifugation for 10 s at 16,363 x *g*. Primers were vortexed for 10 s and incubated on ice for 20 min before storing at -80ºC. Primers were diluted to 5 µM before use in the PCR reaction.

Component	**Volume (µL)**
H_2O	27
5x Q5® reaction buffer	10
dNTPs (10 mM)	1
Forward primer (5 µM)	5
Reverse primer (5 µM)	5
Q5® High-fidelity DNA polymerase	1
DNA	1
Total volume	**50**

Table 2.9 Reaction components per sample for polymerase chain reaction.

Samples were placed in a Veriti® 96-well Thermal Cycler (Applied Biosystems™, Thermo Fisher Scientific, MA, USA), see Appendix C for programme details. DNA was placed immediately on ice upon completion and stored at -20°C.

Gene target	Forward sequence (5'-3')	Reverse sequence (5'-3')
CTH (g40)	CAGCATATTTGCTTCCCCTC	GCATCCACTAAACTAGAGGC
CTH (g204)	TCTGCTGTCAGCCAATAAGG	CATCCGATACAAAGCTGTGC
CTH (g208)	CCGCTAATAAAATCCACCCC	AATCACCTGAATTTCAGGCC
eIF4A2 (g61)	TGCTGCTTTAGCTTGTGCAG	TGAGCTTGAGCAATCACATC
eIF4A2 (g60)	GTGGGATCGGTAAATGTG	TTTCCCCCAGAGGGTATTG
eIF4A2 (g62)	CATTGATCCTGGAGTTCTGC	CCAAGCGTCTCTGTCTTAC
CA9	CTTGGAAGAAATCGCTGAGG	TGGAAGTAGCGGCTGAAGTC
EPO	GCTGCATGTGGATAAAGCCG	AGACTCGGAAGAGTTTGCGG
β-actin	ATTGGCAATGAGCGGTTC	GGATGCCACAGGACTCCAT

Table 2.10 Forward and reverse PCR primer sequences for genes investigated in this study.

2.8.4 Agarose gel electrophoresis

PCR products were separated using agarose gel electrophoresis. PCR products were separated on a 1.5% agarose gel (3 g agarose in 200 mL 1x Tris-acetate-EDTA [TAE] buffer) containing 10 µL ethidium bromide (Sigma Aldrich, MO, USA). Samples were prepared by adding 10 µL of 6x purple loading dye (New England Biolabs, MA, USA) before loading onto the gel. 10 µL of Quick-load® 1kb DNA ladder (New England Biolabs, MA, USA) was used to determine PCR product size in base pairs. Gels were run at 80 volts for 1-2 hours. Gels were imaged using a Gel Doc™ EZ imager (Bio-rad, CA, USA).

2.8.5 Gel extraction

PCR product bands were excised from the agarose gel using a clean scalpel, the excess gel was removed, and the DNA was weighed in a clean, tared 1.5 mL Eppendorf tube (Starlab, Germany). DNA was extracted from the gel using the GenElute gel extraction kit (Sigma Aldrich, MO, USA). Solutions were prepared and stored according to the manufacturer's instructions. All centrifugation steps were carried out at 12,000 x *g*. Briefly, 3 volumes of gel solubilisation solution were added to the gel slice and incubated at 55ºC for 10 min until the gel slice was completely dissolved. The solution was vortexed every 2 min to help dissolution. The binding columns were prepared by adding 500 µL column preparation solution to binding column G in a 2 mL collection tube.

Columns were centrifuged for 1 min and the flow-through was discarded. 1 gel volume of 100% isopropanol was added to the dissolved gel and mixed thoroughly before being added to the prepared binding column. The columns were centrifuged for 1 min and the flow-through was discarded. The columns were washed with 700 µL wash solution and centrifuged for 1 min before discarding the flow-through. The columns were then centrifuged for an additional 1 min to remove any excess ethanol. The binding columns were transferred to a clean 1.5 mL Eppendorf tube and 35 µL of elution buffer was added to the centre of the column. The elution buffer was pre-heated to 65ºC to increase yield. The columns were incubated for 1 min and then centrifuged for 1 min to elute DNA. The elution was repeated a second time with an additional 35 µL elution buffer. DNA was quantified as described in 2.6.2 and then stored at -20ºC.

2.8.6 DNA Sequencing

30 µL of DNA samples were sent for sequencing along with forward and reverse primers diluted to 10 µM (3 µL per sample). Samples were sequenced using a 3130xl ABI PRISM Genetic Analyzer (Life Technologies, CA, USA) at the DNA sequencing facility at The University of Nottingham. DNA sequencing was analysed using SnapGene (GSL Biotech LLC, CA, USA).

2.8.7 RNA extraction

Trizol reagent:

Cells were cultured to ~ 70% confluency in 10 cm Petri dishes (Corning®, Thermo Fisher Scientific, MA, USA) under appropriate conditions. Dishes were placed on ice and cell culture media was aspirated. Typically, 1 mL of TRI reagent® (Sigma Aldrich, MO, USA) was added per 10cm^2 dish and incubated at room temperature for 5 min. All TRI reagent® was removed from the dishes and placed in a clean 1.5 mL Eppendorf tube. 200 µL of chloroform was added, and samples were mixed by vigorous shaking by hand for 30 s. Samples were centrifuged for 20 min at 12,000 x *g*. 400 µL of the aqueous phase was removed and placed into a fresh 1.5 mL Eppendorf tube containing 500 µL isopropanol. Samples were mixed thoroughly by shaking by hand and then incubated at -80°C for 2 hours or overnight. Samples were centrifuged for 20 min at 12,000 x *g* to pellet the RNA and the supernatant was discarded. The pellet was washed in 1 mL 75% ethanol and then centrifuged at 12,000 x *g* for 5 min. Ethanol was aspirated from the

pellet which was left to air dry for a maximum of 10 min. The pellet was dissolved in 20 µL RNase-free water and incubated on ice for 20 min. The samples were transferred to clean 1.5 mL Eppendorf tubes and stored at -80°C.

Qiagen RNeasy column:

Cells were cultured to ~ 70% confluency in T-25 flasks (Corning®, Thermo Fisher Scientific, MA, USA) under appropriate conditions. Cells were harvested as described previously and rinsed once in PBS before pelleting at 200 x *g* and freezing at -80˚C until required. RNA extraction was carried out using the RNeasy Mini kit (Qiagen, Germany). All centrifugation steps were carried out at 12,000 x *g*. Typically, cell pellets were thawed briefly at room temperature before the addition of 600 µL RLT lysis buffer. Lysates were mixed by vortexing and then homogenised by passing the lysate 10 times through a 20-gauge needle (0.9 mm diameter) and syringe. One volume of 70% ethanol was then added to the lysate and mixed by pipetting. The samples were then added to a RNeasy spin column placed within a 2 mL collection tube and centrifuged for 15 s. The flow-through was discarded. 700 µL of wash buffer RW1 was added to the spin column which was then centrifuged for another 15 s and the flow-through was discarded. 500 µL buffer RPE was then added to the spin column, centrifuged for 2 min, and the flow-through was discarded. The spin column was then transferred to a new 2 mL collection tube and centrifuged for 1 min to remove any residual RPE buffer. The spin column was then placed into a clean 1.5 mL Eppendorf tube and 30 µL of RNAse-free water was added directly to the spin column membrane. The column was then centrifuged for 1 min to elute the RNA and the samples were stored at -80˚C until required.

2.8.8 RNA quantification

RNA quantification was performed using the Nanodrop 2000 spectrophotometer (Thermo Fisher Scientific, MA, USA) by measuring absorbance at 260 nm. The ratio of absorbance at 260 nm and 280 nm was used to assess the purity of the RNA with a ratio of >2.0 being classified as pure.

2.8.9 cDNA synthesis

cDNA synthesis was performed using the High-Capacity cDNA Reverse Transcription Kit (Applied Biosystems™, Thermo Fisher Scientific, MA, USA). 2 µg of total RNA was

used per reaction. As outlined in table 2.11, a reverse transcription reaction master mix was prepared and multiplied by the number of reactions required.

Component	Volume (µL)
10x RT buffer	2.0
25x dNTPs mix (100 mM)	0.8
10x RT random primers	2.0
Ultrapure water	4.2
MultiScribe™ reverse transcriptase	1.0
Total volume	**10**

Table 2.11 Reverse transcription master mix components for the cDNA synthesis reaction

Samples were placed into a Veriti® 96-well Thermal Cycler (Applied Biosystems™, Thermo Fisher Scientific, MA, USA). See appendix C for programme details. cDNA was placed on ice immediately upon completion and stored at -20°C.

2.8.10 Quantitative PCR

Component	Volume (µL)
Forward primer (10 µM)	1.0
Reverse primer (10 µM)	1.0
Ultrapure water	6.0
SYBR Green master mix	10.0
cDNA	2.0
Total volume	**20**

Table 2.12 qRT-PCR master mix components for qPCR reaction.

Quantitative PCR (qPCR) was performed using the LightCycler® 480 Instrument II thermal cycler (Roche Diagnostics Ltd, Switzerland, see appendix C for programme details) and reactions were prepared using the LightCycler® 480 SYBR Green I Master mix (Roche, Switzerland). A qPCR master mix was prepared for each pair of target

primers as outlined in table 2.12. All samples were run in triplicate in a 96-well LightCycler® 480 multiwell plate 96 (Roche, Switzerland). Primers were purchased from Sigma Aldrich (see table 2.10). Actin was used as a housekeeping control probe for all reactions and molecular grade H_2O was used as a negative control. Upon completion, Ct values and melting curves were generated using built-in software and then exported to excel for further analysis.

2.9 RNA Sequencing (Illumina)

2.9.1 Sample preparation and quality control

Total RNA was extracted from HCT116 control and HIF1α and HIF2α knockout cells using the Qiagen RNeasy column extraction method described in 2.8.7 with the addition of an on-column DNase digestion step using the RNAse-free DNase Set (Qiagen, Germany). Briefly, after the addition of the cell lysates to the spin column, 350 µL of wash buffer RW1 was added to the column and centrifuged for 15 s. The flow-through was discarded. 10 µL of DNase I stock solution (1500 Kunitz units in 550 µL RNAse-free water) was mixed gently with 70 µL RDD buffer before being added directly to the spin column membrane and incubated at room temperature for 15 min. An additional 350 µL wash buffer RW1 was then added to the column, centrifuged for 15 s and the flow-through was discarded. The RNeasy mini kit protocol was then resumed with the addition of RPE buffer.

RNA purity was assessed as described in section 2.8.8. RNA integrity was assessed and quantified using an Agilent TapeStation automated electrophoresis workflow. RNA samples were then subjected to eukaryotic mRNA sequencing (Illumina 150PE, 20 million reads) by Novogene (UK).

2.9.2 Eukaryotic RNA-Seq library preparation and sequencing

The following steps were carried out by Novogene UK. Prior to undergoing library preparation, additional quality control steps were carried out. RNA integrity and contamination were assessed by agarose gel electrophoresis. Assessment of RNA integrity and RNA quantification was also performed using an Agilent 2100 bioanalyser. RNA contamination analysis was performed using a Nanodrop 2000.

Briefly, the eukaryotic mRNA library was then prepared by carrying out mRNA enrichment through poly(A) capture followed by RNA fragmentation using enzymatic digestion and subsequent cDNA reverse transcription. The cDNA library then underwent additional quality control steps prior to sequencing. 150 bp paired-end RNA sequencing was carried out on an Illumina NovaSeq 6000 S4 platform with 20 million reads per sample.

2.9.3 Bioinformatic processing

Raw RNA-Sequencing reads in FASTQ format were initially processed to ensure the quality of the sequencing. Sequences with a phred score of >30 (1/1000 error rate) were retained. Adaptor sequences were removed using the Trimgalore wrapper script for Cutadapt and FastQC files to automate adaptor and quality trimming (https://github.com/FelixKrueger/TrimGalore). The resulting quality-controlled reads were aligned to the GRCh38.83 genome (https://www.ncbi.nlm.nih.gov/assembly/GCF_000001405.26/) using the Spliced Transcripts Alignment to a Reference (STAR) algorithm[484].

2.9.4 Differential gene expression analysis

Quantification of gene expression from raw RNA-sequencing counts was carried out using the read summarization program featureCounts[485]. Differential expression analysis of three biological replicates per condition was then performed using the DESeq2 package in R (version 1.36). Briefly, DESeq2 uses a negative binomial distribution model to analyse raw RNA-sequencing counts and perform differential expression hypothesis testing between groups using the Wald test. The p-values generated by the Wald test are corrected for multiple comparisons to reduce the number of false positives using the Benjamini-Hochberg method to control the false discovery rate (FDR). Using this approach, genes are ranked based on their p-value and then the p-value is multiplied by m/rank where m = total number of tests. Genes with an adjusted p-value of <0.05 identified in DESeq2 were assigned as differentially expressed (http://bioconductor.org/packages/devel/bioc/vignettes/DESeq2/inst/doc/DESeq2.html).

Gene ontology (GO) and gene set enrichment analyses (GSEA) were performed with an over-representation analysis (ORA) using WebGestalt. Statistically significant terms were defined by an FDR <0.05[486]. Bubble plots were generated using

https://www.bioinformatics.com.cn/en. KEGG pathway analysis was also performed using GSEA software[487]. Additional analyses were performed using the Protein Analysis Through Evolutionary Relationships (PANTHER) software for comparison[488]. Venn diagrams were generated using Venny 2.1 (Courtesy: Oliveros, J.C (2007-2015) Venny. An interactive tool for comparing lists with Venn's diagrams, https://bioinfogp.cnb.csic.es/tools/venny/).

2.9.5 *De novo* splicing analysis

Initially, raw RNA-sequencing reads underwent the same quality control steps as described in 2.9.3. All reads were then trimmed to 145bp to ensure uniform alignment. Analysis of differential alternative splicing events between the experimental groups from the RNA-sequencing data was performed using the Multivariate Analysis of Transcript Splicing Python script rMATS, version 3.2.5[489]. Using this software, splicing events were separated into five categories: alternative 5' splice site (A5SS), skipped exon (SE), mutually exclusive exon (MXE), alternative 3' splice site (A3SS) and retained intron (RI).

Outputs were filtered to remove non-statistically significant events using an FDR < 0.05. Data was then filtered again by the change in % spliced in index (dPSI) using an absolute dPSI ≥ 5. The remaining dataset gave the total number of transcripts affected in each category. Duplicates were then removed to give the total number of unique genes affected in each category in each experimental comparison. GO and GSEA analysis were carried out as described in section 2.9.4.

2.10 *In vitro* 3-Dimensional OrbiSIMS

2.10.1 *In vitro* 3-D spheroid sample preparation

HCT116 control and HIF1α and HIF2α knockout cells were used to form 3-dimensional spheroids *in vitro* as described in section 2.2.1. Cells were seeded at the optimised seeding densities outlined in table 2.13 to ensure uniform size after 7 days of growth and that the diameter of the spheroids was <600 μm (depth limit of the planchettes used for high-pressure freezing). Cells were seeded in an initial volume of 50 μL DMEM. The following day, an additional 150 μL low-glucose DMEM was added to the wells. Media was changed every other day with the replacement of 150 μl fresh low-glucose DMEM.

Spheroids were cultured for 7 days and imaged on days 3, 5 and 7 as described in 2.2.1. Spheroid diameter was measured using the methods outlined in figure 2.1.

Cell line	Seeding density (cells/50 µL
CTL A3	100
CTL A10	100
HIF1α KO g49	100
HIF1α KO g57	200
HIF2α KO g11	100
HIF2α KO g81	200

Table 2.13 Seeding densities used to generate spheroid samples for 3-D OrbiSIMS.

On Day 7, half of the spheroids for each condition were stained with pimonidazole prior to fixation. 100 mg pimonidazole (Hypoxyprobe, MA, USA) was dissolved in 862 µL sterile PBS to give a final stock concentration of 400 mM which was sterile filtered and stored at -20˚C until required. For spheroid staining, a 400 µM stock in low glucose DMEM was made (1:1000 dilution). 100 µL of media was removed from each well and replaced with 100 µL of the 400 µM pimonidazole solution (final concentration = 200 µM). The spheroid plates were then incubated for 2 hours at 37˚C in a humidified incubator at 5% CO_2. Spheroids were then removed from the wells using a cut p1000 pipette and transferred into 1.5 mL Eppendorf tubes. The spheroids were rinsed once in PBS and then fixed in 1x neutral-buffered formalin overnight at 4˚C. The next day, the neutral-buffered formalin was removed, and the spheroids were stored in PBS at 4˚C until required.

The remaining half of the spheroids were stained with Hoechst solution (Thermo Fisher Scientific, MA, USA) prior to high-pressure freezing. A 33 µM Hoechst solution was prepared in low glucose DMEM from a 1 mg/mL stock. For spheroid staining, 100 µL of media was removed and replaced with 100 µL of the 33 µM Hoechst solution (final concentration = 16.5 µM). The spheroid plates were then incubated at 37˚C for 3 hours at 37˚C in a humidified incubator at 5% CO_2. Spheroids were then removed from the wells using a cut p1000 pipette and transferred into 1.5 mL Eppendorf tubes. The

spheroids were rinsed once in PBS and stored in PBS in preparation for high-pressure freezing.

2.10.2 High-pressure freezing

Spheroid samples were washed three times with the cryoprotectant ammonium formate and then three spheroids per condition per biological replicate were transferred to 6x0.5 mm aluminium planchettes (Leica, Germany) using ammonium formate as a filler solution. Spheroids were then high-pressure frozen using a Leica EM ICE high-pressure freezer (Leica, Germany). Samples were then stored under liquid nitrogen until required.

2.10.3 Secondary ion mass spectrometry (SIMS)

Samples were transferred to the OrbiSIMS instrument using a Leica EM Vacuum Cryo Transfer System (VCT500 Leica, Germany), maintaining cryogenic conditions throughout the transfer. Analysis was performed on a 3-D hybrid SIMS instrument (IONTOF GmbH, Germany) at or below -160˚C. The primary ion beam used was a 20 μm Ar_{3000}+ 20 keV analysis beam, with a duty cycle of 4.4% and a current of ~200 pA. The injection time was 500 ms and the cycle time was 20 μs. The mass range was 75-1125 m/z with a mass accuracy of 1/240000 m/z. The analysis field of view was 450 μm x 450 μm, and a random beam raster was used. Charge compensation was achieved using an argon flood gun, and argon regulation and the target potential were optimised for each sample. Calibration of the OrbiTrap was performed using a silver sample. Data was acquired in both positive and negative polarities. Post-acquisition data analysis was performed using SurfaceLab 7.1 (IONTOF GmbH, Germany).

2.10.4 Freeze-drying

One control spheroid sample was freeze-dried *in situ* in the load lock of the OrbiSIMS instrument prior to analysis at ambient temperature conditions. A dual beam analysis was performed, providing a combination of standard TOF-SIMS images, and OrbiTrap measurements, as previously described (Passarelli *et al*, 2017).

2.11 *In vivo* xenograft and patient-derived xenograft orbiSIMS

2.11.1 FOSL2 knockout xenograft sample preparation

The *in vivo* study was carried out by the Ex Vivo Pharmacology In Vivo Team under Project Licence Number P435A9CF8. HCT116 control and FOSL2 knockout xenografts were grown subcutaneously in CD1 nude mice. Eight mice were used per condition (4 males + 4 females to ensure gender-matched results) with a seeding density of $2x10^6$ cells. Tumours were measured weekly by calliper measurements in line with the project licence. At termination, the xenografts were excised, and half of the tumour tissue was snap-frozen in liquid nitrogen immediately. The other half of the tumour tissue was fixed in neutral-buffered formalin for immunohistochemistry. Three control mice (2x male + 1x female) and three FOSL2 KO mice (2x male + 1x female) were selected for analysis based on matching tumour weight and termination time as close as possible.
Snap-frozen tissue samples from the selected mice were embedded in OCT cryo-embedding matrix and stored at -80°C until required. Prior to cryo-sectioning, samples were placed at -20°C to reach the same temperature as the cryostat. For cryo-sectioning, the OCT blocks were mounted onto a CM1900 rapid sectioning cryostat (Leica, Germany) and cut into 4µm thick sections. The sections were collected onto 1cm circular glass coverslips stuck to polysine microscopy slides and stored at -80°C until required. Slides were transported on dry ice at all times to maintain cryogenic conditions.

2.11.2 Colorectal cancer patient-derived xenograft sample preparation

The *in vivo* study was carried out by the Ex Vivo Pharmacology In Vivo Team under Project Licence Number PP2803268. Individual colorectal tumours were obtained from colorectal cancer patients and inserted subcutaneously with matrigel into RAG-2 mice. Three mice were used to generate three experimental repeats. Tumours were measured weekly by calliper measurements in line with the project licence. At termination, the xenografts were excised, and some of the tumour tissue was immediately snap-frozen in liquid nitrogen. An additional section of the tissue was fixed in neutral-buffered formalin for immunohistochemistry. A third section of the tissue was fixed in HEPES-buffered mammalian ringer's solution (see appendix A for buffer details) containing 2.5% glutaraldehyde and 2% sucrose for resin embedding for electron microscopy.

Snap-frozen tissue samples were embedded and sectioned as described above in section 2.11.1 in preparation for orbiSIMS analysis.

2.11.3 Secondary ion mass spectrometry

Samples were transferred to the OrbiSIMS instrument using a Leica EM Vacuum Cryo Transfer System (VCT500 Leica, Germany), maintaining cryogenic conditions throughout the transfer. Analysis was performed on a 3-D hybrid SIMS instrument (IONTOF GmbH, Germany) at or below -160°C. A 2-dimensional LMIG-ToF scan with an area of 6000 μm x 7000 μm was captured with a raster size of 1536 pixels x 1792 pixels and a cycle time of 200 μs. For orbitrap imaging, the primary ion beam used was a 20 μm Ar_{3000}+ 20 keV analysis beam, with a duty cycle of 4.4% and a current of ~200 pA. The injection time was 500 ms and the cycle time was 20 μs. The mass range was 75-1125 m/z with a mass accuracy of 1/240000 m/z. The analysis field of view was 6000 μm x 200 μm, and a random beam raster was used. Charge compensation was achieved using an argon flood gun, and argon regulation and the target potential were optimised for each sample. Calibration of the OrbiTrap was performed using a silver sample. Data was acquired in both positive and negative polarities. Post-acquisition data analysis was performed using SurfaceLab 7.1 (IONTOF GmbH, Germany).

2.12 Statistical analysis

Statistical analysis was performed using GraphPad Prism ver 9.5.1. For comparisons between two groups an unpaired *t*-test was performed and a two-tailed *p*-value of < 0.05 was used as the threshold to define statistical significance. For comparisons between more than two groups with one independent variable an ordinary one-way ANOVA was performed. Pairwise multiple comparisons were performed post-hoc using Šídák's test. For comparisons between more than two groups with two independent variables (e.g. oxygen concentration and time) an ordinary two-way ANOVA was performed. Multiple comparisons were performed post-hoc using Tukey's test, comparing columns (oxygen concentration) within each row (time). In both cases, a *p*-value of < 0.05 was used as a threshold to define statistical significance. Various data were subjected to tests of normality in order to confirm the normal Gaussian distribution of the data using the Shapiro-Wilk test ($\alpha = 0.05$). Additional normality tests were attempted including the D'Agostino & Pearson test but in many cases the n number was too small. All data were

presented using mean ± SEM in order to compare the differences in mean across multiple samples by estimating the precision of the population mean for each sample.

3. eIF4A2 and eIF4A2-regulated proteins in the metabolic adaptation to hypoxia in colorectal cancer

3.1 Introduction

The importance of the eIF4A RNA helicases in regulating mRNA translation in a variety of cancers have led to the development of therapeutic strategies targetting these proteins[490]. However, much of the current research has assumed that the roles of eIF4A1 and eIF4A2 are functionally interchangeable whereas it is now becoming clear that these paralogues also have distinct functional roles[335]. Previous studies in CRC have shown that eIF4A1 protein expression remains unchanged in hypoxia whilst eIF4A2 mRNA and protein expression is increased and is associated with poor patient prognosis[346,353]. Yet, there is little to no published data investigating the role of eIF4A2 within a hypoxia-specific context in CRC. Previous data generated by the Mcintyre lab indicated that the protein expression of eIF4A2 remains unaltered in CRC cell lines when exposed to different lengths of hypoxia[355]. However, analysis of a CRC tumour microarray of 1000 tumour samples identified a significant correlation between eIF4A2 expression and the hypoxic marker CA9 and eIF4A2 expression correlated with worse patient survival suggesting a role for eIF4A2 in the adaptation to hypoxia[355]. Furthermore, the interactions and binding partners of eIF4A2 have been neglected in the literature, particularly in the context of hypoxia, as has the downstream impact of eI4A2 activity in hypoxia. It is currently unknown which paralogue of the eIF4A protein forms the RNA helicase component of the hypoxia-specific eIF4F^{H} translation initiation complex[316]. The interactions of eIF4A2 with other translation initiation factors as well as with CNOT7, as described previously, have not been fully investigated under hypoxic conditions in CRC[336]. Previous data generated by the Mcintyre lab has shown binding of eIF4A2 to CNOT7 in LS174T cells under normoxic conditions which is drastically reduced when exposed to 48 hours hypoxia[355].

Despite the potential therapeutic significance of discriminating eIF4A1 versus eIF4A2 activity and their downstream targets, there are currently no specific eIF4A2 inhibitors and little work has been done to investigate the functional role of eIF4A2 in colorectal cancer cell survival in hypoxia. Previous data generated by the Mcintyre lab has shown that knockdown of eIF4A2 using either siRNA or shRNA leads to a reduction in cell

survival and cell growth *in vitro* in both normoxia and hypoxia as well as a reduction in 3-D spheroid growth[355]. However, further investigation into the phenotypic role of eIF4A2 using more advanced gene editing techniques would help corroborate these findings. Furthermore, the specific downstream regulatory targets of eIF4A2 have remained largely elusive, especially in the context of hypoxia. Previous work carried out in the Mcintyre lab utilised RIP-sequencing in LS174T CRC cells to identify hypoxia-specific mRNA binding by eIF4A2. Pathway analysis revealed a large number of hypoxic eIF4A2-bound transcripts, including the cysteine biosynthetic enzyme CTH and the endocytic genes EHD1 and KIF5B[355].

This work also showed that the expression of CTH, EHD1 and KIF5B is reduced by eIF4A2 knockdown *in vitro* in CRC cells and knockdown of EHD1 or KIF5B reduces cell surivival[355]. Additional studies have also shown that CTH expression can be induced by periods of cyclic hypoxia in CRC cells whilst pharmacological inhibition of CTH leads to a reduction in CRC tumour growth *in vivo*[491,492]. However, the phenotypic effects of CTH activity specifically in the context of hypoxic CRC has not been investigated. Interestingly, there is very little published data on the hypoxic regulation of EHD1 and KIF5B, despite recent studies identifying a hypoxia-specific internalisation proteome[493]. Therefore, a more detailed investigation into the regulation of these genes by eIF4A2 and the functional impact of this would further our understanding of the complex mechanisms of translational regulation in hypoxic CRC.

3.2 Hypothesis and Aims

In this chapter, the following points were investigated, and the following hypothesis was tested:

- Expression of eIF4A2 and its binding partners and their interactions in hypoxia
- Role of eIF4A2 in colorectal cancer cell growth and survival
- Regulation of downstream targets by eIF4A2 including HIFs, metabolic proteins and endocytic proteins
- Role of CTH and endocytic proteins in colorectal cancer cell growth and survival

I hypothesise that eIF4A2 and eIF4A1 protein expression does not change following hypoxic (1% 0_2) exposure but that under these conditions there is a switch in the binding partners of eIF4A2 that leads to changes in its function and that the protein expression of these binding partners including eIF4G3, eIF4E2 and CNOT7 will change under hypoxia. Secondly, I hypothesise that eIF4A2 knockout will lead to reduced colorectal cancer cell growth and survival in both normoxic and hypoxic conditions with a greater effect seen in hypoxia. Additionally, I hypothesise that eIF4A2 knockout leads to a reduction in 3-dimensional colorectal spheroid growth with an increase in cell necrosis. Thirdly, I hypothesise that eIF4A2 regulates the expression of HIF1α and HIF2α in hypoxia at the translational level as well as downstream metabolic targets including CTH as well as endocytic genes such as EHD1 and KIF5B. Finally, I hypothesise that CTH knockout and knockdown of endocytic genes EHD1 and KIF5B will reduce colorectal cancer cell growth and cell survival in both normoxia and hypoxia with a greater effect seen in hypoxia.

To investigate these hypotheses, I have undertaken the following aims:

1- Evaluate the protein expression levels of eIF4A1 and eIF4A2 as well as eIF4A2-binding partners at different time points in normoxic, physoxic and hypoxic conditions

2- Investigate the interaction of eIF4A2 with possible binding partners in hypoxia

3- Produce and validate eIF4A2 knockout colorectal cancer cell lines

4- Investigate the impact of eIF4A2 knockout on 2-D cell survival *in vitro* and 3-D spheroid growth *in vitro*

5- Investigate the impact of eIF4A2 knockout or knockdown on HIF1α and HIF2α protein expression

6- Evaluate the protein expression levels of eIF4A2-bound metabolic mRNA transcripts at different time points in normoxic, physoxic and hypoxic conditions

7- Investigate the impact of CTH knockout on 2-D cell survival *in vitro* and 3-D spheroid growth *in vitro*

8- Evaluate the impact of eIF4A2 knockdown on eIF4A2-regulated endocytosis-associated proteins

9- Investigate the impact of EHD1 and KIF5B knockdown on 2-D cell survival *in vitro*

3.3 Results

3.3.1 Protein expression of eIF4A1 and eIF4A2 in different oxygen concentrations

In order to evaluate whether the protein levels of the RNA helicases eIF4A1 and eIF4A2 were altered in hypoxia, LS174T (CMS3) and HCT116 (CMS4) colorectal cancer cell lines were exposed to either normoxia (21% pO_2), physoxia (8.5% O_2) or hypoxia (1% O_2) for 12, 24, 48 and 72h and eIF4A1 and eIF4A2 protein expression was analysed by immunoblotting (figure 3.1 and figure 3.2). CA9 expression was measured as a positive control for the induction of hypoxia due to it being a known HIF-1α target gene. Physoxia was used to represent a more physiological oxygen concentration found within tissues such as the 6.8% pO_2 seen found in the colon epithelium[184]. The expression of both eIF4A1 and eIF4A2 remained unaltered in conditions of physoxia or hypoxia compared to normoxia and maintained a generally consistent level of expression across all of the time points (figure 3.1a-c and figure 3.2a-c). There was a significant increase in eIF4A2 expression at 48h physoxia, but not hypoxia, compared to normoxia in HCT116 (figure 3.2b, $p<0.0332$). eIF4A2 expression at 48h hypoxia also displayed a non-significant increasing trend compared to normoxia in both cell lines, however, this was restored at the later time points. There was also a significant reduction in eIF4A1 expression at 24h hypoxia compared to physoxia in LS174T (figure 3.1d, $p<0.0332$) however, this was restored at the later time points.

The significantly increased expression of CA9 in the hypoxic time points in LS174T (figure 3.1d; 48h, $p<0.0001$; 72h, $p<0.0001$) and HCT116 (figure 3.2d; 48h, $p<0.0021$; 72h, $p<0.0001$) compared to normoxia as well as the non-significant induction of CA9 at the 12h (LS174T) and 24h (LS174T and HCT116) time points indicated the induction of the hypoxic response in those samples. No significant difference was found in CA9 expression between the normoxic and physoxic conditions at all time points (figure 3.1d and figure 3.2d).

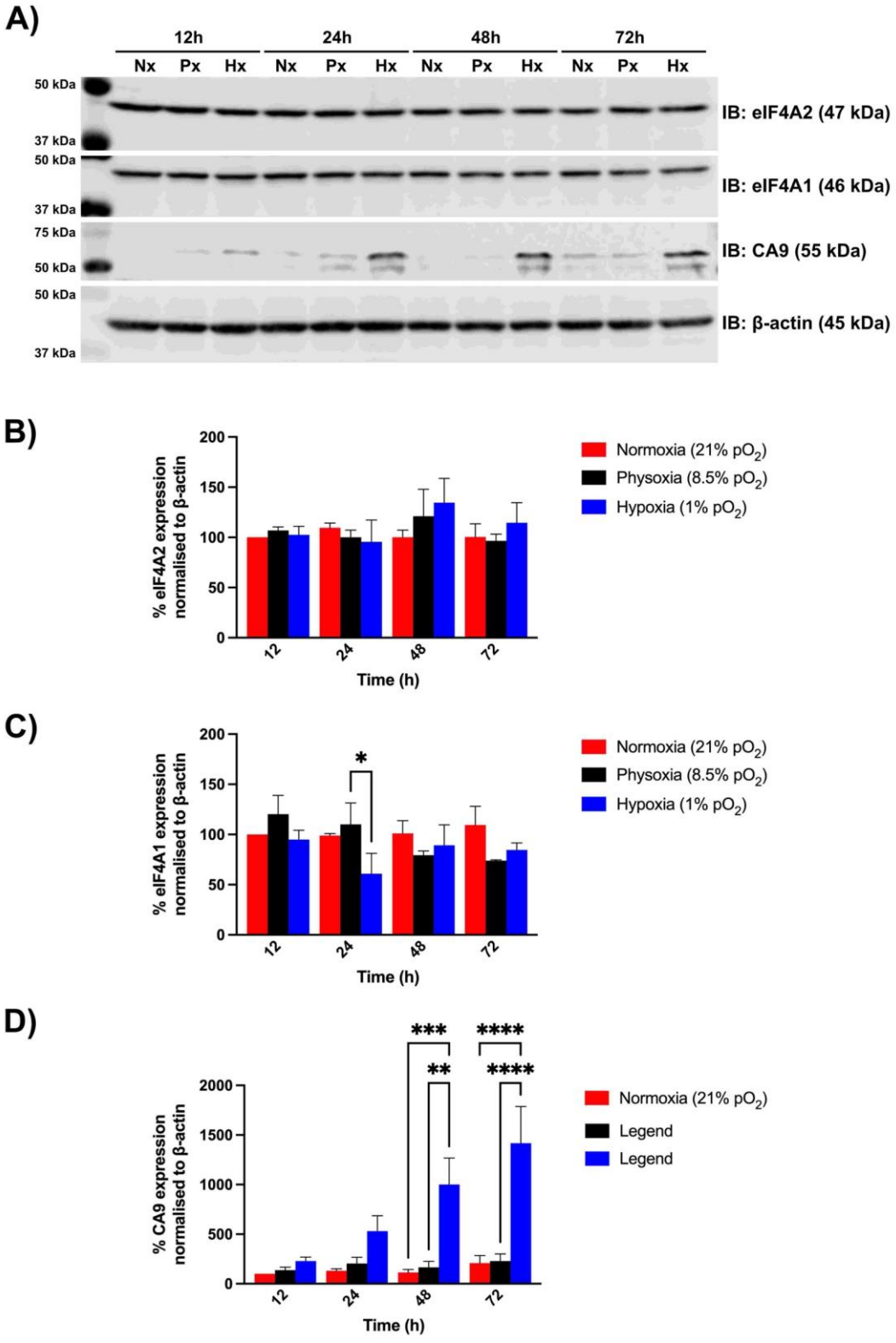

Figure 3.1 eIF4A1 and eIF4A2 protein expression in conditions of normoxia, physoxia and hypoxia are unchanged in LS174T. A) LS174T cells were exposed to 12, 24, 48 or 72h normoxia, physoxia or hypoxia. eIF4A2, eIF4A1 and CA9 protein expression was analysed by immunoblotting. Data analysed by two-way ANOVA comparing normoxia, physoxia and hypoxia for each time point for **B)** eIF4A2, **C)** eIF4A1 and **D)** CA9. *p <0.0332, **p<0.0021, ***p<0.0002, ****P<0.0001. Non-significant comparisons not displayed. Error bars indicate ±SEM. Representative blots are shown. n=3.

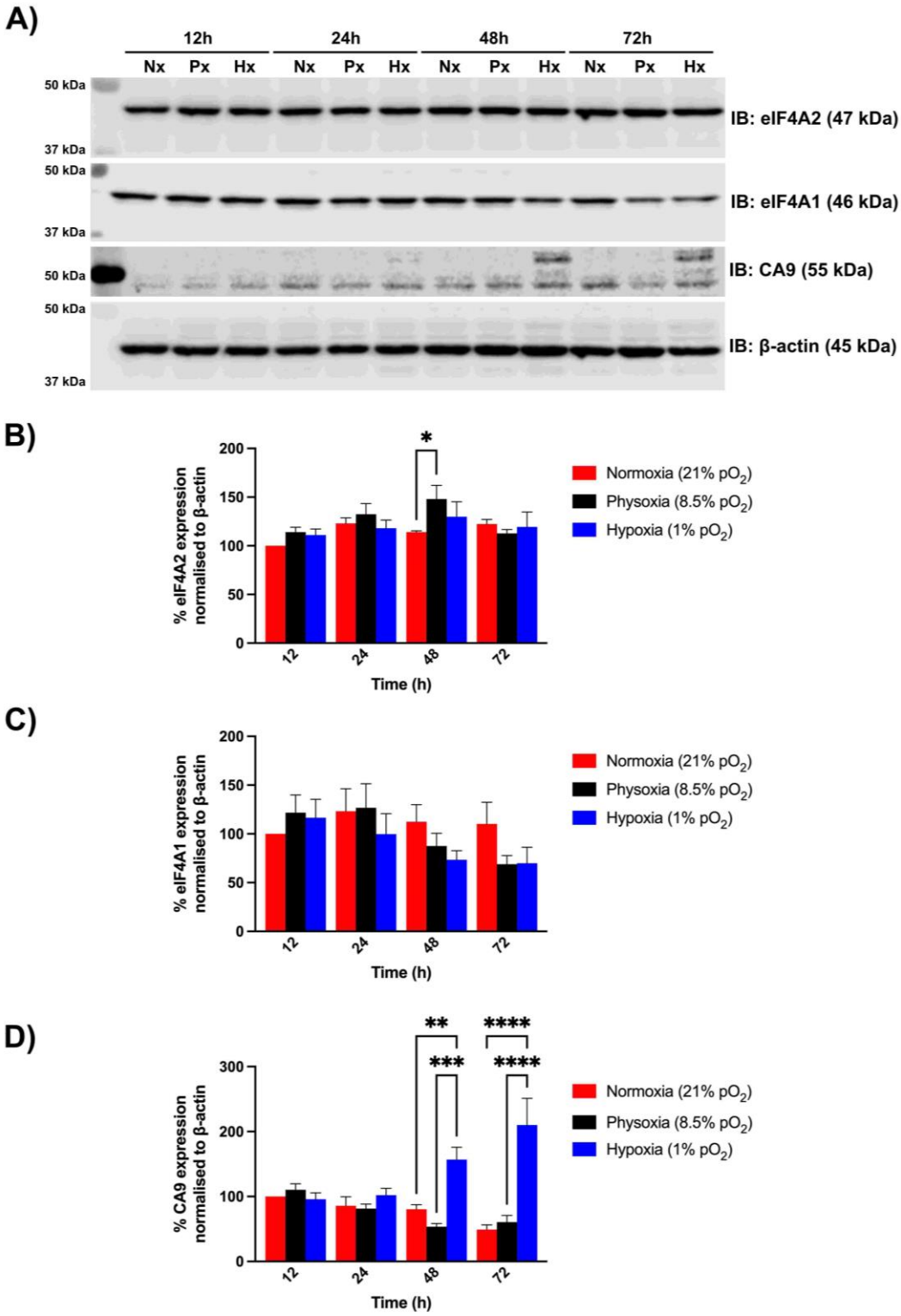

Figure 3.2 eIF4A1 and eIF4A2 protein expression in conditions of normoxia, physoxia and hypoxia are unchanged in HCT116. A) HCT116 cells were exposed to 12, 24, 48 or 72h normoxia, physoxia or hypoxia. eIF4A2, eIF4A1 and CA9 protein expression was analysed by immunoblotting. Data analysed by two-way ANOVA comparing differentially oxygenated conditions within each time point for **B)** eIF4A2, **C)** eIF4A1 and **D)** CA9. *p <0.0332, **p<0.0021, ***p<0.0002, ****P<0.0001. Non-significant comparisons not displayed. Error bars indicate ±SEM. Representative blots are shown. n=3.

3.3.2 Interaction of eIF4A2 with other components of the eIF4F translation initiation complex in hypoxia

Hypoxia has previously been shown to induce a switch in the protein components that form the eIF4F translation initiation complex leading to the formation of an alternative $eIF4F^{H}$ complex consisting of eIF4G3 and eIF4E2 in glioblastoma[316,317]. However, the identity of the eIF4A RNA helicase component has remained unconfirmed. To investigate whether eIF4A2 interacts with eIF4G3 and eIF4E2 in colorectal cancer cells and whether this is regulated by hypoxia, HCT116 and LS174T cells were exposed to 24h normoxia or hypoxia followed by immunoprecipitation of eIF4A2. eIF4A2-bound proteins were analysed by immunoblotting and probed for the presence of eIF4G3 and eIF4E2 as well as the eIF4E paralogue eIF4E1 (figure 3.3 and figure 3.4).

Figure 3.3a and figure 3.4a confirms the pulldown of eIF4A2 in LS174T and HCT116 respectively and also confirms that eIF4A2 expression remains unchanged in hypoxia (figure 3.3e and figure 3.4e). Figure 3.3a and figure 3.4a also show the interaction of eIF4A2 with eIF4G3 in both normoxia and hypoxia. However, this binding was significantly reduced under hypoxic conditions compared to normoxia in both cell lines (figure 3.3f; $p<0.0002$; figure 3.4f; $p<0.0002$). The lack of a significant difference in eIF4G3 expression in the input lanes under normoxic and hypoxic conditions suggests that the results in figures 3.3f and 3.4f are specifically due to a reduction in eIF4A2 binding and not a reduction in protein expression. This is further confirmed by the reduction in hypoxia/normoxia signal ratio for eIF4G3 expression in the IP sample compared to the ratio in the input samples (figure 3.3c and figure 3.4c).

It was not possible to detect an interaction between eIF4A2 and eIF4E2 in either LS174T of HCT116 cell lines. However, as shown in figure 3.3a and figure 3.4a, there was an interaction between eIF4A2 and eIF4E1 in both normoxia and hypoxia (only two replicates in LS174T). This binding showed a decreased trend in hypoxia compared to normoxia in both cell lines (figure 3.3g and figure 3.4g) however, this is possibly due to a reduction in eIF4E1 expression in hypoxia as confirmed by the reduced hypoxia/normoxia signal ratio for eIF4E1 in the input samples (figure 3.3d and figure 3.4d) as well as the decreased expression of eIF4E1 in hypoxia compared to normoxia in the input samples (figure 3.3g; ns; figure 3.4g; $p<0.0001$). This data suggests that there

could be fundamental differences in the binding properties of the different eIF4E paralogues and the way they function within and interact with the eIF4F complex.

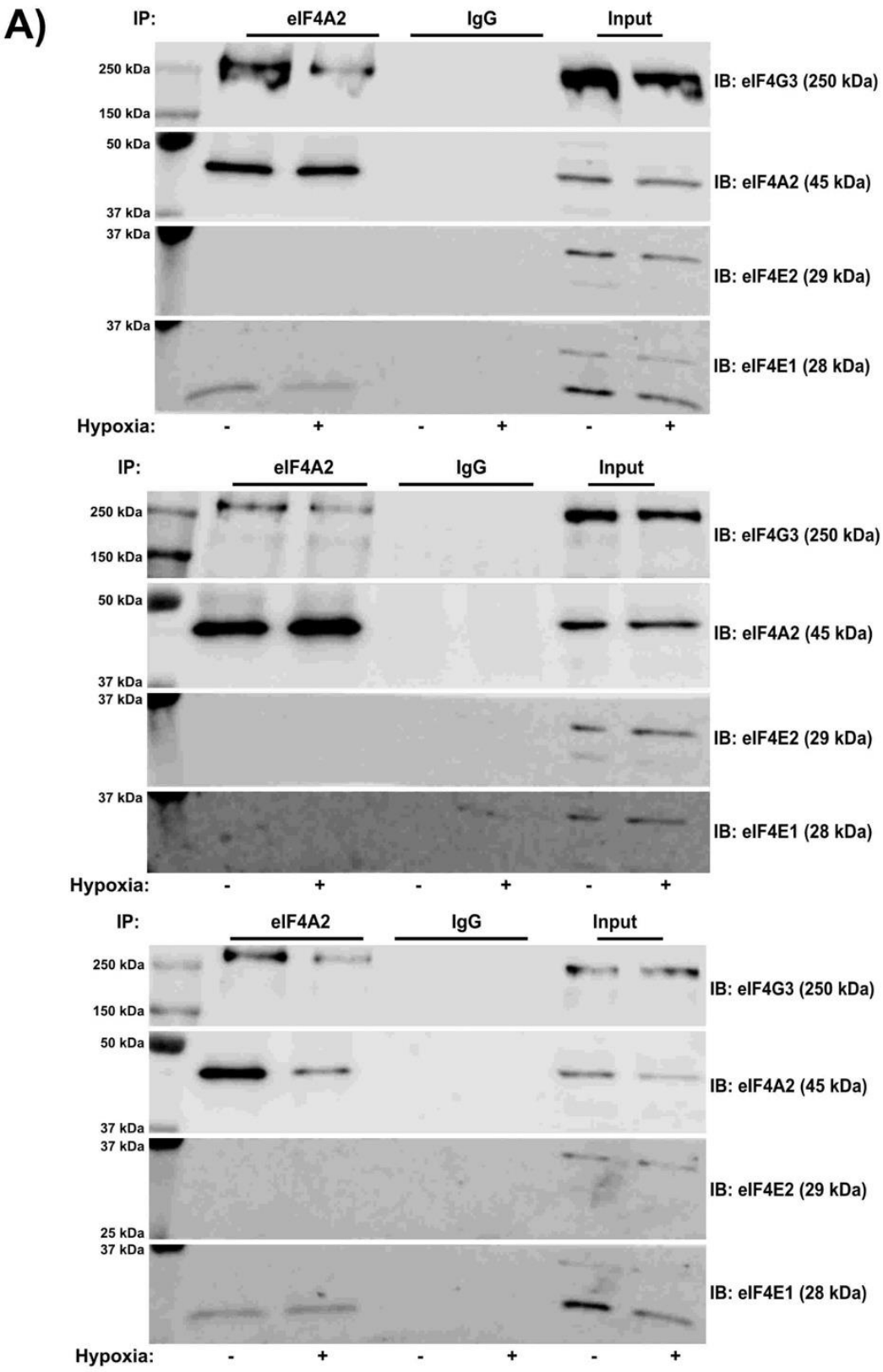
A)
IP:
eIF4A2
IgG
Input
250 kDa
150 kDa
50 kDa
37 kDa
37 kDa
37 kDa
IB: eIF4G3 (250 kDa)
IB: eIF4A2 (45 kDa)
IB: eIF4E2 (29 kDa)
IB: eIF4E1 (28 kDa)
Hypoxia: - + - + - +
IP:
eIF4A2
IgG
Input
250 kDa
150 kDa
50 kDa
37 kDa
37 kDa
37 kDa
IB: eIF4G3 (250 kDa)
IB: eIF4A2 (45 kDa)
IB: eIF4E2 (29 kDa)
IB: eIF4E1 (28 kDa)
Hypoxia: - + - + - +
IP:
eIF4A2
IgG
Input
250 kDa
150 kDa
50 kDa
37 kDa
37 kDa
25 kDa
37 kDa
IB: eIF4G3 (250 kDa)
IB: eIF4A2 (45 kDa)
IB: eIF4E2 (29 kDa)
IB: eIF4E1 (28 kDa)
Hypoxia: - + - + - +

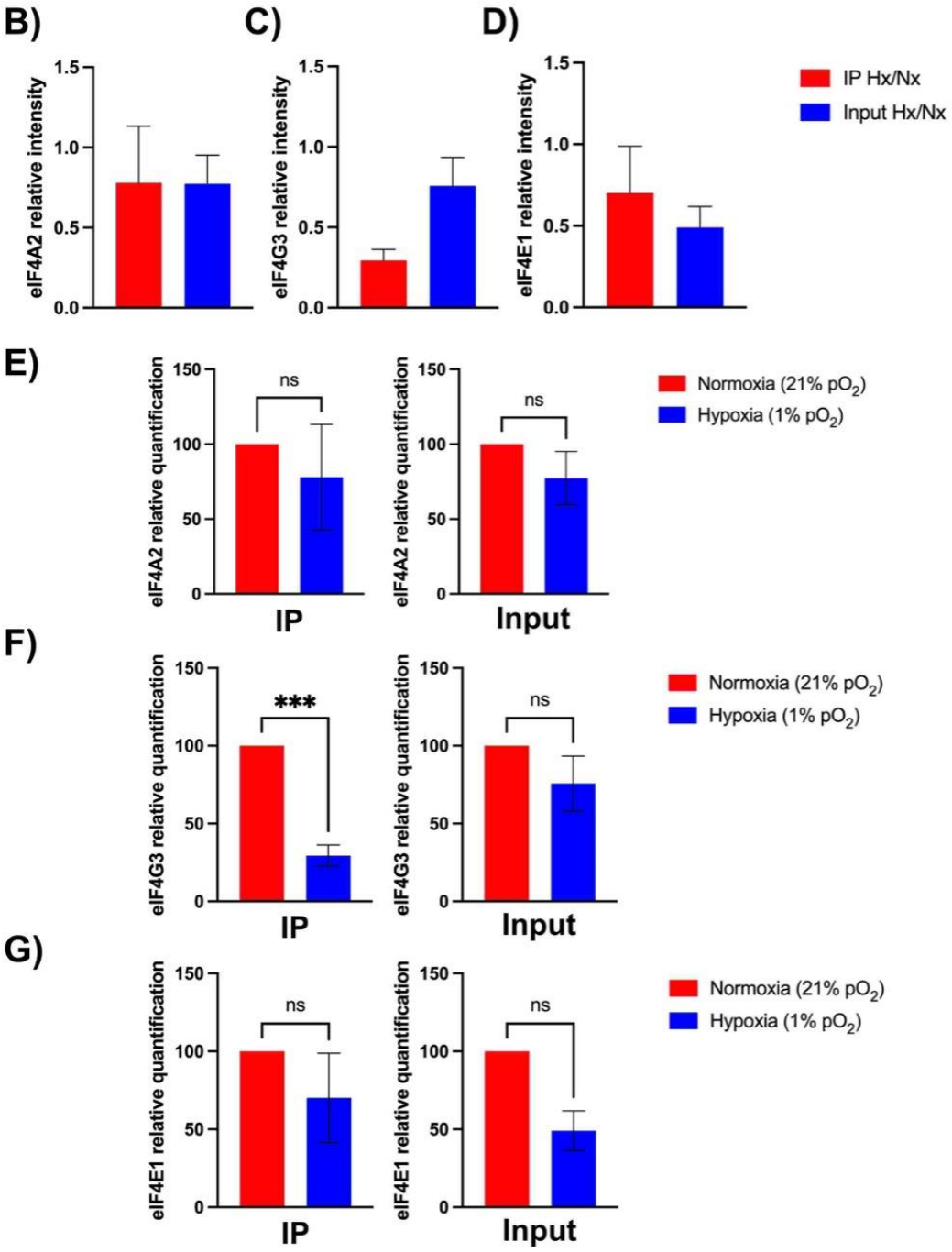

Figure 3.3 eIF4A2 interacts with the eIF4F components eIF4G3 and eIF4E1 in LS174T. A) LS174T cells were exposed to 24h normoxia or hypoxia. Immunoprecipitation was performed with eIF4A2 antibody or IgG as indicated. eIF4A2, eIF4G3, eIF4E1 and eIF4E2 protein expression was analysed by immunoblotting. Densitometry analysis was used to calculate intensity ratios for hypoxia/normoxia in IP and input conditions for **B)** eIF4A2, **C)** eIF4G3 and **D)** eIF4E1. Data was analysed by unpaired t-test comparing hypoxic to normoxic conditions for **E)** eIF4A2 CoIP and input, **F)** eIF4G3 CoIP and input and **G)** eIF4E1 CoIP and input. *p <0.0332, **p<0.0021, ***p<0.0002, ****P<0.0001. Non-significant comparisons not displayed. Error bars indicate ± SEM. n=3 (*n=2 for eIF4E1).

A)

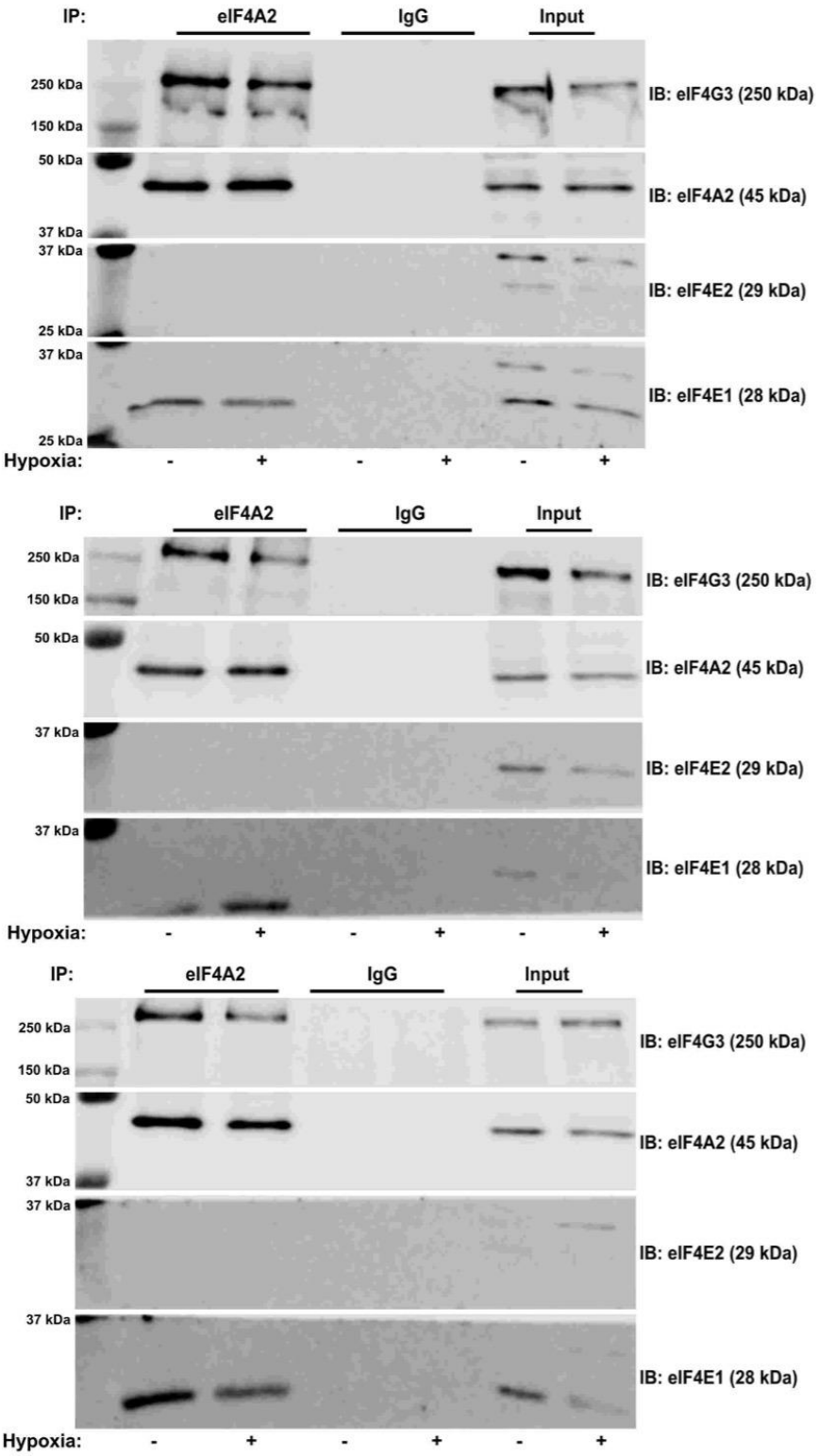
IP:
eIF4A2
IgG
Input
250 kDa
150 kDa
50 kDa
37 kDa
37 kDa
25 kDa
37 kDa
25 kDa
IB: eIF4G3 (250 kDa)
IB: eIF4A2 (45 kDa)
IB: eIF4E2 (29 kDa)
IB: eIF4E1 (28 kDa)
Hypoxia: - + - + - +
IP:
eIF4A2
IgG
Input
250 kDa
150 kDa
50 kDa
37 kDa
37 kDa
IB: eIF4G3 (250 kDa)
IB: eIF4A2 (45 kDa)
IB: eIF4E2 (29 kDa)
IB: eIF4E1 (28 kDa)
Hypoxia: - + - + - +
IP:
eIF4A2
IgG
Input
250 kDa
150 kDa
50 kDa
37 kDa
37 kDa
37 kDa
IB: eIF4G3 (250 kDa)
IB: eIF4A2 (45 kDa)
IB: eIF4E2 (29 kDa)
IB: eIF4E1 (28 kDa)
Hypoxia: - + - + - +

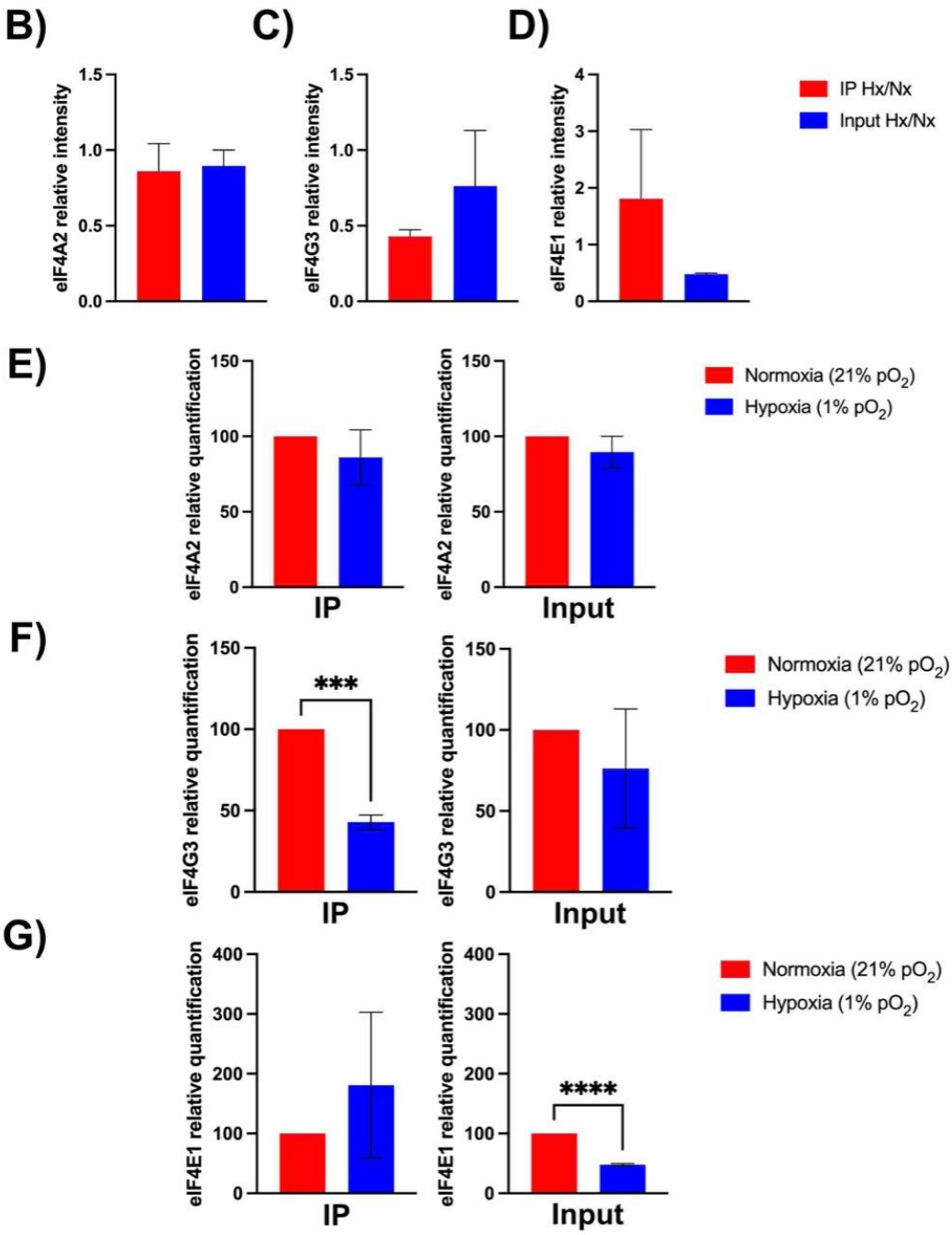

Figure 3.4 eIF4A2 interacts with the eIF4F components eIF4G3 and eIF4E1 in HCT116. **A)** LS174T cells were exposed to 24h normoxia or hypoxia. Immunoprecipitation was performed with eIF4A2 antibody or IgG as indicated. eIF4A2, eIF4G3, eIF4E1 and eIF4E2 protein expression was analysed by immunoblotting. Densitometry analysis was used to calculate intensity ratios for hypoxia/normoxia in IP and input conditions for **B)** eIF4A2, **C)** eIF4G3 and **D)** eIF4E1. Data was analysed by unpaired t-test comparing hypoxic to normoxic conditions for **E)** eIF4A2 CoIP and input, **F)** eIF4G3 CoIP and input and **G)** eIF4E1 CoIP and input. *p <0.0332, **p<0.0021, ***p<0.0002, ****P<0.0001. Non-significant comparisons not displayed. Error bars indicate ± SEM. n=3.

3.3.3 Protein expression of eIF4F components in different oxygen concentrations

Hypoxia has previously been shown to regulate the expression of eIF4E1 in breast cancer[494], whereas eIF4E2 and eIF4G3 expression remains unaltered in glioblastoma despite their involvement in hypoxic translation initiation[316,317]. In order to further understand the regulation of the eIF4F protein machinery by changes in oxygen concentration, LS174T (CMS3) and HCT116 (CMS4) cell lines were exposed to either normoxia, physoxia or hypoxia for 12, 24, 48 or and 72h and eIF4G3, eIF4E2 and eIF4E1 protein expression was analysed by immunoblotting (figure 3.5 and figure 3.6). CA9 expression was measured as a positive control for the induction of hypoxia.

The expression of all three proteins, eIF4G3, eIF4E2 and eIF4E1, displays a similar trend in both cell lines. Maximum expression of these proteins generally occurred at the earlier time points from 12h to 24h and then decreases after 24h (figure 3.5 and figure 3.6). There was a predominantly non-significant increase at the 12h time point for all three proteins, correlating with decreasing oxygen concentration in both cell lines, except for eIF4E2 expression in HCT116 which showed a significant increase in expression in both physoxia and hypoxia at 12h (figure 3.6c; Px, $p<0.0332$; Hx, $P<0.0002$). There was also a significant reduction in eIF4E2 expression at both 24h and 72h in both physoxia and hypoxia in HCT116 (figure 3.6c; 24h Px and Hx, $p<0.0021$; 72h Px and Hx, $p<0.0332$) coinciding with a positive, but non-significant, trend in eIF4E1 expression at 48h (figure 3.6d). However, a significant reduction in eIF4E1 expression was seen at 72h in hypoxia in HCT116 (figure 3.6d; $p<0.0332$). Additionally,
this trend was not observed in the LS174T cell line (figures 3.5c and 3.5d).

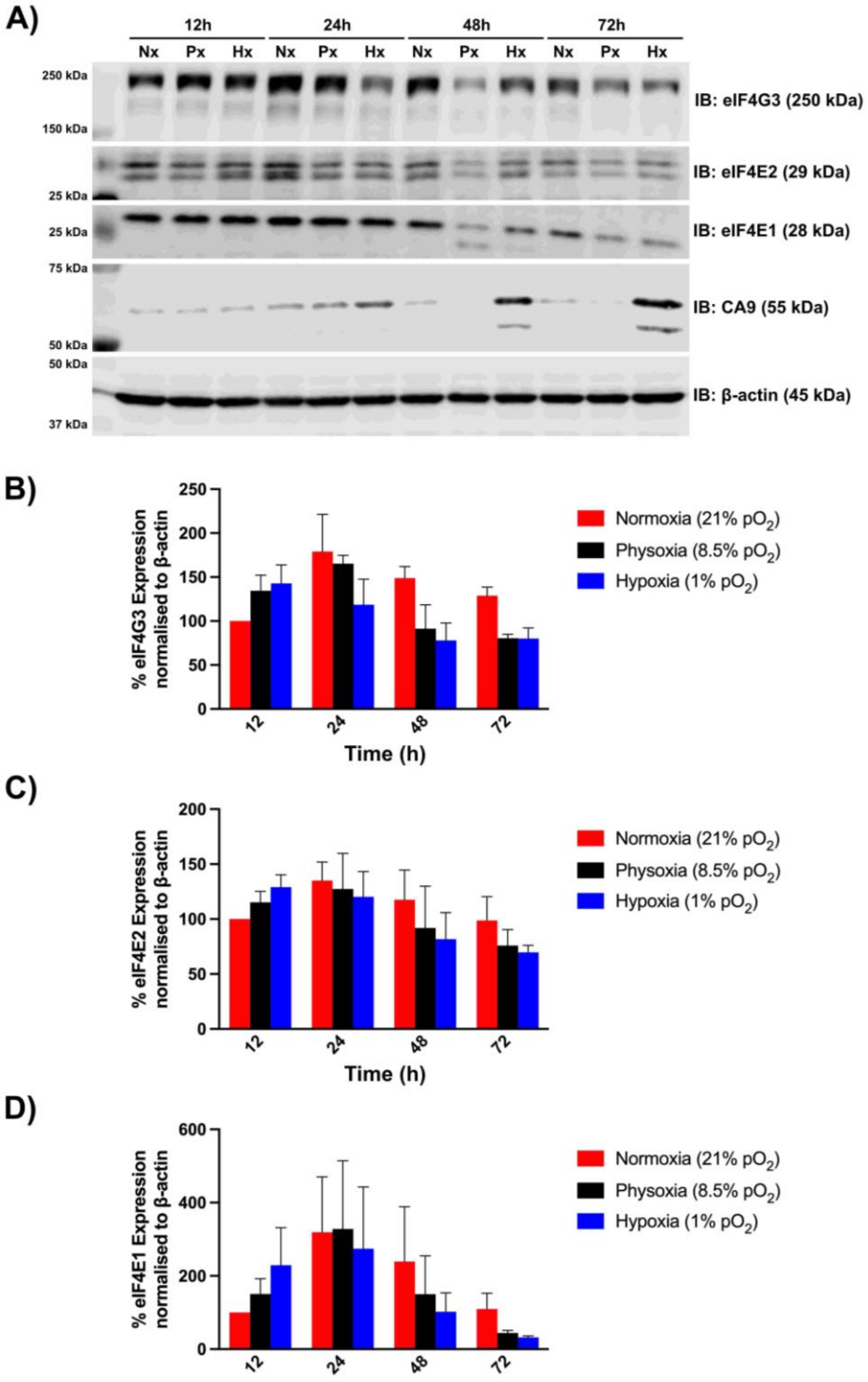

Figure 3.5 eIF4G3, eIF4E2 and eIF4E1 protein expression fluctuates over time under conditions of normoxia, physoxia and hypoxia in LS174T. A) LS174T cells were exposed to 12, 24, 48 or 72h normoxia, physoxia or hypoxia. eIF4G3, eIF4E2 and eIF4E1 protein expression was analysed by immunoblotting. Data analysed by two-way ANOVA comparing normoxia, physoxia and hypoxia for each time point for **B)** eIF4G3, **C)** eIF4E2 and **D)** eIF4E1. *p <0.0332, **p<0.0021, ***p<0.0002, ****P<0.0001. Non-significant comparisons not displayed. Error bars indicate ± SEM. Representative blots are shown. n=3.

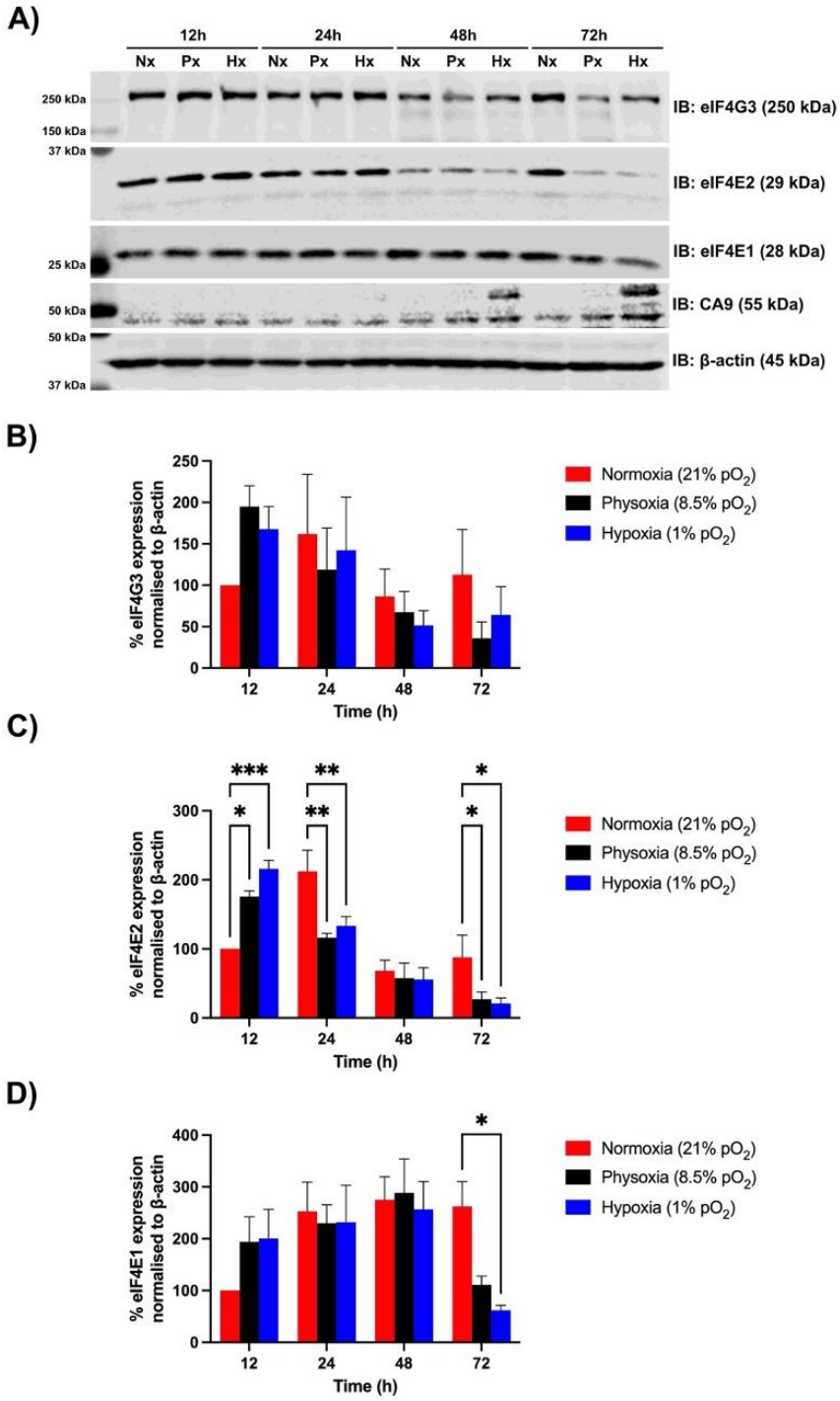

Figure 3.6 eIF4G3, eIF4E2 and eIF4E1 protein expression fluctuates over time under conditions of normoxia, physoxia and hypoxia in HCT116. A) HCT116 cells were exposed to 12, 24, 48 or 72h normoxia, physoxia or hypoxia. eIF4G3, eIF4E2 and eIF4E1 protein expression was analysed by immunoblotting. Data analysed by two-way ANOVA comparing normoxia, physoxia and hypoxia for each time point for **B)** eIF4G3, **C)** eIF4E2 and **D)** eIF4E1. *p <0.0332, **p<0.0021, ***p<0.0002, ****P<0.0001. Non-significant comparisons not displayed. Error bars indicate ± SEM. Representative blots are shown. n=3.

3.3.4 Interaction of eIF4A2 with CNOT7 in hypoxia

eIF4A2 has previously been shown to interact with the microRNA translation repression machinery by binding to the deadenylase component CNOT7 within the Ccr4-Not complex[336]. However, the interaction of eIF4A2 with CNOT7 has not been published using cancer cell lines but has been shown to be present in the LS174T colorectal cancer cell line by immunoprecipitating the CNOT7 protein and probing for eIF4A2 (unpublished data). Furthermore, this interaction was reduced under hypoxic conditions compared to normoxia (unpublished data). To confirm the interaction of eIF4A2 and CNOT7 in colorectal cancer cells and the hypoxic regulation of this interaction, HCT116 and LS174T cells were exposed to 24h normoxia or hypoxia followed by immunoprecipitation of eIF4A2. eIF4A2-bound proteins were analysed by immunoblotting and probed for the presence of CNOT7 (figure 3.7 and figure 3.8).

Figure 3.7a and figure 3.8a confirmed the pulldown of eIF4A2 in LS174T and HCT116 respectively and also confirmed that eIF4A2 expression remained unchanged in hypoxia (figure 3.7a and figure 3.8a). Figure 3.7a and figure 3.8a also confirmed the interaction of CNOT7 with eIF4A2 in both normoxia and hypoxia in both cell lines as indicated by the black arrow denoting the CNOT7 band. However, it was difficult to identify the CNOT7 band on the western blot due to the presence of additional non-specific bands indicated by the red arrows, likely generated from the denatured heavy and light-chain components of the eIF4A2 antibody used for the pulldown. The interaction of eIF4A2 with CNOT7 increased significantly in hypoxia compared to normoxia in HCT116 (figure 3.8c, $p<0.0332$). The lack of significant difference in CNOT7 expression in the input lanes between normoxia and hypoxia confirms that the result in figure 3.8c is due to an increase in CNOT7 binding and not an increase in protein expression. This is further confirmed by the increase in the ratio of hypoxia/normoxia signal for CNOT7 in the pulldown samples compared with the unchanged ratio in the input samples (figure 3.8b). Similarly, despite no significant difference in the binding of CNOT7 to eIF4A2 in LS174T, there is a similar trend of increased CNOT7 binding in hypoxia as indicated by the increased hypoxia/normoxia signal ratio for CNOT7 in the pulldown samples (figure 3.7b) as well as the positive trend in CNOT7 expression in hypoxia compared to normoxia in the pulldown samples accompanied with no difference in expression in the input samples (figure 3.7c).

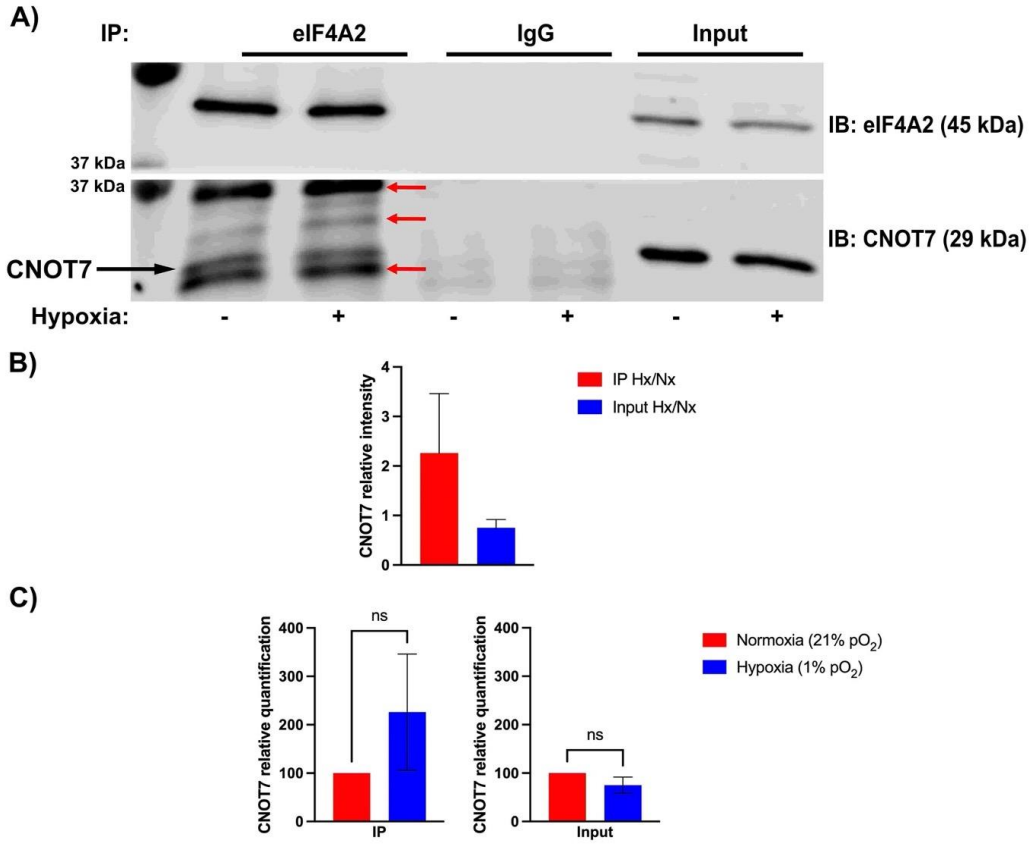

Figure 3.7 eIF4A2 binding to CNOT7 is unchanged in hypoxia in LS174T. LS174T cells were exposed to 24h normoxia or hypoxia. **A)** Immunoprecipitation was performed with eIF4A2 antibody or IgG as indicated. eIF4A2 and CNOT7 protein expression was analysed by immunoblotting. Red arrows represent non-specific bands likely from denatured IP antibody heavy and light chain. **B)** Densitometry analysis was used to calculate intensity ratios for hypoxia/normoxia in IP and input conditions for CNOT7. **C)** Data was analysed by unpaired t-test comparing hypoxic to normoxic conditions for CNOT7 CoIP and input. *p <0.0332, **p<0.0021, ***p<0.0002, ****P<0.0001. Error bars indicate ± SEM. Representative blots are shown. n=3.

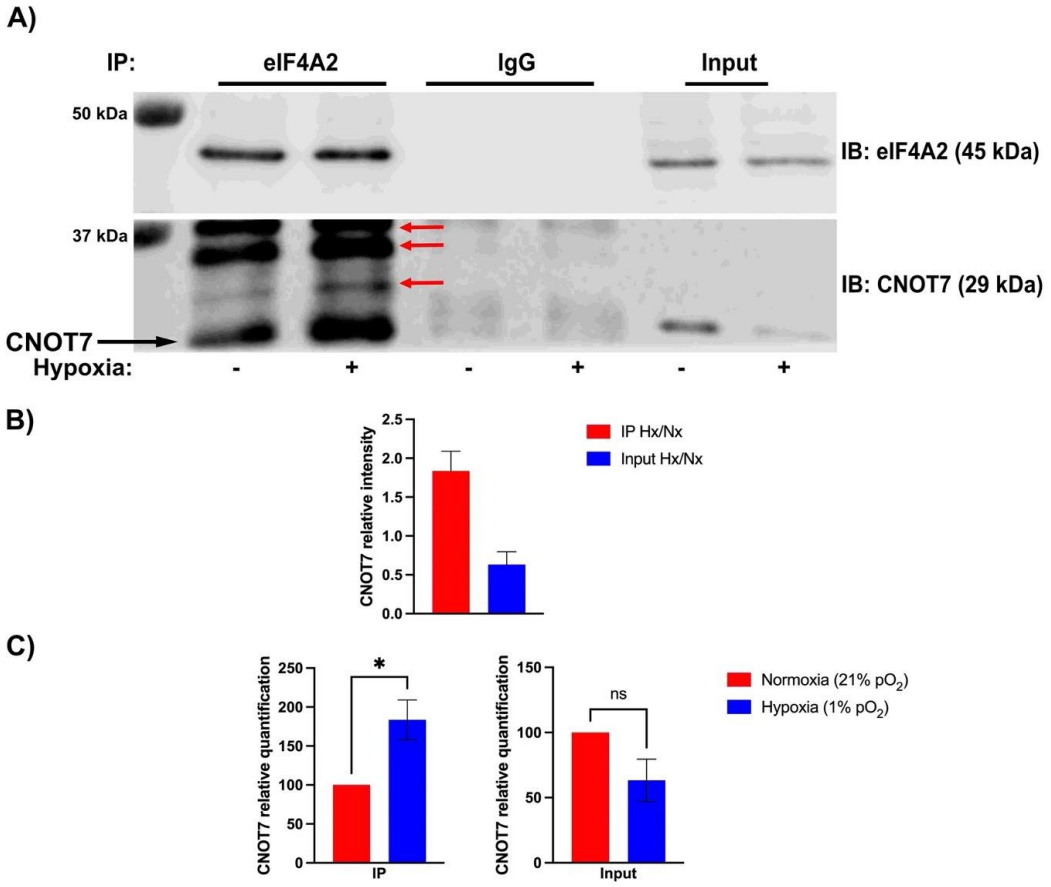

Figure 3.8 eIF4A2 binding to CNOT7 increases in hypoxia in HCT116. HCT116 cells were exposed to 24h normoxia or hypoxia. **A)** Immunoprecipitation was performed with eIF4A2 antibody or IgG as indicated. eIF4A2 and CNOT7 protein expression was analysed by immunoblotting. Red arrows represent non-specific bands likely from denatured IP antibody heavy and light chain. **B)** Densitometry analysis was used to calculate intensity ratios for hypoxia/normoxia in IP and input conditions for CNOT7. **C)** Data was analysed by unpaired t-test comparing hypoxic to normoxic conditions for CNOT7 CoIP and input. *p <0.0332, **p<0.0021, ***p<0.0002, ****P<0.0001. Error bars indicate ± SEM. Representative blots are shown. n=3.

3.3.5 Protein expression of CNOT7 in different oxygen concentrations

The Ccr4-Not complex has previously been implicated in the cellular response to hypoxia in fungi due to a reduction in ATP production[495]. However, the expression of CNOT7 in mammalian cells and specifically in cancer cells in the context of hypoxia has never been studied. In order to further understand the regulation of CNOT7 by changes in oxygen concentration, LS174T (CMS3) and HCT116 (CMS4) cell lines were exposed to either normoxia, physoxia or hypoxia for 12, 24, 48 or and 72h and CNOT7 protein expression was analysed by immunoblotting (figure 3.9 and figure 3.10). CA9 expression was measured as a positive control for the induction of hypoxia.

In both cell lines, maximum hypoxic expression of CNOT7 was observed at the earlier time points of 12h and 24h followed by a non-significant decreasing trend after 24h (figures 3.9 and 3.10). This could explain the increase in CNOT7 binding to eIF4A2 observed at 24h hypoxia as shown in figure 3.8. Interestingly, this also coincided with the maximum expression seen for the hypoxic eIF4F components as shown in figure 3.5 and figure 3.6. However, there was a significant reduction in hypoxic CNOT7 expression at 24h in LS174T compared to normoxia (figure 3.9b; $p<0.0332$). This could explain the lack of a significant difference in CNOT7 binding to eIF4A2 in hypoxia in the LS174T cell line (figure 3.7). Furthermore, there was a significant decrease in CNOT7 expression in both cell lines at 72h in hypoxia compared to normoxia (HCT116 $p<0.0332$; LS174T $p<0.0021$). There was also a significant reduction in CNOT7 expression between physoxia and hypoxia at 72h in LS174T ($p<0.0332$) and between normoxia and physoxia at 72h in HCT116 ($p<0.0332$).

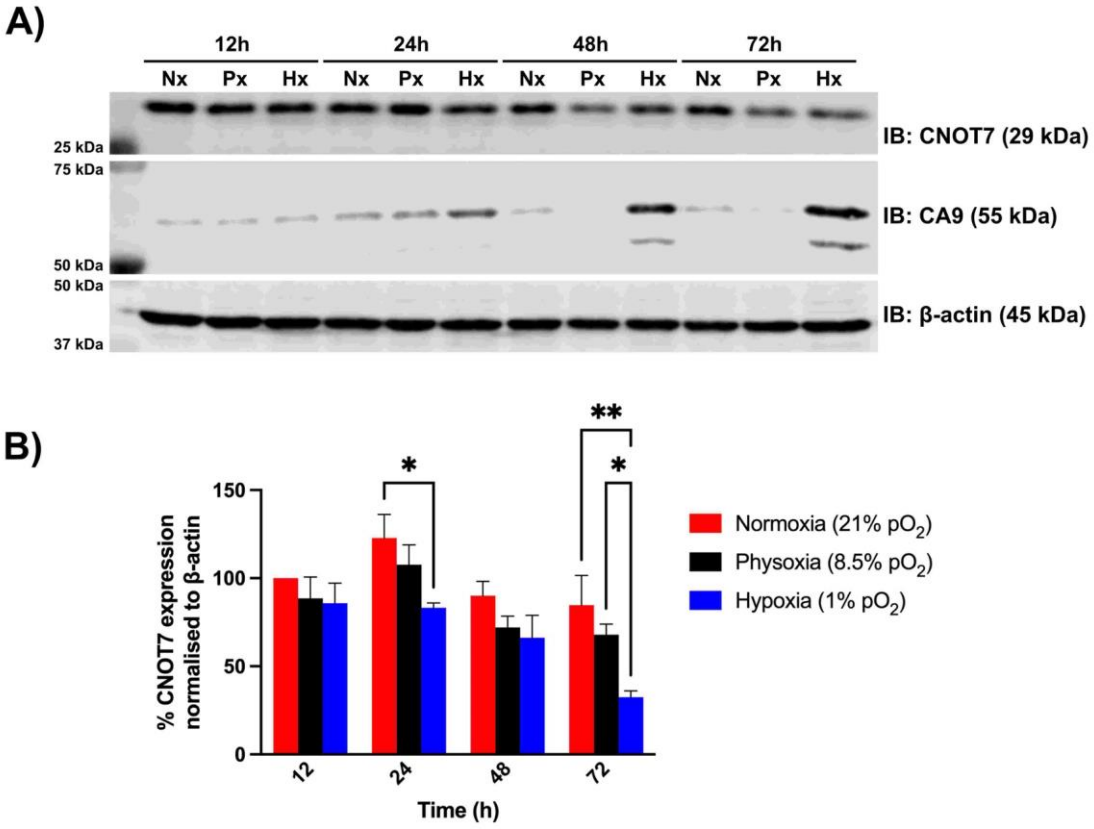

Figure 3.9 CNOT7 protein expression fluctuates over time under conditions of normoxia, physoxia and hypoxia in LS174T. A) LS174T cells were exposed to 12, 24, 48 or 72h normoxia, physoxia or hypoxia. CNOT7 protein expression was analysed by immunoblotting. **B)** Data analysed by two-way ANOVA comparing normoxia, physoxia and hypoxia for each time point. *p <0.0332, **p<0.0021, ***p<0.0002, ****P<0.0001. Non-significant comparisons not displayed. Error bars indicate ± SEM. Representative blots are shown. n=3.

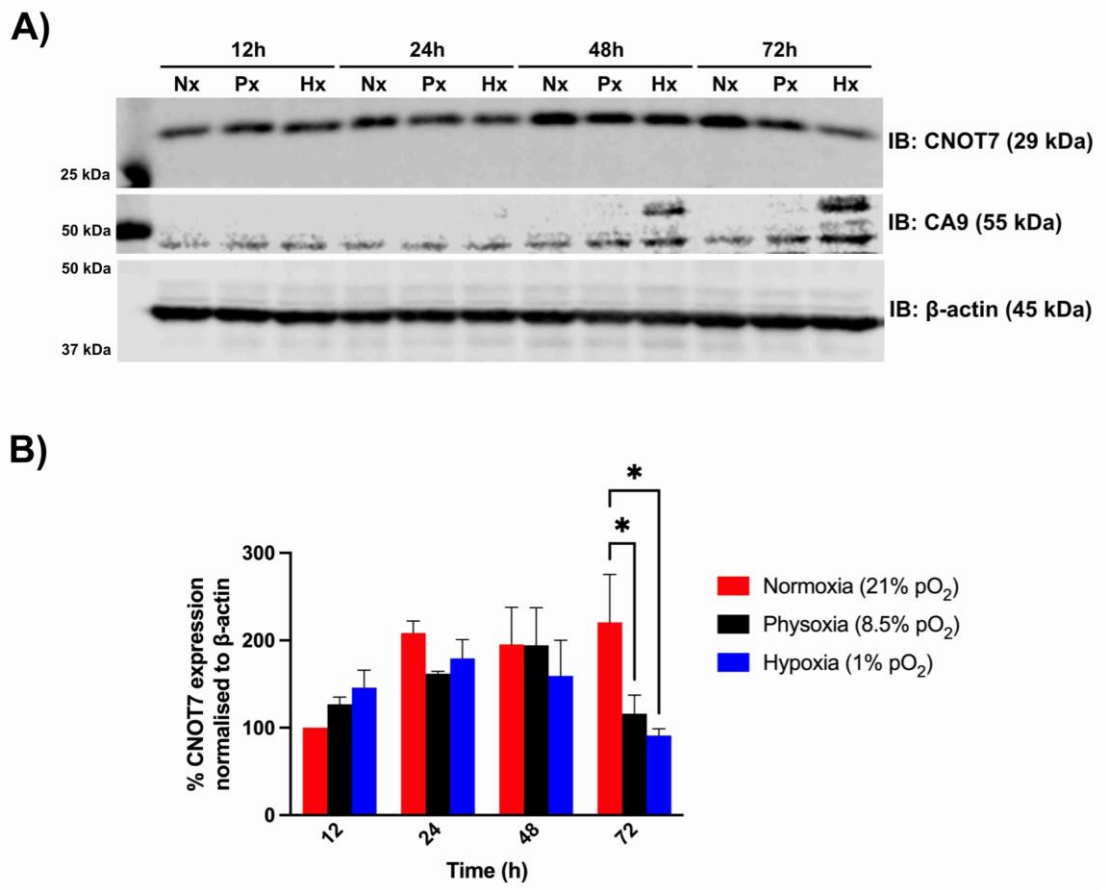

Figure 3.10 CNOT7 protein expression fluctuates over time under conditions of normoxia, physoxia and hypoxia in HCT116. A) HCT116 cells were exposed to 12, 24, 48 or 72h normoxia, physoxia or hypoxia. CNOT7 protein expression was analysed by immunoblotting. **B)** Data analysed by two-way ANOVA comparing normoxia, physoxia and hypoxia for each time point. *p <0.0332, **p<0.0021, ***p<0.0002, ****P<0.0001. Non-significant comparisons not displayed. Error bars indicate ± SEM. Representative blots are shown. n=3.

3.3.6 Generation and validation of LS174T eIF4A2 CRISPR-Cas9 knockout clones

As mentioned in section 3.1, previous work carried out by the Mcintyre lab has investigated the impact of eIF4A2 knockdown using shRNA and shown that eIF4A2 knockdown reduces colorectal cancer cell survival in both 2-D and 3-D *in vitro* in normoxia and hypoxia [355]. Similar results were also obtained in another study using shRNA targetting eIF4A2 or with chemical inhibition using Silvestrol [347]. However, the effect of permanently blocking eIF4A2 protein expression using CRISPR-Cas9 gene editing technology on colorectal cancer cell survival has not been investigated, especially in the context of hypoxia.

Inducible Cas9-expressing colorectal cancer cell lines, termed iCas9, were generated using Edit-R inducible Cas9 lentiviral particles (Horizon Discovery) by lentiviral transduction as described previously. Transfection of LS174T iCas9 colorectal cancer cells with single gRNAs, termed g60 and g61, targetting eIF4A2 alongside a non-targeting control gRNA was performed after doxycycline-induced Cas9 expression as described in section 2.7.2 followed by single-cell clonal selection and expansion as described in section 2.7.3. In order to validate the knockout efficiency, approximately 10 clones per gRNA were cultured and lysed for protein extraction and eIF4A2 protein expression was analysed by immunoblotting (data not shown). The clones with the highest knockout efficiency, termed g60 D9 and g61 F6, were selected for further validation by immunoblotting (figure 3.11). Figure 3.11 shows that eIF4A2 knockout in both g60 D9 and g61 F6 resulted in a significant reduction in eIF4A2 protein expression compared to the non-targeting control (>99%, $p<0.0001$).

In order to confirm that the CRISPR-Cas9-induced mutations in the eIF4A2 DNA sequence were out-of-frame, and therefore unconducive to functional eIF4A2 expression, and to confirm the zygosity of the mutation, Sanger sequencing was performed following DNA extraction on g60 D9 and g61 F6 cells as well as non-targeting control cells as described in section 2.7.4 (figure 3.12). Figure 3.12 highlights the locations of the mutations within the DNA sequence and summarises the type of mutation and the zygosity status of the eIF4A2 knockout clone. g60 D9 was a heterozygous out-of-frame knockout with 1bp and 10bp insertions on the separate alleles whilst g61 F6 was a homozygous out-of-frame knockout with a 1bp insertion.

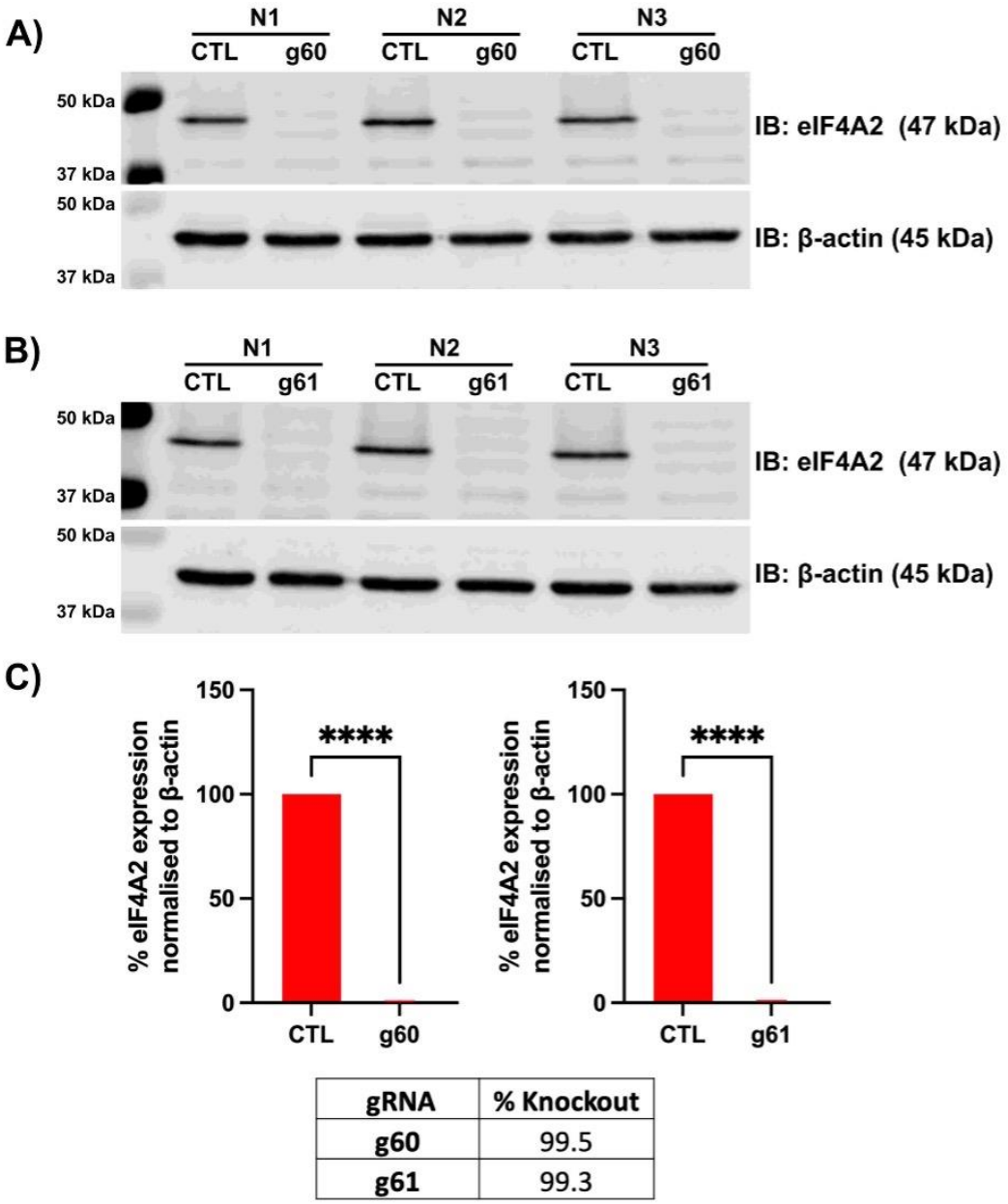

gRNA	% Knockout
g60	99.5
g61	99.3

Figure 3.11 Inducible CRISPR-Cas9 gene editing and clonal selection leads to eIF4A2 knockout in LS174T. Cas9-transduced LS174T cells were treated with 2 μg/mL doxycycline for 48 hours to induce Cas9 expression before transfection with two separate gRNAs g60 and g61 targetting eIF4A2. After 24 hours, cells underwent single cell selection and expansion to generate clonal populations. Once expanded, cells were seeded for 48 hours and lysed for protein extraction. eIF4A2 protein expression was analysed by immunoblotting comparing control lysates with **A)** g60 and **B)** g61 eIF4A2 knockout lysates. **C)** Data analysed by unpaired t-test. *p <0.0332, **p<0.0021, ***p<0.0002, ****P<0.0001. Error bars indicate ± SEM. Percentage knockout calculated by subtraction of eIF4A2 expression in knockout clones from control clones.. n=3.

A)

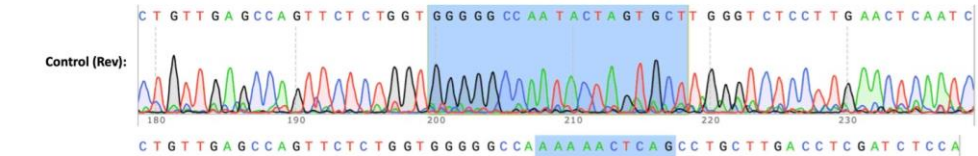

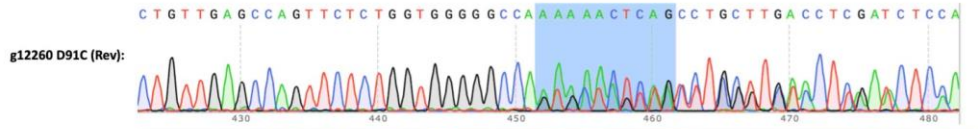

B)

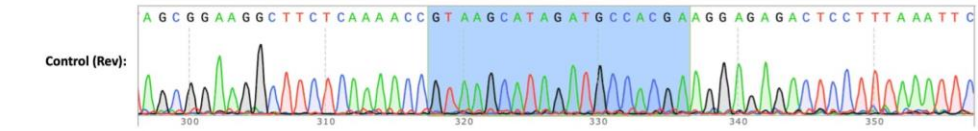

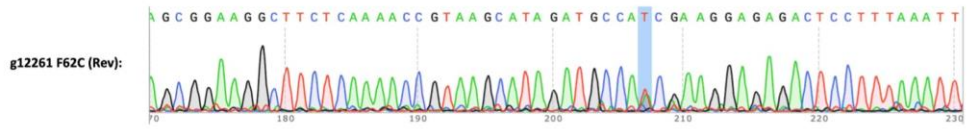

C)

Target	Clone	Sequence	Mutation	Zygosity	KO/KD
eIF4A2 (g60)	D9 1C	Allele 1: GGGGGCCAATACTAGTAGCT Allele 2: GGGGGCCAGAGAACTGTA ATACTAGTGCT	Allele 1: 1bp insertion (A460) Allele 2: 10bp insertion (G452-A461)	Hetero	KO
eIF4A2 (g61)	F6 2C	GTAAGCATAGATGCCATCGA	1bp insertion (T207)	Homo	KO

Figure 3.12 Sanger sequencing of LS174T eIF4A2 knockout clones determines mutation status and zygosity. DNA was extracted from LS174T control and eIF4A2 knockout clonal cell lines, amplified and purified before being sent for Sanger sequencing. **A)** and **B)** Chromatograms of control samples highlight the gRNA sequence used to generate the CRISPR knockout. Chromatograms of eIF4A2 knockout samples **A)** g60 and **B)** g61 indicate the CRISPR-Cas9-induced mutation in the DNA sequence. Chromatograms were analysed using SnapGene. **C)** Summary table indicating the CRISPR-induced mutations highlighted in red within the target gRNA sequence as well as details of the mutation and zygosity status.

3.3.7 Impact of eIF4A2 knockout on cell survival and 3-dimensional spheroid growth using eIF4A2 knockout clones

In order to investigate the impact of eIF4A2 knockout on 3-dimensional spheroid growth, LS174T eIF4A2 knockout clones g60 D9 and g61 F6 cells, as well as control cells, were used to form spheroids as described in section 2.2.1. Spheroids were grown for 10 days with images taken on days 3, 5, 7 and 10 and spheroid volumes were calculated and analysed as described in section 2.2.2. Figure 3.13a displays representative images of the three spheroid conditions at each of the time points measured. Morphologically, the eIF4A2 knockout spheroids displayed less roundedness compared to control spheroids and had an increased propensity for cell protrusions from the spheroid edges. Figure 3.13b shows the average spheroid volume for the control spheroids and the eIF4A2 knockout spheroids and indicates a reduction in spheroid volume with eIF4A2 knockout compared to the control. Linear regression analysis was used to calculate the growth rates for the different spheroids and figure 3.13c confirms that there was a statistically significant reduction in spheroid growth rates in both eIF4A2 knockout clones compared to the control cells (g60, $p<0.0332$; g61, $p<0.0021$). On the other hand, there were no statistically significant differences observed in *in vitro* cell survival measured by clonogenics assay as described in section 2.4 using the LS174T eIF4A2 knockout clones and no differences were observed in colony formation between the normoxic and hypoxic conditions (data not shown). Furthermore, the two eIF4A2 knockout clones appeared to affect colony formation differently as evidenced by the lack of consistency between the two cell lines (data not shown).

This data supports the hypothesis that eIF4A2 is required for the growth of colorectal cancer cells within a 3-dimensional context that is more representative of the tumour microenvironment. However, as these spheroids were formed from cell lines derived from single clones it is possible that the differences in morphology and growth rate are in fact due to genetic variability between the clones. This would also explain the differences observed in the clonogenics assay between the two eIF4A2 knockout cell lines. Therefore, it was decided that a second approach for generating the eIF4A2 knockout cell lines was required to corroborate these findings.

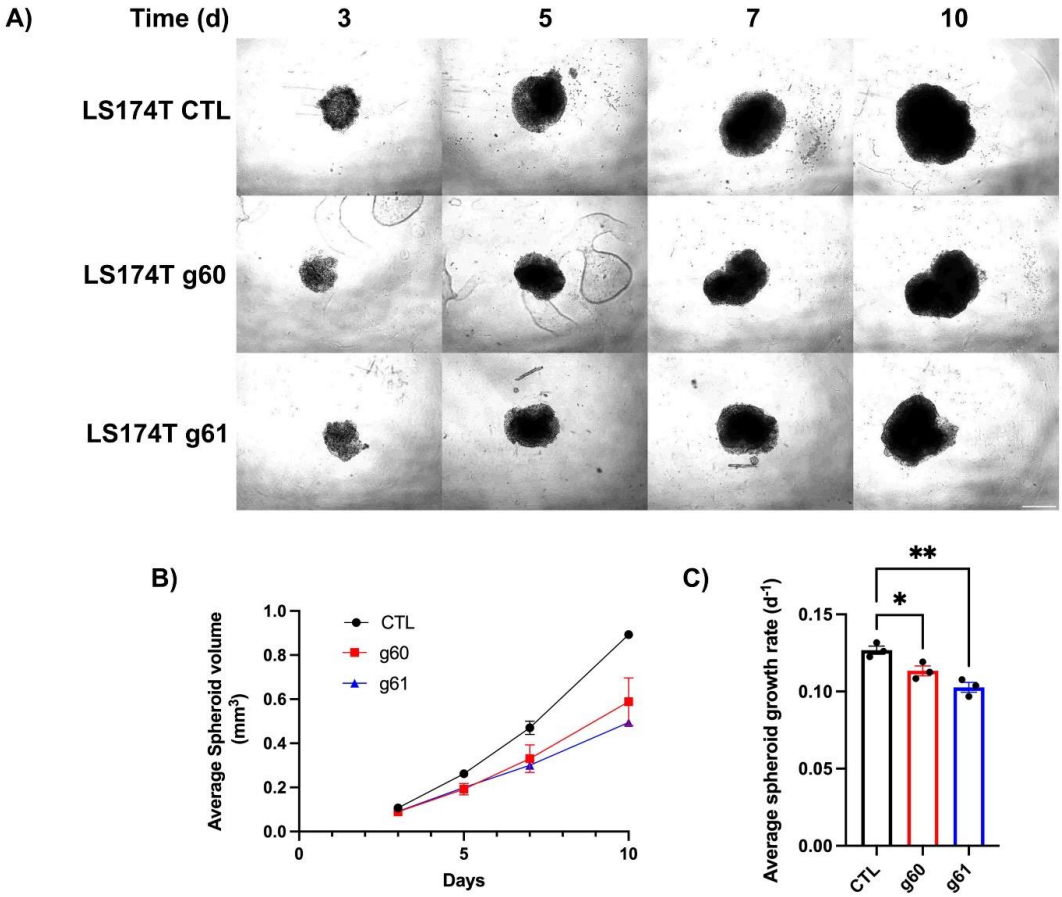

Figure 3.13 eIF4A2 knockout reduces 3-dimensional spheroid growth *in vitro* in LS174T. LS174T iCas9 cells transfected with either non-targeting gRNA control (CTL) or eIF4A2-targeting gRNAs g60 and g61 and isolated into clonal populations were used to form 3-dimensional spheroids *in vitro* at the optimised seeding density of 2000 cells/well. **A)** Representative images from three experimental repeats of LS174T spheroids taken on days 3, 5, 7 and 10 at 4x magnification. Scale bar represents 500µm. **B)** Images were used to calculate the average spheroid volume for CTL, g60 and g61 spheroids on days 3, 5, 7 and 10. **C)** Spheroid volumes were used to calculate growth rates for CTL, g60 and g61 spheroids using linear regression analysis. Data was analysed by one-way ANOVA comparing eIF4A2 knockout spheroid growth rates to the control. *p <0.0332, **p<0.0021, ***p<0.0002, ****P<0.0001. Error bars indicate ± SEM. n=3.

3.3.8 Generation and validation of HCT116 eIF4A2 CRISPR-Cas9 knockout pools

Due to the uncertainty surrounding the use of cell lines derived from individual clones and whether the clonal variation between these cell lines was responsible for the differences in spheroid growth observed in the LS174T cell line (figure 3.13) as well as the mixed effects seen with the eIF4A2 knockout clones on cell survival in 2-D using clonogenics assays (data not shown), an alternative gene editing approach, termed the pooling method, was developed to attempt to overcome this.

Using this method, HCT116 iCas9 cells were transfected with single gRNAs targeting eIF4A2, again termed g60 and g61 plus a third guide g62, along with a control gRNA. However, the transfected cells were then maintained as a mixed population of cells as opposed to undergoing single-cell clonal sorting. These mixed populations of cells were then expanded before undergoing a second round of transfection with the same gRNA. A total of three rounds of transfection were performed to try to progressively increase the knockout efficiency within the pools. After each round of transfection, cells were seeded for protein extraction to assess the knockout efficiency by immunoblotting (figure 3.14). Figure 3.14a and 3.14b display the immunoblotting results after the first round of transfection, termed T1, and the second round of transfection, termed T2, respectively. All three eIF4A2 knockout pools showed a partial knockout of eIF4A2 compared to the control pool after one round of transfection (figure 3.14a). The knockout efficiency following the second round of transfection was enhanced in the g61 and g62 knockout pools but was unchanged in the g60 pool (figure 3.14b). Based on the percentage knockout being <80% in all three pools it was decided a third round of transfection, termed T3, was required to further enhance the knockout efficiency. The third transfection improved the knockout efficiency in all three T3 pools compared to the T2 pools with a statistically significant reduction in eIF4A2 protein expression compared to the control in all three cases (figure 3.14c, $p<0.0001$). Two out of the three T3 pools, g61 and g62, had a percentage knockout >80% and so these two cell lines were selected for downstream experiments.

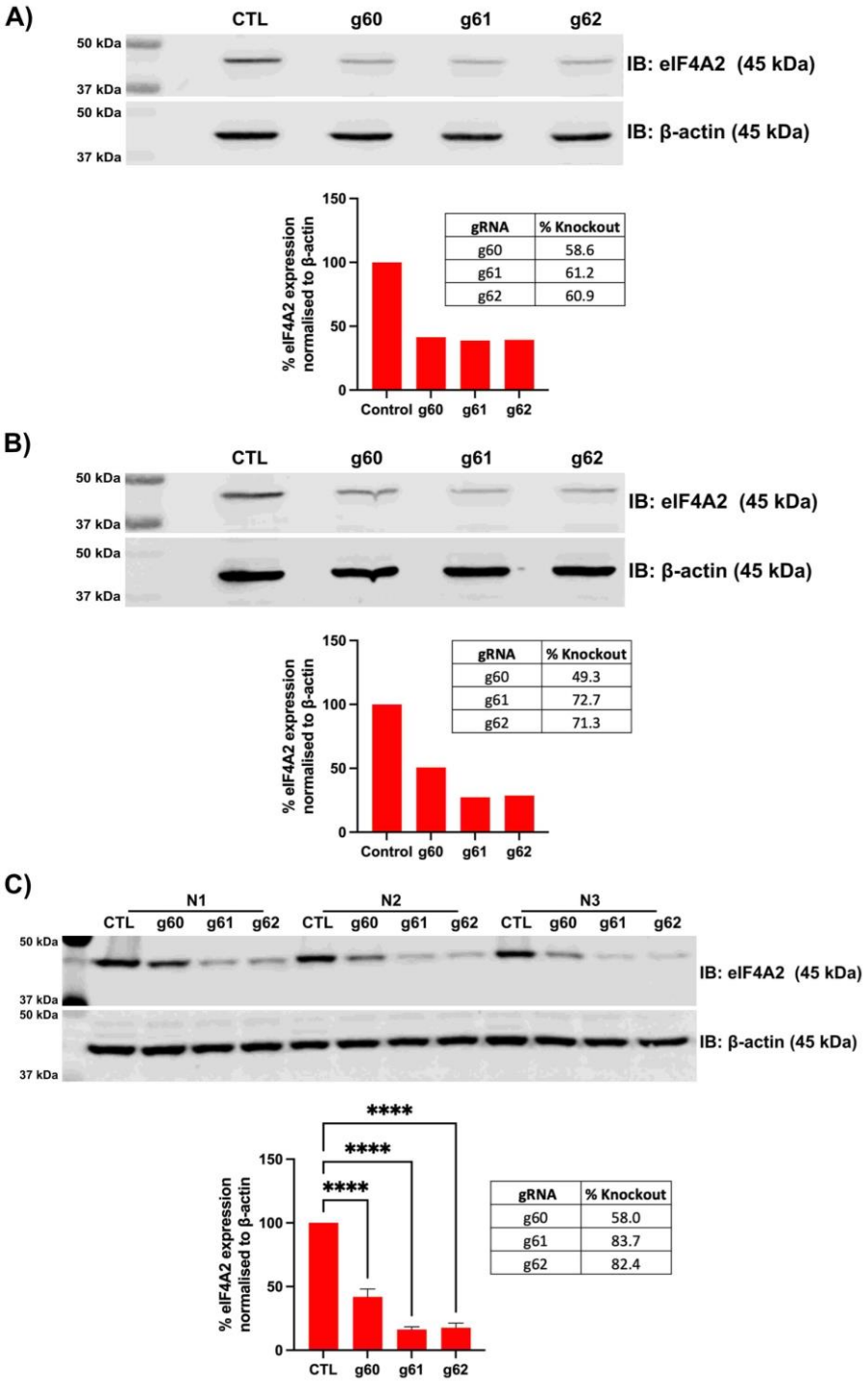

Figure 3.14 Inducible CRISPR-Cas9 gene editing using the pooling method leads to partial eIF4A2 knockout in HCT116. Cas9-transduced HCT116 cells were treated with 2 μg/mL doxycycline for 48 hours to induce Cas9 expression before transfection (T1) with gRNA targetting eIF4A2. After 72 hours, cells were seeded for protein extraction and a second round of transfection (T2). Re-seeded cells underwent a second round of transfection followed by seeding for protein extraction and a third transfection (T3). Cells underwent a third and final transfection followed by seeding for protein extraction. eIF4A2 protein expression was analysed by immunoblotting for **A)** transfection 1, **B)** transfection 2 and **C)** transfection 3. Data analysed by one-way ANOVA comparing eIF4A2 expression in control cells with expression in the knockout pools. *p <0.0332, **p<0.0021, ***p<0.0002, ****P<0.0001. Error bars indicate ± SEM. Percentage knockout calculated by subtraction of eIF4A2 expression in knockout clones from control clones. n=3. *n=1 only for T1 and T2 experiments.

3.3.9 Impact of eIF4A2 knockout on cell survival and 3-dimensional spheroid growth using eIF4A2 knockout pools

In order to first assess the impact of eIF4A2 knockout on cell survival, HCT116 eIF4A2 knockout T3 pools were seeded for clonogenics assay and colonies were stained and counted as described in section 2.4. Cells were exposed to either normoxia or hypoxia for 72h after seeding before being placed in normoxia for two weeks to allow colonies to form. Figure 3.15 displays the results of the clonogenics assay, including representative images of colony formation (3.15a) and analysis of colony counts (3.15b). Following eIF4A2 knockout, no statistically significant difference was observed in cell survival in either normoxia or hypoxia compared to the controls (figure 3.15b). There was also no difference in cell survival between normoxia and hypoxia in the controls suggesting that hypoxia alone does not impact colony formation.

In order to investigate the impact of eIF4A2 knockout on 3-dimensional spheroid growth using the eIF4A2 knockout pools, the HCT116 T3 pools, g61 and g62 cells, as well as control cells, were used to form spheroids as described in section 2.2.1. Spheroids were grown for 10 days with images taken on days 3, 5, 7 and 10 and spheroid volumes were calculated and analysed as described in section 2.2.2. Figure 3.16a displays representative images of the three spheroid conditions at each of the time points measured. Morphologically, there were no visible differences between the eIF4A2 knockout and control spheroids. Figure 3.16b shows the average spheroid volume for the control spheroids and the eIF4A2 knockout spheroids and shows there was no difference in spheroid volume between the conditions. Linear regression analysis was used to calculate the growth rates for the different spheroids and figure 3.16c confirms that there was no reduction in spheroid growth rates in both eIF4A2 knockout clones compared to the control cells.

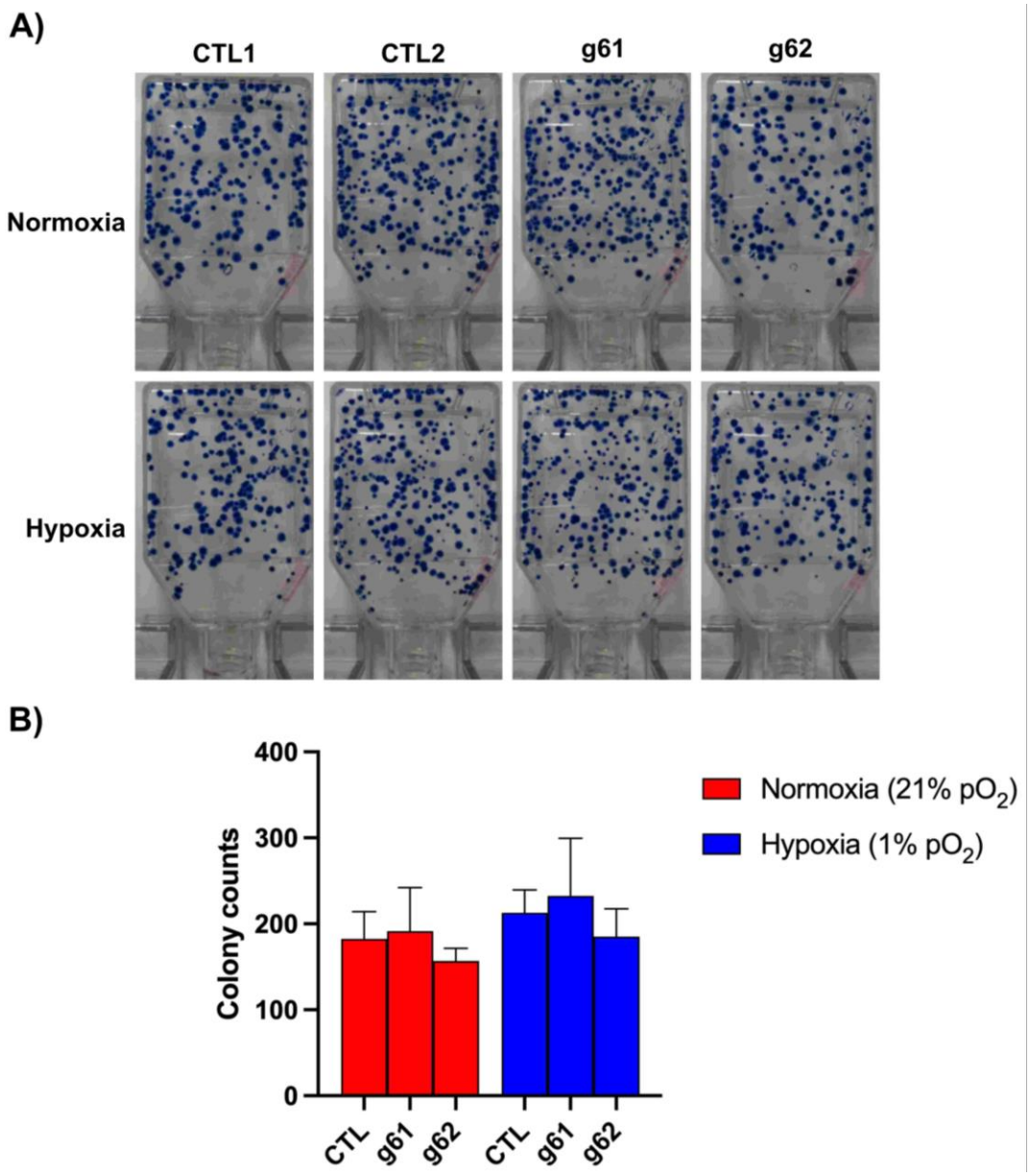

Figure 3.15 eIF4A2 knockout has no effect on cell survival *in vitro* in HCT116. HCT116 iCas9 cells transfected three times with either non-targeting gRNA (CTL) or eIF4A2-targetting gRNAs g61 and g62 were seeded for clonogenics assay *in vitro* at the optimised seeding density of 500 cells/flask. Two technical replicates were seeded per experimental condition. For hypoxic conditions, cells were incubated in hypoxia for 72h and then returned to normoxia for two weeks to allow colonies to form. **A)** Representative images of colony formation for each experimental condition **B)** Data analysed by two-way ANOVA comparing colony counts between CTL and eIF4A2 knockout conditions for both normoxia and hypoxia. *p <0.0332, **p<0.0021, ***p<0.0002, ****P<0.0001. Non-significant comparisons not displayed. Error bars indicate ± SEM. n=3.

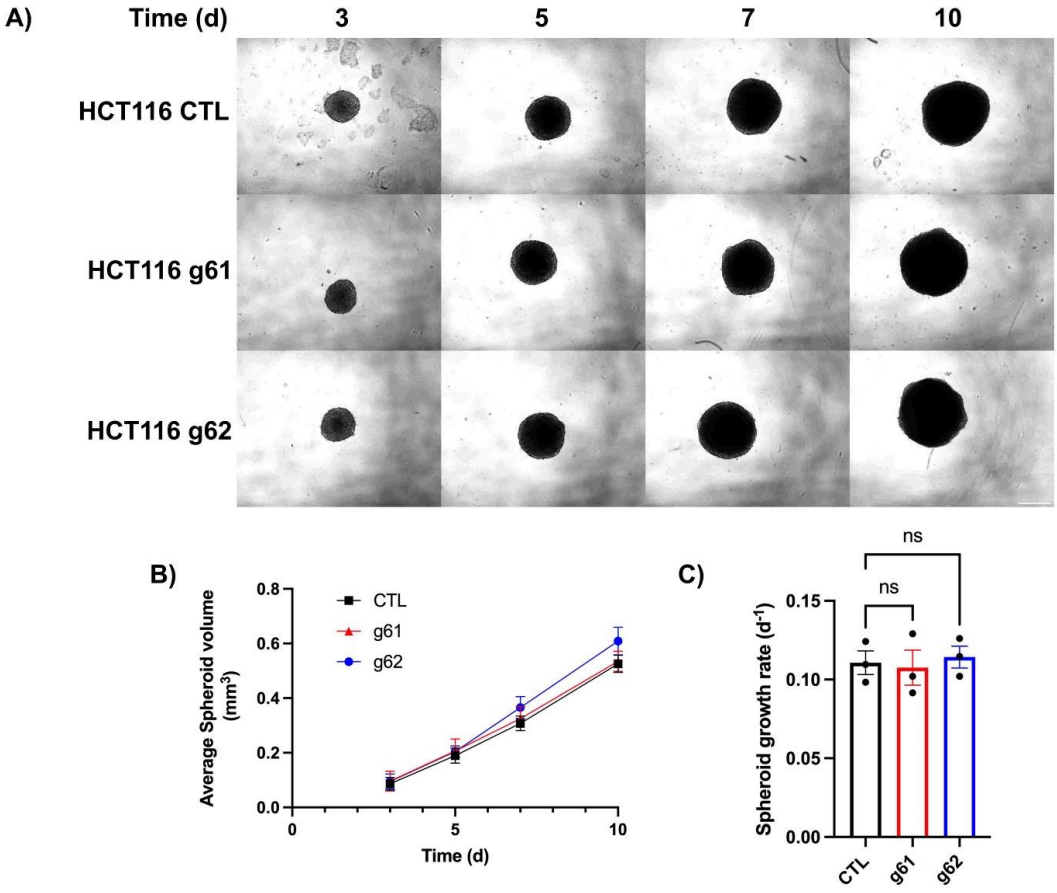

Figure 3.16 eIF4A2 knockout has no effect on 3-dimensional spheroid growth *in vitro* in HCT116. HCT116 iCas9 cells transfected three times with either non-targeting gRNA (CTL) or eIF4A2-targetting gRNAs g61 and g62 were used to form 3-dimensional spheroids *in vitro* at the optimised seeding density of 1000 cells/well. **A)** Representative images from three experimental repeats of HCT116 spheroids taken on days 3, 5, 7 and 10 at 4x magnification. Scale bar represents 500µm. **B)** Images were used to calculate the average spheroid volume for CTL, g61 and g62 spheroids on days 3, 5, 7 and 10. **C)** Spheroid volumes were used to calculate growth rates for CTL, g61 and g62 spheroids using linear regression analysis. Data was analysed by one-way ANOVA comparing eIF4A2 knockout spheroid growth rates to the control. Error bars indicate ± SEM. n=3.

3.3 10 Generation and validation of LS174T lentiviral eIF4A2 CRISPR-Cas9 knockout cell lines

Due to the observed differences in cell survival and 3-D spheroid growth in the LS174T eIF4A2 knockout clones and the HCT116 eIF4A2 knockout pools, it was decided that a new improved CRISPR-Cas9 editing system was required to overcome the issues of clonal variation whilst also improving the knockout efficiency above that seen with the pooling method. LS174T iCas9 cells were therefore transduced with a lentiviral vector harbouring the target gRNA sequence as described in section 2.7.6, in order to generate cell lines stably expressing the gRNA of interest. Gene knockout was then induced as required with the addition of doxycycline to activate the expression of the Cas9 protein.

In order to further assess the impact of eIF4A2 knockout on colorectal cancer cell survival, LS174T iCas9 cells were transduced separately with two lentiviral gRNA vectors, termed g77 and g78, as well as a negative control vector to generate stable cell lines expressing eIF4A2 gRNA. Knockout of eIF4A2 was induced with the addition of doxycycline and cells were seeded for protein extraction to assess the efficiency of the knockout by measuring eIF4A2 protein expression by immunoblotting (figure 3.17). Cell lines without the addition of doxycycline were included as additional controls to monitor the efficiency of Cas9 induction and to account for any potential doxycycline-associated toxicity. Doxycycline effectively induced the expression of Cas9 in all three cell lines whereas Cas9 expression was absent in the samples without doxycycline addition (figure 3.17a). There was a statistically significant reduction in eIF4A2 expression in both the g77 and g78 cell lines with doxycycline addition compared to the negative control (figure 3.17b, $p<0.0001$). There was a greater level of eIF4A2 knockout in the g78 cell line compared to g77 as evidenced by their respective percentage knockouts of 71.4% and 86.1%. There was no statistically significant difference in eIF4A2 expression in the negative control cell line with or without doxycycline addition. A similar reduction in eIF4A2 expression in the g77 and g78 cell lines without doxycycline addition compared to the same cell lines with doxycycline addition was also observed (figure 3.17a).

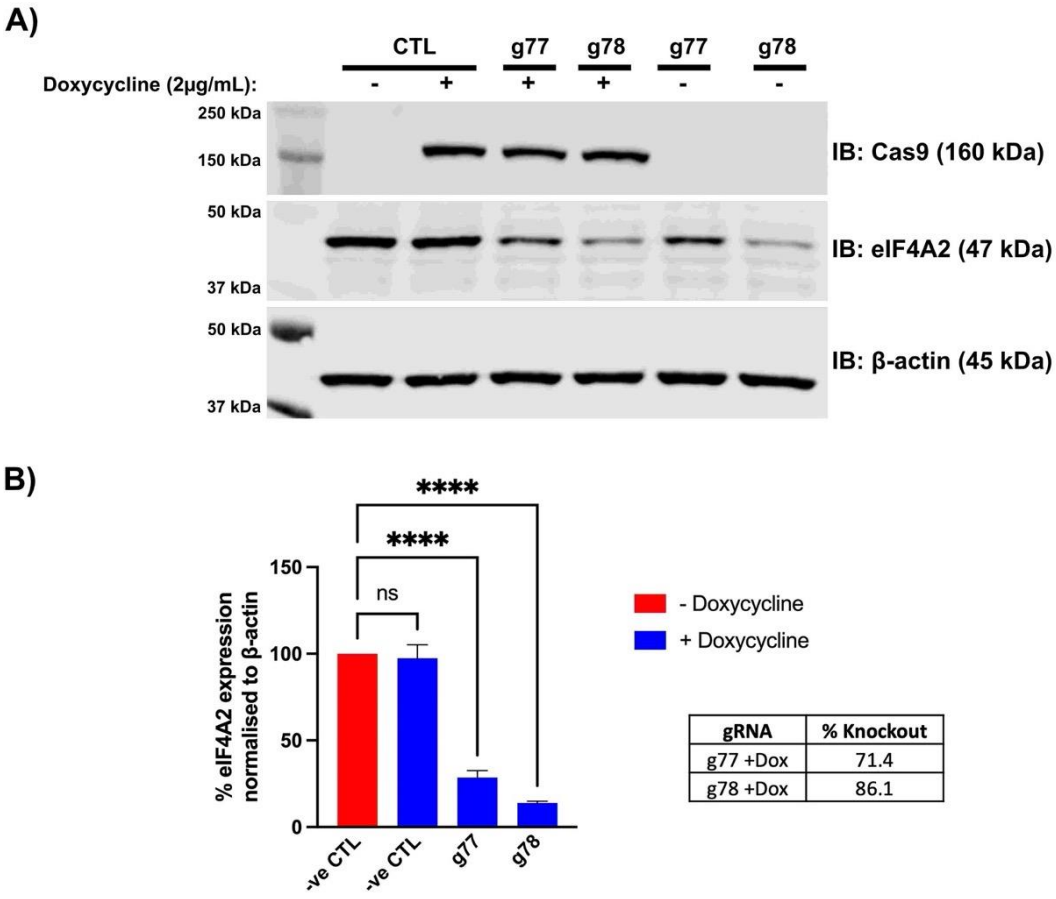

Figure 3.17 Inducible CRISPR-Cas9 gene editing with lentiviral transduction leads to partial eIF4A2 knockout in LS174T. Doxycycline inducible Cas9-transduced LS174T cells were transduced with a lentiviral vector containing eIF4A2-targeting gRNAs g77 or g78 and selected under puromycin 48 hours post-transduction. Cells were then treated with 2 µg/mL doxycycline for 96 hours to induce Cas9 expression. **A)** eIF4A2 protein expression was analysed by immunoblotting in negative control and eIF4A2 knockout lysates g77 and g78 **B)** Data was analysed by one-way ANOVA comparing eIF4A2 expression in negative control cells without doxycycline to knockout cells. *p <0.0332, **p<0.0021, ***p<0.0002, ****P<0.0001. Error bars indicate ± SEM. Percentage knockout calculated by subtraction of eIF4A2 expression in knockout clones from control clones. n=3.

3.3.11 Impact of eIF4A2 knockout on cell survival and 3-dimensional spheroid growth using lentiviral eIF4A2 knockout cells

The impact of eIF4A2 knockout on cell survival was measured by clonogenics assay as described in section 2.4 using the LS174T g77 and g78 lentiviral eIF4A2 knockout cell lines with doxycycline addition as well as the negative control cell line ± doxycycline to account for any toxicity effects. Cells were exposed to either normoxia or hypoxia for 72h after seeding before being placed in normoxia for two weeks to allow colonies to form. Figure 3.18 displays the results of the clonogenics assay, including representative images of colony formation (3.18a) and analysis of colony counts (3.18b). No statistically significant differences were observed in cell survival in normoxia in any of the conditions. There was also no significant difference in colony counts in the control conditions with or without doxycycline addition in either normoxia or hypoxia, suggesting there were no toxicity effects associated with the drug treatment (3.18b). However, following eIF4A2 knockout there was a statistically significant reduction in cell survival in the g78 cell line compared to the control in hypoxia (3.18b, $p<0.0332$). This suggests that there could be a hypoxia-specific role for eIF4A2 in regulating cell survival in LS174T depending on the level of eIF4A2 loss as the same result was not seen with the second eIF4A2 knockout cell line, g77, which had a lower knockout efficiency compared to g78 (see figure 3.17).

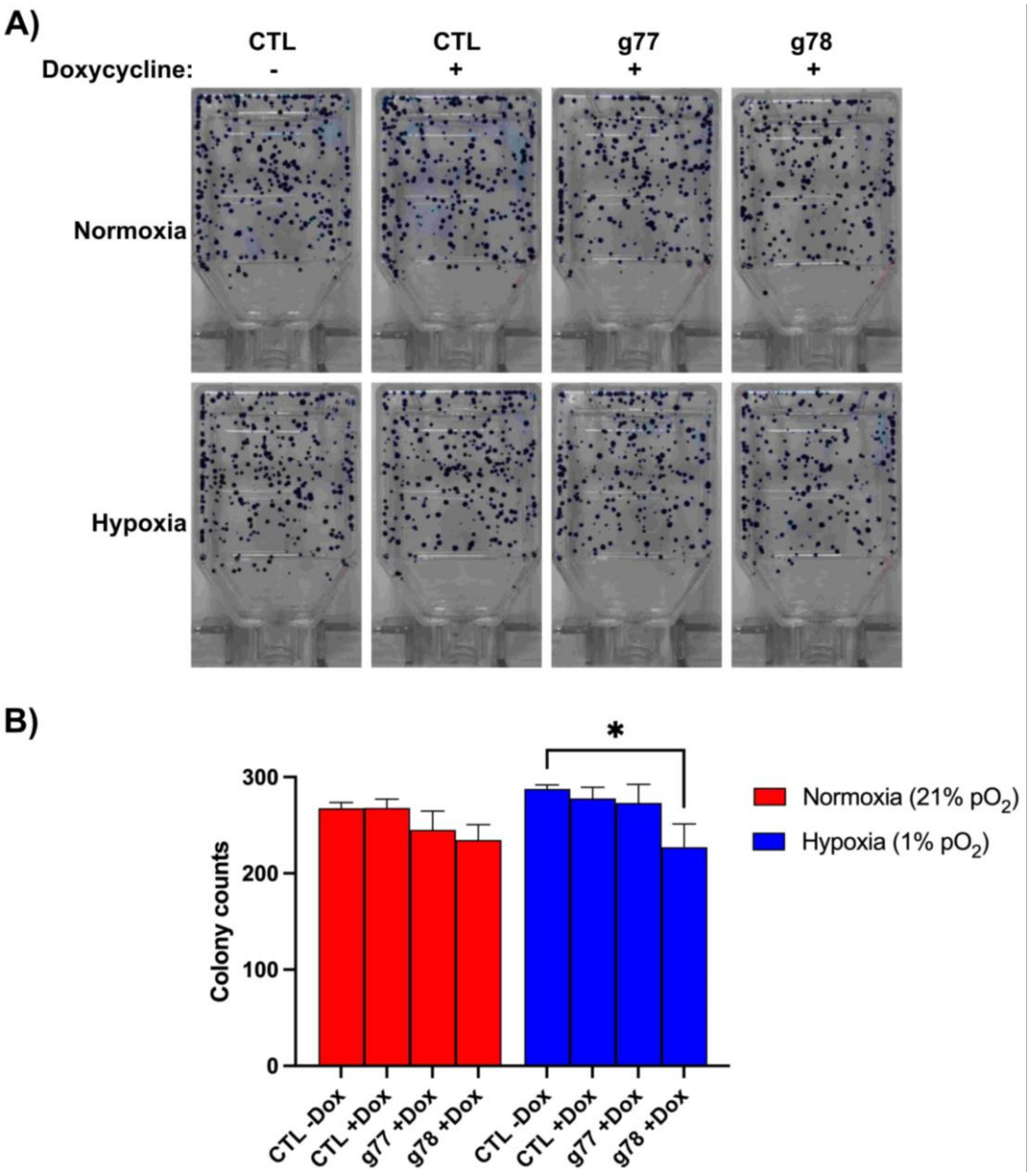

Figure 3.18 Lentiviral eIF4A2 knockout reduces cell survival in hypoxia *in vitro* in LS174T. Lentiviral LS174T negative control (CTL) and doxycyline (Dox)-induced eIF4A2 knockout cell lines g77 and g78 were seeded for clonogenics assay. Two technical replicates were seeded per experimental condition. For hypoxic conditions, cells were incubated in hypoxia (Hx, 1% pO_2) for 72h and then returned to normoxia (Nx, 21% pO_2) for two weeks to allow colonies to form. **A)** Representative images of colony formation for each experimental condition **B)** Data analysed by two-way ANOVA comparing CTL -Dox to CTL, g77 and g78 +Dox for both normoxia and hypoxia. *p <0.0332, **p<0.0021, ***p<0.0002, ****P<0.0001. Error bars indicate ± SEM. n=3.

Optimisation of the seeding densities (data not shown) and the type and concentration of extracellular matrix (ECM) component for the generation of lentiviral-transduced LS174T spheroids was carried out using the negative control cell line. Cells were seeded with either no ECM additive, basement membrane extract (BME) at final concentrations of 100 μg/mL, 200 μg/mL or 400 μg/mL or matrigel at final concentrations of 5% or 10% (figure 3.19). Spheroids were cultured for 10 days and imaged as described in section 2.2. LS174T cells require an ECM matrix in order to effectively form spheroids *in vitro* as evidenced by the lack of spheroid formation without any additives in figure 3.19. Both the 100 μg/mL and 5% matrigel led to partial spheroid formation however the spheroids were more diffuse, less compact and prone to disintegration when disturbed. Both the 200 μg/mL and 400 μg/mL BME conditions as well as the 10% matrigel condition produced more compact and stable spheroids, however, the use of matrigel led to the formation of additional small cell clusters within the wells and so BME was selected as the ECM component moving forwards at a concentration of 200 μg/mL.

The impact of eIF4A2 knockout on 3-dimensional spheroid growth was measured by seeding the LS174T g77 and g78 eIF4A2 knockout cell lines plus doxycycline alongside negative control cells ± doxycycline at the optimised density of 2000 cells/well containing 200 μg/mL BME as described in section 2.2.1. The spheroids were cultured for 10 days and images were taken on days 3, 5, 7 and 10. The images were used to calculate and analyse spheroid growth as described in section 2.2.2. Spheroids were formed successfully in all four conditions tested and figure 3.20a displays representative images of the spheroids at each of the time points investigated. No statistically significant differences in spheroid volume or spheroid growth rate were observed between any of the four conditions tested including between the negative control spheroids and eIF4A2 knockout spheroids (figure 3.20b and figure 3.20c). No statistically significant difference was observed in the negative control spheroids with or without doxycycline addition suggesting that there were no visible toxicity effects (figure 3.20c). Upon termination of the experiment, the spheroids were fixed and embedded for immunohistochemical analysis as described in sections 2.2.4 and 2.2.5.

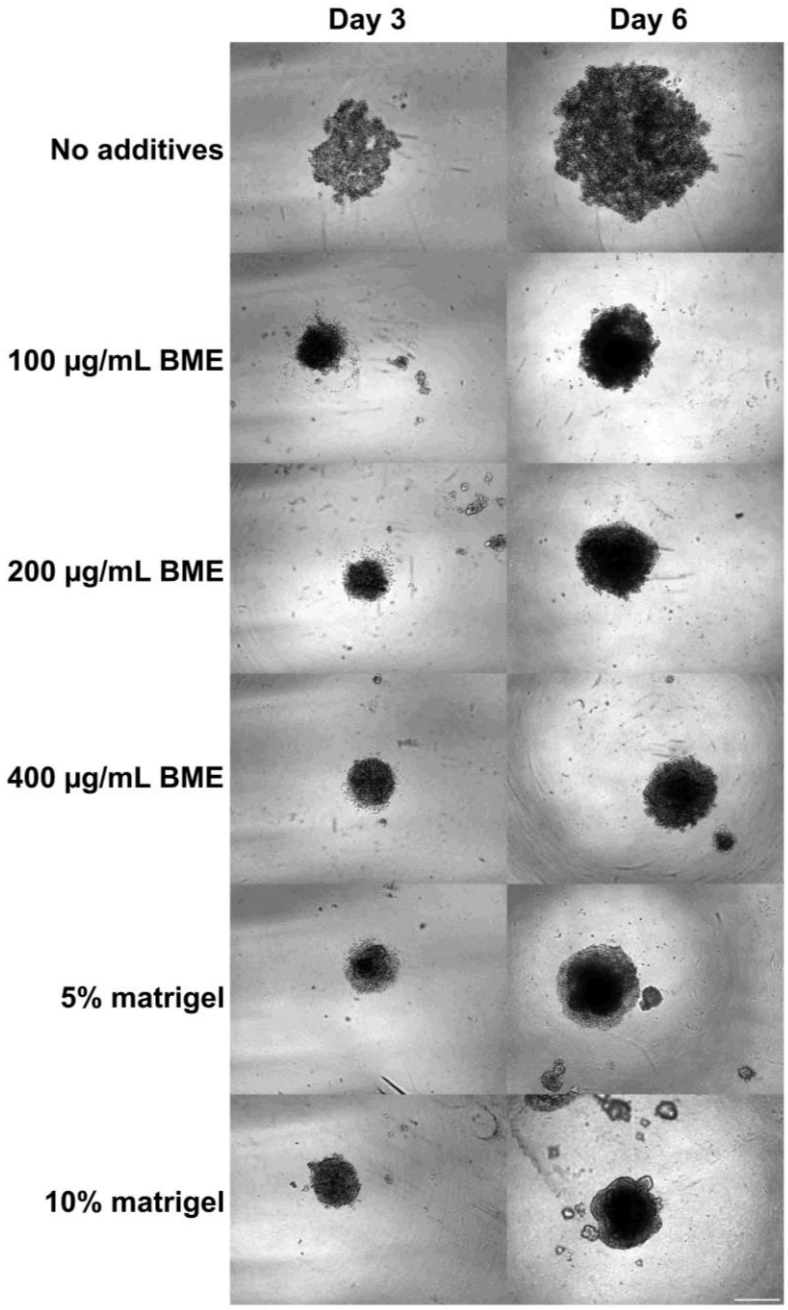

Figure 3.19 Optimisation of culture conditions for lentiviral-transduced LS174T cells. LS174T iCas9 negative control (-ve CTL) transduced cells were used to form 3-dimensional spheroids *in vitro* at the optimised seeding density of 2000 cells/well. Spheroids were seeded either without any additives or with basement membrane extract (BME) at concentrations of 100, 200 or 400 µg/mL or matrigel at concentrations of 5% or 10%. Representative images are shown from one experimental repeat of LS174T -ve CTL spheroids taken on days 3 and 6 at 4x magnification. Scale bar represents 500µm. n=1.

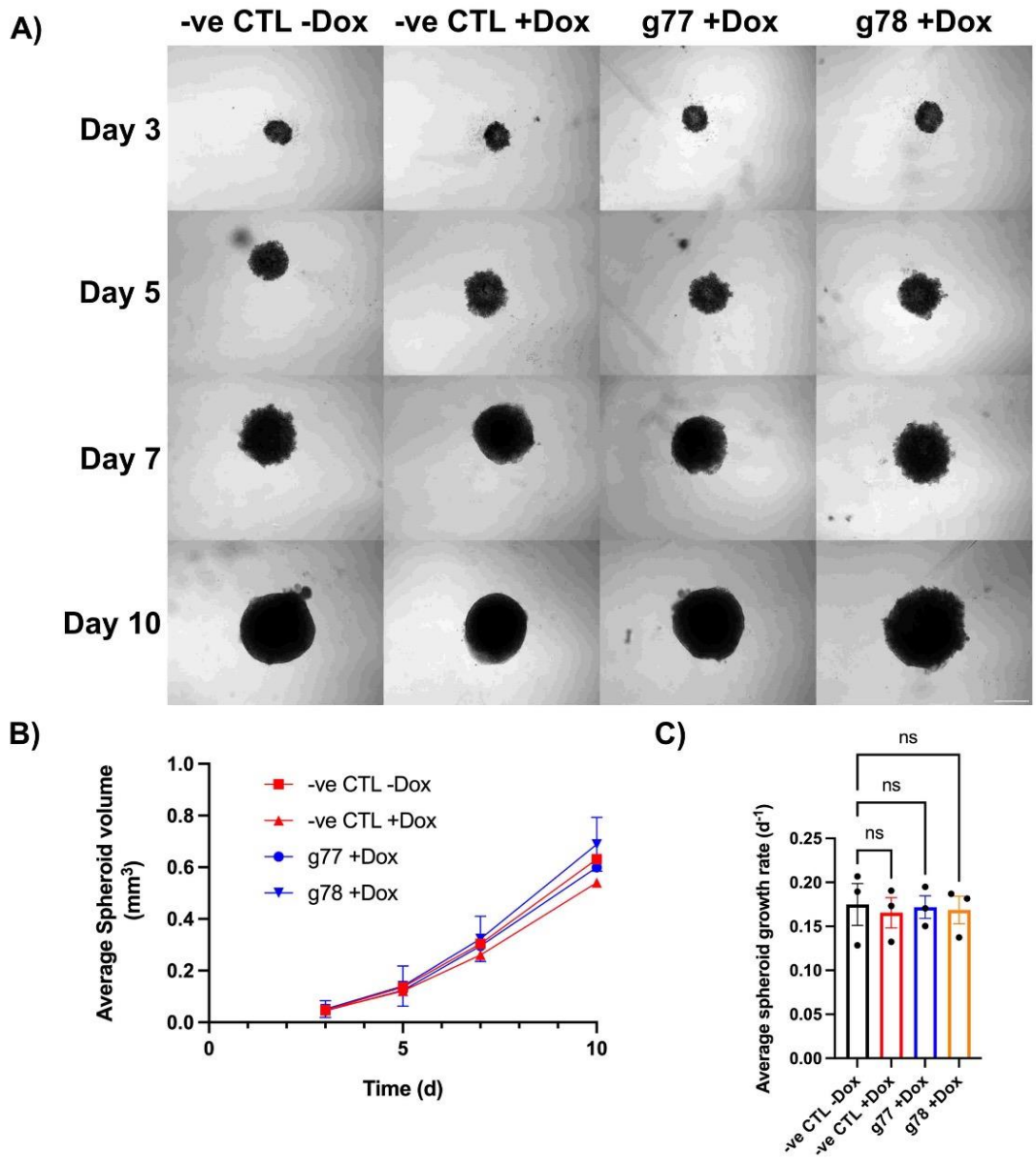

Figure 3.20 Lentiviral eIF4A2 knockout has no effect on 3-dimensional spheroid growth *in vitro* in LS174T. Lentiviral LS174T negative control (-ve CTL) and doxycycline (Dox)-induced eIF4A2 knockout cell lines g77 and g78 were used to form 3-dimensional spheroids *in vitro* at the optimised seeding density of 2000 cells/well + 200µg/mL basement membrane extract. **A)** Representative images from three experimental repeats of LS174T spheroids taken on days 3, 5, 7 and 10 at 4x magnification. Scale bar represents 500µm. **B)** Images were used to calculate the average spheroid volume for -ve CTL ±Dox, g77 +Dox and g78 +Dox spheroids on days 3, 5, 7 and 10. **C)** Spheroid volumes were used to calculate growth rates for -ve CTL ±Dox, g77 +Dox and g78 +Dox spheroids using linear regression analysis. Data was analysed by one-way ANOVA comparing eIF4A2 knockout spheroid growth rates to the control. Error bars indicate ± SEM. n=3.

3.3.12 Immunohistochemical analysis of LS174T lentiviral eIF4A2 knockout spheroids

Previous *in vivo* HCT116 eIF4A2 knockdown xenograft data generated by the Mcintyre Lab indicated that eIF4A2 knockdown significantly increased the levels of necrosis in the tumour tissue compared to the control, despite there being no significant changes in tumour growth[355]. Therefore, it was decided to analyse the levels of necrosis in the LS174T lentiviral eIF4A2 knockout spheroids. LS174T negative control spheroids ± doxycycline as well as eIF4A2 knockout spheroids g77 + doxycycline and g78 + doxycycline were stained with H&E to assess necrosis. Figure 3.21a displays representative images of the H&E-stained spheroids. The eIF4A2 knockout spheroids can be characterised by large amounts of central necrosis. After visually scoring necrosis levels, there was an observed increase in the amount of necrosis in both of the eIF4A2 knockout spheroids compared to the negative control (figure 3.21b). No difference was observed in the negative control with or without doxycycline treatment, confirming the drug treatment did not have an impact on cell death.

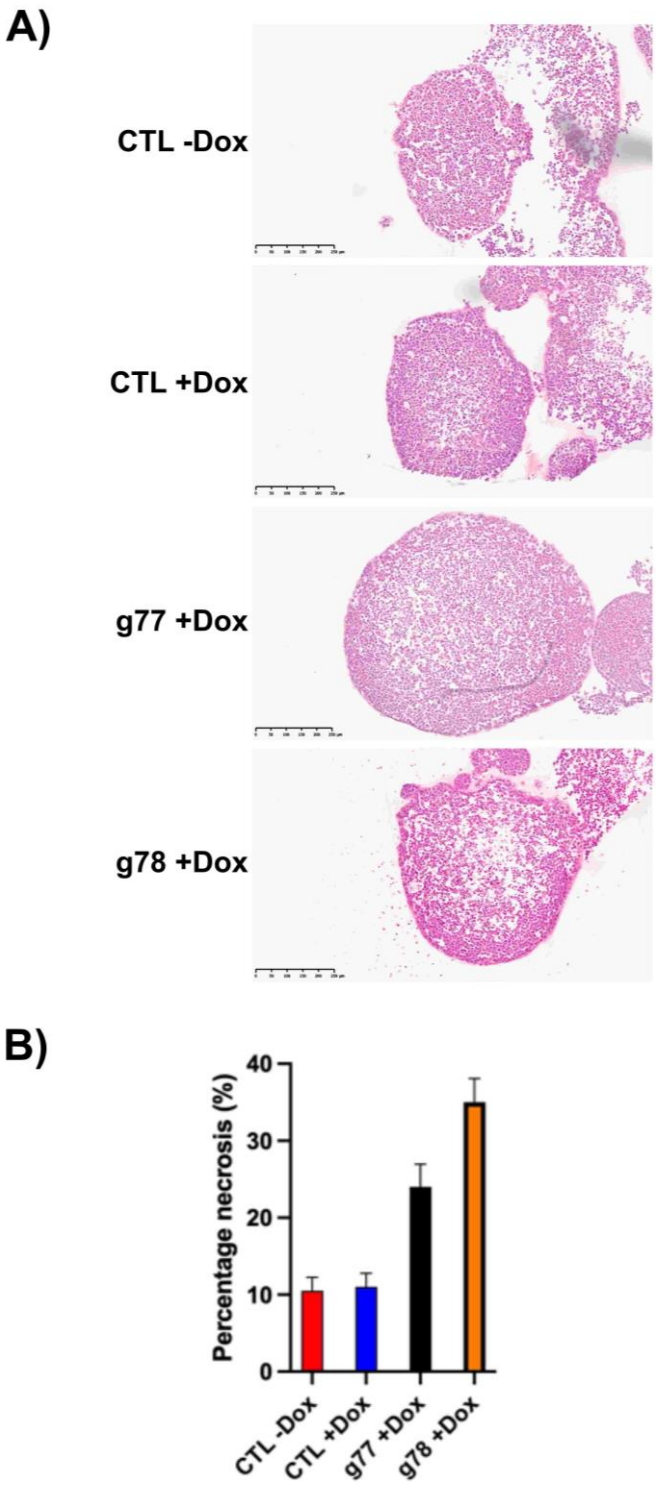

Figure 3.21 Lentiviral eIF4A2 knockout leads to increased necrosis in 3-dimensional spheroids in LS174T. Lentiviral eIF4A2 knockout and negative control (-ve CTL) LS174T spheroids were stained with haematoxylin and eosin (H&E) to assess necrosis. **A)** Representative images of H&E stained spheroids. Images were taken at 10x magnification. Scale bare represents 250μm. **B)** Levels of necrosis within the spheroids were visually scored using histomorphological features including nuclear shape and staining and independently verified by a histopathologist. Data was analysed by one-way ANOVA comparing percentage necrosis in the control + doxycycline and eIF4A2 knockout spheroids to the control – doxycycline spheroids. Error bars indicate ± SEM. n=1.

3.3.13 Regulation of HIF1α and HIF2α protein expression by eIF4A2

Clonal HIF1α and HIF2α knockout HCT116 and LS174T colorectal cancer cell lines generated in the Mcintyre lab (by Dr T. Potgieter) were previously used to investigate the regulation of eIF4A1 and eIF4A2 by the HIF proteins. Both eIF4A1 and eIF4A2 mRNA expression increased in response to both HIF1α and HIF2α knockout in hypoxia in the HCT116 cell line whereas eIF4A2 protein expression was unchanged[355]. Contrastingly, a significant reduction in both eIF4A1 and eIF4A2 mRNA expression was observed only in the LS174T HIF2α knockout cell line in hypoxia and eIF4A2 protein expression was similarly reduced in response to HIF2α knockout[355]. However, much of this data involved clonal cell lines, which could account for the differences between the cell lines. Furthermore, the regulation of HIF1α and HIF2α protein expression by eIF4A2 has not been investigated.

In order to investigate the regulation of HIF1α and HIF2α protein expression by eIF4A2, eIF4A2 knockout was induced in LS174T lentiviral g77 (4A2 KO 1) and g78 (4A2 KO 2) cell lines with the addition of doxycycline for 96 hours in culture. The eIF4A2 knockout cell lines, along with a negative control cell line, were then exposed to either normoxia or hypoxia for 48 hours and HIF1α and HIF2α protein expression was analysed by immunoblotting (figure 3.22a). Cell lines without the addition of doxycycline were also included on the blot as an additional control to confirm any differences in expression were due to the eIF4A2 knockout. CA9 protein expression was also measured as a positive control for the induction of hypoxia as well as to assess any downstream impact of changes in HIF protein expression as a known HIF1α target. There was a statistically significant reduction in eIF4A2 expression in normoxia and hypoxia with the addition of doxycycline in both g77 and g78 cell lines (figure 3.22e, $p<0.0001$) confirming the successful knockout of eIF4A2. An average knockout of 55% and 78% was achieved for the g77 and g78 cell lines respectively. There was no difference in eIF4A2 expression in the negative control sample between normoxia and hypoxia. There was also a significant reduction in eIF4A2 expression in hypoxia without any doxycycline addition (data not shown), suggesting that there was non-induced leaking of Cas9 protein expression, similar to the results seen in figure 3.17. There was a statistically significant increase in CA9 expression in the hypoxic control compared to normoxia indicative of the activation of the hypoxic response in those samples ($p<0.0021$).

There was no significant difference in HIF1α protein expression in hypoxia in the eIF4A2 knockout cell lines compared to the negative control (figure 3.22b) suggesting that HIF1α is not under translational regulation by eIF4A2 in hypoxia. eIF4A2 knockout also had no impact on CA9 expression, confirming that eIF4A2 was not regulating HIF1α expression (figure 3.22d). Interestingly, there was a statistically significant increase in HIF2α protein expression in hypoxia in both the g77 ($p<0.0021$) and g78 ($p<0.0332$) eIF4A2 knockout cell lines compared to the negative control (figure 3.22c).

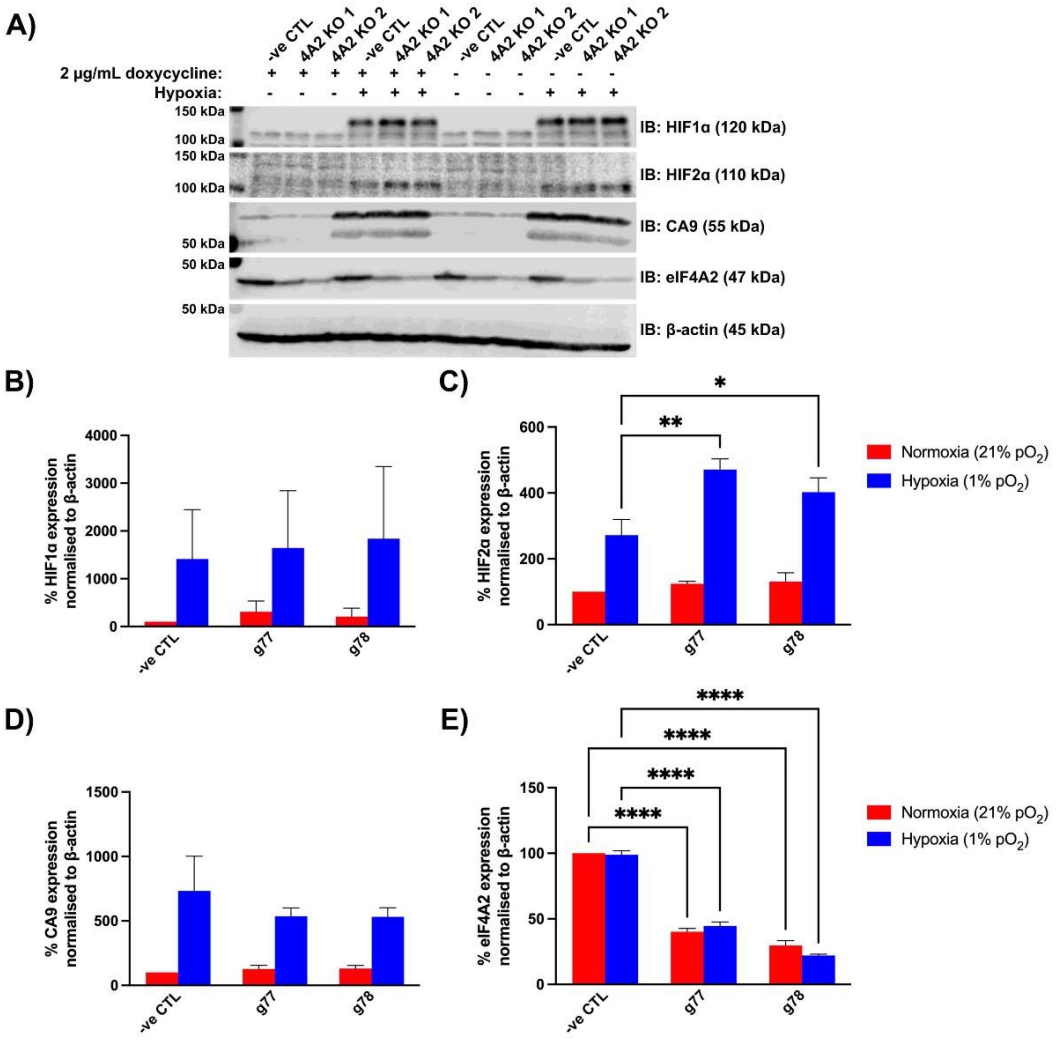

Figure 3.22 eIF4A2 knockout has no impact on HIF1α but increases HIF2α protein expression in LS174T. Inducible Cas9-transduced LS174T cells were selected in 4 µg/mL puromycin for 48 hours and eIF4A2 knockout induced by treating with 2 µg/mL doxycycline (Dox) for 96 hours. **A)** Cells were then seeded and exposed to 48h normoxia or hypoxia. HIF1α, HIF2α, eIF4A2 and CA9 protein expression was analysed by immunoblotting. Data analysed by two-way ANOVA comparing negative control to 4A2 knockout in normoxia and hypoxia for **B)** HIF1α, **C)** HIF2α, **D)** CA9 and **E)** eIF4A2. *p <0.0332, **p<0.0021, ***p<0.0002, ****P<0.0001. Non-significant comparisons not displayed. Error bars indicate ± SEM. Representative blots are shown. n=3.

Similarly, the role of eIF4A2 in the regulation of HIF1α and HIF2α expression was also investigated in HCT116 using previously generated inducible eIF4A2 shRNA knockdown HCT116 clonal cell lines. eIF4A2 knockdown was induced with 1mM IPTG treatment for 72 hours in culture. The eIF4A2 knockdown cell lines sh69 (sheIF4A2 1) and sh84 (sheIF4A2 2), along with a non-targeting control cell line, were then exposed to either normoxia or hypoxia for 48 hours and HIF1α and HIF2α protein expression was analysed by immunoblotting (figure 3.23a). Cell lines without the addition of IPTG were also included on the blot as an additional control to confirm any differences in expression were due to the eIF4A2 knockdown. CA9 protein expression was again measured as a positive control for the induction of hypoxia as well as to assess any downstream impact of changes in HIF protein expression.

There was a statistically significant reduction in eIF4A2 expression in normoxia and hypoxia with the addition of IPTG in both sh69 and sh84 cell lines (figure 3.23e, $p<0.0001$) confirming the successful knockdown of eIF4A2. An average knockdown of 51% and 57% was achieved for the hypoxic sh69 and s84 cell lines respectively. There was no difference in eIF4A2 expression in the negative control sample between normoxia and hypoxia. There was also a significant reduction in eIF4A2 expression in hypoxia without any IPTG addition (figure 3.23a) suggesting that there was possibly some constitutive, non-induced expression of the eIF4A2-targeting shRNA plasmid similar to that seen with the lentiviral knockout system. There was a statistically significant increase in CA9 expression in the hypoxic control compared to normoxia confirming the induction of hypoxia ($p<0.0002$).

eIF4A2 knockdown had no impact on either HIF1α or HIF2α expression in hypoxia however, a decreasing trend in HIF2α expression compared to the control was observed suggesting there may be a role for eIF4A2 in positively regulating HIF2α translation (figures 3.23b and 3.23c). However, this is opposite to the increase in HIF2α expression seen with eIF4A2 knockout in the LS174T cell line (figure 3.22c). Furthermore, a non-significant decrease in HIF1α expression in the sh84 eIF4A2 knockdown cell line was observed as well as a significant decrease in CA9 expression in that cell line in hypoxia (figure 3.23d, $p<0.0002$). However, as this was only observed in one of the clones, it is likely that this effect was a result of clonal variability as opposed to an eIF4A2-dependent effect given the issues already discussed surrounding the use of clones in these studies.

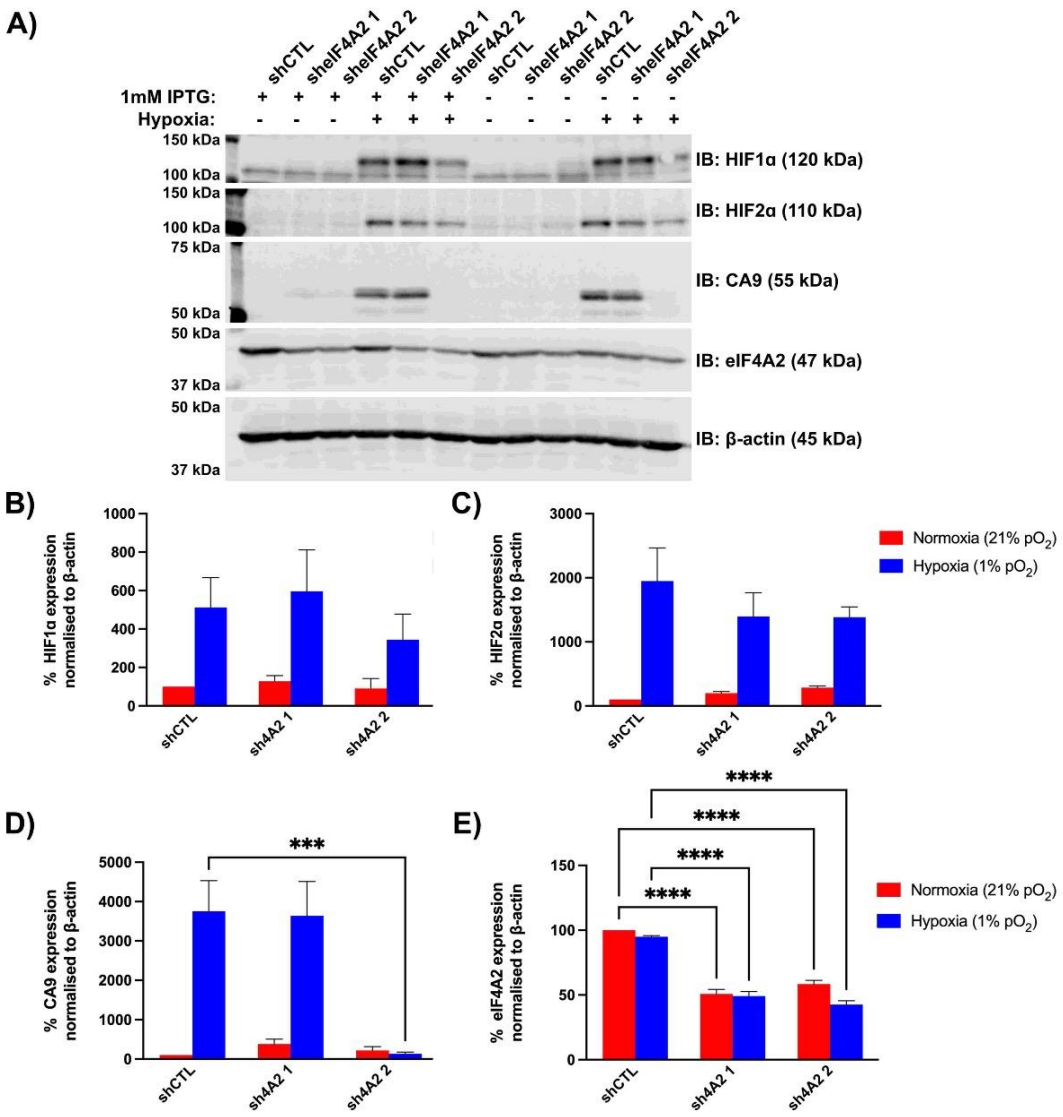

Figure 3.23 eIF4A2 knockdown has no impact on HIF1α or HIF2α protein expression in HCT116. shRNA-expressing HCT116 cells were selected in 4 μg/mL puromycin for 24 hours and eIF4A2 knockdown induced by treating with 1mM IPTG for 72 hours. Cells were then seeded and exposed to 48h normoxia or hypoxia. **A)** HIF1α, HIF2α, eIF4A2 and CA9 protein expression was analysed by immunoblotting. Data analysed by two-way ANOVA comparing shRNA control to 4A2 knockout in normoxia and hypoxia for **B)** HIF1α, **C)** HIF2α, **D)** CA9 and **E)** eIF4A2. *p <0.0332, **p<0.0021, ***p<0.0002, ****P<0.0001. Non-significant comparisons not displayed. Error bars indicate ± SEM. Representative blots are shown. n=3.

3.3.14 Protein expression of hypoxia-specific eIF4A2-bound target genes in different oxygen concentrations

As discussed previously, RIP-sequencing data investigating hypoxia-specific eIF4A2-bound mRNA transcripts identified a large number of metabolic genes as targets of eIF4A2 binding in hypoxic conditions. In particular, genes associated with the KEGG pathway biosynthesis of amino acids were enriched for eIF4A2 binding in hypoxia including IRP1, ALDH18A1, PHGDH, GPT2, SHMT2, ASS1, CTH and BCAT1[355]. Furthermore, as discussed in chapter 1.5, many of these genes are upregulated under hypoxic conditions in several cancer types. Therefore, the regulation of these genes in response to changes in oxygen concentration was investigated in the LS174T CRC cell line. This cell line was selected based on its categorisation as a CMS3 subtype cell line which is characterised by high levels of metabolic adaptation[496]. This cell line was also used in the RIP-sequencing experiment that led to the identification of the eIF4A2-bound mRNAs in hypoxia. LS174T cells were exposed to either normoxia, physoxia or hypoxia for 12, 24, 48 or and 72h and IRP1, ALDH18A1, PHGDH, GPT2, SHMT2, ASS1, CTH and BCAT1 protein expression was analysed by immunoblotting (figure 3.24). eIF4A2 protein expression was also analysed for comparison and CA9 expression was measured as a positive control for the induction of hypoxia.

Several of the target genes, IRP1, ALDH18A1, PHGDH, GPT2 and ASS1 maintained steady levels of protein expression across all of the time points and no statistically significant differences were observed between normoxia, physoxia or hypoxia (figure 3.24b, c, d, e and g). There was a statistically significant increase in SHMT2 expression at the 48h time point between physoxia and hypoxia, but not normoxia and hypoxia, agreeing with the literature describing the role of serine synthesis pathway genes in hypoxia (figure 3.24f, $p<0.0332$). There was also a statistically significant decrease in BCAT1 expression between normoxia and hypoxia at 24, 48 and 72h (figure 3.24i; 24h, $p<0.0021$; 48h, $p<0.0332$; 72h, $p<0.0332$). Despite there being no significant difference in CTH protein expression, a positive trend in expression in both physoxia and hypoxia was observed at the 48h and 72h time points compared to normoxia suggesting eIF4A2 could be playing a role in regulating CTH expression as previously identified in the lab. The increase in CA9 expression observed in the hypoxic conditions at all time points confirmed the induction of hypoxia (figure 3.24a).

A)

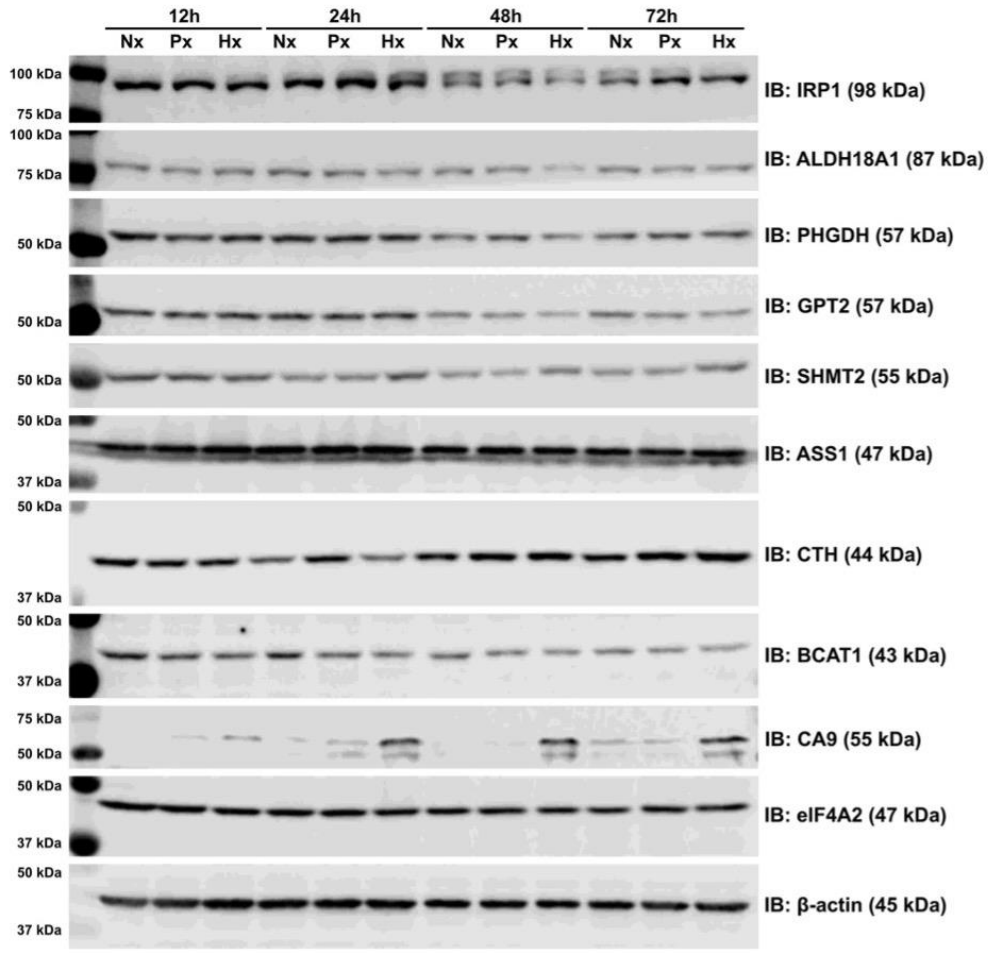
12h
24h
48h
72h
Nx Px Hx Nx Px Hx Nx Px Hx Nx Px Hx
100 kDa
75 kDa
IB: IRP1 (98 kDa)
100 kDa
75 kDa
IB: ALDH18A1 (87 kDa)
50 kDa
IB: PHGDH (57 kDa)
50 kDa
IB: GPT2 (57 kDa)
50 kDa
IB: SHMT2 (55 kDa)
50 kDa
37 kDa
IB: ASS1 (47 kDa)
50 kDa
37 kDa
IB: CTH (44 kDa)
50 kDa
37 kDa
IB: BCAT1 (43 kDa)
75 kDa
50 kDa
IB: CA9 (55 kDa)
50 kDa
37 kDa
IB: eIF4A2 (47 kDa)
50 kDa
37 kDa
IB: β-actin (45 kDa)

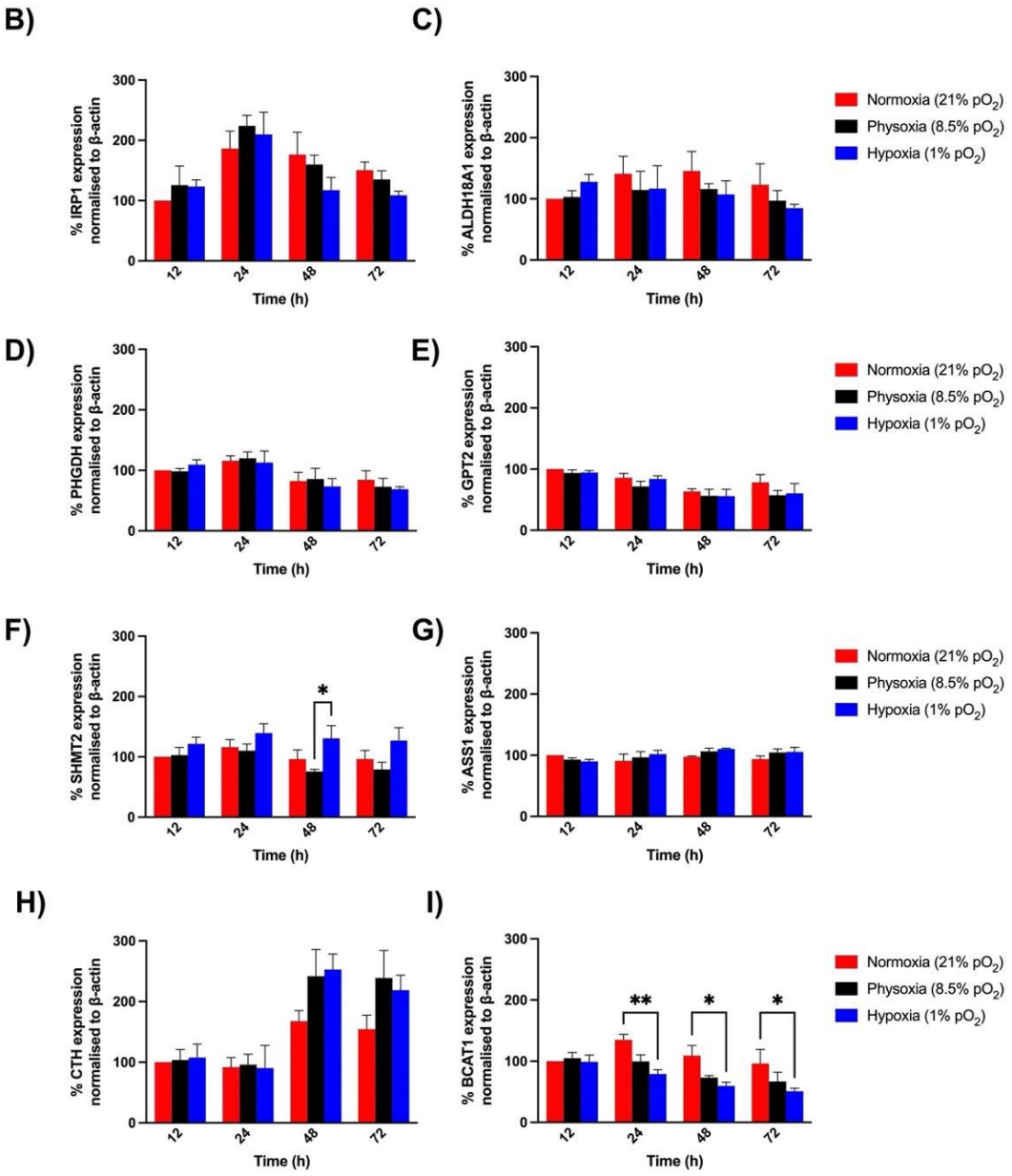

Figure 3.24 Protein expression of eIF4A2 RNA-immunoprecipitation sequencing target genes in normoxia, physoxia and hypoxia in LS174T. A) LS174T cells were exposed to 12, 24, 48 or 72h normoxia, physoxia or hypoxia. IRP1, ALDH18A1, GPT2, SHMT2, ASS1, CTH and BCAT1 protein expression was analysed by immunoblotting. **B-I)** Data analysed by two-way ANOVA comparing normoxia, physoxia and hypoxia for each time point. *p <0.0332, **p<0.0021, ***p<0.0002, ****P<0.0001. Error bars indicate ± SEM. Representative blots are shown. CA9 and eIF4A2 blots duplicated for illustrative purposes only. n=3.

3.3.15 Generation and validation of LS174T CTH CRISPR-Cas9 knockout clones

As discussed previously, RIP-sequencing data investigating hypoxia-specific eIF4A2-bound mRNA transcripts identified the enzyme CTH as one of the most enriched mRNAs for eIF4A2 binding in hypoxic conditions. However, the effect of permanently blocking CTH protein expression using CRISPR-Cas9 gene editing technology on colorectal cancer cell survival has not been investigated, especially in the context of hypoxia.

In order to generate CTH knockout colorectal cancer cell lines, transfection of LS174T iCas9 cells with single gRNAs, termed g40, g204 and g208, targetting CTH alongside a non-targeting control gRNA was performed after doxycycline-induced Cas9 expression as described in section 2.7.2. This was followed by single-cell clonal selection and expansion as described in section 2.7.3. In order to validate the knockout efficiency, approximately 10 clones per gRNA were cultured and lysed for protein extraction and CTH protein expression was analysed by immunoblotting (data not shown). The clones with the highest knockout efficiency termed g40 G2, g204 F5 and g208 F9, were selected for further validation by immunoblotting (figure 3.25a-c). Figure 3.25d shows that CTH knockout in all three cell lines resulted in a statistically significant reduction in CTH protein expression compared to the non-targeting control (>97%, $p<0.0001$).

In order to confirm that the CRISPR-Cas9-induced mutations in the CTH DNA sequence were out-of-frame, and therefore unconducive to functional CTH expression, and to confirm the zygosity of the mutation, Sanger sequencing was performed following DNA extraction on g40 G2, g204 F5 and g208 F9 cells as well as non-targeting control cells as described in section 2.7.4 (figure 3.26). Figure 3.26 highlights the locations of the mutations within the DNA sequence and summarises the type of mutation and the zygosity status of the eIF4A2 knockout clone. Both g40 G2 and g204 F5 were homozygous out-of-frame knockouts with a 1bp insertion whilst g208 F9 was a homozygous out-of-frame knockout with a 13bp deletion.

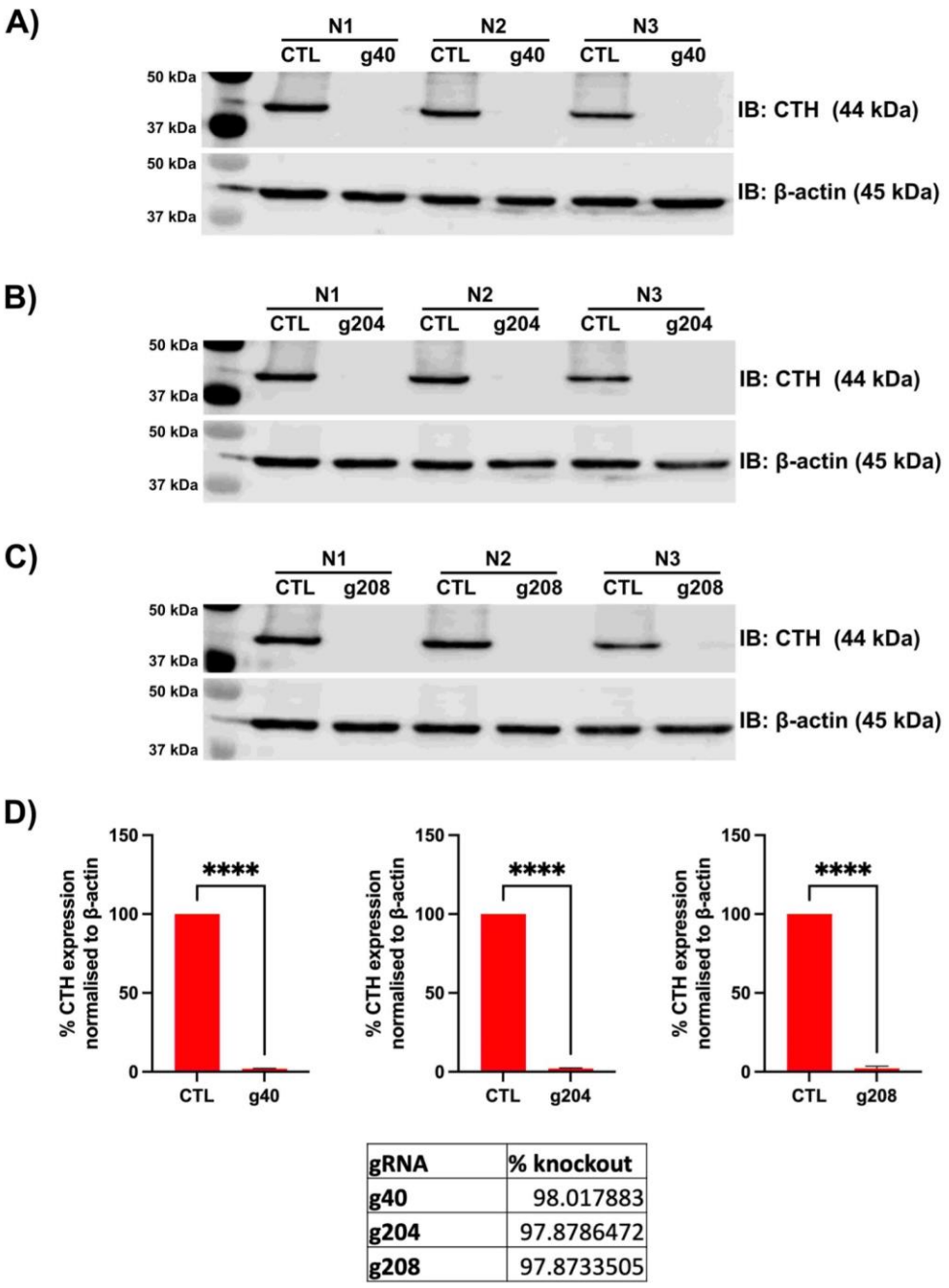

gRNA	% knockout
g40	98.017883
g204	97.8786472
g208	97.8733505

Figure 3.25 Inducible CRISPR-Cas9 gene editing and clonal selection leads to CTH knockout in LS174T. Cas9-transduced LS174T cells were treated with 2 μg/mL doxycycline for 48 hours to induce Cas9 expression before transfection with three separate gRNAs g40, g204 and g208 targetting CTH. After 24 hours, cells underwent single cell selection and expansion to generate clonal populations. Once expanded, cells were seeded for 48 hours and lysed for protein extraction. CTH protein expression was analysed by immunoblotting comparing control lysates with **A)** g40, **B)** g204 and **C)** g208 CTH knockout lysates. **D)** Data analysed by unpaired t-test. *p <0.0332, **p<0.0021, ***p<0.0002, ****P<0.0001. Error bars indicate ± SEM. Percentage knockout calculated by subtraction of eIF4A2 expression in knockout clones from control clones. n=3.

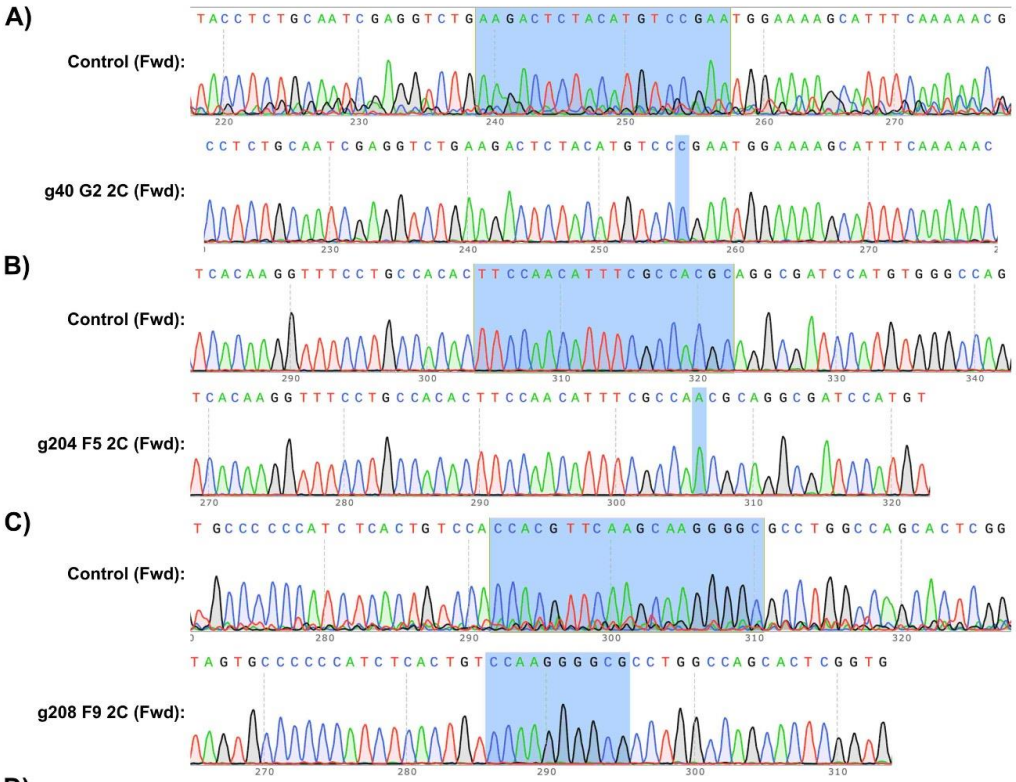

D)

Target	Clone	Sequence	Mutation	Zygosity	KO/KD
CTH (g40)	G2 2C	TTCGG**G**ACATGTAGAGTCTT	1bp insertion (C256)	Homo	KO
CTH (g204)	F5 2C	TTCCAACATTTCGCCA**A**CGC	1bp insertion (A306)	Homo	KO
CTH (g208)	F9 2C	TGTCCA**xxxxxxxxxxxxx**AGGGGCG	13bp deletion (C292-A304)	Homo	KO

Figure 3.26 Sanger sequencing of LS174T CTH knockout clones determines mutation status and zygosity. DNA was extracted from LS174T control and CTH knockout clonal cell lines, amplified and purified before being sent for Sanger sequencing. **A-C)** Chromatograms of control samples highlight the gRNA sequence used to generate the CRISPR knockout. Chromatograms of CTH knockout samples **A)** g40, **B)** g204 and **C)** g208 indicate the CRISPR-Cas9 induced mutation in the DNA sequence. Chromatograms were analysed using SnapGene. **D)** Summary table indicating the CRISPR-induced mutations highlighted in red within the target gRNA sequence as well as details of the mutation and zygosity status.

3.3.16 Impact of CTH knockout on cell survival and 3-dimensional spheroid growth using CTH knockout clones

In order to investigate the impact of CTH knockout on 3-dimensional spheroid growth, LS174T CTH knockout clones g40 G2 and g204 F5 cells, as well as control cells (CTL1 and CTL2), were used to form spheroids as described in section 2.2.1. Spheroids were grown for 10 days with images taken on days 3, 5, 7 and 10 and spheroid volumes were calculated and analysed as described in section 2.2.2. Figure 3.27a displays representative images of the three spheroid conditions at each of the time points measured. Morphologically, the CTH knockout spheroids displayed similar roundedness compared to control spheroids however the g40 CTH knockout spheroids displayed some distortion around the edges, particularly by Day 7 (figure 3.27a). Figure 3.27b shows the average spheroid volume for the control spheroids and the CTH knockout spheroids and indicates no difference in spheroid volume with CTH knockout compared to the control. Linear regression analysis was used to calculate the growth rates for the different spheroids and figure 3.27c confirms that there was no statistically significant reduction in spheroid growth rates in both CTH knockout clones compared to the control cells. On the other hand, there were no statistically significant differences observed in *in vitro* cell survival measured by clonogenics assay as described in section 2.4 using the LS174T CTH knockout clones and no differences were observed in colony formation between the normoxic and hypoxic conditions (data not shown). Furthermore, the two CTH knockout clones appeared to affect colony formation differently as evidenced by the lack of consistency between the two cell lines (data not shown).

This data suggests that CTH does not impact CRC cell survival in hypoxia and has no effect on 3-D CRC cell growth. However, as these spheroids were formed from cell lines derived from single clones it is possible that the lack of differences in cell survival and growth rates are due to the inherent genetic properties of the clonal cell lines selected in the study. In order to verify the results obtained with the clonal CTH knockout cell lines it was decided that CTH knockouts generated by the pooling method would be tested as well.

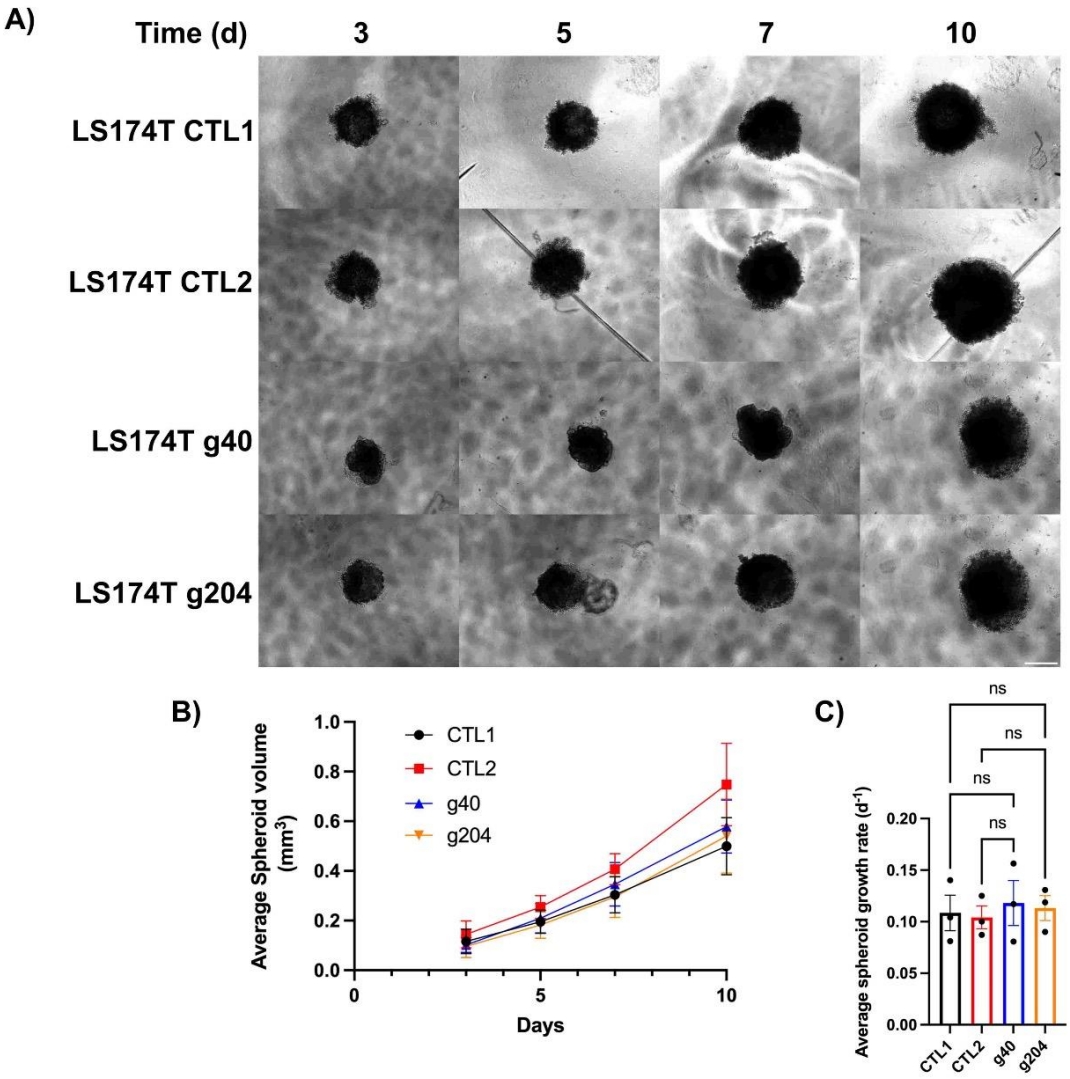

Figure 3.27 CTH knockout has no effect on 3-dimensional spheroid growth *in vitro* in LS174T. LS174T iCas9 cells transfected with either non-targetting gRNA (CTL1 and CTL2) or CTH-targetting gRNAs g40 and g204 and isolated into clonal populations were used to form 3-dimensional spheroids *in vitro* at the optimised seeding density of 2000 cells/well. **A)** Representative images from three experimental repeats of LS174T spheroids taken on day 3, 5, 7 and 10 at 4x magnification. Scale bar represents 500μm. **B)** Images were used to calculate average spheroid volume for CTL1, CTL2, g40 and g204 spheroids on day 3, 5, 7 and 10. **C)** Spheroid volumes were used to calculate growth rates for CTL1, CTL2, g40 and g6204 spheroids using linear regression analysis. Data was analysed by one-way ANOVA comparing CTH knockout spheroid growth rates to the controls. Error bars indicate ± SEM. n=3.

3.3.17 Generation and validation of HCT116 CTH CRISPR-Cas9 knockout pools

Using the aforementioned pooling method, HCT116 iCas9 cells were transfected with single gRNAs targeting CTH, again termed g40, g204 and g208 along with a control gRNA (CTL). However, the transfected cells were then maintained as a mixed population of cells as opposed to undergoing single-cell clonal sorting. A total of three rounds of transfection were carried out with cells seeded for protein extraction to assess the knockout efficiency by immunoblotting after each transfection (figure 3.28). Figure 3.28a and 3.28b display the immunoblotting results after the first round of transfection, termed T1, and the second round of transfection, termed T2, respectively. All three CTH knockout pools showed a partial knockout of CTH compared to the control pool after one round of transfection (figure 3.28a). The knockout efficiency following the second round of transfection was reduced in all three CTH knockout pools (figure 3.28b). Based on the percentage knockout being <80% in all three pools it was decided that a third round of transfection, termed T3, should be attempted to further enhance the knockout efficiency. However, the third transfection reduced the knockout efficiency in all three T3 pools compared to the T2 pools (figure 3.28c). Still, there was a statistically significant reduction in CTH protein expression compared to the control in all three cases (figure 3.28d, $p<0.0001$).

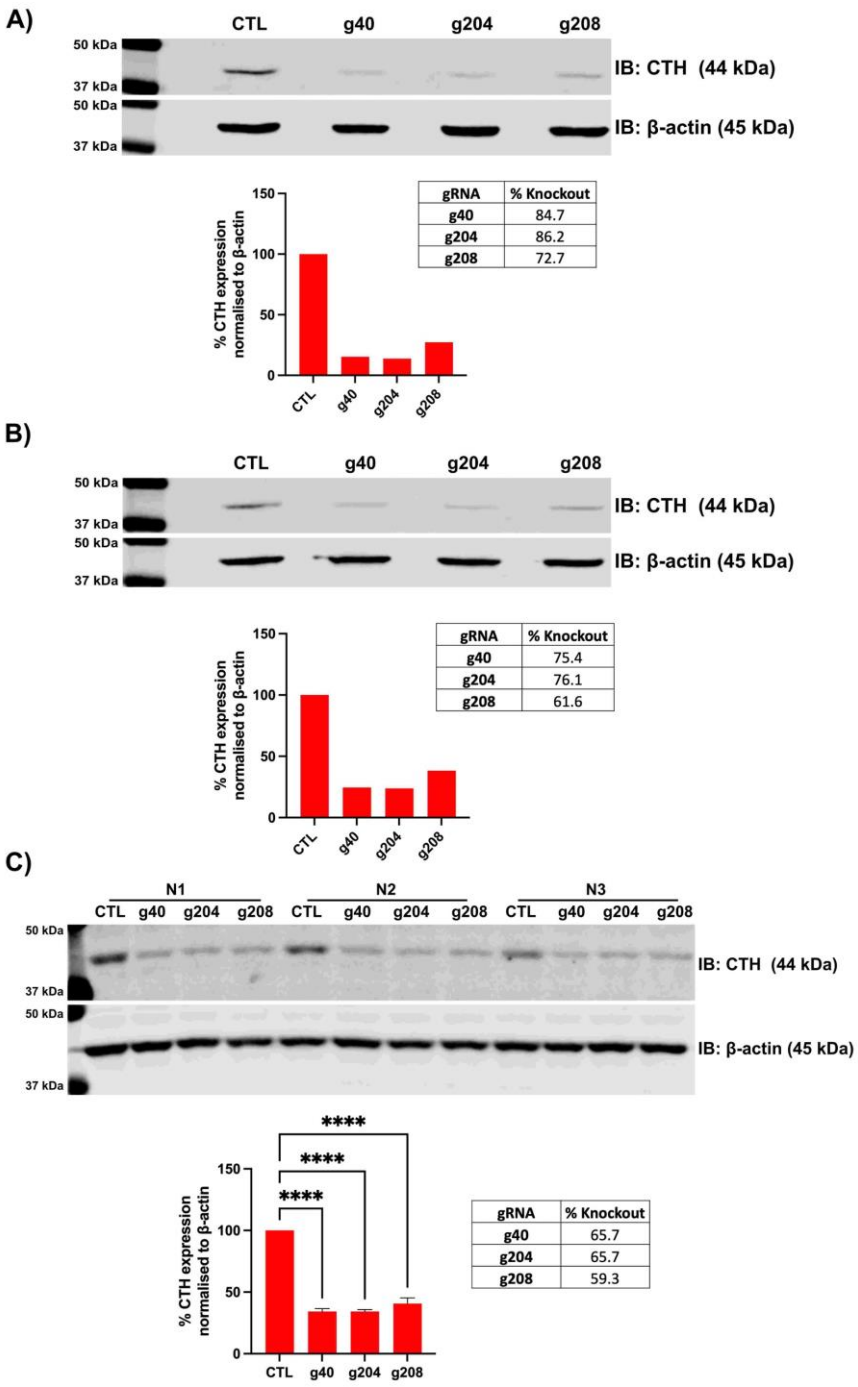

Figure 3.28 Inducible CRISPR-Cas9 gene editing using the pooling method leads to partial CTH knockout in HCT116. Cas9-transduced HCT116 cells were treated with 2 μg/mL doxycycline for 48 hours to induce Cas9 expression before transfection (T1) with gRNA targetting CTH. After 72 hours, cells were seeded for protein extraction and a second round of transfection (T2). Re-seeded cells underwent a second round of transfection followed by seeding for protein extraction and a third transfection (T3). Cells underwent a third and final transfection followed by seeding for protein extraction. CTH protein expression was analysed by immunoblotting for **A)** transfection 1, **B)** transfection 2 and **C)** transfection 3. Data analysed by one-way ANOVA comparing CTH expression in control cells with expression in the knockout pools. *p <0.0332, **p<0.0021, ***p<0.0002, ****P<0.0001. Error bars indicate ± SEM. Percentage knockout calculated by subtraction of eIF4A2 expression in knockout clones from control clones. n=3. *n=1 only for T1 and T2 experiments.

3.3.18 Impact of CTH knockout on cell survival and 3-dimensional spheroid growth using CTH knockout pools

In order to first assess the impact of CTH knockout on cell survival, HCT116 CTH knockout T3 pools were seeded for clonogenics assay and colonies were stained as described in section 2.4. Cells were exposed to either normoxia or hypoxia for 72h after seeding before being placed in normoxia for two weeks to allow colonies to form. Figure 3.29 displays the results of the clonogenics assay, including representative images of colony formation (3.29a) and analysis of colony counts (3.29b). Following CTH knockout, no statistically significant difference was observed in cell survival in either normoxia or hypoxia compared to the control (figure 3.29b). There was also no difference in cell survival between normoxia and hypoxia in the controls suggesting that hypoxia alone does not impact colony formation. This agrees with the previous clonogenics data obtained using the LS174T CTH knockout clones (data not shown). This data suggests that CTH knockout has no impact on cell survival in either normoxia or hypoxia *in vitro*.

In order to investigate the impact of CTH knockout on 3-dimensional spheroid growth using the CTH knockout pools, the HCT116 T3 pools, g40 and g204 cells, as well as control cells, were used to form spheroids as described in section 2.2.1. Spheroids were grown for 10 days with images taken on days 3, 5, 7 and 10 and spheroid volumes were calculated and analysed as described in section 2.2.3. Figure 3.30a displays representative images of the three spheroid conditions at each of the time points measured. Morphologically, there were no visible differences between the CTH knockout and control spheroids. Figure 3.30b shows the average spheroid volume for the control spheroids and the CTH knockout spheroids and shows there was no difference in spheroid volume between the conditions. Linear regression analysis was then used to calculate the growth rates for the different spheroids and figure 3.30c confirms that there was no reduction in spheroid growth rates in both CTH knockout cell lines compared to the control cells.

Together, this data agrees with the previous data obtained using LS174T CTH knockout clones that CTH is not required for the survival of CRC cells in hypoxia or for the 3-D growth of CRC cells. Therefore, it was decided not to continue any follow-up work investigating the role of CTH further.

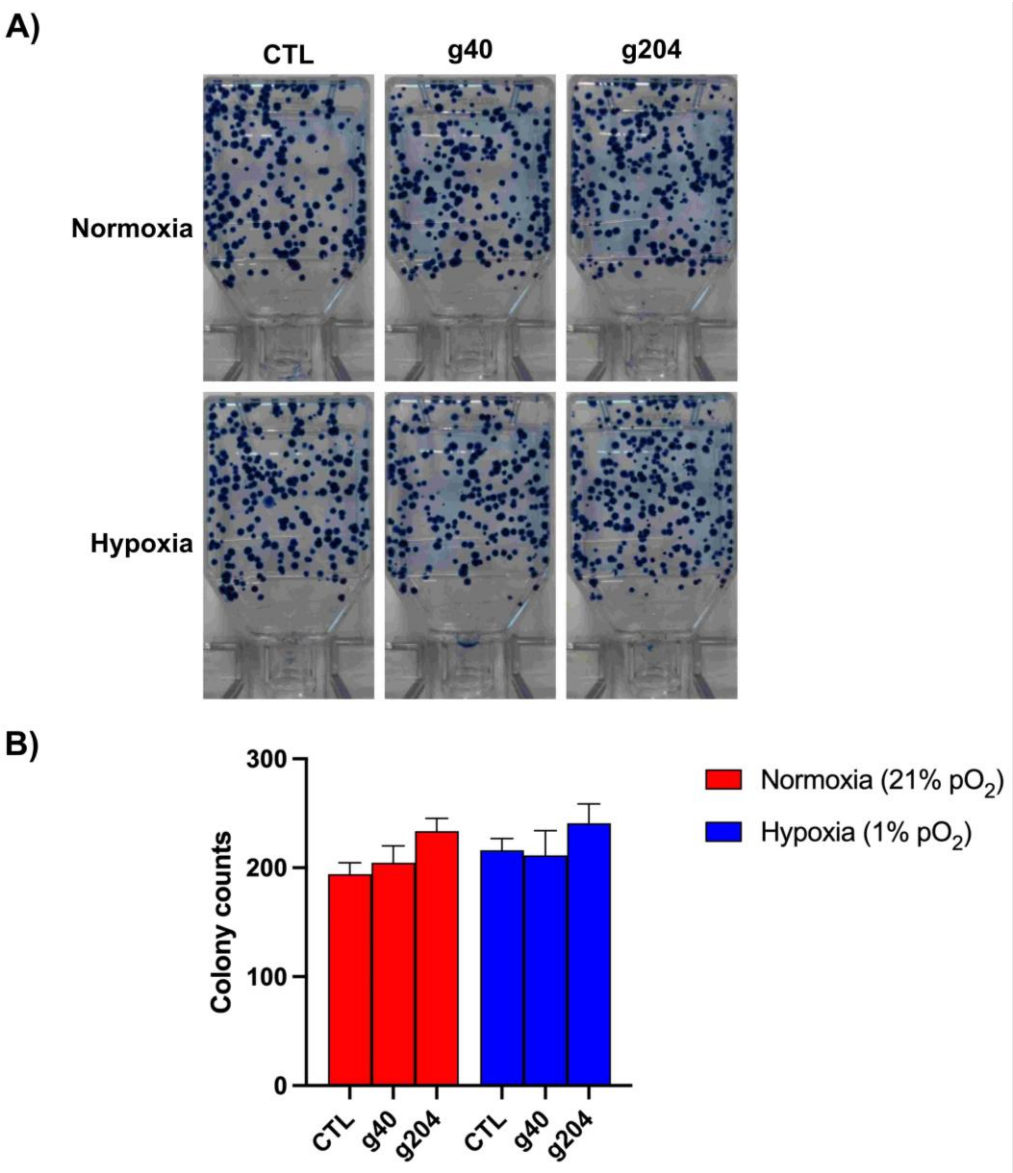

Figure 3.29 CTH knockout has no effect on cell survival *in vitro* in HCT116. HCT116 iCas9 cells transfected three times with either non-targeting gRNA (CTL) or CTH-targetting gRNAs g40 and g204 were seeded for clonogenics assay *in vitro* at the optimised seeding density of 500 cells/flask. Two technical replicates were seeded per experimental condition. For hypoxic conditions, cells were incubated in hypoxia for 72h and then returned to normoxia for two weeks to allow colonies to form. **A)** Representative images of colony formation for each experimental condition **B)** Data analysed by two-way ANOVA comparing colony counts between CTL and CTH knockout conditions for both normoxia and hypoxia. *p <0.0332, **p<0.0021, ***p<0.0002, ****P<0.0001. Non-significant comparisons not displayed. Error bars indicate ± SEM. n=3.

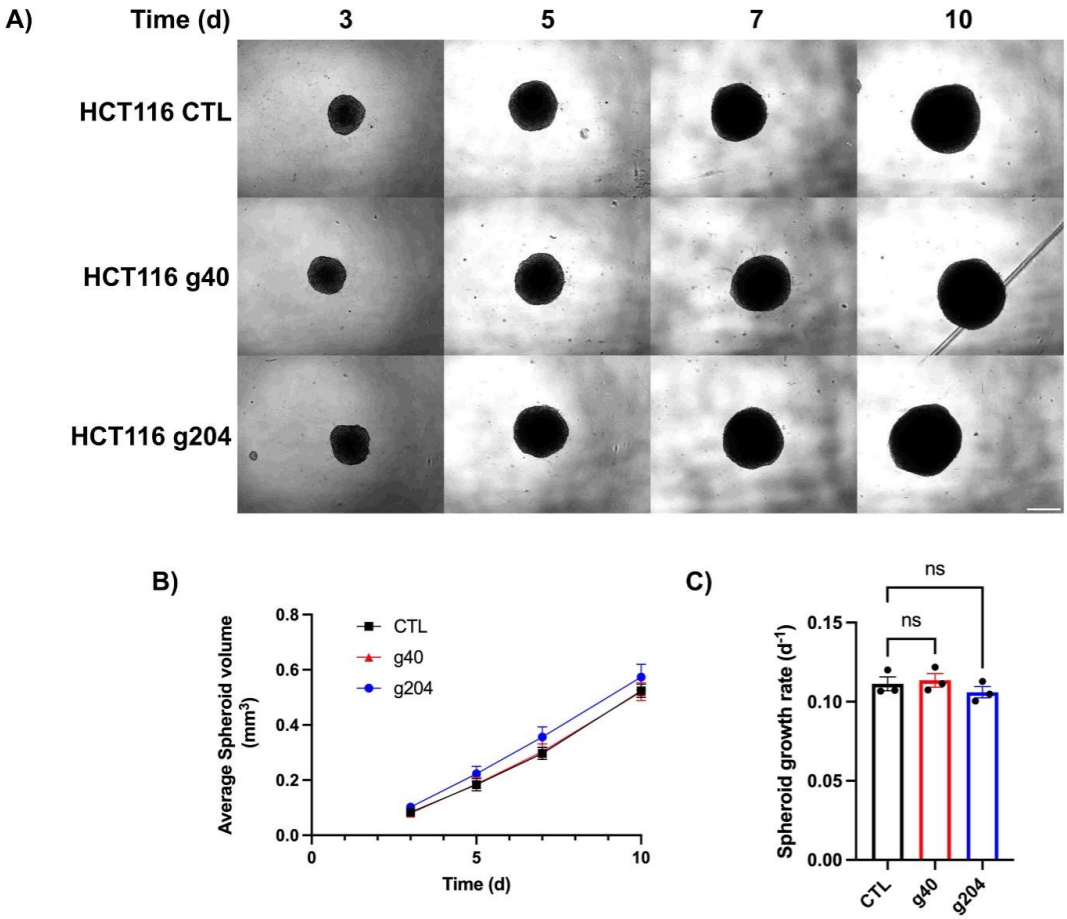

Figure 3.30 CTH knockout has no effect on 3-dimensional spheroid growth *in vitro* in HCT116. HCT116 iCas9 cells transfected three times with either non-targetting gRNA control (CTL) or CTH-targetting gRNAs g40 and g204 were used to form 3-dimensional spheroids *in vitro* at the optimised seeding density of 1000 cells/well. **A)** Representative images from three experimental repeats of HCT116 spheroids taken on day 3, 5, 7 and 10 at 4x magnification. Scale bar represents 500µm. **B)** Images were used to calculate average spheroid volume for CTL, g40 and g204 spheroids on day 3, 5, 7 and 10. **C)** Spheroid volumes were used to calculate growth rates for CTL, g40 and g204 spheroids using linear regression analysis. Data was analysed by one-way ANOVA comparing CTH knockout spheroid growth rates to the control. Error bars indicate ± SEM. n=3.

3.3.19 Impact of eIF4A2 knockdown on metabolic and endocytosis-associated gene expression in hypoxia

Alongside the previous RIP-sequencing identification of metabolic mRNAs bound by eIF4A2 in hypoxia, the second most significantly enriched pathway for increased eIF4A2 binding in hypoxia was endocytosis[355]. Furthermore, eIF4A2 knockdown reduced the expression of endocytosis-associated genes EHD1 and KIF5B as well as the known hypoxia-activated metabolic gene SHMT2 in LS174T[355]. In order to validate these previous findings and confirm the regulation of these genes by eIF4A2, the expression of EHD1, KIF5B and SHMT2 in response to eIF4A2 knockdown was investigated in a second cell line using previously generated inducible eIF4A2 shRNA knockdown HCT116 clonal cell lines. eIF4A2 knockdown was induced with 1mM IPTG treatment for 72 hours in culture. The eIF4A2 knockdown cell lines sh69 (sheIF4A2 1) and sh84 (sheIF4A2 2), along with a non-targeting control cell line, were then exposed to either normoxia or hypoxia for 48 hours and EHD1, KIF5B, SHMT2 and eIF4A2 protein expression was analysed by immunoblotting (figure 3.31a). Cell lines without the addition of IPTG were also included on the blot as an additional control to confirm any differences in expression were due to the eIF4A2 knockdown.

A statistically significant reduction was observed in eIF4A2 expression in the two knockdown clones in hypoxia compared to the shCTL ($p<0.0001$) confirming the successful knockdown of eIF4A2 in the two cell lines (figure 3.31d). An average of 70% knockdown efficiency was achieved in both the sh69 and s84 clonal lines. Following eIF4A2 knockdown, a statistically significant reduction in SHMT2 expression was observed in both sh69 and sh84 cell lines compared to the shCTL in normoxia (figure 3.31d; sh69, $p<0.0021$; sh84, $p<0.0001$) as well as in hypoxia for the sh84 cell line ($p<0.0021$). Additionally, a hypoxia-specific reduction in EHD1 expression was observed in response to eIF4A2 knockdown in both sh69 and sh84 cell lines (figure 3.31c, $p<0.0332$). However, no differences in KIF5B expression were observed in either normoxia or hypoxia in response to eIF4A2 knockdown (figure 3.31b). Taken together, this data indicates a role for eIF4A2 in the regulation of both SHMT2 and EHD1, but not KIF5B, and that the regulation of EHD1 is hypoxia specific.

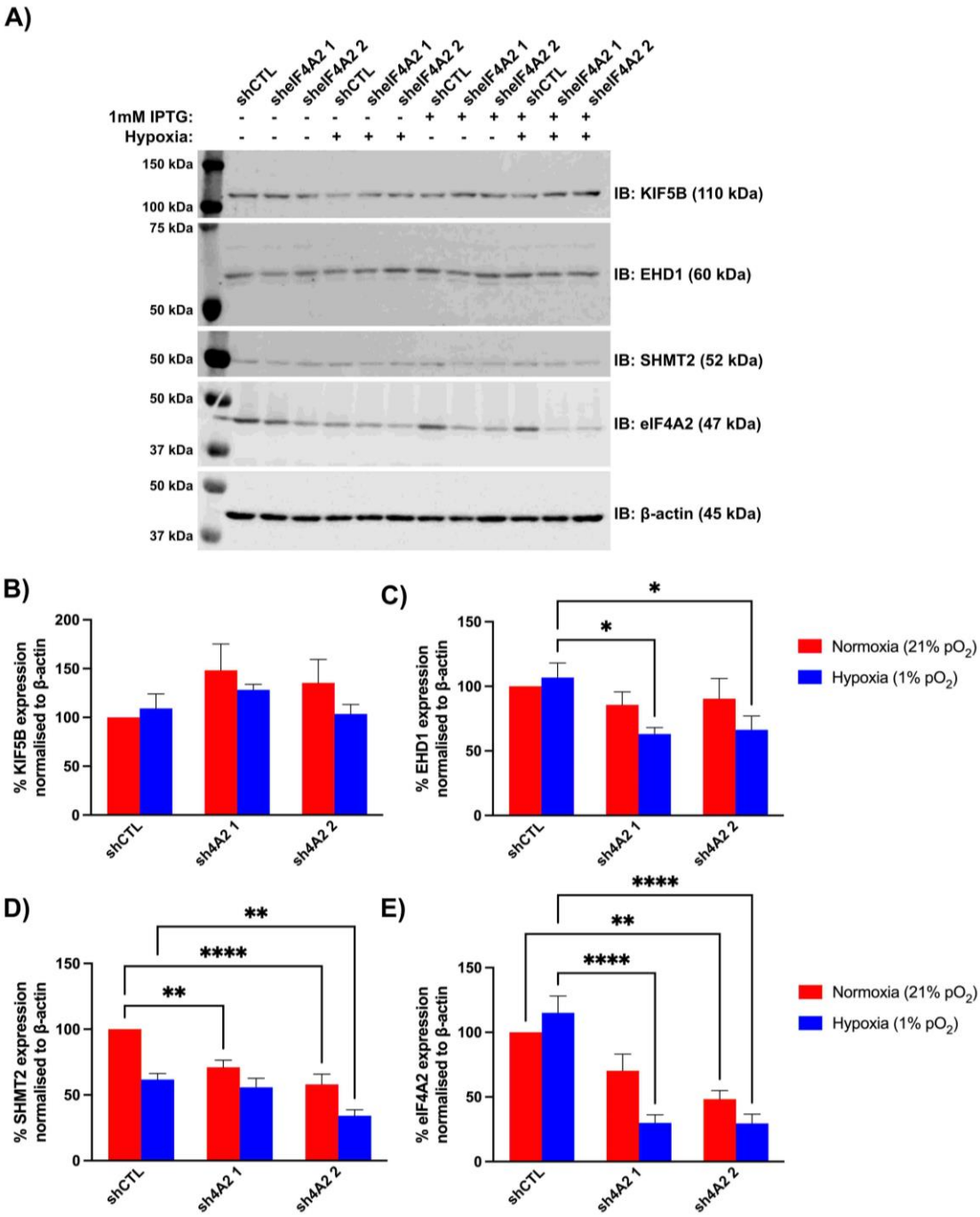

Figure 3.31 eIF4A2 knockdown reduces EHD1 and SHMT2 protein expression in hypoxia in HCT116. shRNA-expressing HCT116 cells were selected in 4 μg/mL puromycin for 24 hours and eIF4A2 knockdown induced by treating with 1mM IPTG for 72 hours. Cells were then seeded and exposed to 48h normoxia or hypoxia. **A)** KIF5B, EHD1, SHMT2 and eIF4A2 protein expression was analysed by immunoblotting. Data analysed by two-way ANOVA comparing shRNA control to 4A2 knockout in normoxia and hypoxia for **B)** KIF5B, **C)** EHD1, **D)** SHMT2 and **E)** eIF4A2. *p <0.0332, **p<0.0021, ***p<0.0002, ****P<0.0001. Non-significant comparisons not displayed. Error bars indicate ± SEM. Representative blots are shown. n=3.

3.3.20 Generation and validation of EHD1 and KIF5B siRNA knockdown HCT116 cell lines

Previous work subsequently carried out in the Mcintyre lab showed that siRNA knockdown of EHD1 and KIF5B led to a reduction in cell survival in both normoxia and hypoxia in LS174T assessed by clonogenics assay[355]. In order to validate these findings and confirm that these endocytosis genes are required for cell survival in hypoxia, these studies were repeated in a second cell line. EHD1 and KIF5B knockdown cell lines were first generated by transfecting HCT116 cells with siRNA targeting EHD1 or KIF5B. A non-targeting control cell line was also generated. Following transfection, cells were seeded for protein extraction and harvested after 48h. Knockdown efficiency was assessed by immunoblotting for EHD1 and KIF5B protein expression. Figure 3.32 displays the knockdown efficiency for the siEHD1 and siKIF5B cell lines compared to the siCTL cell line. A statistically significant reduction was achieved for both EHD1 ($p<0.0001$) and KIF5B ($p<0.0002$) protein expression compared to the control indicating successful knockdown of the two targets (figure 3.32b and 3.32d). The average knockdown efficiency was 85% and 66% for EHD1 and KIF5B respectively.

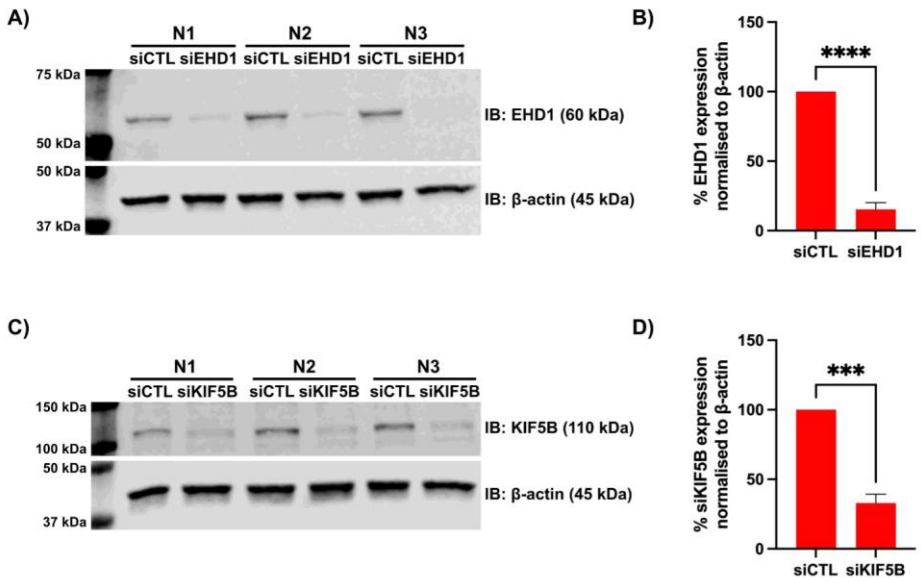

Figure 3.32 siRNA knockdown of EHD1 and KIF5B in HCT116. Wild-type HCT116 cells were transfected with siRNA targetting EHD1 or KIF5B or a non-targetting siRNA control. Cells were seeded for protein extraction after 24h and harvested 48h later. **A)** EHD1 and **C)** KIF5B protein expression was analysed by immunoblotting. Knockdown efficiency analysed by unpaired t-test for **B)** EHD1 and **D)** KIF5B. *p <0.0332, **p<0.0021, ***p<0.0002, ****P<0.0001. Non-significant comparisons not displayed. Error bars indicate ± SEM. Representative blots are shown. n=3.

3.3.21 Impact of EHD1 and KIF5B knockdown on colorectal cancer cell survival in hypoxia

The impact of EHD1 and KIF5B knockdown on cell survival was then investigated by clonogenics assay in order to validate the functional effects of these genes seen previously in the LS174T cell line. HCT116 siEHD1 and siKIF5B cell lines, as well as a siCTL cell line, were seeded for clonogenics assay and stained as described in section 2.4. Cells were exposed to either normoxia or hypoxia for 72h after seeding before being placed in normoxia for two weeks to allow colonies to form. Figure 3.33 and figure 3.34 display the results of the clonogenics assay for EHD1 and KIF5B knockdown respectively, including representative images of colony formation (figure 3.33a and 3.34a) and analysis of colony counts (figure 3.33b and 3.34b). There was no difference in cell survival between normoxia and hypoxia in the siCTL condition showing that hypoxia alone does not impact colony formation. A significant reduction in cell survival in both normoxic ($p<0.0021$) and hypoxic ($p<0.0021$) conditions was observed following EHD1 knockdown compared to the siCTL (figure 3.33b). However, no significant difference was observed in cell survival in either normoxia or hypoxia following KIF5B knockdown compared to the siCTL (figure 3.34b). This data demonstrates that knockdown of the eIF4A2-regulated endocytosis gene EHD1, but not KIF5B, reduces CRC cell survival in both normoxic and hypoxic conditions.

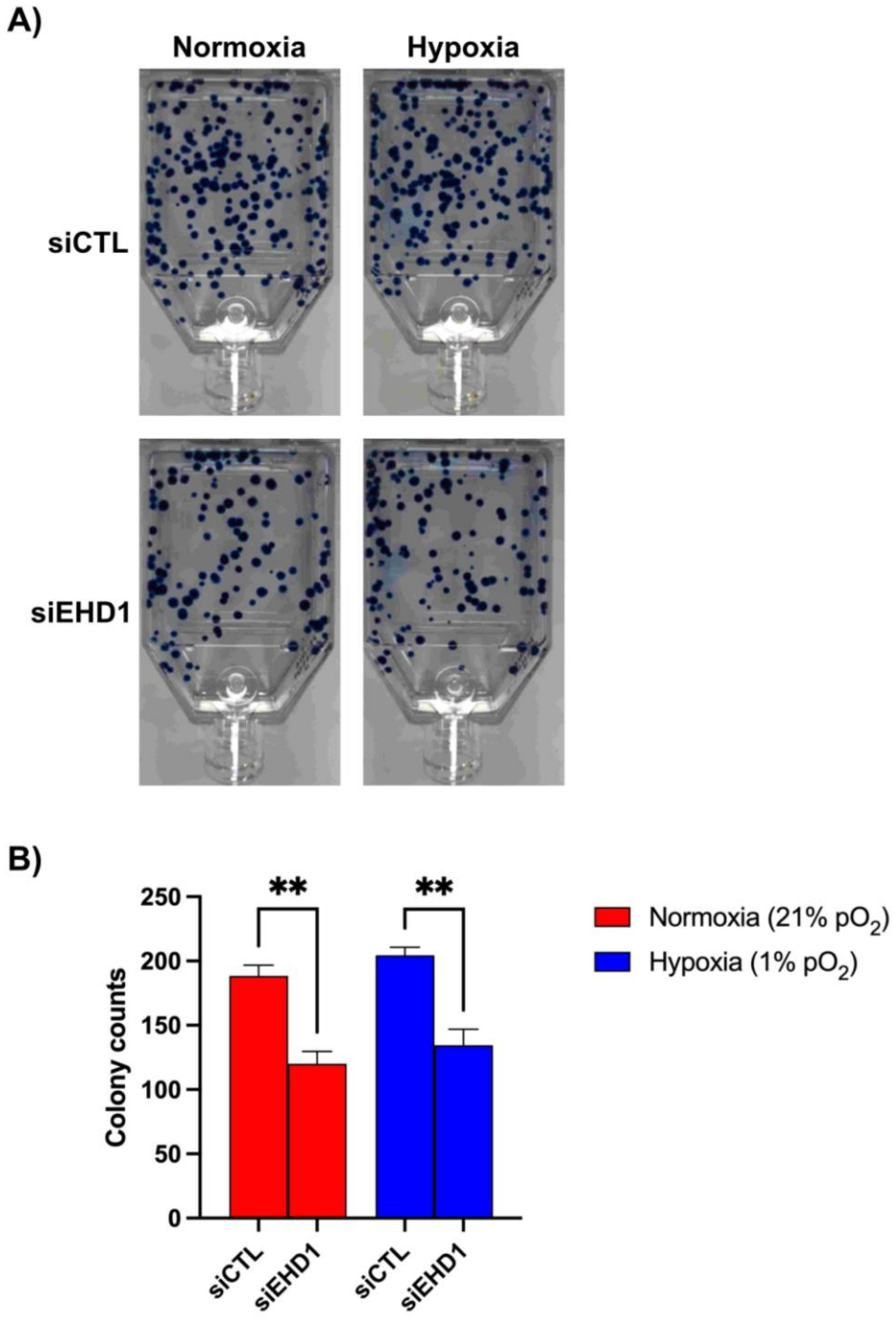

Figure 3.33 Knockdown of EHD1 reduces cell survival in both normoxia and hypoxia in HCT116 with clonogenics assay. EHD1 knockdown in HCT116 was achieved using siRNA as previously described and cells were seeded for clonogenics assay. Two technical replicates were seeded per experimental condition. For hypoxic conditions, cells were incubated in hypoxia for 72h and then returned to normoxia for two weeks to allow colonies to form. **A)** Representative images of colony formation for each experimental condition **B)** Data analysed by two-way ANOVA comparing siCTL to siEHD1 for both normoxia and hypoxia. *p <0.0332, **p<0.0021, ***p<0.0002, ****P<0.0001. Error bars indicate ± SEM. n=3.

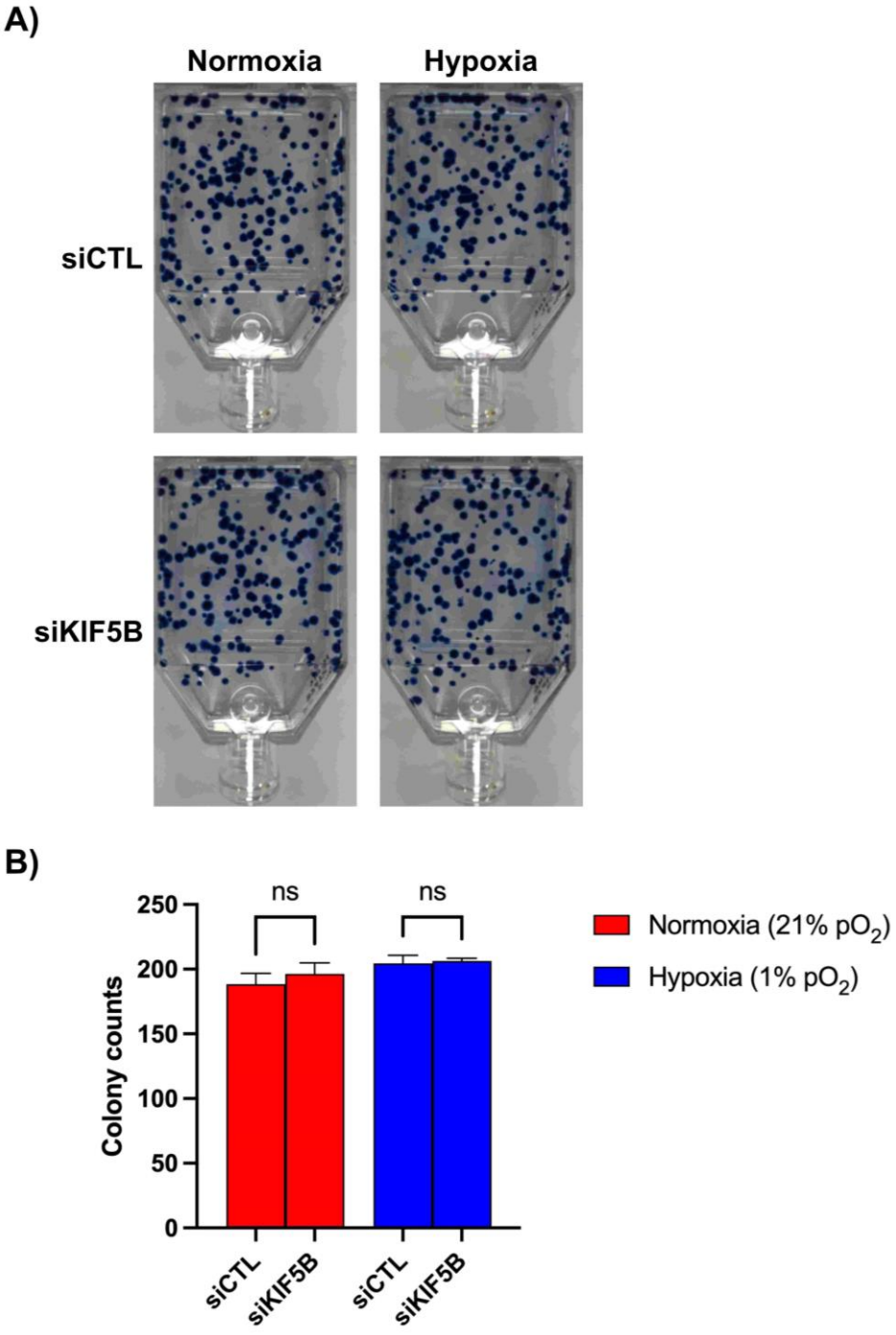

Figure 3.34 Knockdown of KIF5B has no impact on cell survival in both normoxia and hypoxia in HCT116 with clonogenics assay. KIF5B knockdown in HCT116 was achieved using siRNA as previously described and cells were seeded for clonogenics assay. Two technical replicates were seeded per experimental condition. For hypoxic conditions, cells were incubated in hypoxia for 72h and then returned to normoxia for two weeks to allow colonies to form. **A)** Representative images of colony formation for each experimental condition **B)** Data analysed by two-way ANOVA comparing siCTL to siKIF5B for both normoxia and hypoxia. *p <0.0332, **p<0.0021, ***p<0.0002, ****P<0.0001. Error bars indicate ± SEM. n=3.

3.4 Discussion

The aims of this chapter were to investigate the regulation of eIF4A2 and its potential binding partners in response to changes in oxygen concentration and assess the downstream impact of eIF4A2 knockout on colorectal cancer cell growth and survival. Additionally, the hypoxic regulation of several possible downstream targets of eIF4A2 including amino acid biosynthesis and endocytosis genes was investigated as was the possible regulation of HIF1α and HIF2α by eIF4A2. Finally, the impact of several of these target genes including CTH, EHD1 and KIF5B on colorectal cancer cell growth and survival was investigated.

3.4.1 Regulation of eIF4A2 and its binding partners in response to changes in oxygen concentration

In HCT116 and LS174T CRC cell lines, the temporal expression of both eIF4A1 and eIF4A2 expression was not altered by changes in oxygen concentration despite some fluctuations that were likely to be non-specific. eIF4A1 has previously been shown to remain unaltered in response to hypoxia, so constant eIF4A1 expression levels were anticipated[339,346]. Similarly, previous data has shown that eIF4A2 protein expression levels are also unaltered by changes in oxygen tension[355]. Despite this, I have shown that eIF4A2 expression remains constant in hypoxia suggesting it could still be playing a regulatory role under these conditions through additional mechanisms such as post-translational modifications and protein-protein interactions. Previously, sumoylation of eIF4A2 in response to cellular stress was shown to increase its recruitment to stress granules to regulate the reinitiation of translation[497]. eIF4A2 has also been shown to form a complex with NCBP3 and METTL3 within the 5'UTR of target genes to regulate m^6A methylation and hypoxic mRNA translation in cardiomyocytes despite no change in protein expression, suggesting that protein-protein interactions are the main determinant of eIF4A2 activity[498]. Therefore, I hypothesised that interactions with the hypoxic eIF4F complex components could be regulating eIF4A2 activity in hypoxia. Interactions of eIF4A2 with both eIF4G3 and eIF4E1 were observed in hypoxia and normoxia, but not with eIF4E2. Alternative antibodies against eIF4E2 were also used in order to confirm that no technical problems, such as sequestration of the antibody binding site on eIF4E2, were responsible for the lack of interaction. Furthermore, the expression of eIF4E2 was significantly reduced in hypoxia in HCT116 after 24h hypoxia whilst maximum eIF4E1

expression was observed at the 24h and 48h time points in both HCT116 and LS147T, which could explain the differences in the interactions observed in the CoIP study done at 24h. Previously, both eIF4E1 and 4E-BP1 have been shown to be upregulated in a panel of CRC cell lines whereas no work has looked specifically at eIF4E2 expression in hypoxic CRC[499,500]. However, after 24h hypoxia, the level of phosphorylated 4E-BP1 remains the same as normoxia which would prevent 4E-BP1 from sequestering and inactivating eIF4E1, thus allowing it to take part in translation initiation[499]. Due to the well-documented inhibition of mTOR signalling in hypoxia, a possible alternative mechanism of 4E-BP1 phosphorylation may be functioning in CRC to allow the continued activity of eIF4E1[501]. eIF4A2 has also previously been shown to interact directly with eIF4G3 via interactions with the middle and C-terminal domains of eIF4G3, however, my work demonstrates a hypoxia-specific interaction for the first time[275,502]. Whereas, only indirect eIF4A:eIF4E interactions have been shown previously, mediated by eIF4G3 binding[503]. It would be interesting to identify whether the eIF4A2:eIF4E1 interactions identified in this work were due to 4A:4E dimer formation or due to eIF4E1 binding to eIF4G3 and how this might explain the differences seen in eIF4E1 and eIF4E2 binding, possibly through the use of alternative binding sites that become exposed or sequestered hypoxic conditions.

In addition to eIF4F interactions, my work has identified a hypoxia-specific increase in eIF4A2 binding to CNOT7 for the first time. This suggests a potential role for eIF4A2 in protecting selected mRNAs from hypoxia-induced degradation by incorporation into the CCR4-NOT complex and inhibition of CNOT7-mediated RNA degradation[336,341]. Recently, a novel RNA-binding protein TAB182 was shown to be responsible for the selective recruitment of either eIF4A2 or DDX6 into the CCR4-NOT complex to regulate the fate of target mRNAs[341]. Interestingly, the role of TAB182 in hypoxia has not been investigated; this work would provide further insight into whether there is preferential recruitment of eIF4A2 over DDX6 into the CCR4-NOT complex in hypoxic conditions. The majority of proteins that have been investigated in eIF4A2 knockdown CRC cells show reduced expression, suggesting a positive role for eIF4A2 in their regulation[355].

3.4.2 Impact of eIF4A2 knockout on colorectal cancer cell growth and survival

eIF4A2 knockout led to a reduction in 3-dimensional CRC spheroid growth using LS174T clones but not with HCT116 pools or LS174T lentiviral 4A2 knockout cells. Similar heterogeneous results were also observed with the 2-dimensional clonogenics assay whereas, previous data using eIF4A2 knockdown cells showed a reduction in spheroid growth in CRC cells and CRC cell metastasis through the translational regulation of c-myc[353,355]. There are several possible explanations for the variable results presented in my work. One potential challenge is the genetic variability that arises due to the natural accumulation of mutations in the parental cell line selected for CRISPR which is magnified during clonal isolation and expansion[504]. This can lead to phenotypic variability between clones which subsequently exhibit different responses when used in downstream studies making it difficult to confirm the cause of the experimental outcomes[505,506]. On the other hand, it is becoming increasingly well-documented that genetic compensation, where the expected adverse phenotypic effect is not observed due to compensatory mechanisms triggered by the loss-of-function of a gene, presents a major challenge for CRISPR studies[507]. For example, studies have shown that T lymphocytes and breast cancer cells harbouring an *RBL2* knockout display normal immune function and proliferative capacity due to the upregulation of the paralogue RBL1[508,509]. Furthermore, recent studies have identified that these compensatory mechanisms only occur in knockout models, and not in knockdown systems[507]. For example, siRNA-mediated knockdown of any one of the three cyclin D family members inhibits cell proliferation in glioblastoma and pancreatic cancer cells whereas *Cyclin D2* mutant B lymphocytes show no adverse proliferative phenotype due to the upregulation of *Cyclin D3*[510–512]. This could explain the lack of phenotypic effect observed with the eIF4A2 knockout cell lines used in this study, whilst an impact on CRC growth was achieved with eIF4A2 knockdown cell lines[355]. Investigating the possible upregulation of related RNA helicases in response to eIF4A2 knockout through protein analysis or RNA-sequencing would help to confirm this.

Interestingly, despite no differences in overall growth, a significant increase in the levels of necrosis in the lentiviral eIF4A2 knockout spheroids was observed. This agrees with previous *in vivo* eIF4A2 knockdown xenograft studies where an increase in necrosis was also observed[355]. Further immunohistochemical analysis of tumour sections looking at markers of cell death, such as cleaved caspase-3, in the context of hypoxic regions

identified with a hypoxic marker such as CA9, would provide further insight into the possible mechanism of eIF4A2-regulated cell death.

3.4.3 eIF4A2-mediated regulation of HIFs and downstream metabolic and endocytic proteins

eIF4A2 knockout led to an increase in HIF-2α expression in LS174T suggesting a negative regulatory role for eIF4A2. Previous work has suggested that eIF4A2 expression is directly regulated by the HIF2α-RBM4-eIF4E2 complex by binding to the rHRE present within the 3'UTR of eIF4A2[316,355]. One explanation is that eIF4A2 is able to repress HIF2α translation, possibly through its role in the CCR4-NOT complex. Previous RIP-sequencing data has shown that eIF4A2 binding to HIF-2α mRNA increases significantly in hypoxia[355]. It would be interesting to identify through additional RIP-sequencing and IP studies, whether eIF4A2 is binding to HIF-2α as part of a larger complex such as eIF4F or CCR4-NOT and how that determines the impact on HIF-2α expression. Furthermore, there is a complex network of RNA binding proteins (RBPS) that are known to regulate HIFα subunit translation. RNA binding motif protein 38 (RBM38) interacts with the 5'UTR of HIF-1α and prevents the binding of eIF4E to block cap-dependent translation in a p53-dependent manner[513]. Therefore, the regulation of HIFα by eIF4A2 is likely to be further complicated by a network of hypoxia-responsive RBPs which have recently been identified as key regulators of metabolic adaptation to hypoxia through translational control[514].

Several genes encoding amino acid biosynthetic enzymes have previously been identified as eIF4A2 binding targets in hypoxia[355]. However, I have shown that the expression of ALDH18A1, ASS1, IRP1, GPT2 and PHGDH remains unchanged in hypoxic conditions in LS174T. Interestingly, I also observed a downregulation in PHGDH and GPT2 gene expression in hypoxia in HCT116 from 48h hypoxia RNA-seq data and, furthermore, no significant changes in gene expression were observed for ALDH18A1, IRP1 or ASS1. ASS1 expression has previously been shown to be downregulated in hypoxia in HCT116 after 24h hypoxia whereas PHGDH was shown to be upregulated[515,516]. This highlights the importance of considering the temporal regulation of the hypoxic response in these studies. Previous work has also shown that eIF4A2 knockdown leads to a reduction in SHMT2 and CTH protein expression after 24h

hypoxia in LS174T CRC cell line, indicating a positive role for eIF4A2 in regulating the translation of these proteins[355]. I also identified an increase in SHMT2 expression after 48h hypoxia as well as an increasing trend in CTH expression, consistent with previous findings. Interestingly, in the HCT116 RNA-seq data CTH expression was not significantly changed and SHMT2 expression was downregulated in hypoxia, suggesting there may be a cell line-specific response elicited by LS174T. As a member of the CMS3 subtype of CRC, LS174T are characterised by a high degree of metabolic reprogramming which may explain these cell line-dependent differences[170].

3.4.4 Impact of CTH knockout on colorectal cancer cell growth and survival

CTH was previously identified as the most significantly enriched mRNA for eIF4A2 binding under hypoxic conditions and is expressed in hypoxia in an eIF4A2-dependent manner[355]. In addition, CTH overexpression in CRC leads to increased cell proliferation, migration and tumour growth[427]. Taken together, this suggests eIF4A2 could play an important role in regulating hypoxic CRC cell survival. However, my work demonstrated that CTH knockout has no impact on cell survival in hypoxia or 3-dimensional CRC cell growth. Most of the pro-tumourigenic effects of CTH are attributed to its production of H_2S and its stimulatory effect on growth factor signalling, as seen in both CRC and hepatocellular carcinoma[425,517]. However, a significant proportion of endogenous H_2S is synthesised by two closely related enzymes CBS and 3-mercaptopyruvate sulfurtransferase (3-MST)[518]. Furthermore, CBS is commonly overexpressed in CRC and at consistently higher levels than CTH, leading to increased H_2S production[519,520]. Thus, the H_2S generated by CBS overexpression coupled with 3-MST activity is likely able to compensate for the loss of CTH-mediated H_2S production and therefore mitigate the impact of CTH knockout or inhibition, possibly through genetic compensation as discussed earlier. Investigating the regulation of additional H_2S-synthesising enzymes in the context of CTH knockout would provide valuable insight into this mechanism. Furthermore, only a limited number of phenotypic assays were employed in my study. Additional work assessing the impact of CTH and H_2S on CRC migration and invasion, which has been described previously in several cancers, as well as the impact of ROS production, as cysteine generated by CTH serves as a precursor to glutathione, on apoptosis and necrosis in the context of hypoxic regions would help further our understanding of CTH in hypoxic CRC[521,522].

3.4.5 Impact of endocytic gene knockdown on colorectal cancer cell survival

Endocytosis was previously identified as an eIF4A2-regulated pathway in hypoxia based on the characterisation of eIF4A2-bound mRNAs in hypoxia[355]. In my work, a hypoxia-specific reduction in EHD1 expression was observed in response to eIF4A2 knockdown in agreement with previous data using a different CRC cell line and EHD1 knockdown led to a reduction in CRC cell survival in both normoxia and hypoxia. Previous studies have shown that EHD1 is overexpressed in lung cancer patient samples and correlates with worse tumour size and disease-free survival[523,524]. Furthermore, EHD1 knockdown was shown to induce the expression of epithelial markers whilst reducing mesenchymal marker expression to inhibit EMT[523]. *In vivo*, EHD1 overexpression stimulates EMT and increases the formation of lung metastatic nodules[523]. More recently, EHD1 has been implicated in the trafficking of EGFR to the cell surface as EHD1 knockdown leads to reduced EGFR presentation at the cell membrane and an accumulation of EGFR-containing vesicles within the Golgi in both breast and pancreatic cancer cell lines[525]. Therefore, it is plausible that the eIF4A2-mediated translation of EHD1 in hypoxic CRC cells leads to elevated growth factor receptor recycling and cell surface presentation leading to sustained growth signalling and cell proliferation. Investigating the impact of both eIF4A2 and EHD1 knockout on cell-surface receptor presentation through FACS analysis as well as the localisation of growth factor receptors through immunofluorescence would further our understanding of this potential mechanism. The reintroduction of eIF4A2 or EHD1 through rescue experiments would also confirm this.

3.4.6 Concluding statements

In summary, the work presented in this chapter investigated the expression and interactions of eIF4A2 and its binding partners in hypoxia, the role of eIF4A2 in CRC cell growth and survival, the regulation of downstream eIF4A2 targets and the roles of CTH and endocytic proteins in CRC cell growth and survival. As hypothesised, the expression of both eIF4A2 and eIF4A1 is not altered with changing oxygen concentration however, new interacting partners of eIF4A2 under hypoxic conditions were identified. This work has shown, for the first time, that eIF4A2 interacts with both eIF4G3 and eIF4E1, but not eIF4E2, in hypoxic CRC cells and also displays increased binding to CNOT7 in hypoxia. Additionally, complete knockout of eIF4A2, achieved through CRISPR clonal selection, led to a reduction in 3-dimensional CRC spheroid growth as hypothesised. Similarly, eIF4A2 knockout appeared to increase the amount of

necrosis within the spheroids in line with my hypothesis, however further validation of this result is required. Despite this, no effect was seen in 2-dimensional cell survival assays and so the oxygen-dependency of this effect could not be determined. Furthermore, this effect could not be reproduced utilising alternative CRISPR gene-editing methods and different cell lines.

I hypothesised that eIF4A2 regulates the expression of HIF-1α and HIF-2α in hypoxia and demonstrated that eIF4A2 knockout was shown to increase the hypoxia-specific expression of HIF-2α in LS174T. But this effect was not seen in additional CRC cell lines and no impact on HIF-1α was observed. I also hypothesised that eIF4A2 regulates the hypoxic expression of downstream targets such as CTH, EHD1 and KIF5B. eIF4A2 knockdown led to a hypoxia-specific reduction in EHD1 expression however no effect was observed on KIF5B expression and the impact of eIF4A2 loss on CTH expression was not investigated. Finally, I hypothesised that CTH knockout and knockdown of EHD1 or KIF5B would reduce CRC cell growth and survival in hypoxia. I have demonstrated that EHD1 knockdown led to a reduction in CRC cell survival in both normoxia and hypoxia whereas no effect was seen for KIF5B knockdown or CTH knockout in 2-D and 3-D assays.

These results led to the conclusion that eIF4A2 regulates the hypoxic translation of specific target mRNAs, such as EHD1, governed by its interactions with translation regulatory protein complexes including eIF4F and CCR4-NOT, to regulate CRC cell survival and 3-dimensional growth.

4. The role of HIF-1α and HIF-2α in the spatial regulation of metabolic adaptation to hypoxia in colorectal cancer

4.1 Introduction

Hypoxia is well known to induce large-scale gene expression changes, coordinated primarily by the HIF-1α and HIF-2α transcription factors[526]. Recent advances in high-throughput microarray analysis and transcriptomics have led to a large number of studies investigating the transcriptional response to hypoxia in many cell types and across multiple cancer types[527–530]. The majority of hypoxia-responsive genes are involved in coordinating metabolic reprogramming, the inhibition of cell proliferation and the stimulation of angiogenesis[531]. Furthermore, many attempts have been made to identify and distinguish HIF-1α versus HIF-2α gene selectivity, but this remains a significant challenge due to the complexity of the HIF regulatory network along with the difference in response seen within different cancer types[526]. For example, the hypoxic response in endothelial and breast cancer cells is coordinated predominantly by HIF-1α whereas HIF-2α appears to play a dominant role in renal cell carcinoma and neuroblastomas[532,533]. Evidence also suggests that the HIF-1α and HIF-2α-dependent responses to hypoxia are regulated in a temporal manner where the acute hypoxic response (< 24h) is governed primarily by HIF-1α but switches to a HIF-2α-mediated programme during longer periods of chronic hypoxia[227,534]. Despite this, the vast majority of studies investigating the HIF-transcriptional response in solid tumours do not go beyond 24h hypoxia and could explain the lack of literature surrounding HIF-2α-regulated gene expression compared with HIF-1α[526,534].

In CRC, the role of HIF-1α has been extensively studied and shown to regulate many of the major hallmarks of cancer including metabolism, proliferation and angiogenesis[535–537]. However, there is a significant lack of research focusing on the role of HIF-2α in colorectal cancer, despite it being overexpressed in CRC tumours and shown to promote tumour progression[538]. More importantly, the role of HIF-2α in metabolic adaptation to hypoxia remains largely unclear. This is possibly due to the majority of studies focusing on shorter hypoxic time points of ≤ 24h[539].

In addition to changes in gene expression, hypoxia has also been shown to regulate alternative splicing and hypoxia-induced splicing is now recognised as an emerging hallmark of cancer[540]. Hypoxia has been shown to regulate alternative splicing in several cancer types including liver cancer (3,059 splicing events) and breast cancer (~ 2,000 splicing events)[541,542]. However, the relationship between alternative splicing and hypoxia in CRC has not been studied in detail. Furthermore, hypoxia promotes the alternative splicing of both HIF-dependent and HIF-independent genes with the majority of HIF-dependent spliced genes regulating metabolic processes such as glycolysis and glucose uptake[543]. For example, hypoxia promotes the HIF-1α-dependent expression of the PKM2 splice variant of pyruvate kinase which displays weaker enzymatic activity than the PKM1 variant and results in an accumulation of glycolytic intermediates[544]. In addition, HIF-dependent alternative splicing of PDK1 leads to the inhibition of pyruvate dehydrogenase and promotes glycolysis over oxidative phosphorylation[543]. However, most of the current research into hypoxia-regulated alternative splicing has not focused on deciphering the specific roles of HIF-1α and HIF-2α in this process and even less work has investigated the role of alternative splicing in the regulation of metabolic adaptation to hypoxia, especially in the context of CRC. In addition, most of the current work on hypoxia-induced alternative splicing has been limited to acute hypoxia ≤ 24h[541,543].

Metabolic reprogramming is now widely recognised as being at the forefront of tumour adaptation to hypoxia and this has led to the rapid growth of research into the use of metabolomics for identifying biomarkers of tumour hypoxia[545]. Hypoxia-associated metabolic adaptation can give rise to a hypoxia-specific metabolic phenotype that can be used clinically as a diagnostic tool, to aid therapeutic selection and as a marker of therapeutic response[545,546]. However, tumours have been shown to consist of highly heterogeneous populations of cells each with distinct metabolic phenotypes[432]. Therefore, to accurately measure and analyse metabolic adaptation in hypoxic tumours, spatial metabolomics is required with subcellular resolution. Here, the 3-D OrbiSIMS hybrid mass analyser becomes a desirable instrument for carrying out this analysis. The OrbiSIMS has previously been used to identify metabolic responses to drug treatment at the single-cell level and has been used to distinguish and characterise metabolically distinct subpopulations of cells, highlighting its potential applicability to studying metabolic changes across the oxygen gradient found within tumours[462,547]. However, little work has so far utilised the OrbiSIMS technology for analysing spatial metabolism within tumours. One previous study using LC/MS was able to identify

metabolite differences between CRC tumour and normal colon samples in both FFPE and fresh-frozen samples with almost three times more metabolites detected in the frozen compared to FFPE samples[548]. However, the impact of oxygen concentration on the distribution of these metabolites was not investigated. Furthermore, the use of cryogenic conditions for maintaining physiological metabolite distribution in combination with OrbiSIMS analysis has not been used to analyse CRC samples, especially in the context of hypoxia. Additionally, the use of 3-dimensional spheroid models, which more closely represent the oxygen gradient found with solid tumours, in combination with OrbiSIMS analysis, has never been developed or utilised to investigate the spatial regulation of metabolic adaptation to hypoxia in CRC.

4.2 Hypothesis and aims

In this chapter, the following points were investigated, and the following hypotheses were tested:

- Role of HIF-1α and HIF-2α in the regulation of CRC growth
- Role of hypoxia, HIF-1α and HIF-2α in the regulation of gene expression and metabolic gene expression
- Role of hypoxia, HIF-1α and HIF-2α in the regulation of the alternative splicing of genes and metabolic genes
- Role of hypoxia, HIF-1α and HIF-2α in the spatial regulation of metabolic adaptation in CRC

I hypothesise that HIF-1α and HIF-2α regulate CRC growth and that knockout of HIF-1α and HIF-2α reduces CRC growth. Secondly, I hypothesise that hypoxia induces large-scale changes in gene expression and, in particular, changes in metabolic gene expression and that this regulation is controlled by HIF-1α and HIF-2α. Additionally, I hypothesise that hypoxia is associated with the alternative splicing of genes and, in particular, metabolic genes and that both HIF-1α and HIF-2α regulate changes in the alternative splicing of metabolic genes. Finally, I hypothesise that changes in the oxygen gradient within 3-dimensional models alter the spatial regulation of metabolic adaptation to hypoxia and that this regulation is impacted by the loss of HIF-1α and HIF-2α function.

In order to test these hypotheses, I have undertaken the following aims:

1- Validate HIF-1α and HIF-2α knockout cell lines and investigate the impact of HIF-1α and HIF-2α knockout on 3-dimensional spheroid growth *in vitro*
2- Validate the major time point of induction of HIF-1α and HIF-2α expression in the HCT116 CRC cell line
3- Generate and validate normoxic and hypoxic control, as well as hypoxic HIF-1α and HIF-2α knockout, RNA samples for RNA sequencing
4- Investigate the role of hypoxia in the regulation of overall gene expression and metabolic gene expression

5- Investigate the role of HIF-1α and HIF-2α in the regulation of overall gene expression and metabolic gene expression

6- Investigate the role of hypoxia, HIF-1α and HIF-2α in the regulation of the alternative splicing of genes, in particular, metabolic genes

7- Develop a 3-D spheroid model and high-pressure freezing workflow for the spatial analysis of metabolites using secondary ion mass spectrometry

8- Investigate the role of hypoxia, HIF-1α and HIF-2α in the spatial regulation of metabolic adaptation in 3-D CRC models using secondary ion mass spectrometry

4.3 Results

4.3.1 Validation of HCT116 HIF-1α and HIF-2α knockout cell lines

HCT116 HIF-1α and HIF-2α knockout clonal cell lines were generated by Dr T. Potgieter, using the clonal selection CRISPR-Cas9 method as described previously. HCT116 iCas9 cells were transfected with either non-targeting gRNA control, HIF-1α-targeting gRNAs g49 and g57 or HIF-2α-targeting gRNAs g11 and g81. The knockout of HIF-1α and HIF-2α in the four clonal cell lines was validated at the protein level by immunoblotting (figure 4.1). The two HIF-1α knockout cell lines, g49 and g57, showed a statistically significant reduction in HIF-1α expression (figure 4.1b, $p<0.0001$) and achieved an 86% and 88% decrease in protein levels respectively. Similarly, the two HIF-2α knockout cell lines, g11 and g81, showed a statistically significant reduction in HIF-2α expression (figure 4.1d, $p<0.0001$) and achieved a 91% and 84% decrease in protein levels respectively.

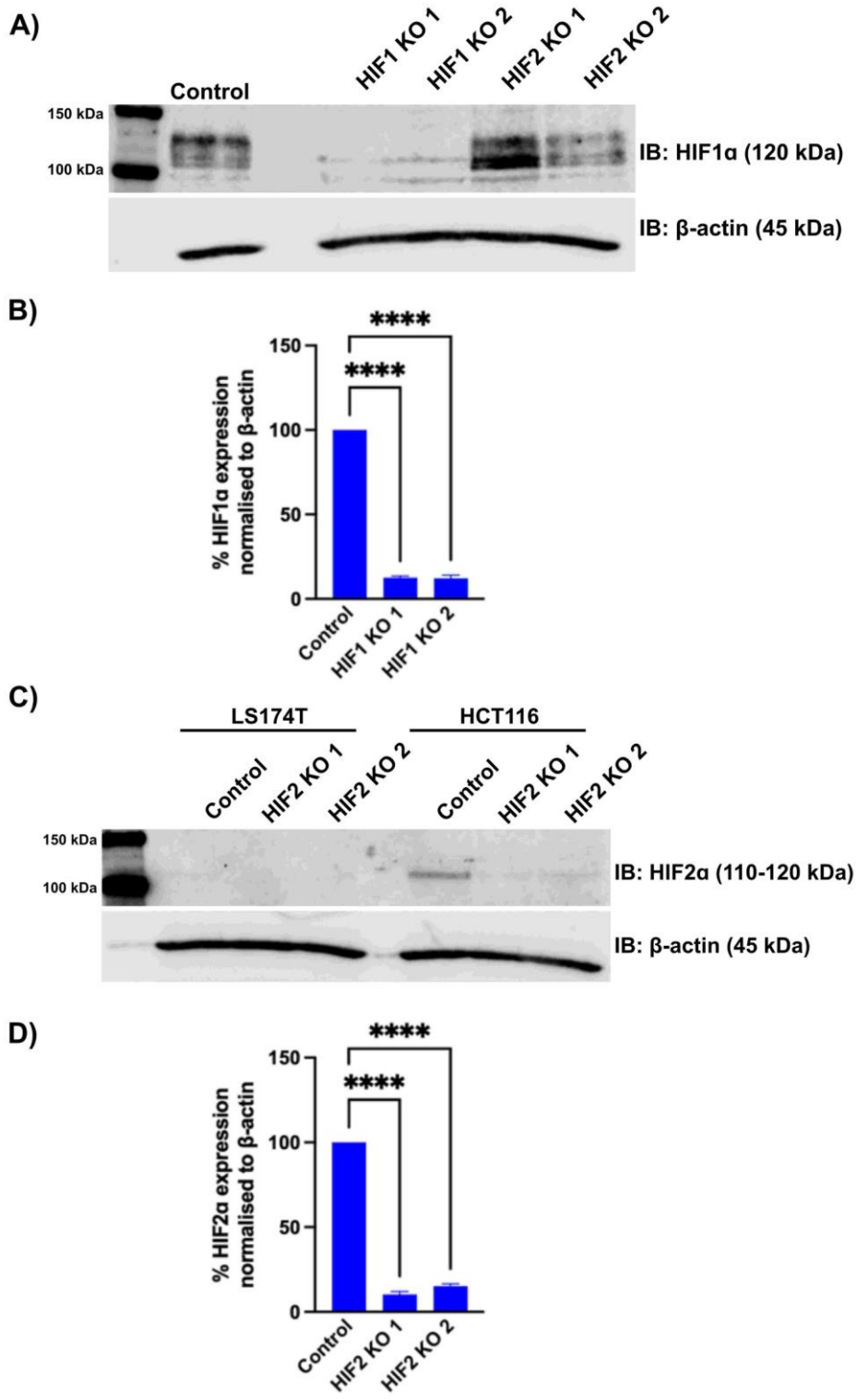

Figure 4.1 Validation of HCT116 HIF-1α and HIF-2α knockout cell lines. Inducible Cas9-expressing HCT116 cells transfected with non-targeting gRNA control, HIF-1α-targeting gRNAs g49 and g57, or HIF-2α-targeting gRNAs g11 and g81 were selected for clonal expansion and seeded for protein extraction. **A, C)** HIF-1α and HIF-2α protein expression was analysed by immunoblotting. **B, D)** Data analysed by one-way ANOVA comparing control to HIF knockout protein expression. *p <0.0332, **p<0.0021, ***p<0.0002, ****P<0.0001. Error bars indicate ± SEM. Representative blots are shown. n=3.

4.3.2 Impact of HIF-1α and HIF-2α knockout on 3-dimensional spheroid growth

In order to confirm that knockout of HIF-1α and HIF-2α leads to the expected reduction in 3-dimensional spheroid growth the HCT116 knockout cell lines, as well as control cells, were used to form spheroids as described in section 2.2.1. Spheroids were grown for 10 days with images taken on days 3, 5, 7 and 10. Spheroid volumes and growth rates were calculated and analysed as described in section 2.2.3. Figure 4.2a displays representative images at each of the time points measured. Morphologically, there were no visible differences between the HIF knockout and control spheroids. The HIF-1α knockout g57 cell line and the HIF-2α knockout g81 cell line had a reduced average spheroid volume compared to the two controls (figure 4.2b) and there was a statistically significant difference in spheroid volume on Day 10 in these two cell lines compared to the control A3 (figure 4.2d, $p<0.0332$). There was no difference in average spheroid volume or day 10 spheroid volume with the other knockout cell lines. Despite the reduction in overall spheroid size, there was no difference in the growth rates of the g57 and g81 spheroids compared to the controls. There was a statistically significant increase in the growth rates of the g49 and g11 spheroids compared to the controls (figure 4.2c, $p<0.0002$). Therefore, the A3 control cell line along with the g57 HIF-1α knockout and g81 HIF-2α knockout cell lines were selected for downstream analysis.

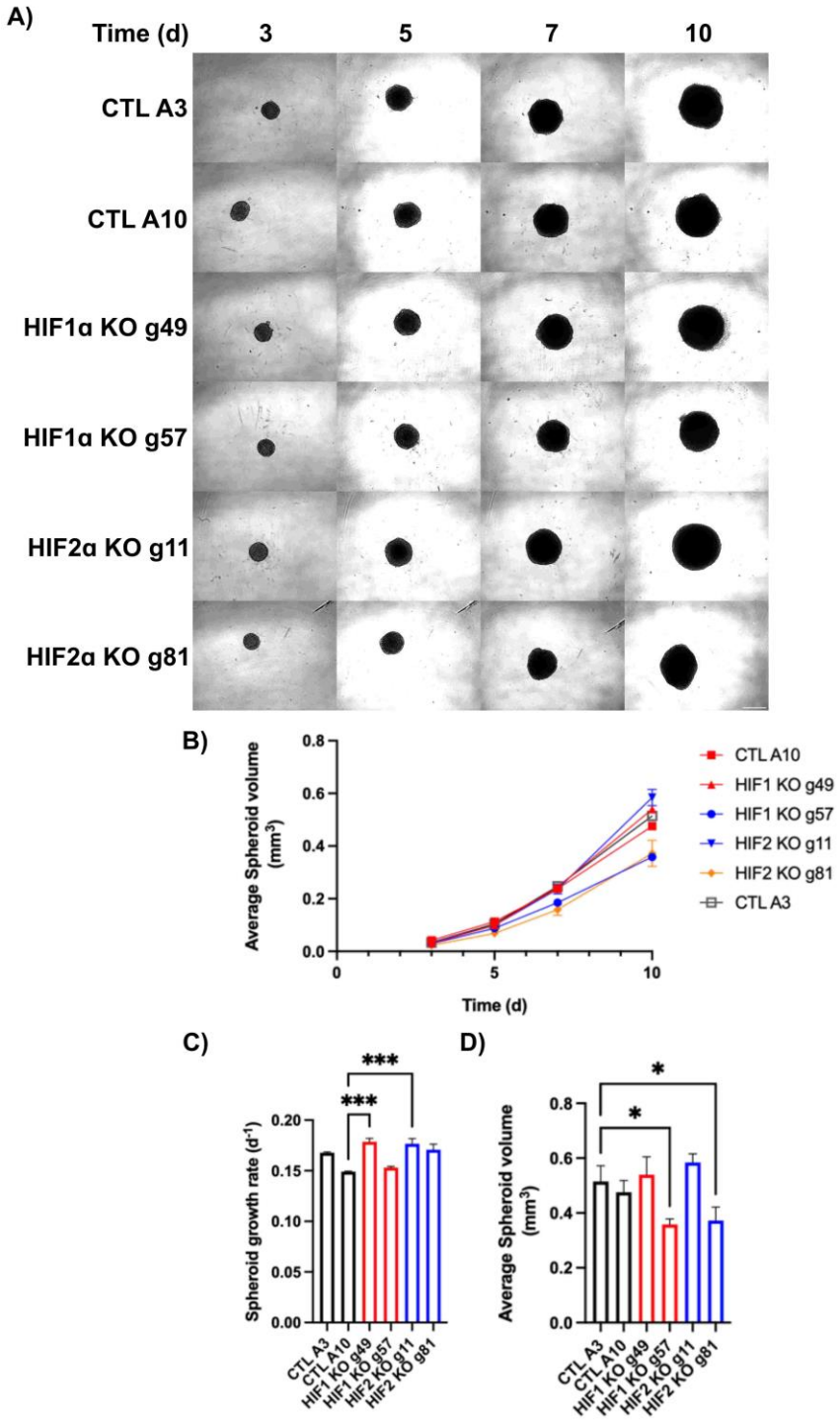

Figure 4.2 HIF-1α and HIF-2α knockout reduce 3-dimensional spheroid growth *in vitro*. HCT116 iCas9 cells transfected with either non-targeting gRNA controls A3 and A10, HIF-1α-targeting gRNAs g49 and g57 or HIF-2α-targeting gRNAs g11 and g81 were isolated into clonal populations and used to form 3-dimensional spheroids *in vitro* at the optimised seeding density of 1000 cells/well. **A)** Representative images from three experimental repeats of HCT116 spheroids taken on days 3, 5, 7 and 10 at 4x magnification. Scale bar represents 500µm. **B)** Images were used to calculate average spheroid volumes on days 3, 5, 7 and 10. **C)** Spheroid volumes were used to calculate growth rates using linear regression analysis. **D)** Comparison of average spheroid volumes on Day 10 of growth. Data was analysed by one-way ANOVA comparing HIF-1α and HIF-2α knockout spheroid growth rates to control A3 and control A10. *p <0.0332, **p<0.0021, ***p<0.0002, ****P<0.0001. Error bars indicate + SEM, n=3

4.3.3 Time-dependence of HIF-1α and HIF-2α protein expression in hypoxia

In order to identify the best time point to use to enable the investigation of both HIF-1α and HIF-2α in the regulation of metabolic gene expression by RNA-sequencing, the expression of HIF-1α and HIF-2α was investigated in normoxia and hypoxia at different time points. Wild-type HCT116 cells were exposed to either normoxia or hypoxia for 24, 48 and 72h and HIF-1α and HIF-2α expression was analysed by immunoblotting (figure 4.3a,c). CA9 protein expression was also measured as a positive control for the induction of hypoxia. Despite a lack of significance, maximum expression of HIF-1α in hypoxia was observed at the 48h time point (figure 4.3b). There was also a statistically signficant increase in HIF-2α expression in hypoxia compared to normoxia at the 48h time point which coincided with maximum HIF-2α expression (figure 4.3d, $p<0.0332$). The increasing trend in hypoxic CA9 expression over time and the statistically significant increase in CA9 expression at the 72h time point confirmed the induction of hypoxia in the samples (figure 4.3e, $p<0.0332$). Therefore, the 48h time point was selected for further analysis based on the combined maximum expression of both HIF-1α and HIF-2α at that time point.

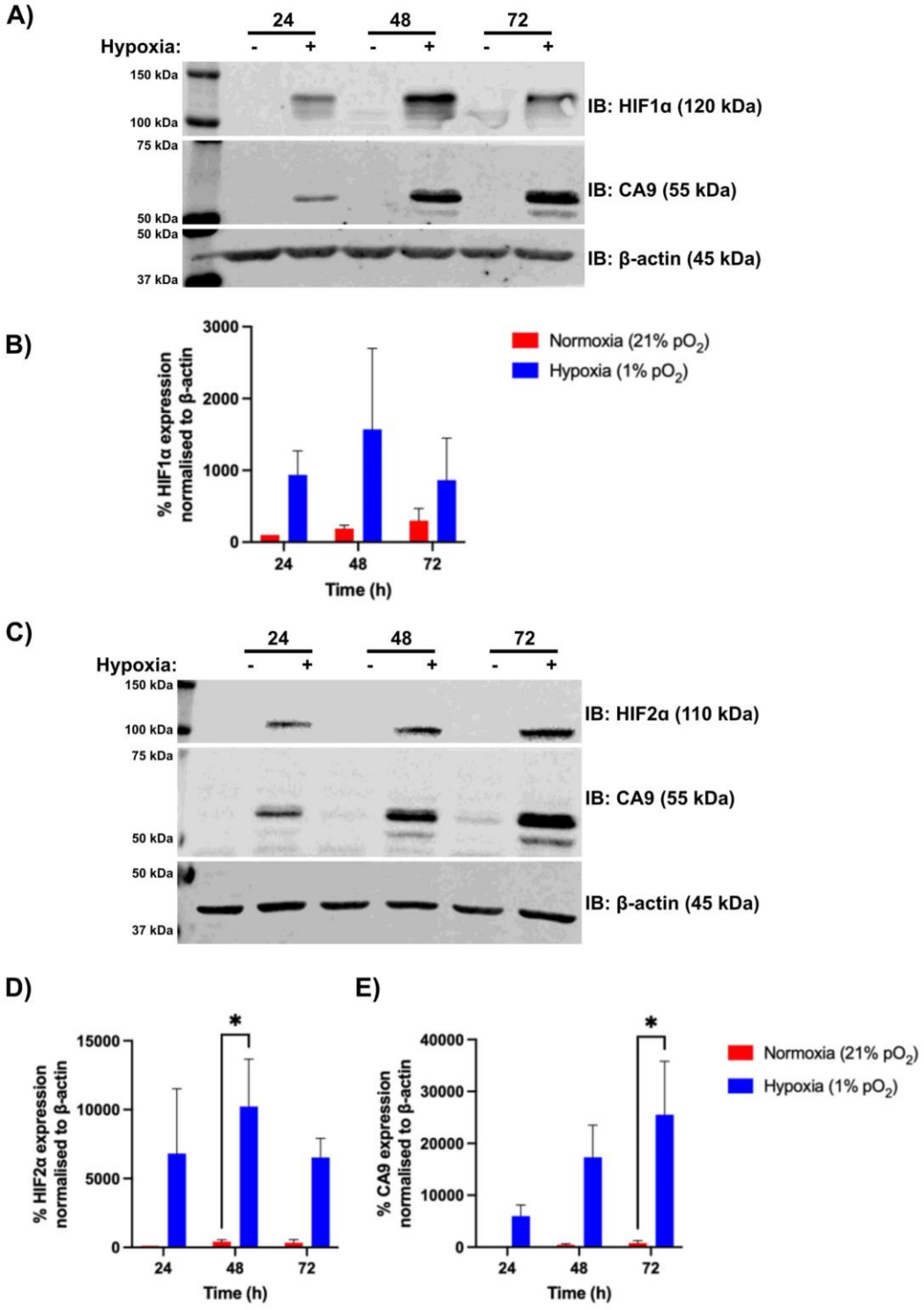

Figure 4.3 HIF-1α, HIF-2α and CA9 protein expression in HCT116 under normoxic and hypoxic conditions at different time points. Wild-type HCT116 cells were exposed to either normoxia or hypoxia for 24, 48 or 72h. **A, C)** HIF-1α, HIF-2α and CA9 protein expression was analysed by immunoblotting. Quantification of **B)** HIF-1α, **D)** HIF-2α and **E)** CA9 expression analysed by two-way ANOVA comparing normoxia and hypoxia at each time point. *p <0.0332, **p<0.0021, ***p<0.0002, ****P<0.0001. Non-significant comparisons not displayed. Error bars indicate ±SEM. Representative blots are shown. n=3.

4.3.4 Validation and quality control of HCT116 HIF-1α and HIF-2α knockout RNA samples for RNA sequencing

HCT116 control A3, HIF-1α knockout g57 and HIF-2α knockout g81 cell lines were exposed to either normoxia or hypoxia for 48h prior to RNA extraction using the column extraction method with DNase digestion as described in section 2.9.1. RNA extracts were prepared from three experimental repeats in order to investigate the hypoxia and HIF-dependent regulation of metabolism in CRC. Prior to submission for RNA sequencing, RNA sample purity was assessed using the A260/A280 absorbance ratio as described in section 2.8.8. All of the samples had an A260/A280 ratio of > 2.0 indicative of pure RNA with no DNA or protein contamination (figure 4.4b). RNA samples were also submitted to Deep-Seq (The University of Nottingham) in order to assess RNA integrity using the Agilent TapeStation. The RNA samples were given an RNA integrity number (RIN) ranging from 1-10 with 10 representing intact RNA with no degradation. 10 out of the 12 RNA samples had a RIN value of 10 whilst the remaining two were 9.9 and 9.7, indicating that all of the samples were intact and there was no degradation (figure 4.4b). Furthermore, gel electrophoresis of the RNA samples identified two clear, distinct bands representing the 28s rRNA and 18s rRNA subunits (figure 4.4a). The sharpness of the two bands and the absence of any smearing confirmed the integrity of the samples and the lack of any sample degradation. CA9 mRNA expression was also measured by qPCR in all of the RNA samples in order to confirm the induction of hypoxia in the hypoxic control sample and to validate the expected reduction in CA9 levels in the HIF-1α knockout condition. A 24-fold increase in CA9 mRNA expression was observed in hypoxia compared to normoxia and this increase was ablated in the HIF-1α knockout sample (figure 4.4c, $p<0.0332$). The identification of a suitable HIF-2α specific target was unsuccessful. Based on these results the RNA samples were submitted to Novogene for 150bp paired-end RNA sequencing.

A)

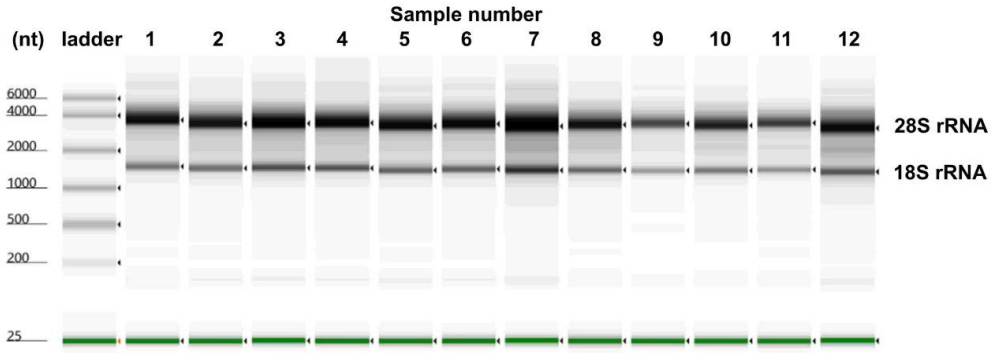

B)

	Sample	A260/280 ratio	RIN
N1	CTL Nx	2.07	10.0
	CTL Hx	2.05	10.0
	HIF1α KO Hx	2.08	10.0
	HIF2α KO Hx	2.06	10.0
N2	CTL Nx	2.07	10.0
	CTL Hx	2.08	10.0
	HIF1α KO Hx	2.08	9.9
	HIF2α KO Hx	2.07	10.0
N3	CTL Nx	2.08	10.0
	CTL Hx	2.06	10.0
	HIF1α KO Hx	2.06	10.0
	HIF2α KO Hx	2.07	9.7

C)

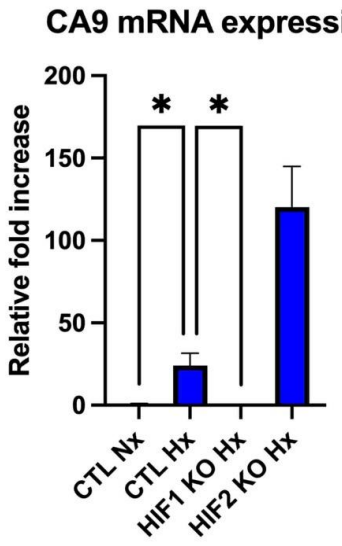

Figure 4.4 Validation of HCT116 control, HIF-1α and HIF-2α knockout RNA samples prior to RNA-sequencing. HCT116 iCas9 control A3, HIF-1α KO g57 and HIF-2α KO g81 cells were exposed to either normoxia or hypoxia for 48h and RNA was extracted using the column extraction method as previously described. **A)** RNA sample integrity was assessed by gel electrophoresis. **B)** Summary table of RNA sample purity and integrity as determined by A260/A280 absorbance ratios and RIN number validation. **C)** CA9 mRNA expression in the different experimental conditions measured by qPCR. Data was analysed by one-way ANOVA comparing control Nx to control Hx as well as control Nx with HIF KO Hx conditions. *p <0.0332, **p<0.0021, ***p<0.0002, ****P<0.0001. Error bars indicate ± SEM. n=3.

4.3.5 The hypoxia-regulated transcriptome

Prior to sequencing, additional quality control steps were carried out by Novogene including the reassessment of RNA integrity and purity. All samples passed the quality control tests. RNA samples then underwent cDNA library preparation prior to undergoing 150bp paired-end RNA sequencing on an Illumina NovaSeq 6000 S4 platform with 20 million reads per sample. The downstream bioinformatic processing and data analysis was carried out in-house (see sections 2.9.4 and 2.9.5 for details). In order to confirm the upregulation of hypoxia-regulated genes and investigate the biological significance of hypoxia-regulated genes differential gene expression (DEG) analysis was carried out between the control normoxia and control hypoxia conditions. Overall, 6,295 genes were significantly differentially expressed between hypoxia and normoxia with 3,220 genes upregulated and 3,075 genes downregulated under hypoxic conditions compared to normoxia (figure 4.5). Approximately 15,000 genes were not significantly differentially expressed between the two conditions after filtering the data by adjusted p-value (padj) < 0.05.

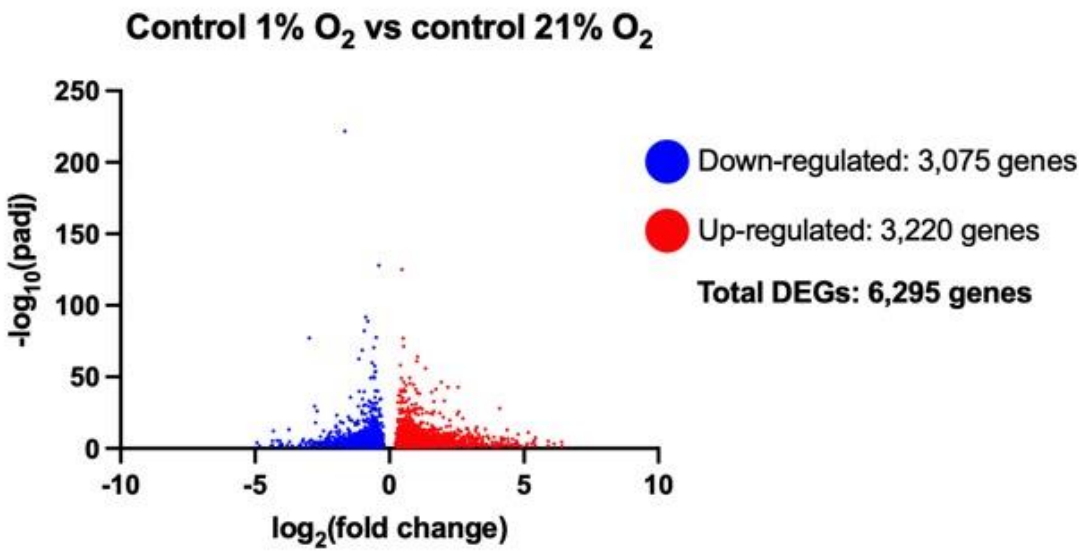

Figure 4.5 Hypoxia induces gene expression changes in the HCT116 cell line. HCT116 iCas9 cells treated with non-targeting gRNA control were exposed to normoxia or hypoxia for 48h and analysed by RNA-sequencing to identify DEGs. The distribution of DEGs in the control hypoxia vs control normoxia samples are shown using log2fold change and the -LOG_{10} of the adjusted p-value. Genes upregulated in hypoxia are shown in red and genes downregulated in hypoxia are shown in blue. Significant gene expression: FDR < 0.05. n=3.

Table 4.1 shows the top 30 most significantly upregulated DEGs in hypoxia compared to normoxia sorted by log2FoldChange (log2FC). There were a large number of long non-coding RNAs, antisense RNAs and pseudogenes within the top 30. A couple of known HIF-1α target genes also featured in the top 30, including CA9 and ANGPTL4. Table 4.2 summarises these genes along with other selected HIF-1α target genes including *LDHA, VEGFA* and *GLUT1 (SLC2A1)*. Several AP-1 subunit genes were also identified as significantly upregulated. Interestingly, HIF-2α was also upregulated in hypoxia (log2FC = 0.89) as was the HIF-1α antisense RNA-2 (HIF1A-AS2, log2FC = 2.7), but not HIF-1α itself. These results confirmed the induction of the established hypoxic response within the control hypoxia sample as well as provided evidence for the role of hypoxia in regulating cellular metabolism.

KEGG pathway analysis was used to identify which pathways containing upregulated DEGs were significantly enriched in hypoxia compared to normoxia. A total of 66 pathways were significantly enriched for genes upregulated in hypoxia. The top 20 most enriched pathways are shown in figure 4.6 measured by their enrichment ratio (ER), which represents the ratio of the observed number of genes to the expected number of genes for that pathway. As expected, 'HIF-1α signalling' was one of the most enriched pathways (ER = 2.5949) and contained many genes associated with glycolysis as well as growth factor signalling. Several other metabolic pathways, highlighted in figure 4.6, were also enriched including 'galactose metabolism' (ER = 2.2623) and 'AMPK signalling' (ER = 1.9871). Outside of the top 20, 'carbon metabolism' was also significantly enriched with an ER of 1.6324.

Gene name	log2FoldChange	padj
RPL7P19	6.4	1.37E-05
AC025259.3	6.4	1.12E-13
AC073410.1	6.1	0.00083289
CCL20	5.9	0.00044895
TRPC5OS	5.9	0.0005029
SSTR3	5.4	0.00383132
AC107021.2	5.4	0.00061143
AC147651.4	5.4	0.00432074
CXCL8	5.4	2.56E-14
AC100791.1	5.3	0.00329388
POU5F1P3	5.2	0.00167212
CIB4	5.1	0.00265533
HCG4B	5.1	3.11E-08
ANGPTL4	4.9	7.67E-129
HLA-V	4.9	5.12E-38
KRT7-AS	4.8	0.01110812
BX539320.1	4.8	0.00863411
CYP4X1	4.8	**0.01142186**
RF00012	4.7	0.01309413
GAPDHP69	4.7	0.00829965
PTPRN	4.7	5.16E-12
CCDC158	4.6	0.01789543
AP002380.1	4.5	0.00082417
KRT34	4.5	0.03172694
PPP1R16B	4.5	0.01482797
AC004448.2	4.4	0.01062711
CA9	4.4	**1.34E-07**
AL137013.1	4.4	7.61E-07
LUCAT1	4.4	2.00E-40
AC103923.1	4.3	0.03812798

Table 4.1 Top 30 differentially expressed upregulated genes in hypoxia compared to normoxia. The top 30 upregulated hypoxia-associated genes sorted by log2FoldChange are displayed along with adjusted p-values. Metabolism-associated genes are highlighted in red. Significant gene expression: padj < 0.05. n=3.

Gene name	log2FoldChange	padj
ANGPTL4	4.9	7.675E-129
CA9	4.4	1.3357E-07
FOSB	4.1	3.4662E-71
ENO2	3.6	5.3714E-83
SLC2A1	2.2	7.2224E-34
VEGFA	1.8	1.0055E-11
LDHA	2.0	4.9737E-42
PFKFB4	3.1	1.389E-222
HK2	3.1	1.8985E-40
BNIP3	2.8	6.937E-126
JUN	2.1	5.5024E-42

Table 4.2 Differentially expressed upregulated hypoxia-regulated genes in hypoxia compared to normoxia. A selection of known hypoxia-regulated genes sorted by log2FoldChange are displayed along with adjusted p-values. Significant gene expression: padj < 0.05. n=3.

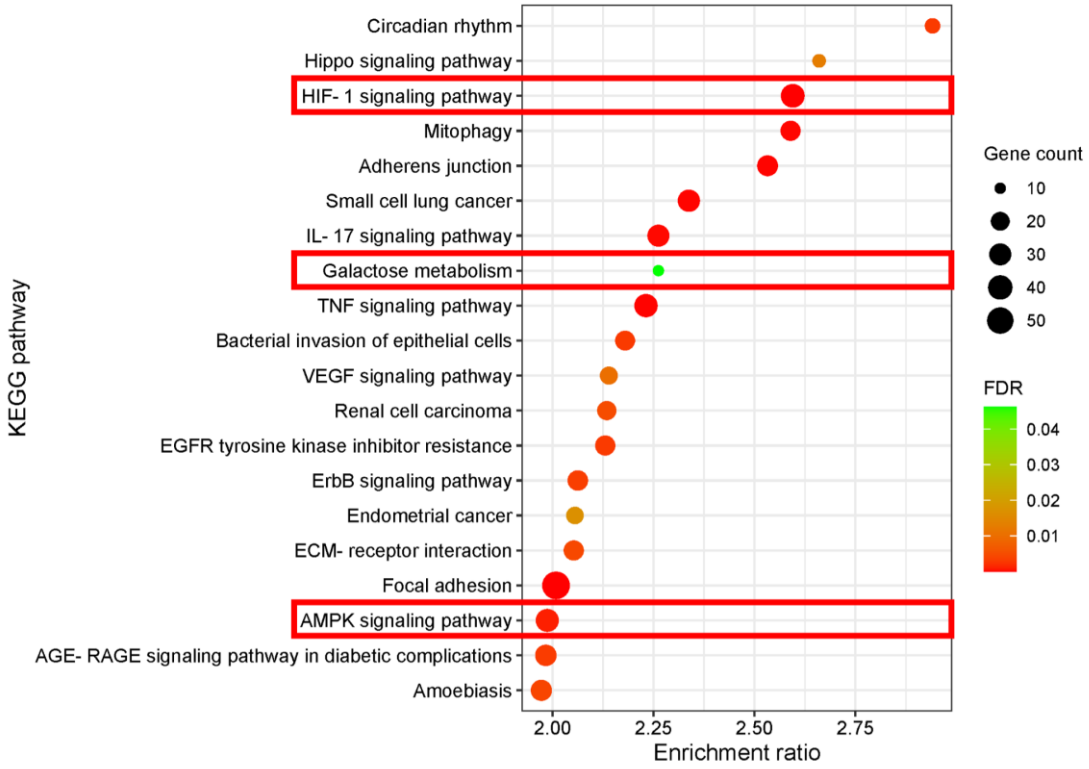

Figure 4.6 Top 20 significantly enriched KEGG pathways for significantly upregulated genes in hypoxia. KEGG pathway analysis of significantly upregulated genes in control hypoxia vs control normoxia samples. Significant KEGG pathways were plotted on the y-axis against their enrichment ratio on the x-axis. The bubble size represents the gene count whilst the colour represents the significance level measured by FDR. The red boxes indicate pathways associated with metabolism. Significant pathways: FDR < 0.05. n=3.

In order to further confirm that the control hypoxia results displayed the expected hypoxic response, the 3,075 differentially expressed downregulated genes were also analysed in more detail to identify the genes and pathways negatively regulated by hypoxia. Table 4.3 shows the top 30 most significantly downregulated DEGs in hypoxia compared to normoxia sorted by log2FC. Similarly to the upregulated genes, there were a large number of long non-coding RNAs and pseudogenes within the top 30. Interestingly, HIF-1α was also found to be downregulated (log2FC = -0.49).

KEGG pathway analysis was used to identify which pathways containing downregulated DEGs were significantly enriched in hypoxia compared to normoxia. A total of 27 pathways were significantly enriched for genes downregulated in hypoxia. The top 20 most enriched pathways are shown in figure 4.7. As expected, many pathways associated with DNA repair and the cell cycle including 'DNA replication' (ER = 5.3731), 'mismatch repair' (ER = 4.6120), 'homologous recombination' (ER = 3.5004) and 'base excision repair' (ER = 3.4035) were enriched for downregulated genes in hypoxia. Furthermore, several metabolic pathways were also enriched including 'one carbon pool by folate' (ER = 3.4319), 'folate biosynthesis' (ER = 2.8799), 'pyrimidine metabolism' (ER = 2.5330), 'fatty acid elongation' (ER = 2.4959), 'pyruvate metabolism' (ER = 2.3999) and 'valine, leucine and isoleucine degradation' (ER = 2.2099). These results further validated the induction of the expected hypoxic response in the hypoxic control samples and provided additional evidence supporting the role of hypoxia in regulating a wide range of metabolic pathways.

Gene name	log2FoldChange	padj
LAMA1	-4.9	0.00185112
HPGD	-4.8	0.04272767
AC131025.1	-4.4	0.03443198
LONRF2	-4.3	5.83E-08
HSPA8P1	-4.3	0.00965452
AC007389.4	-4.3	0.03573444
STAT5A	-4.2	0.03368468
AL117328.1	-4.1	0.01991775
AL021391.1	-4.1	0.0133308
ACP5	-4.1	0.02661939
SNORD12C	-4.0	0.03751325
RN7SL403P	-4.0	0.03075353
AC091152.4	-3.8	0.00835335
AC024884.2	-3.7	0.04209075
CU634019.6	-3.7	0.00015128
LINC00412	-3.6	0.04093048
CCIN	-3.4	0.01238817
Z83851.1	-3.3	7.48E-06
SLC1A4	**-3.3**	**1.64E-43**
RIMBP3	-3.2	0.00664297
NDUFB2-AS1	-3.2	0.03282728
EEF1E1P1	-3.1	0.03506481
FZD8	-3.1	0.00555983
AC093901.1	-3.1	0.01127995
AC019069.1	-3.0	6.01E-09
HLA-DPB1	-3.0	0.02690488
AL590705.5	-2.9	0.00673275
AC010615.1	-2.9	3.96E-05
OVOL2	-2.9	5.37E-06
CCDC96	-2.9	0.00808037

Table 4.3 Top 30 differentially expressed downregulated genes in hypoxia compared to normoxia. The top 30 downregulated hypoxia-associated genes sorted by log2FoldChange are displayed along with adjusted p-values. Metabolism-associated genes are highlighted in red. Significant gene expression: padj < 0.0.5. n=3.

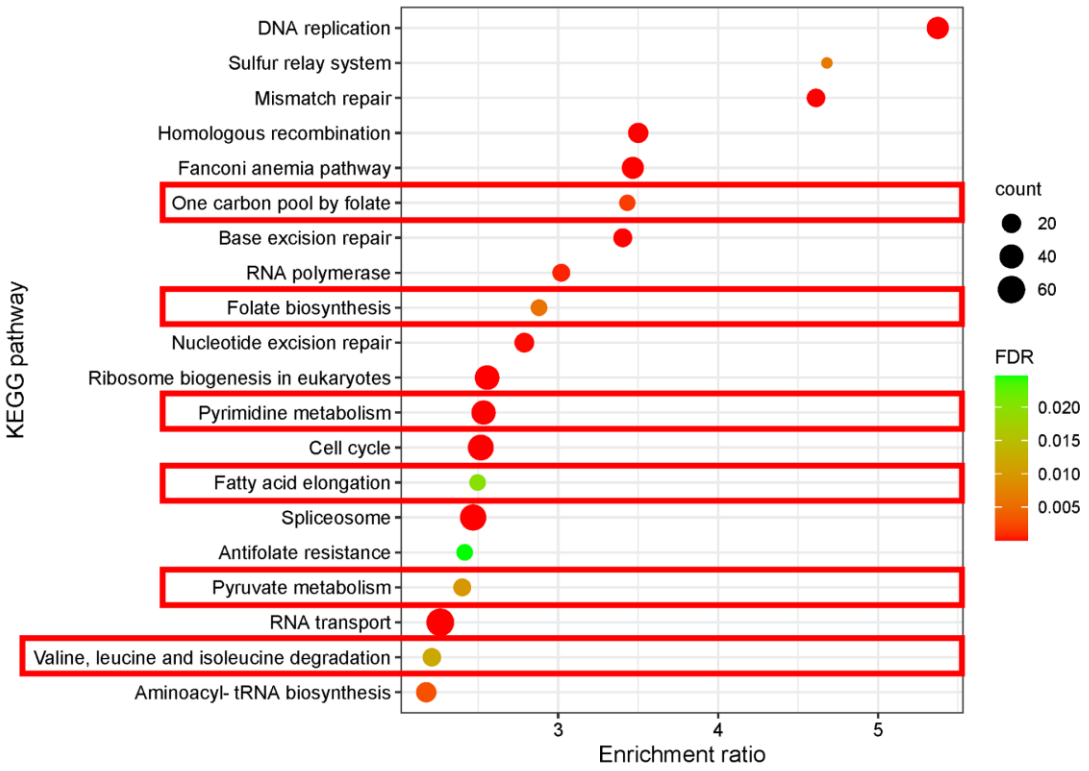

Figure 4.7 Top 20 significantly enriched KEGG pathways for significantly downregulated genes in hypoxia. KEGG pathway analysis of significantly downregulated genes in control hypoxia vs control normoxia samples. Significant KEGG pathways were plotted on the y-axis against their enrichment ratio on the x-axis. The bubble size represents the gene count whilst the colour represents the significance level measured by FDR. The red boxes indicate pathways associated with metabolism. Significant pathways: FDR < 0.05. n=3.

4.3.6 Metabolic adaptation to hypoxia in colorectal cancer

In order to investigate the role of hypoxia in the regulation and reprogramming of cellular metabolism in CRC, the RNA sequencing data was filtered to focus on the complete list of known human metabolic genes comprising 2,752 genes[549]. Overall, 772 metabolic genes, representing 28% of all metabolic genes, were significantly differentially expressed between hypoxia and normoxia with 346 genes upregulated and 426 genes downregulated under hypoxic conditions compared to normoxia. (figure 4.8).

Table 4.4 shows the top 30 most significantly upregulated metabolic DEGs in hypoxia compared to normoxia sorted by log2FC. A large number of HIF-regulated glycolytic enzymes were some of the most upregulated genes including *ENO2* (log2FC = 3.6), *PFKFB4* (log2FC = 3.1) and *HK2* (log2FC = 3.1) along with several glucose transporters and fatty acid metabolism enzymes. KEGG pathway analysis was used to identify which metabolic pathways the significantly upregulated metabolic DEGs belonged to. Importantly, this analysis was not used to infer which pathways were most significantly enriched as the inputs had already been enriched for metabolic genes. A total of 40 pathways were identified associated with the upregulated metabolic DEGs in hypoxia and 20 of those pathways are shown in figure 4.9. The majority of the pathways identified encompassed those associated with central carbon and carbohydrate metabolism but also included amino acid and steroid biosynthetic pathways.

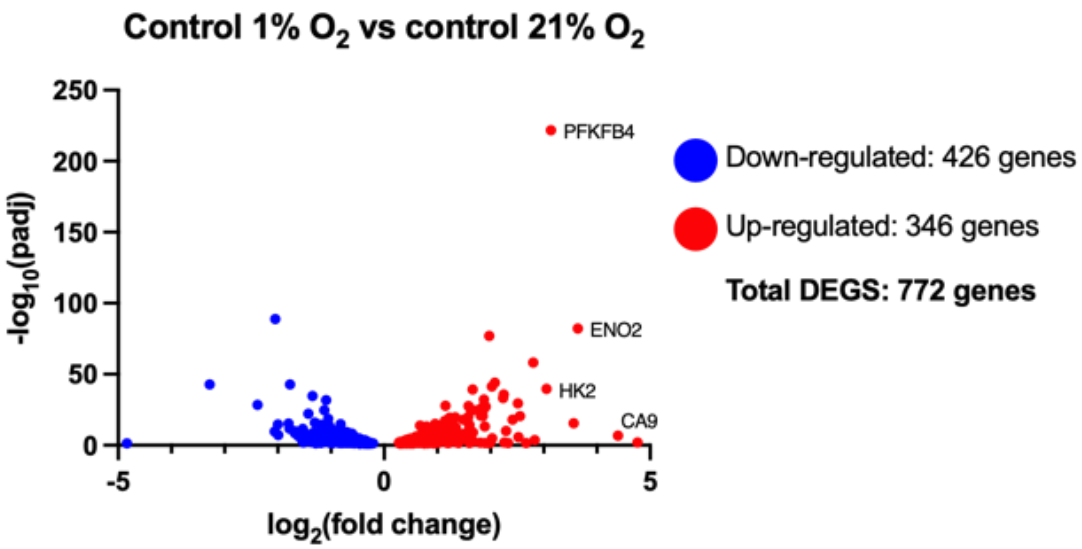

Figure 4.8 Hypoxia induces changes in metabolic gene expression in the HCT116 cell line. HCT116 iCas9 cells treated with non-targeting gRNA control were exposed to normoxia or hypoxia for 48h and analysed by RNA-sequencing to identify metabolic DEGs. The distribution of metabolic DEGs in the control hypoxia vs control normoxia samples are shown using log2fold change and the -LOG$_{10}$ of the adjusted p-value. Genes upregulated in hypoxia are shown in red and genes downregulated in hypoxia are shown in blue. Significant gene expression: FDR < 0.05. n=3.

Gene name	log2FoldChange	padj
CYP4X1	4.8	0.01142186
CA9	**4.4**	**1.3357E-07**
ENO2	**3.6**	**5.3714E-83**
SLC2A3	**3.6**	**2.6501E-16**
PFKFB4	**3.1**	**1.389E-222**
HK2	3.1	**1.8985E-40**
SLC5A10	2.8	0.00022145
FUT11	2.8	6.3915E-59
STRA6	2.7	0.03155466
ALDOC	**2.6**	**2.4566E-21**
SLCO1B3	2.5	1.8828E-06
AGPAT4	2.5	3.9528E-30
GPI	2.4	1.1155E-18
KCNMA1	2.3	0.02861302
ABCB6	2.3	9.2962E-11
NOS2	2.3	0.01004126
ALDOA	**2.2**	**1.9639E-36**
SLC2A1	**2.2**	**7.2224E-34**
GBE1	2.1	9.995E-45
KCNK3	2.0	1.2044E-05
LDHA	**2.0**	**4.9737E-42**
KCNJ1	2.0	0.01447875
NMNAT2	2.0	0.03559945
PGK1	2.0	1.1899E-77
LPIN1	1.9	5.8994E-28
KCNJ9	1.9	0.03463415
FA2H	1.9	5.5607E-14
GAPDH	**1.9**	**5.4656E-33**
AMPD3	1.9	3.1694E-25
DPYSL4	1.9	7.7946E-28

Table 4.4 Top 30 differentially expressed upregulated metabolic genes in hypoxia compared to normoxia. The top 30 upregulated metabolic genes sorted by log2FoldChange are displayed along with adjusted p-values. Selected HIF-regulated genes are highlighted in red. Significant gene expression: padj< 0.05. n=3.

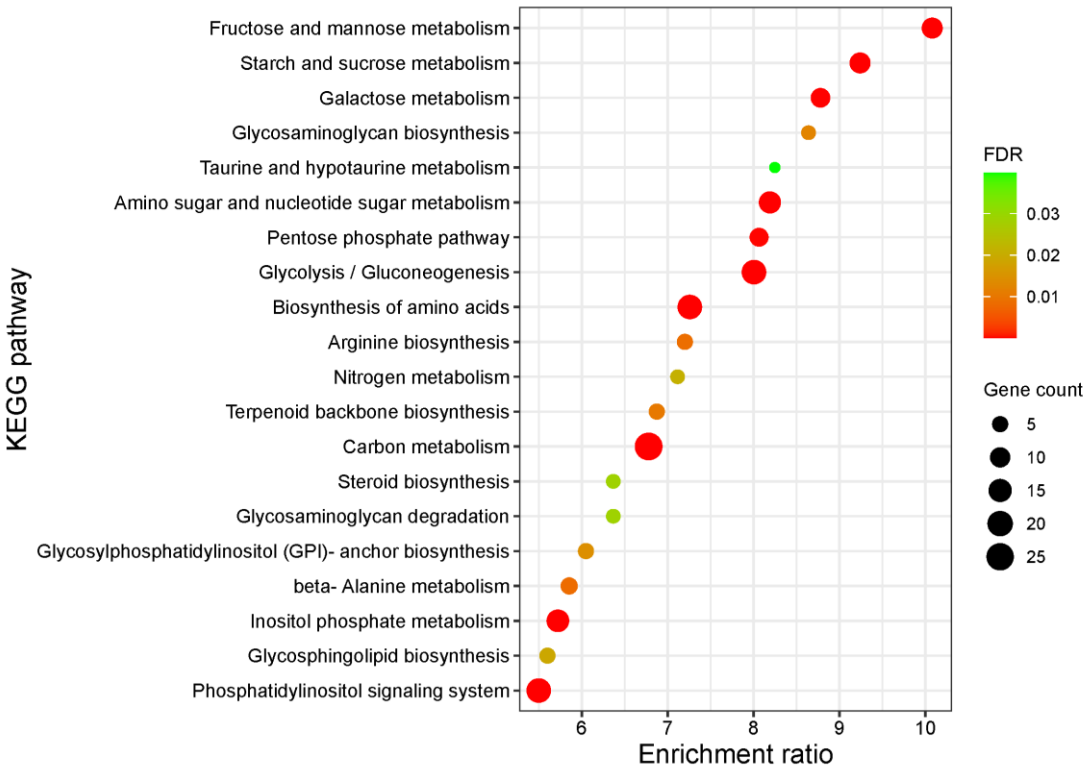

Figure 4.9 KEGG pathway classification for significantly upregulated metabolic genes in hypoxia. KEGG pathway analysis of significantly upregulated metabolc genes in control hypoxia vs control normoxia samples. Significant KEGG pathways were plotted on the y-axis against their enrichment ratio on the x-axis. The bubble size represents the gene count whilst the colour represents the significance level measured by FDR. Significant pathways: FDR < 0.05. n=3.

On the other hand, table 4.5 shows the top 30 most significantly downregulated metabolic DEGs in hypoxia compared to normoxia sorted by log2FC. This included several amino acid and small molecule transporters such as *SLC1A4* (-3.3) and *SLC6A9* (-2.4), members of the cytochrome P450 enzyme family such as *CYB5RL* (-2.1) and *CYP24A1* (-2.0) and several enzymes involved in the serine synthesis pathway and one-carbon metabolism such as *PHGDH* (-1.8) and *DHFR* (-1.5). KEGG pathway analysis identified a total of 46 pathways associated with the downregulated metabolic DEGs in hypoxia and 20 of those pathways are shown in figure 4.10. The majority of the pathways identified were associated with amino acid biosynthesis, folate metabolism and those associated with oxidative phosphorylation including 'pyruvate metabolism' and 'citrate cycle (TCA cycle)'.

Gene name	log2FoldChange	padj
HPGD	-4.8	0.04272767
SLC1A4	-3.3	1.6391E-43
SLC6A9	-2.4	3.8364E-29
CYB5RL	-2.1	1.98E-10
PCK2	-2.0	1.6435E-89
CYP24A1	-2.0	1.8331E-15
GGT5	-2.0	5.6999E-08
ASNS	-1.8	4.9988E-16
SLC25A10	-1.8	1.4608E-12
PHGDH	-1.8	1.2873E-43
DGAT2	-1.7	2.2918E-09
MANEAL	-1.7	7.0962E-10
SFXN2	-1.7	1.5488E-10
SLC43A2	-1.6	1.0039E-08
ASRGL1	-1.6	8.7419E-09
CHRNA5	-1.6	2.3991E-07
KHK	-1.6	3.1809E-07
SLC7A11	-1.5	9.7848E-10
DPYSL5	-1.5	4.5089E-09
KCNK13	-1.5	0.0013195
GBA	-1.5	2.4291E-12
B3GAT1	-1.5	0.01191716
DHFR	-1.5	0.00529388
FOXRED2	-1.5	3.4804E-09
HCN4	-1.5	2.7248E-08
SLC7A5	-1.4	5.4065E-23
NDUFA4L2	-1.4	0.00043957
GLRX2	-1.4	1.8284E-07
SLC43A3	-1.4	1.2022E-07
SLC38A6	-1.4	0.00651766

Table 4.5 Top 30 differentially expressed downregulated metabolic genes in hypoxia compared to normoxia. The top 30 downregulated metabolic genes sorted by log2FoldChange are displayed along with adjusted p-values. Significant gene expression: padj < 0.05. n=3.

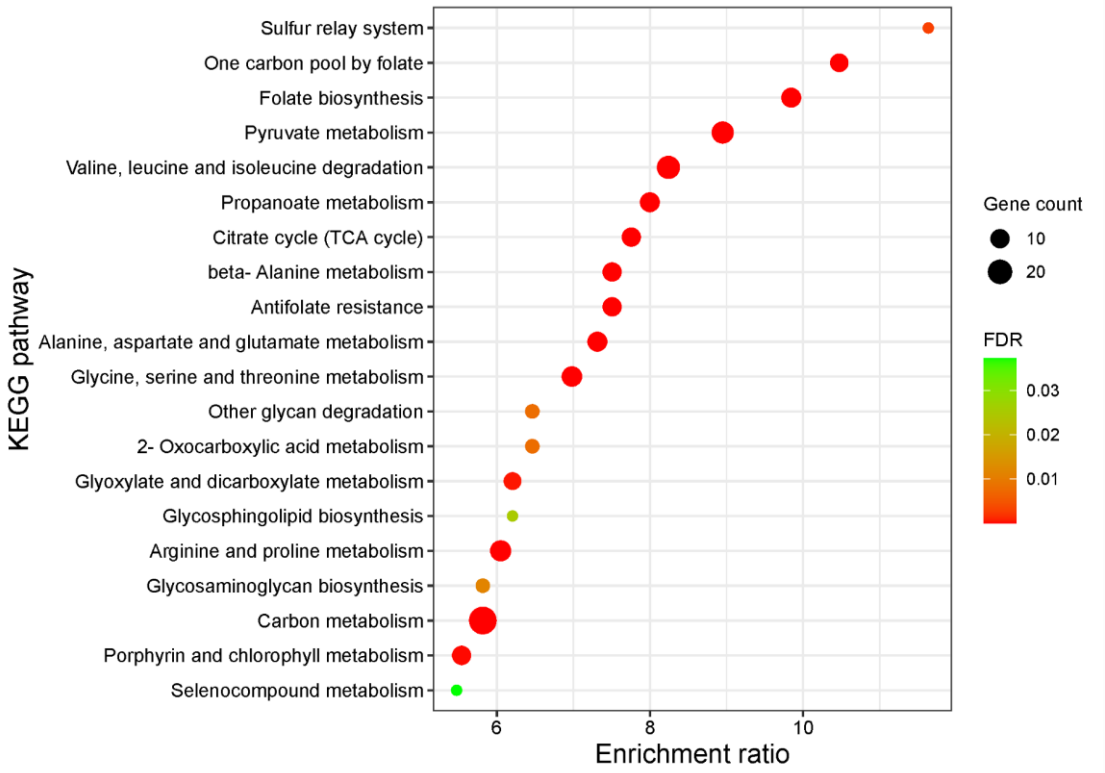

Figure 4.10 KEGG pathway classification for significantly downregulated metabolic genes in hypoxia. KEGG pathway analysis of significantly downregulated metabolic genes in control hypoxia vs control normoxia samples. Significant KEGG pathways were plotted on the y-axis against their enrichment ratio on the x-axis. The bubble size represents the gene count whilst the colour represents the significance level measured by FDR. Significant pathways: FDR < 0.05. n=3.

4.3.7 The role of HIF-1α and HIF-2α-dependent regulation of the hypoxic response

In order to investigate the HIF-1α and HIF-2α-dependent regulation of the transcriptional response to hypoxia the HIF-1α and HIF-2α knockout conditions were compared to the hypoxic control condition. Overall, 3,814 genes were significantly differentially expressed between the HIF-1α knockout and control hypoxia conditions with 1,957 genes upregulated and 1,875 genes downregulated in the HIF-1α knockout compared to the control (figure 4.11). Similarly, 4,346 genes were significantly differentially expressed between the HIF-2α knockout and control hypoxia conditions with 2,188 genes upregulated and 2,158 genes downregulated in the HIF-2α knockout compared to the control (figure 4.12). Approximately 15,000 genes were not significantly differentially expressed between either of the HIF knockout conditions and the control after filtering the data by adjusted p-value (padj) < 0.05.

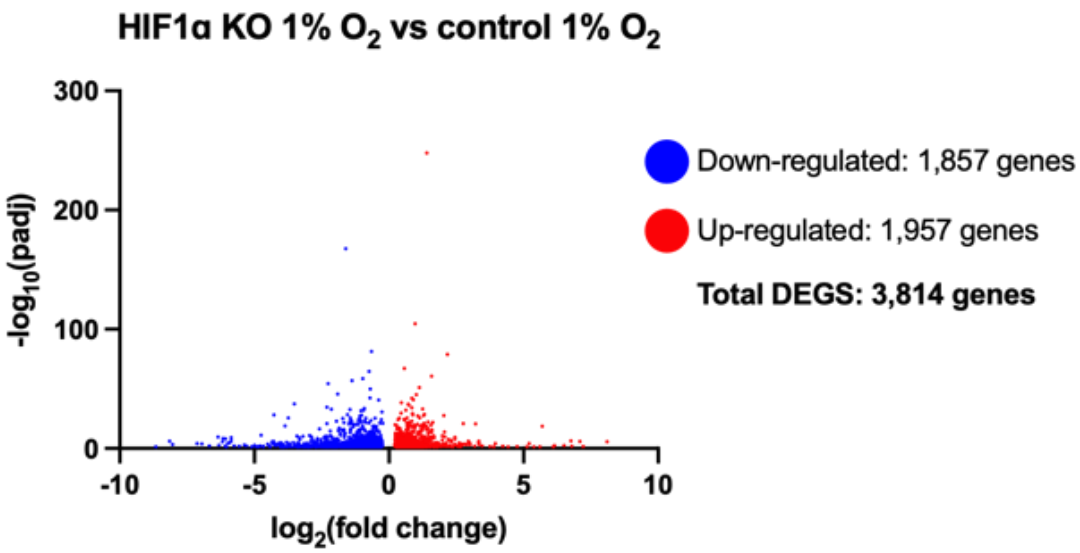

Figure 4.11 HIF-1α knockout induces changes in gene expression in the HCT116 cell line. HCT116 iCas9 cells treated with either non-targeting gRNA control or HIF-1α-targeting gRNA control were exposed to hypoxia for 48h and analysed by RNA-sequencing to identify DEGs. The distribution of DEGs in the HIF-1α knockout vs control samples are shown using log2fold change and the -LOG$_{10}$ of the adjusted p-value. Genes upregulated with HIF-1α knockout are shown in red and genes downregulated with HIF-1α knockout are shown in blue. Significant gene expression: FDR < 0.05. n=3.

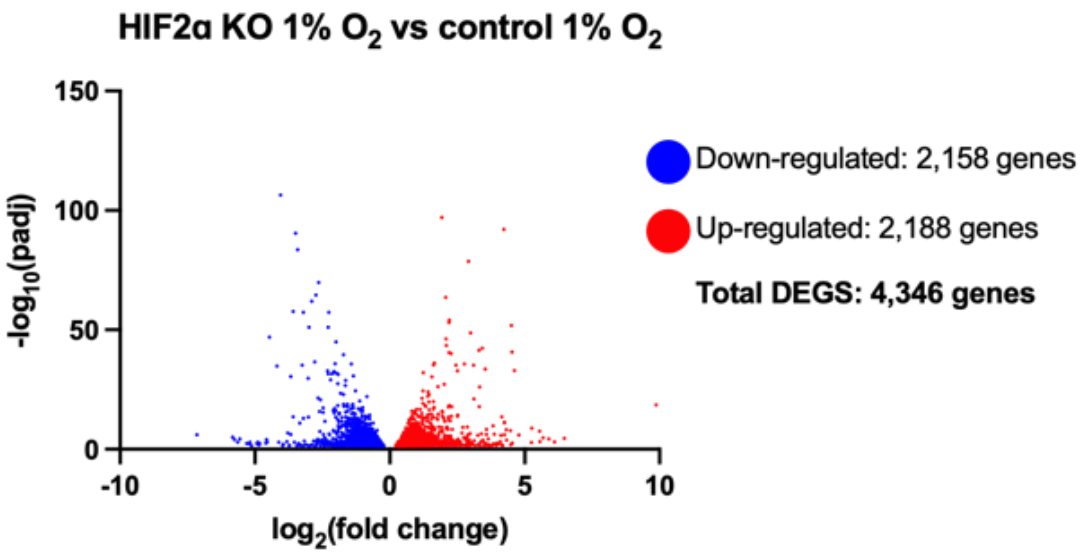

Figure 4.12 HIF-2α knockout induces changes in gene expression in the HCT116 cell line. HCT116 iCas9 cells treated with either non-targeting gRNA control or HIF-2α-targeting gRNA control were exposed to hypoxia for 48h and analysed by RNA-sequencing to identify DEGs. The distribution of DEGs in the HIF-2α knockout vs control samples are shown using log2fold change and the -LOG$_{10}$ of the adjusted p-value. Genes upregulated with HIF-2α knockout are shown in red and genes downregulated with HIF-2α knockout are shown in blue. Significant gene expression: FDR < 0.05. n=3.

In order to identify HIF-1α or HIF-2α-dependent gene expression changes, DEGs that were significantly upregulated in hypoxia but significantly downregulated with loss of either HIF-1α or HIF-2α in hypoxia were identified (figure 4.13). 988 genes were identified that were upregulated in hypoxia but downregulated with HIF-1α knockout. 869 genes were downregulated with HIF-1α knockout but were not upregulated in hypoxia. 1,133 genes were identified that were upregulated in hypoxia but downregulated with HIF-2α knockout. 1,025 genes were downregulated with HIF-2α knockout but were not upregulated in hypoxia. Interestingly, 134 out of the 1,957 upregulated genes in the HIF-1α knockout were also upregulated in the hypoxic control. Similarly, 143 out of the 2,188 upregulated genes in the HIF-2α knockout were also upregulated in the hypoxic control.

However, in order to focus on genes that were only influenced by loss of either HIF-1α or HIF-2α, but not both, any overlapping downregulated genes between the HIF-1α and HIF-2α knockout conditions were excluded prior to further analysis (figure 4.14). 545 out of the 988 genes that were upregulated in hypoxia and downregulated with HIF-1α knockout, were independent of HIF-2α status. Another 654 genes were downregulated with HIF-1α knockout, but not upregulated in hypoxia, independently of HIF-2α status. A total of 1,199 HIF-1α-associated genes were thus identified and selected for downstream analysis (figure 4.14). 690 out of the 1,133 genes that were upregulated in hypoxia and downregulated with HIF-2α knockout, were independent of HIF-1α status. Another 810 genes were downregulated with HIF-2α knockout, but not upregulated in hypoxia, independently of HIF-1α status. A total of 1,500 HIF-2α-associated genes were thus identified and selected for downstream analysis (figure 4.14). 658 genes were downregulated in both the HIF-1α and HIF-2α knockout conditions, 443 of which were upregulated in hypoxia and 215 which were independent of hypoxia. These genes were excluded from any downstream analysis.

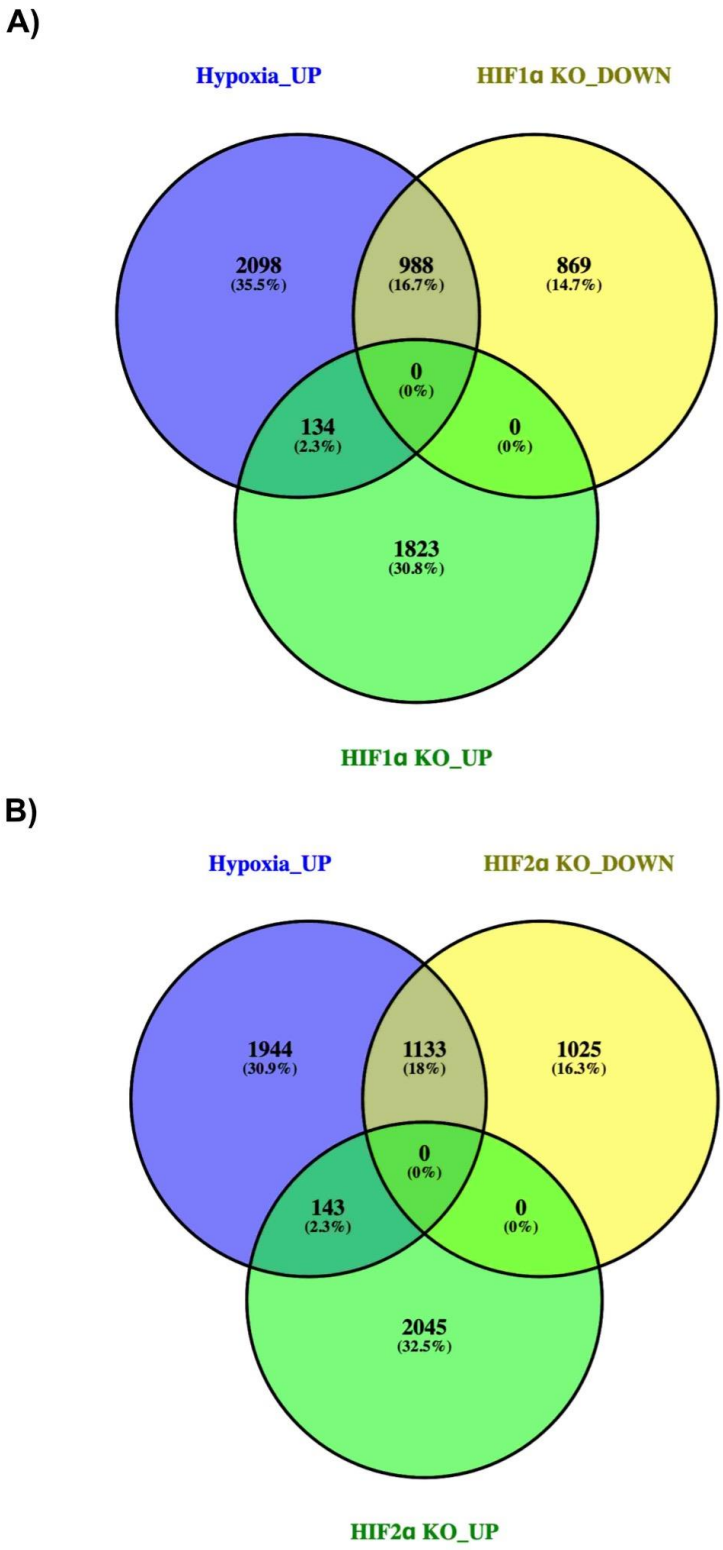

Figure 4.13 Hypoxia induces HIF-dependent changes in gene expression. Venn diagram of overlapping DEGs that were upregulated in hypoxia and differentially expressed in the **A)** HIF-1α and **B)** HIF-2α knockout conditions. The sum of the numbers in each circle represents the total DEG list for that condition. n=3.

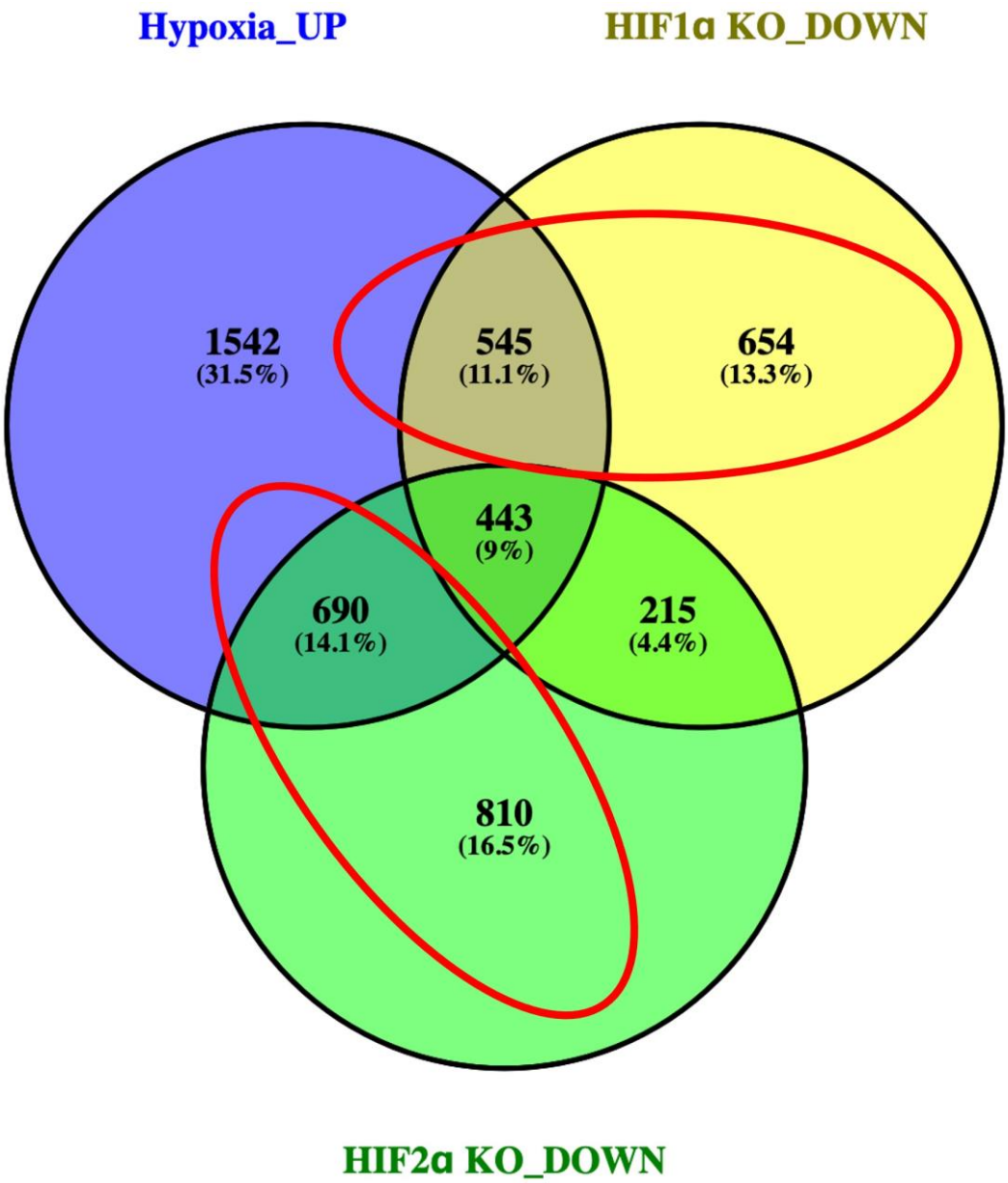

Figure 4.14 Hypoxia induces HIF-1α specific and HIF-2α specific changes in gene expression. Venn diagram of overlapping DEGs that were upregulated in hypoxia and downregulated in either the HIF-1α or HIF-2α knockout conditions. The sum of the numbers in each circle represents the total DEG list for that condition. The red circles highlight those genes identified as either HIF-1α or HIF-2α specific. n=3.

Table 4.6 shows the top 30 most significantly downregulated DEGs out of the 1,199 genes identified as HIF-1α-dependent sorted by log2FC. There were a few long non-coding RNAs and antisense RNAs within the top 30 as well as genes involved in the inflammatory response and apoptosis. Several known HIF-1α target genes also featured in the top 30, including *CA9*. Table 4.7 summarises a selection of HIF-1α target genes including *BNIP3*, *LDHA* and *VEGFA*, and confirms the downregulation of these genes in response to HIF-1α knockout. HIF-1α gene expression was also downregulated in the HIF-1α knockout condition (log2FC = -1.6). These results confirmed the expected reduction in HIF-1α target gene expression in the HIF-1α knockout condition.

KEGG pathway analysis identified a total of 10 pathways that were significantly enriched for HIF-1α-dependent genes (figure 4.15). 7 out of the 10 enriched pathways were metabolic pathways and included 'fructose and mannose metabolism' (ER = 4.6073), 'biosynthesis of amino acids' (ER = 3.9463), 'arginine and proline metabolism' (ER = 3.4209), 'glycolysis/gluconeogenesis' (ER = 3.3538), 'central carbon metabolism in cancer' (ER = 3.2162) and 'carbon metabolism' (ER = 2.6214). The 'HIF-1 signalling pathway' was also significantly enriched as expected based on the impact of HIF-1α knockout on these genes.

Gene name	log2FoldChange	padj
ZNF502	-8.2	1.3711E-09
ARHGEF25	-8.0	1.0862E-09
LRP1B	-7.1	5.7441E-07
LINC00992	-6.9	5.6369E-07
DIRC3	-6.7	1.2368E-08
CASP4	-6.4	6.4763E-08
CA8	**-6.2**	**1.258E-05**
AC025165.1	-6.2	4.0638E-05
AC093752.2	-6.0	0.00016007
TNFSF18	-5.9	3.3249E-05
AC008549.1	-5.9	0.0003692
DCLK1	-5.9	1.0642E-06
CARD11	-5.6	0.00071288
TSPAN2	-5.4	5.336E-08
NRG1	-5.3	0.00074715
KCNJ4	-5.1	0.0015908
STC1	-5.0	0.00560601
AL359273.1	-5.0	0.0040936
PTGDS	-4.9	0.00207338
AL121899.1	-4.8	0.00262064
RF00432	-4.8	0.00960807
PTPRN	-4.7	1.3182E-09
OSR1	-4.7	1.6896E-23
RP11-382A18.2	-4.7	0.00594696
SCN3A	-4.5	0.01501941
RAB19	-4.4	0.00903939
C1GALT1C1L	-4.4	0.00872609
P4HA3	**-4.3**	**7.2162E-05**
CARMN	-4.3	0.02199281
CA9	**-4.3**	**2.4808E-06**

Table 4.6 Top 30 differentially expressed downregulated HIF-1α-dependent genes in HIF-1α knockout compared to the control in hypoxia. The top 30 downregulated HIF-1α-dependent genes sorted by log2FoldChange are displayed along with adjusted p-values. Genes of interest including metabolic genes are highlighted. Significant gene expression: padj< 0.05. n=3.

Gene name	log2FoldChange	padj
CA9	-4.3	2.4808E-06
PFKFB4	-3.4	1.747E-248
BNIP3	-3.3	2.133E-168
ENO2	-3.0	1.3652E-57
HK2	-2.2	1.4744E-20
LDHA	-1.2	2.2141E-14
ANGPTL4	-1.2	0.00010243
VEGFA	-0.9	0.00576813
FOSB	-0.8	0.04660135

Table 4.7 Differentially expressed downregulated HIF-1α-regulated genes in HIF-1α knockout compared to control in hypoxia. A selection of known HIF-1α-regulated genes sorted by log2FoldChange are displayed along with adjusted p-values. Significant gene expression: padj < 0.05. n=3.

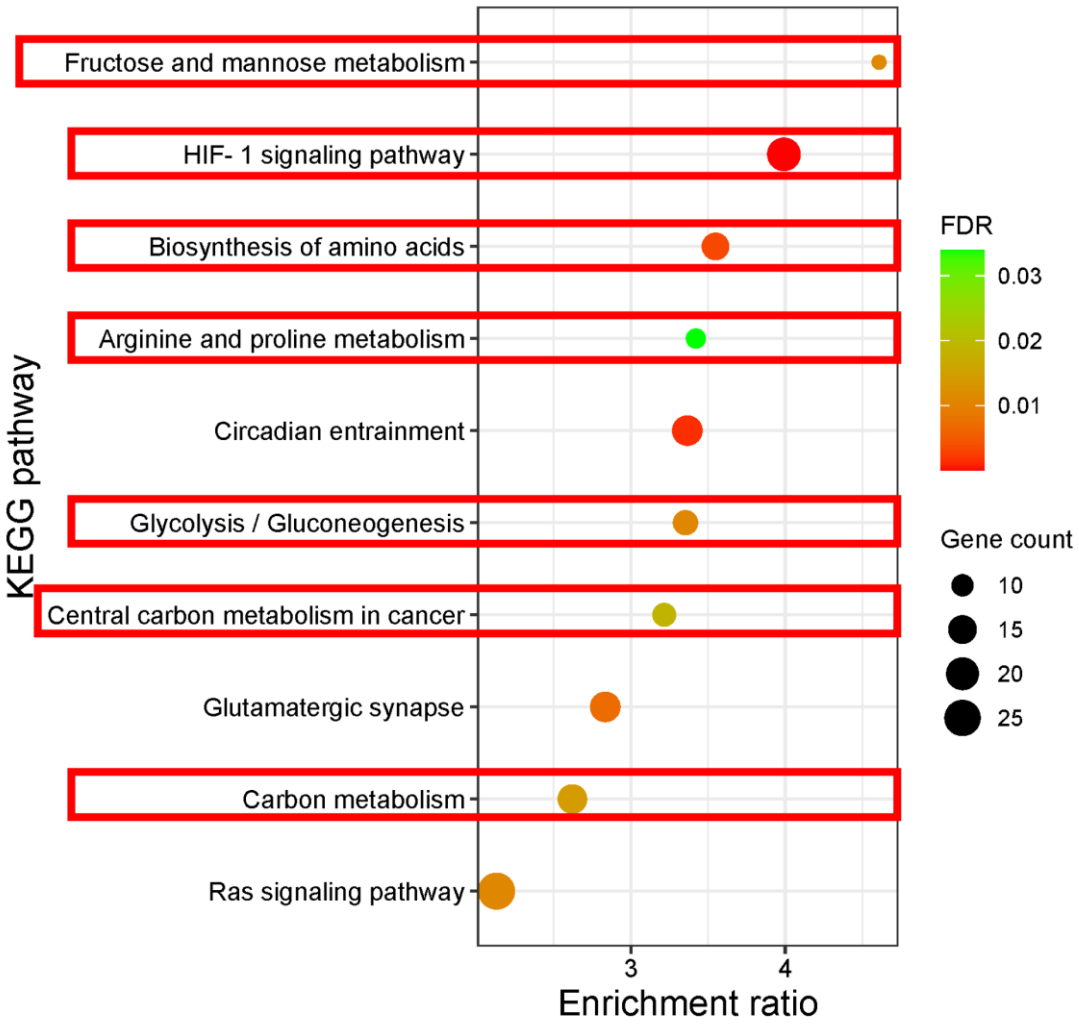

Figure 4.15 Significantly enriched KEGG pathways for downregulated HIF-1α-dependent genes. KEGG pathway analysis of significantly downregulated genes in HIF-1α knockout vs control samples in hypoxia. Significant KEGG pathways were plotted on the y-axis against their enrichment ratio on the x-axis. The bubble size represents the gene count whilst the colour represents the significance level measured by FDR. The red boxes indicate pathways associated with metabolism. Significant pathways: FDR < 0.05. n=3.

Table 4.8 shows the top 30 most significantly downregulated DEGs out of the 1,500 genes identified as HIF-2α-dependent sorted by log2FC. There were several genes associated with membrane transporters and growth factor signalling along with metabolic genes such as *GALNT13* (log2FC = -4.6) and *GRM8* (log2FC = -3.4). HIF-2α (*EPAS1)* was also identified in the top 30 most downregulated genes (log2FC = -3.4). Table 4.9 summarises a selection of HIF-2α target genes including *CXCL8*, *CXCL4, CXCR4* and *YAP1* and confirms the downregulation of these genes in response to HIF-2α knockout. These results confirmed the expected reduction in HIF-2α target gene expression in the HIF-2α knockout condition.

KEGG pathway analysis identified a total of 19 pathways that were significantly enriched for HIF-2α-dependent genes (figure 4.16). The top 3 most enriched pathways were metabolic pathways and included 'steroid biosynthesis' (ER = 6.1637), 'fatty acid biosynthesis' (ER = 5.0047) and 'terpenoid backbone biosynthesis' (ER = 4.7317). These results provided further evidence supporting a role for HIF_2α in regulating metabolic adaption to hypoxia.

Gene name	log2FoldChange	padj
PQLC2L	-7.1	7.6455E-07
AC068633.1	-5.8	8.4242E-05
RIMS4	-5.6	0.0010311
AC009716.1	-5.3	0.00396122
SNX18P9	-5.2	0.00561514
RF00019	-5.1	0.03928135
PDE4D	-4.9	0.00113257
CACNA2D1	-4.9	0.01226651
FXYD1	-4.8	0.01578748
MYRFL	-4.8	0.0032382
RPS15AP30	-4.6	0.00311153
GALNT13	**-4.6**	**8.7956E-05**
NOS1	-4.6	0.00125988
DSC3	-4.5	1.2854E-47
SATB1	-4.2	1.5173E-35
KCNJ9	-4.1	0.00102255
RNF43	-4.1	3.669E-107
RP11-541P9.3	-4.0	0.03331395
RFPL3S	-4.0	0.00857142
TRHDE	-3.8	1.4757E-07
FGF9	-3.7	0.03112124
GCM1	-3.7	0.02578106
LUCAT1	-3.7	4.0439E-31
CPEB2	-3.6	2.455E-14
HOXB4	-3.6	2.1003E-58
RHOT1P1	-3.4	0.03499817
EPAS1	**-3.4**	**2.9013E-84**
GRM8	**-3.4**	**0.02161555**
AC092798.1	-3.4	0.00379966
RUNX2	-3.3	1.0707E-11

Table 4.8 Top 30 differentially expressed downregulated HIF-2α-dependent genes in HIF-2α knockout compared to the control in hypoxia. The top 30 downregulated HIF-2α-dependent genes sorted by log2FoldChange are displayed along with adjusted p-values. Genes of interest including metabolic genes are highlighted. Significant gene expression: padj < 0.05. n=3.

Gene name	log2FoldChange	padj
CXCL8	-2.5	0.00093505
ZNF704	-2.0	1.1337E-45
PTCH1	-1.9	6.7305E-16
EPHA8	-1.8	0.02710269
CXCL1	-1.7	0.00837449
CXCR4	-1.5	7.686E-06
NKX6-1	-1.1	4.4286E-06
ANGPTL4	-1.1	1.7973E-06
SEMA4B	-1.0	6.6649E-08
YAP1	-0.8	4.0899E-11
VEGFA	-0.7	0.01438098

Table 4.9 Differentially expressed downregulated HIF-2α-regulated genes in HIF-2α knockout compared to control in hypoxia. A selection of known HIF-2α-regulated genes sorted by log2FoldChange are displayed along with adjusted p-values. Significant gene expression padj < 0.05. n=3.

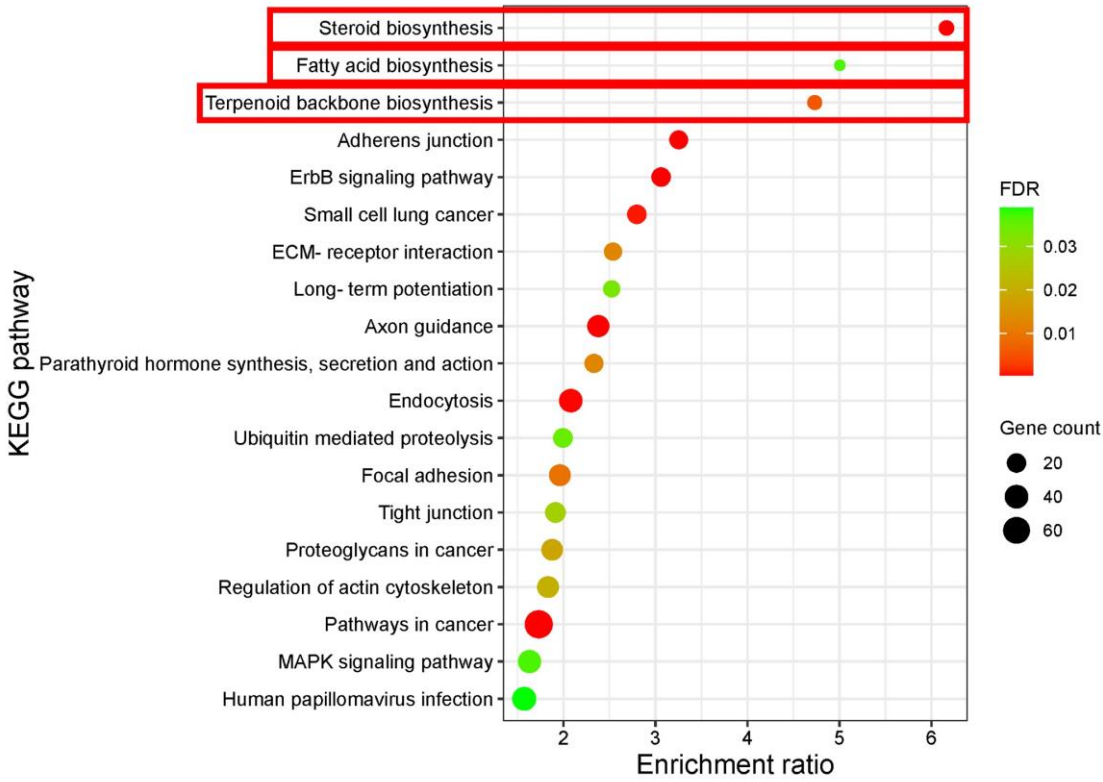

Figure 4.16 Significantly enriched KEGG pathways for downregulated HIF-2α-dependent genes in hypoxia. KEGG pathway analysis of significantly downregulated genes in HIF-2α vs control samples in hypoxia. Significant KEGG pathways were plotted on the y-axis against their enrichment ratio on the x-axis. The bubble size represents the gene count whilst the colour represents the significance level measured by FDR. The red boxes indicate pathways associated with metabolism. Significant pathways: FDR <0.05. n=3.

4.3.8 The role of HIF-1α and HIF-2α-dependent regulation of metabolic adaptation to hypoxia

In order to further analyse the specific roles of HIF-1α and HIF-2α in the regulation and reprogramming of cellular metabolism in CRC, the differential expression of the 2,752 metabolic genes between the HIF knockout and control hypoxia conditions was investigated. Overall, 510 metabolic genes, representing 18.5% of all metabolic genes, were significantly differentially expressed between the HIF-1α knockout and control hypoxia conditions with 256 genes upregulated and 254 genes downregulated in the HIF-1α knockout compared to the control (figure 4.17). Similarly, 533 metabolic genes were significantly differentially expressed between the HIF-2α knockout and control hypoxia conditions with 292 genes upregulated and 241 genes downregulated in the HIF-2α knockout compared to the control (figure 4.18).

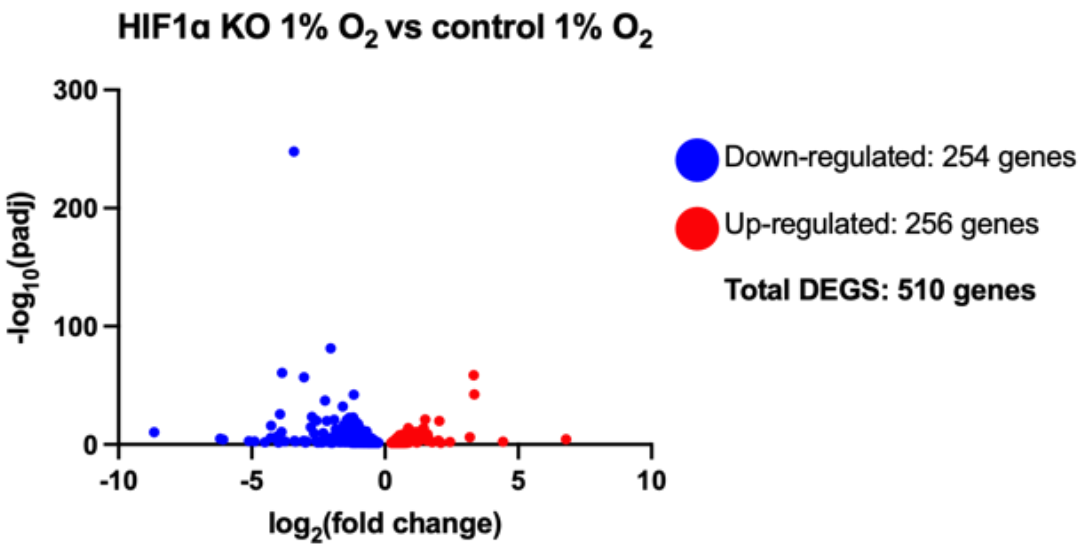

Figure 4.17 HIF-1α knockout induces changes in metabolic gene expression in the HCT116 cell line. HCT116 iCas9 cells treated with either non-targeting gRNA control or HIF-1α-targeting gRNA control were exposed to hypoxia for 48h and analysed by RNA-sequencing to identify metabolic DEGs. The distribution of metabolic DEGs in the HIF-1α knockout vs control samples are shown using log2fold change and the -LOG_{10} of the adjusted p-value. Genes upregulated with HIF-1α knockout are shown in red and genes downregulated with HIF-1α knockout are shown in blue. Significant gene expression: FDR < 0.05. n=3.

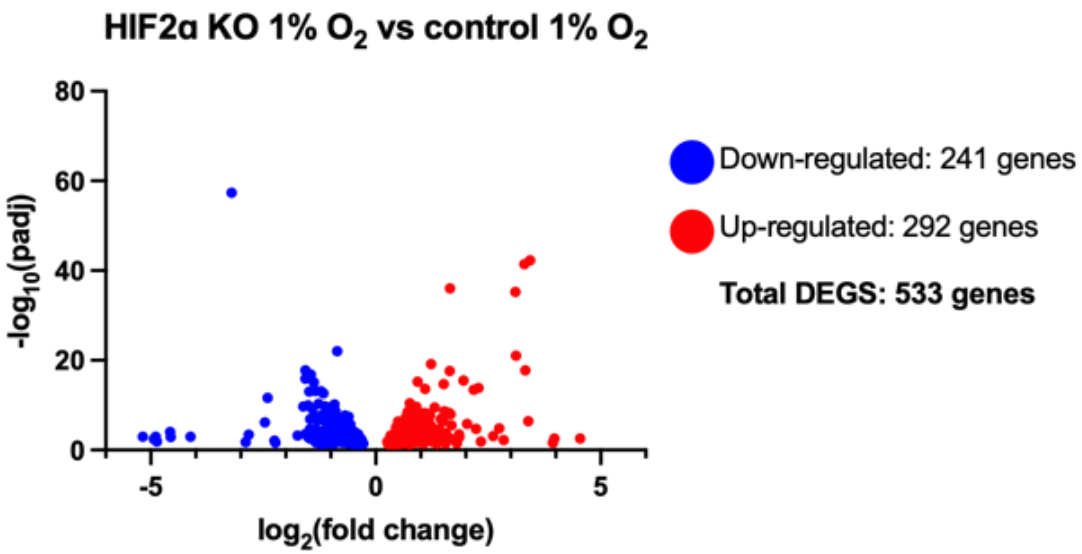

Figure 4.18 HIF-2α knockout induces changes in metabolic gene expression in the HCT116 cell line. HCT116 iCas9 cells treated with either non-targeting gRNA control or HIF-2α-targeting gRNA control were exposed to hypoxia for 48h and analysed by RNA-sequencing to identify metabolic DEGs. The distribution of metabolic DEGs in the HIF-2α knockout vs control samples are shown using log2fold change and the -LOG_{10} of the adjusted p-value. Genes upregulated with HIF-2α knockout are shown in red and genes downregulated with HIF-2α knockout are shown in blue. Significant gene expression: FDR < 0.05. n=3.

In order to identify HIF-1α or HIF-2α-dependent metabolic genes, any overlapping downregulated metabolic genes between the HIF-1α and HIF-2α knockout conditions were excluded prior to further analysis (figure 4.19). 83 out of the 254 metabolic genes that were downregulated with HIF-1α knockout but upregulated in the hypoxic control, were independent of HIF-2α status. Another 103 metabolic genes were downregulated following HIF-1α knockout, but not upregulated in hypoxia, independently of HIF-2α status. A total of 186 HIF-1α associated metabolic genes were thus identified and selected for downstream analysis (figure 4.19). 75 out of the 241 metabolic genes that were downregulated with HIF-2α knockout but upregulated in the hypoxic control, were independent of HIF-1α status. Another 98 metabolic genes were downregulated following HIF-2α knockout, but not upregulated in hypoxia, independently of HIF-1α status. A total of 173 HIF-2α associated metabolic genes were thus identified and selected for downstream analysis (figure 4.19). 68 genes were downregulated in both the HIF-1α and HIF-2α knockout conditions, 40 of which were upregulated in hypoxia and 28 which were independent of hypoxia. These genes were excluded from any downstream analysis.

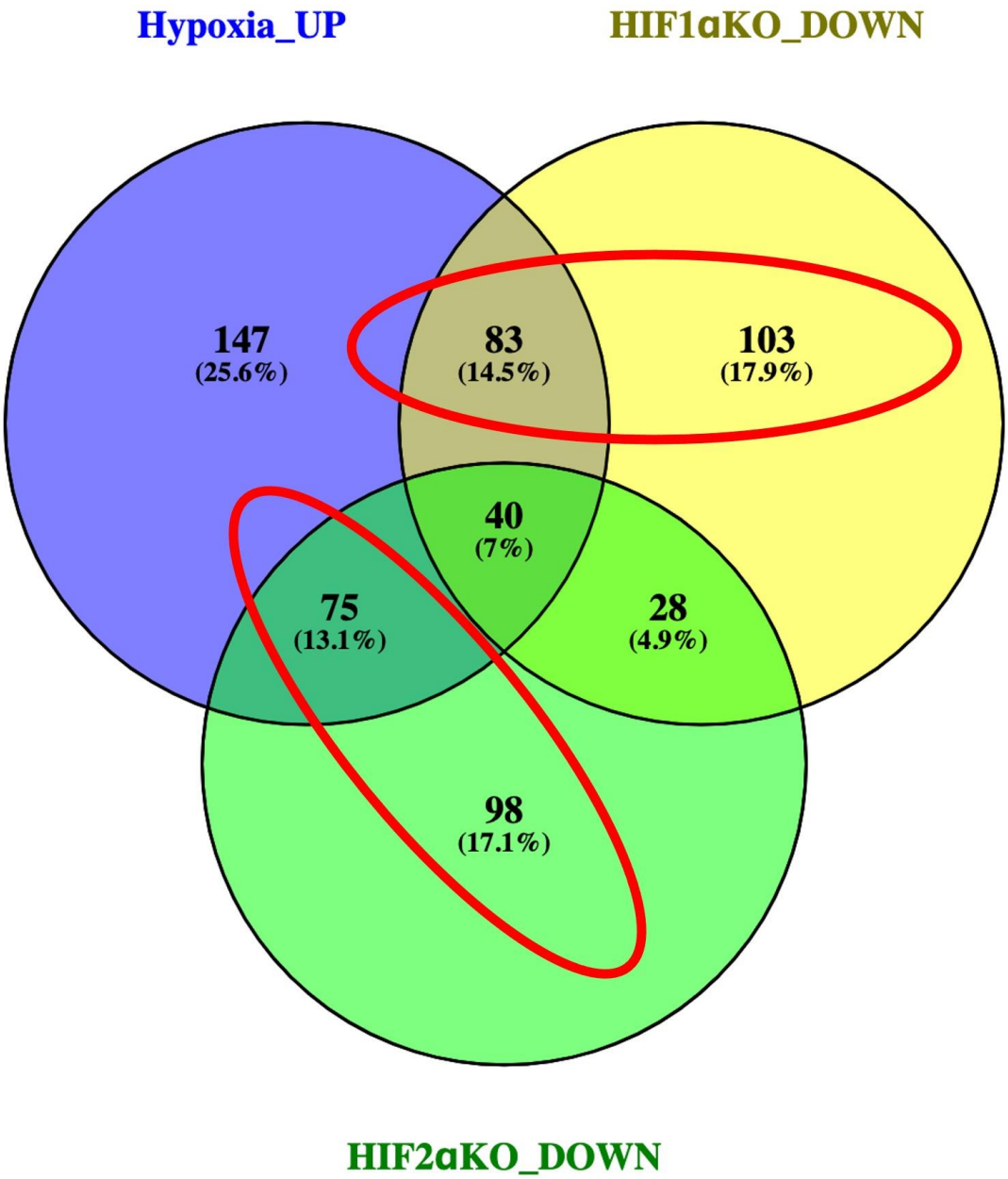

Figure 4.19 Hypoxia induces HIF-1α specific and HIF-2α specific changes in metabolic gene expression. Venn diagram of overlapping metabolic DEGs that were upregulated in hypoxia and downregulated in either the HIF-1α or HIF-2α knockout conditions. The sum of the numbers in each circle represents the total DEG list for that condition. The red circles highlight those genes identified as either HIF-1α or HIF-2α specific. n=3.

Table 4.10 shows the top 30 most significantly downregulated metabolic DEGs out of the 186 metabolic genes identified as HIF-1α-dependent sorted by log2FC. Several known HIF-1α regulated metabolic genes were downregulated including *CA9* (log2FC = -4.3), *PFKFB4* (log2FC = -3.4), *ALDOC* (log2FC = -2.7), *GPI* (log2FC = -2.6) and *NOS2* (log2FC = -2.5). KEGG pathway analysis was used to identify which metabolic pathways the significantly downregulated metabolic DEGs were classified in. A total of 21 pathways were identified associated with the downregulated HIF-1α-dependent metabolic DEGs (figure 4.20). Many pathways identified corresponded to central carbon and carbohydrate metabolism but also included amino acid metabolic pathways.

Gene symbol	log2FoldChange	padj
CA8	-6.2	1.25803E-05
KCNJ4	-5.1	0.001590798
PTGDS	-4.9	0.002073384
SCN3A	-4.5	0.015019407
CA9	**-4.3**	**2.48077E-06**
PLA2G4D	-4.0	0.024822031
GRIN2B	-3.9	2.82006E-26
MMEL1	-3.9	2.04995E-11
DPYSL4	-3.9	1.97834E-61
ALOX15	-3.8	0.001889186
PFKFB4	**-3.4**	**1.7474E-248**
SLC26A10	-3.4	0.000847007
KCNF1	-3.1	0.000896089
SLCO5A1	-3.0	0.003134193
SULT1C2	-2.8	1.90146E-15
ALDOC	**-2.7**	**3.63773E-24**
PLCH2	-2.7	4.055E-10
GPI	-2.6	**5.7205E-21**
ATP4A	-2.5	0.030386777
NOS2	**-2.5**	**0.011688495**
CLCNKA	-2.4	0.004066756
ABCA10	-2.4	0.021152138
KCNQ3	-2.3	0.015032803
GGT5	-2.3	0.000283903
ABCB6	**-2.3**	**2.10456E-10**
TRPV4	-2.3	0.001920161
GCNT2	-2.3	0.00577375
HS6ST3	-2.3	1.6488E-05
FUT11	-2.2	9.30178E-38
SLC5A10	-2.1	0.007742874

Table 4.10 Top 30 differentially expressed downregulated HIF-1α-dependent metabolic genes in HIF-1α knockout compared to the control in hypoxia. The top 30 downregulated HIF-1α-dependent metabolic genes sorted by log2FoldChange are displayed along with adjusted p-values. Known HIF-1α regulated metabolic genes are highlighted. Significant gene expression: padj < 0.05. n=3.

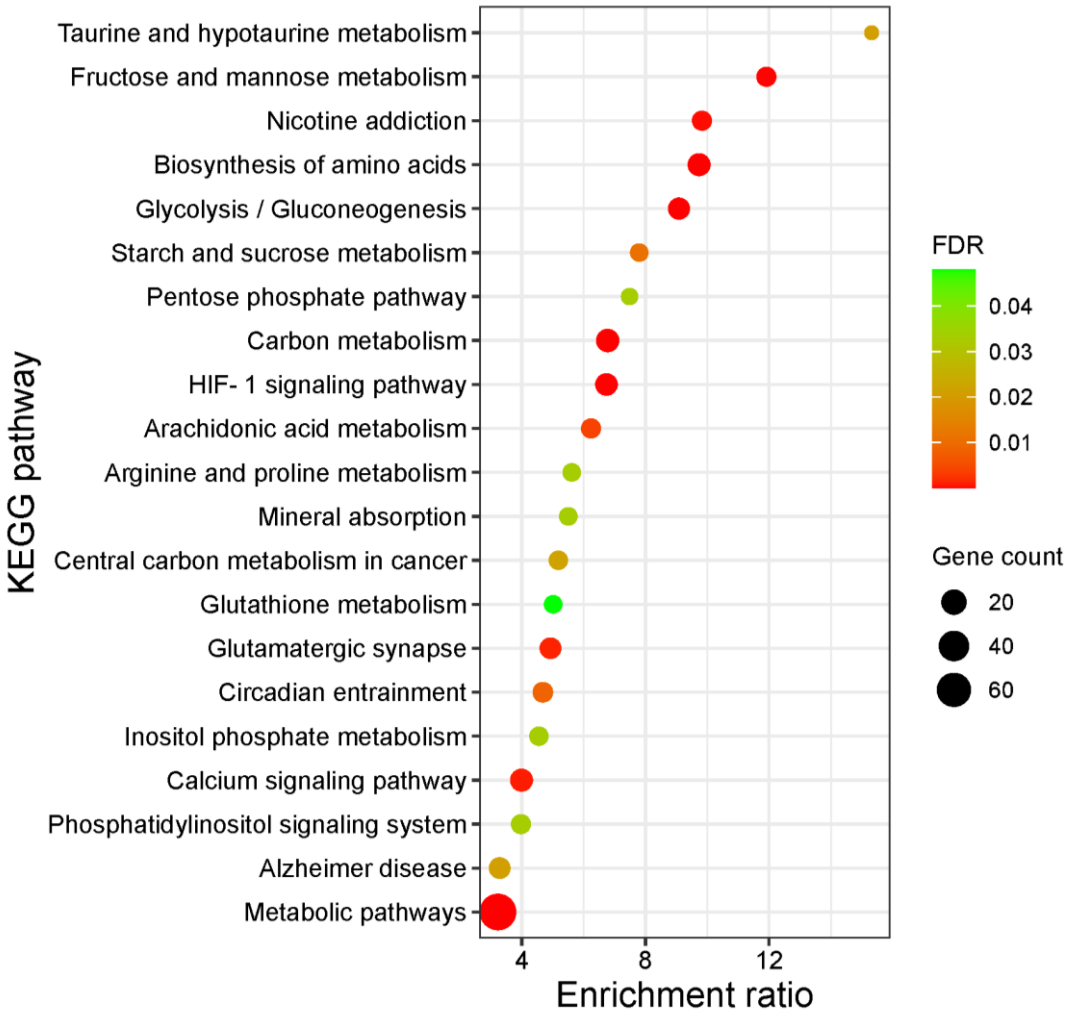

Figure 4.20 KEGG pathway classification of downregulated HIF-1α-dependent metabolic genes in hypoxia. KEGG pathway analysis of significantly downregulated metabolic genes in HIF-1α vs control samples in hypoxia. Significant KEGG pathways were plotted on the y-axis against their enrichment ratio on the x-axis. The bubble size represents the gene count whilst the colour represents the significance level measured by FDR. Significant pathways: FDR < 0.05. n=3.

Table 4.11 shows the top 30 most significantly downregulated metabolic DEGs out of the 173 metabolic genes identified as HIF-2α-dependent sorted by log2FC. These genes were divided across a large number of metabolic pathways with many of them being the rate-limiting enzymes of their respective pathways including *HMGCS1* (log2FC = -1.6), *IDI1* (log2FC = -1.5), *FDFT1* (log2FC = -1.4), *LPIN1* (log2FC = -1.3), *PLA2G4A* (log2FC = -1.2), *NT5E* (log2FC = -1.2) and *CYP51A1* (log2FC = -1.2). KEGG pathway analysis was used to identify which metabolic pathways the significantly downregulated metabolic DEGs were classified in. A total of 14 pathways were identified associated with the downregulated HIF-2α-dependent metabolic DEGs (figure 4.21). Many pathways identified corresponded to pathways involved in both fatty acid and steroid metabolism. Taken together, this data highlights a key role for both HIF-1α and HIF-2α in the regulation of various metabolic pathways. HIF-1α appeared to act as the dominant regulator of central carbon metabolism encompassing glycolysis, PPP and amino acid biosynthesis whereas HIF-2α has a role in the regulation of sterol and fatty acid metabolism.

Gene name	log2FoldChange	padj
PDE4D	-4.9	0.00113257
CACNA2D1	-4.9	0.01226651
GALNT13	-4.6	8.7956E-05
NOS1	-4.6	0.00125988
KCNJ9	-4.1	0.00102255
KCNMA1	-2.9	0.01754003
CATSPERB	-2.3	0.0074278
GALNT3	-1.6	2.0375E-10
HMGCS1	**-1.6**	**1.7962E-18**
ITPR2	-1.6	1.3283E-16
ARSJ	-1.6	0.0002636
KCNB1	-1.5	0.00144569
IDI1	**-1.5**	**9.5284E-14**
GABRG2	-1.5	0.00252008
NDUFV2	-1.4	0.00025142
FDFT1	**-1.4**	**6.553E-10**
CA14	-1.4	0.00301743
PTGS2	-1.4	0.00062114
ABCB1	-1.4	0.00198392
MVD	-1.4	3.6418E-08
LPIN1	**-1.3**	**6.3829E-14**
ST8SIA6	-1.3	0.01979494
NPC1	-1.3	2.6777E-07
PDE5A	-1.3	0.00811149
HSD17B7	-1.3	4.9048E-11
KCTD16	-1.2	0.02961573
PLA2G4A	**-1.2**	**2.4429E-08**
NT5E	**-1.2**	**8.0979E-14**
SLC26A4	-1.2	0.04996716
CYP51A1	**-1.2**	**0.00012934**

Table 4.11 Top 30 differentially expressed downregulated HIF-2α-dependent metabolic genes in HIF-2α knockout compared to the control in hypoxia. The top 30 downregulated HIF-2α-dependent metabolic genes sorted by log2FoldChange are displayed along with adjusted p-values. Genes encoding rate-limiting enzymes are highlighted. Significant gene expression: padj < 0.05. n=3.

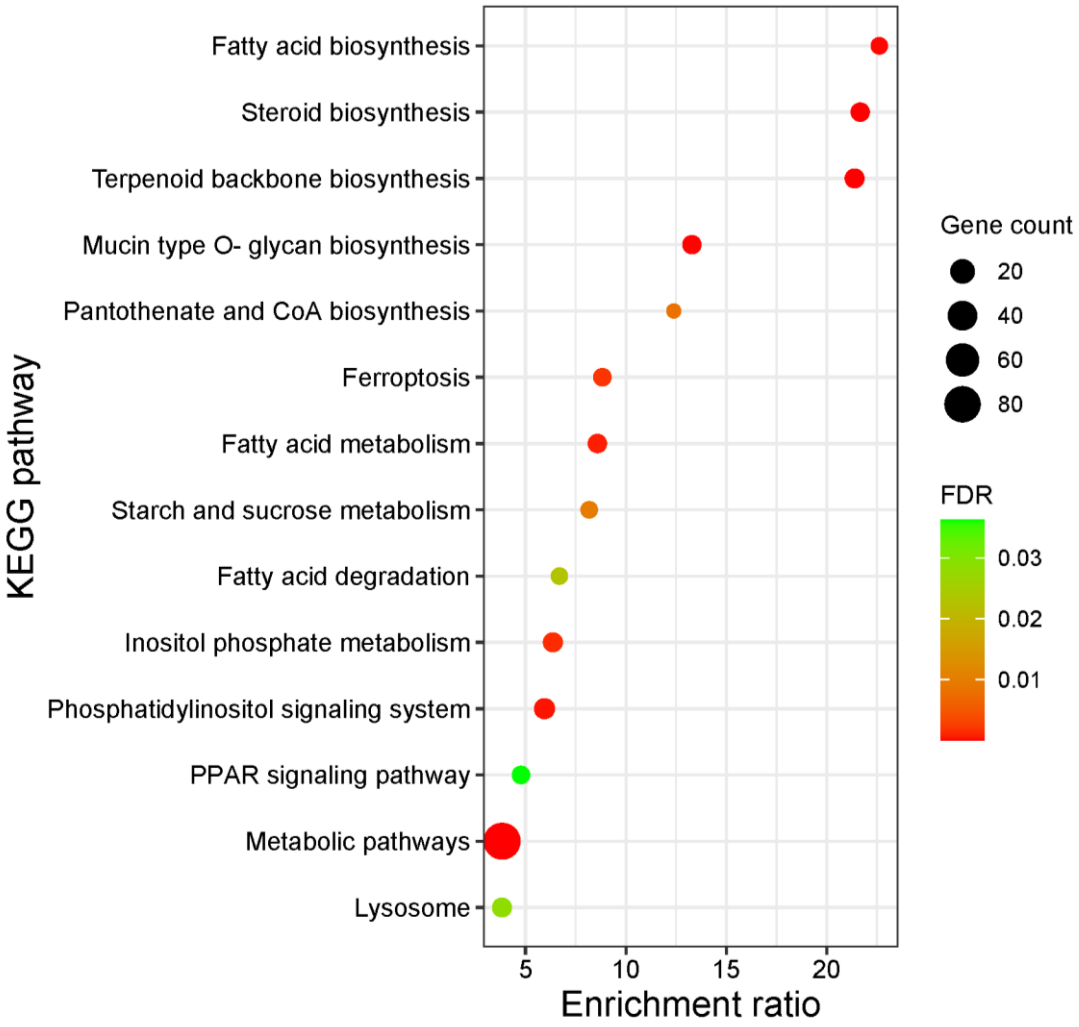

Figure 4.21 KEGG pathway classification of downregulated HIF-2α-dependent metabolic genes in hypoxia. KEGG pathway analysis of significantly downregulated genes in HIF-2α vs control samples in hypoxia. Significant KEGG pathways were plotted on the y-axis against their enrichment ratio on the x-axis. The bubble size represents the gene count whilst the colour represents the significance level measured by FDR. Significant pathways: FDR < 0.05. n=3.

4.3.9 Hypoxia-regulated alternative splicing

In order to identify whether hypoxia was regulating alternative splicing and to examine the biological significance of this regulation the RNA sequencing data was probed for differential alternative splicing events between the experimental groups, as described in section 2.9.6. Overall, a total of 8,591 alternative splicing events, with 4,000 genes associated with those events, were induced by hypoxia (figure 4.22). The majority of hypoxia-induced alternative splicing events were skipped exons (SE) accounting for 60.07% of events (5,161 events) with 2,793 unique genes identified. Mutually exclusive exons (MXE) accounted for 14.29% of events (1,228 events, 770 unique genes), alternative 3' splice site usage (A3SS) accounted for 9.64% of events (828 events, 669 unique genes, alternative 5' splice site usage (A5SS) accounted for 8,24% of events (708 events, 578 unique genes) and retained introns (RI) accounted for 7.75% of events (666 events, 564 unique genes). The top 30 alternatively spliced genes induced by hypoxia are shown in table 4.12. This data provided evidence to suggest that hypoxia is inducing large-scale changes in the alternative splicing of genes in CRC cell lines.

In order to identify what pathways hypoxia-induced alternatively spliced genes were involved in, KEGG pathway analysis was used. Pathway analysis revealed a total of 15 pathways that were significantly enriched for alternatively spliced genes induced by hypoxia (figure 4.23). Many pathways involved in RNA and protein processing and transport were identified such as 'RNA transport' (ER = 1.5806), 'RNA degradation' (ER = 2.3027) and 'endocytosis' (ER = 1.5337) as well as several metabolic pathways including 'inositol phosphate metabolism' (ER = 1.9667), 'lysine degradation' (ER = 1.85) and 'glycerophospholipid metabolism' (ER = 1.7147). This suggests that hypoxia regulates the splicing and function of metabolic genes. The 'spliceosome' (ER = 1.7843) pathway was also identified suggesting that hypoxia might also be inducing direct changes in the splicing machinery.

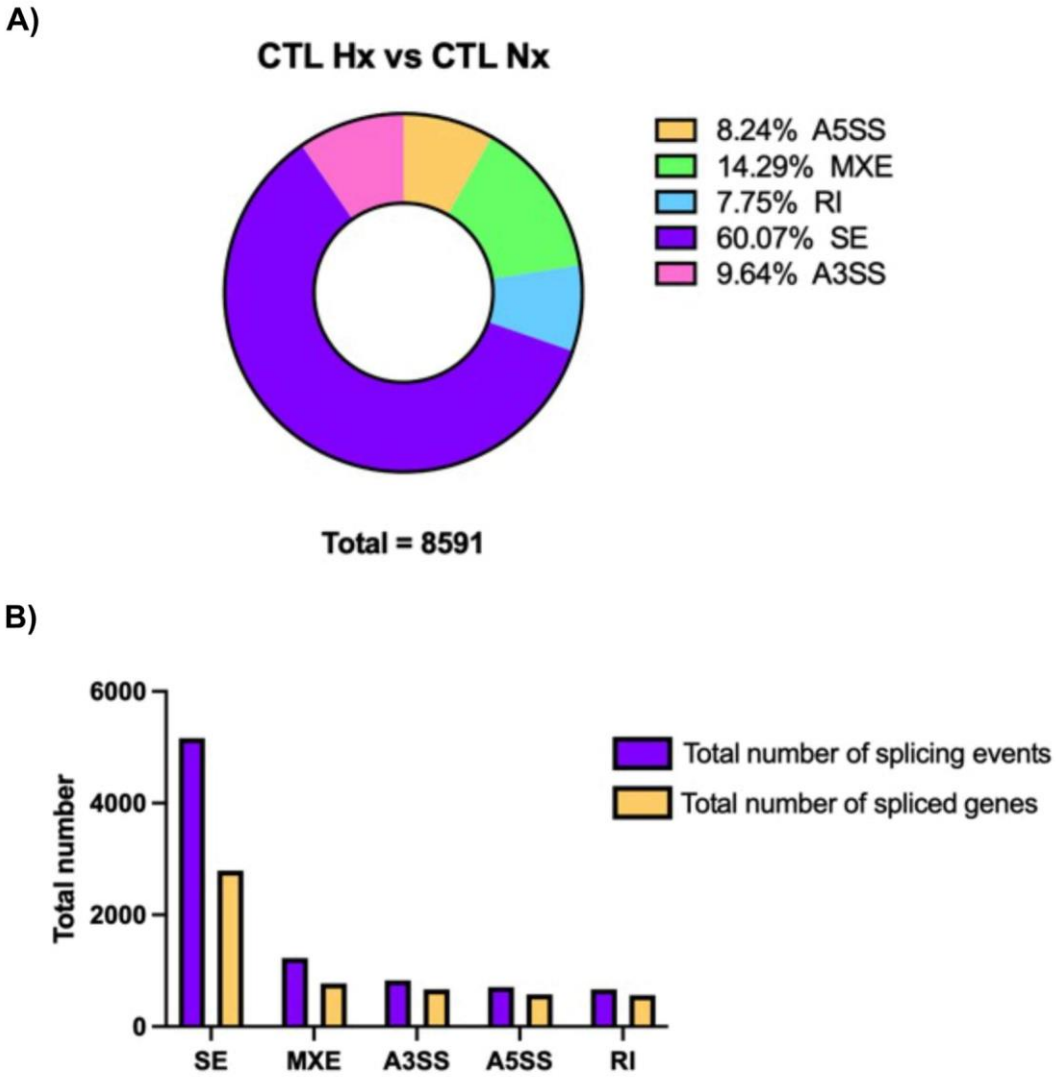

Figure 4.22 Hypoxia regulates alternative splicing in HCT116 cell line. HCT116 iCas9 cells treated with non-targeting gRNA control were exposed to normoxia or hypoxia for 48h and analysed by RNA-sequencing to identify differential splicing events. **A)** The distribution of differential splicing events between the control hypoxia vs control normoxia samples are displayed. **B)** The number of unique genes contributing to the total number of splicing events are displayed. Significant splicing events: dPSI ≥ 5% and FDR < 0.05. SE = skipped exon, MXE = mutually exclusive exon, RI = retained intron, A5SS = alternative 5' splice site, A3SS = alternative 3' splice site. n=3.

Gene symbol	FDR	Abs dPSI
ZSWIM7	0	100
SAR1A	1.444E-10	100
DMKN	1.6398E-10	100
MLPH	4.6491E-10	100
BICD1	5.2601E-10	100
SPIN3	1.7374E-11	100
SAXO2	3.2624E-11	96.6
SPIN1	0	93.4
TM7SF3	4.2413E-06	91.9
NPIPB4	2.8641E-07	91.5
CARS	0.00010587	89.4
PRKAA2	5.7408E-08	87.4
SSPO	2.874E-09	86.9
TTLL6	0	86.2
TMEM161A	3.0596E-12	85.7
TRIM69	1.4353E-10	85.2
RP11-286N22.8	2.4647E-05	84.6
DDOST	**1.03E-06**	**83.2**
RAPGEFL1	0.00279259	83.2
HDLBP	3.0613E-07	83.1
RAVER1	4.2123E-08	82.8
IQUB	1.8845E-06	82.7
CYBA	1.0167E-09	82.3
DCST2	8.2056E-06	81.7
LMNA	3.0859E-07	81.6
ADCK4	**1.6065E-08**	**81.5**
GRID2IP	5.3602E-09	80.3
LINC01057	1.7484E-07	80.1
SPIN1	1.9742E-05	80
RMI1	2.2169E-08	79.8

Table 4.12 Top 30 alternatively spliced genes induced by hypoxia. The top 30 alternatively spliced genes in control hypoxia vs control normoxia samples sorted by dPSI are displayed along with FDR. Metabolic genes are highlighted. Significant splicing events: dPSI >5, FDR < 0.05. n=3.

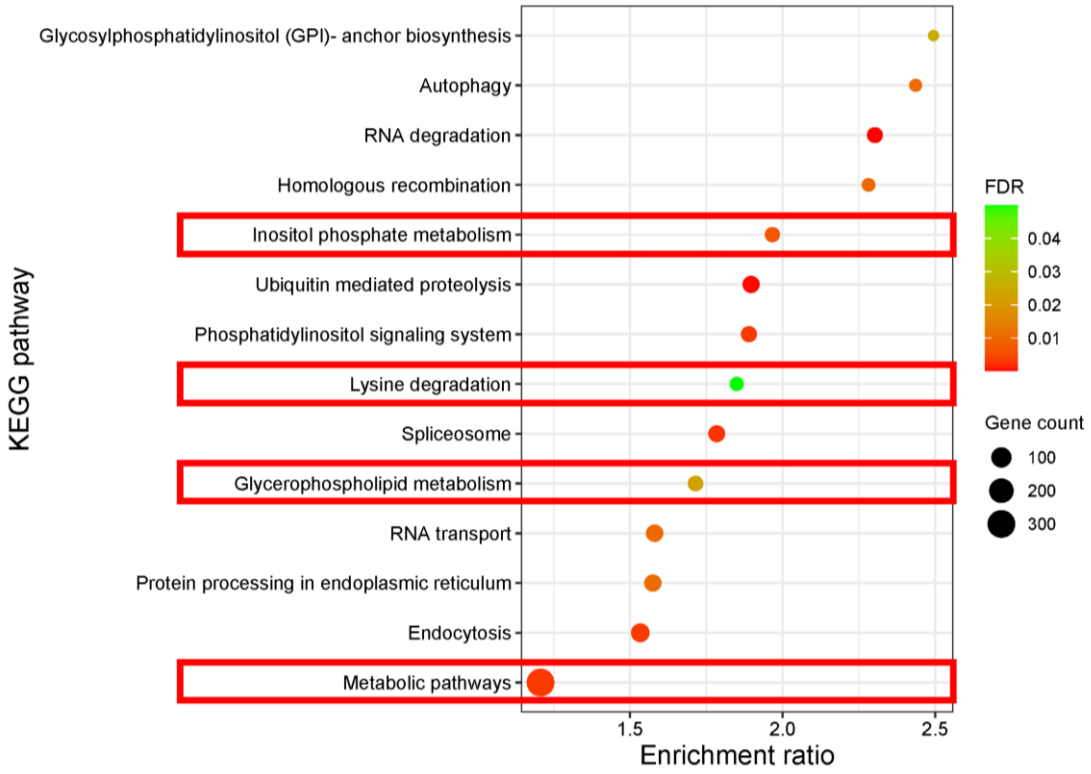

Figure 4.23 Significantly enriched KEGG pathways for alternatively spliced genes in hypoxia. KEGG pathway analysis of differentially spliced genes in control hypoxia vs control normoxia samples. Significant KEGG pathways were plotted on the y-axis against their enrichment ratio on the x-axis. The bubble size represents the gene count whilst the colour represents the significance level measured by FDR. The red boxes indicate pathways associated with metabolism. Significant pathways: FDR < 0.05. n=3.

4.3.10 Hypoxia-regulated alternative splicing of metabolic genes

In order to further analyse the role of hypoxia-induced alternative splicing in the regulation of metabolic reprogramming in CRC, alternatively spliced metabolic genes were identified using the list of 2,752 metabolic genes described previously in comparison with the total number of alternatively spliced genes (figure 4.24). 530 metabolic genes, accounting for 19% of all metabolic genes, were identified as alternatively spliced in hypoxia. The top 30 alternatively spliced metabolic genes induced by hypoxia are shown in table 4.13.

In order to identify what pathways hypoxia-induced alternatively spliced metabolic genes were involved in, KEGG pathway analysis was used. Pathway analysis revealed a total of 47 pathways that were significantly enriched for alternatively spliced genes induced by hypoxia (figure 4.25). Many known hypoxia-regulated metabolic pathways were identified including 'phosphatidylinositol signaling system', 'biosynthesis of amino acids', 'pentose phosphate pathway', 'citrate cycle (TCA cycle)' and 'pyruvate metabolism'. Furthermore, many of the pathways identified correlated with HIF-1α and HIF-2α-regulated differentially expressed metabolic genes. Overall, these results suggest that hypoxia is regulating metabolic adaptation through additional mechanisms alongside gene expression, including the regulation of the alternative splicing of metabolic genes.

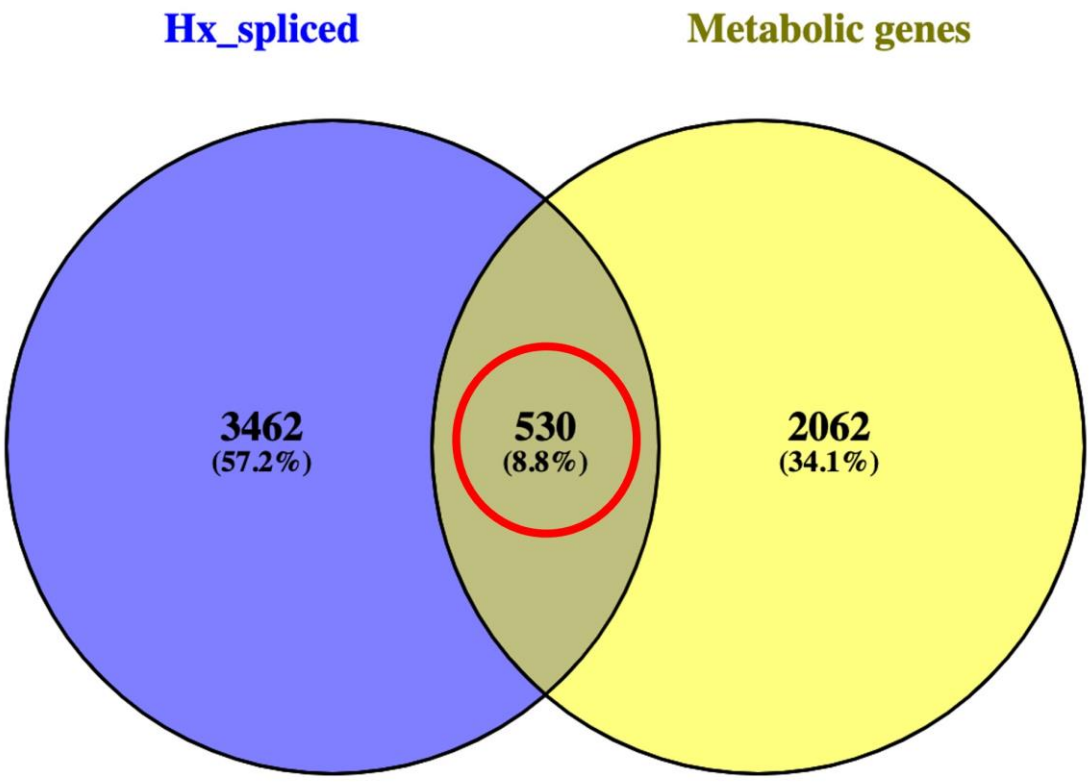

Figure 4.24 Hypoxia induces the alternative splicing of metabolic genes. Venn diagram of overlapping alternatively spliced genes in hypoxia and total metabolic genes. The sum of the numbers in each circle represents the total number of genes for that condition. The red circle highlights metabolic genes identified as alternatively spliced in hypoxia. n=3.

Gene symbol	FDR	Abs dPSI
DDOST	1.03E-06	83.2
CYBA	1.0167E-09	82.3
MCOLN3	9.2332E-11	77.6
HACL1	0.0078019	75.1
HMGCL	9.9587E-08	72
CACNB3	1.075E-06	70.5
IP6K2	0.02236285	70.4
ST6GAL1	0.00820791	70.2
MMAB	4.9784E-07	69.4
GSTZ1	3.8819E-07	67.3
PDE9A	0.00096148	66.7
ISCA2	0.0463005	66.7
POFUT2	0.00547354	66.7
KCNK6	1.0806E-05	66.7
MGST1	2.5135E-05	66.7
RRM2	0.00200815	66.7
CANT1	0.00075242	65.5
ABCB8	4.4497E-09	65.5
ABCD4	8.6941E-05	65
SLC10A7	0.0061192	63.5
ETFA	0.00011123	63.5
GLUD1	0.0005005	62.1
PFKL	0.00021146	61.7
PIGB	6.1096E-05	61.6
PLA2G4B	1.9856E-09	61.6
SLC22A15	0.00051334	61
SLC35D2	0.04140606	60.8
FRRS1	0.00059605	60.3
TBXAS1	3.371E-06	59.9
DECR2	0.00024295	59.1

Table 4.13 Top 30 alternatively spliced metabolic genes induced by hypoxia. The top 30 alternatively spliced metabolic genes in control hypoxia samples sorted by dPSI are displayed along with FDR. Significant splicing events: dPSI >5, FDR < 0.05. n=3.

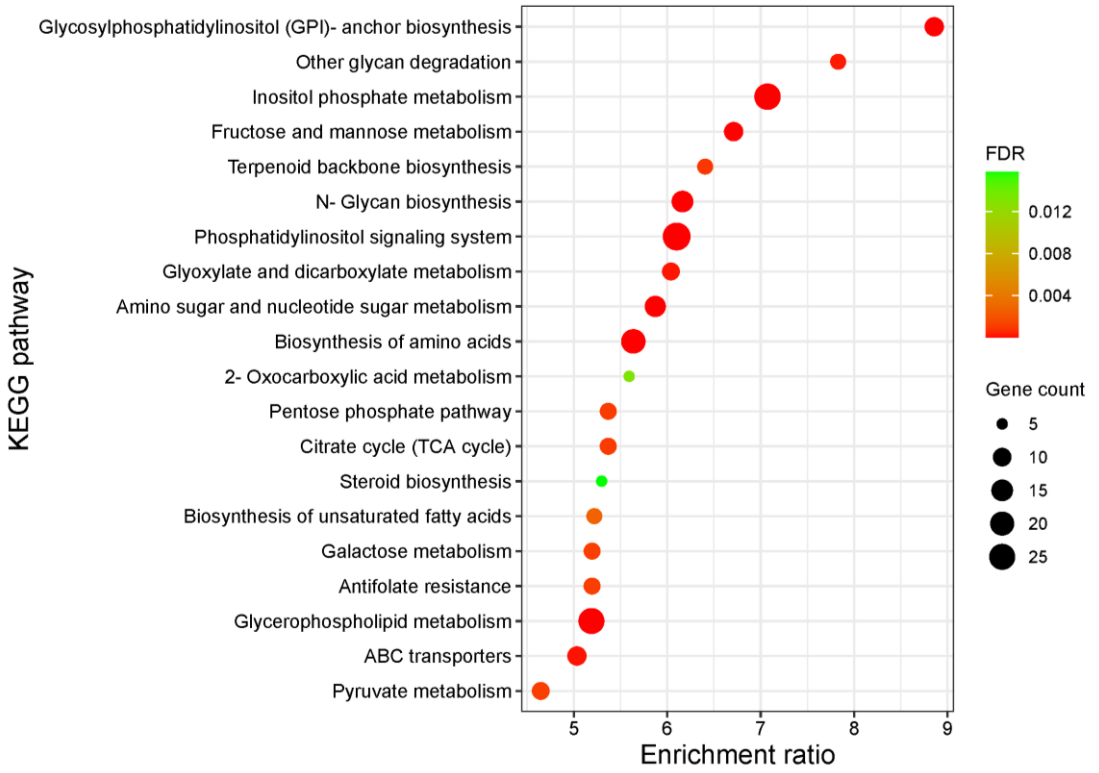

Figure 4.25 KEGG pathway classification for alternatively spliced metabolic genes in hypoxia. KEGG pathway analysis of alternatively spliced metabolic genes in control hypoxia samples. The top 20 significant KEGG pathways were plotted on the y-axis against their enrichment ratio on the x-axis. The bubble size represents the gene count whilst the colour represents the significance level measured by FDR. Significant pathways: FDR < 0.05. n=3.

4.3.11 The role of HIF-1α and HIF-2α-associated alternative splicing

In order to identify whether HIF-1α or HIF-2α were regulating hypoxia-induced alternative splicing events and to identify the biological significance of this regulation, differential alternative splicing events between the control and HIF knockout hypoxic conditions were identified. Overall, a total of 4,621 alternative splicing events, with 2,560 genes associated with those events, were associated with HIF-1α knockout (figure 4.26). The majority of HIF-1α-associated alternative splicing events were SE accounting for 59.01% of events (2,727 events) with 1,745 unique genes identified. MXE accounted for 16.30% of events (753 events, 472 unique genes), A3SS accounted for 8.72% of events (403 events, 344 unique genes), A5SS accounted for 8.44% of events (390 events, 336 unique genes) and RI accounted for 7.53% of events (348 events, 310 unique genes). The top 30 HIF-1α-associated alternatively spliced genes are shown in table 4.14. This data provided evidence to suggest that HIF-1α is associated with large-scale changes in the alternative splicing of genes in CRC cell lines.

In order to identify what pathways HIF-1α-associated alternatively spliced genes were involved in, KEGG pathway analysis was used. Pathway analysis revealed a total of 5 pathways that were significantly enriched for alternatively spliced genes associated with HIF-1α knockout (figure 4.27). A couple of metabolic pathways were identified including 'fructose and mannose metabolism' (ER = 3.0313) and 'metabolic pathways' (ER = 1.252). The 'spliceosome' (ER = 1.8663) pathway was also identified suggesting that HIF-1α might also be associated with changes in the splicing machinery. Overall, a total of 208 genes were present within the enriched metabolic pathways associated with HIF-1α knockout suggesting that HIF-1α is regulating changes the alternative splicing of metabolic genes.

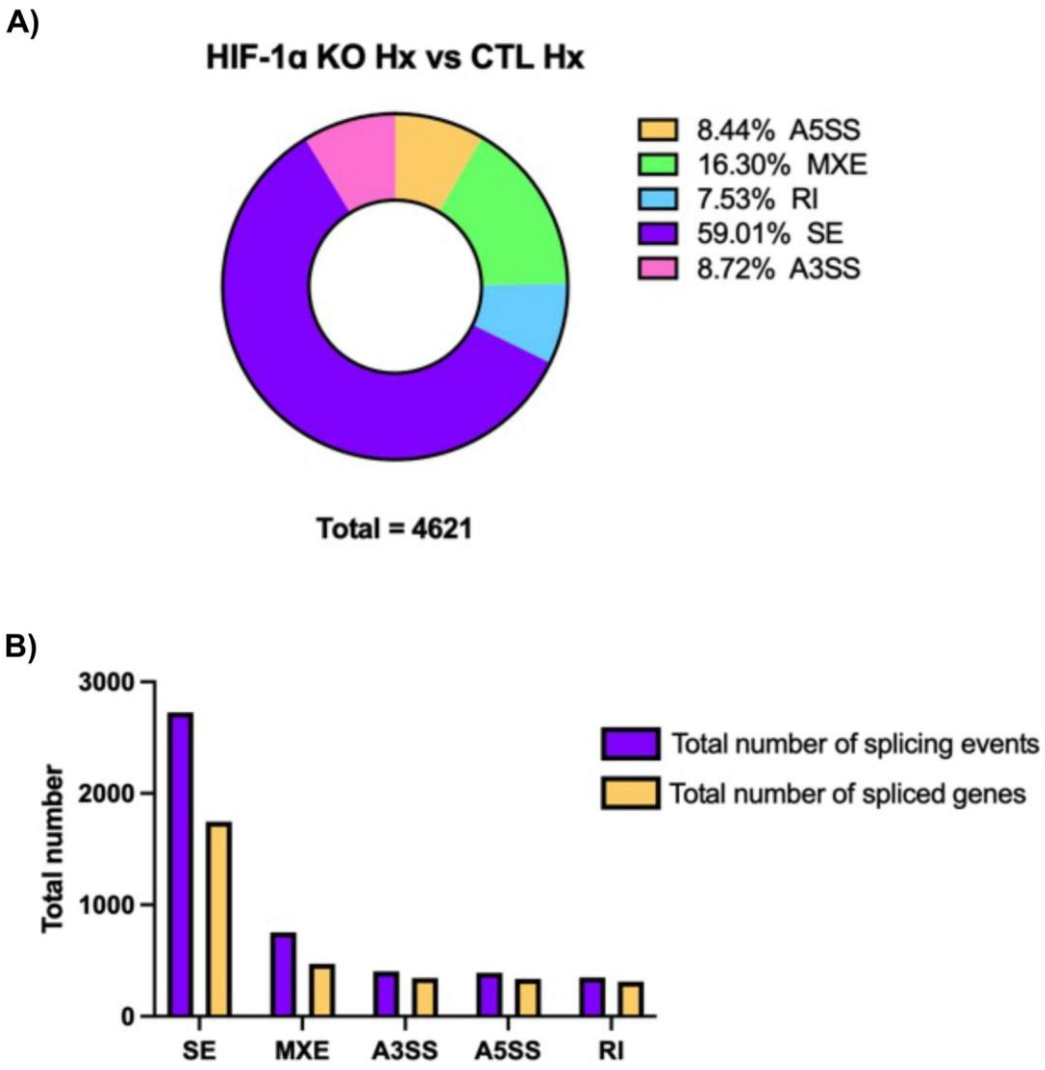

Figure 4.26 HIF-1α regulates alternative splicing in HCT116 cell line. HCT116 iCas9 cells treated with non-targeting gRNA control or HIF-1α-targeting gRNA, g57, were exposed to normoxia (21% pO_2) or hypoxia (1% pO_2) for 48h and analysed by RNA-sequencing to identify differential splicing events. **A)** The distribution of differential splicing events between the control hypoxia vs HIF-1α knockout hypoxia samples are displayed. **B)** The number of unique genes contributing to the total number of splicing events are displayed. Significant splicing events: dPSI ≥ 5% and FDR < 0.05. SE = skipped exon, MXE = mutually exclusive exon, RI = retained intron, A5SS = alternative 5' splice site, A3SS = alternative 3' splice site. n=3.

Gene symbol	FDR	Abs dPSI
ZMYND8	9.9981E-11	100
DRICH1	1.5235E-11	100
CFAP69	3.6116E-10	100
LINC00894	6.9963E-10	100
SEC61A2	5.2404E-09	100
HIF1A	1.6076E-10	99
UHRF2	6.0019E-10	92.2
TM7SF3	7.6172E-06	91.9
HIF1A	1.8223E-11	89.2
P3H1	3.3808E-08	88.6
HRK	2.6262E-05	87.7
CNTNAP3	7.7026E-08	87.3
LA16c-380H5.3	5.4551E-09	85.5
COL17A1	0.00119079	85.2
ZDHHC16	1.7142E-08	84.9
FAM114A2	1.6466E-05	84.6
ABHD10	**5.1815E-07**	**84.5**
SS18	4.5964E-07	83.9
SPIN1	1.2079E-05	83.9
NOLC1	2.3676E-10	83.5
ARNT	0.00021953	83.2
SYT17	2.3979E-05	83.1
RP11-166B2.1	1.8989E-06	82.5
CCSER1	9.9944E-06	81.7
INVS	6.2821E-06	81.5
NAP1L4	1.0696E-06	81.4
GUSBP11	1.5199E-06	81.1
RTKN	6.2109E-11	81
KITLG	3.8057E-06	80.8
LYRM1	1.1545E-06	80.7

Table 4.14 Top 30 HIF-1α-associated alternatively spliced genes. The top 30 alternatively spliced genes in control hypoxia vs HIF-1α knockout hypoxia samples sorted by dPSI are displayed along with FDR. Metabolic genes are highlighted. Significant splicing events: dPSI >5, FDR < 0.05. n=3.

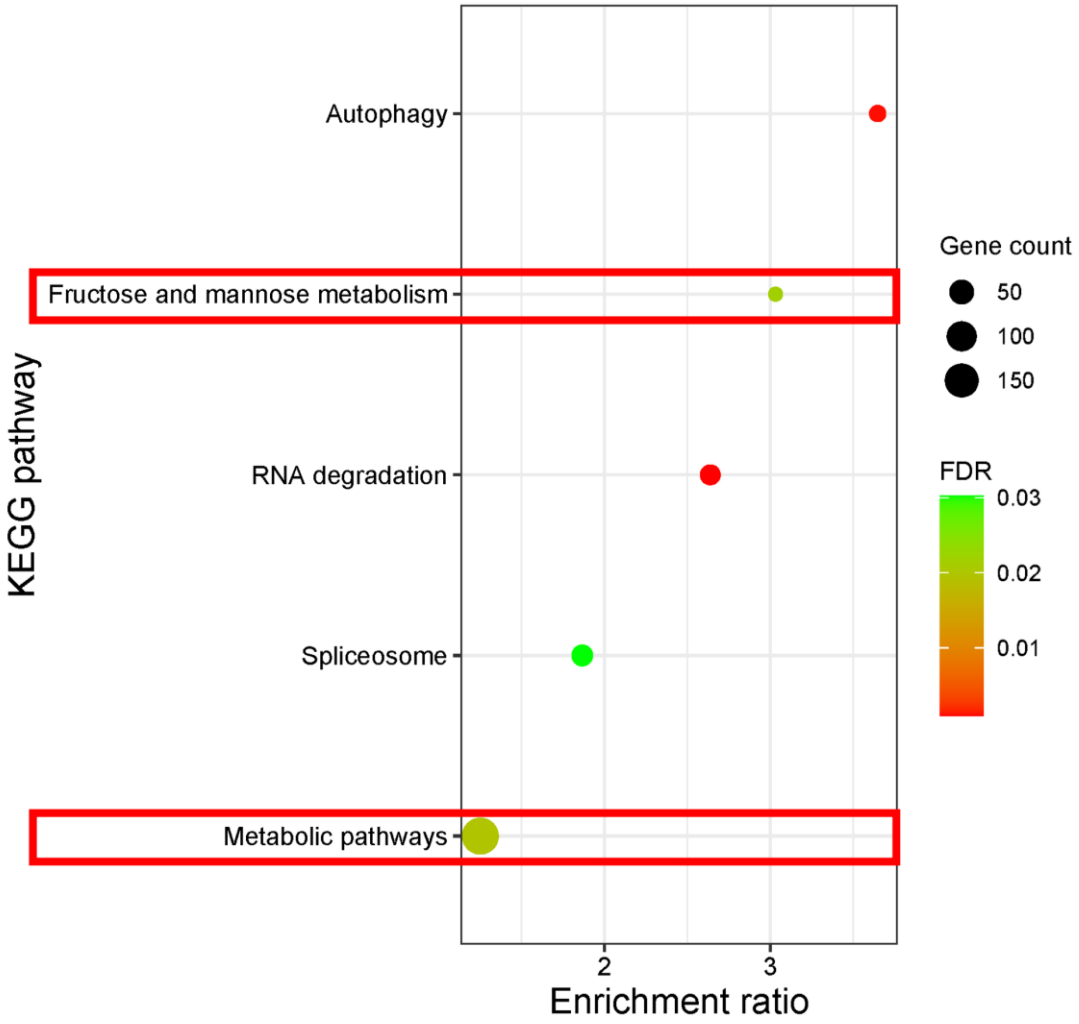

Figure 4.27 Significantly enriched KEGG pathways for HIF-1α-associated alternatively spliced genes. KEGG pathway analysis of differentially spliced genes in control hypoxia vs HIF-1α knockout hypoxia samples. Significant KEGG pathways were plotted on the y-axis against their enrichment ratio on the x-axis. The bubble size represents the gene count whilst the colour represents the significance level measured by FDR. The red boxes indicate pathways associated with metabolism. Significant pathways: FDR < 0.05. n=3.

Overall, a total of 5,807 alternative splicing events, with 3,037 genes associated with those events, were associated with HIF-2α knockout (figure 4.28). The majority of HIF-2α-associated alternative splicing events were SE accounting for 64.49% of events (3,745 events) with 2,228 unique genes identified. MXE accounted for 14.02% of events (814 events, 498 unique genes), A3SS accounted for 8.70% of events (505 events, 428 unique genes), A5SS accounted for 7.35% of events (427 events, 360 unique genes) and RI accounted for 5.44% of events (316 events, 280 unique genes). The top 30 HIF-2α-associated alternatively spliced genes are shown in table 4.15. This data provided evidence to suggest that HIF-2α is associated with large-scale changes in the alternative splicing of genes in CRC cell lines.

In order to identify what pathways HIF-2α-associated alternatively spliced genes were involved in, KEGG pathway analysis was used. Pathway analysis revealed a total of 7 pathways that were significantly enriched for alternatively spliced genes associated with HIF-2α knockout (figure 4.29). Several metabolic pathways were identified including 'terpenoid backbone biosynthesis' (ER = 3.5365), 'lysine degradation' (ER = 2.1578), phosphatidylinositol signaling system' (ER = 1.9290) and 'metabolic pathways' (ER = 1.2195). Overall, a total of 281 genes were present within the enriched metabolic pathways associated with HIF-2α knockout suggesting that HIF-2α is regulating the alternative splicing of metabolic genes.

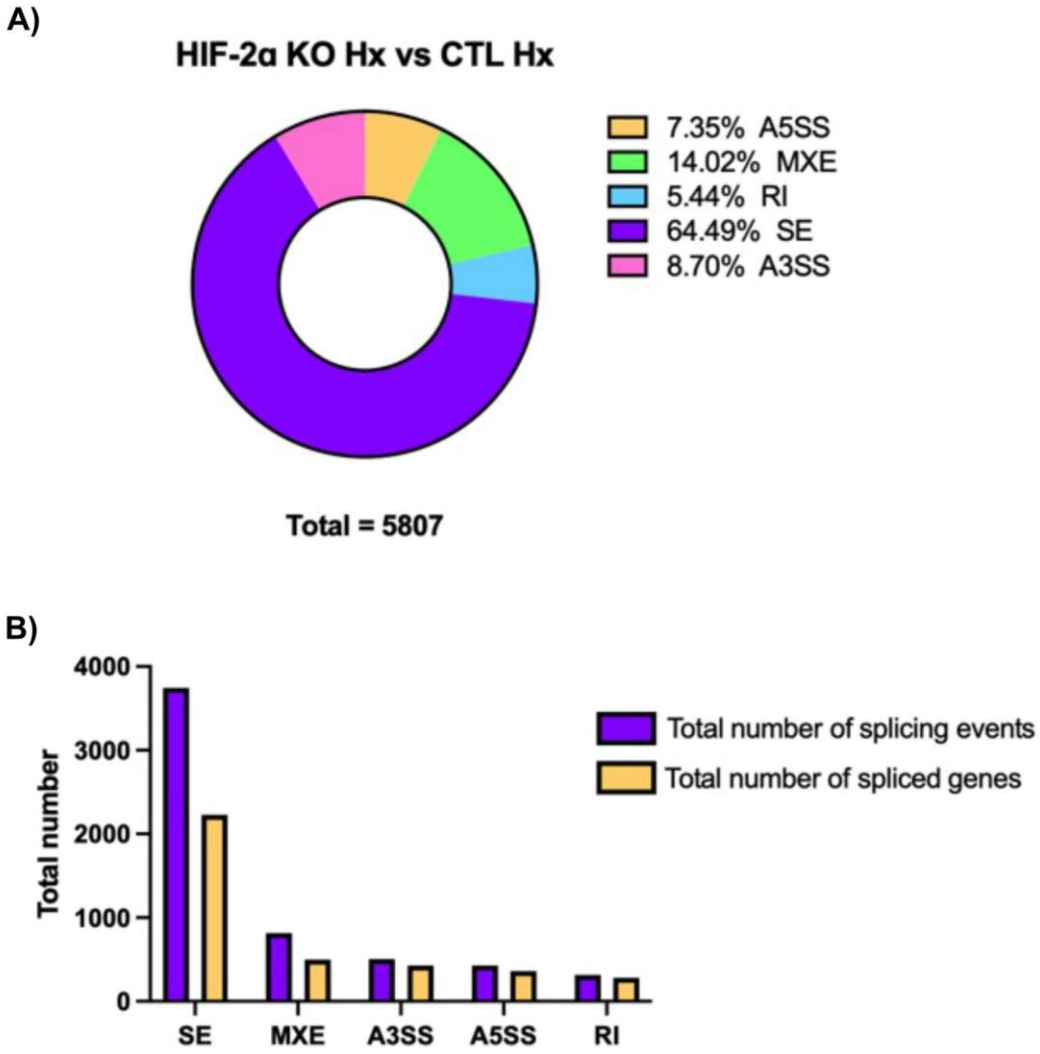

Figure 4.28 HIF-2α regulates alternative splicing in HCT116 cell line. HCT116 iCas9 cells treated with non-targeting gRNA control or HIF-2α-targeting gRNA, g81, were exposed to normoxia (21% pO_2) or hypoxia (1% pO_2) for 48h and analysed by RNA-sequencing to identify differential splicing events. **A)** The distribution of differential splicing events between the control hypoxia vs HIF-2α knockout hypoxia samples are displayed. **B)** The number of unique genes contributing to the total number of splicing events are displayed. Significant splicing events: dPSI ≥ 5% and FDR < 0.05. SE = skipped exon, MXE = mutually exclusive exon, RI = retained intron, A5SS = alternative 5' splice site, A3SS = alternative 3' splice site. n=3.

Gene symbol	FDR	Abs dPSI
RAB11FIP2	1.4135E-09	100
ANXA5	1.9119E-06	93.4
CD9	1.158E-10	92.2
AHSA2	4.2453E-08	92.2
TM7SF3	5.9108E-06	91.9
AC007773.2	1.2211E-08	89.5
DDX31	3.4197E-13	88.9
GAPDH	**0.00020572**	**88.5**
SYT17	2.177E-05	87.8
ZNF607	6.2431E-06	87.1
COL27A1	2.3474E-06	86.9
PABPC1	9.4903E-06	86.3
CDC16	1.2027E-07	86.2
CEP104	1.158E-10	85.9
MLPH	4.6446E-07	85.3
GPR89A	8.0677E-08	85
LGALS9	1.8142E-08	84.6
COMMD4	2.8165E-10	84.5
RMI1	4.8885E-10	84.1
SYT12	6.2791E-07	84.1
AP1G1	6.8726E-09	84
SPIN1	9.5402E-06	83.9
PDPK1	**8.9913E-07**	**83.5**
DIS3L2	2.6064E-07	83.3
RPP30	0	83.2
CCDC159	3.2647E-06	82.9
MAP2K5	1.8445E-09	82.5
AC005592.2	2.5965E-07	82.3
IGF2BP3	**0.00112661**	**82.1**
STEAP3	1.6819E-05	82.1

Table 4.15 Top 30 HIF-2α-associated alternatively spliced genes. The top 30 alternatively spliced genes in control hypoxia vs HIF-2α knockout hypoxia samples sorted by dPSI are displayed along with FDR. Metabolic genes are highlighted. Significant splicing events: dPSI >5, FDR < 0.05. n=3.

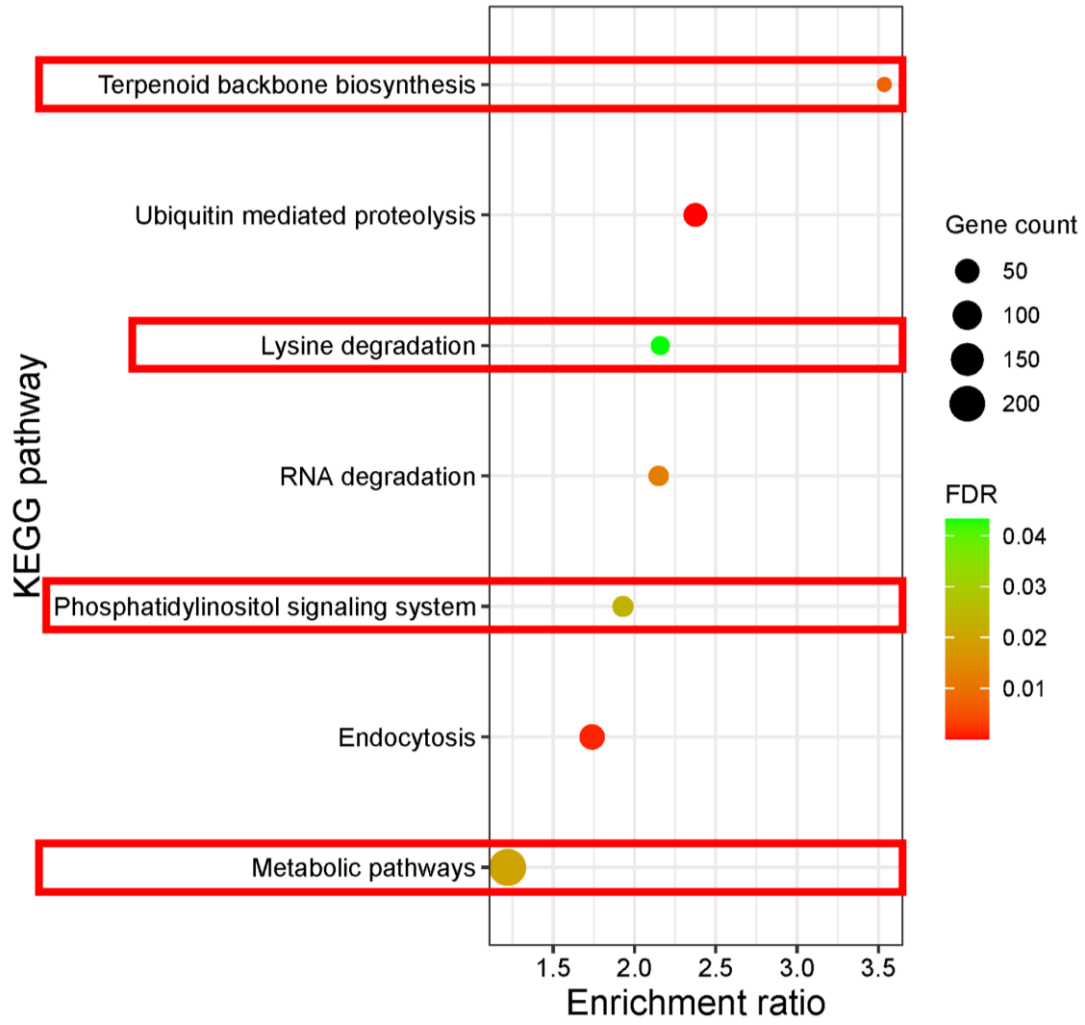

Figure 4.29 Significantly enriched KEGG pathways for HIF-2α-associated alternatively spliced genes. KEGG pathway analysis of differentially spliced genes in control hypoxia vs HIF-2α knockout hypoxia samples. Significant KEGG pathways were plotted on the y-axis against their enrichment ratio on the x-axis. The bubble size represents the gene count whilst the colour represents the significance level measured by FDR. The red boxes indicate pathways associated with metabolism. Significant pathways: FDR < 0.05. n=3.

4.3.12 Optimisation of HIF-1α and HIF-2α knockout spheroids for OrbiSIMS analysis

In order to generate HCT116 control (CTL), HIF-1α and HIF-2α knockout spheroids of comparable size to allow for direct comparison in the OrbiSIMS, due to the differences in growth between the CTL and knockout conditions (see figure 4.2), optimisation of the seeding densities for each condition was required. In addition, the 600 μm depth limit of the planchette holders used in the high-pressure freezing (HPF) sample preparation meant the spheroid diameter could not exceed 600 μm.

Initially, two seeding densities of 500 cells/well and 1000 cells/well were tested for each of the six experimental conditions: CTL A3, CTL A10, HIF-1α knockout g49, HIF-1α knockout g57, HIF-2α knockout g11 and HIF-2α knockout g81, however, the spheroids exceeded the 600 μm limit in all conditions after 7 days of growth (data not shown). A 7-day growth period was selected in order to allow enough time for hypoxia to develop within the spheroid core once the spheroid diameter exceeded the oxygen diffusion limit (~ 180 μm) after approximately 3 days (data not shown). Additionally, optimisation of the culture conditions using both high-glucose (4.5 g/L) and low-glucose (1.0 g/L) DMEM media was considered to try and reduce the effects of media-derived glucose on the metabolism of the spheroids in culture. However, spheroid formation in low-glucose media was unsuccessful (data not shown). Therefore, it was decided to seed the spheroids in an initial 50 μL of high-glucose media followed by a top-up with 150 μL low-glucose media on Day 3, then a subsequent media change on Day 5 removing 100 μL and replacing with 100 μL low-glucose media. This led to an approximate 4.7-fold decrease in glucose concentration by day 5.

The final seeding density optimisation involved two seeding densities for the control conditions: 100 cells/well and 200 cells/well and four conditions for the knockout cell lines: 100, 200, 300 and 400 cells/well. Figure 4.30 shows the average spheroid volumes and average spheroid diameter for each of the conditions tested. Based on these results the following seeding densities were selected: CTL A3, CTL A10, HIF-1α g49 and HIF-2α g11 = 100 cells/well; HIF-1α g57 and HIF-2α g81 = 200 cells/well.

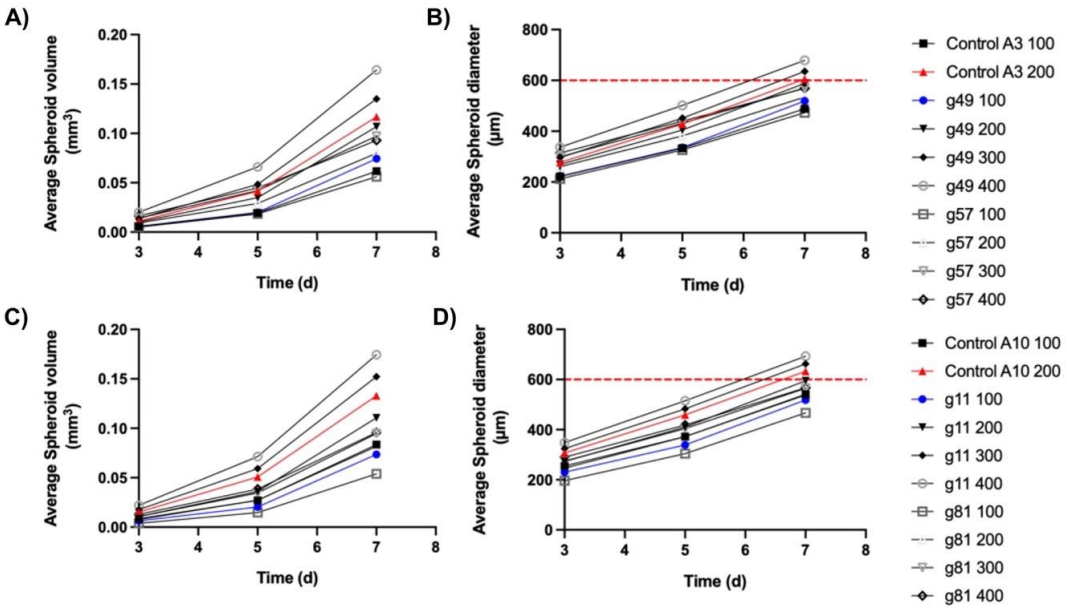

Figure 4.30 Optimisation of seeding conditions for HIF-1α and HIF-2α knockout spheroids. HCT116 iCas9 cells transfected with either non-targeting gRNA controls A3 and A10, HIF-1α-targeting gRNAs g49 and g57 or HIF-2α-targeting gRNAs g11 and g81 were isolated into clonal populations and used to form 3-dimensional spheroids *in vitro* at seeding densities of 100-400 cells/well. Images of HCT116 spheroids were taken on days 3, 5 and 7 at 4x magnification. **A, C)** Images were used to calculate average spheroid volumes on days 3, 5 and 7. **B, D)** Spheroid volumes were used to calculate spheroid diameter on days 3, 5 and 7. The red line indicates the 600 µm size limit. n=1.

4.3.13 Generation of HIF-1α and HIF-2α knockout spheroids for orbiSIMS analysis

Based on the previous analysis investigating the impact of HIF-1α and HIF-2α knockout clones on HCT116 spheroid growth (see figure 4.2) the HIF-1α knockout g57 and HIF-2α knockout g81 cell lines were selected for OrbiSIMS analysis along with the CTL A3 and A10 cell lines. Spheroids were seeded at the optimised seeding densities described above and cultured as described above for 7 days. Figure 4.31a displays representative images at each of the time points measured. Morphologically, there were no visible differences between the HIF knockout and control spheroids. There were no differences in average spheroid volume between the control spheroids and either of the HIF knockout cell lines (figure 4.31b) and there was no difference in the average volume of the spheroids on day 7 (figure 4.31d). Furthermore, no differences were observed in either the overall growth rates of the spheroids (figure 4.31c) or the average spheroid diameter on day 7 (figure 4.31e). The average spheroid diameters for all three conditions were also below the 600 μm size limit required for orbiSIMS sample preparation (figure 4.31e). Taken together, these results confirmed the successful generation of comparably sized spheroids that could be used for orbiSIMS analysis.

A total of 20 spheroids were seeded per experimental condition. 3 spheroids per condition were selected for high-pressure freezing and downstream orbiSIMS analysis based on selection criteria of spheroid diameter = 550 μm ± 10%. These spheroids were stained with Hoechst to allow visualisation and identification of the spheroids within the planchettes following high-pressure freezing and prior to orbiSIMS analysis using cryolight microscopy (see 2.10.1; figure 4.32)[550]. Cryolight imaging was able to identify and locate the spheroids within the planchettes following high-pressure freezing.

In order to confirm the development of hypoxia within the core of the spheroids, the remaining size-conforming spheroids were stained with pimonidazole prior to fixing in neutral-buffered formalin (see 2.10.1). Immunohistochemical analysis of spheroid sections identified hypoxic regions within the control, HIF-1α and HIF-2α knockout spheroids (see 2.3.3; figure 4.33a). An isogenic IgG control was included to confirm the specificity of the staining observed. A negative trend in the amount of hypoxia was observed in both the HIF-1α and HIF-2α knockout spheroids with a larger decrease seen with HIF-2α knockout compared to HIF-1α (figure 4.33b). Central necrotic cores

were also visualised in the control and HIF-1α knockout spheroids but were not observed in the HIF-2α knockout condition. The hypoxic region in the HIF-2α knockout spheroids was found within the core of the spheroids (figure 4.33a).

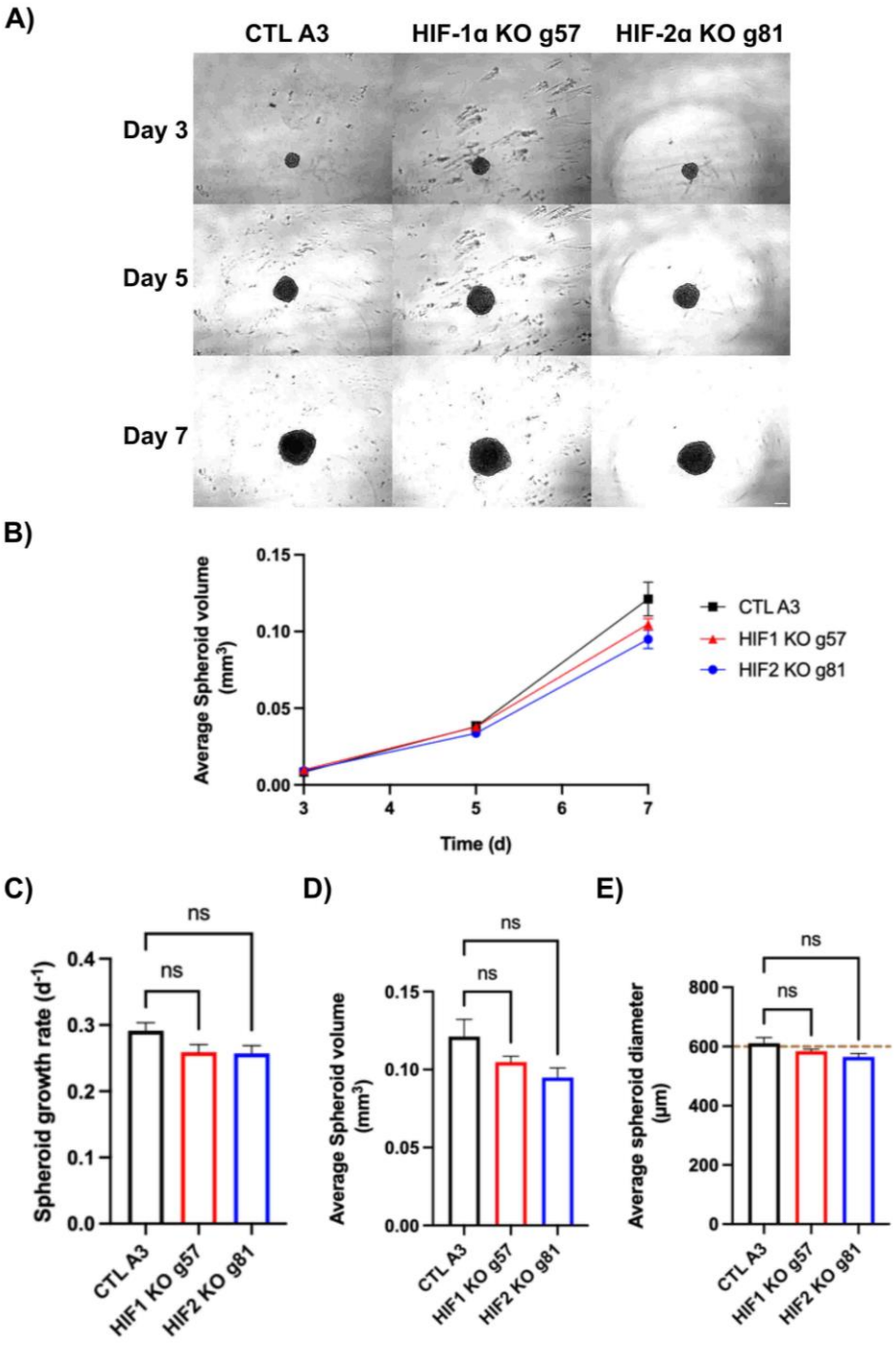

Figure 4.31 Generation of HIF-1α and HIF-2α knockout spheroids for orbiSIMS analysis. HCT116 iCas9 cells transfected with either non-targeting gRNA control A3, HIF-1α-targeting gRNA g57 or HIF-2α-targeting gRNA g81 were isolated into clonal populations and used to form 3-dimensional spheroids *in vitro* at the optimised seeding densities of 100 cells/well (CTL A3) and 200 cells/well (g57 and g81). **A)** Representative images from four experimental repeats of HCT116 spheroids taken on days 3, 5 and 7 at 4x magnification. Scale bar represents 200µm. **B)** Images were used to calculate average spheroid volumes on days 3, 5 and 7. **C)** Spheroid volumes were used to calculate growth rates using linear regression analysis. **D)** Comparison of average spheroid volumes on day 7 of growth. **E)** Comparison of average spheroid diameter on day 7 of growth. The brown line represents the 600 µm size limit. Data was analysed by one-way ANOVA comparing HIF-1α and HIF-2α knockout spheroids to control A3. *p <0.0332, **p<0.0021, ***p<0.0002, ****P<0.0001. Error bars indicate ± SEM.

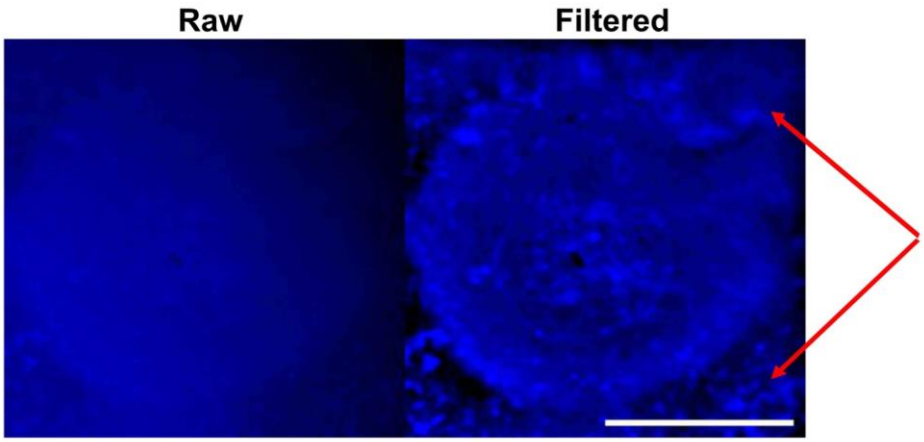

Figure 4.32 Cryolight image of high-pressure frozen spheroid in planchette. HCT116 CTL A3 spheroids were high-pressure frozen in 0.6 mm planchettes and imaged using cryolight microscopy to visualise the position of the spheroids within the planchette. The left-hand image represents the raw output image. The right-hand image was filtered using a bandpass filter (large structure limit = 50 pixels, small structures limit = 1 pixel) and autoscaled after filtering to preserve intensity. The red arrows indicate the location of ice crystals. Scale bar represents 200 μm.

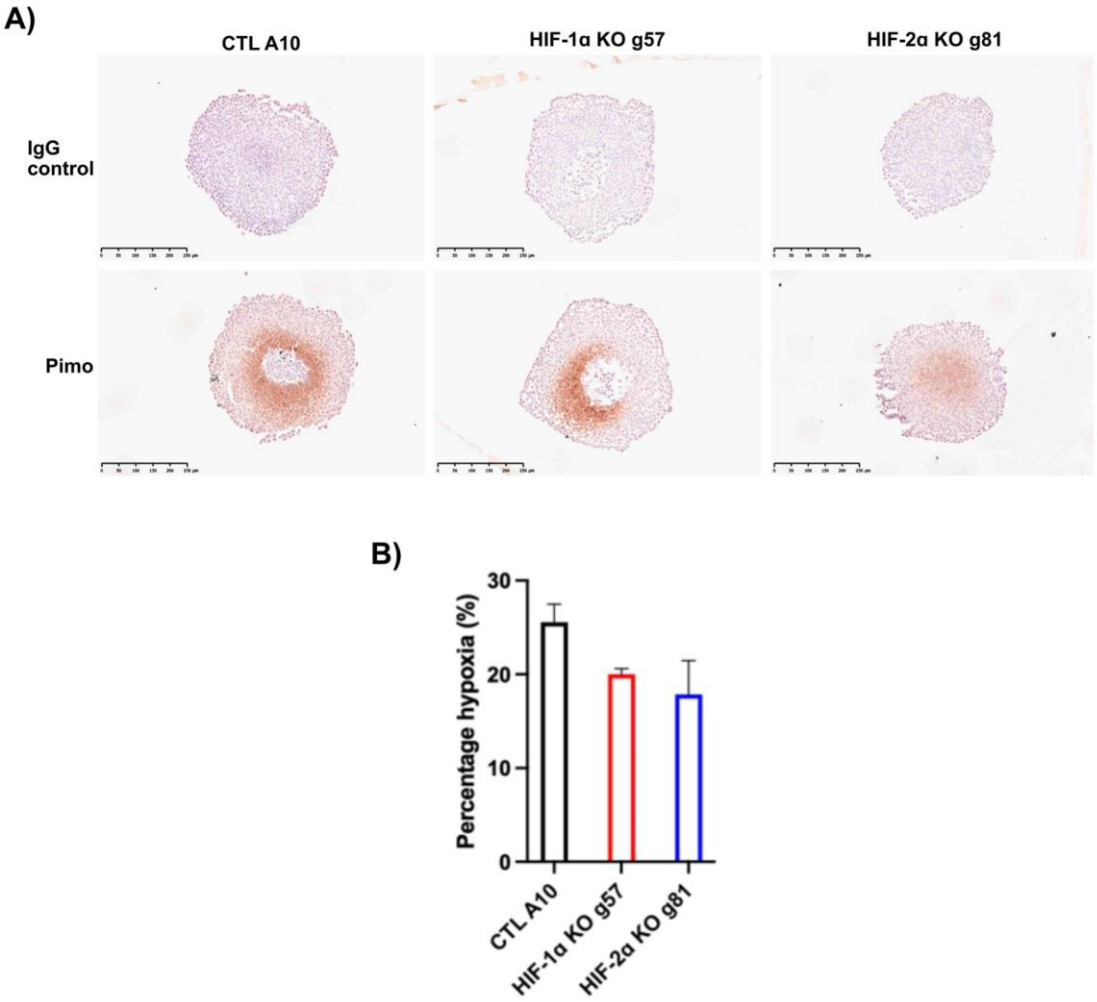

Figure 4.33 Quantification and localisation of the hypoxic core in HIF-1α and HIF-2α knockout spheroids. HCT116 iCas9 cells transfected with either non-targeting gRNA control A10, HIF-1α-targeting gRNA g57 or HIF-2α-targeting gRNA g81 were isolated into clonal populations and used to form 3-dimensional spheroids *in vitro* at the optimised seeding densities of 100 cells/well (CTL A10) and 200 cells/well (g57 and g81). Spheroids were stained with 200 μM pimonidazole prior to fixation and immunohistochemical analysis. **A)** Representative images of pimonidazole staining of HCT116 spheroids taken with a 40x objective. Scale bar represents 250 μm. **B)** Levels of hypoxia were assessed visually and subsequently quantified in ImageJ by calculating the percetange hypoxia (based on positive staining area) as a fraction of the total area of the spheroid section. n=1.

4.3.14 Development and optimisation of an orbiSIMS analysis workflow for 3-dimensional spheroids

Due to the novelty of analysing *in vitro* 3-dimensional spheroids under cryogenic conditions using orbiSIMS mass spectrometry, the development and optimisation of a reproducible and efficient workflow was required. HCT116 CTL A3, CTL A10, HIF-1α knockout g57 and HIF-2α knockout g81 spheroids were cultured and selected for high-pressure freezing as described in 4.3.13. Three spheroids per condition were high-pressure frozen in 0.6mm (2 x 0.3mm) deep planchettes. The spheroids were then transferred to the orbiSIMS instrument under cryogenic conditions and maintained at cryogenic temperatures during the analysis. For the initial development and optimisation of the analysis, the CTL A3 and CTL A10 samples were used. Adenine was selected as an appropriate control marker for identifying cells and was used as a control for all downstream analyses. In order to confirm that the detection of small metabolites, such as adenine, was possible, an initial cycle of milling into the spheroid sample using the LMIG ion beam followed by Ar_{3000+} GCIB orbitrap MS analysis was employed with multiple scan acquisitions. Figure 4.34 displays part of the negative polarity mass spectrum obtained for the HCT116 CTL A10 spheroid. The major negative adenine ion was identified as $C_5H_4N_5^-$ (m/z 134.0472) along with minor peaks for additional possible adenine ions (figure 4.34a). In addition, the isotope distribution of the $C_5H_4N_5^-$ ion confirmed that was the most abundant ion and identified additional minor isotopes consisting of ^{13}C and ^{15}N atoms (figure 4.34b). No isotopes containing deuterium (^2H) were detected (min. % abundance = 0.0001%). Based on this data, the $C_5H_4N_5^-$ ion was selected for further analysis and a similar analysis was carried out for all additional ions of interest.

A total of five scans were taken in the negative polarity for the adenine ion $C_5H_4N_5^-$ (m/z 134.0472) along with the total ion count (TIC). Figure 4.35 shows orbitrap MS images of the individual scans along with an image of the combined scans. The ion counts were normalised by dividing the adenine signal by the TIC signal. No signal was detected in scan 3. The signal detected in scans 2 and 5 appeared to be background noise. Scan 1 partially detected the adenine signal within the spheroid sample but with low intensity. Scan 4 displayed the greatest detection of the adenine signal, and the outline of the spheroid can also be clearly visualised within the image. Therefore, scans 1, 2,3 and 5

were excluded and scan 4 was selected for the subsequent analysis of additional metabolites and small molecules in the control samples.

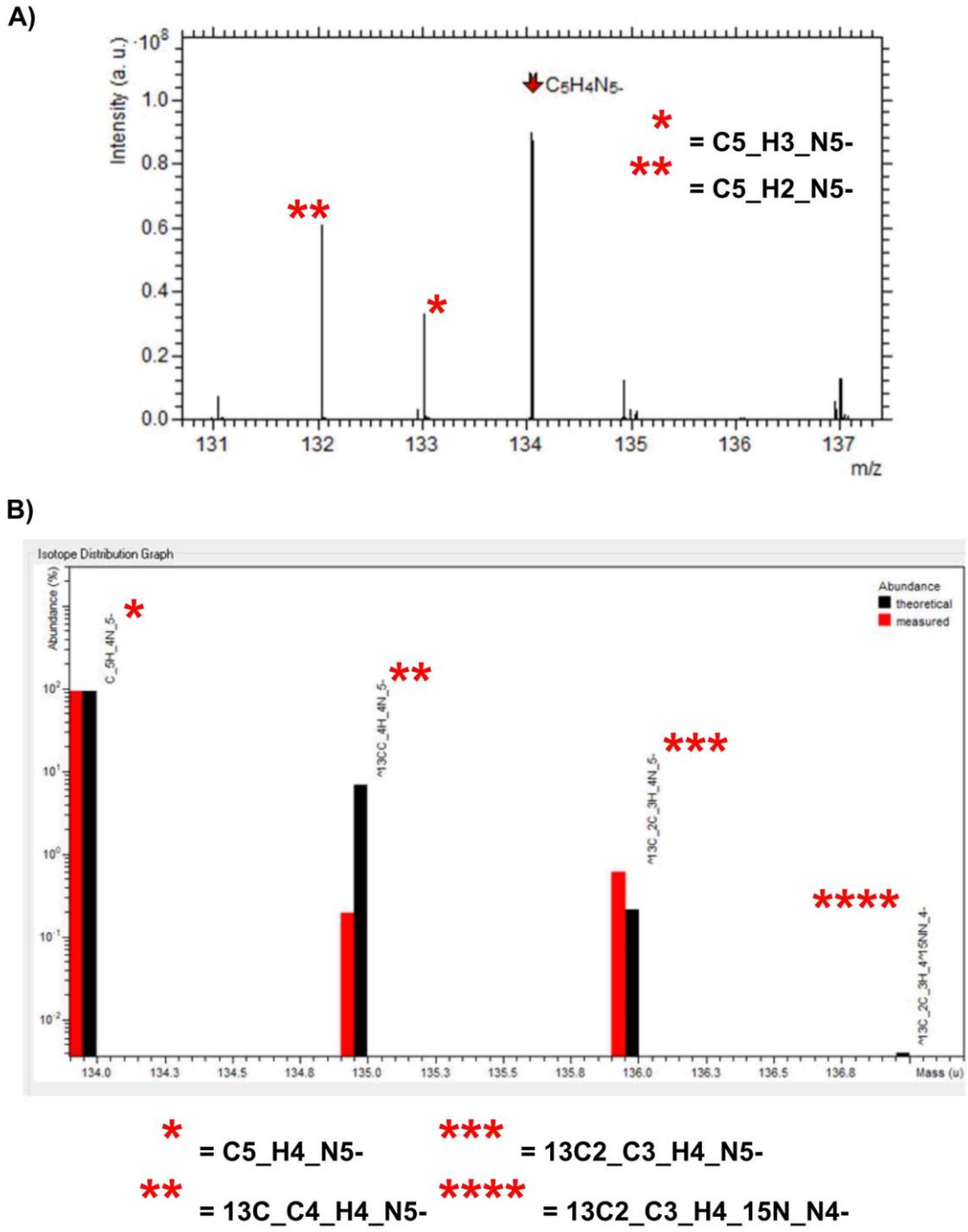

Figure 4.34 GCIB-orbitrap MS identifies the dominant negative ion fragment of adenine and distinguishes it from minor isotopes. 20μm 20keV Ar_{3000+} Orbitrap MS negative polarity mass spectrum from HCT116 CTL A10 spheroids. **A)** Mass spectrum of adenine (*m/z* 134.0472, $C_5H_4N_5^-$) indicating major and minor possible ions. **B)** Isotope distribution of the adenine ion. % abundance is displayed on a log scale. Minimum abundance = 0.0001%. Data analysis performed using SurfaceLab 7.1 (IONTOF GmbH). n=1.

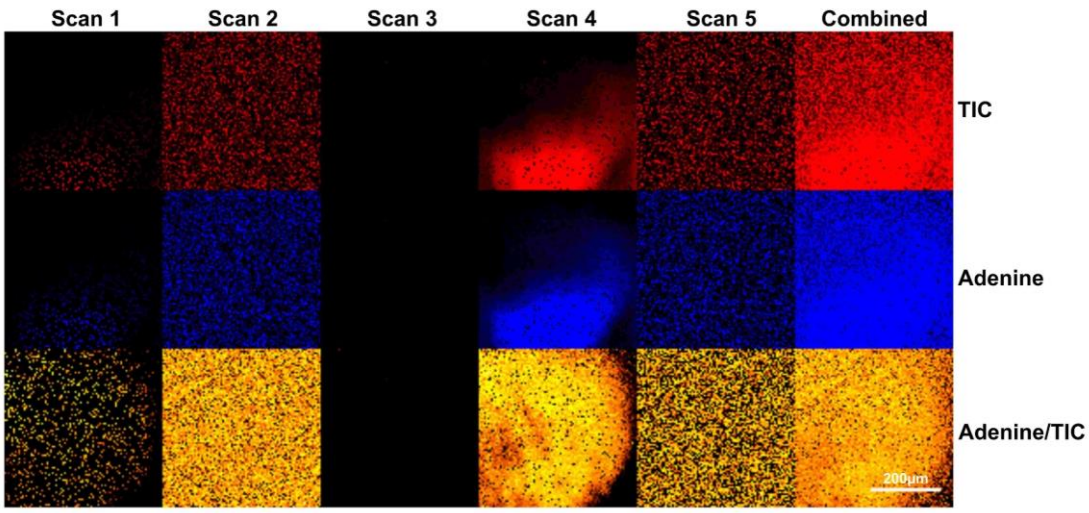

Figure 4.35 Cryo-orbiSIMS GCIB negative polarity orbitrap image analysis of adenine distribution within spheroids. 20µm 20keV Ar_{3000+} Orbitrap MS negative polarity images of adenine (m/z 134.0472, $C_5H_4N_5^-$) and total ion count (TIC) signals from HCT116 CTL A10 spheroids. Signal normalisation was performed using adenine/TIC. Scale bar represents 200 µm. Post-acquisition analysis was carried out using SurfaceLab 7.1 (IONTOF GmbH). n=1.

After confirming the ability of the orbiSIMS to detect metabolites within the spheroid sample it was important to determine whether the use of the negative or positive polarity spectra gave better signal detection. Therefore, the analysis was repeated as described above but in the positive polarity with the acquisition of a single scan. Figure 4.36 displays part of the positive polarity mass spectrum obtained for the HCT116 CTL A10 spheroid. The major positive adenine ion was identified as $C_5H_6N_5^+$ (m/z 136.0472) along with minor peaks for additional possible adenine ions (figure 4.36a). In addition, the isotope distribution of the $C_5H_6N_5^+$ ion confirmed that was the most abundant ion and identified additional minor isotopes consisting of ^{13}C and ^{15}N atoms (figure 4.36b). No isotopes containing deuterium (^2H) were detected (min. % abundance = 0.0001%). Based on this data, the $C_5H_6N_5^+$ ion was selected for further analysis.

Figure 4.37 shows the orbitrap MS images of the positive polarity scan for the adenine ion $C_5H_6N_5^+$ (m/z 136.0472) along with the TIC and normalised image. Figure 4.38 shows the negative polarity scan 4 compared with the positive polarity scan for adenine and TIC. The detection of the adenine signal appeared higher in the negative polarity compared to the positive polarity and the ability to visualise the edge of the spheroid was greatly enhanced in the negative polarity. There was also a large amount of non-specific background detected in the positive polarity. Therefore, it was decided to focus on using the negative polarity spectra for the analysis of additional metabolites.

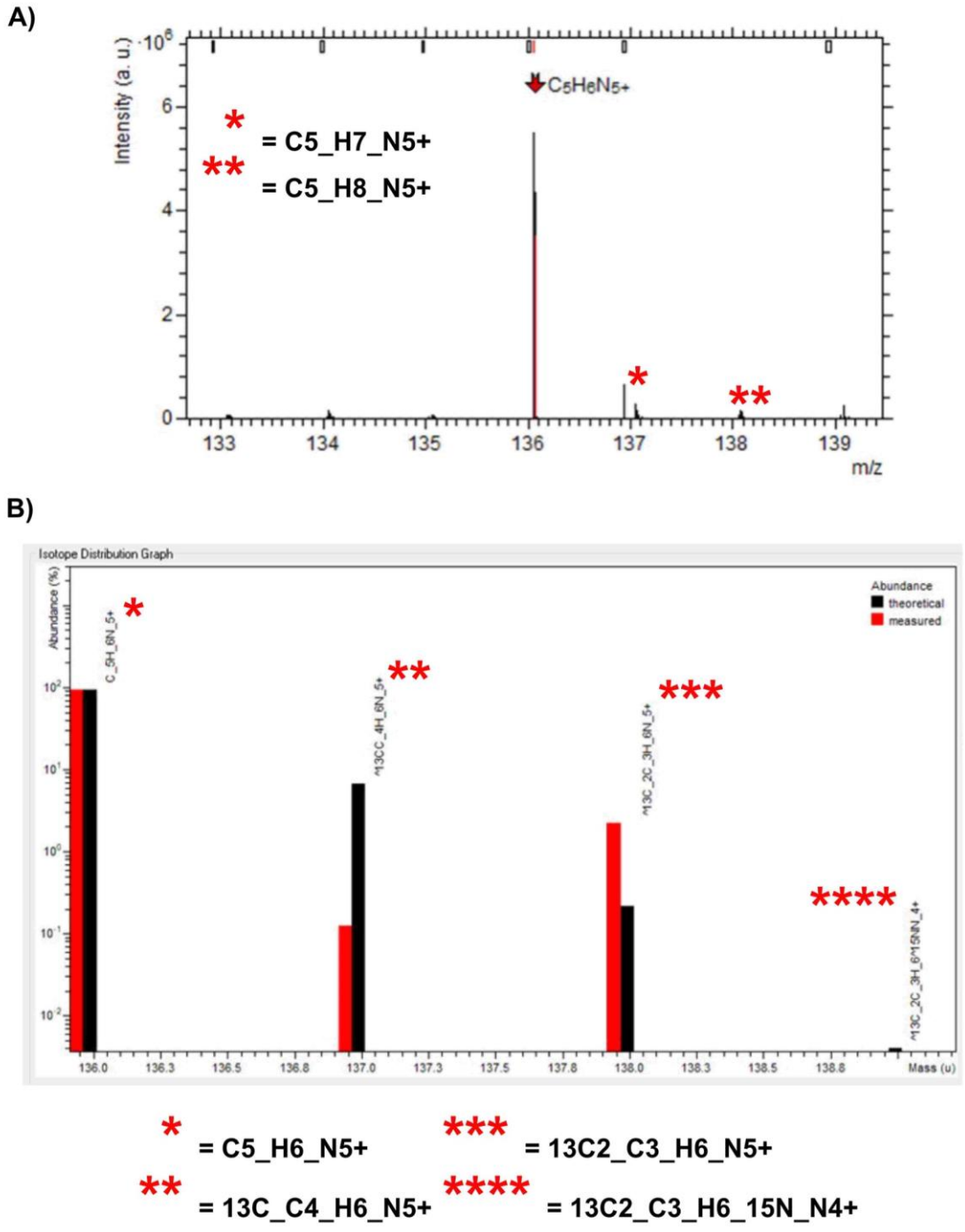

Figure 4.36 GCIB-orbitrap MS identifies the dominant positive ion fragment of adenine and distinguishes it from minor isotopes. 20µm 20keV Ar_{3000+} Orbitrap MS positive polarity mass spectrum from HCT116 CTL A10 spheroids. **A)** Mass spectrum of adenine (m/z 136.0472, $C_5H_6N_5^+$) indicating major and minor possible ions. **B)** Isotope distribution of the adenine ion. % abundance is displayed on a log scale. Minimum abundance = 0.0001%. Data analysis performed using SurfaceLab 7.1 (IONTOF GmbH). n=1.

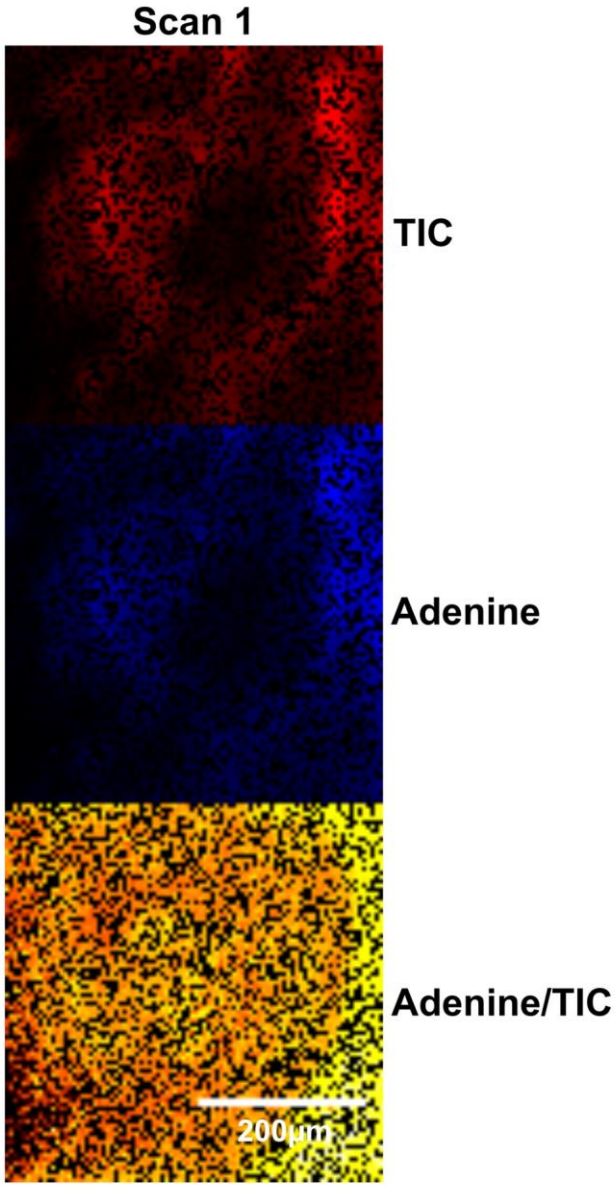

Figure 4.37 Cryo-orbiSIMS GCIB positive polarity orbitrap image analysis of adenine distribution within spheroids. 20µm 20keV Ar_{3000+} Orbitrap MS positive polarity images of adenine (m/z 136.0472, $C_5H_6N_5^+$) and total ion count (TIC) signals from HCT116 CTL A10 spheroids. Signal normalisation was performed using adenine/TIC. Scale bar represents 200 µm. Post-acquisition analysis was carried out using SurfaceLab 7.1 (IONTOF GmbH). n=1.

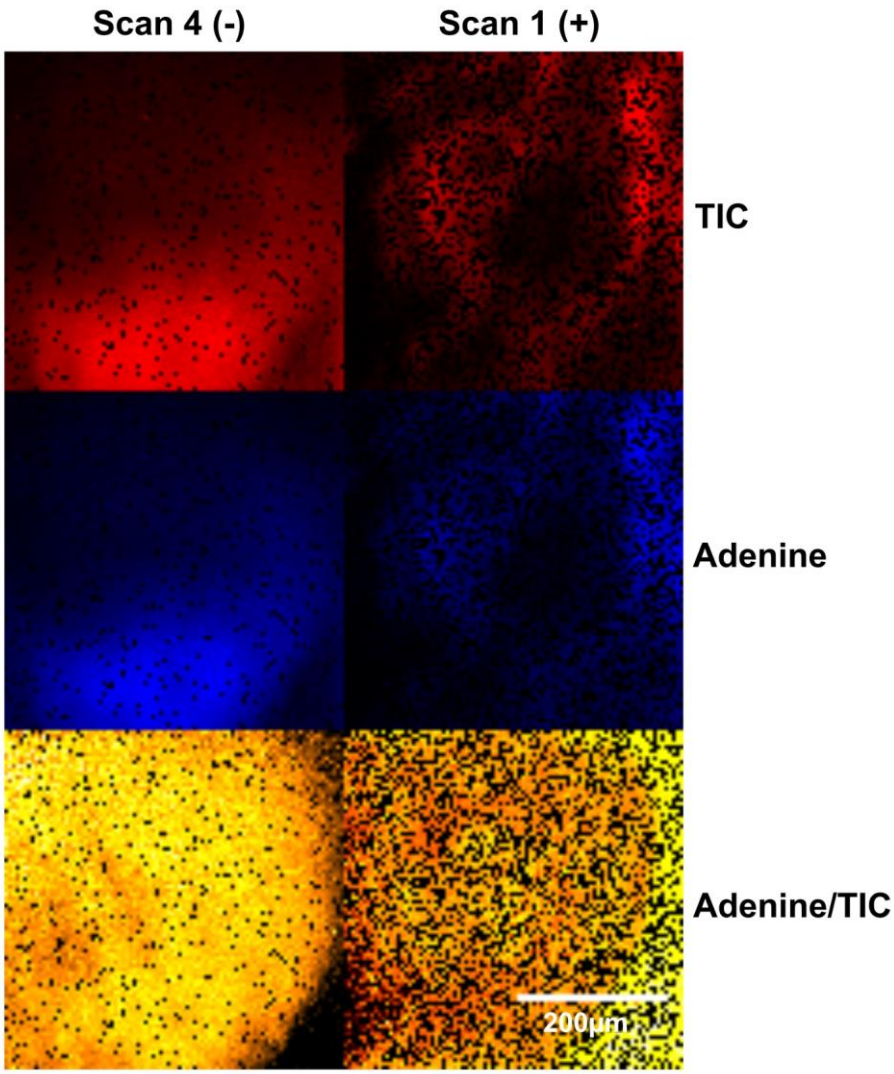

Figure 4.38 Comparison of negative and positive polarity orbitrap image analysis of adenine distribution within spheroids. 20µm 20keV Ar_{3000+} Orbitrap MS negative (m/z 134.0472, $C_5H_4N_5^-$) and positive (m/z 136.0472, $C_5H_6N_5^+$) polarity images of adenine and total ion count (TIC) signals from HCT116 CTL A10 spheroids. Signal normalisation was performed using adenine/TIC. Scale bar represents 200 µm. Post-acquisition analysis was carried out using SurfaceLab 7.1 (IONTOF GmbH). n=1.

4.3.15 Comparison of sample preparation methods for metabolite detection using orbiSIMS

Based on previous work suggesting that the use of cryogenic conditions for studying small molecules by SIMS is important for preventing the unwanted redistribution and migration of metabolites during analysis, it was decided to compare the use of cryogenic conditions for analysing the physiological distribution of metabolites in the spheroid samples compared to the standard freeze-drying preparative method[465]. Several metabolites including glucose and lactate were chosen for comparison along with several lipid molecules: SAPI and DOPI based on differences in the polarity of these molecules. Phosphate was also included due to its presence in the spheroid storage buffer, and adenine was used as the control. Cryogenic sample preparation greatly enhanced the signal detection for glucose, lactate, SAPI and DOPI but had no effect on adenine detection or overall TIC (figure 4.39a). On the other hand, phosphate detection was improved under the freeze-dried condition compared to the cryogenic sample. Cryogenic sample preparation improved the detection of glucose 18-fold, lactate 5-fold, SAPI 9-fold and DOPI 6-fold (figure 4.39b). Whereas freeze-drying improved phosphate detection by ~2.7-fold. Sample preparation had no effect on adenine signal detection (ratio 1.125) and further confirmed its applicability as a control marker for further analysis. Based on the improved detection seen for the majority of small molecules with the cryogenic method, it was decided to use cryogenic sample preparation for all downstream analysis.

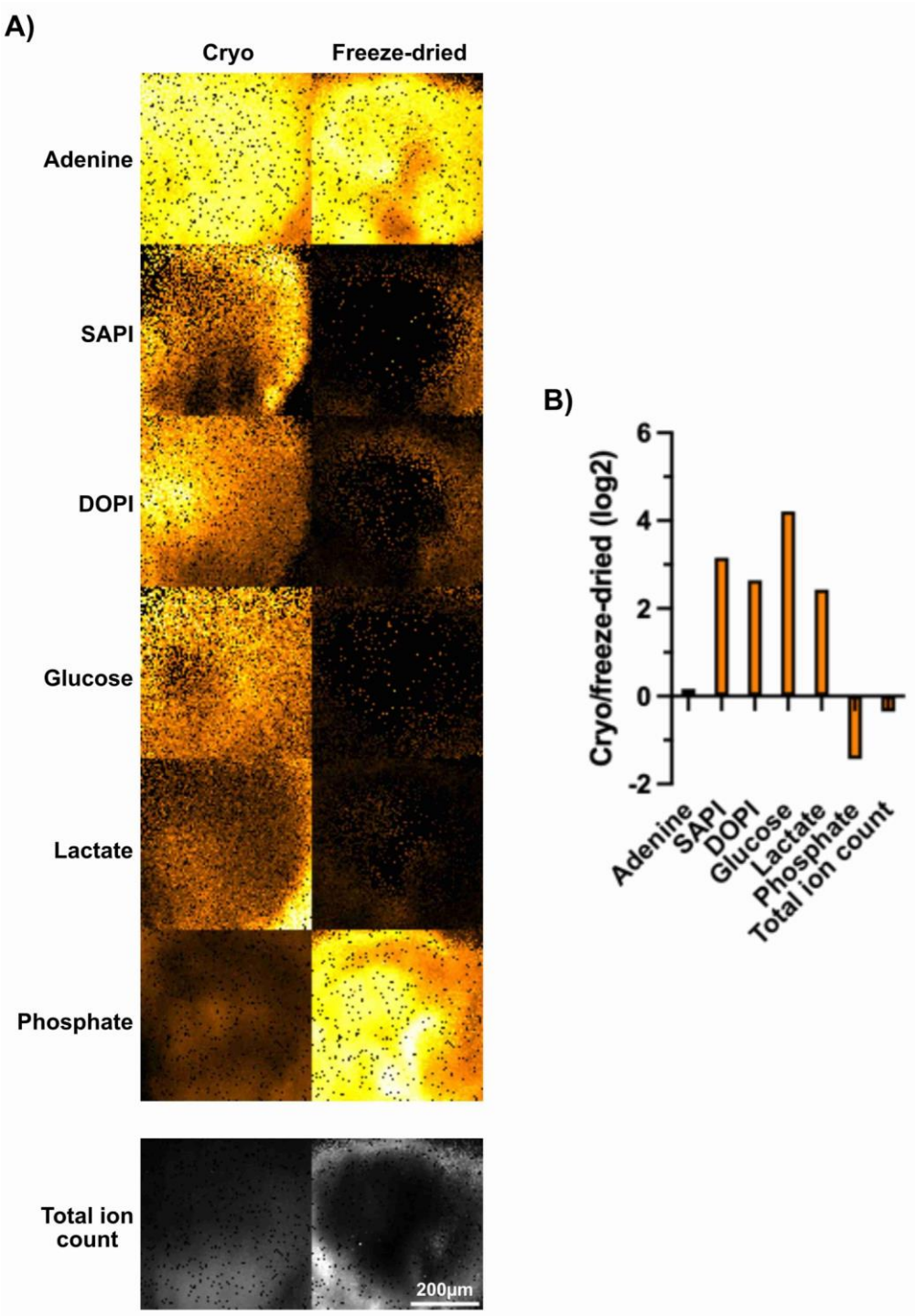

Figure 4.39 Cryogenic sample preparation for orbiSIMS analysis improves relative detection in a molecule-dependent manner. HCT116 CTL A10 and CTL A3 spheroids were prepared for orbiSIMS analysis by high-pressure freezing (cryo) and freeze-drying respectively. **A)** 20µm 20keV Ar_{3000+} Orbitrap MS negative polarity images of metabolites and lipids: adenine (m/z 134.0472, $C_5H_4N_5^-$), SAPI (m/z 885.5499, $C_{47}H_{82}PO_{13}^-$), DOPI (m/z 861.5500, $C_{45}H_{82}PO_{13}^-$), Glucose (m/z 179.0462, $C_6H_{11}O_6^-$), Lactate (m/z 89.0243, $C_3H_5O_3^-$) and phosphate (m/z 78.9588, PO_3^-) normalised to total ion count. **B.** Ratio of ion counts for cryogenic and freeze-dried conditions for a range of metabolites and lipids (log2 scale). Post-acquisition analysis was carried out using SurfaceLab 7.1 (IONTOF GmbH). n=1.

4.3.16 Development of a concentric circle analysis for analysing the spatial distribution of metabolites in spheroids

In order to analyse the spatial distribution of metabolites within the spheroids considering the oxygen gradient present from the periphery to the core, a novel analytical method was required. Initially, a line profiling analysis was developed to measure the ion counts for individual metabolites along defined lines extending from the spheroid core to the periphery (figure 4.40a). Three profiling lines were defined at set lengths and start and finish coordinates at 45° angles using ImageJ software. The ion counts for each metabolite of interest were measured along the three lines (figure 4.40b). The ion counts for each metabolite of interest were then normalised to the total molecule count along each line (sum of ion counts for that metabolite). The average ion counts from the three individual line measurements were plotted for each metabolite against the distance from the spheroid periphery to the spheroid core in order to represent the oxygen gradient. Figure 4.40c shows the profiles for adenine, lactate and glucose. The steady-state levels of adenine observed confirmed that adenine was not impacted by oxygen concentration and was therefore a suitable control marker. A peak in glucose was observed approximately 170 μm into the spheroid coinciding with the previously proposed oxygen diffusion limit, followed by a gradual decrease (figure 4.40c)[551]. Conversely, lactate levels remained low until approximately 300 μm into the spheroid where the levels rose rapidly as glucose levels decreased. Taken together these results provided evidence to support the use of the orbiSIMS for spatially defining metabolite changes along the oxygen gradient within spheroids. However, the use of line profiles meant a large proportion of the date collected from the mass spectrometry images was being ignored and so an alternative, improved method of analysis using concentric circles was developed.

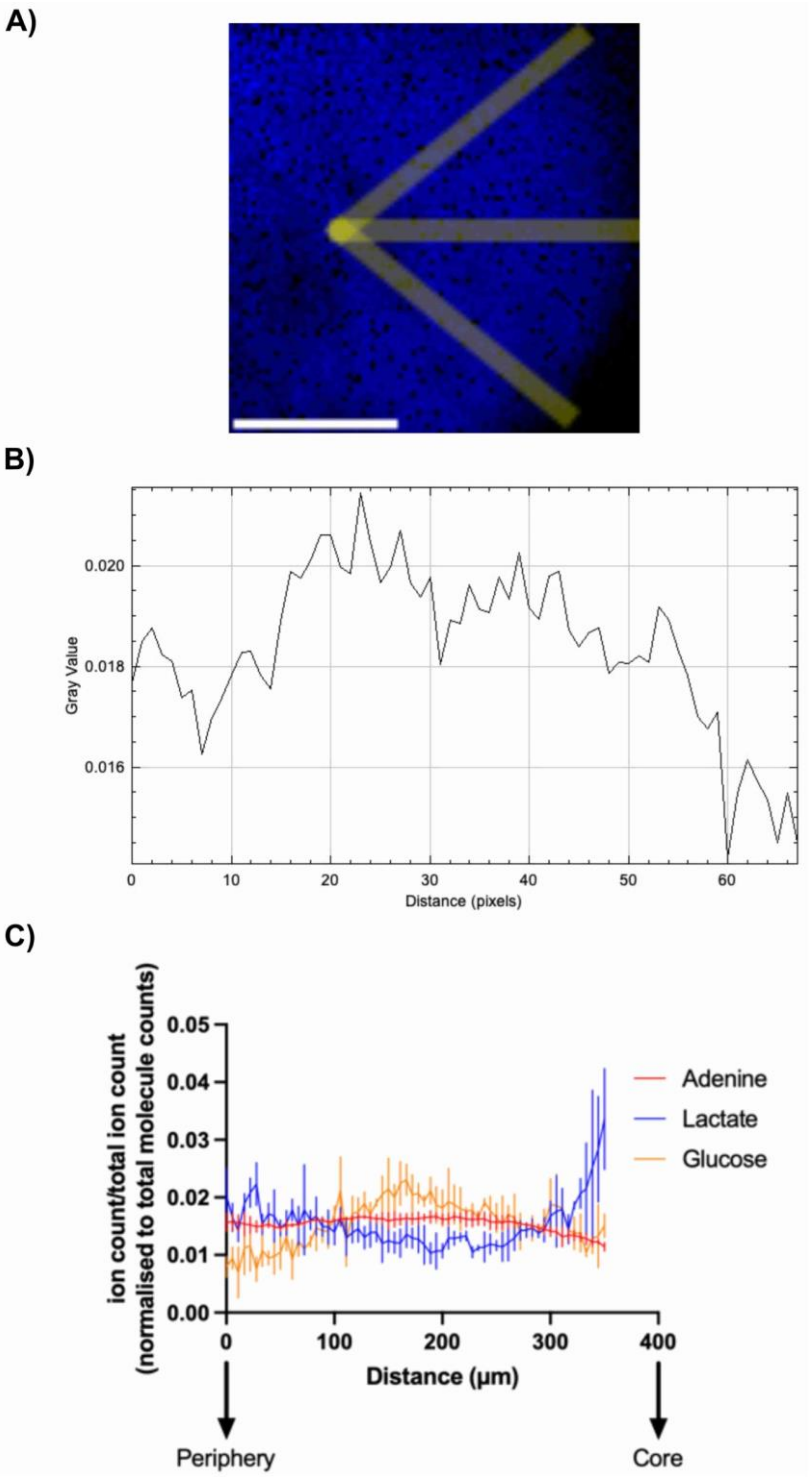

Figure 4.40 Line profiling analysis of spatial metabolite distribution in spheroids using orbiSIMS mass spectrometry imaging. HCT116 CTL A10 spheroids were prepared for orbiSIMS analysis by high-pressure freezing. **A)** 20μm 20keV Ar_{3000+} Orbitrap MS negative polarity image of adenine (m/z 134.0472, $C_5H_4N_5^-$) normalised to total ion count. The yellow lines represent the three line profiles used to measure the ion counts. Scale bar represents 200 μm. **B)** Example line profile for adenine ion count generated in ImageJ. **C)** Average ion count profiles for adenine, lactate and glucose normalised to total molecule counts over distance from the spheroid periphery to the core. Image analysis was carried out in ImageJ. n=1.

Due to the spherical nature of spheroids, it was decided that a concentric circle-based approach to analysing metabolite distribution would be more appropriate and representative of the changes in oxygen concentration across the spheroid. Therefore, a macro was scripted in ImageJ to generate a series of concentric circles centred around the spheroid core at defined intervals (figure 4.41a). The location of the spheroid core was defined based on the calculated radius of the outer circle using the curvature of an arc macro calculation described below. Importantly, the images were rotated 180 degrees prior to analysis so that the zones were defined starting at the periphery on the left-hand side and finishing at the core. The area of each circle along with mean signal intensity and raw integrated density (sum of pixel values) was then calculated for each metabolite of interest (figure 4.41a). The spheroid was then divided into zones by calculating the differences in area and raw integrated density between adjacent circles (figure 4.41b). Raw integrated density values were converted into density/pixel by dividing by zone area and then calculating the square root (figure 4.41b). The density/pixel for each metabolite within each zone was then plotted as shown for adenine in figure 4.41c. The lack of fluctuation in adenine signal across the zones again indicated that adenine was not influenced by changes in oxygen concentration and therefore served as an appropriate control.

A)

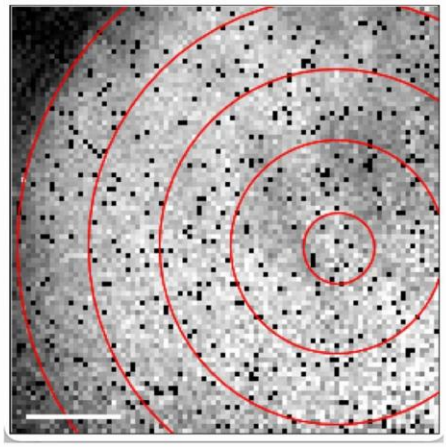

Circle	Area (pixels^2)	Mean	RawIntDen
1	7160	0.018	129.007
2	5658	0.019	104.705
3	3576	0.019	66.662
4	1508	0.018	27.762
5	164	0.018	2.989

B)

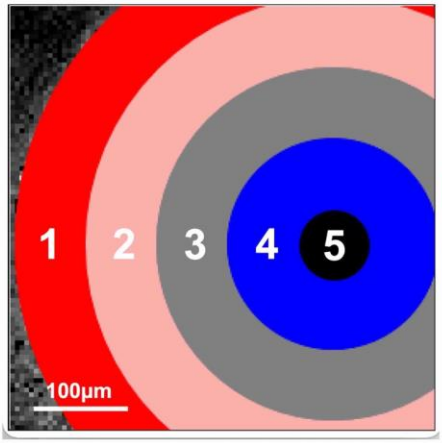

Zone	Area (pixels^2)	RawIntDen	Density/pixel^2	Density/pixel
1	1502	24.302	0.01617976	0.127199687
2	2082	38.043	0.018272334	0.135175199
3	2068	38.9	0.018810445	0.137151175
4	1344	24.773	0.018432292	0.135765576
5	164	2.989	0.01822561	0.135002258

C)

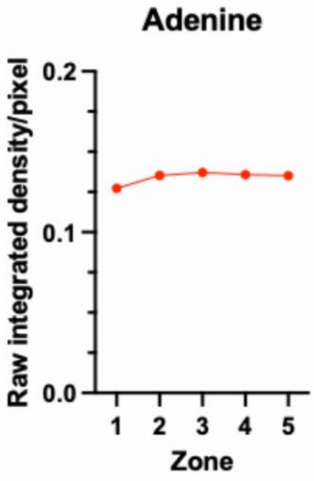

Figure 4.41 Concentric circle analysis of spatial metabolite distribution in spheroids using orbiSIMS mass spectrometry imaging. HCT116 CTL A10 spheroids were prepared for orbiSIMS analysis by high-pressure freezing. **A)** 20µm 20keV Ar_{3000+} Orbitrap MS negative polarity image of adenine (m/z 134.0472, $C_5H_4N_5^-$) normalised to total ion count. The red circles represent the macro-generated concentric circles used to measure signal density. Scale bar represents 100 µm. The table shows the area of each circle along with the mean intensity and raw integrated signal density. **B)** The division of the spheroid image into zones based on the difference in area between adjacent circles. The table shows the area of each zone along with the raw integrated density, density/pixel^2 and density/pixel. **C)** Plot of integrated signal density/pixel for adenine in each zone. Image analysis was carried out in ImageJ. n=1.

However, it was then decided that increasing the number of circles in the analysis would improve the spatial information obtained regarding the distribution of metabolites along the oxygen gradient in the spheroids. Therefore, the concentric circle macro was adapted to generate 10 concentric circles instead and compared with the results obtained from the 5-circle analysis (figure 4.42a). The radii of each circle were also calculated based on a macro for calculating the radius of a circle from the curvature of an arc, as the orbiSIMS images did not encompass the entire spheroid: https://gist.github.com/lacan/42f4abe856f697e664d1062c200fd21f (figure 4.42b). This enabled the calculated density/pixel for each metabolite of interest to be plotted over distance in order to interpret the spatial distribution of the metabolites more accurately. The distances plotted for the signal density values were defined as the mid-points of each zone (between adjacent circles). Importantly. the distance between circles in the 5-circle analysis was calculated to be 75 μm and 35 μm for the 10-circle analysis. Identifying the most physiologically relevant increment in relation to the changes in oxygen concentration would be important for the development of this method.

Figure 4.42c shows the results obtained comparing the 5-circle and 10-circle analyses for adenine. It is worth noting that the edge of the spheroids appeared slightly distorted which led to an underestimation of the signal at the spheroid edge compared with the near periphery approximately 50 μm into the spheroid. Despite this, the overall observed distribution of adenine was similar between the two analyses as expected however, increasing the number of data points obtained with the 10-circle analysis provided more spatial information and so was chosen for the downstream analysis of hypoxia and HIF-regulated metabolites.

A)

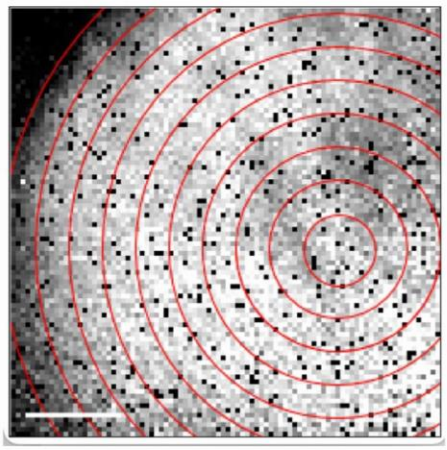

B)

x5	Radius (pixels)	Radius (µm)
Circle 1	67.5	337.5
Circle 2	52.5	262.3
Circle 3	37.5	187.4
Circle 4	22.5	112.4
Circle 5	7.5	37.4

x10	Radius (pixels)	Radius (µm)
Circle 1	70.5	352.5
Circle 2	63.5	317.4
Circle 3	56.5	282.3
Circle 4	49.5	247.3
Circle 5	42.5	212.4
Circle 6	35.5	177.4
Circle 7	28.5	142.4
Circle 8	21.5	107.4
Circle 9	14.5	72.3
Circle 10	7.5	37.4

C)

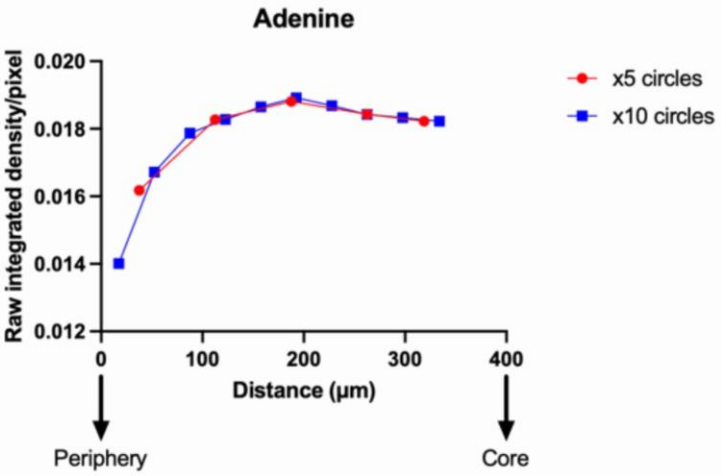

Figure 4.42 A 10-circle concentric circle analysis improves the analysis of the spatial metabolite distribution in spheroids using orbiSIMS mass spectrometry imaging. HCT116 CTL A10 spheroids were prepared for orbiSIMS analysis by high-pressure freezing. **A)** 20µm 20keV Ar_{3000+} Orbitrap MS negative polarity image of adenine (m/z 134.0472, $C_5H_4N_5^-$) normalised to total ion count. The red circles represent the macro-generated concentric circles used to measure signal density. Scale bar represents 100 µm. **B)** The radii of each circle in the 5-circle and 10-circle analysis calculated based on the curvature of an arc. **C)** Plot of integrated signal density/pixel for adenine over distance from the spheroid periphery to the core. Image analysis carried out in ImageJ. n=1.

4.3.17 Investigating the spatial distribution of hypoxia-regulated metabolites using orbiSIMS

In order to investigate the impact of the oxygen gradient on the spatial distribution of metabolites, several hypoxia-upregulated metabolites including *cis*-aconitate, NAD^+ and AMP were selected for analysis along with several hypoxia-downregulated metabolites including fumarate, malate and phosphocreatine based on previous work investigating the role of hypoxia and HIF-1α in the regulation of metabolite levels in hypoxic HCT116 spheroids and 2-D cell culture[371]. Figure 4.43 displays the orbitrap negative polarity MS images for the selected metabolites along with total ion count and adenine as a control marker in the HCT116 CTL A10, HIF-1α knockout g57 and HIF-2α knockout g81 spheroids. In general, the signal outputs from the HIF-1α g57 knockout spheroid data were low compared to those obtained with the CTL and HIF-2α knockout samples. However, in some cases, it was still possible to visualise the periphery of the spheroid (see malate for example). The lack of sphericity seen in the HIF-2α knockout spheroid images was possibly due to some compression of the spheroid during the high-pressure freezing process.

The optimised concentric circle analysis method described in 4.3.16 was used to measure the spatial distribution of the metabolites in figure 4.43 in relation to the distance from the periphery to the core of the spheroid to mimic the decreasing oxygen concentration. Figures 4.44 and 4.45 show the metabolite profiles for the hypoxia-upregulated and hypoxia-downregulated metabolites respectively along with adenine. As mentioned previously, the low signal obtained with the HIF-1α knockout sample led to a reduction in the signal density outputs collected during the analysis. Adenine levels remained constant across the spheroids as expected. With the hypoxia-upregulated metabolites, *cis*-aconitate levels initially decreased followed by a substantial increase around 200 μm into the core of the CTL spheroid whereas a generally negative trend was observed in *cis*-aconitate levels in the HIF-1α and HIF-2α knockout spheroids (figure 4.44b). NAD^+ levels increased gradually down the oxygen gradient for around 200 μm before decreasing, except in the HIF-1α knockout which displayed a negative trend (figure 4.44c). AMP levels showed a decreasing trend in all three experimental conditions (figure 4.44d).

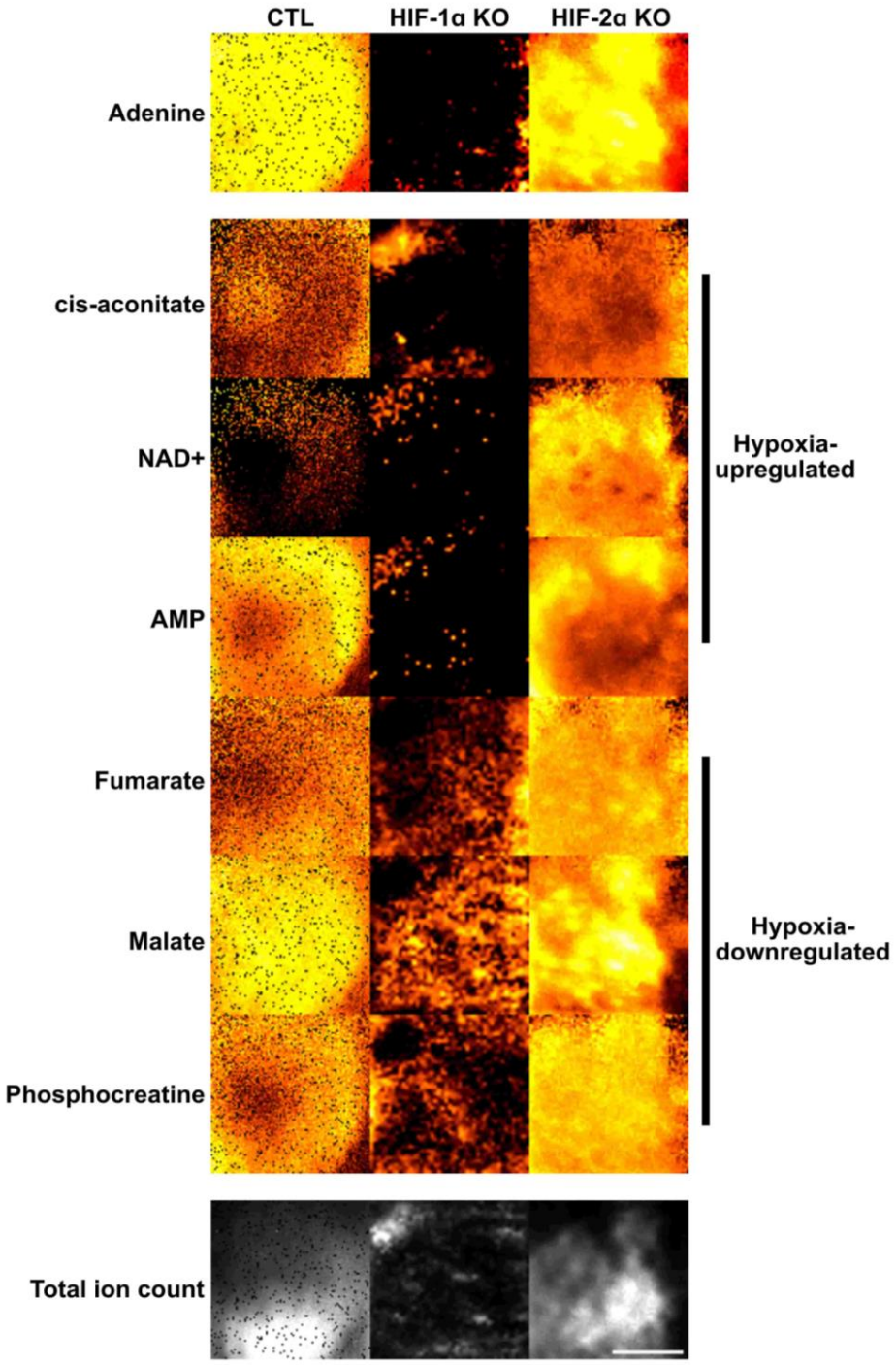

Figure 4.43 Hypoxia regulates the spatial distribution of metabolites across the oxygen gradient in a CRC spheroid model. 20μm 20keV Ar_{3000+} Orbitrap MS negative polarity images of adenine (*m/z* 134.0472, $C_5H_4N_5^-$), *cis*-aconitate (*m/z* 173.0567, $C_6H_5O_6^-$), AMP (*m/z* 346.0558, $C_{10}H_{13}N_5O_7P^-$), NAD^+ (*m/z* 662.1022, $C_{21}H_{26}N_7O_{14}P_2^-$), fumarate (*m/z* 115.0037, $C_4H_3O_4^-$), malate (*m/z* 133.0156, $C_4H_5O_5^-$), phosphocreatine (*m/z* 210.0884, $C_4H_9N_3O_5P^-$) and total ion count (TIC) signals from HCT116 CTL A10, HIF-1α knockout g57 and HIF-2α knockout g81 spheroids. Signal normalisation was performed by dividing by TIC. Scale bar represents 200 μm. Image analysis was carried out in ImageJ. n=1.

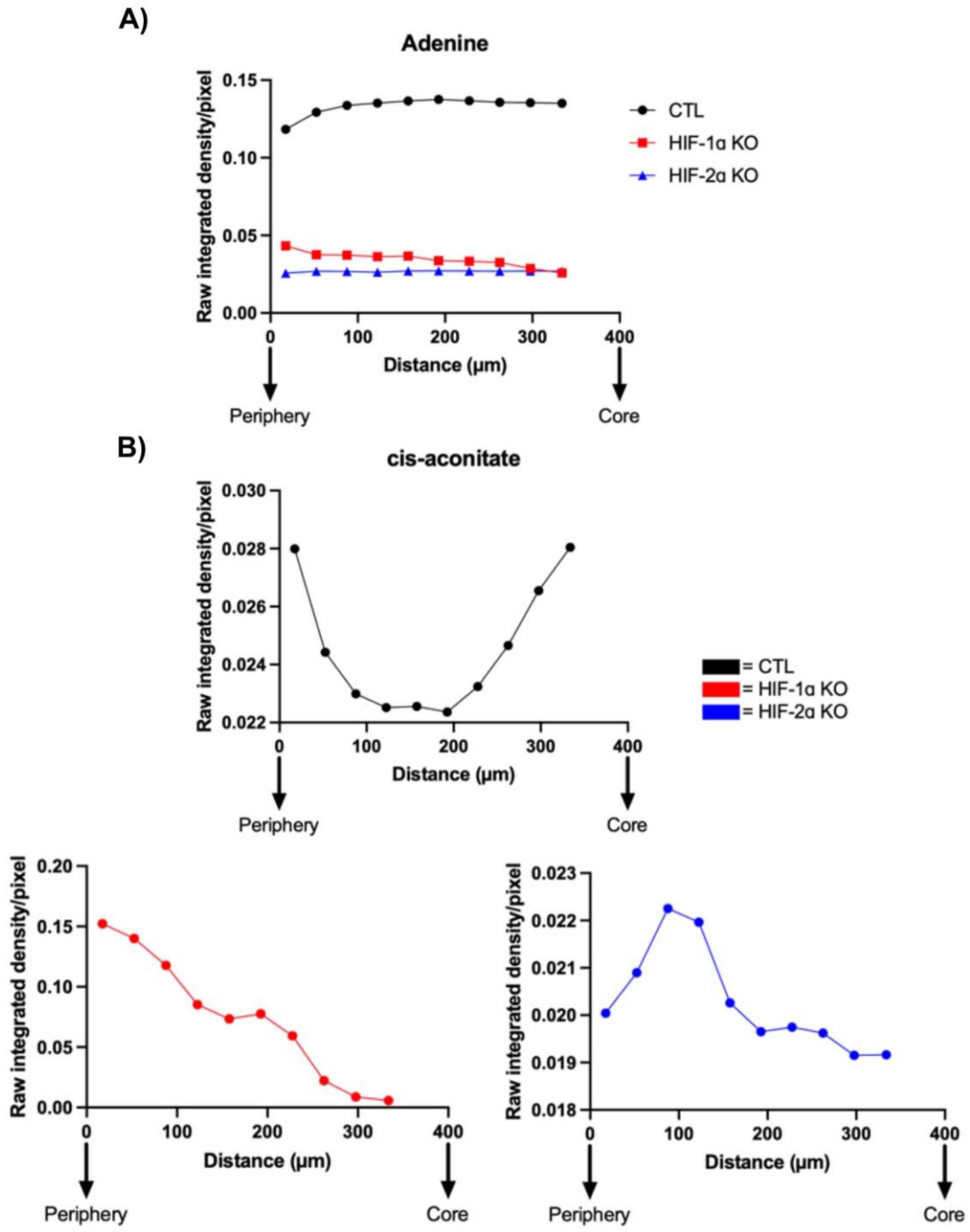
A)
Adenine
Raw integrated density/pixel
0.15
0.10
0.05
0.00
0
100
200
300
400
Distance (µm)
Periphery
Core
CTL
HIF-1α KO
HIF-2α KO
B)
cis-aconitate
Raw integrated density/pixel
0.030
0.028
0.026
0.024
0.022
0
100
200
300
400
Distance (µm)
Periphery
Core
= CTL
= HIF-1α KO
= HIF-2α KO
Raw integrated density/pixel
0.20
0.15
0.10
0.05
0.00
0
100
200
300
400
Distance (µm)
Periphery
Core
Raw integrated density/pixel
0.023
0.022
0.021
0.020
0.019
0.018
0
100
200
300
400
Distance (µm)
Periphery
Core

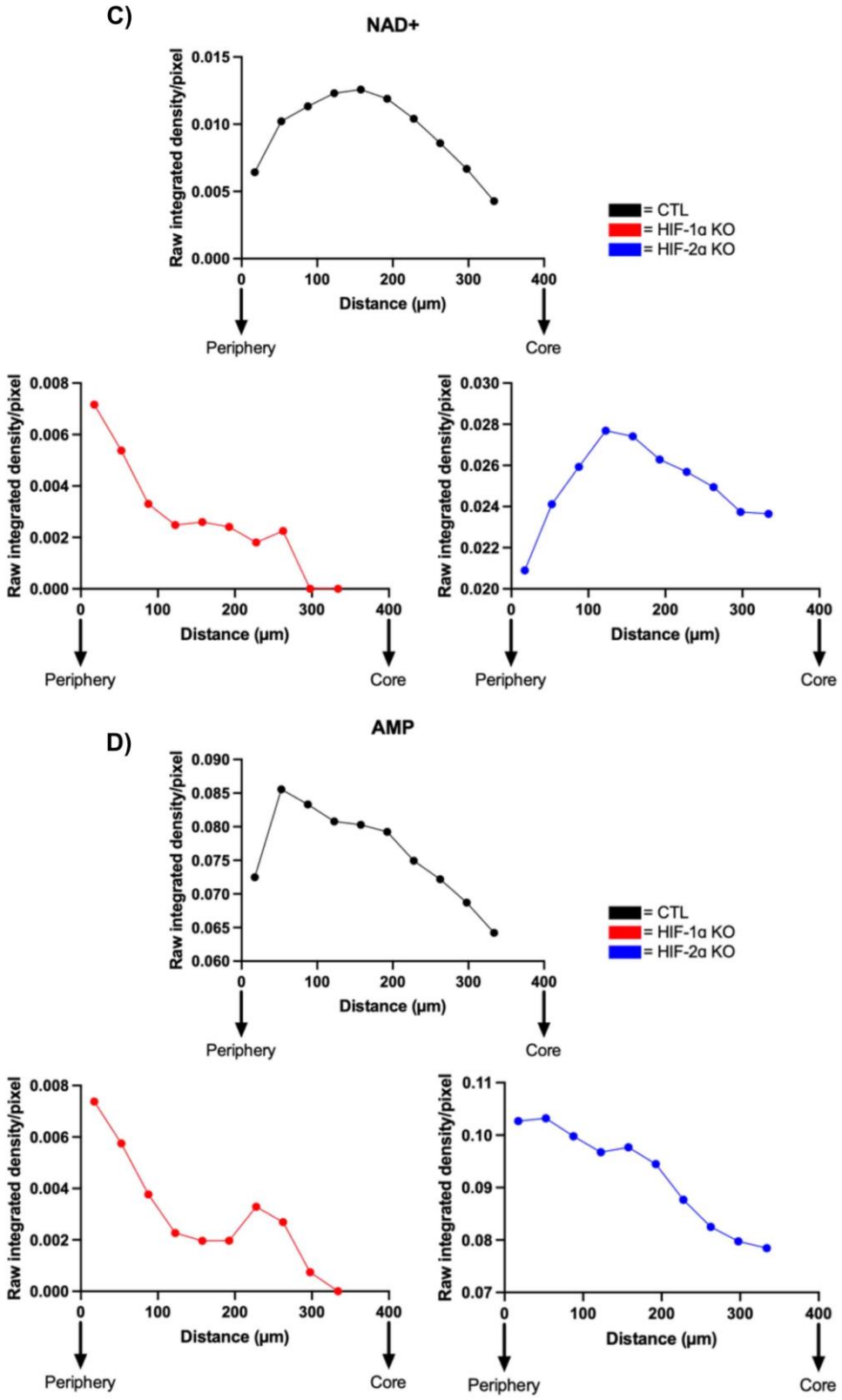

Figure 4.44 The oxygen gradient regulates the spatial distribution of hypoxia-induced metabolites in a CRC spheroid model. A-D) Concentric circle analysis was employed on orbitrap MS images of adenine, *cis*-aconitate, NAD^+ and AMP to measure the change in metabolite signal across the oxygen gradient in HCT116 CTL A10, HIF-1α knockout g57 and HIF-2α knockout g81 spheroids. Image analysis was performed in ImageJ using an in-house macro. n=1.

With the hypoxia-downregulated metabolites, fumarate levels decreased down the oxygen gradient in the CTL spheroid however, this was reversed with HIF-1α knockout (figure 4.45b). Similarly, malate levels displayed an increasing trend in both the HIF-1α and HIF-2α knockout spheroids, and to a lesser extent in the CTL, until around 300 μm (figure 4.45c). Phosphocreatine levels decreased substantially going from the periphery to the core in both the CTL and HIF-1α knockout conditions but increased with HIF-2α knockout (figure 4.45d).

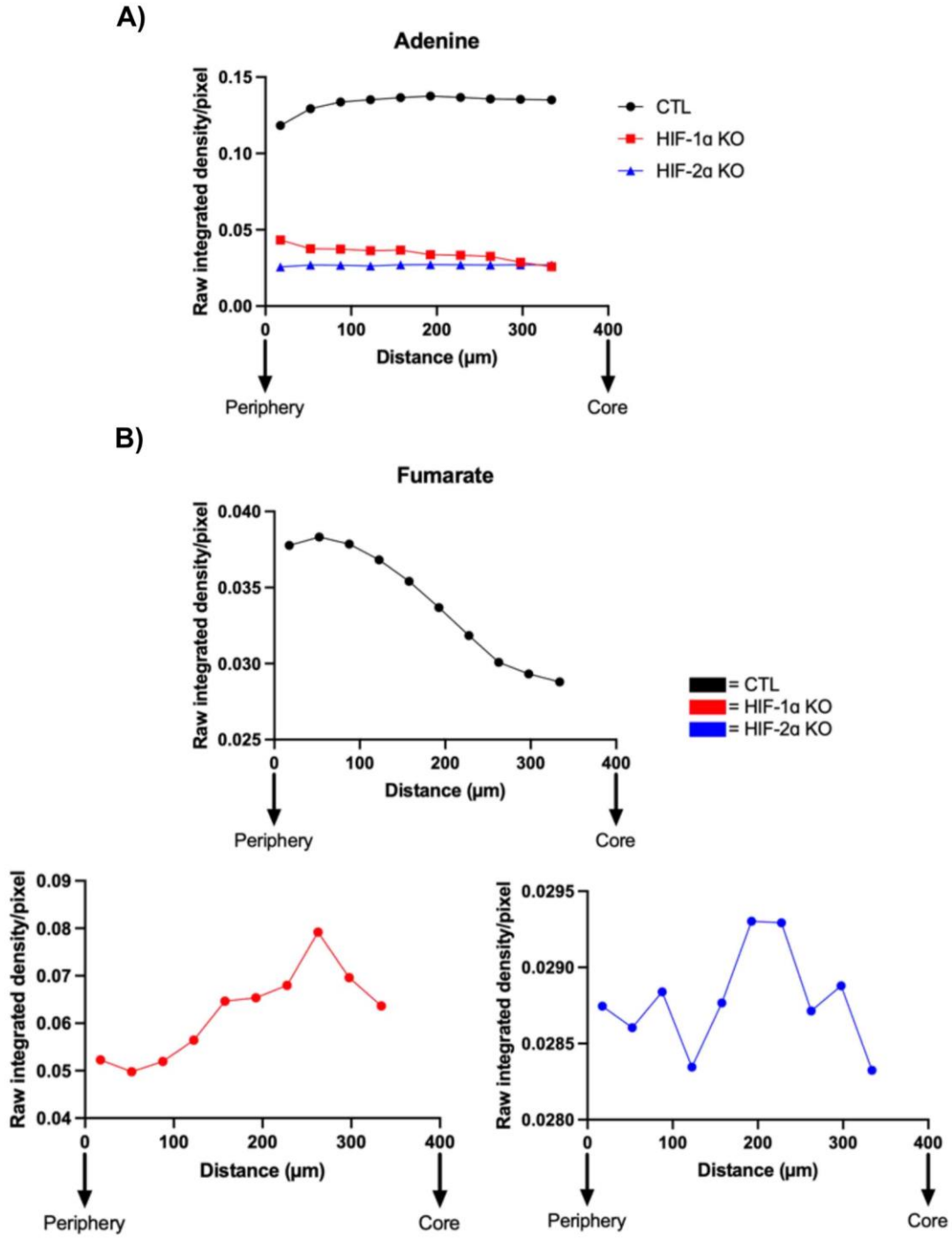
A)
Adenine
Raw integrated density/pixel
0.15
0.10
0.05
0.00
0
100
200
300
400
Distance (μm)
Periphery
Core
CTL
HIF-1α KO
HIF-2α KO
B)
Fumarate
Raw integrated density/pixel
0.040
0.035
0.030
0.025
0
100
200
300
400
Distance (μm)
Periphery
Core
= CTL
= HIF-1α KO
= HIF-2α KO
Raw integrated density/pixel
0.09
0.08
0.07
0.06
0.05
0.04
0
100
200
300
400
Distance (μm)
Periphery
Core
Raw integrated density/pixel
0.0295
0.0290
0.0285
0.0280
0
100
200
300
400
Distance (μm)
Periphery
Core

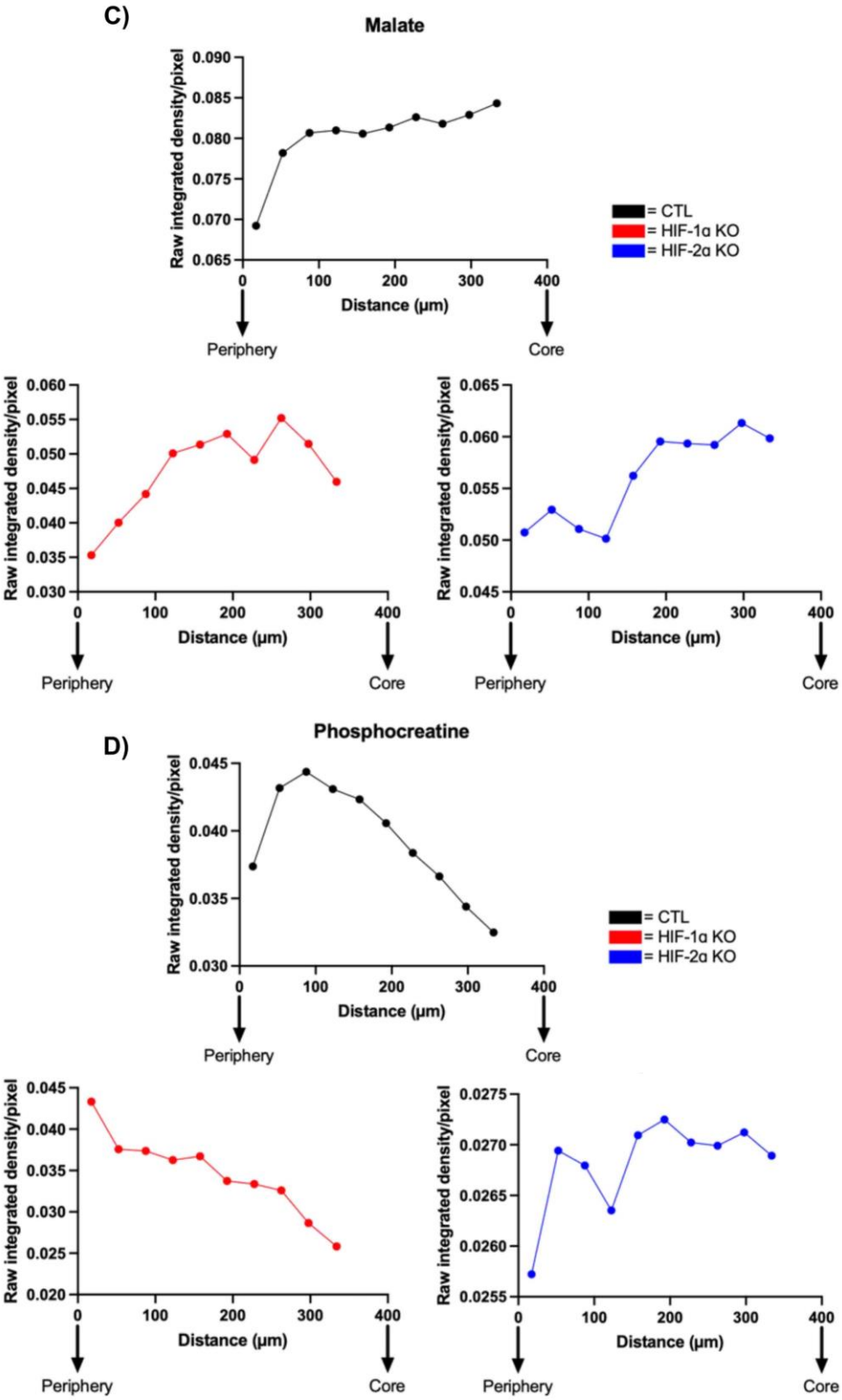

Figure 4.45 The oxygen gradient regulates the spatial distribution of downregulated metabolites in hypoxia in a CRC spheroid model. A-D) Concentric circle analysis was employed on orbitrap MS images of adenine, fumarate, malate and phosphocreatine to measure the change in metabolite signal across the oxygen gradient in HCT116 CTL A10, HIF-1α knockout g57 and HIF-2α knockout g81 spheroids. Image analysis was performed in ImageJ using an in-house macro. n=1.

4.3.18 Investigating the spatial distribution of acidosis-regulated metabolites using orbiSIMS

Acidosis is another phenotype often seen in solid tumours that is commonly observed in conjunction with hypoxia and which generates a pH gradient similar to that of oxygen[552]. It has also been shown to be important in the regulation of cancer cell metabolism[552]. Therefore, in order to investigate the impact of the oxygen gradient on the spatial distribution of acidosis-associated metabolites, several metabolites proposed to be upregulated in acidic conditions, including phenylalanine, palmitic acid and acetyl-CoA were selected for analysis along with several acidosis-downregulated metabolites including alanine, threonine and glutamic acid[553]. Figure 4.46 displays the orbitrap MS images for the selected metabolites along with total ion count and adenine as a control marker in the HCT116 CTL A10, HIF-1α knockout g57 and HIF-2α knockout g81 spheroids. Visually, the potential central necrotic core of the spheroid was identified, particularly in the CTL.

Figures 4.47 and 4.48 display the metabolic profiles for the acidosis-upregulated and acidosis-downregulated metabolites respectively. With the acidosis-upregulated metabolites, going from the periphery to the core, an overall increasing trend in phenylalanine was observed in all three conditions but decreased after ~ 300 μm in the CTL and HIF-1α knockout conditions (figure 4.47b). Palmitic acid levels increased down the oxygen gradient in the CTL spheroid and this was attenuated with both HIF-1α and HIF-2α knockout (figure 4.47c). Similarly, acetyl-CoA levels showed an increasing trend in the CTL condition which was reversed with knockout of both HIF-1α and HIF-2α (figure 4.47d).

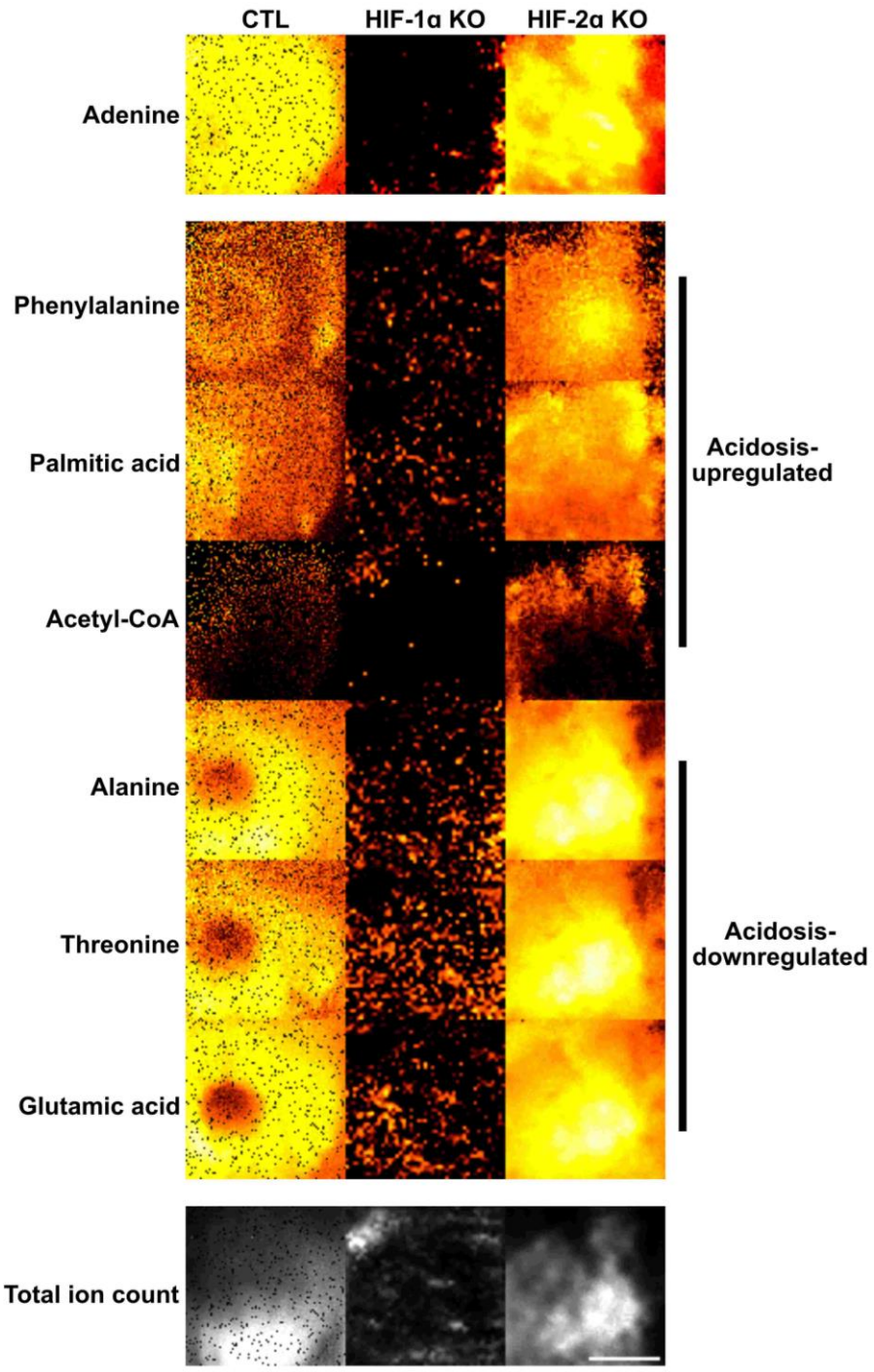

Figure 4.46 Hypoxia regulates the spatial distribution of acidosis-associated metabolites across the oxygen gradient in a CRC spheroid model. 20μm 20keV Ar_{3000+} Orbitrap MS negative polarity images of adenine (*m/z* 134.0472, $C_5H_4N_5^-$), phenylalanine (*m/z* 164.0718, $C_9H_{10}NO_2^-$), palmitic acid (*m/z* 255.2333, $C_{16}H_{31}O_2^-$), acetyl-CoA (*m/z* 796.3861, $C_{23}H_{37}N_7O_{17}P_3S^-$), alanine (*m/z* 88.0404, $C_3H_6NO_2^-$), threonine (*m/z* 118.0512, $C_4H_8NO_3^-$), glutamic acid (*m/z* 146.0457, $C_5H_8NO_4^-$) and total ion count (TIC) signals from HCT116 CTL A10, HIF-1α knockout g57 and HIF-2α knockout g81 spheroids. Signal normalisation was performed by dividing by TIC. Scale bar represents 200 μm. Image analysis was carried out in ImageJ. n=1.

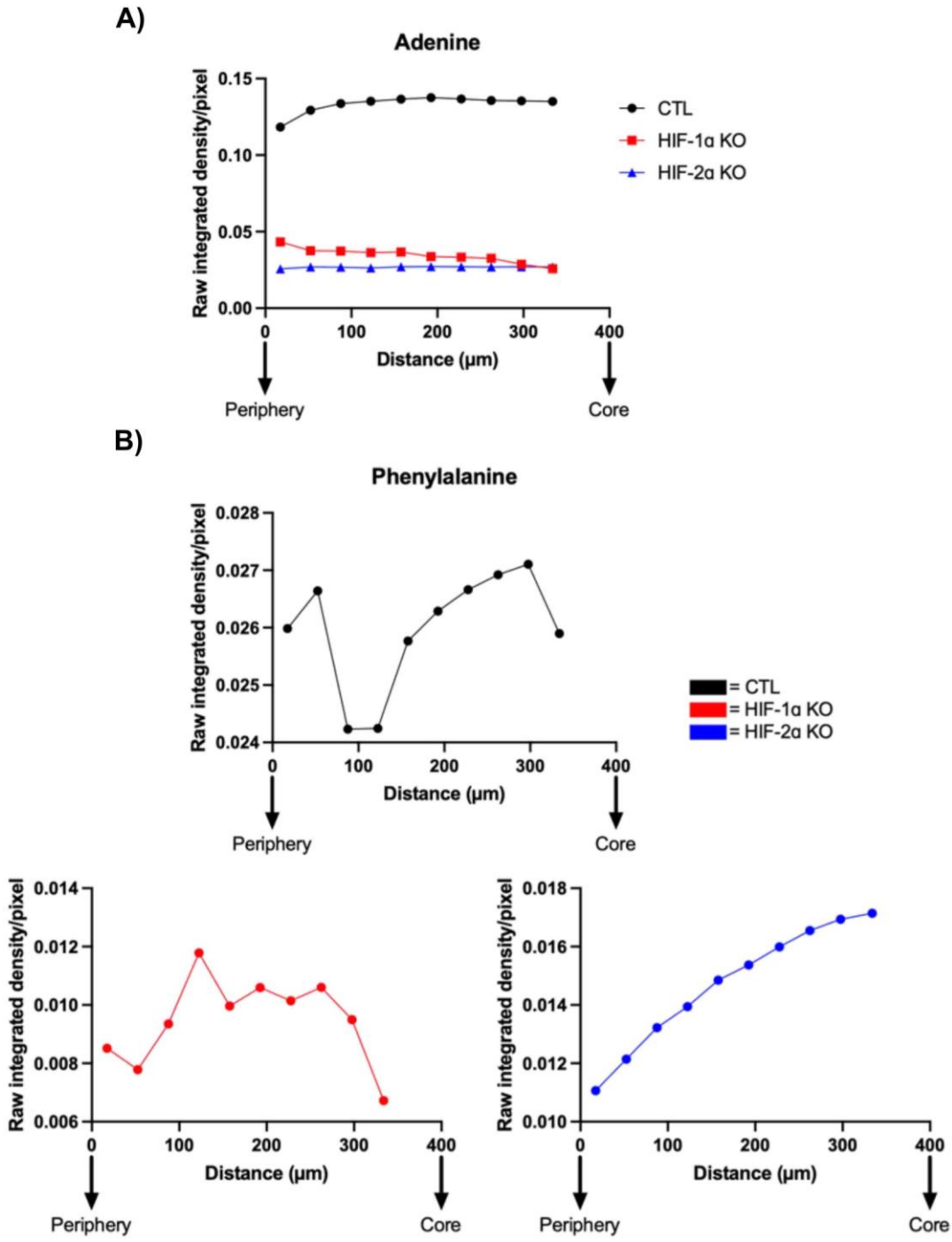
A)
Adenine
Raw integrated density/pixel
0.15
0.10
0.05
0.00
0
100
200
300
400
Distance (µm)
Periphery
Core
CTL
HIF-1α KO
HIF-2α KO
B)
Phenylalanine
Raw integrated density/pixel
0.028
0.027
0.026
0.025
0.024
0
100
200
300
400
Distance (µm)
Periphery
Core
= CTL
= HIF-1α KO
= HIF-2α KO
Raw integrated density/pixel
0.014
0.012
0.010
0.008
0.006
0
100
200
300
400
Distance (µm)
Periphery
Core
Raw integrated density/pixel
0.018
0.016
0.014
0.012
0.010
0
100
200
300
400
Distance (µm)
Periphery
Core

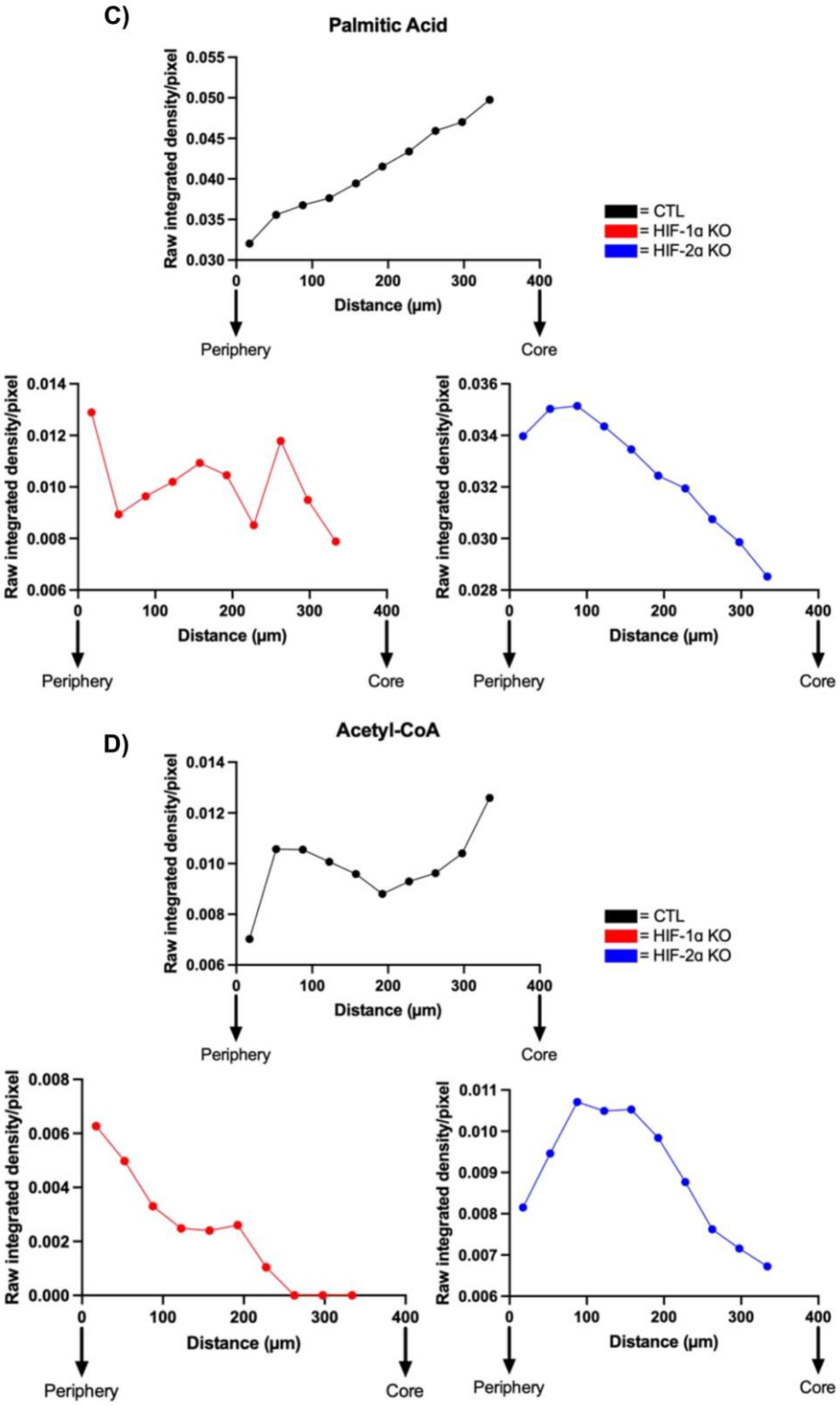

Figure 4.47 The oxygen gradient regulates the spatial distribution of acidosis-induced metabolites in a CRC spheroid model. A-D) Concentric circle analysis was employed on orbitrap MS images of adenine, phenylalanine, palmitic acid and acetyl-CoA to measure the change in metabolite signal across the oxygen gradient in HCT116 CTL A10, HIF-1α knockout g57 and HIF-2α knockout g81 spheroids. Image analysis was performed in ImageJ using an in-house macro. n=1.

With the acidosis-downregulated metabolites, alanine levels decreased from the periphery to the core of the CTL spheroid however, the opposite trend was seen with HIF-2α knockout (figure 4.48b). Similar results were also observed for both threonine and glutamic acid where the decrease in metabolite levels was reversed by HIF-2α knockout (figures 4.48c and 4.48d). Alanine and threonine levels displayed a similar pattern in the HIF-1α knockout spheroid where an initial decrease was observed at the periphery followed by an increase and then a sharp decrease around 300 μm. A gradual decreasing trend was seen for glutamic acid in the HIF-1α knockout spheroid.

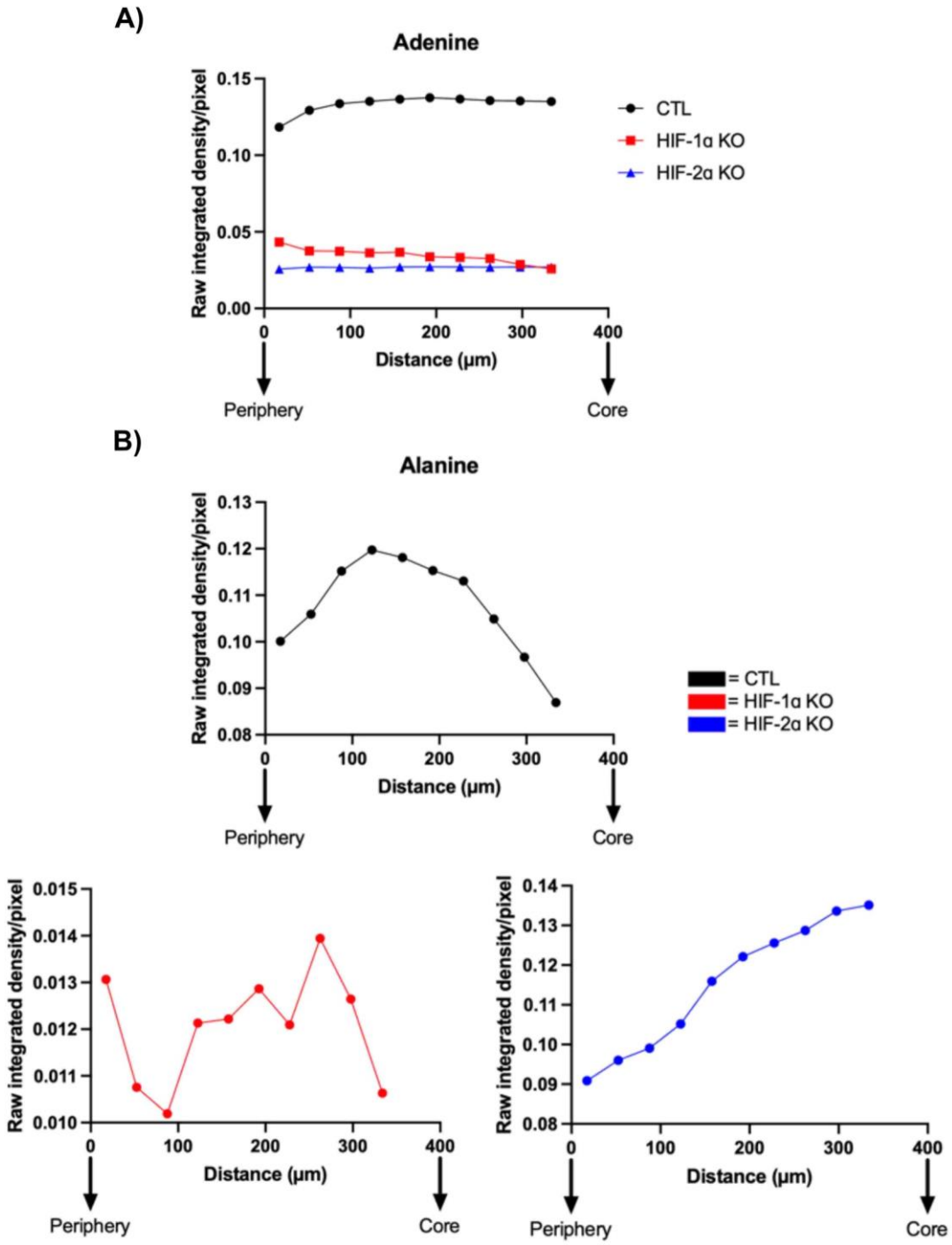
A)
Adenine
Raw integrated density/pixel
0.15
0.10
0.05
0.00
0
100
200
300
400
Distance (µm)
Periphery
Core
CTL
HIF-1α KO
HIF-2α KO
B)
Alanine
Raw integrated density/pixel
0.13
0.12
0.11
0.10
0.09
0.08
0
100
200
300
400
Distance (µm)
Periphery
Core
= CTL
= HIF-1α KO
= HIF-2α KO
Raw integrated density/pixel
0.015
0.014
0.013
0.012
0.011
0.010
0
100
200
300
400
Distance (µm)
Periphery
Core
Raw integrated density/pixel
0.14
0.13
0.12
0.11
0.10
0.09
0.08
0
100
200
300
400
Distance (µm)
Periphery
Core

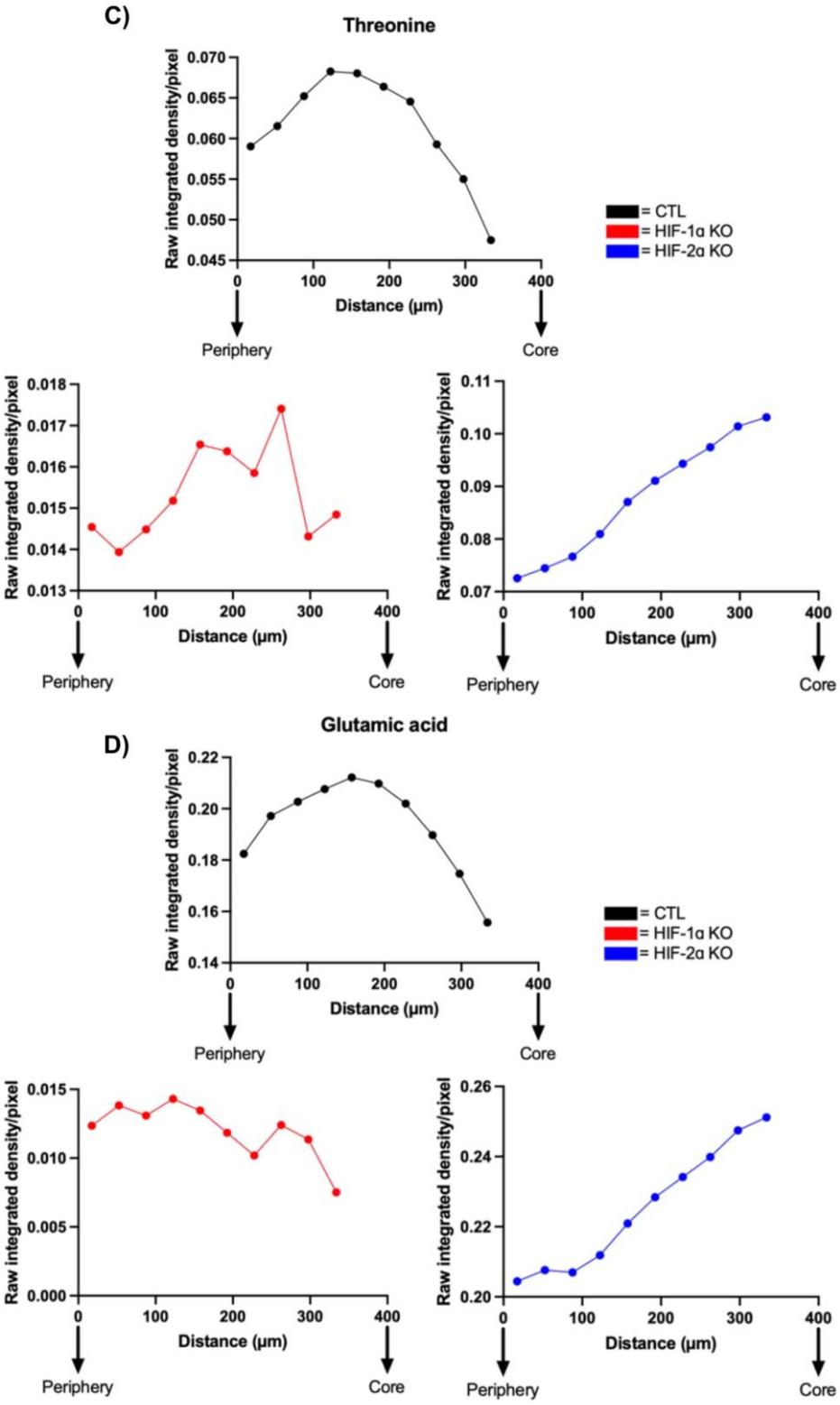

Figure 4.48 The oxygen gradient regulates the spatial distribution of downregulated metabolites in acidosis in a CRC spheroid model. A-D) Concentric circle analysis was employed on orbitrap MS images of adenine, alanine, threonine and glutamic acid to measure the change in metabolite signal across the oxygen gradient in HCT116 CTL A10, HIF-1α knockout g57 and HIF-2α knockout g81 spheroids. Image analysis was performed in ImageJ using an in-house macro. n=1.

4.3.18 Investigating the impact of HIF-1α and HIF-2α knockout on the spatial distribution of HIF-1α-regulated metabolites

Based on the RNA-sequencing results presented earlier in this chapter it was decided to investigate whether the orbiSIMS approach could be used to identify and spatially resolve HIF-1α and HIF-2α-dependent metabolic changes. Therefore, glycolytic intermediates that are the end products of the most upregulated HIF-1α-dependent differentially expressed metabolic genes, identified in the RNA-sequencing data, were selected for orbiSIMS analysis. This included lactate, F-2,6-BP, dihydroxyacetone phosphate (DHAP), fructose-6-phosphate (F-6-P), and phosphoenolpyruvate (PEP) as well as adenine as a control. Figure 4.49 displays the orbitrap MS images for the selected metabolites along with total ion count and adenine as a control marker in the HCT116 CTL A10, HIF-1α knockout g57 and HIF-2α knockout g81 spheroids.

Figure 4.50 displays the metabolic profiles for the HIF-1α-regulated metabolites. F-6-P levels increased down the oxygen gradient in the CTL spheroid but decreased in both the HIF-1α and HIF-2α knockout spheroids. The observed HIF-1α knockout decrease was sharpest around 250 μm (figure 4.50a). F-2,6-BP levels displayed a slight gradual decrease in the CTL spheroid however, a sharp decrease in F-2,6-BP levels was observed in the HIF-1α knockout and, to a lesser extent, in the HIF-2α knockout (figure 4.50b). A substantial reduction in DHAP levels was observed in the CTL spheroid from the periphery. Whereas DHAP levels increased in the HIF-1α and HIF-2α knockout for the first ~ 150 μm followed by a sharp decrease (figure 4.50c). A HIF-1α-specific decrease in PEP levels was observed compared to the increase seen in the CTL and HIF-2α knockout spheroids (figure 4.50d). Despite an initial decrease, an increasing trend in lactate levels was observed in all the conditions until ~ 280 μm where a decrease in lactate was seen only in the HIF-1α knockout spheroid.

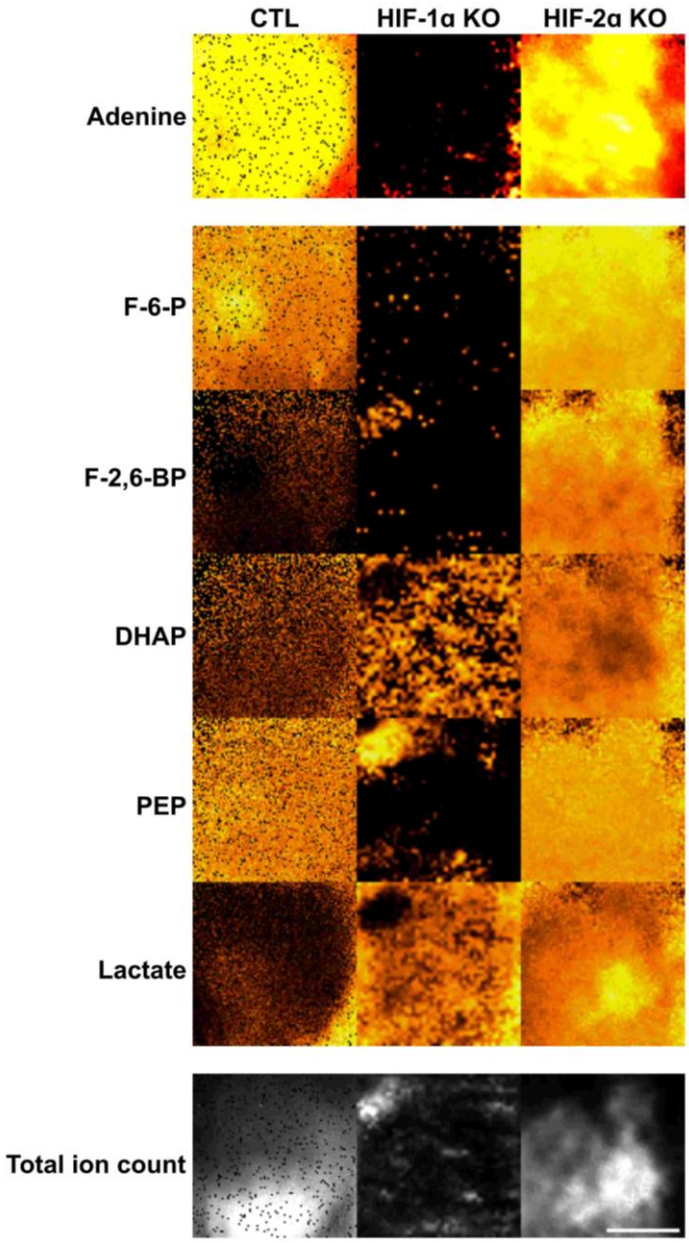

Figure 4.49 Loss of HIF-1α and HIF-2α leads to changes in the spatial distribution of HIF-1α-regulated metabolites across the oxygen gradient in a CRC spheroid model. 20μm 20keV Ar_{3000+} Orbitrap MS negative polarity images of adenine (*m/z* 134.0472, $C_5H_4N_5^-$), fructose-6-phosphate (*m/z* 259.0227, $C_6H_{12}O_9P^-$), fructose-2,6-bisphosphate (*m/z* 338.9890, $C_6H_{13}O_{12}P_2^-$), dihydroxyacetone phosphate (*m/z* 168.9909, $C_4H_8NO_3^-$), phosphoenolpyruvate (*m/z* 167.0463, $C_3H_4O_6P^-$), lactate (*m/z* 89.0244, $C_3H_5O_3^-$) and total ion count (TIC) signals from HCT116 CTL A10, HIF-1α knockout g57 and HIF-2α knockout g81 spheroids. Signal normalisation was performed by dividing by TIC. Scale bar represents 200 μm. Image analysis was carried out in ImageJ. n=1.

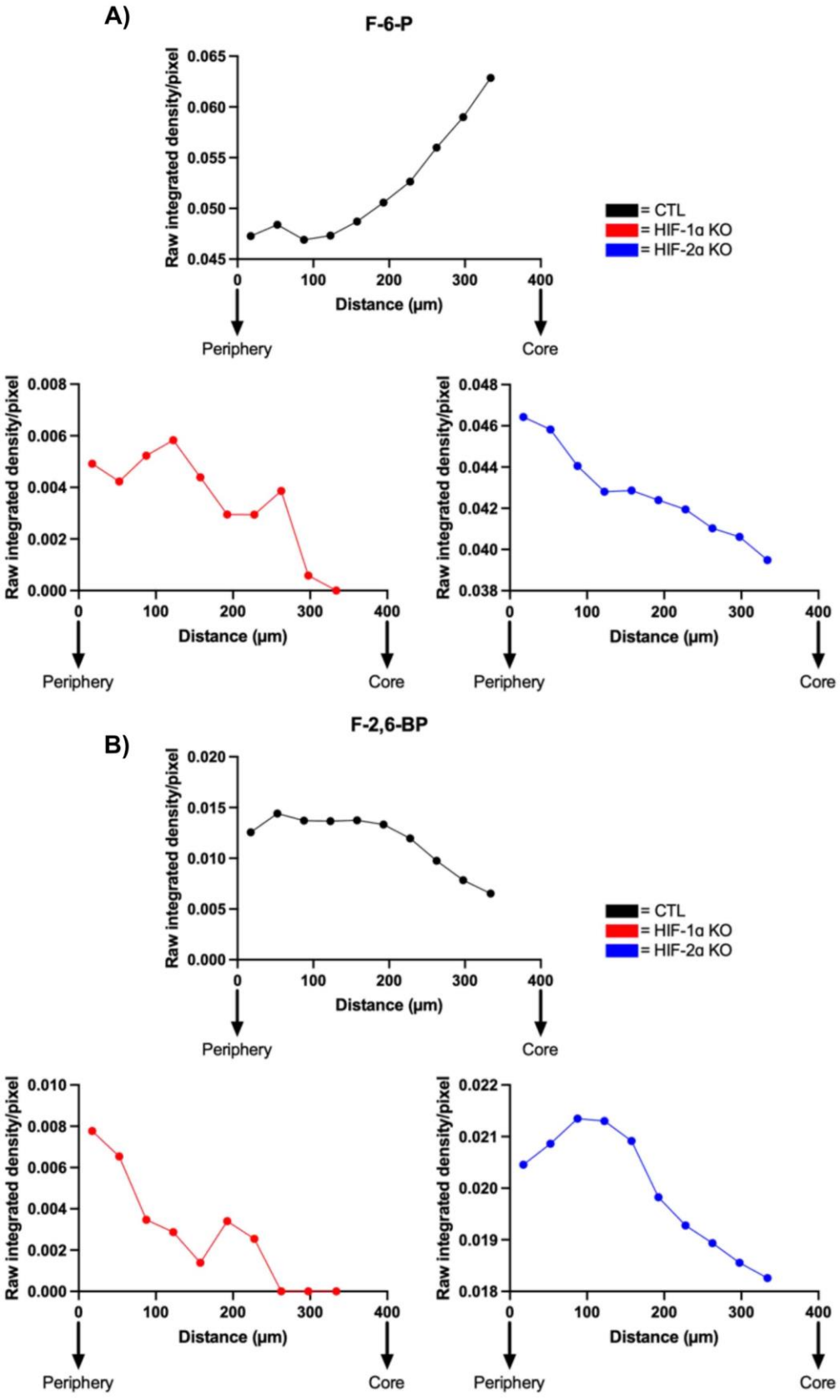
A)
F-6-P
Raw integrated density/pixel
0.065
0.060
0.055
0.050
0.045
0
100
200
300
400
Distance (μm)
Periphery
Core
= CTL
= HIF-1α KO
= HIF-2α KO
0.008
0.006
0.004
0.002
0.000
0.048
0.046
0.044
0.042
0.040
0.038
B)
F-2,6-BP
0.020
0.015
0.010
0.005
0.000
0.010
0.008
0.006
0.004
0.002
0.000
0.022
0.021
0.020
0.019
0.018

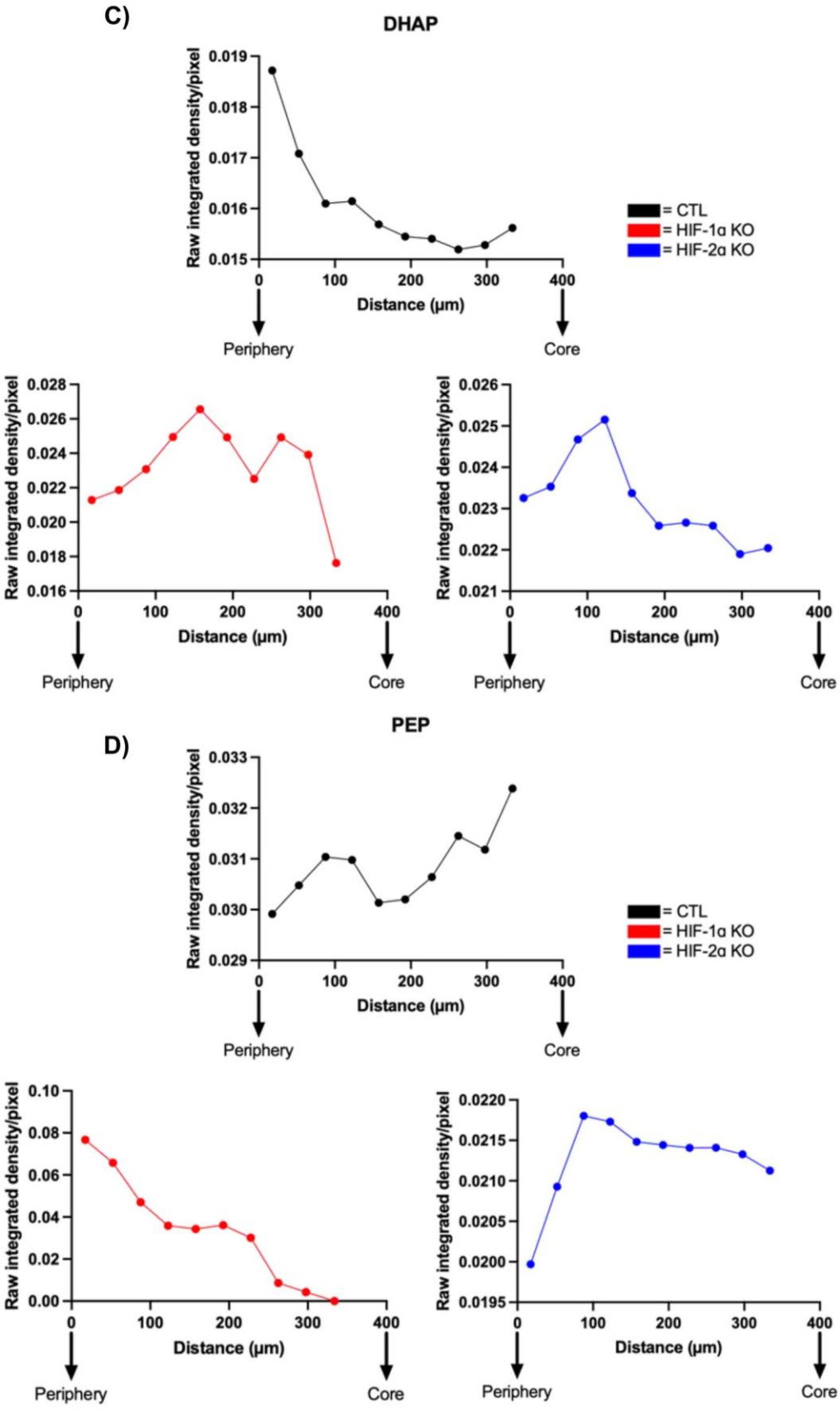
C)
DHAP
Raw integrated density/pixel
Distance (µm)
Periphery
Core
= CTL
= HIF-1α KO
= HIF-2α KO
D)
PEP

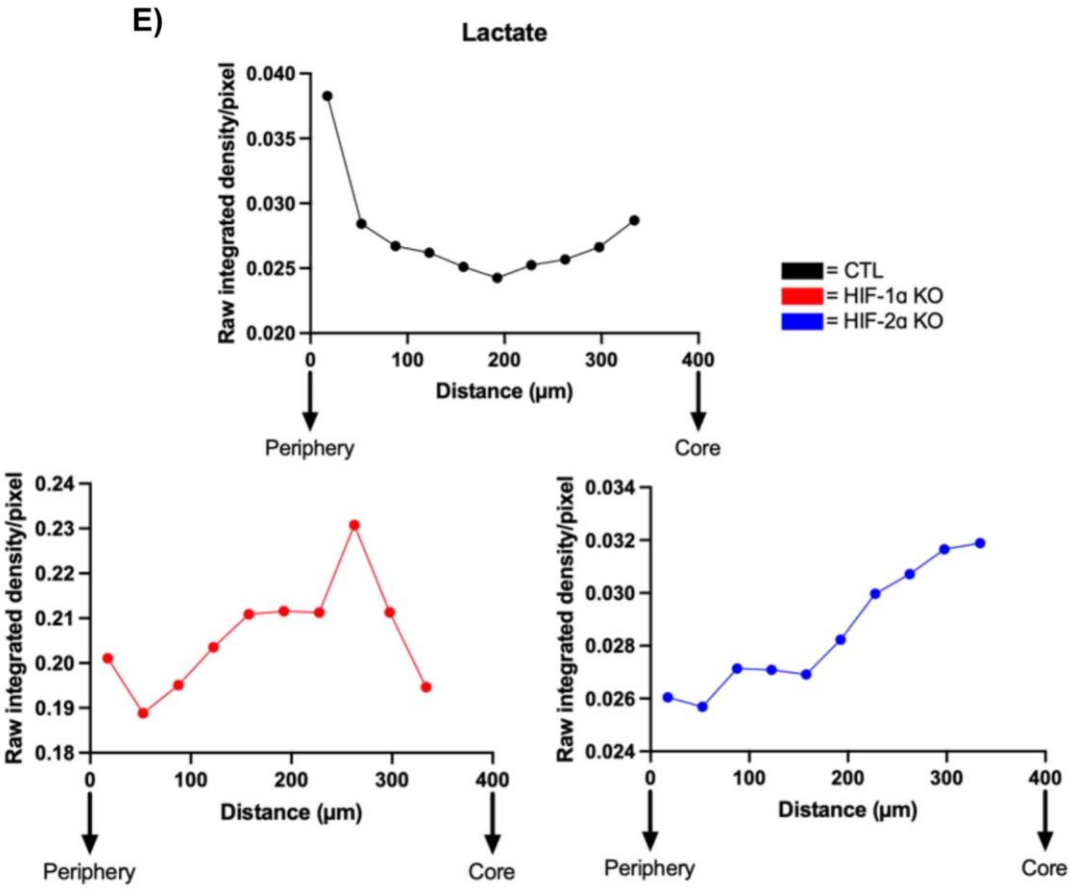

Figure 4.50 Loss of HIF-1α leads to a spatially resolved reduction in HIF-1α-regulated metabolites across the oxygen gradient in a CRC spheroid model. A-E) Concentric circle analysis was employed on orbitrap MS images of F-6-P, F-2,6-BP, DHAP, PEP and lactate to measure the change in metabolite signal across the oxygen gradient in HCT116 CTL A10, HIF-1α knockout g57 and HIF-2α knockout g81 spheroids. Image analysis was performed in ImageJ using an in-house macro. n=1.

4.3.19 Investigating the impact of HIF-1α and HIF-2α knockout on the spatial distribution of HIF-2α-regulated metabolites

Similar to the experimental design described in section 4.3.18 for investigating HIF-1α-regulated metabolic changes, metabolites identified as the end products of the most upregulated HIF-2α-dependent differentially expressed metabolic genes, identified in the RNA sequencing data, were selected for orbiSIMS analysis. This included 3-hydroxy-3-methylglutaryl-CoA (HMG-CoA), squalene, dimethylallyl pyrophosphate/isopentenyl pyrophosphate (DMAPP/IPP), diacylglycerol (DAG), 17-β-estradiol as well as adenine as a control. Figure 4.51 displays the orbitrap MS images for the selected metabolites along with total ion count and adenine as a control marker in the HCT116 CTL A10, HIF-1α knockout g57 and HIF-2α knockout g81 spheroids.

Figure 4.52 displays the metabolic profiles for the HIF-2α-regulated metabolites. HMG-CoA levels decreased gradually in the CTL spheroid from the periphery to the core and this was also observed in the HIF-2α knockout spheroid but included a substantially rapid decrease at ~ 120 μm before recovering after 200 μm (figure 4.52a). Squalene levels increased in the CTL over the first 100-200 μm and then decreased gradually. Whereas a steady decrease in squalene levels was observed across the whole distance in both the HIF-1α and HIF-2α knockout spheroids (figure 4.52b). DMAPP levels rose and fell in the CTL spheroid whereas a steady increase in DMAPP levels was observed with HIF-2α knockout. DMAPP levels also increased in the HIF-1α knockout spheroid until ~ 250 μm where a rapid decrease was observed (figure 4.52c). DAG levels showed a constant increase from the periphery to the core of the CTL spheroid which was reversed in both the HIF-1α and HIF-2α knockout spheroids but to a greater extent with loss of HIF-1α (figure 4.52d). Finally, 17-β-estradiol levels appeared to fluctuate quite substantially across the CTL spheroid whereas opposing effects were seen with the HIF knockouts. HIF-2α knockout led to a steady increase in 17-β-estradiol levels whilst a gradual reduction was observed with HIF-1α knockout (figure 4.52e).

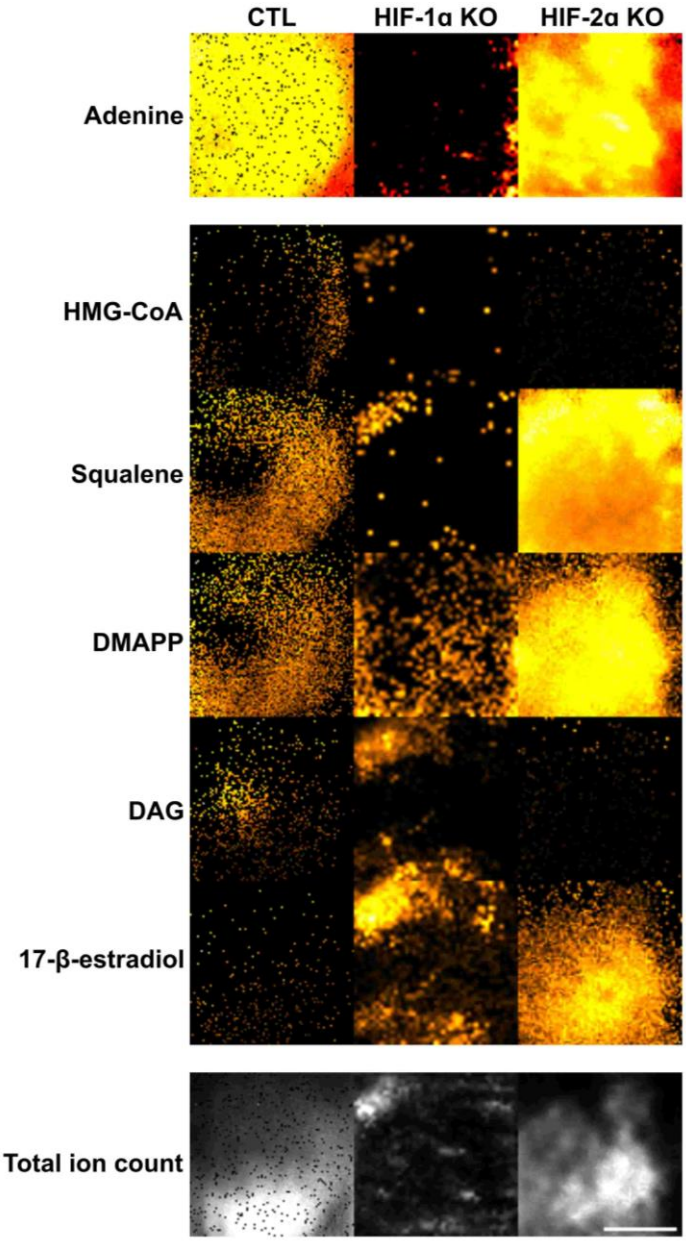

Figure 4.51 Loss of HIF-1α and HIF-2α leads to changes in the spatial distribution of HIF-2α-regulated metabolites across the oxygen gradient in a CRC spheroid model. 20μm 20keV Ar_{3000+} Orbitrap MS negative polarity images of adenine (*m/z* 134.0472, $C_5H_4N_5^-$), 3-hydroxy-3-methylglutaryl CoA (*m/z* 910.0864, $C_{27}H_{43}N_7O_{20}P_3S^-$), squalene (*m/z* 409.3793, $C_{30}H_{49}^-$), dimethylallyl pyrophosphate (*m/z* 245.0434, $C_5H_{11}O_7P_2^-$), diacylglycerol (*m/z* 592.0854, $C_{37}H_{69}O_5^-$), 17-β-estradiol (*m/z* 270.9420, $C_{18}H_{23}O_2^-$) and total ion count (TIC) signals from HCT116 CTL A10, HIF-1α knockout g57 and HIF-2α knockout g81 spheroids. Signal normalisation was performed by dividing by TIC. Scale bar represents 200 μm. Image analysis was carried out in ImageJ. n=1.

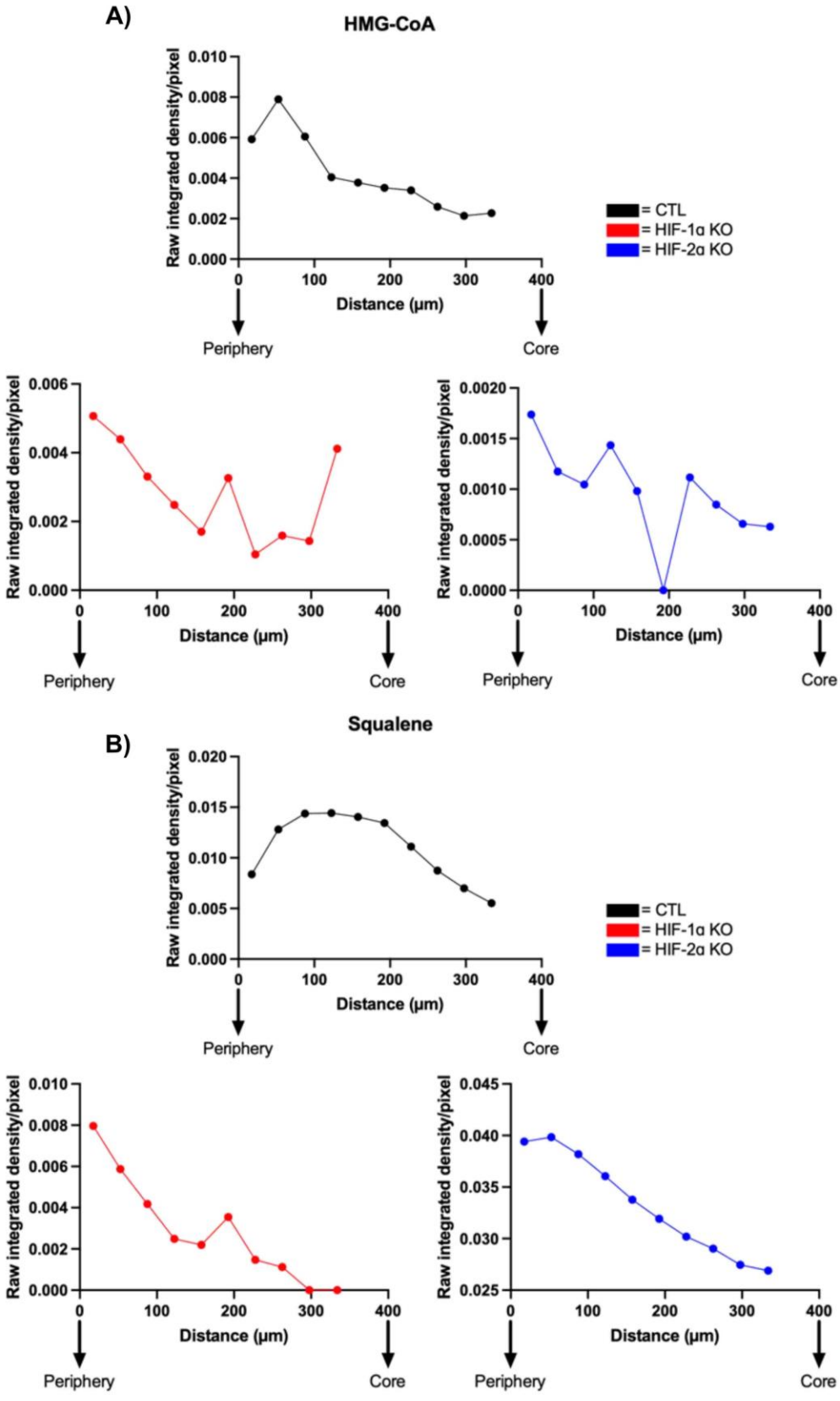
A)
HMG-CoA
Raw integrated density/pixel
0.010
0.008
0.006
0.004
0.002
0.000
0
100
200
300
400
Distance (µm)
Periphery
Core
= CTL
= HIF-1α KO
= HIF-2α KO
0.006
0.004
0.002
0.000
0.0020
0.0015
0.0010
0.0005
0.0000
B)
Squalene
0.020
0.015
0.010
0.005
0.000
0.045
0.040
0.035
0.030
0.025

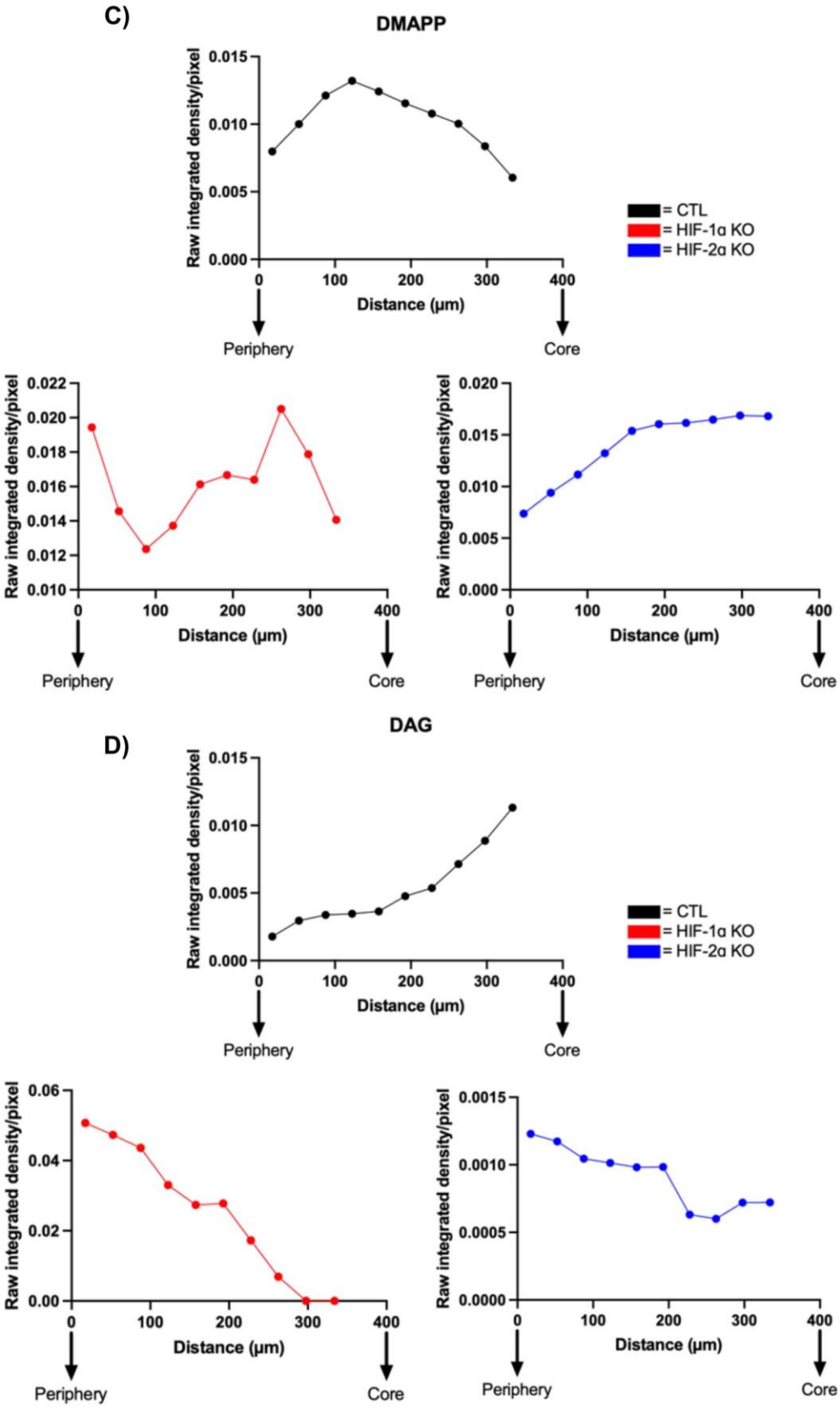
C)
DMAPP
Raw integrated density/pixel
0.015
0.010
0.005
0.000
0
100
200
300
400
Distance (μm)
Periphery
Core
= CTL
= HIF-1α KO
= HIF-2α KO
Raw integrated density/pixel
0.022
0.020
0.018
0.016
0.014
0.012
0.010
Distance (μm)
Periphery
Core
Raw integrated density/pixel
0.020
0.015
0.010
0.005
0.000
Distance (μm)
Periphery
Core
D)
DAG
Raw integrated density/pixel
0.015
0.010
0.005
0.000
Distance (μm)
Periphery
Core
= CTL
= HIF-1α KO
= HIF-2α KO
Raw integrated density/pixel
0.06
0.04
0.02
0.00
Distance (μm)
Periphery
Core
Raw integrated density/pixel
0.0015
0.0010
0.0005
0.0000
Distance (μm)
Periphery
Core

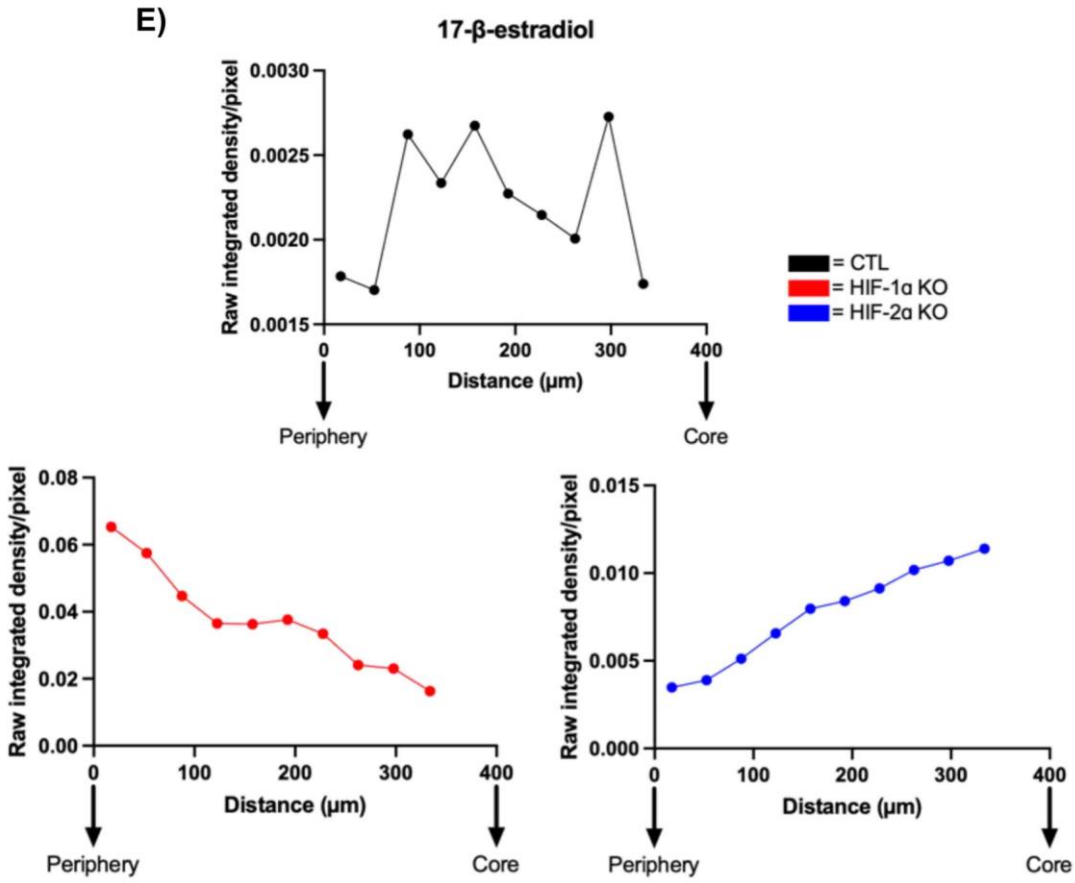

Figure 4.52 Loss of HIF-2α leads to spatially resolved changes in HIF-2α-regulated metabolites across the oxygen gradient in a CRC spheroid model. A-E) Concentric circle analysis was employed on orbitrap MS images of HMG-CoA, squalene, DMAPP, DAG and 17-β-estradiol to measure the change in metabolite signal across the oxygen gradient in HCT116 CTL A10, HIF-1α knockout g57 and HIF-2α knockout g81 spheroids. Image analysis was performed in ImageJ using an in-house macro. n=1.

4.4 Discussion

The aims of this chapter were to investigate the roles of hypoxia, and specifically HIF-1α and HIF-2α, in the regulation of gene expression and alternative splicing, with a particular focus on metabolic genes. Additionally, a novel cryogenic orbiSIMS mass spectrometry imaging protocol was developed for analysing the spatial regulation of metabolites in a 3-D CRC spheroid model. This model was employed to investigate the impact of the oxygen gradient, as well as loss of HIF-1α and HIF-2α activity, on the spatial regulation of metabolites in a CRC.

4.4.1 Impact of HIF-1α and HIF-2α knockout on colorectal cancer cell growth

In HCT116 spheroids, growth was significantly impacted by the loss of either HIF-1α or HIF-2α, supporting a role for both HIF-1α and HIF-2α in CRC growth. This is further evidenced by previous studies that show both HIFα isoforms are co-expressed in CRC cells and HIF knockdown or pharmacological inhibition reduces tumour growth *in vivo* and sensitizes CRC cells to therapeutic intervention[554–556]. However, most studies investigating HIF inhibition do not distinguish between HIF-1α and HIF-2α-specific responses despite both isoforms having increased expression correlating with poor prognosis in CRC tumours[557,558]. Studies looking at the individual roles of HIF-1α and HIF-2α in CRC have shown that HIF-1α knockout reduces growth in a 3-D spheroid model whereas HIF-2α appears to suppress growth, as demonstrated in a mouse xenograft model[213,371]. These previous findings coupled with the large number of HIF-1α and HIF-2α-dependent gene expression changes presented in my work, suggest that both HIF-1α and HIF-2α play important roles in CRC, but further delineation of their individual roles is needed.

4.4.2 Temporal regulation of HIF-1α and HIF-2α expression in colorectal cancer

Investigation of the temporal regulation of HIF-1α and HIF-2α protein expression in HCT116 cells showed that both isoforms were expressed at 24h, 48h and 72h after hypoxic exposure. However, maximum expression of both isoforms occurred at 48h after which HIF-1α levels decreased whereas HIF-2α levels remained stable. Previous studies in other cancer types such as neuroblastoma and bladder cancer have shown that HIF-1α is induced rapidly during acute periods of hypoxia (< 24h) and then decreases

whereas HIF-2α expression gradually increases over time during chronic hypoxia[559,560]. This has led to the proposal of the 'HIF switch' where HIF-1α provides a rapid, but transient, response to acute hypoxia followed by activation of HIF-2α during prolonged hypoxia[534,561]. Importantly, most studies investigating HIF regulation in CRC have used < 24h hypoxia and the temporal expression of the HIF isoforms has not been considered. The data presented here suggests maximum HIF expression occurs at later time points in CRC, particularly for HIF-2α. Interestingly, the stabilisation of HIF-2α expression levels as opposed to a continued increase from 48h onwards could be due to the binding of eIF4A2, as part of the CCR4-NOT complex, to HIF-2α mRNA to prevent its degradation. Investigating the binding of eIF4A2 and its interaction partners to the HIF proteins across different hypoxic time points would help identify this mechanism.

4.4.3 Hypoxia-regulated gene expression in colorectal cancer

The RNA-sequencing data presented in this work identified a large number of DEGs both upregulated and downregulated by hypoxia, many of which were associated with metabolic pathways. Interestingly, PHD2 as well as the HIF-1α antisense RNA, HIF1A-AS2 were upregulated in hypoxia as was HIF-2α itself. PHD2 is known to be upregulated by HIF-1α in hypoxia and subsequently can promote HIF-1α degradation as part of a negative feedback mechanism to reduce HIF-1α mRNA stability during chronic hypoxia[562]. Furthermore, PHD2 displays preferential hydroxylation activity towards HIF-1α over HIF-2α[563]. In addition, HIF1A-AS2 has previously been shown to be upregulated in chronic hypoxia and destabilise HIF-1α mRNA in lung cells[564]. In CRC, pro-tumourigenic, HIF-independent roles of HIF1A-AS2 have also been identified[565]. My work demonstrates, for the first time, an upregulation of HIF-2α gene expression as well as multiple negative regulatory proteins of HIF-1α after 48h hypoxia, thus providing evidence for the HIF switch in CRC during chronic hypoxia.

Components of the translation regulation machinery were also identified as downregulated in hypoxia including eIF4E and eIF4G1. Inhibition of translation in hypoxia occurs primarily through the sequestration of eIF4E by 4E-BP1 which is overexpressed in hypoxic CRC cell lines[566]. eIF4E has also been reported to be overexpressed in CRC patients with enhanced metastatic potential, however, this was independent of oxygen status[567]. Similarly, both eIF4E and eIF4G1 have been shown to be upregulated by hypoxia in breast cancer, however, this was only studied after 24h of

hypoxia[494]. Furthermore, the amount of phosphorylated 4E-BP1 is not reduced after 24h hypoxia, preventing the inhibition of eIF4E[499]. It is possible that the dephosphorylation of 4E-BP1 and subsequent inhibition of eIF4E occurs as part of the 'late' hypoxic response, possibly through HIF-2α-dependent regulation. This could represent a novel mechanism promoting the switch to the use of the hypoxic cap-binding complex consisting of eIF4E2 and eIF4G3. Furthermore, a significant overlap between hypoxia-upregulated genes and genes previously identified as being bound by eIF4A2 in hypoxia by RIP-Seq was identified (figure 4.53). 7 out of the top 10 most enriched KEGG pathways for these genes were metabolic pathways (data not shown). Taken together, this provides additional evidence for the role of eIF4A2, possibly in conjunction with eIF4E2 and eIF4G3, in driving the hypoxic translation of metabolic genes in CRC, as discussed in chapter 3, but also suggests a potential synergistic partnership between HIF and eIF4A2.

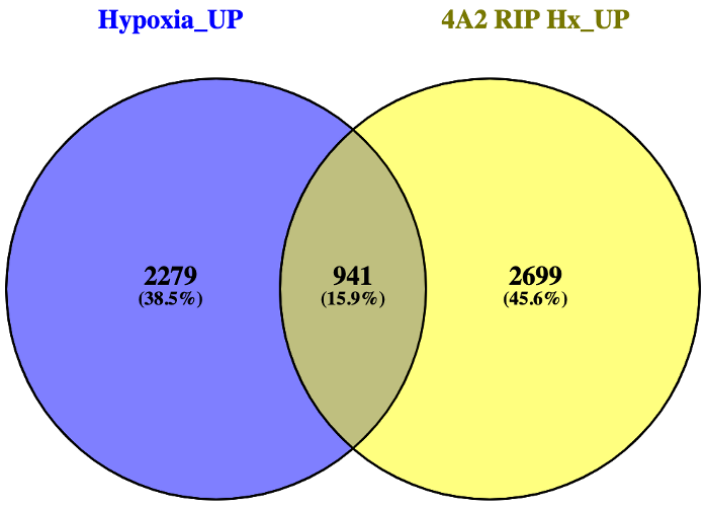

Figure 4.53 Hypoxia-upregulated genes are also bound by eIF4A2 under hypoxic conditions. Venn diagram of overlapping hypoxia-upregulated genes and eIF4A2-bound genes in hypoxia. The sum of the numbers in each circle represents the total number of genes for that condition.

Identification of HIF-1α and HIF-2α-regulated genes in hypoxia revealed a larger number of and more significantly enriched KEGG pathways related to HIF-2α-dependent genes compared to HIF-1α. As discussed previously, the majority of hypoxic gene expression analysis in CRC has been limited to ≤ 24h hypoxia where HIF-1α may dominate[534,564]. Here, I demonstrate a more prominent role for HIF-2α at the later time points used in this study as evidenced by the increase in HIF-2α-regulated genes. Interestingly, around 25% of both HIF-1α and HIF-2α-regulated genes were identified as

metabolic genes, highlighting the importance of their roles in metabolic reprogramming in CRC[356]. The role of HIF-1α in the regulation of glycolysis and associated pathways such as the PPP is well-documented, and this was confirmed in the data presented here with the majority of HIF-1α-regulated metabolic genes converging on these pathways[568]. On the other hand, the role of HIF-2α in metabolic regulation, particularly in CRC, is very poorly understood. HIF-2α has only thoroughly been studied in the context of liver disease where it has been shown to regulate hepatic lipid metabolism[569]. In my work, I identified that HIF-2α-regulated metabolic genes were mostly involved in fatty acid and steroid metabolism. Interestingly, 7 of the top 30 HIF-2α-regulated metabolic genes: *HMGCS1*, *IDI1*, *FDFT1*, *LPIN1*, *PLA2G4A*, *NT5E* and *CYP51A1*, encode rate-limiting enzymes within their associated metabolic pathways[570–576]. This work provides new evidence indicating a role for HIF-2α in the regulation of lipid and steroid metabolism in chronic hypoxia in CRC and suggests a possible mechanism where HIF-2α exhibits high selectivity for rate-limiting enzymes within its target pathways as opposed to broad regulation.

4.4.3 Hypoxia-regulated alternative splicing in colorectal cancer

In addition to its role in regulating gene expression, hypoxia has been shown to regulate the alternative splicing of genes[540]. In this work, hypoxia resulted in a large number of alternative splicing events and pathway analysis revealed an enrichment of metabolic pathways. 19% of all metabolic genes were alternatively spliced in hypoxia across 47 metabolic KEGG pathways, many of which were also transcriptionally regulated by HIF-1α and HIF-2α. Previous studies have identified hypoxia-induced alternative splicing events in HIF-target genes belonging predominantly to the glycolytic pathway[543]. Interestingly, a large number of genes involved in the regulation of mRNA stability and translation underwent novel alternative splicing in hypoxia including components of the CCR4-NOT complex: CNOT7, CNOT1, CNOT2, CNOT8 and CNOT10, as well as translation initiation factors: eIF4G3, eIF4G1, eIF4B and eIF4H. A splice variant of CNOT7, CNOT7v2, has previously been reported in the breast cancer cell line MCF7 and was shown to lack deadenylation activity despite still binding to the CCR4-NOT complex[577]. However, the splicing of CNOT7 has not been investigated in CRC nor in hypoxia. It would be interesting to identify if this is a hypoxia-specific splice variant and whether or not that influences the interaction between CNOT7 and eIF4A2, as discussed

in chapter 3, to modulate hypoxic mRNA stability. Furthermore, an alternative isoform of eIF4G3 has previously been described utilising an alternative initiation codon leading to the extension of the eIF4G3 N-terminus[578]. It is possible the N-terminal sequence could provide a hypoxia-specific binding site for alternative translation initiation factor binding, such as eIF4A2, however, this requires further investigation. Similarly, alternative isoforms of eIF4H and eIF4B have previously been identified[579,580]. The cancer-specific eIF4H isoform 1 has been shown to promote CRC progression *in vivo* but has not been investigated in hypoxia[579]. The eIF4B isoform was predicted to disrupt eIF4G1 binding and so it would be interesting to study whether this promoted alternative interactions with eIF4G3[579]. Additionally, it is possible that alternative isoforms of the eIF4A-stimulating 4H and 4B proteins display a preference for eIF4A2 over eIF4A1 in hypoxia.

4.4.3 Comparison of ionisation modes and sample preparation techniques for orbiSIMS-based metabolomics

As part of the development of the orbiSIMS imaging technique, the use of negative and positive polarity GCIB orbitrap mass spectra were compared with the negative ion mode providing greater ionisation efficiency and improved signal-to-noise ratio for the majority of molecules investigated. Previously, electrospray ionisation (ESI) has been the most commonly employed ionisation technique for mass spectrometry-based metabolomics and a comparison of the two polarities has shown that the negative ion mode provides enhanced sensitivity and lower detection limits[581]. However, this is highly molecule dependent. For example, most fatty acids readily form negative ions, $[M-H]^-$, due to deprotonation of the carboxylic acid functional group[582]. Whereas for chemically diverse molecules such as phospholipids the nature of the polar head group drives preference for $[M-H]^-$ or positive ions, $[M+H]^+$[583]. Importantly, previous MS-based metabolomics of sugars and glycolytic intermediates have shown that the negative ion mode provides a greater ion intensity, likely due to deprotonation of polar hydroxyl groups[584].

Similarly, the use of cryogenic conditions for sample preparation was shown to improve ion detection and signal-to-noise ratio, but in a molecule-dependent manner. It has previously been shown that cryogenic mass spectrometry can reduce the unwanted redistribution and migration of small molecules that often occurs with standard freeze-drying methods and can greatly enhance signal intensity[465,466]. Cryogenic sample

preparation employed in my work resulted in an average 6-fold increase in signal intensity compared to frozen samples that were subsequently freeze-dried, thus highlighting the importance of considering sample preparative methods prior to MS analysis.

4.4.4 Spatial regulation of metabolic adaptation to hypoxia

Using the HCT116 CRC spheroid model in combination with the concentric circle analysis, I was able to define the spheroids in the GCIB-orbitrap images based on the visualisation of the spheroid periphery and signals for a large range of metabolites were detectable by negative ion mode MS imaging and measured across the oxygen gradient of the spheroid. Adenine was confirmed as a suitable control marker as the signal intensity remained consistent across the spheroid and appeared unaffected by changes in oxygen tension or by HIF knockout. However, one of the major challenges identified with this analysis was not knowing what depth into the spheroid the images were taken at. Correlation of the pimonidazole staining of hypoxic regions within the spheroid with the calculations made to estimate the spheroid core, and therefore diameter, in the orbitrap images provided the best possible assumption. One alternative method that could be tested would be to freeze-fracture the spheroids into two half-spheres in order to expose the spheroid core. However, the use of this technique for spheroids has not been tested extensively and has predominantly been used in the study of membrane-bound structures such as extracellular vesicles[585,586]. Alternatively, using adjacent cryosections of the spheroids for both pimonidazole staining and orbiSIMS analysis could simplify the workflow, as I have since developed a method of cryosectioning for orbiSIMS as discussed in Chapter 5, however this employed standard freezing instead of HPF.

Furthermore, a large range of signal intensities were observed for the metabolites investigated for which there are several possible explanations. One possibility is that metabolites for which a reduced signal intensity was observed more readily form $[M+H]^+$ as opposed to $[M-H]^-$ ions. However, the majority of metabolites investigated here produced a detectable and measurable negative ion signal. The metabolites that had a reduced signal intensity, such as NAD+, acetyl-CoA and HMG-CoA were large, complex structures with a large number of protonation/deprotonation sites. It is likely that a more detailed analysis of additional ion fragments for these molecules would have identified an improved signal. In some cases, a signal was also observed outside of the spheroid

periphery which led to an unexpectedly high signal intensity. It is possible that during the period of transferring the spheroids from their culture vessel to the HPF instrument, which was done at ambient temperatures, certain metabolites migrated into the cryoprotectant solution added prior to HPF. Importantly perhaps, most of these mobile metabolites that displayed this 'edge effect', including fumarate, malate and lactate, are highly polar molecules that have a higher propensity for unwanted molecule migration as demonstrated previously[465,466]. However, it is interesting to note this increased signal present at the well-oxygenated periphery of the spheroid.

Analysis of predicted hypoxia-upregulated metabolites revealed a similar pattern of decreasing signal intensity for both NAD+ and AMP as well as for the hypoxia-downregulated metabolites fumarate and phosphocreatine. Furthermore, the spatial distribution of acidosis-regulated metabolites all displayed the expected patterns of up or downregulation down the oxygen gradient. The use of the concentric circle analysis was able to spatially resolve these changes and identify possible mechanisms of HIF-dependent regulation. For example, the opposing increase and decrease in *cis*-aconitate levels observed 200 μm into the control and HIF-1α knockout spheroids respectively could be due to the HIF-1α-dependent activation of glutamate reductive carboxylation in hypoxia and subsequent increase in isocitrate to citrate conversion for fatty acid biosynthesis[381]. The utilisation of glutamate for energy production in hypoxia could also explain the decrease in glutamate signal observed in the control spheroid that was ablated with HIF knockout[587]. Similarly, the predicted acidosis-mediated downregulation of both alanine and threonine was also observed but an opposite effect was seen with HIF-2α knockout, suggesting HIF-2α may play a role in regulating the catabolism of these amino acids. On the other hand, both HIF-1α and HIF-2α knockout reversed the observed increase in acidosis-induced metabolites palmitic acid and acetyl-CoA from 50-200 μm into the spheroid. Loss of acetyl-CoA in response to HIF-1α knockout is unsurprising given the known role of HIF-1α in the inhibition of PDH[369,370]. Interestingly, the HIF-2α-dependent effect on palmitic acid agrees with the RNA-sequencing data reported here, along with previous work carried out in liver cells, identifying a regulatory role for HIF-2α in fatty acid metabolism[569]. Previously, it has been reported that hepatoma cells can promote glycolysis by increasing the AMP/ATP ratio to allosterically activate PFK-1 activity in the absence of HIF-1α[588]. However, the HIF-independent decrease in AMP observed here suggests an alternative use for AMP levels, possibly in the production of

ADP for subsequent use in the dephosphorylation of phosphocreatine to generate creatine and ATP by creatine kinase to sustain energy levels[589]. CRC cells have previously been shown to regulate the localisation of creatine kinase enzymes which are reported to be under HIF-2α-regulated control in hypoxia[590,591]. This would explain the lack of phosphocreatine utilisation observed in the HIF-2α knockout spheroids.

Analysis of glycolytic intermediate signal intensities across the oxygen gradient enabled the visualisation of the expected inhibition of glycolysis with HIF-1α knockout, further confirming the success of the methodology developed in this study[568]. Interestingly, a similar decrease in glycolytic intermediates was observed in the HIF-2α knockout spheroids. Further inspection of the RNA-sequencing data identified that HIF-2α regulated the expression of several glycolytic enzymes including HK2, ALDOA and ENO2 as well as HIF-1α. It is therefore possible that as part of the switch from HIF-1α to HIF-2α regulation under chronic hypoxia that I have demonstrated in this study, glycolytic flux can be maintained by HIF-2α-mediated pathways in CRC. However, this has not been studied in the literature and warrants further investigation.

The RNA-sequencing data also identified a role for HIF-2α in the regulation of fatty acid and sterol metabolism and OrbiSIMS analysis revealed a general decreasing trend in most of the metabolites investigated in these pathways. Interestingly, around 200 μm into the spheroid there was an opposing increase and decrease in HMG-CoA signal with the loss of HIF-1α and HIF-2α respectively. HIF-1α has previously been shown to regulate HMG-CoA reductase which catalyses the breakdown of HMG-CoA to mevalonate[592]. However, I have shown for the first time that HIF-2α regulates HMG-CoA synthase expression and this translates into a reduction in HMG-CoA production in HIF-2α knockout spheroids. Interestingly, in the hypoxic region of the control and HIF-1α-depleted spheroids an overall reduction in DMAPP levels was observed yet an increase was observed with HIF-2α knockout. The RNA-sequencing data identified the enzyme IDI1, previously reported to be upregulated in hypoxia, as a HIF-2α target which catalyses the interconversion between DMAPP and its isomer IPP[575,593]. IDI1 synthesises IPP:DMAPP in a ratio of 85:15 however, how hypoxia and specifically HIF-2α influence the selectivity of IDI1 and the IPP:DMAPP ratio is unclear and would be interesting to study further[594].

4.4.5 Concluding statements

In summary, the work presented in this chapter investigated the role of HIF-1α and HIF-2α in the regulation of 3-dimensional CRC spheroid growth along with their role in the regulation of hypoxic gene expression and hypoxia-associated alternative splicing, with a focus on metabolic genes. This chapter also presented the development of a novel secondary ion mass spectrometry imaging technique, 3-D orbiSIMS, for measuring and analysing the oxygen and HIF-dependent spatial regulation of metabolites within 3-dimensional spheroids.

As hypothesised, knockout of either HIF-1α or HIF-2α led to a reduction in CRC spheroid growth suggesting a role for both HIF-1α and HIF-2α in regulating CRC cell growth. However, these effects were only seen in individual knockout clones of HIF-1α and HIF-2α, and additional validation of these results would be beneficial. Furthermore, this work demonstrated a role for both HIF-1α and HIF-2α in the regulation of gene expression in response to chronic hypoxia in CRC as hypothesised, but interestingly, HIF-2α appears to play a larger role. This work also reported that both HIF-1α and HIF-2α regulate metabolic reprogramming in hypoxia, in agreement with my hypothesis, and highlighted HIF-1α regulated pathways associated with glycolysis and carbon metabolism and HIF-2α regulated pathways such as fatty acid and sterol metabolism. Similarly, I hypothesised that hypoxia as well as both HIF-1α and HIF-2α regulate the alternative splicing of genes. I have demonstrated that hypoxia is associated with large-scale changes in alternative splicing and that both HIF-1α and HIF-2α regulate alternative splicing in hypoxia, and in particular, the splicing of genes associated with metabolic pathways.

This work also demonstrates the use of a novel cryogenic 3-dimensional orbiSIMS mass spectrometry imaging workflow and concentric circle analysis for analysing the spatial regulation of metabolites along the oxygen gradient of a 3-dimensional CRC spheroid model. I hypothesised that the oxygen gradient regulates the spatial distribution of metabolites and that this was further regulated by HIF-1α and HIF-2α. This novel methodology spatially resolved known hypoxia and acidosis-associated metabolites as well as identified HIF-1α and HIF-2α-regulated metabolites including glycolytic intermediates and steroid biosynthetic intermediates. Thus, showing the potential of

using this method in the analysis and identification of novel hypoxia-regulated metabolic changes for therapeutic targetting.

5. The spatial regulation of metabolic adaptation to hypoxia in FOSL2 knockout and patient-derived colorectal cancer xenografts

5.1 Introduction

Clinically, hypoxia is a leading cause of therapeutic failure due to the increased resistance to radiotherapy, chemotherapy, immunotherapy and molecular targeted therapies[229]. Furthermore, tumour hypoxia is associated with poor patient prognosis and increased metastatic potential in almost every clinical setting independently of cancer type or grade[229,230]. Many of these features can be attributed to the large-scale changes in metabolic reprogramming that occur in response to hypoxia and increased HIF activity[231]. Due to the many challenges associated with targeting hypoxia and HIF activity directly, the identification of novel targets for therapeutic exploitation, particularly ones involved in hypoxia-induced metabolic reprogramming, is becoming increasingly important[260,595].

In vitro cancer cell line systems remain the most common models used to study cancer biology and identify and test new therapeutic targets despite there being several challenges associated with them[596]. For example, the number of passages that cancer cell lines undergo in culture can lead to genotypic and phenotypic changes, such as copy number variations and alterations to the transcriptome, that can differ greatly from the characteristics of the tumour of origin including [596,597]. Furthermore, it is clear that cells grown in culture cannot fully recapitulate the complex vascular network of human tumours despite advances in 3-dimensional cell culture technologies[598,599]. In the context of hypoxia, this becomes even more important as the aberrant vasculature of solid tumours is critical for the development of hypoxic regions[189]. *In vivo* animal models have been used extensively and have been shown to more accurately reproduce the oxygen gradients found in human tumours[600,601]. More recently, patient-derived xenograft (PDX) models have been developed and have been shown to consistently maintain the genetic and transcriptomic profiles from the parental patient tumour[602,603]. Importantly, the native tumour microenvironment can greatly influence the metabolism of cancer cells, particularly in hypoxic regions, and so the use of suitable models for studying metabolic changes to hypoxia becomes very important[604].

CRC PDX models have been developed recently to study the therapeutic responses and metabolic reprogramming of colorectal tumours. One study utilised a panel of 49 PDX samples to identify mechanisms of therapeutic resistance to common CRC therapeutics such as novel HER2 mutations providing resistance to cetuximab[605]. Furthermore, CRC PDX models in combination with GC-MS based metabolomics analysis have been used to identify changes in circulating metabolites in tumour vs non-tumour serum[606]. Importantly, serum levels of amino acids such as aspartate and phenylalanine were found to be reduced in the PDX samples suggesting an increased utilization of amino acids by CRC cells[606]. However, the spatial regulation of metabolites within CRC tumours in relation to the oxygen gradient has never been studied. Furthermore, previous work carried out in the Mcintyre lab identified the AP-1 subunit FOSL2 as a key regulator of the molecular adaptation to hypoxia in CRC and RNA-sequencing analysis revealed a large number of metabolic pathways that were regulated by FOSL2 in hypoxia (unpublished data). However, the impact of FOSL2 on the spatial regulation of metabolites in response to changes in oxygen concentration has not been studied.

5.2 Hypothesis and aims

In this chapter, the following points were investigated, and the following hypotheses were tested:

- Role of hypoxia and FOSL2 in the spatial regulation of metabolic adaptation *in vivo*
- Role of hypoxia in the spatial regulation of metabolic adaptation in CRC patient-derived xenografts

I hypothesise that changes in the oxygen gradient within CRC tumour xenografts and patient-derived xenografts (PDXs) lead to alterations in the spatial distribution of metabolites in response to hypoxia and that this regulation is impacted by the loss of FOSL2 function. Specifically, I hypothesise that hypoxia leads to changes in the spatial regulation of metabolites associated with FOSL2 and HIF-regulated gene expression including glycolytic intermediates and metabolites related to fatty acid and steroid metabolism.

In order to test these hypotheses, I have undertaken the following aims:

1. Validate FOSL2 knockout in HCT116 mouse xenograft samples by immunohistochemical staining
2. Investigate the role of hypoxia and FOSL2 in the spatial regulation of metabolic adaptation in HCT116 mouse xenograft samples using secondary ion mass spectrometry
3. Investigate the role of hypoxia in the spatial regulation of metabolic adaptation in CRC patient-derived xenograft samples using secondary ion mass spectrometry

5.3 Results

5.3.1 Impact of FOSL2 knockout on tumour growth *in vivo*

The following xenograft study is credited to Dr T. Potgieter, and the data is presented here with permission. In order to determine the role of FOSL2 in regulating CRC tumour growth *in vivo*, HCT116 control (CTL) and FOSL2 knockdown (FOSL2 KO) cells were generated as previously described and implanted into CD1 nude mice to monitor tumour growth. Cell lines were treated with 2 μg/mL doxycycline for 5 days to induce Cas9 expression prior to implantation. $2x10^6$ cells prepared with matrigel in a 100 μL dosing volume were injected subcutaneously into the flank of CD1 nude mice. Each experimental group consisted of 8 mice. Tumours were established in the mice after approximately 11 days and calliper measurements were recorded every 3 days to measure tumour volume and diameter (figure 5.1).

As shown in figure 5.1a, the volumes of the HCT116 CTL and FOSL2 KO tumours were similar for the first 45 days of growth. From day 45 onwards the FOSL2 KO tumour volumes were smaller than the CTL tumours. Following the termination of the final CTL tumour on day 59, the CTL tumour average volume was 292 mm^3 greater than the average tumour volume for the FOSL2 KO tumours. Similarly, the diameters of the CTL and FOSL2 KO tumours were similar for the first 45 days of growth followed by a reduction in FOSL2 KO tumour diameter compared to the CTL tumours (figure 5.1b). This data suggested that FOSL2 knockdown was reducing the growth rates of the HCT116 xenografts. However, calculations of the tumour growth rates (see spheroid growth rate calculation in section 2.2.2) showed there was no significant difference in the growth rates of the FOSL2 KO tumours compared to the CTL tumours (figure 5.2).

A)

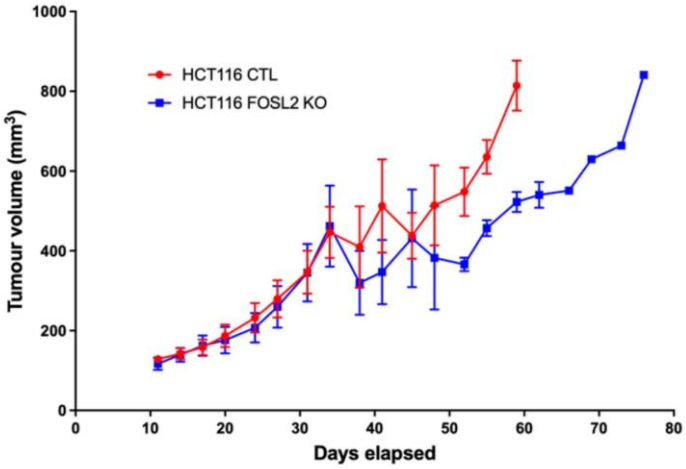

B)

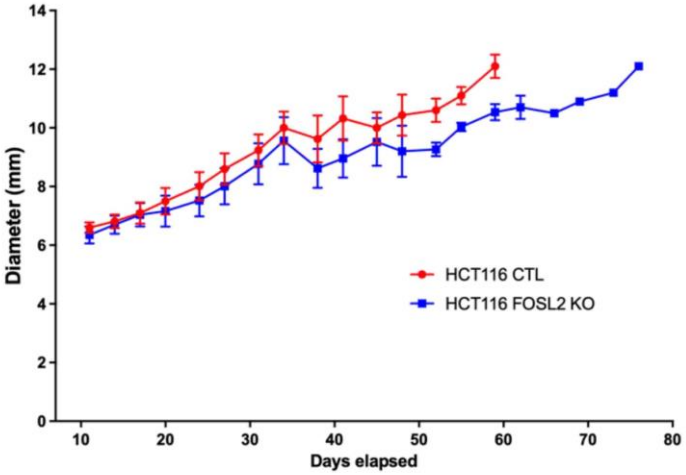

C)

	Mouse	Day of term.
HCT116 CTL	1	34
	2	34
	3	34
	4	34
	5	49
	6	59
	7	59
	8	41
HCT116 FOSL2 KO	9	34
	10	59
	11	62
	12	76
	13	34
	14	45
	15	34
	16	49

Figure 5.1 FOSL2 knockout reduces tumour volume and diameter in HCT116 xenografts. The height, width and depth of HCT116 CTL and HCT116 FOSL2 knockout xenografts were measured every 3 days by calliper measurements. **A)** Average tumour volumes displayed in mm^3 of the CTL and FOSL2 knockout xenografts. **B)** Average tumour diameters displayed in mm of the CTL and FOSL2 knockout xenografts. **C)** Summary table of mouse termination days. Error bars represent ± SEM. n=8 mice per group.

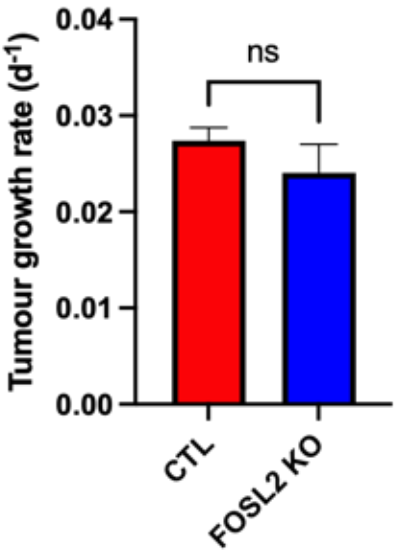

Figure 5.2 FOSL2 knockout has no impact on tumour growth rate *in vivo*. HCT116 control and FOSL2 knockout cells were injected subcutaneously into CD1 nude mice and tumour volume was measured every 3 days. Tumour growth rates were calculated by Log10 transforming the tumour volumes and carrying out linear regression analysis. Data was analysed by unpaired t-test. Error bars represent ± SEM. n=8 mice per group.

5.3.2 Validation of FOSL2 knockout in HCT116 mouse xenograft samples

The following immunohistochemical analysis is credited to Dr R. Mahmoud and the data is presented here with permission. In order to confirm FOSL2 knockdown in the HCT116 cells utilised in the xenograft study, immunohistochemical staining of FOSL2 expression was performed. Figure 5.3a shows representative images of the FOSL2 staining of HCT116 CTL and HCT116 FOSL2 KO xenograft FFPE sections along with a no antibody negative control. The absence of staining in the negative control confirmed there was no background staining and that the staining observed was specifically due to the antibody:antigen interaction. A reduction in FOSL2 staining in all three of the knockout xenografts could be identified visually.

In order to quantify the reduction in FOSL2 expression, the percentage of FOSL2 staining in the CTL and FOSL2 KO sections was visually scored. There was a statistically significant decrease in FOSL2 staining in the FOSL2 KO sections compared to the CTL equating to an approximately 3-fold reduction in FOSL2 expression (figure 5.3b, $p<0.0332$). This data confirmed that FOSL2 knockdown was achieved in the FOSL2 KO xenografts.

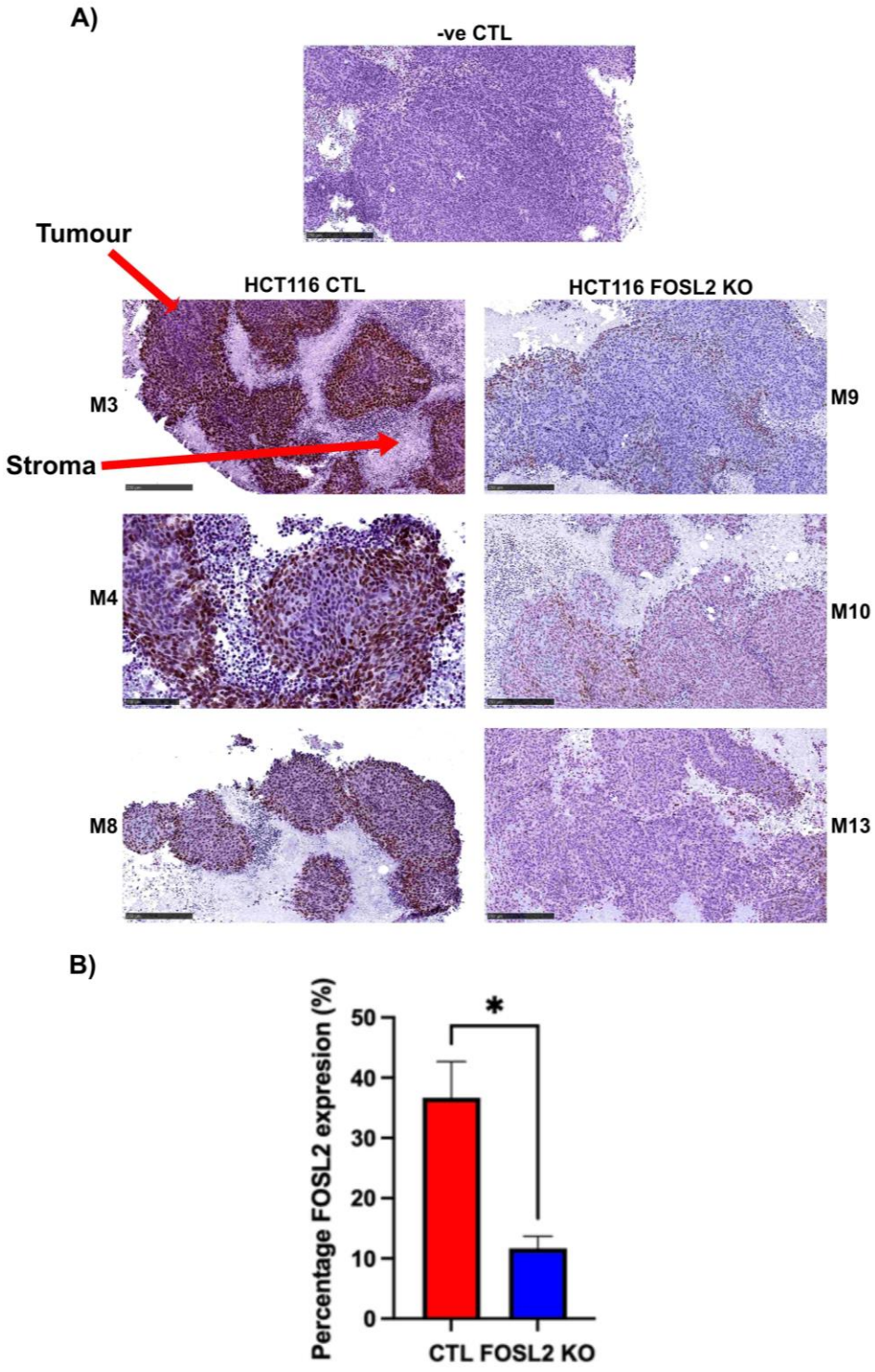

Figure 5.3 Validation of FOSL2 knockout in HCT116 xenograft tumours. HCT116 control xenografts 3, 4 and 8 along with FOSL2 KO xenografts 9, 10 and 13 were analysed by immunohistochemical staining for FOSL2 expression. A no antibody negative control was included. **A)** Representative images of FOSL2 staining in the CTL and FOSL2 KO xenograft sections taken with a 10x objective on a slide scanner (Hamamatsu NanoZoomer). Scale bar represents 250 μm. **B)** FOSL2 expression was visually scored and analysed by unpaired t-test. *p <0.0332, **p<0.0021, ***p<0.0002, ****P<0.0001. Error bars represent ± SEM. n=3. *Experiments performed and analysed by Dr R. Mahmoud.

5.3.3 Investigating the spatial distribution of hypoxia-associated metabolites across the oxygen gradient using orbiSIMS in an HCT116 mouse xenograft model

In order to investigate whether the orbiSIMS methodology developed in Chapter 3 could be used on *in vivo* tumour samples to identify spatial changes in metabolites in response to changes in oxygen tension, the HCT116 CTL and FOSL2 KO xenografts were cryo-sectioned and submitted for orbiSIMS analysis (see 2.11.1 and 2.11.3). In order to identify regions of interest (ROI) within the sample it was decided to take an initial tilescan of the section using the LMIG ToF mode on the orbiSIMS and then identify a 'strip' for GCIB orbitrap image analysis that covered from the centre of the sample to the periphery to capture regions of necrosis and hypoxia along with proliferating cells (figure 5.4). The LMIG bismuth cluster ion beam combined with ToF analysis allowed for the rapid acquisition of an overview image but with increased molecular fragmentation. Figure 5.5a displays the LMIG-ToF tilescan obtained for the HCT116 control xenograft from mouse 4 (M4) and indicates the 'strip' that was selected for GCIB-orbitrap imaging. The selected 'strip' is shown in figure 5.5b and highlights the region of the 'strip' that was utilised for downstream analysis encompassing the tumour sample from the core to the periphery. Figure 5.5c displays the region of the 'strip' used in downstream analysis, which was 5400 μm x 200 μm. A line profiling analysis, as described in section 4.3.16, using a single line of width 200 μm to cover the tumour ROI was used to measure the metabolite signal along the oxygen gradient (figure 5.5d).

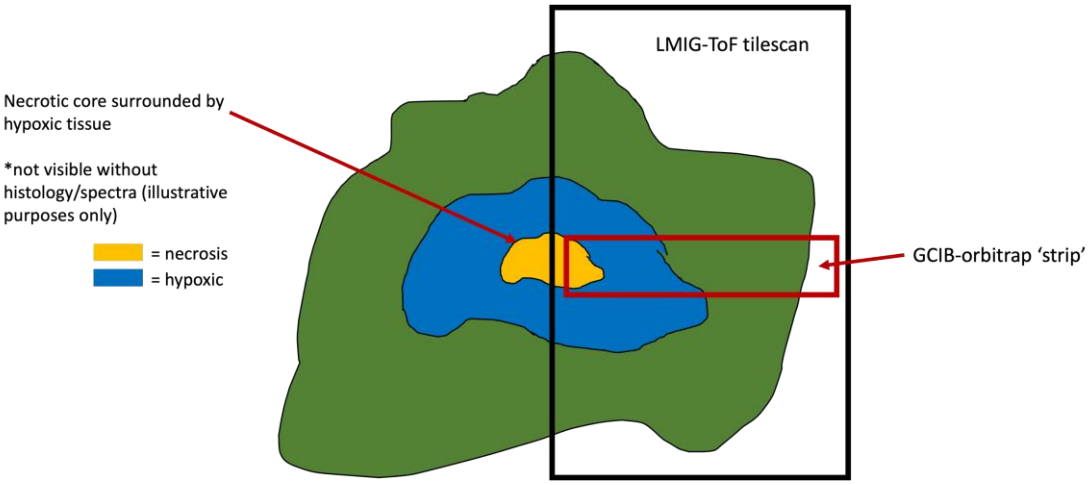

Figure 5.4 Diagrammatic representation of orbiSIMS methodology for analysis of tumour sections. An LMIG-ToF tilescan of 6000 μm x 7000 μm was obtained to acquire an overview scan of the sample and to enable the selection of the sample 'strip' for GCIB-orbitrap imaging containing the required regions of interest within the tumour sample.

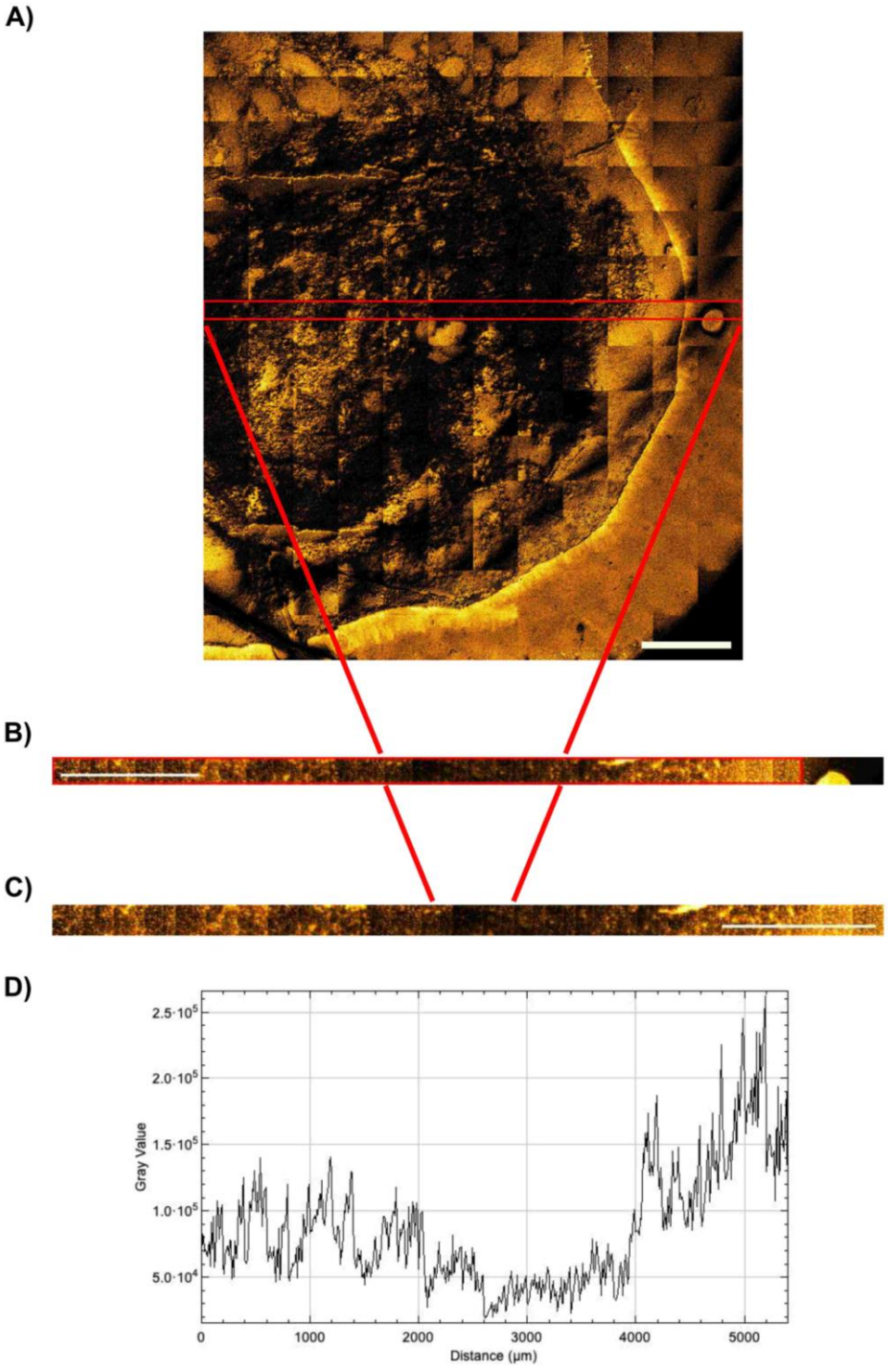

Figure 5.5 Identification of ROI for GCIB orbitrap image analysis and line profile analysis from LMIG-ToF tilescan. A) A 6000 µm x 7000 µm (1536 pixels x 1792 pixels) LMIG-ToF tilescan of the HCT116 CTL4 xenograft sample with a cycle time of 200 µs. The red box highlights the 'strip' selected for GCIB-orbitrap image analysis **B)** The 6000 µm x 200 µm sample 'strip' selected for GCIB-orbitrap image analysis. The red box highlights the region of interest capturing the tumour tissue. **C)** The tumour ROI covering from the core (left) to the periphery (right) of the xenograft section. **D)** Line profile analysis of the tumour ROI using a line width of 200 µm. Scale bar represents 1 mm. n=1.

The same hypoxia-regulated metabolites that were investigated in Chapter 4 were selected for *in vivo* orbiSIMS analysis along with glucose and lactate. NAD+ and AMP were not included due to the lack of signal obtained. Figure 5.6 displays the GCIB orbitrap negative polarity images for the selected metabolites along with the total ion count for the control xenograft and FOSL2 knockout xenograft cryosections. Adenine was once again selected as a control marker. Overall, a better signal was achieved with the control sample compared to the knockout however, the variation in signal intensities appeared to be mostly molecule dependent.

A line profile analysis, similar to the method described in section 4.3.16, but using a line width of 200 μm in order to cover the entire sample 'strip' in the measurement was employed to investigate the spatial distribution of metabolites across the oxygen gradient within the tumour samples from the periphery to the core. Figures 5.7 and 5.8 show the metabolite line profiles for the hypoxia-upregulated and hypoxia-downregulated metabolites respectively along with adenine. Despite an increase close to the periphery of the tumour, which could be due to the increased proliferative rates of viable cells at the tumour edge, adenine levels remained consistent across the tumour but with a much weaker signal in the FOSL2 knockout sample (figure 5.7a). Glucose levels fluctuated consistently along the oxygen gradient in both the control and knockout samples (figure 5.7b). A rapid increase and then decrease was observed in the lactate signal in both samples followed by a very gradual increase across the tumour down the oxygen gradient (figure 5.7c). *cis*-aconitate levels increased initially around 600 μm from the periphery of the tumour and then remained high across the sample (figure 5.7d). An even greater increase was observed with FOSL2 knockout, but much further into the tumour around 2.4 mm.

Regarding the hypoxia-downregulated metabolites, the fumarate signal increased slightly around 600 μm from the tumour periphery but remained low across the sample (figure 5.8b). A larger increase was observed in the FOSL2 knockout sample starting around 2.4 mm into the tumour. An initial increase in the malate signal was also seen in both conditions followed by a large decrease starting around 600 μm (figure 5.8c). The phosphocreatine signal fluctuated rapidly across the oxygen gradient with a generally higher signal observed in the control compared to the knockout sample (figure 5.8d).

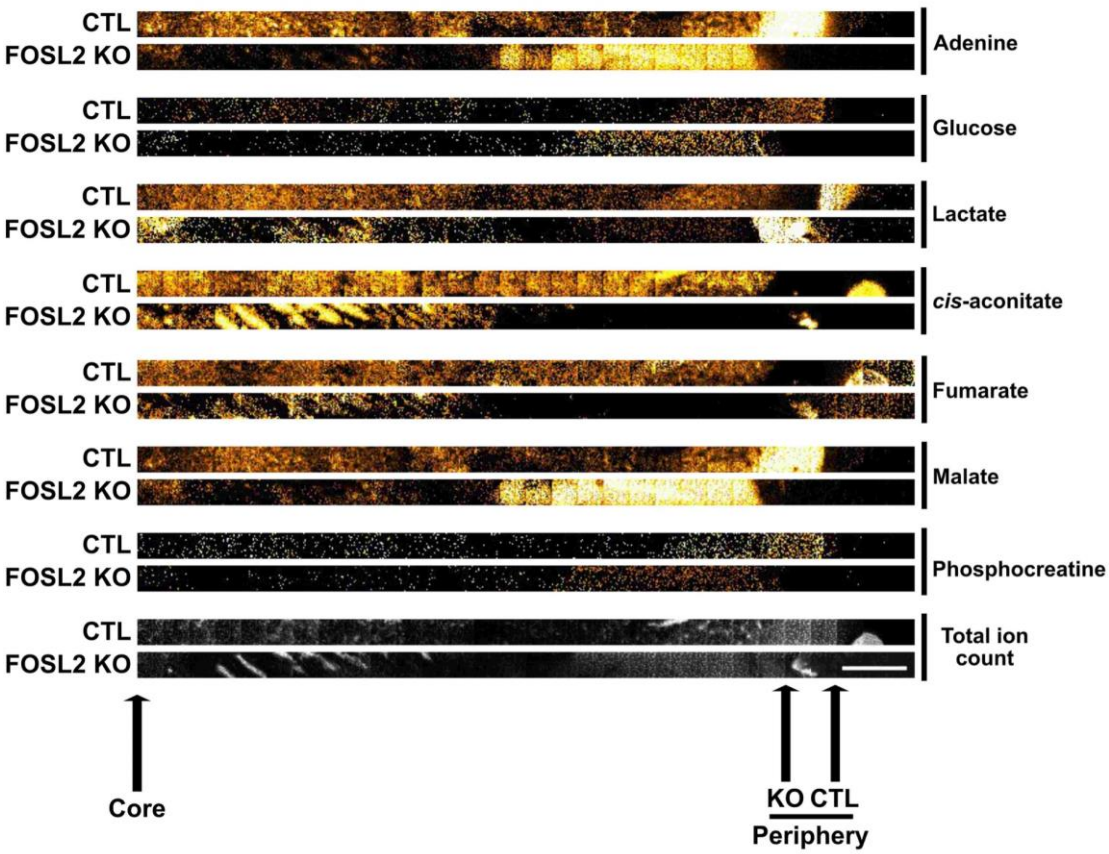

Figure 5.6 Hypoxia regulates the spatial distribution of metabolites across the oxygen gradient in HCT116 CRC xenografts *in vivo*. 20μm 20keV Ar_{3000+} Orbitrap MS negative polarity images of adenine (*m/z* 134.0472, $C_5H_4N_5^-$), glucose (*m/z* 179.0463, $C_6H_{11}O_6^-$), lactate (*m/z* 89.0243, $C_3H_5O_3^-$), cis-aconitate (*m/z* 173.0567, $C_6H_5O_6^-$), fumarate (*m/z* 115.0037, $C_4H_3O_4^-$), malate (*m/z* 133.0156, $C_4H_5O_5^-$), phosphocreatine (*m/z* 210.0884, $C_4H_9N_3O_5P^-$) and total ion count (TIC) signals from HCT116 CTL M4 and FOSL2 KO M10 xenograft sections. Signal normalisation was performed by dividing by TIC. Scale bar represents 500 μm. n=1.

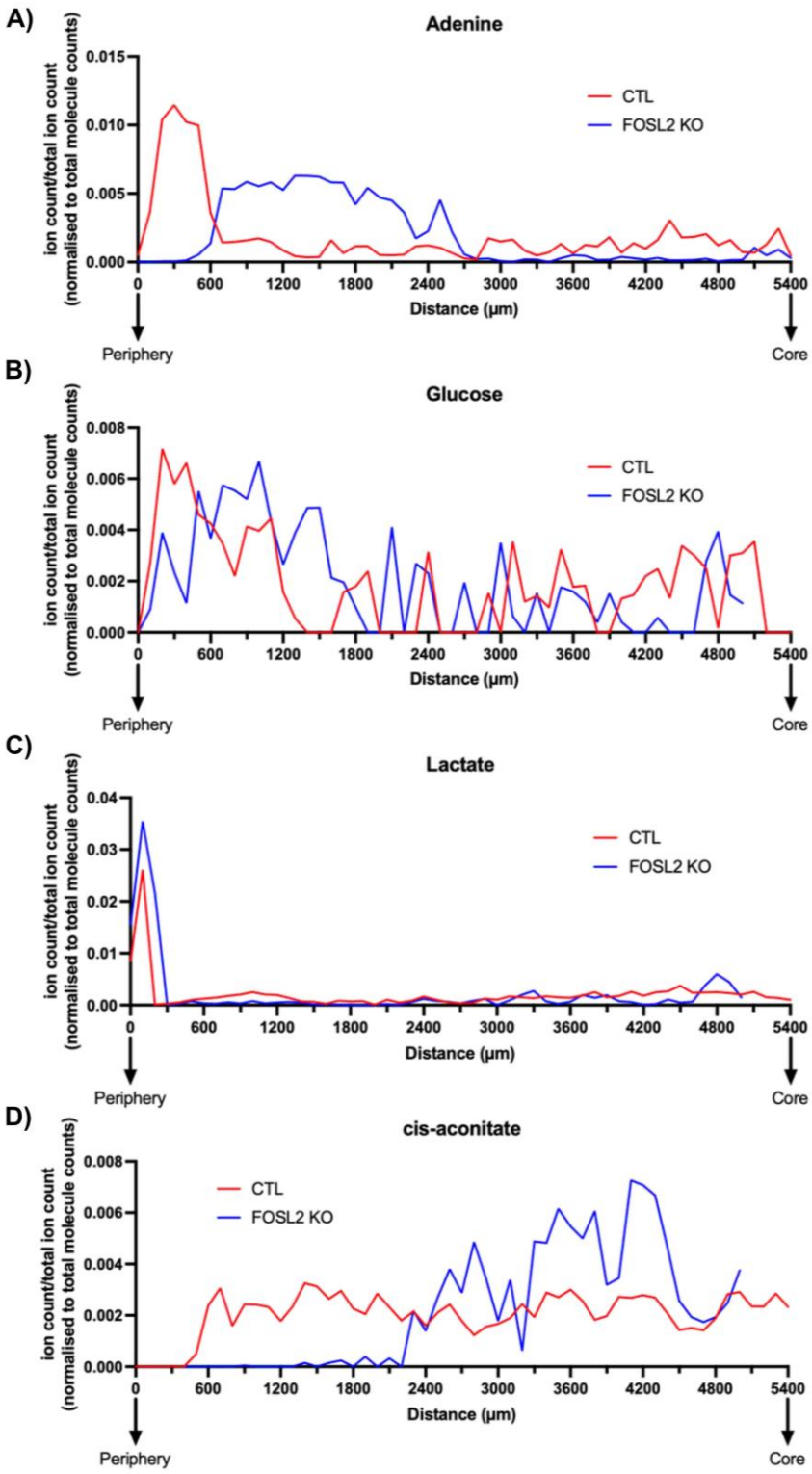

Figure 5.7 The spatial distribution of hypoxia-induced metabolites fluctuates across the oxygen gradient in a CRC xenograft model. A-D) Line profile analysis was employed on GCIB orbitrap negative polarity MS images of adenine, glucose, lactate and *cis*-aconitate to measure the change in metabolite signal across the oxygen gradient in HCT116 control and FOSL2 knockout xenograft sections. Image analysis was performed in ImageJ. n=1.

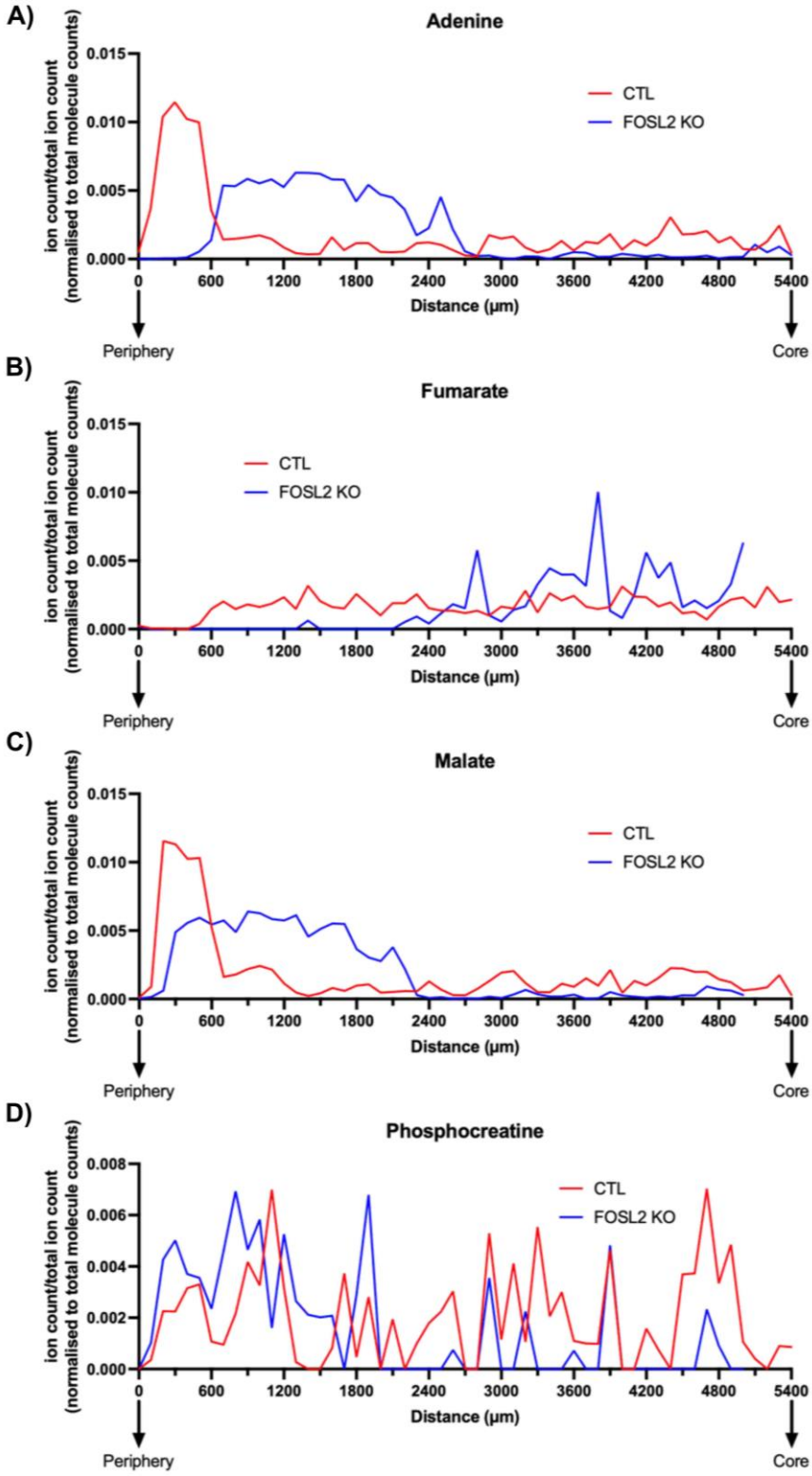

Figure 5.8 The spatial distribution of hypoxia-downregulated metabolites fluctuates across the oxygen gradient in a CRC xenograft model. A-D) Line profile analysis was employed on GCIB orbitrap negative polarity MS images of adenine, fumarate, malate and -phosphocreatine to measure the change in metabolite signal across the oxygen gradient in HCT116 control and FOSL2 knockout xenograft sections. Image analysis was performed in ImageJ. n=1.

5.3.3 Investigating the spatial distribution of acidosis-associated metabolites across the oxygen gradient using orbiSIMS in an HCT116 mouse xenograft model

The same acidosis-regulated metabolites that were investigated in Chapter 4 were also selected for *in vivo* orbiSIMS analysis to investigate the impact of acidosis on the spatial regulation of metabolites in tumour samples. Figure 5.9 displays the GCIB orbitrap negative polarity images for the selected metabolites along with the total ion count and adenine for the control and FOSL2 knockout xenograft cryosections. Figures 5.10 and 5.11 display the metabolite line profiles for the acidosis-upregulated and downregulated metabolites respectively along with adenine. Similar results were observed for the phenylalanine and acetyl-CoA signals in both the control and knockout samples, with the highest signal occurring within the first 1.2-1.8 mm followed by a decrease (figures 5.10b and 5.10d). The palmitic acid signal remained consistently low across the majority of both the control and knockout tumours; however, an increase began deep into the tumour around 4.5 mm (figure 5.10c).

Regarding the acidosis-downregulated metabolites, an initial rapid increase in alanine signal was observed followed by an equally rapid decrease around 150 μm from the tumour periphery after which, only a very weak signal was obtained (figure 5.11b). Similarly, both the threonine and glutamate signals increased steadily over the first 300 μm and 600 μm respectively from the tumour periphery followed by a gradual decrease until ~ 1.8 mm (figures 5.11c and 5.11d). After this, a slight increasing trend in the signals was observed, with consistent fluctuations, going towards the tumour core. A greater increase was seen in the control sample.

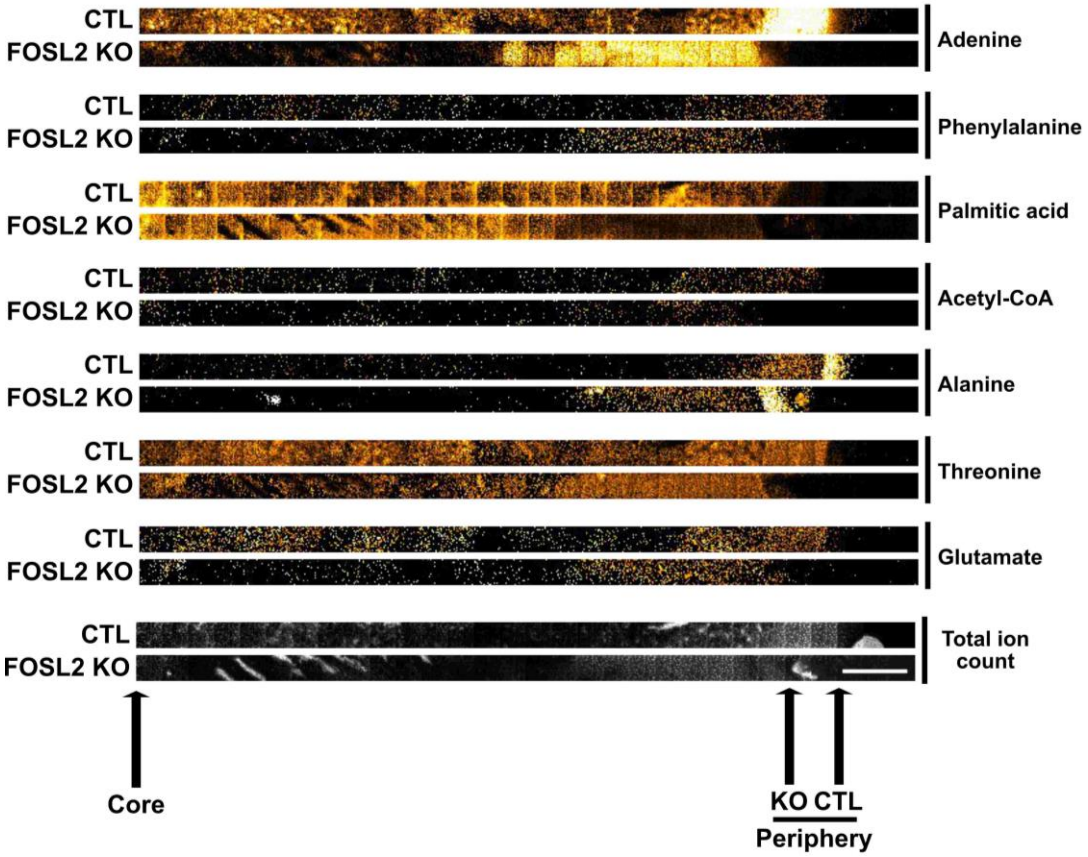

Figure 5.9 Hypoxia regulates the spatial distribution of acidosis-regulated metabolites across the oxygen gradient in HCT116 CRC xenografts *in vivo*. 20μm 20keV Ar_{3000+} Orbitrap MS negative polarity images of adenine (*m/z* 134.0472, $C_5H_4N_5^-$), phenylalanine (*m/z* 164.0718, $C_9H_{10}NO_2^-$), palmitic acid (*m/z* 255.2333, $C_{16}H_{31}O_2^-$), acetyl-CoA (*m/z* 796.3861, $C_{23}H_{37}N_7O_{17}P_3S^-$), alanine (*m/z* 88.0404, $C_3H_6NO_2^-$), threonine (*m/z* 118.0512, $C_4H_8NO_3^-$), glutamate (*m/z* 146.0457, $C_5H_8NO_4^-$) and total ion count (TIC) signals from HCT116 CTL M4 and FOSL2 KO M10 xenograft sections. Signal normalisation was performed by dividing by TIC. Scale bar represents 500 μm. n=1.

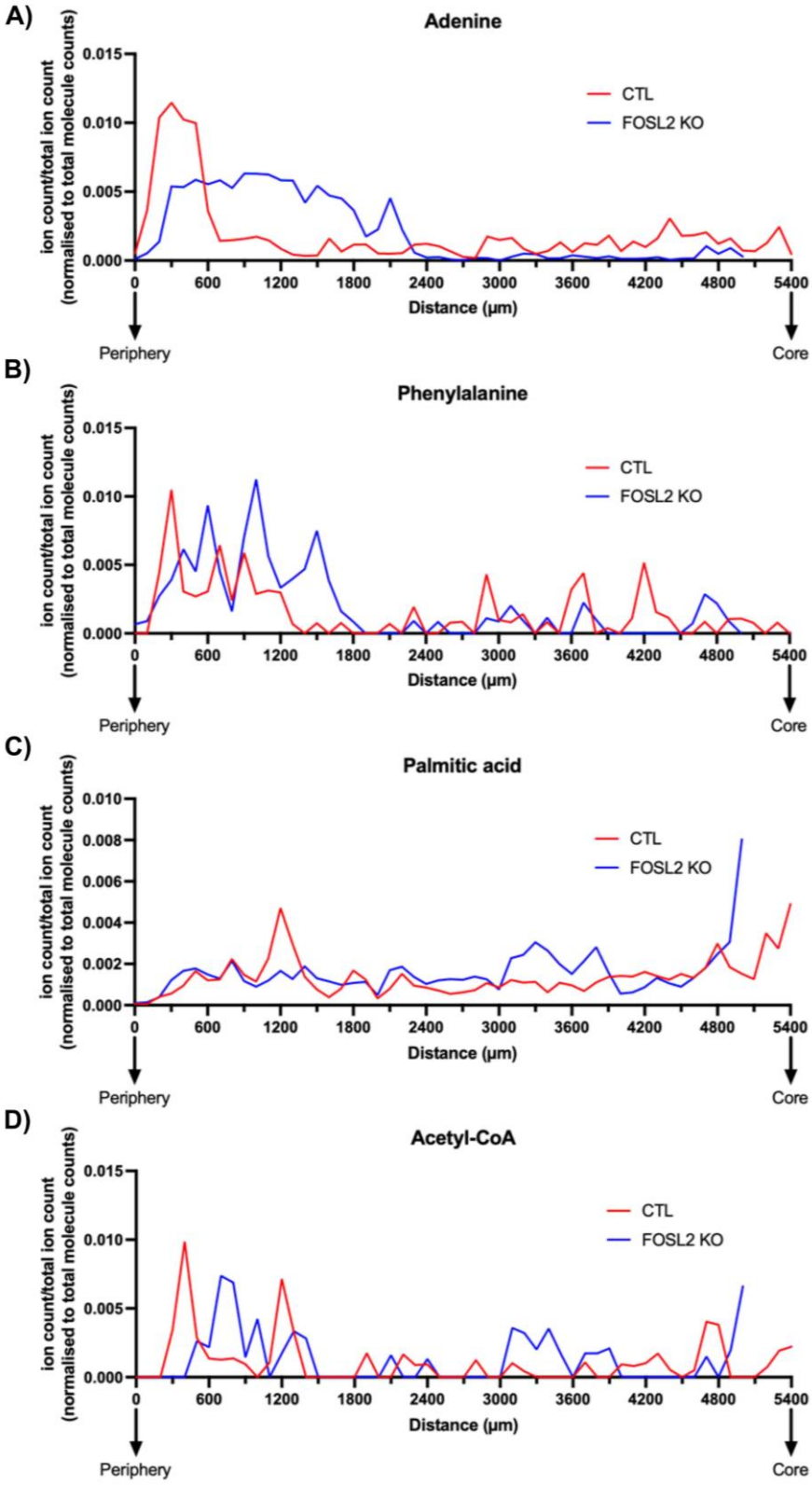

Figure 5.10 The spatial distribution of acidosis-induced metabolites fluctuates across the oxygen gradient in a CRC xenograft model. A-D) Line profile analysis was employed on GCIB orbitrap negative polarity MS images of adenine, phenylalanine, palmitic acid and acetyl-CoA to measure the change in metabolite signal across the oxygen gradient in HCT116 control and FOSL2 knockout xenograft sections. Image analysis was performed in ImageJ. n=1.

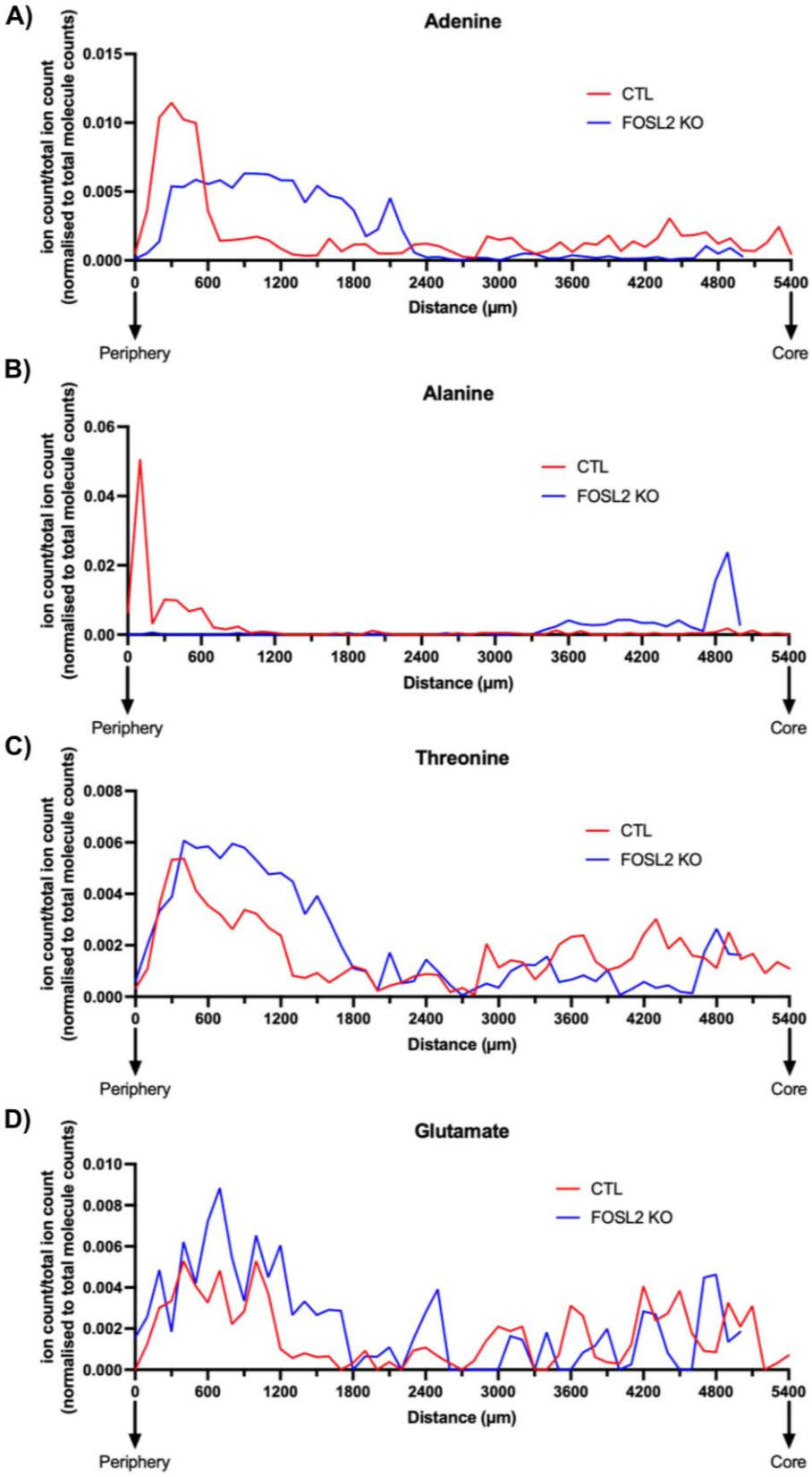

Figure 5.11 The spatial distribution of acidosis-downregulated metabolites fluctuates across the oxygen gradient in a CRC xenograft model. A-D) Line profile analysis was employed on GCIB orbitrap negative polarity MS images of adenine, alanine, threonine and -glutamate to measure the change in metabolite signal across the oxygen gradient in HCT116 control and FOSL2 knockout xenograft sections. Image analysis was performed in ImageJ. n=1.

5.3.4 Investigating the spatial distribution of glycolytic intermediates across the oxygen gradient using orbiSIMS in an HCT116 mouse xenograft model

Previous LS174T CRC cell line FOSL2 siRNA knockdown hypoxia vs control hypoxia RNA-sequencing data, generated by Dr E. Vancauwenberghe and used with permission, was studied to identify whether FOSL2-regulated genes were involved in metabolic regulation in hypoxia. In order to identify what pathways FOSL2-regulated genes were involved in KEGG pathway analysis was used. Pathway analysis revealed a total of 9 pathways that were significantly enriched for downregulated FOSL2-dependent DEGs (figure 5.12). Importantly, all 9 of the enriched pathways corresponded to metabolic pathways including major known hypoxia-regulated pathways such as glycolysis and amino acid biosynthesis. Furthermore, filtering of the downregulated DEGs to identify metabolic genes revealed that 5 of the top 20 downregulated FOSL2-regulated DEGs belonged to the glycolytic pathway (data not shown). Therefore, it was decided to investigate the spatial regulation of glycolytic intermediates in the HCT116 FOSL2 knockout xenograft samples by orbiSIMS analysis.

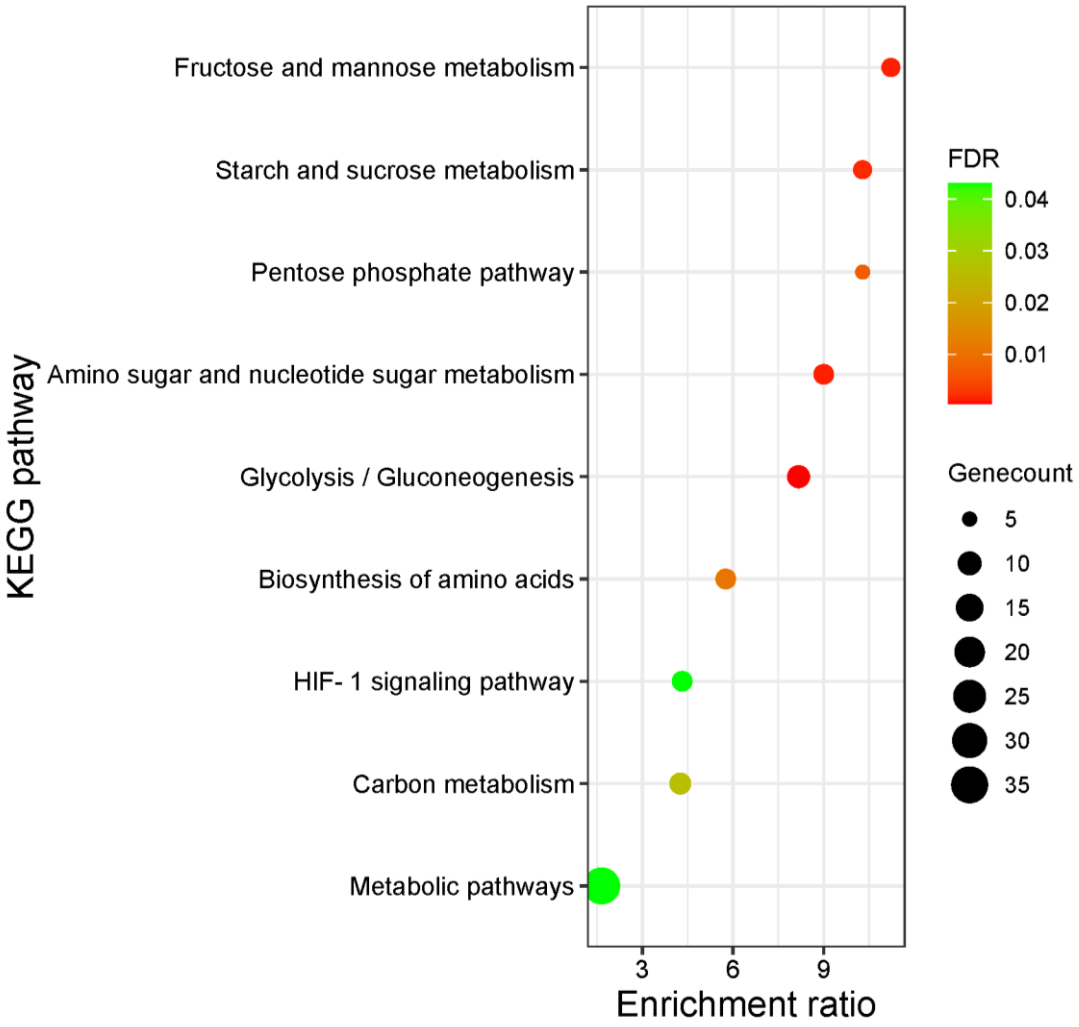

Figure 5.12 KEGG pathway classification of downregulated FOSL2-dependent genes in hypoxia. KEGG pathway analysis of significantly downregulated genes in siFOSL2 vs control samples in hypoxia. Significant KEGG pathways were plotted on the y-axis against their enrichment ratio on the x-axis. The bubble size represents the gene count whilst the colour represents the significance level measured by FDR. Significant pathways: FDR < 0.05. n=3.

Some of the glycolytic intermediates investigated in Chapter 4 in the context of HIF-1α-regulated metabolism were also used here including F-6-P, F-2,6-BP, DHAP and PEP with the addition of glycerol-3-phosphate (G-3-P). Figure 5.13 displays the GCIB orbitrap negative polarity images for the selected metabolites along with the total ion count and adenine for the control and FOSL2 knockout xenograft cryosections. Figures 5.14 displays the metabolite line profiles for the glycolytic intermediates along with adenine. Similar results were observed for F-2,6-BP and DHAP in both the control and knockout samples with the only signal detected within the first 1.8 mm into the tumour sections (figures 5.14c and 5.14d). Conversely, G-3-P was only strongly detected in the FOSL2 knockout sample closer to the tumour core from 3 mm inwards (figure 5.14e). Similar trends were also observed for both F-6-P and PEP in the control and FOSL2 knockout samples and displayed high degrees of fluctuation across the tumours (figures 5.14b and 5.14f).

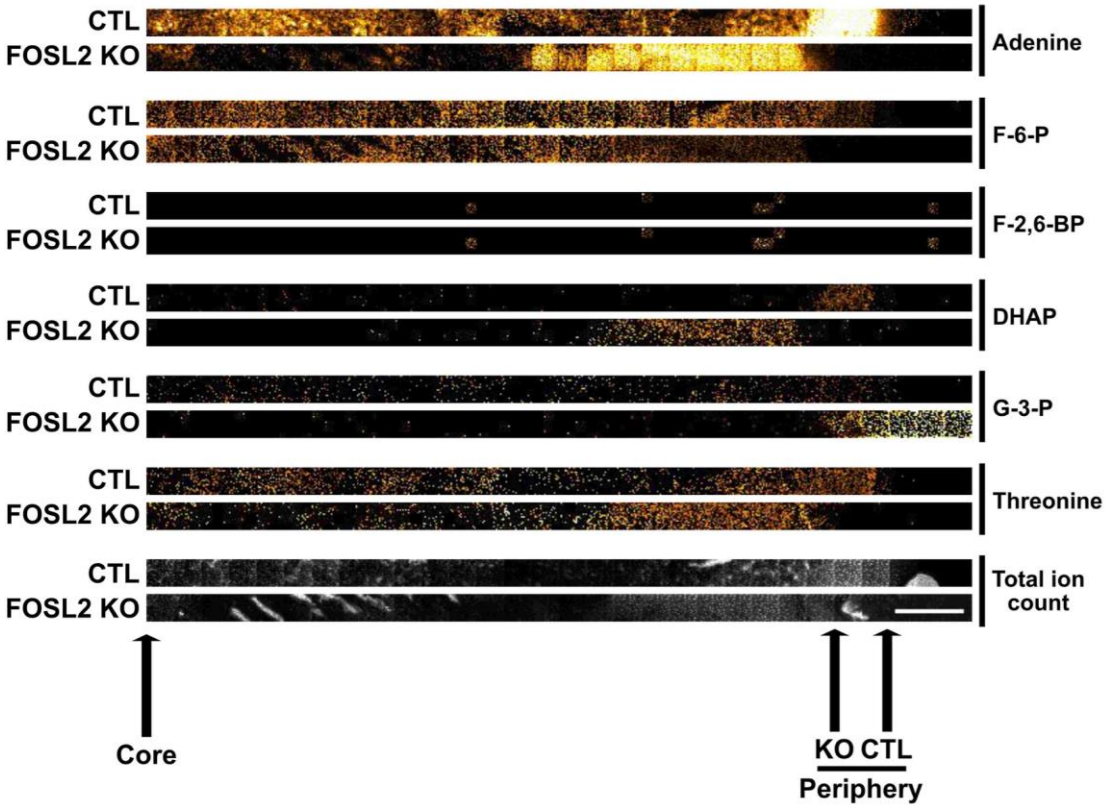

Figure 5.13 Loss of FOSL2 leads to changes in the spatial distribution of glycolytic intermediates across the oxygen gradient in HCT116 CRC xenografts *in vivo*. 20μm 20keV Ar_{3000+} Orbitrap MS negative polarity images of adenine (*m/z* 134.0472, $C_5H_4N_5^-$), fructose-6-phosphate (*m/z* 259.0227, $C_6H_{12}O_9P^-$), fructose-2,6-bisphosphate (*m/z* 338.9890, $C_6H_{13}O_{12}P_2^-$), dihydroxyacetone phosphate (*m/z* 168.9909, $C_4H_8NO_3^-$), glycerol-3-phosphate (*m/z* 171.0452, $C_3H_8O_6P^-$), phosphoenolpyruvate (*m/z* 167.0463, $C_3H_4O_6P^-$) and total ion count (TIC) signals from HCT116 CTL M4 and FOSL2 KO M10 xenograft sections. Signal normalisation was performed by dividing by TIC. Scale bar represents 500 μm. n=1.

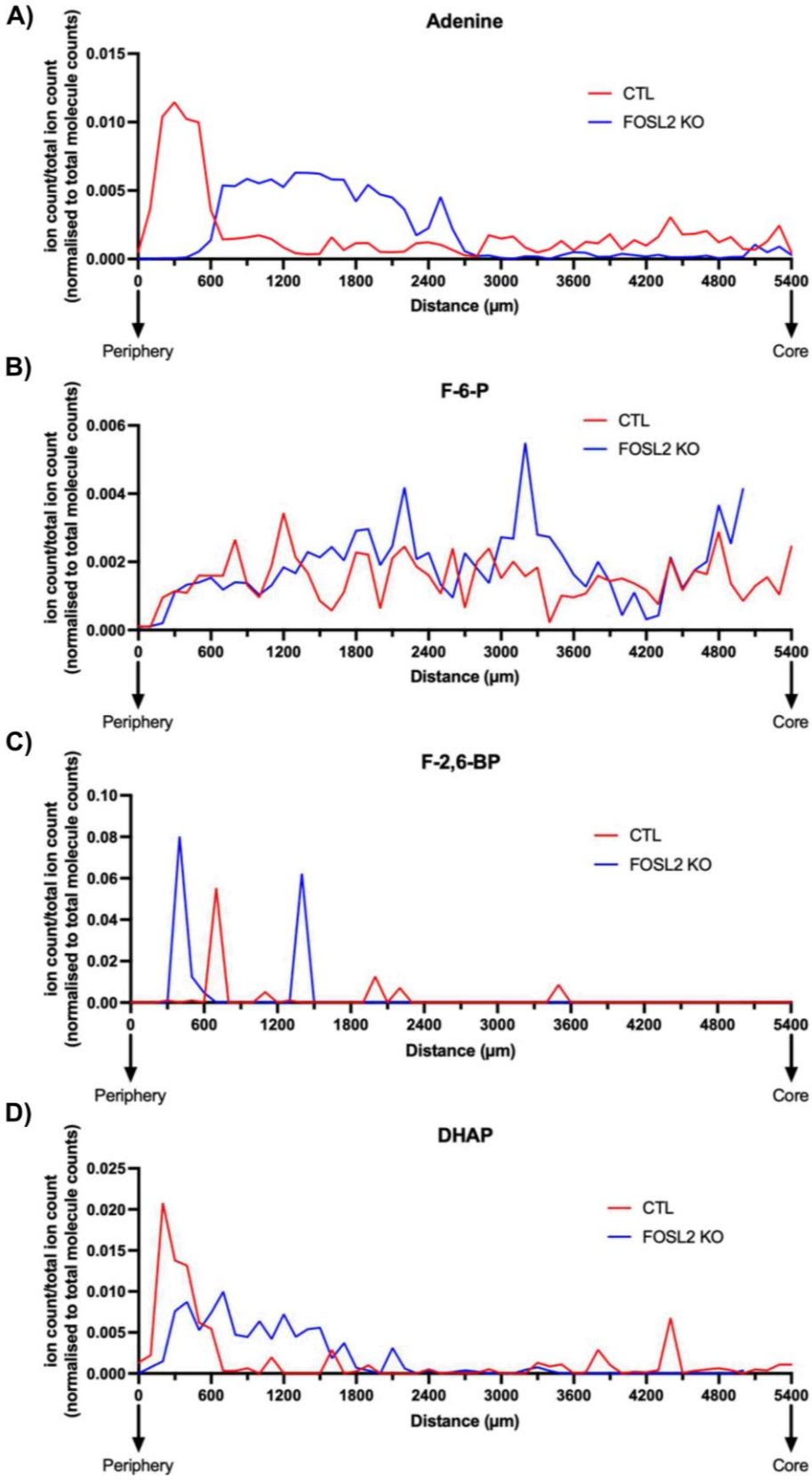
A)
Adenine
ion count/total ion count (normalised to total molecule counts)
0.015
0.010
0.005
0.000
CTL
FOSL2 KO
0
600
1200
1800
2400
3000
3600
4200
4800
5400
Distance (µm)
Periphery
Core
B)
F-6-P
ion count/total ion count (normalised to total molecule counts)
0.006
0.004
0.002
0.000
CTL
FOSL2 KO
0
600
1200
1800
2400
3000
3600
4200
4800
5400
Distance (µm)
Periphery
Core
C)
F-2,6-BP
ion count/total ion count (normalised to total molecule counts)
0.10
0.08
0.06
0.04
0.02
0.00
CTL
FOSL2 KO
0
600
1200
1800
2400
3000
3600
4200
4800
5400
Distance (µm)
Periphery
Core
D)
DHAP
ion count/total ion count (normalised to total molecule counts)
0.025
0.020
0.015
0.010
0.005
0.000
CTL
FOSL2 KO
0
600
1200
1800
2400
3000
3600
4200
4800
5400
Distance (µm)
Periphery
Core

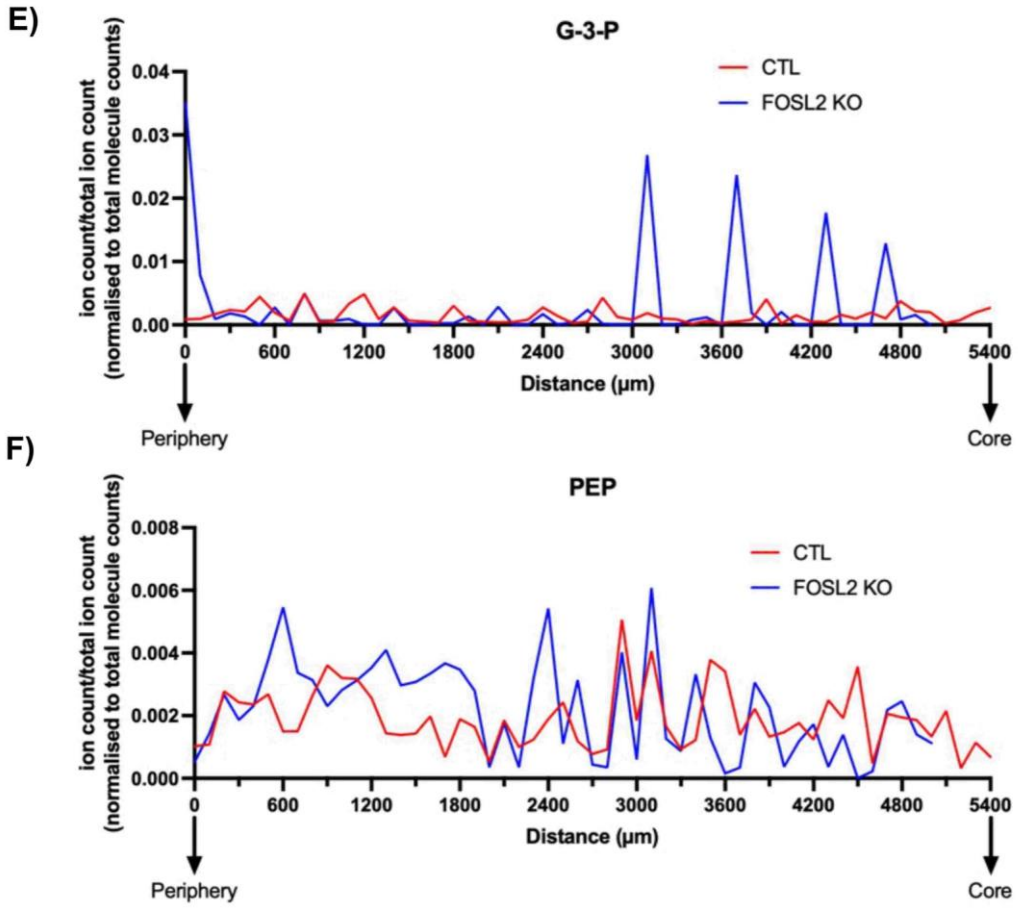

Figure 5.14 The spatial distribution of glycolytic intermediates fluctuates across the oxygen gradient in a CRC xenograft model. A-F) Line profile analysis was employed on GCIB orbitrap negative polarity MS images of adenine, F-6-P, F-2,6-BP, DHAP, G-3-P and PEP measure the change in metabolite signal across the oxygen gradient in HCT116 control and FOSL2 knockout xenograft sections. Image analysis was performed in ImageJ. n=1.

5.3.5 Investigating the spatial distribution of hypoxia-associated metabolites using orbiSIMS in CRC patient-derived xenografts

In order to further examine the applicability of the orbiSIMS methodology developed in Chapter 3 for use in a clinical setting, an analysis of the spatial distribution of hypoxia-associated metabolites was also carried out on CRC PDX cryosections (see 2.11.2 and 2.11.3). The same experimental setup as described in section 5.3.3 was employed here including the use of an LMIG-ToF tilescan and identification of GCIB-orbitrap 'strip' for imaging, followed by line profiling analysis. Importantly, for technical reasons, only positive polarity GCIB-orbitrap MS analysis was performed as opposed to the negative ion mode used throughout this study.

The same hypoxia-regulated metabolites analysed in the HCT116 xenograft samples in section 5.3.3 were selected for analysis here. Figure 5.15 displays the GCIB orbitrap positive polarity images for the selected metabolites along with the total ion count and adenine for a single CRC PDX cryosection. Figures 5.16 and 5.17 display the metabolite line profiles for the hypoxia-upregulated and downregulated metabolites respectively along with adenine. Similar trends were observed for malate and phosphocreatine with generally low signals detected across the tumour apart from a large spike in signal intensity around 1.8 mm and 3.6 mm into the tumour respectively (figures 5.17c and 5.17d). Highly fluctuating signals were observed across the tumour section for both glucose and *cis*-aconitate (figures 5.16b and 5.16d). A similar pattern was also seen for both lactate and fumarate with a large increase in signal around 300 μm into the tumour section followed by a sustained high signal throughout (figure 5.16c and figure 5.17b).

Following this, attempts were made to also investigate the acidosis-regulated metabolites and glycolytic intermediates studied in the HCT166 CRC xenograft sections previously however low/no signal was obtained for the majority of the metabolites searched for and so the data was not included. This is possibly due to the switch in polarities used for the acquisition of the MS data. Repeating the PDX analysis using the negative ion mode could improve the detection of these metabolites.

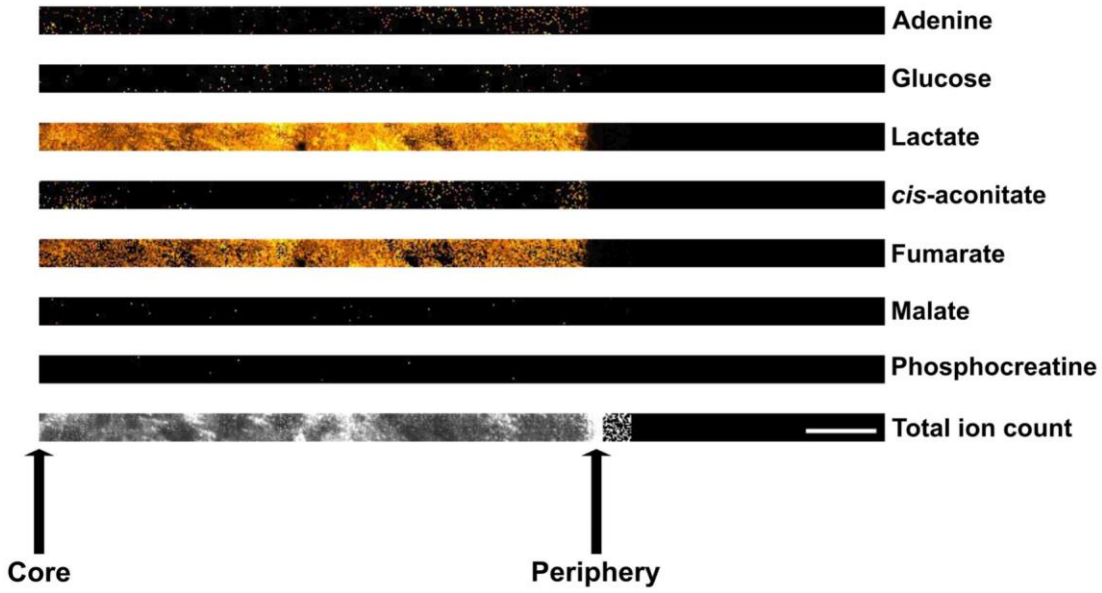

Figure 5.15 Hypoxia regulates the spatial distribution of metabolites across the oxygen gradient in CRC patient-derived xenografts *in vivo*. 20μm 20keV Ar_{3000+} Orbitrap MS positive polarity images of adenine (*m/z* 134.0472, $C_5H_4N_5^-$), glucose (*m/z* 179.0463, $C_6H_{11}O_6^-$), lactate (*m/z* 89.0243, $C_3H_5O_3^-$), cis-aconitate (*m/z* 173.0567, $C_6H_5O_6^-$), fumarate (*m/z* 115.0037, $C_4H_3O_4^-$), malate (*m/z* 133.0156, $C_4H_5O_5^-$), phosphocreatine (*m/z* 210.0884, $C_4H_9N_3O_5P^-$) and total ion count (TIC) signals from a CRC patient-derived xenograft section. Signal normalisation was performed by dividing by TIC. Scale bar represents 500 μm. n=1.

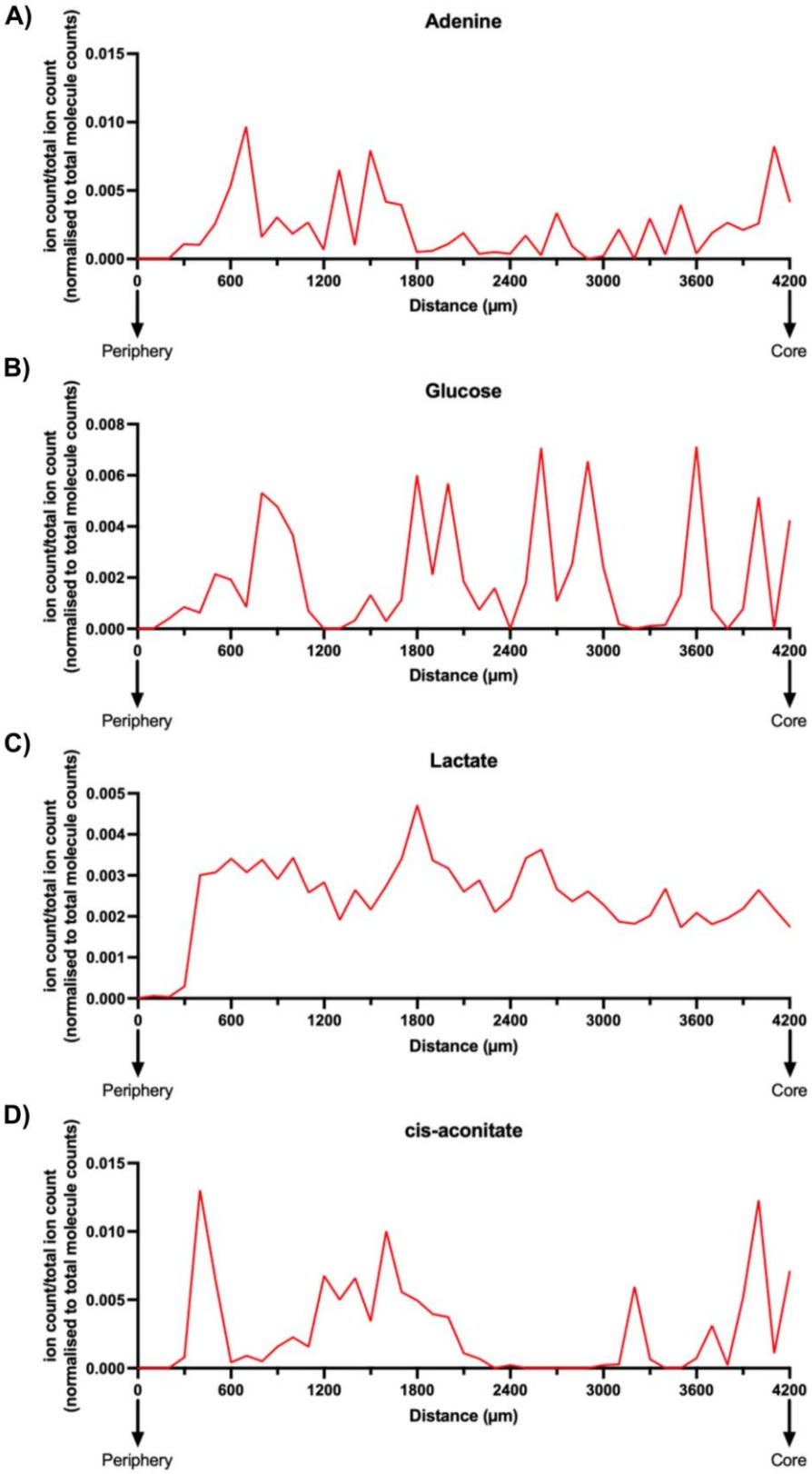

Figure 5.16 The spatial distribution of hypoxia-induced metabolites fluctuates across the oxygen gradient in a CRC patient-derived xenograft model. A-D) Line profile analysis was employed on GCIB orbitrap positive polarity MS images of adenine, glucose, lactate and *cis*-aconitate to measure the change in metabolite signal across the oxygen gradient in a CRC patient-derived xenograft section. Image analysis was performed in ImageJ. n=1.

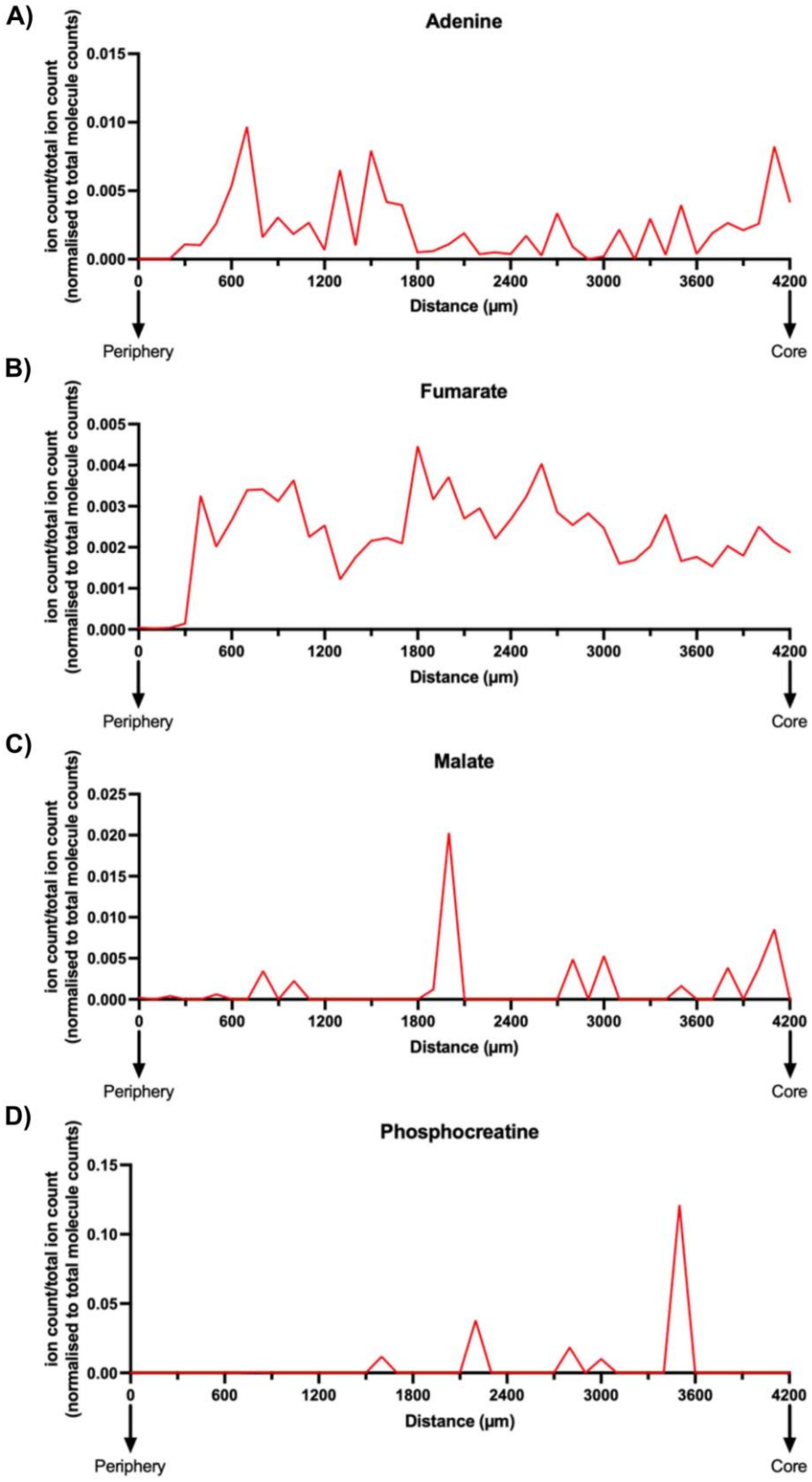

Figure 5.17 The spatial distribution of hypoxia-downregulated metabolites fluctuates across the oxygen gradient in a CRC patient-derived xenograft model. A-D) Line profile analysis was employed on GCIB orbitrap positive polarity MS images of adenine, fumarate, malate and phosphocreatine to measure the change in metabolite signal across the oxygen gradient in a CRC patient-derived xenograft section. Image analysis was performed in ImageJ.

5.4 Discussion

5.4.1 A FOSL2 knockout HCT116 mouse xenograft model

Tumour growth in response to FOSL2 knockout exhibited a biphasic response. In the first phase, the knockout tumour grew similarly to the control for approximately 40 days after which a plateau phase occurred for approximately 10 days. A second phase of growth then followed. However, the start of this second phase for the knockout tumours was delayed compared to the control. This could explain the difference in tumour volume observed without any significant change in the overall growth rate. Interestingly, most previous studies that have mathematically modelled tumour growth observe an asymptotical growth curve without this second phase[607,608]. It would be interesting to identify the mechanisms behind this second phase of tumour growth and the delay observed with FOSL2 knockout. This could be due to a reduction in the availability of metabolites needed to continue the rapid rates of proliferation and growth caused by the loss of FOSL2. Furthermore, if this occurs within hypoxic regions of the tumour, it is possible that a gradual replenishment of these metabolites through hypoxia-induced metabolic reprogramming could promote the reinitiation of tumour growth.

5.4.2 Applicability of the orbiSIMS approach for spatially resolving metabolic adaptation to hypoxia using *in vivo* xenograft models

The cryo-orbiSIMS workflow developed in this study was able to successfully detect and measure metabolite distribution for a wide range of metabolites, including both polar and non-polar molecules, in the HCT116 mouse xenograft sections using a negative ion polarity mode. However, only a few small, polar molecules such as lactate, glucose and fumarate were detected in the CRC PDX samples. Importantly, the PDX sample was only analysed in the positive ion mode whereas, throughout this study, I have demonstrated the improved signal detection and ionisation efficiency achieved with the negative ion mode for the metabolites I have investigated. Therefore, further analysis of the PDX sections in the negative ion mode would help resolve this.

The high vacuum operating conditions required for orbiSIMS analysis means specialised sample preparation is needed[547]. A typical procedure involves drying following either chemical or cryogenic sample fixation[463]. Here, I have shown that the snap-freezing of tumour sections in liquid nitrogen followed by cryosectioning and negative polarity

orbiSIMS analysis under cryogenic conditions is suitable for maintaining the physiological distribution of metabolites within *in vivo* tumour samples. Previous studies comparing room temperature and cryogenic orbiSIMS for the detection of lipids and semi-volatile molecules, such as free fatty acids, demonstrated the improved ionisation yield and improved spatial resolution under cryogenic conditions[609]. Furthermore, other studies have also shown that the size and structure of lipids and sterols are also altered during the drying process[464,610]. For example, cholesterol redistribution occurred in brain tissue analysed by ToF-SIMS following freeze-drying[464]. My work, combined with these studies, indicates the importance of maintaining cells and tissues in their native hydrated state through cryogenic sample preparation for metabolomic studies. Furthermore, I have demonstrated, for the first time, the use of a cryogenic transfer system to maintain cryogenic conditions when transferring HPF cell and tissue samples to the orbiSIMS instrument. Importantly, this prevents the unwanted condensation of water on the sample surface that can occur when the transfer is carried out at ambient temperatures which could interfere with data acquisition, as previously demonstrated in ToF-SIMS studies of unicellular organisms[452].

However, several metabolites including AMP, NAD+ as well as sterol intermediates failed to be detected using the methodology developed in my work. The low signal detection for these metabolites was also observed in the spheroid analysis discussed in chapter 4. The molecular complexity of these molecules warrants a more detailed analysis to identify the most likely candidate ion fragments. Previous studies have also discussed the challenges associated with carrying out mass spectrometry-based analyses of sterols due to their low ionisation efficiencies and poor isomer separation[611,612]. This could explain the low signals detected for the sterol intermediates investigated in my work, in both the *in vitro* and *in vivo* systems, and suggests that this workflow may not be applicable for the analysis of sterol derivatives. Positive mode ESI is typically used for these molecules due to the formation of adducts such as $[M+NH_4]^+$ and [M+ alkali metal ion]$^+$[613]. However, the formation of these ions was not investigated in this study. A more detailed analysis of the mass spectra for these metabolites could identify the formation of these adducts. In addition, it is possible that the use of different cryoprotectant solutions could be used to improve signal detection, however previous studies investigating membrane lipids in leukocytes by ToF-SIMS used ammonium formate, as used in my work, to successfully detect cholesterol[614].

5.4.3 Spatial regulation of metabolic adaptation to hypoxia in HCT116 mouse xenografts

Adenine was used as a control marker to identify cells within the tumour sections. Previous work using cryo-orbiSIMS to analyse bacterial biofilms demonstrated the applicability of adenine as an identifier of cells based on its incorporation into nucleic acids[466]. Interestingly, in the control tumour, a short peak was observed which dropped close to 0 after the first 300 μm from the periphery whereas a longer peak was observed in the knockout tumour over the first ~ 1.5 mm which then dropped to below detectable limits. A similar trend was also observed for malate and the glycolytic intermediate DHAP. This suggests there could be a difference in the size of the necrotic core within the two tumours with a smaller core in the knockout. However, immunohistochemical analysis of cell death markers such as cleaved caspase-3 or PARP in the tumour sections would help confirm this[615]. Importantly, the two tumours selected for orbiSIMS analysis were chosen based on size-matching as close as possible. However, as the knockout tumour took an additional 24 days to reach a comparable size to the control it is possible that the necrotic core also developed at a slower rate. In addition, due to the larger expected size of the necrotic core in tumour samples compared to spheroids, it is possible this effect would not be observed with the spheroid model[616].

The same edge effects observed with lactate in the spheroid model were also observed in the tumour sections. As discussed previously, this is possibly due to the leakage of small, polar metabolites out of the sample during the cryoprotectant washing stages prior to HPF. It would be interesting to compare samples that forego the additional washing steps to identify if washing was causing any metabolite migration. However, it is well-documented that cryoprotectants are important for the prevention of alterations to cellular structures and to reduce salt formation on the sample surface[617,618]. Interestingly, after this apparent peak at the tumour periphery little to no lactate was detected in the FOSL2 knockout sample whereas a small but steady increase was seen in the control tumour. It is possible that changes in the activity of glycolytic enzymes in response to FOSL2 knockout are leading to diminished anaerobic glycolysis and reduced lactate production. Interestingly, larger and more sustained signals were observed for several glycolytic intermediates including F-6-P and DHAP in the FOSL2 knockout compared to the control. Carrying out a spatial transcriptomics analysis of the tumour sections

would be interesting to correlate spatially resolved changes in the expression of glycolytic enzymes with the metabolite changes observed with FOSL2 knockout.

Several metabolites including glucose and phosphocreatine displayed high degrees of fluctuation across the tumour sections. It is difficult to confirm whether these fluctuations are due to a reduced signal-to-noise ratio for these ions or if they are biologically relevant effects induced by fluctuating oxygen concentrations. Reducing the number of data points presented could help to distinguish any background from true biologically relevant effects. It is also important to consider the physiological differences between the spheroid models used in chapter 4 and the tumour sections used here. The oxygen gradient within tumours is not a well-defined linear change as local fluctuations in oxygen tension occur depending on the proximity and viability of nearby blood vessels and interactions with the extracellular matrix, both of which are not present in spheroids[619]. It is feasible that by spatially probing tumour sections we are capturing these fluctuations in oxygen tension through the similar fluctuations seen for certain metabolites. Accurately identification of the hypoxic regions of the tumour sections will enable correlation between oxygen levels and metabolite changes. Both pimonidazole and EF5 staining have been used previously in the detection of hypoxia in snap-frozen tissue samples and this could be coupled with immunohistochemical staining for vascular markers such as CD31 to identify the tumour vasculature[620,621].

Interestingly, both threonine and glutamate, along with phenylalanine, all displayed similar trends in the tumour samples, and these were largely in agreement with the patterns observed in the spheroid model from Chapter 4. In the control tumours, a peak in signal intensity was observed at the periphery over the first 300-600 μm after which it decreased close to 0 at around 1.2 mm. A similar peak was seen in the knockout tumour however this peak was larger than that of the control and occurred slightly deeper into the tumour, peaking at around 900 μm followed by a similar decrease towards 0 at around 1.8 mm. Following the decreases in signal, a slow but steady increase in these signals was observed moving towards the core of the tumours. The accumulation of amino acids 300-900 μm into the tumour is suggestive of increased amino acid biosynthesis which has been reported to occur in response to hypoxia in multiple cancer types including CRC[387]. The decreased TCA cycle activity observed in hypoxia leads to elevated glutamine catabolism which produces glutamate in a HIF-1α-dependent manner

for fatty acid biosynthesis and the synthesis of additional amino acids[587]. Furthermore, HIF-2α has been shown to increase the expression of the phenylalanine transporter LAT1 to increase phenylalanine uptake[406]. Importantly, the role of FOSL2 in regulating amino acid biosynthesis and transport has not been investigated, especially in the context of hypoxia and CRC. The prolonged signals observed for the amino acids investigated here in the FOSL2 knockout tumours compared to the controls suggest a role for FOSL2 in the regulation of amino acid metabolism. Probing of the previously mentioned FOSL2 knockdown RNA-sequencing data identified several amino acid transporters regulated by FOSL2 in hypoxia, however, further investigation into this was outside the scope of this study.

5.4.4 Concluding statements

In summary, the work presented in this chapter successfully built upon the orbiSIMS-based metabolomics analysis developed in Chapter 4 and applied this technique to the spatial analysis of hypoxia-regulated metabolites from FOSL2 knockout CRC tumour xenografts as well as CRC PDX samples. In line with the hypothesis, hypoxia-associated metabolites across the oxygen gradient within the CRC tumour samples were spatially resolved and this identified oxygen tension-dependent changes in metabolite distribution. Furthermore, loss of FOSL2 function led to the identification of FOSL2-regulated metabolites including phenylalanine, threonine and glutamate, suggesting a possible role for FOSL2 in the regulation of amino acid metabolism in hypoxic CRC.

As hypothesised, the hypoxic regulation of glycolytic intermediates including F-6-P, G-3-P and PEP in CRC tumour xenografts was also characterized and loss of FOSL2 was shown to alter their spatial distribution. However, the analysis failed to detect hypoxia-regulated fatty acid and sterol metabolic intermediates and so that hypothesis could not be tested in this work. In addition, this analysis also failed to detect glycolytic, fatty acid and sterol intermediates in the CRC PDX samples. Additional analysis of these samples using negative ion polarity SIMS would provide further spatial information regarding the role of hypoxia in the regulation of these metabolites in patient samples. Finally, the work presented here also highlights the challenges associated with analysing more complex biological samples, such as tumour tissue, and identifies additional considerations that need to be taken into account for the future development of the technique.

Conclusions and future directions

Role of eIF4A2

Data presented in this thesis follows on from previous work investigating the role of eIF4A2 in the regulation of adaptation to hypoxia in colorectal cancer through reprogramming mRNA translation. My work has demonstrated eIF4A2 is able to interact with other translation regulatory proteins in hypoxia including eIF4G3, eIF4E1 and CNOT7. However, how these protein:protein interactions coordinate eIF4A2 mRNA selectivity and activity in hypoxia is a pertinent question? Incorporation of eIF4A2 into the CCR4-NOT complex does not require helicase activity, and so functions as an mRNA chaperone as opposed to an initiator of translation. Additional RIP-Seq experiments comparing the overlap between eIF4A1 or CNOT7-bound mRNAs with eIF4A2-bound mRNAs in hypoxia would help further delineate the individual roles of eIF4A1 and eIF4A2 and identify what ratio of hypoxic mRNAs are also bound by CNOT7, which would confirm the dominant role of eIF4A2 as either a translation activator or RNA chaperone. Furthermore, additional immunoprecipitation studies and mass spectrometry could identify the binding of other factors such as eIF4B and eIF4H as well as novel hypoxia responsive RBPs such as TAB182. It would also be interesting to conduct some follow-up studies based on the splicing analysis I have presented here and whether hypoxia-specific splice variants of these translation initiation factors are responsible for selective eIF4A2 recruitment over other RNA helicases and what structural determinants might possibly be behind this.

Role of eIF4A2-target proteins

Data presented in chapter 3 suggests that loss of CTH activity does not impact CRC cell spheroid growth or cell survival following hypoxic exposure. However, as discussed earlier, a limited number of phenotypic assays were employed in this study and additional assays could identify, as of yet, unidentified roles for CTH in hypoxic CRC. Assessing the role of H_2S generated by CTH overexpression in hypoxic CRC cells would be vital to understanding the impact of CTH activity on CRC cell migration and invasion, particularly in 3-D cell models where a gradient of H_2S could be established.

Data presented here also identified a role for eIF4A2 in the hypoxic regulation of the endocytosis protein EHD1 and showed that EHD1 knockdown reduces CRC cell

survival after hypoxic exposure. As discussed in chapter 3, studying the impact of both eIF4A2 and EHD1 knockout on cell surface receptors, such as EGFR, localisation through FACS and immunofluorescent staining could provide insight into the hypoxic regulation of endocytosis. Furthermore, pulse-chase assays could be employed to measure endocytic recycling rates of receptors and identify whether hypoxia leads to changes in receptor recycling.

orbiSIMS-based spatial metabolomics

This thesis has revealed a pioneering new mass spectrometry-based technique for the simultaneous measurement of metabolites *in situ* in their native hydrated state in tumours and spheroid models using a high-pressure frozen orbiSIMS workflow. However, further optimisation and development of the methodology and sample preparation techniques is required to allow the system to evolve. Some of the major challenges with this technology are the technical and logistical issues surrounding the use of the orbiSIMS instrument. For example, access to the instrument is severely limited and so acquiring sufficient machine time to improve the method of data collection e.g. testing of different polarity modes, different pixel sizes, alternative acquisition modes is difficult but these would be worthwhile tests for the development of the technique. In addition, analysis of a single sample used in my work cost approximately £1000 per run, so testing new ways of reducing the run-time required to acquire data would help overcome the financial barrier. Previously discussed techniques such as freeze-fracturing or spheroid sectioning could help reduce run time.

Future work utilising the orbiSIMS technique developed here should focus on the analysis of spatial metabolite patterns within tumour material, as initially studied here in Chapter 5. Applying this technique directly to patient-derived tumour samples from the clinic would be vital for understanding the unique metabolic patterns induced by the oxygen gradient within individual tumours. These metabolic changes could help guide personalised therapeutic strategies and help predict therapeutic outcome whilst also identifying novel targets for new therapeutic development. This could be further aided through correlation with *in situ* spatial transcriptomics such as 10x Genomics or NanoString to identify gene expression changes associated with the metabolite patterns observed with orbiSIMS analysis. Another powerful opportunity with this technology would be the identification of different populations of cells within tumours based on

their metabolic profiles. For example, identifying metabolic signatures in hypoxic cells with enhanced metastatic potential could help predict the likelihood of metastasis within patient tumours and could help identify the subpopulation of cells where metastasis originates.

Appendices

Appendix A – Buffer recipes

SDS-PAGE running buffer (1L):

30 g Tris base (250 mM)

144 g glycine (1.92 M)

10 g SDS (1%)

Adjust pH to 8.3 with HCl

Make up to 1 L with ultrapure H_2O

*Dilute to 1x before use with ultrapure H_2O

Turbo Transfer buffer (1L):

200 mL 5x Turbo transfer buffer (Bio-Rad)

200 mL 100% ethanol (reagent grade)

600 mL ultrapure H_2O

10x TBS (1L):

87.7 g NaCl (1.5 M)

100 mL 1 M Tris-HCl, pH 7.5 (100 mM)

900 mL ultrapure H_2O

*Dilute to 1x before use with ultrapure H_2O

1x TBS (1L):

100 mL 10x TBS

900 mL distilled H_2O

Co-IP lysis buffer (1L):

50 mL Tris, pH 7.4 (50 mM)

8.76 g NaCl (150 mM)

10 mL Nonidet P-40 (1%)

2.5 g sodium deoxycholate (0.25%)

0.38 g EGTA (1 mM)

0.04 g NaF (1 mM)

0.184 g Na_3VO_4 (1 mM)

10 μL/mL PMSF (1 mM)

10 μL/mL protease inhibitor cocktail (1%)

940 mL distilled H_2O

Co-IP wash buffer (500 mL):

500 mL PBS

500 μL Tween20 (0.1%)

Co-IP elution buffer (500 mL):

7.5 g glycine (200 mM)

Adjust pH to 2.5 with HCl

Co-IP neutralisation buffer (100 mL):

12.1 g Tris base (1 M)

Adjust pH to 11.0 with NaOH

Urea buffer (50 mL):

12 g urea (4 M final)

2.5 mL glycerol (5% final)

1.0 mL 0.5M Tris pH 6.8 (10 mM final)

prior to use:

5 μL 10% SDS per mL (0.05% final)

10 μL 100 mM DTT per mL (1 mM final)

10 μL/mL protease inhibitor cocktail

Mammalian Ringer's solution:

154 mM NaCl

5.64 mM KCl

2.16 mM $CaCl_2$

10 mM glucose

5.5 mM HEPES

Adjust pH to 7.3 with HCl and NaOH

Appendix B – Polyacrylamide gel recipes

Recipe for 1x 1.0 mm polyacrylamide gel (resolving gel):

	Resolving gel %		
Reagent	**8%**	**10%**	**12%**
H_2O	4.2 mL	3.8 mL	3.4 mL
Acrylamide (40%)	1.6 mL	2.0 mL	2.4 mL
1.5M Tris pH 8.8	2.0 mL	2.0 mL	2.0 mL
10% SDS	80 µL	80 µL	80 µL
10% APS	80 µL	80 µL	80 µL
TEMED	8 µL	8 µL	8 µL

Recipe for 1x 1.0 mm polyacrylamide gel (stacking gel):

	Stacking gel %	
Reagent	**4%**	**6%**
H_2O	3.1 mL	2.9 mL
Acrylamide (40%)	500 µL	750 µL
0.5M Tris pH 6.8	1.25 mL	1.25 mL
10% SDS	50 µL	50 µL
10% APS	50 µL	50 µL
TEMED	5 µL	5 µL

Appendix C – PCR programmes

PCR thermal cycling conditions:

Settings	Step 1	Step 2	Step 3	Step 4	Step 5
Temperature (˚C)	95	60	72	72	4
Time (seconds)	60	50	60	420	Hold

cDNA synthesis cycling conditions:

Settings	Step 1	Step 2	Step 3	Step 4
Temperature (˚C)	25	37	85	4
Time (minutes)	10	120	5	Hold

qRT-PCR cycling conditions:

Settings	Step 1	Step 2	Step 3	Step 4
Temperature (˚C)	95	95	60	4
Time (minutes)	10	0.25	1	Hold

Professional Internship Placement: Reflective statement

Note to Examiners:

This statement is included as an appendix to the thesis in order that the thesis accurately captures the PhD training experienced by the candidate as a BBSRC Doctoral Training Partnership student. The Professional Internship for PhD Students (PIP) is a compulsory 3-month placement which must be undertaken by DTP students. It is usually centred on a specific project and must not be related to the PhD project. However, exceptions to this were made in the wake of the COVID-19 pandemic such that PIP projects relating to the PhD project were allowed in order to help mitigate lost research time.

Reflective statement

I completed my PIP from 14th July – 14th October 2022. However, flexibility was granted due to the lost lab time that students faced due to the COVID-19 pandemic, so I was able to continue my lab work as well during this time period. I completed my placement at the University of Nottingham Biodiscovery Institute under the supervision of Prof Nigel Mongan whose research focuses on nuclear receptor-mediated transcriptional regulation of stem cells. embryonic development and cancer and has expertise in bioinformatics and large-scale sequencing analyses.

My project involved the preparation and analysis of an RNA-sequencing experiment investigating the role of HIFs on metabolic adaptation to hypoxia in colorectal cancer (as discussed in Chapter 4). This project was ultimately selected in order to recover some of the research time that was lost due to the COVID-19 pandemic. However, my intention for my PIP was always to gain experience in bioinformatics and sequencing data analysis and this work enabled me to do that whilst also contributing to the continuation of my PhD. Initially, the work involved learning and understanding the correct techniques for sample preparation such as the RNA extraction method, followed by quality control assessment including submitting samples for RIN number validation. I was responsible for coordinating with Novogene to request the correct sequencing experiment and to organise sample preparation and shipping. After receiving the raw sequencing data back from Novogene, I worked closely with Prof Mongan who took me through all the stages

of data analysis. This included quality control data filtering and trimming, genome alignment, gene expression quantification and differential gene expression analysis using the DESeq2 package in R. I also learnt about a variety of pathway and gene ontology analysis websites and programs including, WebGestalt, Panther and GSEA as well as different techniques and methods for presenting RNA sequencing data. Following this, we decided to carry out a more complicated splicing analysis to identify hypoxia-induced changes in splicing. This involved learning an alternative script called rMATS along with different filtering and quality control steps.

I would like to thank Prof Mongan for his fantastic teaching and guidance during my placement and for showing such a keen interest in my work.

Bibliography

1. Bray F, Ferlay J, Soerjomataram I, Siegel RL, Torre LA, Jemal A. Global cancer statistics 2018: GLOBOCAN estimates of incidence and mortality worldwide for 36 cancers in 185 countries. *CA Cancer J Clin*. 2018;68(6):394-424. doi:10.3322/caac.21492
2. Hanahan D, Weinberg RA. The Hallmarks of Cancer. *Cell*. 2000;100(1):57-70. doi:10.1016/S0092-8674(00)81683-9
3. Chaffer CL, Weinberg RA. A Perspective on Cancer Cell Metastasis. *Science (80-)*. 2011;331(6024):1559-1564. doi:10.1126/science.1203543
4. Omran AR. The epidemiologic transition. A theory of the epidemiology of population change. *Milbank Mem Fund Q*. 1971;49(4):509-538.
5. Lengauer C, Kinzler KW, Vogelstein B. Genetic instabilities in human cancers. *Nature*. 1998;396(6712):643-649. doi:10.1038/25292
6. Cahill DP, Kinzler KW, Vogelstein B, Lengauer C. Genetic instability and darwinian selection in tumours. *Trends Biochem Sci*. 1999;24(12):M57-M60. doi:10.1016/S0968-0004(99)01466-8
7. Wu X, Pandolfi PP. Mouse models for multistep tumorigenesis. *Trends Cell Biol*. 2001;11:S2-S9. doi:10.1016/S0962-8924(01)82000-6
8. Knudson AG, Jr. Mutation and cancer: statistical study of retinoblastoma. *Proc Natl Acad Sci U S A*. 1971;68(4):820-823. doi:10.1073/pnas.68.4.820
9. Rous P. A transmissible avian neoplasm. (sarcoma of the common fowl.). *J Exp Med*. 1910;12(5):696-705. doi:10.1084/jem.12.5.696
10. Iba H, Takeya T, Cross FR, Hanafusa T, Hanafusa H. Rous sarcoma virus variants that carry the cellular src gene instead of the viral src gene cannot transform chicken embryo fibroblasts. *Proc Natl Acad Sci U S A*. 1984;81(14 I):4424-4428. doi:10.1073/pnas.81.14.4424
11. Bishop JM. Molecular themes in oncogenesis. *Cell*. 1991;64(2):235-248. doi:10.1016/0092-8674(91)90636-D
12. Weinberg RA. Oncogenes and tumor suppressor genes. *CA Cancer J Clin*. 1994;44(3):160-170. doi:10.3322/canjclin.44.3.160
13. Yeang C-H, McCormick F, Levine A. Combinatorial patterns of somatic gene mutations in cancer. *FASEB J*. 2008;22(8):2605-2622. doi:10.1096/fj.08-108985
14. Fernández-Medarde A, Santos E. Ras in cancer and developmental diseases. *Genes and Cancer*. 2011;2(3):344-358. doi:10.1177/1947601911411084
15. Khan AQ, Kuttikrishnan S, Siveen KS, et al. RAS-mediated oncogenic signaling pathways in human malignancies. *Semin Cancer Biol*. 2019;54:1-13. doi:10.1016/j.semcancer.2018.03.001
16. Pylayeva-Gupta Y, Grabocka E, Bar-Sagi D. RAS oncogenes: Weaving a tumorigenic web. *Nat Rev Cancer*. 2011;11(11):761-774. doi:10.1038/nrc3106
17. Albertson DG. Gene amplification in cancer. *Trends Genet*. 2006;22(8):447-455. doi:10.1016/j.tig.2006.06.007
18. Windle BE, Wahl GM. Molecular dissection of mammalian gene amplification: New mechanistic insights revealed by analyses of very early events. *Mutat Res Genet Toxicol*. 1992;276(3):199-224. doi:10.1016/0165-1110(92)90009-X
19. O'Hagan RC, Chang S, Maser RS, et al. Telomere dysfunction provokes regional amplification and deletion in cancer genomes. *Cancer Cell*. 2002;2(2):149-155. doi:10.1016/S1535-6108(02)00094-6
20. Dang C V. MYC on the path to cancer. *Cell*. 2012;149(1):22-35. doi:10.1016/j.cell.2012.03.003
21. Savelyeva L, Schwab M. Amplification of oncogenes revisited: From expression

profiling to clinical application. *Cancer Lett*. 2001;167(2):115-123. doi:10.1016/S0304-3835(01)00472-4
22. Knudson AG. Mutation and cancer: statistical study of retinoblastoma. *Proc Natl Acad Sci U S A*. 1971;68(4):820-823. doi:10.1073/pnas.68.4.820
23. Sherr CJ. Principles of Tumor Suppression. *Cell*. 2004;116(2):235-246. doi:10.1016/S0092-8674(03)01075-4
24. Comings DE. A general theory of carcinogenesis. *Proc Natl Acad Sci U S A*. 1973;70(12 (I)):3324-3328. doi:10.1073/pnas.70.12.3324
25. Müller H, Helin K. The E2F transcription factors: Key regulators of cell proliferation. *Biochim Biophys Acta - Rev Cancer*. 2000;1470(1):M1. doi:10.1016/S0304-419X(99)00030-X
26. Weinberg RA. The retinoblastoma protein and cell cycle control. *Cell*. 1995;81(3):323-330. doi:10.1016/0092-8674(95)90385-2
27. Kandoth C, McLellan MD, Vandin F, et al. Mutational landscape and significance across 12 major cancer types. *Nature*. 2013;502(7471):333-339. doi:10.1038/nature12634
28. Appella E, Anderson CW. Post-translational modifications and activation of p53 by genotoxic stresses. *Eur J Biochem*. 2001;268(10):2764-2772. doi:10.1046/j.1432-1327.2001.02225.x
29. Prives C. Signaling to p53: Breaking the MDM2-p53 circuit. *Cell*. 1998;95(1):5-8. doi:10.1016/S0092-8674(00)81774-2
30. Hanahan D, Weinberg RA. Hallmarks of Cancer: The Next Generation. *Cell*. 2011;144(5):646-674. doi:10.1016/J.CELL.2011.02.013
31. Colotta F, Allavena P, Sica A, Garlanda C, Mantovani A. Cancer-related inflammation, the seventh hallmark of cancer: Links to genetic instability. *Carcinogenesis*. 2009;30(7):1073-1081. doi:10.1093/carcin/bgp127
32. Negrini S, Gorgoulis VG, Halazonetis TD. Genomic instability an evolving hallmark of cancer. *Nat Rev Mol Cell Biol*. 2010;11(3):220-228. doi:10.1038/nrm2858
33. Witsch E, Sela M, Yarden Y. Roles for Growth Factors in Cancer Progression. *Physiology*. 2010;25(2):85-101. doi:10.1152/physiol.00045.2009
34. Sporn MB, Todaro GJ. Autocrine Secretion and Malignant Transformation of Cells. *N Engl J Med*. 1980;303(15):878-880. doi:10.1056/NEJM198010093031511
35. HAMMACHER A, NISTÉR M, WESTERMARK B, HELDIN C -H. A human glioma cell line secretes three structurally and functionally different dimeric forms of platelet-derived growth factor. *Eur J Biochem*. 1988;176(1):179-186. doi:10.1111/j.1432-1033.1988.tb14266.x
36. Ciardiello E, Kim N, Mcgeady ML, et al. Expression of transforming growth factor alpha (TGFα) in breast cancer. *Ann Oncol*. 1991;2(3):169-182. doi:10.1093/oxfordjournals.annonc.a057897
37. Di Fiore PP, Pierce JH, Kraus MH, Segatto O, King CR, Aaronson SA. ErbB-2 is a potent oncogene when overexpressed in NIH/3T3 cells. *Science (80-)*. 1987;237(4811):178-182. doi:10.1126/science.2885917
38. Su Huang HJ, Nagane M, Klingbeil CK, et al. The enhanced tumorigenic activity of a mutant epidermal growth factor receptor common in human cancers is mediated by threshold levels of constitutive tyrosine phosphorylation and unattenuated signaling. *J Biol Chem*. 1997;272(5):2927-2935. doi:10.1074/jbc.272.5.2927
39. Ascierto PA, Kirkwood JM, Grob JJ, et al. The role of BRAF V600 mutation in melanoma. *J Transl Med*. 2012;10(1):85. doi:10.1186/1479-5876-10-85
40. Medema RH, Bos JL. The role of p21ras in receptor tyrosine kinase signaling. *Crit*

Rev Oncog. 1993;4(6):615-661. doi:10.1007/978-3-0348-9057-1_1
41. Amin ARMR, Karpowicz PA, Carey TE, et al. Evasion of anti-growth signaling: A key step in tumorigenesis and potential target for treatment and prophylaxis by natural compounds. *Semin Cancer Biol*. 2015;35:S55-S77. doi:10.1016/j.semcancer.2015.02.005
42. Fynan TM, Reiss M. Resistance to inhibition of cell growth by transforming growth factor-beta and its role in oncogenesis. *Crit Rev Oncog*. 1993;4(5):493-540.
43. Moll UM, Petrenko O. The MDM2-p53 Interaction. *Mol Cancer Res*. 2003;1(14):1001-1008.
44. Fernald K, Kurokawa M. Evading apoptosis in cancer. *Trends Cell Biol*. 2013;23(12):620-633. doi:10.1016/j.tcb.2013.07.006
45. Fortin A, Cregan SP, MacLaurin JG, et al. APAF1 is a key transcriptional target for p53 in the regulation of neuronal cell death. *J Cell Biol*. 2001;155(2):207-216. doi:10.1083/jcb.200105137
46. Nakano K, Vousden KH. PUMA, a novel proapoptotic gene, is induced by p53. *Mol Cell*. 2001;7(3):683-694. doi:10.1016/S1097-2765(01)00214-3
47. Oda E, Ohki R, Murasawa H, et al. Noxa, a BH3-only member of the Bcl-2 family and candidate mediator of p53-induced apoptosis. *Science (80-)*. 2000;288(5468):1053-1058. doi:10.1126/science.288.5468.1053
48. Beroukhim R, Mermel CH, Porter D, et al. The landscape of somatic copy-number alteration across human cancers. *Nature*. 2010;463(7283):899-905. doi:10.1038/nature08822
49. Tonon G, Wong KK, Maulik G, et al. High-resolution genomic profiles of human lung cancer. *Proc Natl Acad Sci U S A*. 2005;102(27):9625-9630. doi:10.1073/pnas.0504126102
50. Tsujimoto Y, Gorham J, Cossman J, Jaffe E, Croce CM. The t(14;18) chromosome translocations involved in B-cell neoplasms result from mistakes in VDJ joining. *Science (80-)*. 1985;229(4720):1390-1393. doi:10.1126/science.3929382
51. Yaswen P, MacKenzie KL, Keith WN, et al. Therapeutic targeting of replicative immortality. *Semin Cancer Biol*. 2015;35(Suppl):S104-S128. doi:10.1016/j.semcancer.2015.03.007
52. Kipling D, Wynford-Thomas D, Jones CJ, et al. Telomere-dependent senescence [1] (multiple letters). *Nat Biotechnol*. 1999;17(4):313-314. doi:10.1038/7827
53. Counter CM, Avilion AA, LeFeuvre CE, et al. Telomere shortening associated with chromosome instability is arrested in immortal cells which express telomerase activity. *EMBO J*. 1992;11(5):1921-1929. doi:10.1002/j.1460-2075.1992.tb05245.x
54. Morin GB. The human telomere terminal transferase enzyme is a ribonucleoprotein that synthesizes TTAGGG repeats. *Cell*. 1989;59(3):521-529. doi:10.1016/0092-8674(89)90035-4
55. Shay JW, Bacchetti S. A survey of telomerase activity in human cancer. *Eur J Cancer Part A*. 1997;33(5):787-791. doi:10.1016/S0959-8049(97)00062-2
56. Dilley RL, Greenberg RA. ALTernative Telomere Maintenance and Cancer. *Trends in Cancer*. 2015;1(2):145-156. doi:10.1016/j.trecan.2015.07.007
57. Hanahan D, Folkman J. Patterns and emerging mechanisms of the angiogenic switch during tumorigenesis. *Cell*. 1996;86(3):353-364. doi:10.1016/S0092-8674(00)80108-7
58. Gupta MK, Qin RY. Mechanism and its regulation of tumor-induced angiogenesis. *World J Gastroenterol*. 2003;9(6):1144-1155. doi:10.3748/wjg.v9.i6.1144

59. Veikkola T, Alitalo K. VEGFs, receptors and angiogenesis. *Semin Cancer Biol.* 1999;9(3):211-220. doi:10.1006/scbi.1998.0091
60. Mazure NM, Chen EY, Laderoute KR, Giaccia AJ. Induction of vascular endothelial growth factor by hypoxia is modulated by a phosphatidylinositol 3-kinase/Akt signaling pathway in Ha-ras- transformed cells through a hypoxia inducible factor-1 transcriptional element. *Blood.* 1997;90(9):3322-3331. doi:10.1182/blood.v90.9.3322
61. Pepper MS, Ferrara N, Orci L, Montesano R. Vascular endothelial growth factor (VEGF) induces plasminogen activators and plasminogen activator inhibitor-1 in microvascular endothelial cells. *Biochem Biophys Res Commun.* 1991;181(2):902-906. doi:10.1016/0006-291X(91)91276-I
62. Baeriswyl V, Christofori G. The angiogenic switch in carcinogenesis. *Semin Cancer Biol.* 2009;19(5):329-337. doi:10.1016/j.semcancer.2009.05.003
63. Meirson T, Gil-Henn H, Samson AO. Invasion and metastasis: the elusive hallmark of cancer. *Oncogene.* 2020;39(9):2024-2026. doi:10.1038/s41388-019-1110-1
64. Valastyan S, Weinberg RA. Tumor metastasis: Molecular insights and evolving paradigms. *Cell.* 2011;147(2):275-292. doi:10.1016/j.cell.2011.09.024
65. Thiery JP, Acloque H, Huang RYJ, Nieto MA. Epithelial-Mesenchymal Transitions in Development and Disease. *Cell.* 2009;139(5):871-890. doi:10.1016/j.cell.2009.11.007
66. Peri AK, Wilgenbus P, Dahl U, Semb H, Christofori G. A causal role for E-cadherin in the transition from adenoma to carcinoma. *Nature.* 1998;392(6672):190-193. doi:10.1038/32433
67. Babey H, Quéré G, Descourt R, et al. Immune-checkpoint inhibitors to treat cancers in specific immunocompromised populations: a critical review. *Expert Rev Anticancer Ther.* 2018;18(10):981-989. doi:10.1080/14737140.2018.1499468
68. Jacobs JFM, Nierkens S, Figdor CG, de Vries IJM, Adema GJ. Regulatory T cells in melanoma: The final hurdle towards effective immunotherapy? *Lancet Oncol.* 2012;13(1):e32-e42. doi:10.1016/S1470-2045(11)70155-3
69. Curiel TJ, Coukos G, Zou L, et al. Specific recruitment of regulatory T cells in ovarian carcinoma fosters immune privilege and predicts reduced survival. *Nat Med.* 2004;10(9):942-949. doi:10.1038/nm1093
70. Fantini MC, Becker C, Monteleone G, Pallone F, Galle PR, Neurath MF. Cutting Edge: TGF-β Induces a Regulatory Phenotype in CD4 + CD25 − T Cells through Foxp3 Induction and Down-Regulation of Smad7 . *J Immunol.* 2004;172(9):5149-5153. doi:10.4049/jimmunol.172.9.5149
71. Garcia-Lora A, Algarra I, Garrido F. MHC class I antigens, immune surveillance, and tumor immune escape. *J Cell Physiol.* 2003;195(3):346-355. doi:10.1002/jcp.10290
72. Matsuda M, Salazar F, Petersson M, et al. Interleukln 10 pretreatment protects target cells from tumor- and allo-specific cytotoxic T cells and downregulates HLA class I expression. *J Exp Med.* 1994;180(6):2371-2376. doi:10.1084/jem.180.6.2371
73. Lin EY, Gouon-Evans V, Nguyen A V., Pollard JW. The macrophage growth factor CSF-1 in mammary gland development and tumor progression. *J Mammary Gland Biol Neoplasia.* 2002;7(2):147-162. doi:10.1023/A:1020399802795
74. Heiden MGV, Cantley LC, Thompson CB. Understanding the Warburg effect: the metabolic requirements of cell proliferation. *Science.* 2009;324(5930):1029-1033. doi:10.1126/SCIENCE.1160809
75. Warburg O. On the origin of cancer cells. *Science (80-).* 1956;123(3191):309-314.

doi:10.1126/science.123.3191.309
76. Weinhouse S, Warburg O, Burk D, Schade AL. On respiratory impairment in cancer cells. *Science (80-)*. 1956;124(3215):267-272. doi:10.1126/science.124.3215.267
77. Semenza GL. HIF-1: upstream and downstream of cancer metabolism. *Curr Opin Genet Dev*. 2010;20(1):51-56. doi:10.1016/j.gde.2009.10.009
78. DeBerardinis RJ, Sayed N, Ditsworth D, Thompson CB. Brick by brick: metabolism and tumor cell growth. *Curr Opin Genet Dev*. 2008;18(1):54-61. doi:10.1016/j.gde.2008.02.003
79. Heiden MGV, Cantley LC, Thompson CB. Understanding the warburg effect: The metabolic requirements of cell proliferation. *Science (80-)*. 2009;324(5930):1029-1033. doi:10.1126/science.1160809
80. Greaves M, Maley CC. Clonal evolution in cancer. *Nature*. 2012;481(7381):306-313. doi:10.1038/nature10762
81. Negrini S, Gorgoulis VG, Halazonetis TD. Genomic instability an evolving hallmark of cancer. *Nat Rev Mol Cell Biol*. 2010;11(3):220-228. doi:10.1038/nrm2858
82. Lengauer C, Kinzler KW, Vogelstein B. Genetic instability in colorectal cancers. *Nature*. 1997;386(6625):623-627. doi:10.1038/386623a0
83. Al-Tassan N, Chmiel NH, Maynard J, et al. Inherited variants of MYH associated with somatic G:C→T:A mutations in colorectal tumors. *Nat Genet*. 2002;30(2):227-232. doi:10.1038/ng828
84. Loeb LA. Mutator phenotype may be required for multistage carcinogenesis. *Cancer Res*. 1991;51(12):3075-3079. http://www.ncbi.nlm.nih.gov/pubmed/2039987. Accessed May 28, 2020.
85. Halazonetis TD, Gorgoulis VG, Bartek J. An oncogene-induced DNA damage model for cancer development. *Science (80-)*. 2008;319(5868):1352-1355. doi:10.1126/science.1140735
86. Gorgoulis VG, Vassiliou LVF, Karakaidos P, et al. Activation of the DNA damage checkpoint and genomic instability in human precancerous lesions. *Nature*. 2005;434(7035):907-913. doi:10.1038/nature03485
87. Bartkova J, Hořejší Z, Koed K, et al. DNA damage response as a candidate anti-cancer barrier in early human tumorigenesis. *Nature*. 2005;434(7035):864-870. doi:10.1038/nature03482
88. Balkwill F, Mantovani A. Inflammation and cancer: Back to Virchow? *Lancet*. 2001;357(9255):539-545. doi:10.1016/S0140-6736(00)04046-0
89. Flier JS, Underhill LH, Dvorak HF. Tumors: Wounds That Do Not Heal. *N Engl J Med*. 1986;315(26):1650-1659. doi:10.1056/NEJM198612253152606
90. Pagano JS, Blaser M, Buendia MA, et al. Infectious agents and cancer: Criteria for a causal relation. *Semin Cancer Biol*. 2004;14(6):453-471. doi:10.1016/j.semcancer.2004.06.009
91. Grivennikov SI, Greten FR, Karin M. Immunity, Inflammation, and Cancer. *Cell*. 2010;140(6):883-899. doi:10.1016/j.cell.2010.01.025
92. B. Vendramini-Costa D, E. Carvalho J. Molecular Link Mechanisms between Inflammation and Cancer. *Curr Pharm Des*. 2012;18(26):3831-3852. doi:10.2174/138161212802083707
93. Mantovani A, Allavena P, Sica A, Balkwill F. Cancer-related inflammation. *Nature*. 2008;454(7203):436-444. doi:10.1038/nature07205
94. Abraham D, Zins K, Sioud M, et al. Stromal cell-derived CSF-1 blockade prolongs xenograft survival of CSF-1-negative neuroblastoma. *Int J Cancer*. 2010;126(6):1339-1352. doi:10.1002/ijc.24859

95. Qian BZ, Li J, Zhang H, et al. CCL2 recruits inflammatory monocytes to facilitate breast-tumour metastasis. *Nature*. 2011;475(7355):222-225. doi:10.1038/nature10138
96. Condeelis J, Pollard JW. Macrophages: Obligate partners for tumor cell migration, invasion, and metastasis. *Cell*. 2006;124(2):263-266. doi:10.1016/j.cell.2006.01.007
97. Mantovani A, Marchesi F, Malesci A, Laghi L, Allavena P. Tumour-associated macrophages as treatment targets in oncology. *Nat Rev Clin Oncol*. 2017;14(7):399-416. doi:10.1038/nrclinonc.2016.217
98. Shojaei F, Zhong C, Wu X, Yu L, Ferrara N. Role of myeloid cells in tumor angiogenesis and growth. *Trends Cell Biol*. 2008;18(8):372-378. doi:10.1016/j.tcb.2008.06.003
99. O'Sullivan C, Lewis CE, McGee JOD, Harris AL. Secretion of epidermal growth factor by macrophages associated with breast carcinoma. *Lancet*. 1993;342(8864):148-149. doi:10.1016/0140-6736(93)91348-P
100. Wu Y, Antony S, Meitzler JL, Doroshow JH. Molecular mechanisms underlying chronic inflammation-associated cancers. *Cancer Lett*. 2014;345(2):164-173. doi:10.1016/j.canlet.2013.08.014
101. Abbas Z, Rehman S. An Overview of Cancer Treatment Modalities. In: *Neoplasm*. InTech; 2018. doi:10.5772/intechopen.76558
102. DeVita VT, Chu E. A history of cancer chemotherapy. *Cancer Res*. 2008;68(21):8643-8653. doi:10.1158/0008-5472.CAN-07-6611
103. Ralhan R, Kaur J. Alkylating agents and cancer therapy. *Expert Opin Ther Pat*. 2007;17(9):1061-1075. doi:10.1517/13543776.17.9.1061
104. Tiwari M. Antimetabolites: Established cancer therapy. *J Cancer Res Ther*. 2012;8(4):510-519. doi:10.4103/0973-1482.106526
105. Liang X, Wu Q, Luan S, et al. A comprehensive review of topoisomerase inhibitors as anticancer agents in the past decade. *Eur J Med Chem*. 2019;171:129-168. doi:10.1016/j.ejmech.2019.03.034
106. Debnath B, Singh WS, Das M, et al. Role of plant alkaloids on human health: A review of biological activities. *Mater Today Chem*. 2018;9:56-72. doi:10.1016/j.mtchem.2018.05.001
107. Padma VV. An overview of targeted cancer therapy. *Biomed*. 2015;5(4):1-6. doi:10.7603/s40681-015-0019-4
108. Gerber DE. Targeted therapies: A new generation of cancer treatments. *Am Fam Physician*. 2008;77(3):311-319.
109. Slamon DJ, Clark GM, Wong SG, Levin WJ, Ullrich A, McGuire WL. Human breast cancer: Correlation of relapse and survival with amplification of the HER-2/neu oncogene. *Science (80-)*. 1987;235(4785):182-191. doi:10.1126/science.3798106
110. Cardones A, Banez L. VEGF Inhibitors in Cancer Therapy. *Curr Pharm Des*. 2005;12(3):387-394. doi:10.2174/138161206775201910
111. Hurwitz H, Saini S. Bevacizumab in the Treatment of Metastatic Colorectal Cancer: Safety Profile and Management of Adverse Events. *Semin Oncol*. 2006;33(SUPPL. 10). doi:10.1053/j.seminoncol.2006.08.001
112. Sandler AB, Johnson DH, Herbst RS. Anti-vascular endothelial growth factor monoclonals in non-small cell lung cancer. In: *Clinical Cancer Research*. Vol 10. Clin Cancer Res; 2004. doi:10.1158/1078-0432.CCR-040023
113. O'Brien SG, Guilhot F, Larson RA, et al. Imatinib compared with interferon and low-dose cytarabine for newly diagnosed chronic-phase chronic myeloid leukemia. *N Engl J Med*. 2003;348(11):994-1004. doi:10.1056/NEJMoa022457
114. Halliday GM, Patel A, Hunt MJ, Tefany FJ, Barnetson RSC. Spontaneous

regression of human melanoma/nonmelanoma skin cancer: association with infiltrating CD4+ T cells. *World J Surg*. 1995;19(3):352-358. doi:10.1007/BF00299157
115. Waldman AD, Fritz JM, Lenardo MJ. A guide to cancer immunotherapy: from T cell basic science to clinical practice. *Nat Rev Immunol 2020 2011*. 2020;20(11):651-668. doi:10.1038/s41577-020-0306-5
116. Fife BT, Bluestone JA. Control of peripheral T-cell tolerance and autoimmunity via the CTLA-4 and PD-1 pathways. *Immunol Rev*. 2008;224(1):166-182. doi:10.1111/J.1600-065X.2008.00662.X
117. Linsley PS, Brady W, Urnes M, Grosmaire LS, Damle NK, Ledbetter JA. CTLA-4 is a second receptor for the B cell activation antigen B7. *J Exp Med*. 1991;174(3):561-569. doi:10.1084/JEM.174.3.561
118. Hodi FS, O'Day SJ, McDermott DF, et al. Improved survival with ipilimumab in patients with metastatic melanoma. *N Engl J Med*. 2010;363(8):711-723. doi:10.1056/NEJMOA1003466
119. Parry R V., Chemnitz JM, Frauwirth KA, et al. CTLA-4 and PD-1 receptors inhibit T-cell activation by distinct mechanisms. *Mol Cell Biol*. 2005;25(21):9543-9553. doi:10.1128/MCB.25.21.9543-9553.2005
120. Gong J, Chehrazi-Raffle A, Reddi S, Salgia R. Development of PD-1 and PD-L1 inhibitors as a form of cancer immunotherapy: a comprehensive review of registration trials and future considerations. *J Immunother cancer*. 2018;6(1). doi:10.1186/S40425-018-0316-Z
121. Herbst RS, Baas P, Kim DW, et al. Pembrolizumab versus docetaxel for previously treated, PD-L1-positive, advanced non-small-cell lung cancer (KEYNOTE-010): a randomised controlled trial. *Lancet (London, England)*. 2016;387(10027):1540-1550. doi:10.1016/S0140-6736(15)01281-7
122. Perica K, Varela JC, Oelke M, Schneck J. Adoptive T Cell Immunotherapy for Cancer. *Rambam Maimonides Med J*. 2015;6(1):e0004. doi:10.5041/RMMJ.10179
123. Rosenberg SA, Packard BS, Aebersold PM, et al. Use of tumor-infiltrating lymphocytes and interleukin-2 in the immunotherapy of patients with metastatic melanoma. A preliminary report. *N Engl J Med*. 1988;319(25):1676-1680. doi:10.1056/NEJM198812223192527
124. Porter DL, Levine BL, Kalos M, Bagg A, June CH. Chimeric antigen receptor-modified T cells in chronic lymphoid leukemia. *N Engl J Med*. 2011;365(8):725-733. doi:10.1056/NEJMOA1103849
125. Fry TJ, Shah NN, Orentas RJ, et al. CD22-targeted CAR T cells induce remission in B-ALL that is naive or resistant to CD19-targeted CAR immunotherapy. *Nat Med*. 2018;24(1):20-28. doi:10.1038/NM.4441
126. Offit K. Personalized medicine: New genomics, old lessons. *Hum Genet*. 2011;130(1):3-14. doi:10.1007/s00439-011-1028-3
127. Verma M. Personalized medicine and cancer. *J Pers Med*. 2012;2(1):1-14. doi:10.3390/jpm2010001
128. Brauch H, Mürdter TE, Eichelbaum M, Schwab M. Pharmacogenomics of tamoxifen therapy. *Clin Chem*. 2009;55(10):1770-1782. doi:10.1373/clinchem.2008.121756
129. Brauch H, Jordan VC. Targeting of tamoxifen to enhance antitumour action for the treatment and prevention of breast cancer: The "personalised" approach? *Eur J Cancer*. 2009;45(13):2274-2283. doi:10.1016/j.ejca.2009.05.032
130. Day DW. The adenoma-carcinoma sequence. *Scand J Gastroenterol Suppl*. 1984;19(104):99-107.
131. Simon K. Colorectal cancer development and advances in screening. *Clin Interv*

Aging. 2016;11:967-976. doi:10.2147/CIA.S109285
132. Leslie A, Carey FA, Pratt NR, Steele RJC. The colorectal adenoma-carcinoma sequence. *Br J Surg*. 2002;89(7):845-860. doi:10.1046/j.1365-2168.2002.02120.x
133. Fleming M, Ravula S, Tatishchev SF, Wang HL. Colorectal carcinoma: Pathologic aspects. *J Gastrointest Oncol*. 2012;3(3):153-173. doi:10.3978/j.issn.2078-6891.2012.030
134. Yamagishi H, Kuroda H, Imai Y, Hiraishi H. Molecular pathogenesis of sporadic colorectal cancers. *Chin J Cancer*. 2016;35(1). doi:10.1186/s40880-015-0066-y
135. Cannon-Albright LA, Skolnick MH, Bishop DT, Lee RG, Burt RW. Common Inheritance of Susceptibility to Colonic Adenomatous Polyps and Associated Colorectal Cancers. *N Engl J Med*. 1988;319(9):533-537. doi:10.1056/NEJM198809013190902
136. Rustgi AK. The genetics of hereditary colon cancer. *Genes Dev*. 2007;21(20):2525-2538. doi:10.1101/gad.1593107
137. Fearon ER, Vogelstein B. A genetic model for colorectal tumorigenesis. *Cell*. 1990;61(5):759-767. doi:10.1016/0092-8674(90)90186-I
138. Grady WM, Carethers JM. Genomic and Epigenetic Instability in Colorectal Cancer Pathogenesis. *Gastroenterology*. 2008;135(4):1079-1099. doi:10.1053/j.gastro.2008.07.076
139. Armaghany T, Wilson JD, Chu Q, Mills G. Genetic alterations in colorectal cancer. *Gastrointest Cancer Res*. 2012;5(1):19-27. /pmc/articles/PMC3348713/?report=abstract. Accessed June 18, 2020.
140. Markowitz SD, Bertagnolli MM. Molecular basis of colorectal cancer. *N Engl J Med*. 2009;361(25):2449. doi:10.1056/NEJMra0804588
141. Powell SM, Zilz N, Beazer-Barclay Y, et al. APC mutations occur early during colorectal tumorigenesis. *Nature*. 1992;359(6392):235-237. doi:10.1038/359235a0
142. Coppedè F, Lopomo A, Spisni R, Migliore L. Genetic and epigenetic biomarkers for diagnosis, prognosis and treatment of colorectal cancer. *World J Gastroenterol*. 2014;20(4):943-956. doi:10.3748/wjg.v20.i4.943
143. Esteller M. Epigenetic lesions causing genetic lesions in human cancer: Promoter hypermethylation of DNA repair genes. *Eur J Cancer*. 2000;36(18):2294-2300. doi:10.1016/S0959-8049(00)00303-8
144. Kinzler KW, Vogelstein B. Lessons from hereditary colorectal cancer. *Cell*. 1996;87(2):159-170. doi:10.1016/S0092-8674(00)81333-1
145. Lustig B, Behrens J. The Wnt signaling pathway and its role in tumor development. *J Cancer Res Clin Oncol*. 2003;129(4):199-221. doi:10.1007/s00432-003-0431-0
146. Stanczak A, Stec R, Bodnar L, et al. Prognostic significance of Wnt-1, β-catenin and E-cadherin expression in advanced colorectal carcinoma. *Pathol Oncol Res*. 2011;17(4):955-963. doi:10.1007/s12253-011-9409-4
147. Arrington AK, Heinrich EL, Lee W, et al. Prognostic and predictive roles of KRAS mutation in colorectal cancer. *Int J Mol Sci*. 2012;13(10):12153-12168. doi:10.3390/ijms131012153
148. Neumann J, Zeindl-Eberhart E, Kirchner T, Jung A. Frequency and type of KRAS mutations in routine diagnostic analysis of metastatic colorectal cancer. *Pathol Res Pract*. 2009;205(12):858-862. doi:10.1016/j.prp.2009.07.010
149. Mao M, Tian F, Mariadason JM, et al. Resistance to BRAF inhibition in BRAF-mutant colon cancer can be overcome with PI3K inhibition or demethylating agents. *Clin Cancer Res*. 2013;19(3):657-667. doi:10.1158/1078-0432.CCR-11-1446
150. Liu Y, Bodmer WF. Analysis of P53 mutations and their expression in 56 colorectal cancer cell lines. *Proc Natl Acad Sci U S A*. 2006;103(4):976-981.

doi:10.1073/pnas.0510146103
151. López I, Oliveira LL, Tucci P, Álvarez-Valín F, A. Coudry R, Marín M. Different mutation profiles associated to P53 accumulation in colorectal cancer. *Gene*. 2012;499(1):81-87. doi:10.1016/j.gene.2012.02.011
152. Nakayama M, Oshima M. Mutant p53 in colon cancer. *J Mol Cell Biol*. 2019;11(4):267-276. doi:10.1093/JMCB/MJY075
153. Zarzour P, Boelen L, Luciani F, et al. Single nucleotide polymorphism array profiling identifies distinct chromosomal aberration patterns across colorectal adenomas and carcinomas. *Genes Chromosom Cancer*. 2015;54(5):303-314. doi:10.1002/gcc.22243
154. Thiagalingam S, Lengauer C, Leach FS, et al. Evaluation of candidate tumour suppressor genes on chromosome 18 in colorectal cancers. *Nat Genet*. 1996;13(3):343-346. doi:10.1038/ng0796-343
155. Shi Y, Hata A, Lo RS, Massagué J, Pavletich NP. A structural basis for mutational inactivation of the tumour suppressor Smad4. *Nature*. 1997;388(6637):87-93. doi:10.1038/40431
156. Alazzouzi H, Alhopuro P, Salovaara R, et al. SMAD4 as a prognostic marker in colorectal cancer. *Clin Cancer Res*. 2005;11(7):2606-2611. doi:10.1158/1078-0432.CCR-04-1458
157. Nguyen HT, Duong HQ. The molecular characteristics of colorectal cancer: Implications for diagnosis and therapy (review). *Oncol Lett*. 2018;16(1):9-18. doi:10.3892/ol.2018.8679
158. Loeb LA. Cancer cells exhibit a mutator phenotype. *Adv Cancer Res*. 1997;72:25-56. doi:10.1016/s0065-230x(08)60699-5
159. Herman JG, Umar A, Polyak K, et al. Incidence and functional consequences of hMLH1 promoter hypermethylation in colorectal carcinoma. *Proc Natl Acad Sci U S A*. 1998;95(12):6870-6875. doi:10.1073/pnas.95.12.6870
160. Boland CR, Thibodeau SN, Hamilton SR, et al. A National Cancer Institute Workshop on Microsatellite Instability for Cancer Detection and Familial Predisposition: Development of International Criteria for the Determination of Microsatellite Instability in Colorectal Cancer. *Cancer Res*. 1998;58(22).
161. Biswas S, Trobridge P, Romero-Gallo J, et al. Mutational inactivation of TGFBR2 in microsatellite unstable colon cancer arises from the cooperation of genomic instability and the clonal outgrowth of transforming growth factor β resistant cells. *Genes, Chromosom Cancer*. 2008;47(2):95-106. doi:10.1002/GCC.20511
162. Parsons R, Myeroff LL, Liu B, et al. Microsatellite Instability and Mutations of the Transforming Growth Factor β Type II Receptor Gene in Colorectal Cancer. *Cancer Res*. 1995;55(23).
163. Kondo Y, Issa JPJ. Epigenetic changes in colorectal cancer. *Cancer Metastasis Rev*. 2004;23(1-2):29-39. doi:10.1023/A:1025806911782
164. Van Rijnsoever M, Grieu F, Elsaleh H, Joseph D, Iacopetta B. Characterisation of colorectal cancers showing hypermethylation at multiple CpG islands. *Gut*. 2002;51(6):797-802. doi:10.1136/gut.51.6.797
165. Ogino S, Cantor M, Kawasaki T, et al. CpG island methylator phenotype (CIMP) of colorectal cancer is best characterised by quantitative DNA methylation analysis and prospective cohort studies. *Gut*. 2006;55(7):1000-1006. doi:10.1136/gut.2005.082933
166. Weisenberger DJ, Siegmund KD, Campan M, et al. CpG island methylator phenotype underlies sporadic microsatellite instability and is tightly associated with BRAF mutation in colorectal cancer. *Nat Genet*. 2006;38(7):787-793. doi:10.1038/ng1834

167. Shen L, Toyota M, Kondo Y, et al. Integrated genetic and epigenetic analysis identifies three different subclasses of colon cancer. *Proc Natl Acad Sci U S A*. 2007;104(47):18654-18659. doi:10.1073/pnas.0704652104
168. Ogino S, Kawasaki T, Kirkner GJ, Ohnishi M, Fuchs CS. 18q loss of heterozygosity in microsatellite stable colorectal cancer is correlated with CpG island methylator phenotype-negative (CIMP-0) and inversely with CIMP-low and CIMP-high. *BMC Cancer*. 2007;7. doi:10.1186/1471-2407-7-72
169. Singh MP, Rai S, Pandey A, Singh NK, Srivastava S. Molecular subtypes of colorectal cancer: An emerging therapeutic opportunity for personalized medicine. *Genes Dis*. 2019;8(2):133-145. doi:10.1016/J.GENDIS.2019.10.013
170. Guinney J, Dienstmann R, Wang X, et al. The consensus molecular subtypes of colorectal cancer. *Nat Med 2015 2111*. 2015;21(11):1350-1356. doi:10.1038/nm.3967
171. Berg KCG, Eide PW, Eilertsen IA, et al. Multi-omics of 34 colorectal cancer cell lines - a resource for biomedical studies. *Mol Cancer*. 2017;16(1):1-16. doi:10.1186/S12943-017-0691-Y/FIGURES/6
172. Sinicrope FA, Shi Q, Smyrk TC, et al. Molecular Markers Identify Subtypes of Stage III Colon Cancer Associated with Patient Outcomes. *Gastroenterology*. 2015;148(1):88. doi:10.1053/J.GASTRO.2014.09.041
173. Daaboul HE, El-Sibai M. Treatment Strategies in Colorectal Cancer. In: *Colorectal Cancer - Diagnosis, Screening and Management*. InTech; 2018. doi:10.5772/intechopen.71620
174. Dotan E, Cohen SJ. Challenges in the management of stage II colon cancer. *Semin Oncol*. 2011;38(4):511-520. doi:10.1053/j.seminoncol.2011.05.005
175. Watanabe T, Wu TT, Catalano PJ, et al. Molecular predictors of survival after adjuvant chemotherapy for colon cancer. *N Engl J Med*. 2001;344(16):1196-1206. doi:10.1056/NEJM200104193441603
176. Aran V, Victorino AP, Thuler LC, Ferreira CG. Colorectal Cancer: Epidemiology, Disease Mechanisms and Interventions to Reduce Onset and Mortality. *Clin Colorectal Cancer*. 2016;15(3):195-203. doi:10.1016/j.clcc.2016.02.008
177. Van Cutsem E, Oliveira J, ESMO Guidelines Working Group. Advanced colorectal cancer: ESMO clinical recommendations for diagnosis, treatment and follow-up. *Ann Oncol Off J Eur Soc Med Oncol*. 2009;20 Suppl 4:61-63. doi:10.1093/annonc/mdp130
178. Vatandoust S, Price TJ, Karapetis CS. Colorectal cancer: Metastases to a single organ. *World J Gastroenterol*. 2015;21(41):11767-11776. doi:10.3748/wjg.v21.i41.11767
179. OConnell JB, Maggard MA, Ko CY. Colon Cancer Survival Rates With the New American Joint Committee on Cancer Sixth Edition Staging. *J Natl Cancer Inst*. 96(19):1420-1425. doi:10.1093/jnci/djh275
180. Nordlinger B, Sorbye H, Glimelius B, et al. Perioperative chemotherapy with FOLFOX4 and surgery versus surgery alone for resectable liver metastases from colorectal cancer (EORTC Intergroup trial 40983): a randomised controlled trial. *Lancet*. 2008;371(9617):1007-1016. doi:10.1016/S0140-6736(08)60455-9
181. Mitry E, Fields ALA, Bleiberg H, et al. Adjuvant chemotherapy after potentially curative resection of metastases from colorectal cancer: A pooled analysis of two randomized trials. *J Clin Oncol*. 2008;26(30):4906-4911. doi:10.1200/JCO.2008.17.3781
182. Van Cutsem E, Cervantes A, Nordlinger B, Arnold D. Metastatic colorectal cancer: ESMO Clinical Practice Guidelines for diagnosis, treatment and follow-up †. *Ann Oncol*. 25(suppl3):iii1-iii9. doi:10.1093/annonc/mdu260

183. Grothey A, Van Cutsem E, Sobrero A, et al. Regorafenib monotherapy for previously treated metastatic colorectal cancer (CORRECT): An international, multicentre, randomised, placebo-controlled, phase 3 trial. *Lancet*. 2013;381(9863):303-312. doi:10.1016/S0140-6736(12)61900-X
184. McKeown SR. Defining normoxia, physoxia and hypoxia in tumours - Implications for treatment response. *Br J Radiol*. 2014;87(1035). doi:10.1259/bjr.20130676
185. Carreau A, Hafny-Rahbi B El, Matejuk A, Grillon C, Kieda C. Why is the partial oxygen pressure of human tissues a crucial parameter? Small molecules and hypoxia. *J Cell Mol Med*. 2011;15(6):1239-1253. doi:10.1111/j.1582-4934.2011.01258.x
186. Vaupel P, Höckel M, Mayer A. Detection and characterization of tumor hypoxia using pO2 histography. *Antioxidants Redox Signal*. 2007;9(8):1221-1235. doi:10.1089/ars.2007.1628
187. Höckel M, Vaupel P. Tumor hypoxia: Definitions and current clinical, biologic, and molecular aspects. *J Natl Cancer Inst*. 2001;93(4):266-276. doi:10.1093/jnci/93.4.266
188. Pollheimer MJ, Kornprat P, Lindtner RA, et al. Tumor necrosis is a new promising prognostic factor in colorectal cancer. *Hum Pathol*. 2010;41(12):1749-1757. doi:10.1016/j.humpath.2010.04.018
189. Brown JM, Giaccia AJ. The unique physiology of solid tumors: Opportunities (and problems) for cancer therapy. *Cancer Res*. 1998;58(7):1408-1416.
190. Yoshimura H, Dhar DK, Kohno H, et al. Prognostic impact of hypoxia-inducible factors 1α and 2α in colorectal cancer patients: Correlation with tumor angiogenesis and cyclooxygenase-2 expression. *Clin Cancer Res*. 2004;10(24):8554-8560. doi:10.1158/1078-0432.CCR-0946-03
191. Koukourakis MI, A. G, J. S, et al. Hypoxia inducible factor (HIF-1a and HIF-2a) expression in early esophageal cancer and response to photodynamic therapy and radiotherapy. *Cancer Res*. 2001;61(5):1830-1832. http://www.embase.com/search/results?subaction=viewrecord&from=export&id=L32691993. Accessed May 5, 2020.
192. Harris AL. Hypoxia — a key regulatory factor in tumour growth. *Nat Rev Cancer*. 2002;2(1):38-47. doi:10.1038/nrc704
193. Vaupel P, Kallinowski F, Okunieff P. Blood Flow, Oxygen and Nutrient Supply, and Metabolic Microenvironment of Human Tumors: A Review. *Cancer Res*. 1989;49(23):6449-6465.
194. Folkman J. What is the evidence that tumors are angiogenesis dependent? *J Natl Cancer Inst*. 1990;82(1):4-7. doi:10.1093/jnci/82.1.4
195. Dewhirst MW, Ong ET, Braun RD, et al. Quantification of longitudinal tissue pO2 gradients in window chamber tumours: Impact on tumour hypoxia. *Br J Cancer*. 1999;79(11-12):1717-1722. doi:10.1038/sj.bjc.6690273
196. Vaupel P. The Role of Hypoxia-Induced Factors in Tumor Progression. *Oncologist*. 2004;9(S5):10-17. doi:10.1634/theoncologist.9-90005-10
197. Cárdenas-Navia LI, Yu D, Braun RD, Brizel DM, Secomb TW, Dewhirst MW. Tumor-dependent Kinetics of Partial Pressure of Oxygen Fluctuations during Air and Oxygen Breathing. *Cancer Res*. 2004;64(17):6010-6017. doi:10.1158/0008-5472.CAN-03-0947
198. Hoogsteen IJ, Marres HAM, van der Kogel AJ, Kaanders JHAM. The Hypoxic Tumour Microenvironment, Patient Selection and Hypoxia-modifying Treatments. *Clin Oncol*. 2007;19(6):385-396. doi:10.1016/j.clon.2007.03.001
199. Liu W, Shen SM, Zhao XY, Chen Dr. GQ. Targeted genes and interacting

proteins of hypoxia inducible factor-1. *Int J Biochem Mol Biol*. 2012;3(2):165. /pmc/articles/PMC3388736/. Accessed November 4, 2022.
200. Semenza GL. Targeting HIF-1 for cancer therapy. *Nat Rev Cancer*. 2003;3(10):721-732. doi:10.1038/NRC1187
201. Semenza GL, Wang GL. A nuclear factor induced by hypoxia via de novo protein synthesis binds to the human erythropoietin gene enhancer at a site required for transcriptional activation. *Mol Cell Biol*. 1992;12(12):5447-5454. doi:10.1128/mcb.12.12.5447
202. Wang GL, Jiang BH, Rue EA, Semenza GL. Hypoxia-inducible factor 1 is a basic-helix-loop-helix-PAS heterodimer regulated by cellular O2 tension. *Proc Natl Acad Sci U S A*. 1995;92(12):5510-5514. doi:10.1073/pnas.92.12.5510
203. Tian H, McKnight SL, Russell DW. Endothelial PAS domain protein 1 (EPAS1), a transcription factor selectively expressed in endothelial cells. *Genes Dev*. 1997;11(1):72-82. doi:10.1101/gad.11.1.72
204. Semenza GL. Hypoxia-inducible factor 1: Master regulator of O2 homeostasis. *Curr Opin Genet Dev*. 1998;8(5):588-594. doi:10.1016/S0959-437X(98)80016-6
205. Bersten DC, Sullivan AE, Peet DJ, Whitelaw ML. BHLH-PAS proteins in cancer. *Nat Rev Cancer*. 2013;13(12):827-841. doi:10.1038/nrc3621
206. Huang LE, Gu J, Schau M, Bunn HF. Regulation of hypoxia-inducible factor 1α is mediated by an O2-dependent degradation domain via the ubiquitin-proteasome pathway. *Proc Natl Acad Sci U S A*. 1998;95(14):7987-7992. doi:10.1073/pnas.95.14.7987
207. Arany Z, Huang LE, Eckner R, et al. An essential role for p300/CBP in the cellular response to hypoxia. *Proc Natl Acad Sci U S A*. 1996;93(23):12969-12973. doi:10.1073/pnas.93.23.12969
208. Wiener CM, Booth G, Semenza GL. In vivo expression of mRNAs encoding hypoxia-inducible factor 1. *Biochem Biophys Res Commun*. 1996;225(2):485-488. doi:10.1006/bbrc.1996.1199
209. O'Rourke JF, Tian YM, Ratcliffe PJ, Pugh CW. Oxygen-regulated and transactivating domains in endothelial PAS protein 1: Comparison with hypoxia-inducible factor-1α. *J Biol Chem*. 1999;274(4):2060-2071. doi:10.1074/jbc.274.4.2060
210. Wiesener MS, Turley H, Allen WE, et al. Induction of Endothelial PAS Domain Protein-1 by Hypoxia: Characterization and Comparison With Hypoxia-Inducible Factor-1α. *Blood*. 1998;92(7):2260-2268. doi:10.1182/blood.V92.7.2260
211. Wiesener MS, Jürgensen JS, Rosenberger C, et al. Widespread hypoxia-inducible expression of HIF-2alpha in distinct cell populations of different organs. *FASEB J*. 2003;17(2):271-273. doi:10.1096/fj.02-0445fje
212. Keith B, Johnson RS, Simon MC. HIF1 α and HIF2 α: sibling rivalry in hypoxic tumour growth and progression. *Nat Rev Cancer*. 2012;12(1):9-22. doi:10.1038/nrc3183
213. Imamura T, Kikuchi H, Herraiz MT, et al. HIF-1α and HIF-2α have divergent roles in colon cancer. *Int J Cancer*. 2009;124(4):763-771. doi:10.1002/ijc.24032
214. Hu C-J, Wang L-Y, Chodosh LA, Keith B, Simon MC. Differential Roles of Hypoxia-Inducible Factor 1α (HIF-1α) and HIF-2α in Hypoxic Gene Regulation. *Mol Cell Biol*. 2003;23(24):9361-9374. doi:10.1128/mcb.23.24.9361-9374.2003
215. Takeda N, Maemura K, Imai Y, et al. Endothelial PAS domain protein 1 gene promotes angiogenesis through the transactivation of both vascular endothelial growth factor and its receptor, Flt-1. *Circ Res*. 2004;95(2):146-153. doi:10.1161/01.RES.0000134920.10128.b4
216. Nauta TD, van den Broek M, Gibbs S, et al. Identification of HIF-2α-regulated

genes that play a role in human microvascular endothelial sprouting during prolonged hypoxia in vitro. *Angiogenesis*. 2017;20(1):39-54. doi:10.1007/s10456-016-9527-4
217. Jaakkola P, Mole DR, Tian YM, et al. Targeting of HIF-α to the von Hippel-Lindau ubiquitylation complex by O2-regulated prolyl hydroxylation. *Science (80-)*. 2001;292(5516):468-472. doi:10.1126/science.1059796
218. Epstein ACR, Gleadle JM, McNeill LA, et al. C. elegans EGL-9 and mammalian homologs define a family of dioxygenases that regulate HIF by prolyl hydroxylation. *Cell*. 2001;107(1):43-54. doi:10.1016/S0092-8674(01)00507-4
219. Chowdhury R, McDonough MA, Mecinović J, et al. Structural Basis for Binding of Hypoxia-Inducible Factor to the Oxygen-Sensing Prolyl Hydroxylases. *Structure*. 2009;17(7):981-989. doi:10.1016/j.str.2009.06.002
220. Pause A, Lee S, Worrell RA, et al. The von Hippel-Lindau tumor-suppressor gene product forms a stable complex with human CUL-2, a member of the Cdc53 family of proteins. *Proc Natl Acad Sci U S A*. 1997;94(6):2156-2161. doi:10.1073/pnas.94.6.2156
221. Kamura T, Koepp DM, Conrad MN, et al. Rbx1, a component of the VHL tumor suppressor complex and SCF ubiquitin ligase. *Science (80-)*. 1999;284(5414):657-661. doi:10.1126/science.284.5414.657
222. Cockman ME, Masson N, Mole DR, et al. Hypoxia inducible factor-α binding and ubiquitylation by the von Hippel-Lindau tumor suppressor protein. *J Biol Chem*. 2000;275(33):25733-25741. doi:10.1074/jbc.M002740200
223. Kamura T, Sato S, Iwai K, Czyzyk-Krzeska M, Conaway RC, Conaway JW. Activation of HIF1α ubiquitination by a reconstituted von Hippel-Lindau (VHL) tumor suppressor complex. *Proc Natl Acad Sci U S A*. 2000;97(19):10430-10435. doi:10.1073/pnas.190332597
224. Mahon PC, Hirota K, Semenza GL. FIH-1: A novel protein that interacts with HIF-1α and VHL to mediate repression of HIF-1 transcriptional activity. *Genes Dev*. 2001;15(20):2675-2686. doi:10.1101/gad.924501
225. McNeill LA, Hewitson KS, Claridge TD, Seibel JF, Horsfall LE, Schofield CJ. Hypoxia-inducible factor asparaginyl hydroxylase (FIH-1) catalyses hydroxylation at the β-carbon of asparagine-803. *Biochem J*. 2002;367(3):571-575. doi:10.1042/BJ20021162
226. Dames SA, Martinez-Yamout M, De Guzman RN, Jane Dyson H, Wright PE. Structural basis for Hif-1α/CBP recognition in the cellular hypoxic response. *Proc Natl Acad Sci U S A*. 2002;99(8):5271-5276. doi:10.1073/pnas.082121399
227. Koh MY, Lemos R, Liu X, Powis G. The hypoxia-associated factor switches cells from HIF-1α- to HIF-2α-dependent signaling promoting stem cell characteristics, aggressive tumor growth and invasion. *Cancer Res*. 2011;71(11):4015-4027. doi:10.1158/0008-5472.CAN-10-4142
228. Camenisch G, Stroka D, Gassmann M, Wenger R. Attenuation of HIF-1 DNA-binding activity limits hypoxia-inducible endothelin-1 expression. *Pflugers Arch Eur J Physiol*. 2001;443(2):240-249. doi:10.1007/s004240100679
229. Wilson WR, Hay MP. Targeting hypoxia in cancer therapy. *Nat Rev Cancer*. 2011;11(6):393-410. doi:10.1038/nrc3064
230. Vaupel P. Hypoxia and aggressive tumor phenotype: implications for therapy and prognosis. *Oncologist*. 2008;13 Suppl 3(S3):21-26. doi:10.1634/THEONCOLOGIST.13-S3-21
231. VAUPEL P. Oxygenation status of malignant tumors: Pathogenesis of hypoxia and significance for tumor therapy. *Semin Oncol*. 2001;28(2 Suppl 8):29-35. doi:10.1016/s0093-7754(01)90210-6

232. Ward JF. DNA Damage Produced by Ionizing Radiation in Mammalian Cells: Identities, Mechanisms of Formation, and Reparability. *Prog Nucleic Acid Res Mol Biol*. 1988;35(C):95-125. doi:10.1016/S0079-6603(08)60611-X
233. Harrison LB, Chadha M, Hill RJ, Hu K, Shasha D. Impact of Tumor Hypoxia and Anemia on Radiation Therapy Outcomes. *Oncologist*. 2002;7(6):492-508. doi:10.1634/theoncologist.7-6-492
234. GRAY LH, CONGER AD, EBERT M, HORNSEY S, SCOTT OC. The concentration of oxygen dissolved in tissues at the time of irradiation as a factor in radiotherapy. *Br J Radiol*. 1953;26(312):638-648. doi:10.1259/0007-1285-26-312-638
235. Antonovic L, Lindblom E, Dasu A, Bassler N, Furusawa Y, Toma-Dasu I. Clinical oxygen enhancement ratio of tumors in carbon ion radiotherapy: the influence of local oxygenation changes. *J Radiat Res*. 55(5):902-911. doi:10.1093/jrr/rru020
236. Baskar R, Dai J, Wenlong N, Yeo R, Yeoh KW. Biological response of cancer cells to radiation treatment. *Front Mol Biosci*. 2014;1(NOV). doi:10.3389/fmolb.2014.00024
237. Brown JM. Tumor Hypoxia in Cancer Therapy. *Methods Enzymol*. 2007;435:295-321. doi:10.1016/S0076-6879(07)35015-5
238. Barcellos-Hoff MH, Park C, Wright EG. Radiation and the microenvironment - Tumorigenesis and therapy. *Nat Rev Cancer*. 2005;5(11):867-875. doi:10.1038/nrc1735
239. Liao WL, Lin SC, Sunny Sun H, Tsai SJ. Hypoxia-induced tumor malignancy and drug resistance: Role of microRNAs. *Biomarkers Genomic Med*. 2014;6(1):1-11. doi:10.1016/j.bgm.2014.01.003
240. Minchinton AI, Tannock IF. Drug penetration in solid tumours. *Nat Rev Cancer*. 2006;6(8):583-592. doi:10.1038/nrc1893
241. Heldin CH, Rubin K, Pietras K, Östman A. High interstitial fluid pressure - An obstacle in cancer therapy. *Nat Rev Cancer*. 2004;4(10):806-813. doi:10.1038/nrc1456
242. Jing X, Yang F, Shao C, et al. Role of hypoxia in cancer therapy by regulating the tumor microenvironment. *Mol Cancer*. 2019;18(1):1-15. doi:10.1186/s12943-019-1089-9
243. Teicher BA, Lazo JS, Sartorelli AC. Classification of Antineoplastic Agents by their Selective Toxicities toward Oxygenated and Hypoxic Tumor Cells. *Cancer Res*. 1981;41(1):73-81.
244. Tannock IF. Cell kinetics and chemotherapy: a critical review. *undefined*. 1978.
245. Vaupel P, Thews O, Hoeckel M. Treatment resistance of solid tumors: Role of hypoxia and anemia. *Med Oncol*. 2001;18(4):243-259. doi:10.1385/MO:18:4:243
246. Amadori D, Volpi A, Maltoni R, et al. Cell proliferation as a predictor of response to chemotherapy in metastatic breast cancer: A prospective study. *Breast Cancer Res Treat*. 1997;43(1):7-14. doi:10.1023/A:1005780107879
247. Gardner LB, Li Q, Park MS, Flanagan WM, Semenza GL, Dang C V. Hypoxia Inhibits G1/S Transition through Regulation of p27 Expression. *J Biol Chem*. 2001;276(11):7919-7926. doi:10.1074/jbc.M010189200
248. Kim CY, Tsai MH, Osmanian C, et al. Selection of Human Cervical Epithelial Cells That Possess Reduced Apoptotic Potential to Low-Oxygen Conditions. *Cancer Res*. 1997;57(19).
249. Erler JT, Cawthorne CJ, Williams KJ, et al. Hypoxia-Mediated Down-Regulation of Bid and Bax in Tumors Occurs via Hypoxia-Inducible Factor 1-Dependent and -Independent Mechanisms and Contributes to Drug Resistance. *Mol Cell Biol*.

2004;24(7):2875-2889. doi:10.1128/mcb.24.7.2875-2889.2004
250. Dong Z, Venkatachalam MA, Wang J, et al. Up-regulation of apoptosis inhibitory protein IAP-2 by hypoxia: HIF-1-independent mechanisms. *J Biol Chem*. 2001;276(22):18702-18709. doi:10.1074/jbc.M011774200
251. Chen YQ, Zhao CL, Li W. Effect of hypoxia-inducible factor-1 on transcription of survivin in non-small cell lung cancer. *J Exp Clin Cancer Res*. 2009;28(1). doi:10.1186/1756-9966-28-29
252. Jing X, Yang F, Shao C, et al. Role of hypoxia in cancer therapy by regulating the tumor microenvironment. *Mol Cancer*. 2019;18(1). doi:10.1186/s12943-019-1089-9
253. Fardel O, Lecureur V, Guillouzo A. The P-glycoprotein multidrug transporter. *Gen Pharmacol*. 1996;27(8):1283-1291. doi:10.1016/S0306-3623(96)00081-X
254. Ding Z, Yang L, Xie X, et al. Expression and significance of hypoxia-inducible factor-1 alpha and MDR1/P-glycoprotein in human colon carcinoma tissue and cells. *J Cancer Res Clin Oncol*. 2010;136(11):1697-1707. doi:10.1007/s00432-010-0828-5
255. Nooter K, Westerman AM, Flens MJ, et al. Expression of the Multidrug Resistance-associated Protein (MRP) Gene in Human Cancers. *Clin Cancer Res*. 1995;1(11):1301-1310.
256. Padró M, Louie RJ, Lananna B V., Krieg AJ, Timmerman LA, Chan DA. Genome-independent hypoxic repression of estrogen receptor alpha in breast cancer cells. *BMC Cancer*. 2017;17(1):1-16. doi:10.1186/S12885-017-3140-9/FIGURES/5
257. Woo YM, Shin Y, Lee EJ, et al. Inhibition of Aerobic Glycolysis Represses Akt/mTOR/HIF-1α Axis and Restores Tamoxifen Sensitivity in Antiestrogen-Resistant Breast Cancer Cells. *PLoS One*. 2015;10(7). doi:10.1371/JOURNAL.PONE.0132285
258. Meric-Bernstam F, Hurwitz H, Raghav KPS, et al. Pertuzumab and trastuzumab for HER2-amplified metastatic colorectal cancer: an updated report from MyPathway, a multicentre, open-label, phase 2a multiple basket study. *Lancet Oncol*. 2019;20(4):518. doi:10.1016/S1470-2045(18)30904-5
259. Aghazadeh S, Yazdanparast R. Activation of STAT3/HIF-1α/Hes-1 axis promotes trastuzumab resistance in HER2-overexpressing breast cancer cells via down-regulation of PTEN. *Biochim Biophys acta Gen Subj*. 2017;1861(8):1970-1980. doi:10.1016/J.BBAGEN.2017.05.009
260. Kopecka J, Salaroglio IC, Perez-Ruiz E, et al. Hypoxia as a driver of resistance to immunotherapy. *Drug Resist Updat*. 2021;59:100787. doi:10.1016/J.DRUP.2021.100787
261. Raggi F, Pelassa S, Pierobon D, et al. Regulation of human Macrophage M1-M2 Polarization Balance by hypoxia and the Triggering receptor expressed on Myeloid cells-1. *Front Immunol*. 2017;8(SEP):1097. doi:10.3389/FIMMU.2017.01097/BIBTEX
262. Du R, Lu K V., Petritsch C, et al. HIF1α Induces the Recruitment of Bone Marrow-Derived Vascular Modulatory Cells to Regulate Tumor Angiogenesis and Invasion. *Cancer Cell*. 2008;13(3):206-220. doi:10.1016/j.ccr.2008.01.034
263. Vignali DAA, Collison LW, Workman CJ. How regulatory T cells work. *Nat Rev Immunol 2008 87*. 2008;8(7):523-532. doi:10.1038/nri2343
264. Cubillos-Zapata C, Avendaño-Ortiz J, Hernandez-Jimenez E, et al. Hypoxia-induced PD-L1/PD-1 crosstalk impairs T-cell function in sleep apnoea. *Eur Respir J*. 2017;50(4). doi:10.1183/13993003.00833-2017
265. Noman MZ, Desantis G, Janji B, et al. PD-L1 is a novel direct target of HIF-1α, and its blockade under hypoxia enhanced MDSC-mediated T cell activation. *J Exp*

Med. 2014;211(5):781-790. doi:10.1084/JEM.20131916
266. Kafri M, Metzl-Raz E, Jona G, Barkai N. The Cost of Protein Production. *Cell Rep*. 2016;14(1):22. doi:10.1016/J.CELREP.2015.12.015
267. Liu L, Cash TP, Jones RG, Keith B, Thompson CB, Simon MC. Hypoxia Induced Energy Stress Regulates mRNA Translation and Cell Growth. *Mol Cell*. 2006;21(4):521. doi:10.1016/J.MOLCEL.2006.01.010
268. Hershey JWB, Sonenberg N, Mathews MB. Principles of translational control: an overview. *Cold Spring Harb Perspect Biol*. 2012;4(12):a011528-a011528. doi:10.1101/CSHPERSPECT.A011528
269. Hinnebusch AG, Lorsch JR. The mechanism of eukaryotic translation initiation: new insights and challenges. *Cold Spring Harb Perspect Biol*. 2012;4(10). doi:10.1101/CSHPERSPECT.A011544
270. Koumenis C, Naczki C, Koritzinsky M, et al. Regulation of protein synthesis by hypoxia via activation of the endoplasmic reticulum kinase PERK and phosphorylation of the translation initiation factor eIF2alpha. *Mol Cell Biol*. 2002;22(21):7405-7416. doi:10.1128/MCB.22.21.7405-7416.2002
271. Sonenberg N, Hinnebusch AG. Regulation of Translation Initiation in Eukaryotes: Mechanisms and Biological Targets. *Cell*. 2009;136(4):731. doi:10.1016/J.CELL.2009.01.042
272. Phan L, Zhang X, Asano K, et al. Identification of a Translation Initiation Factor 3 (eIF3) Core Complex, Conserved in Yeast and Mammals, That Interacts with eIF5. *Mol Cell Biol*. 1998;18(8):4935. https://www.ncbi.nlm.nih.gov/pmc/articles/PMC109077/. Accessed September 6, 2019.
273. Asano K, Clayton J, Shalev A, Hinnebusch AG. A multifactor complex of eukaryotic initiation factors, eIF1, eIF2, eIF3, eIF5, and initiator tRNAMet is an important translation initiation intermediate in vivo. *Genes Dev*. 2000;14(19):2534. https://www.ncbi.nlm.nih.gov/pmc/articles/PMC316978/. Accessed September 6, 2019.
274. Sonenberg N, Gingras A-C. The mRNA 5' cap-binding protein eIF4E and control of cell growth. *Curr Opin Cell Biol*. 1998;10(2):268-275. doi:10.1016/S0955-0674(98)80150-6
275. Imataka H, Sonenberg N. Human eukaryotic translation initiation factor 4G (eIF4G) possesses two separate and independent binding sites for eIF4A. *Mol Cell Biol*. 1997;17(12):6940. https://www.ncbi.nlm.nih.gov/pmc/articles/PMC232551/. Accessed September 6, 2019.
276. Lamphear BJ, Kirchweger R, Skern T, Rhoads RE. Mapping of Functional Domains in Eukaryotic Protein Synthesis Initiation Factor 4G (eIF4G) with Picornaviral Proteases. *J Biol Chem*. 1995;270(37):21975-21983. doi:10.1074/jbc.270.37.21975
277. Archer SK, Shirokikh NE, Hallwirth C V, Beilharz TH, Preiss T. Probing the closed-loop model of mRNA translation in living cells. *RNA Biol*. 2015;12(3):248-254. doi:10.1080/15476286.2015.1017242
278. Tarun SZ, Jr, Sachs AB. Association of the yeast poly(A) tail binding protein with translation initiation factor eIF-4G. *EMBO J*. 1996;15(24):7168. https://www.ncbi.nlm.nih.gov/pmc/articles/PMC452544/. Accessed September 6, 2019.
279. Uchida N, Hoshino S ichi, Imataka H, Sonenberg N, Katada T. A novel role of the mammalian GSPT/eRF3 associating with poly(A)-binding protein in Cap/Poly(A)-dependent translation. *J Biol Chem*. 2002;277(52):50286-50292.

doi:10.1074/JBC.M203029200
280. Kahvejian A, Svitkin Y V., Sukarieh R, M'Boutchou MN, Sonenberg N. Mammalian poly(A)-binding protein is a eukaryotic translation initiation factor, which acts via multiple mechanisms. *Genes Dev*. 2005;19(1):104-113. doi:10.1101/GAD.1262905
281. Svitkin Y V., Evdokimova VM, Brasey A, et al. General RNA-binding proteins have a function in poly(A)-binding protein-dependent translation. *EMBO J*. 2009;28(1):58-68. doi:10.1038/EMBOJ.2008.259
282. Passmore LA, Schmeing TM, Maag D, et al. The eukaryotic translation initiation factors eIF1 and eIF1A induce an open conformation of the 40S ribosome. *Mol Cell*. 2007;26(1):41-50. doi:10.1016/J.MOLCEL.2007.03.018
283. Cheung YN, Maag D, Mitchell SF, et al. Dissociation of eIF1 from the 40S ribosomal subunit is a key step in start codon selection in vivo. *Genes Dev*. 2007;21(10):1217-1230. doi:10.1101/GAD.1528307
284. Algire MA, Maag D, Lorsch JR. Pi release from eIF2, not GTP hydrolysis, is the step controlled by start-site selection during eukaryotic translation initiation. *Mol Cell*. 2005;20(2):251-262. doi:10.1016/J.MOLCEL.2005.09.008
285. Pestova T V., Lomakin IB, Lee JH, Choi SK, Dever TE, Hellen CUT. The joining of ribosomal subunits in eukaryotes requires eIF5B. *Nature*. 2000;403(6767):332-335. doi:10.1038/35002118
286. Shin BS, Maag D, Roll-Mecak A, et al. Uncoupling of initiation factor eIF5B/IF2 GTPase and translational activities by mutations that lower ribosome affinity. *Cell*. 2002;111(7):1015-1025. doi:10.1016/S0092-8674(02)01171-6
287. Acker MG, Shin BS, Nanda JS, Saini AK, Dever TE, Lorsch JR. Kinetic analysis of late steps of eukaryotic translation initiation. *J Mol Biol*. 2009;385(2):491-506. doi:10.1016/J.JMB.2008.10.029
288. Fulda S, Gorman AM, Hori O, Samali A. Cellular stress responses: cell survival and cell death. *Int J Cell Biol*. 2010;2010. doi:10.1155/2010/214074
289. Pakos-Zebrucka K, Koryga I, Mnich K, Ljujic M, Samali A, Gorman AM. The integrated stress response. *EMBO Rep*. 2016;17(10):1374-1395. doi:10.15252/EMBR.201642195
290. Chee NT, Lohse I, Brothers SP. mRNA-to-protein translation in hypoxia. *Mol Cancer*. 2019;18(1). doi:10.1186/S12943-019-0968-4
291. Martineau Y, Müller D, Pyronnet S. Targeting protein synthesis in cancer cells. *Oncoscience*. 2014;1(7):484. doi:10.18632/ONCOSCIENCE.63
292. Clemens MJ. Initiation factor eIF2 alpha phosphorylation in stress responses and apoptosis. *Prog Mol Subcell Biol*. 2001;27:57-89. http://www.ncbi.nlm.nih.gov/pubmed/11575161. Accessed September 6, 2019.
293. Koritzinsky M, Magagnin MG, Van Den Beucken T, et al. Gene expression during acute and prolonged hypoxia is regulated by distinct mechanisms of translational control. *EMBO J*. 2006;25(5):1114. doi:10.1038/SJ.EMBOJ.7600998
294. Uttam S, Wong C, Price TJ, Khoutorsky A. eIF4E-Dependent Translational Control: A Central Mechanism for Regulation of Pain Plasticity. *Front Genet*. 2018;9. doi:10.3389/FGENE.2018.00470
295. Vadysirisack DD, Ellisen LW. mTOR Activity Under Hypoxia. In: *Methods in Molecular Biology (Clifton, N.J.)*. Vol 821. ; 2012:45-58. doi:10.1007/978-1-61779-430-8_4
296. Jhanwar-Uniyal M, Wainwright J V., Mohan AL, et al. Diverse signaling mechanisms of mTOR complexes: mTORC1 and mTORC2 in forming a formidable relationship. *Adv Biol Regul*. 2019;72:51-62. doi:10.1016/J.JBIOR.2019.03.003

297. Alessi DR, James SR, Downes CP, et al. Characterization of a 3-phosphoinositide-dependent protein kinase which phosphorylates and activates protein kinase Balpha. *Curr Biol*. 1997;7(4):261-269. doi:10.1016/S0960-9822(06)00122-9
298. Hemmings BA, Restuccia DF. PI3K-PKB/Akt Pathway. *Cold Spring Harb Perspect Biol*. 2012;4(9):a011189. doi:10.1101/CSHPERSPECT.A011189
299. Haar E Vander, Lee S il, Bandhakavi S, Griffin TJ, Kim DH. Insulin signalling to mTOR mediated by the Akt/PKB substrate PRAS40. *Nat Cell Biol*. 2007;9(3):316-323. doi:10.1038/NCB1547
300. Parmar N, Tamanoi F. Rheb G-Proteins and the Activation of mTORC1. *Enzym*. 2010;27(C):39. doi:10.1016/S1874-6047(10)27003-8
301. Pópulo H, Lopes JM, Soares P. The mTOR Signalling Pathway in Human Cancer. *Int J Mol Sci*. 2012;13(2):1886-1918. doi:10.3390/ijms13021886
302. Holz MK, Ballif BA, Gygi SP, Blenis J. mTOR and S6K1 mediate assembly of the translation preinitiation complex through dynamic protein interchange and ordered phosphorylation events. *Cell*. 2005;123(4):569-580. doi:10.1016/j.cell.2005.10.024
303. Magnuson B, Ekim B, Fingar DC. Regulation and function of ribosomal protein S6 kinase (S6K) within mTOR signalling networks. *Biochem J*. 2012;441(1):1-21. doi:10.1042/BJ20110892
304. Liu L, Cash TP, Jones RG, Keith B, Thompson CB, Simon MC. Hypoxia-induced energy stress regulates mRNA translation and cell growth. *Mol Cell*. 2006;21(4):521-531. doi:10.1016/J.MOLCEL.2006.01.010
305. Koumenis C, Naczki C, Koritzinsky M, et al. Regulation of protein synthesis by hypoxia via activation of the endoplasmic reticulum kinase PERK and phosphorylation of the translation initiation factor eIF2alpha. *Mol Cell Biol*. 2002;22(21):7405-7416. doi:10.1128/MCB.22.21.7405-7416.2002
306. Uniacke J, Perera JK, Lachance G, Francisco CB, Lee S. Cancer cells exploit eIF4E2-directed synthesis of hypoxia response proteins to drive tumor progression. *Cancer Res*. 2014;74(5):1379-1389. doi:10.1158/0008-5472.CAN-13-2278/651276/AM/CANCER-CELLS-EXPLOIT-EIF4E2-DIRECTED-HYPOXIC
307. Blais JD, Filipenko V, Bi M, et al. Activating Transcription Factor 4 Is Translationally Regulated by Hypoxic Stress. *Mol Cell Biol*. 2004;24(17):7469. doi:10.1128/MCB.24.17.7469-7482.2004
308. Arsham AM, Howell JJ, Simon MC. A novel hypoxia-inducible factor-independent hypoxic response regulating mammalian target of rapamycin and its targets. *J Biol Chem*. 2003;278(32):29655-29660. doi:10.1074/JBC.M212770200
309. Schneider A, Younis RH, Gutkind JS. Hypoxia-Induced Energy Stress Inhibits the mTOR Pathway by Activating an AMPK/REDD1 Signaling Axis in Head and Neck Squamous Cell Carcinoma. *Neoplasia*. 2008;10(11):1295-1302. doi:10.1593/NEO.08586
310. Inoki K, Zhu T, Guan KL. TSC2 Mediates Cellular Energy Response to Control Cell Growth and Survival. *Cell*. 2003;115(5):577-590. doi:10.1016/S0092-8674(03)00929-2
311. Deyoung MP, Horak P, Sofer A, Sgroi D, Ellisen LW. Hypoxia regulates TSC1/2-mTOR signaling and tumor suppression through REDD1-mediated 14-3-3 shuttling. *Genes Dev*. 2008;22(2):239-251. doi:10.1101/GAD.1617608
312. Ellisen LW. Cell Cycle Growth Control Under Stress: mTOR Regulation through the REDD1-TSC Pathway. *Cell Cycle*. 2005;4(11):11. doi:10.4161/cc.4.11.2139
313. Lejbkowicz F, Goyer C, Darveau A, Neron S, Lemieux R, Sonenberg N. A fraction of the mRNA 5' cap-binding protein, eukaryotic initiation factor 4E,

localizes to the nucleus. *Proc Natl Acad Sci U S A*. 1992;89(20):9612-9616. doi:10.1073/PNAS.89.20.9612
314. Dostie J, Ferraiuolo M, Pause A, Adam SA, Sonenberg N. A novel shuttling protein, 4E-T, mediates the nuclear import of the mRNA 5' cap-binding protein, eIF4E. *EMBO J*. 2000;19(12):3142-3156. doi:10.1093/EMBOJ/19.12.3142
315. Koritzinsky M, Magagnin MG, Van Den Beucken T, et al. Gene expression during acute and prolonged hypoxia is regulated by distinct mechanisms of translational control. *EMBO J*. 2006;25(5):1114. doi:10.1038/SJ.EMBOJ.7600998
316. Uniacke J, Holterman CE, Lachance G, et al. An oxygen-regulated switch in the protein synthesis machinery. *Nature*. 2012;486(7401):126-129. doi:10.1038/nature11055
317. Ho JJD, Wang M, Audas TE, et al. Systemic reprograming of translation efficiencies on oxygen stimulus. *Cell Rep*. 2016;14(6):1293. doi:10.1016/J.CELREP.2016.01.036
318. Cordin O, Banroques J, Tanner NK, Linder P. The DEAD-box protein family of RNA helicases. *Gene*. 2006;367(1-2):17-37. doi:10.1016/J.GENE.2005.10.019
319. Gorbalenya AE, Koonin E V. Helicases: amino acid sequence comparisons and structure-function relationships. *Curr Opin Struct Biol*. 1993;3(3):419-429. doi:10.1016/S0959-440X(05)80116-2
320. Tanner NK, Cordin O, Banroques J, Doère M, Linder P. The Q motif: A newly identified motif in DEAD box helicases may regulate ATP binding and hydrolysis. *Mol Cell*. 2003;11(1):127-138. doi:10.1016/S1097-2765(03)00006-6
321. Caruthers JM, McKay DB. Helicase structure and mechanism. *Curr Opin Struct Biol*. 2002;12(1):123-133. doi:10.1016/S0959-440X(02)00298-1
322. Hinnebusch AG. The scanning mechanism of eukaryotic translation initiation. *Annu Rev Biochem*. 2014;83:779-812. doi:10.1146/ANNUREV-BIOCHEM-060713-035802
323. Li Q, Imataka H, Morino S, et al. Eukaryotic translation initiation factor 4AIII (eIF4AIII) is functionally distinct from eIF4AI and eIF4AII. *Mol Cell Biol*. 1999;19(11):7336-7346. doi:10.1128/MCB.19.11.7336
324. Yoder-Hill J, Pause A, Sonenberg N, Merrick WC. The p46 subunit of eukaryotic initiation factor (eIF)-4F exchanges with eIF-4A. *J Biol Chem*. 1993;268(8):5566-5573. doi:10.1016/S0021-9258(18)53358-5
325. Chan CC, Dostie J, Diem MD, et al. eIF4A3 is a novel component of the exon junction complex. *RNA*. 2004;10(2):200-209. doi:10.1261/RNA.5230104
326. Duncan R, Hershey JW. Identification and quantitation of levels of protein synthesis initiation factors in crude HeLa cell lysates by two-dimensional polyacrylamide gel electrophoresis. *J Biol Chem*. 1983;258(11). doi:10.1016/s0021-9258(18)32356-1
327. Rogers GW, Richter NJ, Lima WF, Merrick WC. Modulation of the Helicase Activity of eIF4A by eIF4B, eIF4H, and eIF4F. *J Biol Chem*. 2001;276(33):30914-30922. doi:10.1074/jbc.M100157200
328. Rozovsky N, Butterworth AC, Moore MJ. Interactions between eIF4AI and its accessory factors eIF4B and eIF4H. *RNA*. 2008;14(10). doi:10.1261/rna.1049608
329. Nielsen KH, Behrens MA, He Y, et al. Synergistic activation of eIF4A by eIF4B and eIF4G. *Nucleic Acids Res*. 2011;39(7). doi:10.1093/nar/gkq1206
330. Williams-Hill DM, Duncan RF, Nielsen PJ, Tahara SM. Differential expression of the murine eukaryotic translation initiation factor isogenes eIF4A(I) and eIF4A(II) is dependent upon cellular growth status. *Arch Biochem Biophys*. 1997;338(1):111-120. doi:10.1006/ABBI.1996.9804
331. Nielsen PJ, Trachsel H. The mouse protein synthesis initiation factor 4A gene

family includes two related functional genes which are differentially expressed. *EMBO J*. 1988;7(7):2097-2105. doi:10.1002/J.1460-2075.1988.TB03049.X
332. Galicia-Vázquez G, Chu J, Pelletier J. EIF4AII is dispensable for miRNA-mediated gene silencing. *RNA*. 2015;21(10). doi:10.1261/rna.052225.115
333. Wilczynska A, Gillen SL, Schmidt T, et al. EIF4A2 drives repression of translation at initiation by Ccr4-Not through purine-rich motifs in the 5'UTR. *Genome Biol*. 2019;20(1):1-21. doi:10.1186/S13059-019-1857-2/FIGURES/5
334. Galicia-Vázquez G, Cencic R, Robert F, Agenor AQ, Pelletier J. A cellular response linking eIF4AI activity to eIF4AII transcription. *RNA*. 2012;18(7). doi:10.1261/rna.033209.112
335. Raza F, Waldron JA, Le Quesne J. Translational dysregulation in cancer: eIF4A isoforms and sequence determinants of eIF4A dependence. *Biochem Soc Trans*. 2015;43(6):1227-1233. doi:10.1042/BST20150163
336. Meijer HA, Kong YW, Lu WT, et al. Translational repression and eIF4A2 activity are critical for microRNA-mediated gene regulation. *Science (80-)*. 2013;340(6128):82-85. doi:10.1126/SCIENCE.1231197/SUPPL_FILE/MEIJER-SM.PDF
337. Cooke A, Prigge A, Wickens M. Translational repression by deadenylases. *J Biol Chem*. 2010;285(37):28506-28513. doi:10.1074/JBC.M110.150763
338. Mathys H, Basquin JÔ, Ozgur S, et al. Structural and biochemical insights to the role of the CCR4-NOT complex and DDX6 ATPase in microRNA repression. *Mol Cell*. 2014;54(5):751-765. doi:10.1016/J.MOLCEL.2014.03.036
339. Wilczynska A, Gillen SL, Schmidt T, et al. EIF4A2 drives repression of translation at initiation by Ccr4-Not through purine-rich motifs in the 5'UTR. *Genome Biol*. 2019;20(1):1-21. doi:10.1186/S13059-019-1857-2/FIGURES/5
340. Petit AP, Wohlbold L, Bawankar P, et al. The structural basis for the interaction between the CAF1 nuclease and the NOT1 scaffold of the human CCR4-NOT deadenylase complex. *Nucleic Acids Res*. 2012;40(21):11058-11072. doi:10.1093/NAR/GKS883
341. Meijer HA, Schmidt T, Gillen SL, et al. DEAD-box helicase eIF4A2 inhibits CNOT7 deadenylation activity. *Nucleic Acids Res*. 2019;47(15):8224. doi:10.1093/NAR/GKZ509
342. Liang S, Zhou Y, Chen Y, Ke G, Wen H, Wu X. Decreased expression of EIF4A1 after preoperative brachytherapy predicts better tumor-specific survival in cervical cancer. *Int J Gynecol Cancer*. 2014;24(5):908-915. doi:10.1097/IGC.0000000000000152
343. Gao C, Guo X, Xue A, Ruan Y, Wang H, Gao X. High intratumoral expression of eIF4A1 promotes epithelial-to-mesenchymal transition and predicts unfavorable prognosis in gastric cancer. *Acta Biochim Biophys Sin (Shanghai)*. 2020;52(3). doi:10.1093/abbs/gmz168
344. Modelska A, Turro E, Russell R, et al. The malignant phenotype in breast cancer is driven by eIf4A1-mediated changes in the translational landscape. *Cell Death Dis*. 2015;6(1). doi:10.1038/cddis.2014.542
345. Lin CJ, Cencic R, Mills JR, Robert F, Pelletier J. c-Myc and eIF4F Are Components of a Feedforward Loop that Links Transcription and Translation. *Cancer Res*. 2008;68(13):5326-5334. doi:10.1158/0008-5472.CAN-07-5876
346. Lai MC, Chang CM, Sun HSS. Hypoxia Induces Autophagy through Translational Up-Regulation of Lysosomal Proteins in Human Colon Cancer Cells. *PLoS One*. 2016;11(4):e0153627. doi:10.1371/JOURNAL.PONE.0153627
347. Chen ZH, Qi JJ, Wu QN, et al. Eukaryotic initiation factor 4A2 promotes experimental metastasis and oxaliplatin resistance in colorectal cancer. *J Exp Clin*

Cancer Res. 2019;38(1):1-18. doi:10.1186/S13046-019-1178-Z/FIGURES/7
348. Yan LX, Wu QN, Zhang Y, et al. Knockdown of miR-21 in human breast cancer cell lines inhibits proliferation, in vitro migration and in vivo tumor growth. *Breast Cancer Res*. 2011;13(1). doi:10.1186/bcr2803
349. Shaoyan X, Juanjuan Y, Yalan T, Ping H, Jianzhong L, Qinian W. Downregulation of EIF4A2 in Non–Small-Cell Lung Cancer Associates with Poor Prognosis. *Clin Lung Cancer*. 2013;14(6):658-665. doi:10.1016/j.cllc.2013.04.011
350. Lyu S, Lu J, Chen W, et al. High expression of eIF4A2 is associated with a poor prognosis in esophageal squamous cell carcinoma. *Oncol Lett*. 2020;20(5). doi:10.3892/ol.2020.12038
351. Liu M, Gong C, Xu R, Chen Y, Wang X. MicroRNA-5195-3p enhances the chemosensitivity of triple-negative breast cancer to paclitaxel by downregulating EIF4A2. *Cell Mol Biol Lett*. 2019;24(1). doi:10.1186/s11658-019-0168-7
352. Chen Z-H, Wu Q, Lu J, et al. Eukaryotic initiation factor 4A2 (EIF4A2) expression in colorectal cancer and prediction of prognosis. *https://doi-org.nottingham.idm.oclc.org/101200/JCO2018364_suppl664*. 2018;36(4_suppl):664-664. doi:10.1200/JCO.2018.36.4_SUPPL.664
353. Chen ZH, Qi JJ, Wu QN, et al. Eukaryotic initiation factor 4A2 promotes experimental metastasis and oxaliplatin resistance in colorectal cancer. *J Exp Clin Cancer Res*. 2019;38(1). doi:10.1186/S13046-019-1178-Z
354. Sørensen BS, Busk M, Overgaard J, Horsman MR, Alsner J. Simultaneous Hypoxia and Low Extracellular pH Suppress Overall Metabolic Rate and Protein Synthesis In Vitro. *PLoS One*. 2015;10(8):e0134955. doi:10.1371/JOURNAL.PONE.0134955
355. Bolland H. eIF4A2 is a regulator of hypoxic translation and colorectal tumour cell survival. December 2020.
356. Samanta D, Semenza GL. Metabolic adaptation of cancer and immune cells mediated by hypoxia-inducible factors. *Biochim Biophys Acta - Rev Cancer*. 2018;1870(1):15-22. doi:10.1016/J.BBCAN.2018.07.002
357. Maxwell PH, Dachs GU, Gleadle JM, et al. Hypoxia-inducible factor-1 modulates gene expression in solid tumors and influences both angiogenesis and tumor growth. *Proc Natl Acad Sci U S A*. 1997;94(15):8104-8109. doi:10.1073/PNAS.94.15.8104
358. Chen C, Pore N, Behrooz A, Ismail-Beigi F, Maity A. Regulation of glut1 mRNA by hypoxia-inducible factor-1. Interaction between H-ras and hypoxia. *J Biol Chem*. 2001;276(12):9519-9525. doi:10.1074/JBC.M010144200
359. Mathupala SP, Rempel A, Pedersen PL. Glucose catabolism in cancer cells: Identification and characterization of a marked activation response of the type II hexokinase gene to hypoxic conditions. *J Biol Chem*. 2001;276(46). doi:10.1074/jbc.M108181200
360. DeBerardinis RJ, Lum JJ, Hatzivassiliou G, Thompson CB. The Biology of Cancer: Metabolic Reprogramming Fuels Cell Growth and Proliferation. *Cell Metab*. 2008;7(1):11-20. doi:10.1016/j.cmet.2007.10.002
361. Kathagen A, Schulte A, Balcke G, et al. Hypoxia and oxygenation induce a metabolic switch between pentose phosphate pathway and glycolysis in glioma stem-like cells. *Acta Neuropathol*. 2013;126(5). doi:10.1007/s00401-013-1173-y
362. Iyer N V., Kotch LE, Agani F, et al. Cellular and developmental control of O2 homeostasis by hypoxia- inducible factor 1α. *Genes Dev*. 1998;12(2). doi:10.1101/gad.12.2.149
363. Bartrons R, Simon-Molas H, Rodríguez-García A, et al. Fructose 2,6-bisphosphate

in cancer cell metabolism. *Front Oncol*. 2018;8(SEP). doi:10.3389/fonc.2018.00331
364. Houddane A, Bultot L, Novellasdemunt L, et al. Role of Akt/PKB and PFKFB isoenzymes in the control of glycolysis, cell proliferation and protein synthesis in mitogen-stimulated thymocytes. *Cell Signal*. 2017;34. doi:10.1016/j.cellsig.2017.02.019
365. Minchenko OH, Ochiai A, Opentanova IL, et al. Overexpression of 6-phosphofructo-2-kinase/fructose-2,6-bisphosphatase-4 in the human breast and colon malignant tumors. *Biochimie*. 2005;87(11). doi:10.1016/j.biochi.2005.04.007
366. Minchenko A, Leshchinsky I, Opentanova I, et al. Hypoxia-inducible factor-1-mediated expression of the 6-phosphofructo-2-kinase/fructose-2,6-bisphosphatase-3 (PFKFB3) gene. Its possible role in the Warburg effect. *J Biol Chem*. 2002;277(8):6183-6187. doi:10.1074/JBC.M110978200
367. Firth JD, Ebert BL, Ratcliffe PJ. Hypoxic regulation of lactate dehydrogenase A: Interaction between hypoxia-inducible factor 1 and cAMP response elements. *J Biol Chem*. 1995;270(36). doi:10.1074/jbc.270.36.21021
368. Ullah MS, Davies AJ, Halestrap AP. The plasma membrane lactate transporter MCT4, but not MCT1, is up-regulated by hypoxia through a HIF-1α-dependent mechanism. *J Biol Chem*. 2006;281(14). doi:10.1074/jbc.M511397200
369. Patel MS, Korotchkina LG. Regulation of mammalian pyruvate dehydrogenase complex by phosphorylation: Complexity of multiple phosphorylation sites and kinases. *Exp Mol Med*. 2001;33(4). doi:10.1038/emm.2001.32
370. Kim JW, Tchernyshyov I, Semenza GL, Dang C V. HIF-1-mediated expression of pyruvate dehydrogenase kinase: A metabolic switch required for cellular adaptation to hypoxia. *Cell Metab*. 2006;3(3). doi:10.1016/j.cmet.2006.02.002
371. Valli A, Morotti M, Zois CE, et al. Adaptation to HIF1a deletion in hypoxic cancer cells by upregulation of GLUT14 and creatine metabolism. *Mol Cancer Res*. 2019;17(7):1531-1544. doi:10.1158/1541-7786.MCR-18-0315/81772/AM/ADAPTATION-TO-HIF1-DELETION-IN-HYPOXIC-CANCER
372. Kawai K, Uemura M, Munakata K, et al. Fructose-bisphosphate aldolase A is a key regulator of hypoxic adaptation in colorectal cancer cells and involved in treatment resistance and poor prognosis. *Int J Oncol*. 2017;50(2). doi:10.3892/ijo.2016.3814
373. Currie E, Schulze A, Zechner R, Walther TC, Farese R V. Cellular fatty acid metabolism and cancer. *Cell Metab*. 2013;18(2). doi:10.1016/j.cmet.2013.05.017
374. Mylonis I, Simos G, Paraskeva E. Hypoxia-inducible factors and the regulation of lipid metabolism. *Cells*. 2019;8(3). doi:10.3390/cells8030214
375. Bensaad K, Favaro E, Lewis CA, et al. Fatty acid uptake and lipid storage induced by HIF-1α contribute to cell growth and survival after hypoxia-reoxygenation. *Cell Rep*. 2014;9(1):349-365. doi:10.1016/J.CELREP.2014.08.056
376. Krishnan J, Suter M, Windak R, et al. Activation of a HIF1alpha-PPARgamma axis underlies the integration of glycolytic and lipid anabolic pathways in pathologic cardiac hypertrophy. *Cell Metab*. 2009;9(6):512-524. doi:10.1016/J.CMET.2009.05.005
377. Perman JC, Boström P, Lindbom M, et al. The VLDL receptor promotes lipotoxicity and increases mortality in mice following an acute myocardial infarction. *J Clin Invest*. 2011;121(7):2625-2640. doi:10.1172/JCI43068
378. Castellano J, Aledo R, Sendra J, et al. Hypoxia stimulates low-density lipoprotein receptor-related protein-1 expression through hypoxia-inducible factor-1α in human vascular smooth muscle cells. *Arterioscler Thromb Vasc Biol*. 2011;31(6):1411-1420. doi:10.1161/ATVBAHA.111.225490

379. Mullen AR, Wheaton WW, Jin ES, et al. Reductive carboxylation supports growth in tumour cells with defective mitochondria. *Nature*. 2011;481(7381):385-388. doi:10.1038/NATURE10642
380. Beckner ME, Fellows-Mayle W, Zhang Z, et al. Identification of ATP citrate lyase as a positive regulator of glycolytic function in glioblastomas. *Int J Cancer*. 2010;126(10). doi:10.1002/ijc.24918
381. Metallo CM, Gameiro PA, Bell EL, et al. Reductive glutamine metabolism by IDH1 mediates lipogenesis under hypoxia. *Nature*. 2011;481(7381):380-384. doi:10.1038/NATURE10602
382. Chen R, Xu M, Nagati J, Garcia JA. Coordinate regulation of stress signaling and epigenetic events by Acss2 and HIF-2 in cancer cells. *PLoS One*. 2017;12(12). doi:10.1371/journal.pone.0190241
383. Furuta E, Pai SK, Zhan R, et al. Fatty acid synthase gene is up-regulated by hypoxia via activation of Akt and sterol regulatory element binding protein-1. *Cancer Res*. 2008;68(4):1003-1011. doi:10.1158/0008-5472.CAN-07-2489
384. Liu Y, Ma Z, Zhao C, et al. HIF-1α and HIF-2α are critically involved in hypoxia-induced lipid accumulation in hepatocytes through reducing PGC-1α-mediated fatty acid β-oxidation. *Toxicol Lett*. 2014;226(2). doi:10.1016/j.toxlet.2014.01.033
385. Huang D, Li T, Li X, et al. HIF-1-mediated suppression of acyl-CoA dehydrogenases and fatty acid oxidation is critical for cancer progression. *Cell Rep*. 2014;8(6). doi:10.1016/j.celrep.2014.08.028
386. Du W, Zhang L, Brett-Morris A, et al. HIF drives lipid deposition and cancer in ccRCC via repression of fatty acid metabolism. *Nat Commun*. 2017;8(1). doi:10.1038/s41467-017-01965-8
387. Lieu EL, Nguyen T, Rhyne S, Kim J. Amino acids in cancer. *Exp Mol Med*. 2020;52(1). doi:10.1038/s12276-020-0375-3
388. Wei Z, Liu X, Cheng C, Yu W, Yi P. Metabolism of Amino Acids in Cancer. *Front Cell Dev Biol*. 2021;8. doi:10.3389/fcell.2020.603837
389. Fan J, Kamphorst JJ, Mathew R, et al. Glutamine-driven oxidative phosphorylation is a major ATP source in transformed mammalian cells in both normoxia and hypoxia. *Mol Syst Biol*. 2013;9. doi:10.1038/msb.2013.65
390. Wise DR, Thompson CB. Glutamine addiction: a new therapeutic target in cancer. *Trends Biochem Sci*. 2010;35(8). doi:10.1016/j.tibs.2010.05.003
391. Yang L, Venneti S, Nagrath D. Glutaminolysis: A Hallmark of Cancer Metabolism. *Annu Rev Biomed Eng*. 2017;19(1):163-194. doi:10.1146/annurev-bioeng-071516-044546
392. Fuchs BC, Bode BP. Amino acid transporters ASCT2 and LAT1 in cancer: Partners in crime? *Semin Cancer Biol*. 2005;15(4):254-266. doi:10.1016/J.SEMCANCER.2005.04.005
393. Yoo HC, Park SJ, Nam M, et al. A Variant of SLC1A5 Is a Mitochondrial Glutamine Transporter for Metabolic Reprogramming in Cancer Cells. *Cell Metab*. 2020;31(2):267-283.e12. doi:10.1016/j.cmet.2019.11.020
394. Wise DR, Ward PS, Shay JES, et al. Hypoxia promotes isocitrate dehydrogenasedependent carboxylation of α-ketoglutarate to citrate to support cell growth and viability. *Proc Natl Acad Sci U S A*. 2011;108(49):19611-19616. doi:10.1073/PNAS.1117773108/SUPPL_FILE/PNAS.201117773SI.PDF
395. Xiang L, Mou J, Shao B, et al. Glutaminase 1 expression in colorectal cancer cells is induced by hypoxia and required for tumor growth, invasion, and metastatic colonization. *Cell Death Dis*. 2019;10(2). doi:10.1038/s41419-018-1291-5
396. Gordan JD, Bertout JA, Hu CJ, Diehl JA, Simon MC. HIF-2α Promotes Hypoxic Cell Proliferation by Enhancing c-Myc Transcriptional Activity. *Cancer Cell*.

2007;11(4). doi:10.1016/j.ccr.2007.02.006
397. Jiang ZF, Wang M, Xu JL, Ning YJ. Hypoxia promotes mitochondrial glutamine metabolism through HIF1α-GDH pathway in human lung cancer cells. *Biochem Biophys Res Commun*. 2017;483(1). doi:10.1016/j.bbrc.2017.01.015
398. Sergiy MN, Xenia S, Dragony F, Keith N, Joshua M, Brookes PS. Acidic pH Is a Metabolic Switch for 2-Hydroxyglutarate Generation and Signaling. *J Biol Chem*. 2016;291(38):20188-20197. doi:10.1074/JBC.M116.738799
399. Alberghina L, Gaglio D. Redox control of glutamine utilization in cancer. *Cell Death Dis*. 2014;5(12). doi:10.1038/cddis.2014.513
400. Harding HP, Zhang Y, Zeng H, et al. An integrated stress response regulates amino acid metabolism and resistance to oxidative stress. *Mol Cell*. 2003;11(3). doi:10.1016/S1097-2765(03)00105-9
401. Zhang B, Chen Y, Bao L, Luo W. GPT2 Is Induced by Hypoxia-Inducible Factor (HIF)-2 and Promotes Glioblastoma Growth. *Cells*. 2022;11(16):2597. doi:10.3390/CELLS11162597/S1
402. Gao S, Ge A, Xu S, et al. PSAT1 is regulated by ATF4 and enhances cell proliferation via the GSK3β/β-catenin/cyclin D1 signaling pathway in ER-negative breast cancer. *J Exp Clin Cancer Res*. 2017;36(1). doi:10.1186/s13046-017-0648-4
403. Samanta D, Park Y, Andrabi SA, Shelton LM, Gilkes DM, Semenza GL. PHGDH expression is required for mitochondrial redox homeostasis, breast cancer stem cell maintenance, and lung metastasis. *Cancer Res*. 2016;76(15). doi:10.1158/0008-5472.CAN-16-0530
404. Neinast MD, Jang C, Hui S, et al. Quantitative Analysis of the Whole-Body Metabolic Fate of Branched-Chain Amino Acids. *Cell Metab*. 2019;29(2). doi:10.1016/j.cmet.2018.10.013
405. Yudkoff M. Brain metabolism of branched-chain amino acids. *Glia*. 1997;21(1). doi:10.1002/(SICI)1098-1136(199709)21:1<92::AID-GLIA10>3.0.CO;2-W
406. Elorza A, Soro-Arnáiz I, Meléndez-Rodríguez F, et al. HIF2α Acts as an mTORC1 Activator through the Amino Acid Carrier SLC7A5. *Mol Cell*. 2012;48(5):681-691. doi:10.1016/j.molcel.2012.09.017
407. Häfliger P, Charles RP. The l-type amino acid transporter LAT1—an emerging target in cancer. *Int J Mol Sci*. 2019;20(10). doi:10.3390/ijms20102428
408. Zhang B, Chen Y, Shi X, et al. Regulation of branched-chain amino acid metabolism by hypoxia-inducible factor in glioblastoma. *Cell Mol Life Sci*. 2021;78(1). doi:10.1007/s00018-020-03483-1
409. Maddocks ODK, Athineos D, Cheung EC, et al. Modulating the therapeutic response of tumours to dietary serine and glycine starvation. *Nature*. 2017;544(7650). doi:10.1038/nature22056
410. Morotti M, Bridges E, Valli A, et al. Hypoxia-induced switch in SNAT2/SLC38A2 regulation generates endocrine resistance in breast cancer. *Proc Natl Acad Sci U S A*. 2019;116(25). doi:10.1073/pnas.1818521116
411. Leibovici A, Rossignol C, Montrowl JA, et al. The effects of hypoxia-ischemia on neutral amino acid transporters in the developing rat brain. *Dev Neurosci*. 2007;29(3). doi:10.1159/000097410
412. Locasale JW. Serine, glycine and one-carbon units: Cancer metabolism in full circle. *Nat Rev Cancer*. 2013;13(8). doi:10.1038/nrc3557
413. Samanta D, Semenza GL. Serine synthesis helps hypoxic cancer stem cells regulate redox. *Cancer Res*. 2016;76(22). doi:10.1158/0008-5472.CAN-16-1730
414. Jia XQ, Zhang S, Zhu HJ, et al. Increased expression of PHGDH and prognostic significance in colorectal cancer. *Transl Oncol*. 2016;9(3).

doi:10.1016/j.tranon.2016.03.006
415. Locasale JW, Grassian AR, Melman T, et al. Phosphoglycerate dehydrogenase diverts glycolytic flux and contributes to oncogenesis. *Nat Genet*. 2011;43(9). doi:10.1038/ng.890
416. DeNicola GM, Chen PH, Mullarky E, et al. NRF2 regulates serine biosynthesis in non-small cell lung cancer. *Nat Genet*. 2015;47(12). doi:10.1038/ng.3421
417. Zheng Y, Cantley LC. Toward a better understanding of folate metabolism in health and disease. *J Exp Med*. 2019;216(2). doi:10.1084/jem.20181965
418. Zhu Z, Leung GKK. More Than a Metabolic Enzyme: MTHFD2 as a Novel Target for Anticancer Therapy? *Front Oncol*. 2020;10. doi:10.3389/fonc.2020.00658
419. Tibbetts AS, Appling DR. Compartmentalization of mammalian folate-mediated one-carbon metabolism. *Annu Rev Nutr*. 2010;30. doi:10.1146/annurev.nutr.012809.104810
420. Qiu F, Huang J, Sui M. Targeting arginine metabolism pathway to treat arginine-dependent cancers. *Cancer Lett*. 2015;364(1). doi:10.1016/j.canlet.2015.04.020
421. Silberman A, Goldman O, Assayag OB, et al. Acid-induced downregulation of ASS1 contributes to the maintenance of intracellular pH in cancer. *Cancer Res*. 2019;79(3). doi:10.1158/0008-5472.CAN-18-1062
422. Tang L, Zeng J, Geng P, et al. Global metabolic profiling identifies a pivotal role of proline and hydroxyproline metabolism in supporting hypoxic response in hepatocellular carcinoma. *Clin Cancer Res*. 2018;24(2). doi:10.1158/1078-0432.CCR-17-1707
423. Westbrook RL, Bridges E, Roberts J, et al. Proline Synthesis Through PYCR1 is Required to Support Cancer Cell Proliferation and Survival in Oxygen-Limiting Conditions. *SSRN Electron J*. 2021. doi:10.2139/ssrn.3883636
424. Hellmich MR, Szabo C. Hydrogen Sulfide and Cancer. *Handb Exp Pharmacol*. 2015;230:233-241. doi:10.1007/978-3-319-18144-8_12
425. Zhang J, Xie Y, Xu Y, Pan Y, Shao C. Hydrogen sulfide contributes to hypoxia-induced radioresistance on hepatoma cells. *J Radiat Res*. 2011;52(5):622-628. doi:10.1269/JRR.11004
426. Cai W, Wang M, Ju L, Wang C, Zhu Y. Hydrogen sulfide induces human colon cancer cell proliferation: role of Akt, ERK and p21. *Cell Biol Int*. 2010;34(6):565-572. doi:10.1042/CBI20090368
427. Fan K, Li N, Qi J, et al. Wnt/β-catenin signaling induces the transcription of cystathionine-γ-lyase, a stimulator of tumor in colon cancer. *Cell Signal*. 2014;26(12):2801-2808. doi:10.1016/J.CELLSIG.2014.08.023
428. Dickhout JG, Carlisle RE, Jerome DE, et al. Integrated stress response modulates cellular redox state via induction of cystathionine γ-lyase: cross-talk between integrated stress response and thiol metabolism. *J Biol Chem*. 2012;287(10):7603-7614. doi:10.1074/JBC.M111.304576
429. McIntyre A, Harris AL. Metabolic and hypoxic adaptation to anti-angiogenic therapy: a target for induced essentiality. *EMBO Mol Med*. 2015;7(4):368-379. doi:10.15252/EMMM.201404271
430. Peng X, Chen Z, Farshidfar F, et al. Molecular Characterization and Clinical Relevance of Metabolic Expression Subtypes in Human Cancers. *Cell Rep*. 2018;23(1). doi:10.1016/j.celrep.2018.03.077
431. Li S, Yu J, Huber A, et al. Metabolism drives macrophage heterogeneity in the tumor microenvironment. *Cell Rep*. 2022;39(1):110609. doi:10.1016/J.CELREP.2022.110609
432. Rubakhin SS, Lanni EJ, Sweedler J V. Progress toward single cell metabolomics.

Curr Opin Biotechnol. 2013;24(1):95. doi:10.1016/J.COPBIO.2012.10.021
433. Muhl L, Genové G, Leptidis S, et al. Single-cell analysis uncovers fibroblast heterogeneity and criteria for fibroblast and mural cell identification and discrimination. *Nat Commun*. 2020;11(1). doi:10.1038/s41467-020-17740-1
434. Breslin S, O'Driscoll L. Three-dimensional cell culture: the missing link in drug discovery. *Drug Discov Today*. 2013;18(5-6):240-249. doi:10.1016/J.DRUDIS.2012.10.003
435. Kaddurah-Daouk R, Kristal BS, Weinshilboum RM. Metabolomics: A global biochemical approach to drug response and disease. *Annu Rev Pharmacol Toxicol*. 2008;48. doi:10.1146/annurev.pharmtox.48.113006.094715
436. Chang L, Ni J, Beretov J, et al. Identification of protein biomarkers and signaling pathways associated with prostate cancer radioresistance using label-free LC-MS/MS proteomic approach. *Sci Rep*. 2017;7. doi:10.1038/srep41834
437. Lubes G, Goodarzi M. GC–MS based metabolomics used for the identification of cancer volatile organic compounds as biomarkers. *J Pharm Biomed Anal*. 2018;147. doi:10.1016/j.jpba.2017.07.013
438. Alexandrov T. Spatial Metabolomics and Imaging Mass Spectrometry in the Age of Artificial Intelligence. *Annu Rev Biomed Data Sci*. 2020;3(1). doi:10.1146/annurev-biodatasci-011420-031537
439. Ma X, Fernández FM. Advances in mass spectrometry imaging for spatial cancer metabolomics. *Mass Spectrom Rev*. 2022:e21804. doi:10.1002/MAS.21804
440. Taylor MJ, Lukowski JK, Anderton CR. Spatially Resolved Mass Spectrometry at the Single Cell: Recent Innovations in Proteomics and Metabolomics. *J Am Soc Mass Spectrom*. 2021;32(4):872-894. doi:10.1021/JASMS.0C00439/ASSET/IMAGES/LARGE/JS0C00439_0008.JPEG
441. Passarelli MK, Ewing AG. Single-Cell Imaging Mass Spectrometry. *Curr Opin Chem Biol*. 2013;17(5):854-859. doi:10.1016/J.CBPA.2013.07.017
442. Zenobi R. Single-cell metabolomics: analytical and biological perspectives. *Science*. 2013;342(6163). doi:10.1126/SCIENCE.1243259
443. Weibel KE, Mor JR, Fiechter A. Rapid sampling of yeast cells and automated assays of adenylate, citrate, pyruvate and glucose-6-phosphate pools. *Anal Biochem*. 1974;58(1):208-216. doi:10.1016/0003-2697(74)90459-X
444. Wishart DS, Tzur D, Knox C, et al. HMDB: the Human Metabolome Database. *Nucleic Acids Res*. 2007;35(Database issue):D521. doi:10.1093/NAR/GKL923
445. Watrous JD, Alexandrov T, Dorrestein PC. The evolving field of imaging mass spectrometry and its impact on future biological research. *J Mass Spectrom*. 2011;46(2). doi:10.1002/jms.1876
446. Amstalden van Hove ER, Smith DF, Heeren RMA. A concise review of mass spectrometry imaging. *J Chromatogr A*. 2010;1217(25). doi:10.1016/j.chroma.2010.01.033
447. Buchberger AR, DeLaney K, Johnson J, Li L. Mass Spectrometry Imaging: A Review of Emerging Advancements and Future Insights. *Anal Chem*. 2018;90(1). doi:10.1021/acs.analchem.7b04733
448. Anderton CR, Gamble LJ. Secondary Ion Mass Spectrometry Imaging of Tissues, Cells, and Microbial Systems. *Micros Today*. 2016;24(2). doi:10.1017/s1551929516000018
449. Perry WJ, Patterson NH, Prentice BM, Neumann EK, Caprioli RM, Spraggins JM. Uncovering matrix effects on lipid analyses in MALDI imaging mass spectrometry experiments. *J Mass Spectrom*. 2020;55(4). doi:10.1002/jms.4491
450. Lee JLS, Ninomiya S, Matsuo J, Gilmore IS, Seah MP, Shard AG. Organic depth

profiling of a nanostructured delta layer reference material using large argon cluster ions. *Anal Chem*. 2010;82(1):98-105. doi:10.1021/AC901045Q/SUPPL_FILE/AC901045Q_SI_001.PDF
451. Fletcher JS. Cellular imaging with secondary ion mass spectrometry. *Analyst*. 2009;134(11). doi:10.1039/b913575h
452. Colliver TL, Brummel CL, Pacholski ML, Swanek FD, Ewing AG, Winograd N. Atomic and Molecular Imaging at the Single-Cell Level with TOF-SIMS. *Anal Chem*. 1997;69(13). doi:10.1021/ac9701748
453. Yoon S, Lee TG. Biological tissue sample preparation for time-of-flight secondary ion mass spectrometry (ToF–SIMS) imaging. *Nano Converg*. 2018;5(1). doi:10.1186/s40580-018-0157-y
454. Kollmer F, Paul W, Krehl M, Niehuis E. Ultra high spatial resolution SIMS with cluster ions - Approaching the physical limits. In: *Surface and Interface Analysis*. Vol 45. ; 2013. doi:10.1002/sia.5093
455. Tian H, Maciążek D, Postawa Z, Garrison BJ, Winograd N. CO2 Cluster Ion Beam, an Alternative Projectile for Secondary Ion Mass Spectrometry. *J Am Soc Mass Spectrom*. 2016;27(9). doi:10.1007/s13361-016-1423-z
456. Pareek V, Tian H, Winograd N, Benkovic SJ. Metabolomics and mass spectrometry imaging reveal channeled de novo purine synthesis in cells. *Science (80-)*. 2020;368(6488). doi:10.1126/science.aaz6465
457. Bruinen AL, Fisher GL, Heeren RMA. ToF-SIMS parallel imaging MS/MS of lipid species in thin tissue sections. In: *Methods in Molecular Biology*. Vol 1618. ; 2017. doi:10.1007/978-1-4939-7051-3_14
458. Fisher GL, Bruinen AL, Ogrinc Potočnik N, et al. A New Method and Mass Spectrometer Design for TOF-SIMS Parallel Imaging MS/MS. *Anal Chem*. 2016;88(12). doi:10.1021/acs.analchem.6b01022
459. Passarelli MK, Pirkl A, Moellers R, et al. The 3D OrbiSIMS—label-free metabolic imaging with subcellular lateral resolution and high mass-resolving power. *Nat Methods 2017 1412*. 2017;14(12):1175-1183. doi:10.1038/nmeth.4504
460. Hu Q, Noll RJ, Li H, Makarov A, Hardman M, Cooks RG. The Orbitrap: a new mass spectrometer. *J Mass Spectrom*. 2005;40(4):430-443. doi:10.1002/JMS.856
461. Scheltema RA, Hauschild JP, Lange O, et al. The Q Exactive HF, a Benchtop mass spectrometer with a pre-filter, high-performance quadrupole and an ultra-high-field Orbitrap analyzer. *Mol Cell Proteomics*. 2014;13(12):3698-3708. doi:10.1074/MCP.M114.043489
462. Suvannapruk W, Edney MK, Kim DH, Scurr DJ, Ghaemmaghami AM, Alexander MR. Single-Cell Metabolic Profiling of Macrophages Using 3D OrbiSIMS: Correlations with Phenotype. *Anal Chem*. 2022;94(26):9389-9398. doi:10.1021/ACS.ANALCHEM.2C01375/SUPPL_FILE/AC2C01375_SI_001.PDF
463. Malm J, Giannaras D, Riehle MO, Gadegaard N, Sjövall P. Fixation and drying protocols for the preparation of cell samples for time-of-flight secondary ion mass spectrometry analysis. *Anal Chem*. 2009;81(17). doi:10.1021/ac900636v
464. Sjövall P, Johansson B, Lausmaa J. Localization of lipids in freeze-dried mouse brain sections by imaging TOF-SIMS. *Appl Surf Sci*. 2006;252(19). doi:10.1016/j.apsusc.2006.02.126
465. Fletcher JS, Rabbani S, Henderson A, Lockyer NP, Vickerman JC. Three-dimensional mass spectral imaging of HeLa-M cells - Sample preparation, data interpretation and visualisation. *Rapid Commun Mass Spectrom*. 2011;25(7). doi:10.1002/rcm.4944
466. Zhang J, Brown J, Scurr DJ, et al. Cryo-OrbiSIMS for 3D Molecular Imaging of a

Bacterial Biofilm in Its Native State. *Anal Chem*. 2020;92(13). doi:10.1021/acs.analchem.0c01125
467. McDonald KL, Auer M. High-pressure freezing, cellular tomography, and structural cell biology. *Biotechniques*. 2006;41(2). doi:10.2144/000112226
468. Meurs J, Scurr DJ, Lourdusamy A, et al. Sequential 3D OrbiSIMS and LESA-MS/MS-based metabolomics for prediction of brain tumor relapse from sample-limited primary tissue archives. *bioRxiv*. 2021.
469. Lovitt CJ, Shelper TB, Avery VM. Advanced Cell Culture Techniques for Cancer Drug Discovery. *Biology (Basel)*. 2014;3(2):345. doi:10.3390/BIOLOGY3020345
470. Li ML, Aggeler J, Farson DA, Hatier C, Hassell J, Bissell MJ. Influence of a reconstituted basement membrane and its components on casein gene expression and secretion in mouse mammary epithelial cells. *Proc Natl Acad Sci U S A*. 1987;84(1):136. doi:10.1073/PNAS.84.1.136
471. Ludwig K, Tse ES, Wang JY. Colon cancer cells adopt an invasive phenotype without mesenchymal transition in 3-D but not 2-D culture upon combined stimulation with EGF and crypt growth factors. *BMC Cancer 2013 131*. 2013;13(1):1-12. doi:10.1186/1471-2407-13-221
472. Hirt C, Papadimitropoulos A, Mele V, et al. "In vitro" 3D models of tumor-immune system interaction. *Adv Drug Deliv Rev*. 2014;79-80:145-154. doi:10.1016/J.ADDR.2014.05.003
473. Costa EC, Gaspar VM, Coutinho P, Correia IJ. Optimization of liquid overlay technique to formulate heterogenic 3D co-cultures models. *Biotechnol Bioeng*. 2014;111(8):1672-1685. doi:10.1002/BIT.25210
474. Mcmillin DW, Negri JM, Mitsiades CS. The role of tumour-stromal interactions in modifying drug response: challenges and opportunities. *Nat Rev Drug Discov*. 2013;12(3):217-228. doi:10.1038/NRD3870
475. Nederman T, Norling B, Glimelius B, Carlsson J, Brunk U. Demonstration of an extracellular matrix in multicellular tumor spheroids. *Cancer Res*. 1984.
476. Van Dijk M, Göransson SA, Strömblad S. Cell to extracellular matrix interactions and their reciprocal nature in cancer. *Exp Cell Res*. 2013;319(11):1663-1670. doi:10.1016/J.YEXCR.2013.02.006
477. Mehta G, Hsiao AY, Ingram M, Luker GD, Takayama S. Opportunities and challenges for use of tumor spheroids as models to test drug delivery and efficacy. *J Control Release*. 2012;164(2):192-204. doi:10.1016/J.JCONREL.2012.04.045
478. Trédan O, Galmarini CM, Patel K, Tannock IF. Drug resistance and the solid tumor microenvironment. *J Natl Cancer Inst*. 2007;99(19):1441-1454. doi:10.1093/JNCI/DJM135
479. Luca AC, Mersch S, Deenen R, et al. Impact of the 3D microenvironment on phenotype, gene expression, and EGFR inhibition of colorectal cancer cell lines. *PLoS One*. 2013;8(3). doi:10.1371/JOURNAL.PONE.0059689
480. Chang TT, Hughes-Fulford M. Monolayer and spheroid culture of human liver hepatocellular carcinoma cell line cells demonstrate distinct global gene expression patterns and functional phenotypes. *Tissue Eng Part A*. 2009;15(3):559-567. doi:10.1089/TEN.TEA.2007.0434
481. Tidwell TR, Røsland G V., Tronstad KJ, Søreide K, Hagland HR. Metabolic flux analysis of 3D spheroids reveals significant differences in glucose metabolism from matched 2D cultures of colorectal cancer and pancreatic ductal adenocarcinoma cell lines. *Cancer Metab*. 2022;10(1). doi:10.1186/S40170-022-00285-W
482. Lagies S, Schlimpert M, Neumann S, et al. Cells grown in three-dimensional spheroids mirror in vivo metabolic response of epithelial cells. *Commun Biol 2020*

31. 2020;3(1):1-10. doi:10.1038/s42003-020-0973-6
483. Schindelin J, Arganda-Carreras I, Frise E, et al. Fiji: an open-source platform for biological-image analysis. *Nat Methods 2012 97*. 2012;9(7):676-682. doi:10.1038/nmeth.2019
484. Dobin A, Davis CA, Schlesinger F, et al. STAR: ultrafast universal RNA-seq aligner. *Bioinformatics*. 2013;29(1):15-21. doi:10.1093/BIOINFORMATICS/BTS635
485. Liao Y, Smyth GK, Shi W. featureCounts: an efficient general purpose program for assigning sequence reads to genomic features. *Bioinformatics*. 2014;30(7):923-930. doi:10.1093/BIOINFORMATICS/BTT656
486. Liao Y, Wang J, Jaehnig EJ, Shi Z, Zhang B. WebGestalt 2019: gene set analysis toolkit with revamped UIs and APIs. *Nucleic Acids Res*. 2019;47(W1):W199-W205. doi:10.1093/NAR/GKZ401
487. Subramanian A, Tamayo P, Mootha VK, et al. Gene set enrichment analysis: a knowledge-based approach for interpreting genome-wide expression profiles. *Proc Natl Acad Sci U S A*. 2005;102(43):15545-15550. doi:10.1073/PNAS.0506580102
488. Mi H, Thomas P. PANTHER pathway: an ontology-based pathway database coupled with data analysis tools. *Methods Mol Biol*. 2009;563:123-140. doi:10.1007/978-1-60761-175-2_7
489. Shen S, Park JW, Lu ZX, et al. rMATS: robust and flexible detection of differential alternative splicing from replicate RNA-Seq data. *Proc Natl Acad Sci U S A*. 2014;111(51):E5593-E5601. doi:10.1073/PNAS.1419161111
490. Heerma van Voss MR, van Diest PJ, Raman V. Targeting RNA helicases in cancer: the translation trap. *Biochim Biophys Acta*. 2017;1868(2):510. doi:10.1016/J.BBCAN.2017.09.006
491. Chen S, Bu D, Zhu J, et al. Endogenous hydrogen sulfide regulates xCT stability through persulfidation of OTUB1 at cysteine 91 in colon cancer cells. *Neoplasia*. 2021;23(5):461-472. doi:10.1016/J.NEO.2021.03.009
492. Rouschop KM, Dubois LJ, Keulers TG, et al. PERK/eIF2α signaling protects therapy resistant hypoxic cells through induction of glutathione synthesis and protection against ROS. *Proc Natl Acad Sci U S A*. 2013;110(12):4622-4627. doi:10.1073/PNAS.1210633110/SUPPL_FILE/PNAS.201210633SI.PDF
493. Bourseau-Guilmain E, Menard JA, Lindqvist E, et al. Hypoxia regulates global membrane protein endocytosis through caveolin-1 in cancer cells. *Nat Commun 2016 71*. 2016;7(1):1-13. doi:10.1038/ncomms11371
494. Yi T, Papadopoulos E, Hagner PR, Wagner G. Hypoxia-inducible factor-1α (HIF-1α) promotes cap-dependent translation of selective mRNAs through up-regulating initiation factor eIF4E1 in breast cancer cells under hypoxia conditions. *J Biol Chem*. 2013;288(26):18732-18742. doi:10.1074/JBC.M113.471466
495. Sellam A, van het Hoog M, Tebbji F, Beaurepaire C, Whiteway M, Nantelc A. Modeling the Transcriptional Regulatory Network That Controls the Early Hypoxic Response in Candida albicans. *Eukaryot Cell*. 2014;13(5):675. doi:10.1128/EC.00292-13
496. Berg KCG, Eide PW, Eilertsen IA, et al. Multi-omics of 34 colorectal cancer cell lines - a resource for biomedical studies. *Mol Cancer*. 2017;16(1). doi:10.1186/S12943-017-0691-Y
497. Jongjitwimol J, Baldock RA, Morley SJ, Watts FZ. Sumoylation of eIF4A2 affects stress granule formation. *J Cell Sci*. 2016;129(12):2407. doi:10.1242/JCS.184614
498. Ye F, Wang X, Tu S, et al. The effects of NCBP3 on METTL3-mediated m6A RNA methylation to enhance translation process in hypoxic cardiomyocytes. *J Cell Mol Med*. 2021;25(18):8920. doi:10.1111/JCMM.16852

499. Tam SY, Wu VWC, Law HKW. Dynamics of oxygen level-driven regulators in modulating autophagy in colorectal cancer cells. *Biochem Biophys Res Commun*. 2019;517(2):193-200. doi:10.1016/J.BBRC.2019.07.043
500. Xu T, Zong Y, Peng L, et al. Overexpression of eIF4E in colorectal cancer patients is associated with liver metastasis. *Onco Targets Ther*. 2016;9:815. doi:10.2147/OTT.S98330
501. Arsham AM, Howell JJ, Simon MC. A novel hypoxia-inducible factor-independent hypoxic response regulating mammalian target of rapamycin and its targets. *J Biol Chem*. 2003;278(32):29655-29660. doi:10.1074/JBC.M212770200
502. Robert F, Cencic R, Cai R, Schmeing TM, Pelletier J. RNA-tethering assay and eIF4G:eIF4A obligate dimer design uncovers multiple eIF4F functional complexes. *Nucleic Acids Res*. 2020;48(15). doi:10.1093/nar/gkaa646
503. Krause L, Willing F, Andreou AZ, Klostermeier D. The domains of yeast eIF4G, eIF4E and the cap fine-tune eIF4A activities through an intricate network of stimulatory and inhibitory effects. *Nucleic Acids Res*. 2022;50(11):6497-6510. doi:10.1093/NAR/GKAC437
504. Panda A, Suvakov M, Mariani J, et al. Clonally selected lines after CRISPR/Cas editing are not isogenic. *bioRxiv*. May 2022:2022.05.17.492193. doi:10.1101/2022.05.17.492193
505. Boettcher M, Covarrubias S, Biton A, et al. Tracing cellular heterogeneity in pooled genetic screens via multi-level barcoding. *BMC Genomics*. 2019;20(1):1-9. doi:10.1186/S12864-019-5480-0/FIGURES/3
506. Westermann L, Li Y, Göcmen B, et al. Wildtype heterogeneity contributes to clonal variability in genome edited cells. *Sci Reports 2022 121*. 2022;12(1):1-13. doi:10.1038/s41598-022-22885-8
507. El-Brolosy MA, Stainier DYR. Genetic compensation: A phenomenon in search of mechanisms. *PLOS Genet*. 2017;13(7):e1006780. doi:10.1371/JOURNAL.PGEN.1006780
508. Jackson JG, Pereira-Smith OM. Primary and compensatory roles for RB family members at cell cycle gene promoters that are deacetylated and downregulated in doxorubicin-induced senescence of breast cancer cells. *Mol Cell Biol*. 2006;26(7):2501-2510. doi:10.1128/MCB.26.7.2501-2510.2006
509. Mulligan GJ, Wong J, Jacks T. p130 is dispensable in peripheral T lymphocytes: evidence for functional compensation by p107 and pRB. *Mol Cell Biol*. 1998;18(1):206-220. doi:10.1128/MCB.18.1.206
510. Radulovich N, Pham NA, Strumpf D, et al. Differential roles of cyclin D1 and D3 in pancreatic ductal adenocarcinoma. *Mol Cancer*. 2010;9. doi:10.1186/1476-4598-9-24
511. Wang J, Wang Q, Cui Y, et al. Knockdown of cyclin D1 inhibits proliferation, induces apoptosis, and attenuates the invasive capacity of human glioblastoma cells. *J Neurooncol*. 2012;106(3):473-484. doi:10.1007/S11060-011-0692-4
512. Lam EWF, Glassford J, Banerji L, Thomas NSB, Sicinski P, Klaus GGB. Cyclin D3 compensates for loss of cyclin D2 in mouse B-lymphocytes activated via the antigen receptor and CD40. *J Biol Chem*. 2000;275(5):3479-3484. doi:10.1074/JBC.275.5.3479
513. Cho SJ, Teng IF, Zhang M, et al. Hypoxia-inducible factor 1 alpha is regulated by RBM38, a RNAbinding protein and a p53 family target, via mRNA translation. *Oncotarget*. 2015;6(1). doi:10.18632/oncotarget.2786
514. Ho JJD, Balukoff NC, Theodoridis PR, et al. A network of RNA-binding proteins controls translation efficiency to activate anaerobic metabolism. *Nat Commun 2020 111*. 2020;11(1):1-16. doi:10.1038/s41467-020-16504-1

515. Van de Gucht M, Dufait I, Kerkhove L, et al. Inhibition of Phosphoglycerate Dehydrogenase Radiosensitizes Human Colorectal Cancer Cells under Hypoxic Conditions. *Cancers (Basel)*. 2022;14(20). doi:10.3390/CANCERS14205060/S1
516. Burrows N, Cane G, Robson M, et al. Hypoxia-induced nitric oxide production and tumour perfusion is inhibited by pegylated arginine deiminase (ADI-PEG20). *Sci Rep*. 2016;6. doi:10.1038/SREP22950
517. Cai W, Wang M, Ju L, Wang C, Zhu Y. Hydrogen sulfide induces human colon cancer cell proliferation: role of Akt, ERK and p21. *Cell Biol Int*. 2010;34(6):565-572. doi:10.1042/CBI20090368
518. Kimura H. Hydrogen sulfide: Its production, release and functions. *Amino Acids*. 2011;41(1):113-121. doi:10.1007/S00726-010-0510-X/FIGURES/3
519. Szabo C, Coletta C, Chao C, et al. Tumor-derived hydrogen sulfide, produced by cystathionine-β-synthase, stimulates bioenergetics, cell proliferation, and angiogenesis in colon cancer. *Proc Natl Acad Sci U S A*. 2013;110(30):12474-12479. doi:10.1073/PNAS.1306241110/SUPPL_FILE/PNAS.201306241SI.PDF
520. Wallace JL, Vaughan D, Dicay M, Macnaughton WK, De Nucci G. Hydrogen Sulfide-Releasing Therapeutics: Translation to the Clinic. *https://home.liebertpub.com/ars*. 2018;28(16):1533-1540. doi:10.1089/ARS.2017.7068
521. Fan K, Li N, Qi J, et al. Wnt/β-catenin signaling induces the transcription of cystathionine-γ-lyase, a stimulator of tumor in colon cancer. *Cell Signal*. 2014;26(12):2801-2808. doi:10.1016/J.CELLSIG.2014.08.023
522. You J, Shi X, Liang H, et al. Cystathionine- γ-lyase promotes process of breast cancer in association with STAT3 signaling pathway. *Oncotarget*. 2017;8(39):65677. doi:10.18632/ONCOTARGET.20057
523. Meng Q, Xing Y, Ren T, et al. Mammalian Eps15 homology domain 1 promotes metastasis in non-small cell lung cancer by inducing epithelial-mesenchymal transition. *Oncotarget*. 2017;8(14):22433. doi:10.18632/ONCOTARGET.11220
524. Meng Q, Sun W, Li M, et al. Increased Expression of Eps15 Homology Domain 1 is Associated with Poor Prognosis in Resected Small Cell Lung Cancer. *J Cancer*. 2015;6(10):990. doi:10.7150/JCA.11650
525. Tom EC, Mushtaq I, Mohapatra BC, et al. EHD1 and RUSC2 Control Basal Epidermal Growth Factor Receptor Cell Surface Expression and Recycling. *Mol Cell Biol*. 2020;40(7). doi:10.1128/MCB.00434-19
526. Dengler VL, Galbraith MD, Espinosa JM. Transcriptional Regulation by Hypoxia Inducible Factors. *Crit Rev Biochem Mol Biol*. 2014;49(1):1. doi:10.3109/10409238.2013.838205
527. Semenza GL, Roth PH, Fang HM, Wang GL. Transcriptional regulation of genes encoding glycolytic enzymes by hypoxia-inducible factor 1. *J Biol Chem*. 1994;269(38):23757-23763. doi:10.1016/S0021-9258(17)31580-6
528. Maciej Serda, Becker FG, Cleary M, et al. V-SRC induces expression of hypoxia-inducible factor 1 (HIF-1) and transcription of genes encoding vascular endothelial growth factor and enolase 1: Involvement of HIF-1 in tumor progression. G. Balint, Antala B, Carty C, Mabieme J-MA, Amar IB, Kaplanova A, eds. *Cancer Res*. 1997;57(23):5328-5335. doi:10.2/JQUERY.MIN.JS
529. Kou W, Zhao N, Zhao L, et al. Single-cell characterization revealed hypoxia-induced metabolic reprogramming of gastric cancer. *Heliyon*. 2022;8(11):e11866. doi:10.1016/J.HELIYON.2022.E11866
530. Zhao X, Liu W, Liu B, et al. Exploring the underlying molecular mechanism of liver cancer cells under hypoxia based on RNA sequencing. *BMC Genomic Data*. 2022;23(1):1-11. doi:10.1186/S12863-022-01055-9/FIGURES/7
531. Benita Y, Kikuchi H, Smith AD, Zhang MQ, Chung DC, Xavier RJ. An

integrative genomics approach identifies Hypoxia Inducible Factor-1 (HIF-1)-target genes that form the core response to hypoxia. *Nucleic Acids Res.* 2009;37(14):4587-4602. doi:10.1093/nar/gkp425
532. Holmquist-Mengelbier L, Fredlund E, Löfstedt T, et al. Recruitment of HIF-1alpha and HIF-2alpha to common target genes is differentially regulated in neuroblastoma: HIF-2alpha promotes an aggressive phenotype. *Cancer Cell.* 2006;10(5):413-423. doi:10.1016/J.CCR.2006.08.026
533. Sowter H, Raval R, Moore J, Ratcliffe P, Harris A. Predominant role of hypoxia-inducible transcription factor (Hif)-1alpha versus Hif-2alpha in regulation of the transcriptional response to hypoxia. *Cancer Res.* 2003;63(19).
534. Koh MY, Powis G. Passing the baton: the HIF switch. *Trends Biochem Sci.* 2012;37(9):364-372. doi:10.1016/J.TIBS.2012.06.004
535. Fukuda R, Hirota K, Fan F, Jung Y Do, Ellis LM, Semenza GL. Insulin-like growth factor 1 induces hypoxia-inducible factor 1-mediated vascular endothelial growth factor expression, which is dependent on MAP kinase and phosphatidylinositol 3-kinase signaling in colon cancer cells. *J Biol Chem.* 2002;277(41):38205-38211. doi:10.1074/JBC.M203781200
536. Jubb AM, Pham TQ, Hanby AM, et al. Expression of vascular endothelial growth factor, hypoxia inducible factor 1alpha, and carbonic anhydrase IX in human tumours. *J Clin Pathol.* 2004;57(5):504-512. doi:10.1136/JCP.2003.012963
537. Krishnamachary B, Berg-Dixon S, Kelly B, et al. Regulation of Colon Carcinoma Cell Invasion by Hypoxia-Inducible Factor 1 1. *CANCER Res.* 2003;63:1138-1143. http://aacrjournals.org/cancerres/article-pdf/63/5/1138/2512375/ch0503001138.pdf. Accessed December 18, 2022.
538. Zhao J, Du F, Shen G, Zheng F, Xu B. The role of hypoxia-inducible factor-2 in digestive system cancers. *Cell Death Dis 2015 61.* 2015;6(1):e1600-e1600. doi:10.1038/cddis.2014.565
539. Chen JT, Liu CC, Yu JS, Li HH, Lai MC. Integrated omics profiling identifies hypoxia-regulated genes in HCT116 colon cancer cells. *J Proteomics.* 2018;188:139-151. doi:10.1016/J.JPROT.2018.02.031
540. Farina AR, Cappabianca L, Sebastiano M, Zelli V, Guadagni S, Mackay AR. Hypoxia-induced alternative splicing: The 11th Hallmark of Cancer. *J Exp Clin Cancer Res.* 2020;39(1). doi:10.1186/s13046-020-01616-9
541. Han J, Li J, Ho JC, et al. Hypoxia is a Key Driver of Alternative Splicing in Human Breast Cancer Cells. *Sci Rep.* 2017;7(1). doi:10.1038/s41598-017-04333-0
542. Jimenez M, Arechederra M, Ávila MA, Berasain C. Splicing alterations contributing to cancer hallmarks in the liver: Central role of dedifferentiation and genome instability. *Transl Gastroenterol Hepatol.* 2018;3(October). doi:10.21037/tgh.2018.10.11
543. Sena JA, Wang L, Heasley LE, Hu CJ. Hypoxia regulates alternative splicing of HIF and non-HIF target genes. *Mol Cancer Res.* 2014;12(9). doi:10.1158/1541-7786.MCR-14-0149
544. Williams AL, Khadka V, Tang M, et al. HIF1 mediates a switch in pyruvate kinase isoforms after myocardial infarction. *Physiol Genomics.* 2018;50(7):479-494. doi:10.1152/PHYSIOLGENOMICS.00130.2017
545. Schmidt DR, Patel R, Kirsch DG, Lewis CA, Heiden MG Vander, Locasale JW. Metabolomics in cancer research and emerging applications in clinical oncology. *CA Cancer J Clin.* 2021;71(4):333-358. doi:10.3322/CAAC.21670
546. Armitage EG, Kotze HL, Allwood JW, Dunn WB, Goodacre R, Williams KJ. Metabolic profiling reveals potential metabolic markers associated with Hypoxia Inducible Factor-mediated signalling in hypoxic cancer cells. *Sci Reports 2015 51.*

2015;5(1):1-12. doi:10.1038/srep15649
547. Passarelli MK, Pirkl A, Moellers R, et al. The 3D OrbiSIMS—label-free metabolic imaging with subcellular lateral resolution and high mass-resolving power. *Nat Methods*. 2017;14(12):1175-1183. doi:10.1038/nmeth.4504
548. Arima K, Lau MC, Zhao M, et al. Metabolic Profiling of Formalin-Fixed Paraffin-Embedded Tissues Discriminates Normal Colon from Colorectal Cancer. *Mol Cancer Res*. 2020;18(6):883-890. doi:10.1158/1541-7786.MCR-19-1091
549. Haider S, McIntyre A, van Stiphout RGPM, et al. Genomic alterations underlie a pan-cancer metabolic shift associated with tumour hypoxia. *Genome Biol*. 2016;17(1):1-17. doi:10.1186/S13059-016-0999-8/FIGURES/6
550. Nizamudeen ZA, Timmins P, Allen C, Bates D., Arkill K. Adaptive 3D cryogenic correlative light imaging of native biology using laser free confocal system - 2021 - Wiley Analytical Science. Wiley Analytical Science. https://analyticalscience.wiley.com/do/10.1002/was.00170086. Published 2021. Accessed December 20, 2022.
551. Groebe K, Vaupel P. Evaluation of oxygen diffusion distances in human breast cancer xenografts using tumor-specific in vivo data: role of various mechanisms in the development of tumor hypoxia. *Int J Radiat Oncol Biol Phys*. 1988;15(3):691-697. doi:10.1016/0360-3016(88)90313-6
552. Corbet C, Feron O. Tumour acidosis: from the passenger to the driver's seat. *Nat Rev Cancer 2017 1710*. 2017;17(10):577-593. doi:10.1038/nrc.2017.77
553. Gao J, Guo Z, Cheng J, et al. Differential metabolic responses in breast cancer cell lines to acidosis and lactic acidosis revealed by stable isotope assisted metabolomics. *Sci Rep*. 2020;10(1). doi:10.1038/S41598-020-78955-2
554. Shay JES, Imtiyaz HZ, Sivanand S, et al. Inhibition of hypoxia-inducible factors limits tumor progression in a mouse model of colorectal cancer. *Carcinogenesis*. 2014;35(5):1067. doi:10.1093/CARCIN/BGU004
555. Robles-Flores M, Saint-Martin A, Martínez-Ríos J, et al. Functional Interaction of Hypoxia-Inducible Factor 2-Alpha and Autophagy Mediates Drug Resistance in Colon Cancer Cells. *Cancers (Basel)*. 2019;11(6). doi:10.3390/CANCERS11060755
556. Santoyo-Ramos P, Likhatcheva M, García-Zepeda EA, Cristina Castañeda-Patlan M, Robles-Flores M. Hypoxia-Inducible Factors Modulate the Stemness and Malignancy of Colon Cancer Cells by Playing Opposite Roles in Canonical Wnt Signaling. *PLoS One*. 2014;9(11):112580. doi:10.1371/JOURNAL.PONE.0112580
557. Baba Y, Nosho K, Shima K, et al. HIF1A Overexpression Is Associated with Poor Prognosis in a Cohort of 731 Colorectal Cancers. *Am J Pathol*. 2010;176(5):2292. doi:10.2353/AJPATH.2010.090972
558. Han S, Huang T, Li W, et al. Association Between Hypoxia-Inducible Factor-2α (HIF-2α) Expression and Colorectal Cancer and Its Prognostic Role: a Systematic Analysis. *Cell Physiol Biochem*. 2018;48(2):516-527. doi:10.1159/000491806
559. Guan Z, Ding C, Du Y, et al. HAF drives the switch of HIF-1α to HIF-2α by activating the NF-κB pathway, leading to malignant behavior of T24 bladder cancer cells. *Int J Oncol*. 2014;44(2):393-402. doi:10.3892/IJO.2013.2210/HTML
560. Holmquist-Mengelbier L, Fredlund E, Löfstedt T, et al. Recruitment of HIF-1α and HIF-2α to common target genes is differentially regulated in neuroblastoma: HIF-2α promotes an aggressive phenotype. *Cancer Cell*. 2006;10(5):413-423. doi:10.1016/J.CCR.2006.08.026
561. Cowman SJ, Koh MY. Revisiting the HIF switch in the tumor and its immune microenvironment. *Trends in Cancer*. 2022;8(1):28-42. doi:10.1016/J.TRECAN.2021.10.004
562. Ginouvès A, Ilc K, Macías N, Pouysségur J, Berra E. PHDs overactivation during

chronic hypoxia "desensitizes" HIFα and protects cells from necrosis. *Proc Natl Acad Sci U S A*. 2008;105(12):4745-4750. doi:10.1073/PNAS.0705680105/ASSET/8AC7EBFB-63A8-4206-862B-FBC1012D1B51/ASSETS/GRAPHIC/ZPQ0110898810007.JPEG
563. Berra E, Benizri E, Ginouvès A, Volmat V, Roux D, Pouysségur J. HIF prolyl-hydroxylase 2 is the key oxygen sensor setting low steady-state levels of HIF-1alpha in normoxia. *EMBO J*. 2003;22(16):4082-4090. doi:10.1093/EMBOJ/CDG392
564. Uchida T, Rossignol F, Matthay MA, et al. Prolonged hypoxia differentially regulates hypoxia-inducible factor (HIF)-1alpha and HIF-2alpha expression in lung epithelial cells: implication of natural antisense HIF-1alpha. *J Biol Chem*. 2004;279(15):14871-14878. doi:10.1074/JBC.M400461200
565. Lin J, Shi Z, Yu Z, He Z. LncRNA HIF1A-AS2 positively affects the progression and EMT formation of colorectal cancer through regulating miR-129-5p and DNMT3A. *Biomed Pharmacother*. 2018;98:433-439. doi:10.1016/J.BIOPHA.2017.12.058
566. Chao MW, Wang LT, Lai CY, et al. eIF4E binding protein 1 expression is associated with clinical survival outcomes in colorectal cancer. *Oncotarget*. 2015;6(27):24092. doi:10.18632/ONCOTARGET.4483
567. Xu T, Zong Y, Peng L, et al. Overexpression of eIF4E in colorectal cancer patients is associated with liver metastasis. *Onco Targets Ther*. 2016;9:815. doi:10.2147/OTT.S98330
568. Mole DR, Blancher C, Copley RR, et al. Genome-wide association of hypoxia-inducible factor (HIF)-1alpha and HIF-2alpha DNA binding with expression profiling of hypoxia-inducible transcripts. *J Biol Chem*. 2009;284(25):16767-16775. doi:10.1074/JBC.M901790200
569. Rankin EB, Rha J, Selak MA, et al. Hypoxia-Inducible Factor 2 Regulates Hepatic Lipid Metabolism. *Mol Cell Biol*. 2009;29(16):4527. doi:10.1128/MCB.00200-09
570. Gibbons GF. The role of cytochrome P450 in the regulation of cholesterol biosynthesis. *Lipids*. 2002;37(12):1163-1170. doi:10.1007/S11745-002-1016-X
571. Jiang T, Xu X, Qiao M, et al. Comprehensive evaluation of NT5E/CD73 expression and its prognostic significance in distinct types of cancers. *BMC Cancer*. 2018;18(1). doi:10.1186/S12885-018-4073-7
572. Guo C, Ni X, Zhu P, Li W, Zhu X, Sun K. Induction of progesterone receptor A form attenuates the induction of cytosolic phospholipase A2α expression by cortisol in human amnion fibroblasts. *Reproduction*. 2010;139(5):915-922. doi:10.1530/REP-10-0007
573. He J, Zhang F, Tay LWR, et al. Lipin-1 regulation of phospholipid synthesis maintains endoplasmic reticulum homeostasis and is critical for triple-negative breast cancer cell survival. *FASEB J*. 2017;31(7):2893. doi:10.1096/FJ.201601353R
574. Ha NT, Lee CH. Roles of Farnesyl-Diphosphate Farnesyltransferase 1 in Tumour and Tumour Microenvironments. *Cells*. 2020;9(11):1-33. doi:10.3390/CELLS9112352
575. Berthelot K, Estevez Y, Deffieux A, Peruch F. Isopentenyl diphosphate isomerase: A checkpoint to isoprenoid biosynthesis. *Biochimie*. 2012;94(8):1621-1634. doi:10.1016/J.BIOCHI.2012.03.021
576. Vock C, Döring F, Nitz I. Transcriptional regulation of HMG-CoA synthase and HMG-CoA reductase genes by human ACBP. *Cell Physiol Biochem*. 2008;22(5-6):515-524. doi:10.1159/000185525
577. Chapat C, Chettab K, Simonet P, et al. Alternative splicing of CNOT7 diversifies

CCR4–NOT functions. *Nucleic Acids Res*. 2017;45(14):8508. doi:10.1093/NAR/GKX506
578. Coldwell MJ, Sack U, Cowan JL, et al. Multiple isoforms of the translation initiation factor eIF4GII are generated via use of alternative promoters, splice sites and a non-canonical initiation codon. *Biochem J*. 2012;448(1). doi:10.1042/BJ20111765
579. Climente-González H, Porta-Pardo E, Godzik A, Eyras E. The Functional Impact of Alternative Splicing in Cancer. *Cell Rep*. 2017;20(9). doi:10.1016/j.celrep.2017.08.012
580. Wu D, Matsushita K, Matsubara H, Nomura F, Tomonaga T. An alternative splicing isoform of eukaryotic initiation factor 4H promotes tumorigenesis *in vivo* and is a potential therapeutic target for human cancer. *Int J Cancer*. 2011;128(5):1018-1030. doi:10.1002/ijc.25419
581. Liigand P, Kaupmees K, Haav K, et al. Think Negative: Finding the Best Electrospray Ionization/MS Mode for Your Analyte. *Anal Chem*. 2017;89(11):5665-5668. doi:10.1021/ACS.ANALCHEM.7B00096/ASSET/IMAGES/LARGE/AC-2017-000969_0003.JPEG
582. Murphy RC, Axelsen PH. Mass Spectrometric Analysis of Long-Chain Lipids. *Mass Spectrom Rev*. 2011;30(4):579. doi:10.1002/MAS.20284
583. Han X, Gross RW. Shotgun lipidomics: electrospray ionization mass spectrometric analysis and quantitation of cellular lipidomes directly from crude extracts of biological samples. *Mass Spectrom Rev*. 2005;24(3):367-412. doi:10.1002/MAS.20023
584. Park JH, Lee SY, Sauer M, et al. Liquid Chromatography/Tandem Mass Spectrometry of Glycolytic Intermediates: Deconvolution of Coeluting Structural Isomers Based on Unique Product Ion Ratios. *Anal Chem*. 2009;81(10):4021-4026. doi:10.1021/AC9004698
585. Resnik N, Romih R, Kreft ME, Hudoklin S. Freeze-Fracture Electron Microscopy for Extracellular Vesicle Analysis. *J Vis Exp*. 2022;2022(187). doi:10.3791/63550
586. Rossi MR, Masters JRW, Park S, et al. The immortalized UROtsa cell line as a potential cell culture model of human urothelium. *Environ Health Perspect*. 2001;109(8):801-808. doi:10.1289/EHP.01109801
587. Sun RC, Denko NC. Hypoxic regulation of glutamine metabolism through HIF1 and SIAH2 supports lipid synthesis that is necessary for tumor growth. *Cell Metab*. 2014;19(2). doi:10.1016/j.cmet.2013.11.022
588. Golinska M, Troy H, Chung YL, et al. Adaptation to HIF-1 deficiency by upregulation of the AMP/ATP ratio and phosphofructokinase activation in hepatomas. *BMC Cancer*. 2011;11(1):1-13. doi:10.1186/1471-2407-11-198/FIGURES/5
589. Yan Y Bin. Creatine kinase in cell cycle regulation and cancer. *Amino Acids*. 2016;48(8):1775-1784. doi:10.1007/S00726-016-2217-0
590. Zheng L, Kelly CJ, Colgan SP. Physiologic hypoxia and oxygen homeostasis in the healthy intestine. A Review in the Theme: Cellular Responses to Hypoxia. *Am J Physiol Cell Physiol*. 2015;309(6):C350-C360. doi:10.1152/AJPCELL.00191.2015
591. Loo JM, Scherl A, Nguyen A, et al. Extracellular metabolic energetics can promote cancer progression. *Cell*. 2015;160(3):393-406. doi:10.1016/J.CELL.2014.12.018
592. Pallottini V, Guantario B, Martini C, et al. Regulation of HMG-CoA reductase expression by hypoxia. *J Cell Biochem*. 2008;104(3):701-709. doi:10.1002/JCB.21757

593. Cheng H, Cui C, Lu S, et al. Identification and analysis of hub genes and networks related to hypoxia preconditioning in mice (No 035215). *Oncotarget*. 2018;9(15):11889. doi:10.18632/ONCOTARGET.23555
594. Tritsch D, Hemmerlin A, Bach TJ, Rohmer M. Plant isoprenoid biosynthesis via the MEP pathway: in vivo IPP/DMAPP ratio produced by (E)-4-hydroxy-3-methylbut-2-enyl diphosphate reductase in tobacco BY-2 cell cultures. *FEBS Lett*. 2010;584(1):129-134. doi:10.1016/J.FEBSLET.2009.11.010
595. Miranda-Galvis M, Teng Y. Targeting Hypoxia-Driven Metabolic Reprogramming to Constrain Tumor Progression and Metastasis. *Int J Mol Sci*. 2020;21(15):1-17. doi:10.3390/IJMS21155487
596. Gillet JP, Varma S, Gottesman MM. The clinical relevance of cancer cell lines. *J Natl Cancer Inst*. 2013;105(7). doi:10.1093/jnci/djt007
597. Gillet JP, Calcagno AM, Varma S, et al. Redefining the relevance of established cancer cell lines to the study of mechanisms of clinical anti-cancer drug resistance. *Proc Natl Acad Sci U S A*. 2011;108(46):18708-18713. doi:10.1073/PNAS.1111840108/-/DCSUPPLEMENTAL
598. Rolver MG, Elingaard-Larsen LO, Pedersen SF. Assessing cell viability and death in 3d spheroid cultures of cancer cells. *J Vis Exp*. 2019;2019(148). doi:10.3791/59714
599. Zanoni M, Piccinini F, Arienti C, et al. 3D tumor spheroid models for in vitro therapeutic screening: A systematic approach to enhance the biological relevance of data obtained. *Sci Rep*. 2016;6. doi:10.1038/srep19103
600. Sobhanifar S, Aquino-Parsons C, Stanbridge EJ, Olive P. Reduced expression of hypoxia-inducible factor-1alpha in perinecrotic regions of solid tumors. *Cancer Res*. 2005;65(16):7259-7266. doi:10.1158/0008-5472.CAN-04-4480
601. Ahmed MAM, Nagelkerke A. Current developments in modelling the tumour microenvironment in vitro: Incorporation of biochemical and physical gradients. *Organs-on-a-Chip*. 2021;3:100012. doi:10.1016/J.OOC.2021.100012
602. Zhao X, Liu Z, Yu L, et al. Global gene expression profiling confirms the molecular fidelity of primary tumor-based orthotopic xenograft mouse models of medulloblastoma. *Neuro Oncol*. 2012;14(5):574-583. doi:10.1093/NEUONC/NOS061
603. Reyal F, Guyader C, Decraene C, et al. Molecular profiling of patient-derived breast cancer xenografts. *Breast Cancer Res*. 2012;14(1). doi:10.1186/BCR3095
604. Shi R, Tang YQ, Miao H. Metabolism in tumor microenvironment: Implications for cancer immunotherapy. *MedComm*. 2020;1(1). doi:10.1002/mco2.6
605. Chen Y, Ni J, Gao Y, et al. Integrated proteomics and metabolomics reveals the comprehensive characterization of antitumor mechanism underlying Shikonin on colon cancer patient-derived xenograft model. *Sci Rep*. 2020;10(1). doi:10.1038/s41598-020-71116-5
606. Ni J, Chen Y, Li N, Sun D, Ju H, Chen Z. Combination of GC-MS based metabolomics analysis with mouse xenograft models reveals a panel of dysregulated circulating metabolites and potential therapeutic targets for colorectal cancer. *Transl Cancer Res*. 2021;10(4). doi:10.21037/tcr-20-3406
607. Cabrales LEB, Nava JJG, Aguilera AR, et al. Modified Gompertz equation for electrotherapy murine tumor growth kinetics: predictions and new hypotheses. *BMC Cancer*. 2010;10:589. doi:10.1186/1471-2407-10-589
608. González MM, Joa JAG, Cabrales LEB, et al. Is cancer a pure growth curve or does it follow a kinetics of dynamical structural transformation? *BMC Cancer*. 2017;17(1). doi:10.1186/S12885-017-3159-Y
609. Newell CL, Vorng JL, MacRae JI, Gilmore IS, Gould AP. Cryogenic OrbiSIMS

Localizes Semi-Volatile Molecules in Biological Tissues. *Angew Chemie Int Ed*. 2020;59(41):18194-18200. doi:10.1002/ANIE.202006881
610. Wessman P, Edwards K, Mahlin D. Structural effects caused by spray- and freeze-drying of liposomes and bilayer disks. *J Pharm Sci*. 2010;99(4):2032-2048. doi:10.1002/JPS.21972
611. Li T, Yin Y, Zhou Z, et al. Ion mobility-based sterolomics reveals spatially and temporally distinctive sterol lipids in the mouse brain. *Nat Commun 2021 121*. 2021;12(1):1-13. doi:10.1038/s41467-021-24672-x
612. Murphy RC. Challenges in Mass Spectrometry-based Lipidomics of Neutral Lipids. *Trends Analyt Chem*. 2018;107:91. doi:10.1016/J.TRAC.2018.07.023
613. Randolph CE, Blanksby SJ, McLuckey SA. Enhancing detection and characterization of lipids using charge manipulation in electrospray ionization-tandem mass spectrometry. *Chem Phys Lipids*. 2020;232:104970. doi:10.1016/J.CHEMPHYSLIP.2020.104970
614. Nygren H, Eriksson C, Malmberg P, et al. A cell preparation method allowing subcellular localization of cholesterol and phosphocholine with imaging TOF-SIMS. *Colloids Surfaces B Biointerfaces*. 2003;30(1-2). doi:10.1016/S0927-7765(03)00066-3
615. Bressenot A, Marchal S, Bezdetnaya L, Garrier J, Guillemin F, Plénat F. Assessment of Apoptosis by Immunohistochemistry to Active Caspase-3, Active Caspase-7, or Cleaved PARP in Monolayer Cells and Spheroid and Subcutaneous Xenografts of Human Carcinoma. *J Histochem Cytochem*. 2009;57(4):289. doi:10.1369/JHC.2008.952044
616. Han SJ, Kwon S, Kim KS. Challenges of applying multicellular tumor spheroids in preclinical phase. *Cancer Cell Int 2021 211*. 2021;21(1):1-19. doi:10.1186/S12935-021-01853-8
617. Dahl R, Staehelin LA. High-pressure freezing for the preservation of biological structure: theory and practice. *J Electron Microsc Tech*. 1989;13(3):165-174. doi:10.1002/JEMT.1060130305
618. Meryman HT. Cryopreservation of living cells: Principles and practice. *Transfusion*. 2007;47(5). doi:10.1111/j.1537-2995.2007.01212.x
619. Vaupel P, Mayer A, Höckel M. Tumor Hypoxia and Malignant Progression. *Methods Enzymol*. 2004;381. doi:10.1016/S0076-6879(04)81023-1
620. Aguilera KY, Brekken RA. Hypoxia Studies with Pimonidazole in vivo. *Bio-protocol*. 2014;4(19). doi:10.21769/BIOPROTOC.1254
621. Fenton B, Paoni S, Lee J, Koch C, Lord E. Quantification of tumour vasculature and hypoxia by immunohistochemical staining and HbO2 saturation measurements. *Br J Cancer 1999 793*. 1999;79(3):464-471. doi:10.1038/sj.bjc.6690072